REPORT NO.
UCB/EERC-79/22
AUGUST 1979

EARTHQUAKE ENGINEERING RESEARCH CENTER

EFFECTS OF GENERALIZED LOADINGS ON BOND OF REINFORCING BARS EMBEDDED IN CONFINED CONCRETE BLOCKS

by

S. VIWATHANATEPA
E. P. POPOV
V. V. BERTERO

Report to National Science Foundation

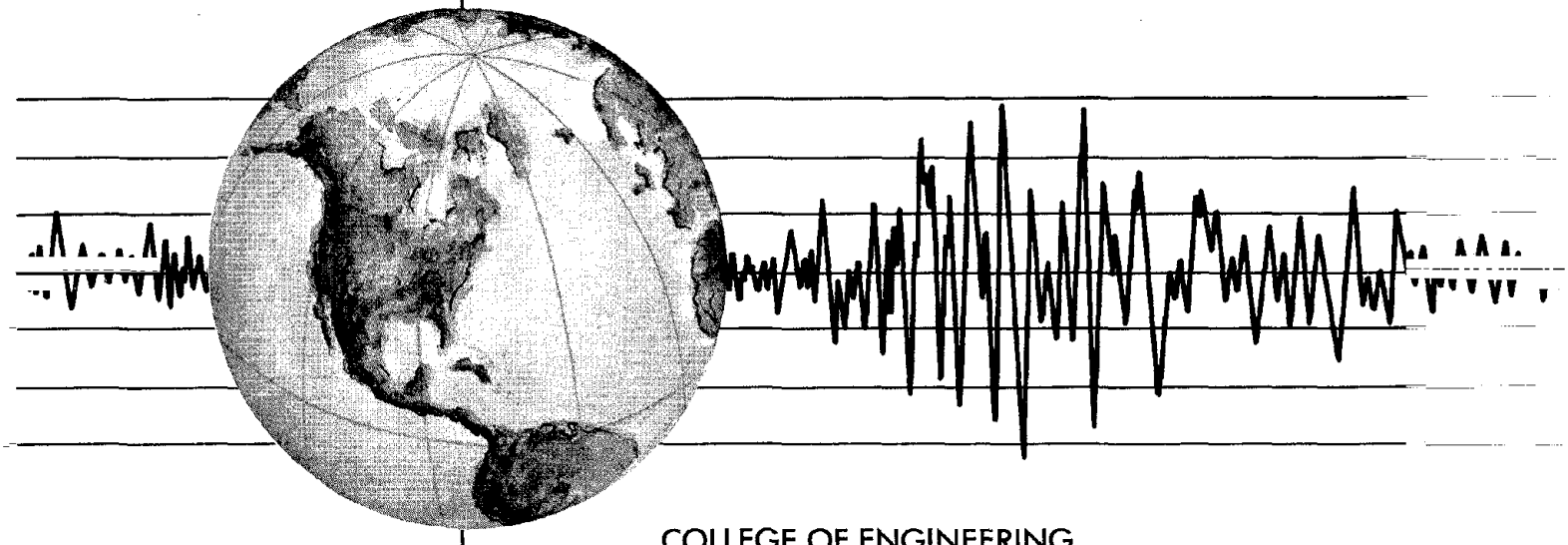

COLLEGE OF ENGINEERING

UNIVERSITY OF CALIFORNIA · Berkeley, California

50272-101

REPORT DOCUMENTATION PAGE	1. REPORT NO. NSF/RA-790526	2.	3. Recipient's Accession No. PB81 124018
4. Title and Subtitle: Effects of Generalized Loadings on Bond of Reinforcing Bars Embedded in Confined Concrete Blocks			5. Report Date: August 1979 6.
7. Author(s): S. Viwathanatepa, E.P. Popov and V.V. Bertero			8. Performing Organization Rept. No. UCB/EERC-79/22
9. Performing Organization Name and Address: Earthquake Engineering Research Center, University of California, Richmond Field Station, 47th and Hoffman Blvd., Richmond, California 94804			10. Project/Task/Work Unit No. 11. Contract(C) or Grant(G) No. (C) (G) ENV-76-04263
12. Sponsoring Organization Name and Address: National Science Foundation, 1800 G Street, N.W., Washington, D. C. 20550			13. Type of Report & Period Covered 14.

15. Supplementary Notes

16. Abstract (Limit: 200 words)

Under reversing lateral loads, such as occur during a major earthquake, cracks can form at column faces of continuous beams framing into joints of moment-resisting frames. Reinforcement may be strained well into the inelastic range and cracks will tend to remain open. During cyclic loading, continuous longitudinal beam bars can be simultaneously pushed and pulled from opposite sides of a column, creating a severe demand on anchorage.

The performance of anchorage under conditions similar to those described above was tested experimentally. Seventeen specimens of single bars embedded in well-confined column stubs were tested under push-pull or only pull loadings. Monotonic as well as cyclic loadings were prescribed. Bar sizes #6, #8, and #10 were tested. The tendency of bond to degrade under cyclic loading was observed. Results obtained from these tests provide essential data from which a mathematical model for predicting the bond behavior that leads to the pull out or push in of a rebar is formulated.

Finite element techniques are employed to predict the cracking behavior of the surrounding concrete since this behavior could not be deduced from the experimental data. The superior performance of a bar subjected to a push load is noted. The discrepancy between the predicted and experimental results is evaluated, and the limitations of the material models used in the present analysis are described.

A model for the hysteretic behavior of a bond element when subjected to generalized loading histories is established from the experimental results. The reliability of the model for monotonic and full reversal loading histories is encouraging.

18. Availability Statement: Release Unlimited	19. Security Class (This Report)	21. No. of Pages: 320
	20. Security Class (This Page)	22. Price

(ANSI 739.18) See Instructions on Reverse

OPTIONAL FORM 272 (4-77) (Formerly NTIS-35) Department of Commerce

EFFECTS OF GENERALIZED LOADINGS ON BOND OF REINFORCING BARS EMBEDDED IN CONFINED CONCRETE BLOCKS

by

S. Viwathanatepa
Research Assistant

E. P. Popov
Professor of Civil Engineering

and

V. V. Bertero
Professor of Civil Engineering

Report to

National Science Foundation

Report No. UCB/EERC-79/22
Earthquake Engineering Research Center
College of Engineering
University of California
Berkeley, California

August 1979

ABSTRACT

Under reversing lateral loads, such as occur during a major earthquake, cracks can form at column faces of continuous beams framing into joints of moment-resisting frames. Reinforcement may be strained well into the inelastic range and cracks will tend to remain open. During cyclic loading, continuous longitudinal beam bars can be simultaneously pushed and pulled from opposite sides of a column, creating a severe demand on anchorage.

The performance of anchorage under conditions similar to those described above was tested experimentally. Seventeen specimens of single bars embedded in well-confined column stubs were tested under push-pull or only pull loadings. Monotonic as well as cyclic loadings were prescribed. Bar sizes #6, #8, and #10 were tested. The tendency of bond to degrade under cyclic loading was observed. Results obtained from these tests provide essential data from which a mathematical model for predicting the bond behavior that leads to the pull out or push in of a rebar is formulated.

Finite element techniques are employed to predict the cracking behavior of the surrounding concrete since this behavior could not be deduced from the experimental data. The superior performance of a bar subjected to a push load is noted. The discrepancy between the predicted and experimental results is evaluated, and the limitations of the material models used in the present analysis are described.

A model for the hysteretic behavior of a bond element when subjected to generalized loading histories is established from the experimental results. The reliability of the model for monotonic and full reversal loading histories is encouraging.

ACKNOWLEDGMENTS

The research reported here was carried out under National Science Foundation Grant No. ENV-76-04263 as part of an investigation on the deterioration of bond in reinforced concrete under generalized loading carried out at the University of California, Berkeley. The present report is based on the doctoral dissertation of S. Viwathanatepa, completed under the direction of Professors E. P. Popov and V. V. Bertero of the Department of Civil Engineering.

The authors also wish to express their appreciation of the work of B. Lotz among the many who help with the experimental program, Drs. Soleimani and Wang who gave much good advice and assisted during various phases of the investigation, and A. Cowell whose editorial assistance during the writing of the work was invaluable.

TABLE OF CONTENTS

Page

Page

LIST OF NOTATION

A_c	area of confined core of a column section
A_g	gross area of section
A_s	area of embedded reinforcing steel
A'_s	area of bottom reinforcing steel
A_{sh}	area of transverse reinforcing steel for confinement
A_v	area of transverse reinforcing steel for shear
C	compression force
d	effective depth (distance from top side to centroid of bottom steel)
d'	distance from bottom side to centroid of bottom steel
D	diameter of reinforcing bar
D_{avg}	average diameter of reinforcing bar
E_c	modulus of elasticity of concrete
E_s	modulus of elasticity of steel
E_{sh}	tangential stiffness of stress strain diagram of steel at onset of strain hardening (in tension)
E_{shc}	tangential stiffness of stress strain diagram of steel at onset of strain hardening (in compression)
f'_c	concrete compressive strength

f_r	modulus of rupture
f_{sp}	tensile strength of concrete from splitting tension test
f_{s1}	stress on embedded reinforcing bar at South face (see Chapter 4)
f_{s2}	stress on embedded reinforcing bar at North face (see Chapter 4)
f_y	yield strength of steel
f_s	stress in embedded reinforcing bar
G	shear modulus of concrete
G*	shear modulus of cracked concrete
h	height of steel lug
k_1	stiffness of hysteretic curve (see Chapter 7)
ℓ_d	development length of anchored bar
ℓ_e	length of shear element
L	embedment length of rebar
L_h	unsupported length of transversed reinforcement
LP	Load Point
M	bending moment
M_u	ultimate moment of a R/C section
N_u	normal force applied on a concrete block section
p	top steel reinforcement ratio, A_s/bd
p'	bottom steel reinforcement ratio, A'_s/bd
P_b	dimensionless constant related to accumulative shear deformations
P_c	dimensionless constant related to accumulative shear deformations
P'_b	dimensionless constant related to accumulative shear deformations
P'_c	dimensionless constant related to accumulative shear deformations
r	polar coordinate
R	force in spring elements
R/C	reinforced concrete

S	spacing of stirrup
t	thickness of concrete soft boundary layer
u_r	displacement component in r direction
u_z	displacement component in z direction
v_c	shear stress capacity contributed by concrete
V_c	$v_c bd$
V_u	ultimate design shear force
w	unit weight of R/C concrete
x	distance along a bar
z	polar axis for axisymmetric element
α_1	a parameter to establish cyclic hysteretic rules
β_1	a parameter to establish cyclic hysteretic rules
γ	shear deformation of soft layer element (see Chapter 7)
τ	shear stress acting on the soft layer element
δ	displacement in general
δ_1	displacement of embedded bar section of South face
δ_2	displacement of embedded bar section of North face
δ_x	displacement of section distance x from South face
ε_c	concrete strain
ε'_c	concrete strain at concrete stress of f'_c
ε_s	steel strain
ε_{sht}	steel strain at point of strain hardening (in monotonic tension)
ε_{shc}	steel strain at point of strain hardening (in monotonic compression)
ε_{smax}	steel strain at maximum tensile stress

θ_{FE} fixed-end rotation of the beam

ν Poisson's ratio

Σ_o perimeter of reinforcing bars

σ_s stress in longitudinal reinforcement (see Appendix A)

u bond stress = $\frac{\Delta f_s A_s}{\Sigma_o \Delta x}$

1. INTRODUCTION

1.1 GENERAL

The ACI-ASCE Committee 352 recognized and clearly pointed out the need for research on deterioration of the anchorage of continuous beam bars passing through interior joints of moment-resisting frames under racking loads such as occur during an earthquake [1]. The problem of deterioration is not of importance in the design of interior joints for gravity loads, nor in the design of these joints against the effects of monotonically increasing lateral loads. In the latter case, if the longitudinal beam bars go into tension, they are anchored, not only in the column but also in the compression zone of the adjoining continuous beam beyond the column. The same approach cannot be applied in the design for repeated and reversed cyclic loadings such as might occur during an earthquake. Furthermore, in all the above cases, there is the problem of evaluating the effect of the deformation of the bars along their embedment length in the joint on the overall behavior of the frame.

Several experiments with subassemblages of ductile R/C moment-resisting frames clearly demonstrated that bond deterioration can take place at the interior beam-column joints [2,3]. This bond deterioration can significantly reduce the joint stiffness which can result in excessive structural and nonstructural damage due to excessive deflections, and in extreme cases, the stability of the whole frame can be jeopardized. At the present time, no guidelines nor provisions are given in the current seismic codes to handle this problem.

The specimens used in the experiments referred to above were one-half scale models of an interior joint subassemblage at the third floor level of a 20-story building. The symmetric cruciform specimens had vertical columns in the middle of a continuous beam. The 9 by 16 in. beams were reinforced with four #6 bars at the top and three #5 bars at the bottom. These half-span beams framed into 17 in. square columns. The longitudinal beam reinforcement was continuous and passed through the column. Schematic diagrams of a specimen terminating with hinges at mid-span of beams and at mid-height of columns are shown in Fig. 1.1.

In addition to the vertically applied force P, the specimens were subjected to pseudo-static cyclic lateral force H, the application of which simulated the effect of earthquake loading. Early significant bond deterioration leading eventually to bond failure of the main longitudinal beam bars within the column occurred. The reason for this failure under severe cyclic loading can be understood by examining a specimen's hysteretic behavior, Fig. 1.2(a) [2]. First, as H increases from O to B, cracks develop on both sides of the column, Fig. 1.2(b). After unloading and applying H in the opposite direction (B to D on the hysteretic loop), diametrically opposed cracks develop in either side of the column, Fig. 1.2(c). If the load reversals applied in both directions are sufficiently severe to cause permanent strains in beam bars, cracks through the entire beam cross section are formed as shown in Fig. 1.2(d). The bars that pass through the column are simultaneously pulled and pushed from opposite sides under cyclic loading. The critical condition develops when a bar is subjected to full reversals of tensile and compressive forces of equal magnitudes simultaneously developing high bond stresses along the bar embedment length within the column.

To simulate the simultaneous push-pull condition of a beam bar in an interior joint, excluding the complexities of the dowel action which is generated by the presence of shear at the column faces and an interaction from the adjacent bars, a simplified model was devised. Single bars were cast into well-confined concrete blocks (Fig. 1.3). The obtained experimental results provide guidance on the two principal areas of concern. First, the data generated enable one to determine the slippage of the bars and consequently the amount of rotation at the fixed-end of beams as is illustrated in Fig. 1.4. From estimates of the amounts of bar pull-out, and the corresponding ones for bar push-in, the fixed-end rotation of a beam framing into a column can be determined. This rotation is usually neglected in the analysis of moment-resisting frames, but may be important. Second, the all important problems of the maximum attainable anchorage within an interior joint can be appraised. The current ACI provisions are silent on this phenomenon, which can contribute to a large loss in joint stiffness, thereby contributing to possible structural and non-structural damage as well as frame instability. Since basketing of the concrete at the column and the beams' critical regions has now been made more stringent [4,5], bond deterioration of main beam bars along the column joint may become one of the crucial problems in the seismic design of moment-resisting R/C frames.

1.2 LITERATURE REVIEW OF STUDY IN BOND DETERIORATION

The nature of deterioration in bond and the problems related to rebar anchorage have received some attention in the past. Some of the earlier work is summarized in the ACI Committee Report [6], "Bond Stress--The State of the Art." In this document, the nature of bond failure is discussed and the influence of splitting on bond is brought out. However, in terms of the needs for seismic-resistant design, this report does not go far enough. Nothing is said regarding the anchorage and bond behavior under severe repeated and reversed loading conditions. Unfortunately, relatively little has been done in this area since. A brief review of the relevant work will be attempted here.

In general, there are two types of problems involved in the interaction of steel and concrete. First, there is the problem of the interaction between the reinforcing steel and concrete in flexural situations where, due to the flexural bending, cracks perpendicular to the bars can form rather readily. This occurs primarily in slabs, beams and beam-columns. The second problem is one of anchorage, and in the analysis of framed structures where under extreme conditions deflection ductilities of 6 to 8 may be expected, even a partial pull-out of the bars is very important. Takeda, Sozen and Nielsen [7] were among the first to note that pull-out of main beam bars from their anchorage causes fixed-end rotations which significantly contribute to the deflection of a frame. In one of their examples, this amounted to over 50 percent of the deflections caused by cracked beam sections. Ismail and Jirsa [8], and Ma, Bertero, and Popov [9] have found this effect also to be very important. The pressing necessity for including such effects in the analysis seems clear.

1.2.1 Steel-Concrete Interaction in Flexural Members

Two schemes have been used to study the transfer of forces from steel to concrete, and vice versa, around stressed tension bars such as occurs in flexure. In both schemes a bar is encased concentrically in a long rectangular prism, or a cylinder, and axial tensile forces are applied to the exposed ends of the bar. In one scheme only the variation in the steel strain is obtained. In the other scheme, ink is injected into tension specimens to determine the cracking pattern. After splitting the specimens longitudinally, the internal crack pattern was studied [10]. The deformation of concrete around a reinforcing steel bar after formation of internal cracks is illustrated in Fig. 1.5. The schematic diagram provides insight into the internal mechanism for monotonic application of force on the bar. One can readily imagine a mirror image of similar cracks that would form if a complete reversal of load were possible, such as would occur in an anchorage under cyclic loading. A large number of similar experiments with monotonically applied end forces was performed by Houde [11], who formulated some bond-slip relations. A refined study with internal instrumentation in the concentric bars for monotonic loading is reported by Nilson [12], who urges further work in this area.

Valuable as the above studies are, they are not sufficient for resolving bond-slip problems under severe cyclic loading. Using the same experimental set-up as described above, Bresler and Bertero [13] studied the bond problem under repeating loading. In this simulation, it is only possible to apply a tensile force and then release it. However, this may be repeated a number of times with a different level of axial

force intensity. Based on these experiments, they reached a number of important conclusions of direct utility in seismic-resistant design. Among these, they noted the loading history dependence of bond deterioration and the great sensitivity to the maximum peak stress level on subsequent behavior.

A more realistic experimental set-up for studying deterioration of bond in flexural members due to cyclic load reversal was used by Zagajeski [14]. In his arrangement a 12 ft. simple span was loaded with reversing third point loads. Therefore, the middle third of the beam was subjected to pure cyclic bending, and it is this region that was studied with regard to the behavior of reinforcing bars in bond. The bars in this region were heavily instrumented, and crack initiators were placed to correlate with the internal gages.

The results of this study led to some significant conclusions. The experiments corroborated the earlier findings that bond effectiveness is sensitive to previous load history. The magnitude of the previous stress level and the sense in which it was acting were found to be important.

1.2.2 Steel-Concrete Interaction in Anchorage Regions

The anchorage of reinforcing steel in concrete is basic to the whole idea of reinforced concrete. Therefore, numerous tests have been conducted on anchorage. Primarily, however these were to determine the required length of embedment for developing the full capacity of a reinforcing bar. The amount of pull-out from the anchoring block as a function of the applied force did not receive sufficient attention.

For gravity load design, provided the capacity of the bar is developed, the problem of excessive slippage of a main rebar from an anchored media rarely occurs. However, in seismic resistant design, at extreme loads, the fixed end rotation caused by the pull-out of the bars may greatly soften the structural system. Therefore, unless this behavior is thoroughly understood and quantified, predictions of structural behavior may be in gross error.

The conventional anchorage bond test consists of a concrete block from which an embedded bar is pulled. In some arrangements the block is held in position by a concentric ring support; in others, the block supporting conditions attempt to simulate a part of a beam or a joint, requiring a clamping device or two or more concentrated supports. Reports on a number of tests with monotonically applied, as well as cyclic, loading are available and are summarized in [6].

Test data on development length and splices for monotonic loadings has been recently re-evaluated by Orangun, Jirsa, and Breen [15]. In their paper an equation is derived for calculating the development and splice length for deformed bars. Emphasis is placed on the amount of cover and spacing of the bars. A more limited aspect of the effect of rib spacings and their heights on bond characteristics of a bar has been reported by Lutz [16].

An extensive study of hooked bar anchorages for monotonic loading is reported in two papers from the University of Texas by Minor and Jirsa [17], and by Marques and Jirsa [18]. In the first paper, primary interest centers on the measurements of slip between the bar and the concrete at several points along the anchored bar. This study shows

that the pull-through of hooked bar anchorages designed according to ACI 1971 is about the same as that of straight bars of the same length, and that 90° hooks are preferable to those of 180°. In the second paper, specimens with hooked bars simulating typical exterior beam-column joints were studied. The degree of concrete confinement at the joint was the principal variable investigated.

Some pull-out tests on #8 bars having embedment lengths of 15 in. and 31 in. were carried out by Houde [11]. The specimens were used to study the combination of pull-out and dowel action. Some empirical bond stress-slip relationships are suggested. Before their general acceptance, a wider range of supporting test data is necessary.

Experimental results on cyclic bond behavior began to appear in the 70's. Such work is of direct importance in seismic design. Some studies of this kind have been conducted in Japan; in the U.S.A. this work is largely centralized at the Universities of Texas, Washington, and California. One of the better known studies in Japan is that of Morita and Kaku [19,20]. In their summary paper [19], various loads histories of bond deterioration of 19 mm bars in 48 mm embedments, and of 25 mm bars in 66 mm, are presented, and an empirical cyclic bond-slip law is proposed. This work is a good beginning for a rational evaluation of cyclic bond behavior. Their more recent paper [20] discusses cyclic splitting bond failure of large 51 mm (2 in.) deformed reinforcing bars.

In a two-paper sequence, Brown and Jirsa [21], and Ismail and Jirsa [8] study the behavior of the anchorage of reinforcing bars in cantilevers when subjected to cyclic overloads. The conditions studied are typical of exterior joints. In the first paper, the fixed end rotation due to slip in the fixed end is clearly

recognized, and some useful experimental data are given. The second paper, specifically directed to the behavior of anchored bars under low cycle overloads, indicates the necessity for increasing the embedment lengths of bars in such cases over and above the current code provisions. These investigators noted that the elongations of the anchored bars contributed between 30% to 45% of the total end deflection of the beams. This conclusion is analogous to that mentioned earlier [7,9].

Recently some very important work on cyclic pull-out tests has been completed by Hassan and Hawkins [22]. In their experiments concrete blocks simulating the conditions existing at a typical exterior beam-column joint were employed. The blocks were 6 in. thick, 24 in. wide, and 18 in. high with the test bars being placed in the middle of the 6 in. dimension at a distance of 6 in. from the top. Two series of experiments were performed with straight #10 Grade 40 bars, and one series with bars terminating in 180° hooks having 18.4 in. lead-in length. As the test blocks simulated a column, four #7 vertical bars were used in the corners, and four #4 Grade 40 closed ties provided concrete confinement. The blocks were held in position by an appropriate system of supports.

As a result of these tests, some empirical formulas were proposed. These express the energy absorbed, crack lengths, and force-deformation for an anchored bar. The latter attempt is particularly important, but unfortunately as yet the available data are too limited for extrapolation to cases other than those analyzed. A study of the report does, however, shed some light on bond deterioration under cyclic loading, which should help in establishing an acceptable force-deformation relation.

1.3 OBJECTIVES AND SCOPE

Because of the urgent need for the information of the deterioration in bond of a bar embedded in a beam column joint, a research program on the bond behavior of such a bar was initiated. The report of the initial phase of the bond research program is given in this dissertation. The objectives of this phase of the investigation are:

(1) To study bond deterioration as influenced by loading history, bar size and column widths. An attempt is made to understand the mechanism of bond deterioration to form a basis for formulating a mathematical rule.

(2) To establish a reliable mathematical model for bond deterioration under generalized loading for predicting experimental results.

To achieve the goal, 17 specimens subjected to pull and simultaneous push, to simulate the condition existing in interior beam column joints, were tested. A pull-only specimen was also included in the test program to provide a basis for evaluating the pushing effect. Based on the information from these tests, a hysteretic rule for a bond element is established. The proposed hysteretic rule for bond was used to predict the experimental response of three monotonic and three cyclic loading cases.

2. TEST SPECIMEN AND MECHANICAL CHARACTERISTICS OF MATERIAL

2.1 TEST SPECIMENS

The test specimens in this series of experiments were intended to simulate a block of well confined concrete column such as exists in an interior beam-column joint of a moment resisting R/C ductile frame. The concrete blocks and their reinforcing cages were designed and detailed according to the to the special requirements of ACI 1971 [24] for an earthquake zone of the highest seismic risk. Detailed calculations for designing the testing specimens is given in Appendix A. Two types of reinforcement were provided: transverse and longitudinal. The transverse reinforcement was provided for shear and confinement; the confinement requirement was a controlling criteria for the design of the specimens. Due to the manner of applying load and transferring reactions, flexural bending moment was introduced in the specimens with maximum bending at the section of pulling and pushing load application (see Appendix A); longitudinal reinforcement was designed to limit the size and extent of the flexural cracks. The specimens were 10 in. in thickness to provide an ample cover against splitting failure. The specimens were made 46 in. high to fit in the test fixture. Because of the amount of reinforcement provided, the concrete in all column stubs could be classified as well confined. The width of the blocks ranged from 15 to 25 in.

The reinforcing cages for 15, 20 and 25 in. column blocks are shown in Figs. 2.1 to 2.3. An embedded bar to be tested was placed at

the center of the block 22 in. from the tops. At 11 in. from an embedded rebar, conduits of 1-1/2 in. diameter were installed to facilitate tying down the specimens in the testing bed. A photograph of a typical reinforcing cage prior to casting is shown in Fig. 2.4.

2.2 MATERIAL PROPERTIES

2.2.1 Concrete

The concrete used was made of normal weight aggregate. The proportions of cement, fine aggregate, and coarse aggregate for a designed strength of 4000 psi at 28 days was 1:.87:2.99, the water-cement ratio was 0.59. Compressive tests, splitting tension tests and flexural tests were performed on samples of each test specimen's concrete following each bond test. Table 2.1 summarizes the actual concrete properties at the time of testing. Note that small values of the standard deviation for ε'_c, f'_c, E_c, f_r, and f_{sp} indicate that a reasonable uniformity of concrete properties was achieved throughout the whole series of tests. The same conclusion can be reached by studying the upper and lower bounds of concrete stress-strain curves given in Fig. 2.5. In average terms, the properties of concrete were ε'_c = .0026 in/in, f'_c = 4.47 ksi, E_c = 3319 ksi, f_r = 584.4 psi and f_{sp} = 470 psi, respectively.

2.2.2 Reinforcing Steel

Grade 60 deformed bars were used for the test bars as well as for the bars of reinforcing cages. The test bar deformation pattern is shown in Fig. 2.6. This particular deformation pattern was selected to be the same as that used in the previous beam-column experiments [3].

The geometry of deformations for #6, #8 and #10 rebars is shown in Fig. 2.7. Note that certain portions along the length of the rebar are inscribed with a manufacturer's mill mark, resulting in fewer deformed lugs in this portion than elsewhere (see Fig. 2.7(b)). Neither the inside nor the outside rebar diameter corresponded to the nominal values generally used in practical design. Although similar in appearance, lug dimensions and spacing were not exactly proportional to the bar diameters and, therefore, the law of simulitude could not be applied to extrapolate the test results from one bar size to another.

All the reinforcing bars have yield strength well above the requirement for grade 60 (see Figs. 2.8 and 2.9). The slight difference between f_s-ε_s curves of the embedded bars shows that their mechanical properties are rather uniform.

Contrary to what has been normally believed, the stress-strain curve of steel, f_s-ε_s, under uni-axial tension was not the same as under uni-axial compression (see Fig. 2.10). Though the elastic portion of the f_s-ε_s curves was practically the same, several different aspects were detected for the post-elastic range. The differences were as follows:

(1) Stress level of initiation of yielding was slightly higher for compression.

(2) Yield plateaus were slightly shorter for compression.

(3) At the onset of strain-hardening range, a higher tangential stiffness, E_{sh}, for compression was observed.

(4) Providing that no buckling failure occurred in compressing a rebar, the stress condinued to increase for increasing strain. Meanwhile, for pulling, tensile stress leveled off because of necking

of the bar section just before fracture.

There is no simple explanation for (1) and (2), unless a detailed study of the metallurgical structure of the medal is made. Numbers (3) and (4) can be accounted for by the Poisson effect, where the Poisson ratio for the inelastic range is about 1/2.

Since the majority of the test specimens were subjected to cyclic loading, the cyclic f_s-ε_s curve for a rebar was needed for interpreting the test data. A typical f_s-ε_s curve for a rebar subjected to a cyclic loading history similar to that applied to the bond test specimens is shown in Fig. 2.11. A pronounced stiffness degradation known as the Bauschinger effect appears on stressing the bar in an opposite sense after it has yielded.

2.3 MANUFACTURE AND CURING

The specimens were cast in wooden forms in an upright position. The concrete was vibrated externally with form vibrators and internally with a plunger vibrator. The forms were removed approximately two days after casting, and the specimens were covered with wet burlap and polyethylene until the time of testing to ensure moist curing conditions (see Fig. 2.12). A few days prior to each test, the specimens were placed in the testing jig and instrumentation was then attached.

3. TEST FACILITY, INSTRUMENTATION AND TEST PROGRAM

3.1 TEST FACILITY

3.1.1 Testing Apparatus

The apparatus to perform the tests described herein is located on the second floor of Davis Hall at the University of California, Berkeley. Figure 3.1 shows the general layout. Large concrete blocks prestressed to the floor serve as reactions to the forces applied to the specimen. The facility is designed to accommodate specimens 46 in. long by 10 in. deep and in widths of 15 in. to 31 in. The device for holding the specimens in place was chosen to minimize local stress-concentrations. Vertical support is provided by wide-flanged beams with a Teflon pad glued on to permit free horizontal movement. Lateral support is provided by prestressing heavy plates (tie-down straps) to the specimen as shown in Fig. 3.1(a). The plates are then connected to the horizontal supports which are in turn anchored against the concrete reaction block. The specimen is thus restrained against the horizontal movement by the friction developed between the plates and the contact surface of the specimen. This scheme of supports is devised to minimize the stress concentration developed in the test specimen. The total prestressing force in each plate was varied from 153 kips for #6 bar 15 in. column to 340 kips for #10 bar 25 in. column.

Load was applied to the specimen by means of hydraulic rams (A), (B) and (C), see Fig. 3.1(a). Two double acting 120-kip rams, (A) and (B), were used to apply load to the test rebar. A 300-kip capacity ram,

(C), applied axial load to the specimen transverse to the direction of the main rams. The main rams (A & B) were actuated by MTS controllers. The tests were to be performed with equal push and pull or pull only. For the condition of pull equal to push, the ram on one side was made a slave. Therefore, only a single input was required to actuate both jacks. Two types of feedback were fed into the controller. The output from force transducers, (load cells C2A and C2B), was used mainly in the working load range to ensure good control at low displacement levels. In most of the cases, displacement feed-back was employed after the completion of working load cycles to prevent the possibility of sudden pullout of the bar. The force was transmitted to the reinforcing bar by means of an assembly shown in Fig. 3.2. The assembly consists of a clevis arrangement which threads into the ram on one side and a large steel pin on the other. The pin threads into a specially fabricated Cadweld device which was welded to the bar prior to fabrication of the specimen. A teflon lined stand supports the pin to ensure accurate alignment, minimize bending and to reduce friction. For convenience, the two sides are designated "north" and "south" according to the orientation in the test bay. The only significance of these designations is that the sense of the cycles was such that the initial force on the south side was tensile.

3.1.2 Data Acquisition

A low-speed data acquisition system was employed to collect and record data from the various external and internal gages used in the test. The data collecting system consists of three major components: a low-speed scanner (a Nova minicomputer), a tape writing machine and a

teletype (see Fig. 3.1(b)). The function of the low-speed scanner is to take readings and carry out simple calculations. After gathering readings from the gages by the scanner, the data is kept in the central memory of the minicomputer, later to be transferred to the tape device and deposited on a magnetic tape. Communication between the scanner and the tape writing machine is possible via manual typing instructions on the teletype to control the process. Raw data from an experiment must be manipulated by data reduction programs on a 6400 CDC Computer before obtaining numerical readings in a desired form, as listings or as curves, depicting the relation of sets of readings. Several computer programs have been developed to facilitate a data reduction task needed for the bond research. A brief description of the computer programs used in the data reduction process is given in Appendix E.

Besides the low-speed data acquisition system, the load-displacement relationships were continuously monitored on X-Y recorders. These plots were necessary for controlling the tests and for evaluating the response during the experiments.

3.2 INSTRUMENTATION

Three quantities were of primary interest regarding experimental measurements. These were the forces applied to the rebar, the strain distribution along the bar, and the displacement of points on the bar originally at the faces of the column. The force and displacement values were measured by means of external devices. The strain distribution was obtained from readings of internal strain gages.

3.2.1 External Instrumentation

Force measurements were obtained by use of carefully calibrated load cells incorporated into the hydraulic rams, see Fig. 3.1(a). The displacements, herein referred to as δ's, were measured in two parts, (see Fig. 3.3 and 3.4). First, linear variable differential transformers (LVDT's), (A)--PS1A and PS1B in South face, PS2A and PS2B in North face, were held fixed relative to the longitudinal centerline by a special aluminum frame. The plungers of the LVDT's rested on a ring attached to the rebar a small distance from the column face. These devices recorded the movement δ plus the elongation of bar in the protruding length. This quantity is referred to as δ'. Second, strain gages were placed on the bar between the face and the ring. By subtracting the elongation component from δ', δ was obtained. Figure 3.5 shows schematically the quantities δ' and δ. The subscripts 1 and 2 used subsequently refer to the south and north sides of the specimen respectively. In addition to the above, a second set of LVDT's, (B)--PC1A and PC1B in South face, P2A and P2B in North face, was attached to the ring with the plunger bearing on the concrete face in the vicinity of the embedded bar. This measured δ' less the bulging of the concrete surface. It should be noted that in order to obtain a reliable value of concrete surface bulge which was highly localized, the LVDT's PC1A, PC1B, PC2A and PC2B should be located as close as possible to the center of the rebar. However, because of congestion of instrumentation at the column faces and the relatively large size of the Cadweld couplers (connectors between the embedded rebar and activating rams), the closest practical positioning was 2 in. from the rebar center line. This may not provide a good picture of bulge. Also,

clip gages were located on the top surface to measure the width of longitudinal cracks, see Fig. 3.3(a).

3.2.2 Internal Instrumentation and Installation

In order to measure strains along the rebar with a minimum of interference with the bond mechanism and still provide a suitable surface for strain gage installation, grooves were machined in the rebar. The grooves run longitudinally on each side of the bar along the initial location of the longitudinal ribs (see Fig. 3.6). The cross-sectional dimensions are shown in Fig. 3.7. It should be noted that the size of the grooves is almost identical for the different bar sizes. This is because the same strain gages, lead wires and waterproofing material must be accommodated. This means that the smaller the bar diameter, the more distortion is introduced by the groove. Table 3.1 gives the measured areas and circumferences of the grooved and ungrooved sections. Note that the arc lengths of either longitudinal ribs or grooves are deducted from the total perimeter to obtain the measured circumferences.

Prior to installing internal strain gages, the bars were cut and trimmed to a designated length. Cadweld couplers were welded to the ends (Fig. 3.8). The grooves were sandblasted to ensure a good bonding between the gages and the steel surface. SR-4 Type post yield strain gages (Micro-Measurements Model EP-08-250 BG-120) were epoxied to the grooved surface with M-Bond Type AE 10/15 adhesive. Coated wires were soldered to the strain gages and run along the grooves (see Fig. 3.9). Finally, M-Coat Type G epoxy adhesive and metal strips were applied for water proofing and protection of the strain gage from damage during casting.

A completely grooved rebar and its section are shown in Fig. 3.10 and 3.11.

A typical layout of strain gages along the rebar is shown in Fig. 3.12. It should be noted that a few locations along the length near protruding ends of a bar were fitted with two diametrically opposite gages. The double gage installation served to eliminate the bending effect introduced in the protruding section.

3.3 TEST PROGRAM

Out of 17 specimens tested, 7 specimens were for monotonic tests while the remaining ten specimens were for cyclic tests, as listed in Table 3.2. Six of the specimens were made of ungrooved bars. The rest were grooved. Ungrooved bar tests were necessary to provide information for evaluating the effect of the grooves. All except one, Specimen No. 3, were subjected to simultaneous push and pull with pull equal to push. Specimen No. 3 was subjected to pull only.

3.4 LOADING HISTORY

Two types of loading were applied to the specimens: monotonic and cyclic loading. In the monotonic experiments, three initial cycles reaching the maximum stress of 10 ksi, followed by three cycles reaching 24 ksi, were applied (see first six cycles of Fig. 3.13). Thereafter, using displacement control, the experiments were continued until, usually, the test bar pulled through the column stub. It should be noted that the first three cycles at 10 ksi were intended for checking

proper instrument response while cycles at 24 ksi were designed to simulate working load excitations.

In the cyclic experiments, after applying the same six preliminary cycles as in the monotonic loading case, the specimens were loaded to the level of 40 ksi, 55 ksi and then yielding of the rebar (see cycle no. 6 to 15 in Fig. 3.14). Three cycles were applied at each prescribed load. The loading history was switched to the displacement control before yielding cycles. The displacement on the tension side was matched to a specified displacement level; meanwhile the compression side was left uncontrolled. The applied force on opposing ends of the bar was maintained equal in magnitude and opposite in sense throughout the test. The displacement levels to be followed after yielding cycles are .04, .07, .125 in. until complete failure in anchorage was evident (see cycle no. 15 to 26 in Fig. 3.14). In case the anchorage strength of the embedded bar was less than the rebar yielding stress, cycles at prescribed loads of 40 ksi and 55 ksi were attempted. However, if this attempt led to excessive pullout (larger than .04 in.), displacement control was imposed. The displacements of .07, .125 in. etc., were then imposed. Such a displacement control history was selected to facilitate the comparison of test results for cyclic loading.

4. EXPERIMENTAL RESULTS AND THEIR INTERPRETATION

4.1 GENERAL

The results of the tested specimens are presented under three classifications. Two of these deal with the case of monotonically applied loads. In the one, a bar subjected only to a pull from one side; in the other, a bar is simultaneously pulled from one side and pushed from the other. The third case was cyclically loaded. All of the 17 specimens were tested until failure caused by a pull-through of the bar. The results of a representative specimen of each group are presented in detail. Significant results for all tests are summarized in tabular form.

The following specimens, representing the three loading conditions mentioned above, are selected as typical for summarizing the different test results: Specimen No. 3 for monotonic pull only, Specimen No. 13 for monotonic push-pull loading, and Specimen No. 14 for cyclic push-pull. All of these selected specimens were made of #8 grooved bars embedded in 25 in. column blocks. The pulled-through strength in each case exceeded the yield strength of the rebars.

For the representative specimens, the main results can be classified as follows:

(1) Load-deformation relations measured at the protruding ends of the rebar. This curve represents the total response of the bar embedded in the column stub system.

(2) Strain distribution along the rebar. Strain variation from point to point along the rebar is depicted in this diagram.

(3) Stress distribution along the rebar. Variation of stress in the rebar under external applied load is described in this diagram.

(4) Bond stress distribution along the rebar. In this diagram, the rate of force dissipation from rebar into surrounding concrete is illustrated.

(5) Local displacement distribution. This diagram shows how much each point along the rebar moves with respect to the center axis of the column. This displacement gives some indication of the magnitude of the relative displacement between the rebar and its adjacent concrete.

In addition to the results of (1) to (5), the behavior from visual observation is also included in the presentation. These results are essential to the study of the mechanism of bond deterioration.

It should be noted that only (1) and (2) were obtained directly from experimental measurements. Numbers (3) through (5) were calculated quantities. In (5) local displacement was computed by integrating the measured strains in (2); therefore better or more reliable data was obtained. To get the rebar stress distribution (3), the stress-strain relation of the reinforcing bar, f_s-ε_s, was needed. The slight discrepancy between the actual stress-strain curve and the mathematical model used in the strain-to-stress conversion can lead to some error. Larger error in converted stress is expected to occur in the regions near the bar ends where Cadweld couplers are connected. Intensive heat applied during the welding of the couplers to the bar ends can significantly modify their stress-strain characteristics. Therefore, some judgment is needed to interpret the stress results.

4.2 VISUAL OBSERVATIONS OF CRACK DEVELOPMENT

4.2.1 Monotonic Pull-Only Specimen

In this specimen considerable cracking occurred at the pull end face, though no visible cracks were observed at the free end. Figs. 4.1(a)

and 4.1(b) show cracks that appeared at the pulled face and on the side of the column stub at different pulling stresses. The sequence of major crack developments were as follows. The first splitting tension crack on the face and the longitudinal crack on the side of the block emerged simultaneously at a pulling stress of about 40 ksi. As loading increased, more splitting cracks were formed and longitudinal cracks extended further toward the free end. At a stress level of about 60 ksi, splitting cracks and longitudinal cracks began to connect. At the yielding stress of the rebar, cracks in the concrete surrounding the rebar at the pull end assumed the shape of a cone that fractured away from the main block (see Fig. 4.2). As load was further increased, the formation of the cone was more evident. At a stress of about 80 ksi, the concrete cone was completely fractured away from the rest of the block (see photo in Fig. 4.3). The dimensions of the cone as roughly described by an approximate radius, r, and depth, d, shown in Fig. 4.4, were 4.5 in. and 3 in., respectively.

Longitudinal cracks did not propagate all the way to the other side of the block. Due to the manner of support and application of load on the specimen, the maximum flexural moment was induced at the section where the bar was embedded (see Fig. 4.5). This moment produced a tension field around the south face and a compression field on the north. The compressive state of stress on the north face inhibited longitudinal crack development.

4.2.2 Monotonic Push-Pull Specimens

A sequence of crack development similar to that for pulling only was observed for the pull and push loading condition, (see Fig. 4.6).

Splitting tension cracks and longitudinal cracks were first seen at a stress of about 40 ksi. Additional splitting tension cracks kept forming until the stress reached as high as 90 ksi. A clear separation of the cone away from the main block occurred as late as 60 ksi, although signs of its first appearance were detected around 40 ksi.

There was, however, a noticeable difference between the crack patterns of pull only and pull-push specimens. On the sides of pull-push blocks, a few diagonal shear cracks were formed in addition to the flexural longitudinal crack at advanced stages of loading. In the push-pull case, the total shear force was almost twice as high as in the case of pull loading only, and these higher shear stresses are more likely to produce diagonal cracking. Also, a few small splitting cracks appeared at the pushed end, as shown in Fig. 4.6(c). The increase of bar diameter due to the Poisson effect is believed to be the major cause of this splitting.

Table 4.1(a) lists the significant stages of crack development for the remaining push-pull specimens. Note that the stress level for the first appearance of splitting tension and longitudinal cracks is almost the same for all cases, i.e., within 36-50 ksi range. The stress levels at which the cone formation was detected at the pull end also show a narrow range of variation, from 45-56 ksi. It is rather interesting to note that all the major cracking occurred before the yielding of the rebar was reached.

4.2.3 Cyclic Push-Pull Specimens

Unlike the monotonic loading cases where extensive cracking developed mostly on one face, cracks appeared on both faces under load

reversals. The sequences of crack development on both faces and on the side of the specimens, however, were not much different from that of the pull face of a monotonically loaded specimen, i.e., simultaneous splitting tension cracks spreading out radially and longitudinal cracks running from one face to the other were the first to be detected; formation of the cones followed (see Fig. 4.7 for typical cracking patterns). It should be noted that the longitudinal cracks in this case ran through the specimen from one face to the other. As a specimen was pulled at the South face, longitudinal cracks would begin to propagate to the North, and vice versa. At $\pm$ 40 ksi stress level, cracks propagating from both sides either connected together or overlapped (Fig. 4.7(a)). The cyclic loading also produced cone formations at both ends at approximately $\pm$ 40 ksi. As a result, the effective length for anchoring the rebar above $\pm$ 40 ksi was substantially reduced; only the inner confined cores of the specimen remained useful.

Table 4.1(b) lists the major sequence of crack development under cyclic loading. Conclusions similar to the monotonic pull-push case can be reached for the cyclic case, i.e., the initiation of splitting and longitudinal cracks vary over a narrow range, i.e., within 40 to 55 ksi stress level. The size of the cones also shows little variation. The depths of the cones vary from 2.8 to 3.5 in. The average radius of the cones range from 3.0 to 4.0 in. It is believed that the cone sizes are controlled by the spacing of the stirrups and the thickness of concrete cover. All the specimens tested have almost the same stirrup spacings and thickness of column covers as shown in Figs. 2.1 to 2.3.

4.3 STRESS-DISPLACEMENT DIAGRAMS OF THE SPECIMENS (f_s-δ)

The overall behavior of an anchored bar, with either pull-only or push-pull loading, is described by the stress-displacement relations measured at protruding ends of the test bar. The force-displacement diagram can also be readily obtained through a scaling of the stress by the cross sectional area of the rebar. The displacements denoted as δ_1 on the South face of δ_2 for the North represent the relative displacements of a bar section at the column face with respect to a fixed axis located at the center of the block (see Fig. 4.8). Adopting the same system of identification as the displacements, f_{s1} denotes the stress applied to the bar at the South face, and f_{s2} refers to the North.

These stress-displacement diagrams provide the most significant data for evaluating the overall performance of the bond test specimens. The amount of energy dissipated by the anchored bar can be estimated from the areas enclosed by the hysteretic loops of the f_{s1}-δ_1 and f_{s2}-δ_2 diagrams for push-pull loading and the f_{s1}-δ_1 diagram for pull-only. The stiffness deterioration and strength characteristics of the specimen can also be readily obtained from this diagram.

4.3.1 Monotonic Pull-Only Specimen

The hysteretic curve f_{s1}-δ_1 at low amplitudes, $\pm$ 10 ksi, and working load level, $\pm$ 24 ksi, is illustrated in Fig. 4.9(a). Note that, although the system showed signs of degradation in stiffness around zero load, no further degradation in stiffness and increment in peak displacements on the next two repeating cycles were observed.

Responses under monotonic increasing load are shown in Fig. 4.9(b). It should be noted that significant degradation in stiffness took place

after the rebar was loaded past yielding stress (point A in the figures). Unloading and reloading at a stress level of 100 ksi, considerably above the rebar yielding stress, produced no significant loss in strength or stiffness (see loops A, A'', A'''). A maximum strength of 102 ksi, close to the maximum strength of the rebar (106 ksi), was developed. The specimen was able to sustain a stress of about 100 ksi until the bar was pulled out 1 in. (see point B in Fig. 4.9(b)) before strength started to decline.

Figure 4.10 shows the displacement of the free end, δ_2. Note that there was virtually no movement before the yielding strength was reached (see point A). The bar end begins to display large displacement from point B to point C, confirming that the rebar was on the verge of pull-through.

From this particular test result, it was clear that a 25 in. well-confirmed column can provide a bond (anchorage) resistance larger than that required to develop the yield strength of the pulled bar. The anchorage length requirement as specified by ACI [23], which is about 20 in. of embedment length, seems to be adequate.

4.3.2 Monotonic Push-Pull Specimens

A typical f_{s1}-δ_1 diagram of the push-pull specimen loaded to maximum stresses of 10 ksi and 24 ksi is shown in Fig. 4.11(a). This response is virtually the same as that of the pulled-only specimen previously presented (see Fig. 4.11(b)). This indicates that at low levels of loading the applied load on one end of the rebar has no influence on the other end. The curves f_{s1}-δ_1 and f_{s2}-δ_2 under monotonically increasing loads are given in Fig. 4.11(c). Again, the similarity

of response at the pulled end between the two specimens, pull only and push-pull, was maintained, i.e., from zero to initiation of yield, a highly stiff response prevailed; beyond the yielding of the rebar a consistent degrading in stiffness was evidenced; and, finally, the embedded bar pulled through at point B. A verification of the bar being pulled through is evidenced by the almost identical appearance of the declining branch, B-C, of the f_{s1}-δ_1 and f_{s2}-δ_2 curve (Fig. 4.12). (Note that the f_{s2}-δ_2 curve was translated and rotated to match point B of the f_{s1}-δ_1 curve in the first quadrant.)

The load-deformation curve for the pushed end was different from that of the pulled end. The difference in response is shown in Fig. 4.13, where the f_{s2}-δ_2 curve was rotated about the origin by 180 degrees. Instead of possessing a long plateau of flat slope in the post-yield range, the response of the specimens showed a small displacement followed by a sudden drop in strength. The causes of these differing responses will become obvious once the data on strain along the rebar is presented.

Values of significant responses for the other specimens are summarized in Table 4.2. It should be noted that all the specimens except Specimen No. 7 which was a #8 bar embedded in a 15-inch column, were able to develop the yield strength of the main rebar. Since Specimen No. 7 did not yield, its displacements at maximum stress were smaller than those of the others.

4.3.3 Cyclic Push-Pull Specimens

A diagram of typical f_{s1}-δ_1 and f_{s2}-δ_2 curves for cyclic loading is shown in Fig. 4.14 and 4.15. The cyclic loading

sequences adopted, incrementally increasing magnitude, tended to produce very similar responses for both South and North Faces. Unlike monotonic loading, a significant degradation in stiffness under cyclic loading was observed at cycles as low as $\pm$ 40 ksi, signifying a considerable reduction in energy absorption capacity. Furthermore, after a number of cycles of load reversal, the loss of stiffness became more pronounced. When subsequent cycles were carried out at equal peak loading value, (for instance, the three cycles at each of the incremental steps, Nos. 3 to 12 identified by LP 3C to 12F in Fig. 4.14(a)), the displacement increased from cycle to cycle and stabilization of the hysteretic loops within the next two cycles of the same load was not achieved. The instability of loops also developed for repeated cycles with peak displacement control (this cycle started with No. 12, as shown by LP 12F, in Fig. 4.14(a), and continued up to the end of the test, Figs. 4.14(a) and (b) and 4.15). This lack of stabilization increased as the end displacement was increased, indicating the bond deterioration was highly susceptible to cyclic loading. Cumulative and irreversable damage was suffered by the concrete layer surrounding the test bar during each loading and unloading cycle.

According to the imposed load-displacement history, specimens either attained yielding of the rebar or initiation of pulling through at LP 15E (See Fig. 3.14). In the case of Specimen No. 14, yielding strength of the rebar and even strain hardening to a stress of 72 ksi was reached (LP 15E to 21E). However, the strength was rapidly degraded once loading went beyond 21E. This by no means was comparable to monotonic loading where the pulled-through stress of 92 ksi could be achieved. One of the reasons the cyclic loading gave rise to a lower pulled-through strength was the considerable loss of effective anchored length due to the fracturing

away of the concrete cone at both loading ends (see Fig. 4.7(a)), thereby leaving as the effective anchorage region the confined core in the middle section of the column. In Specimen No. 14 the depth of cone was about 3 in., leaving about 19 inches of confined core out of 25 in. of initial column width.

A listing of significant results for the complete response of the other cyclically tested specimens is given in Table 4.2(b). Note that the four specimens with 15 in. block widths had pull-through strengths below the yielding strength of the rebars. Displacement at the peak loads of pulling cycles varied over a narrow range, .039 to .071 in., regardless of the block width and bar diameter. In addition, the development of a higher average bond stress for narrower columns was also observed for cyclic push-pull loading. For instance, in a 15 in. #6 grooved bar (Specimen No. 4), a bond strength of 1.73 ksi was attained while a 1.58 ksi bond strength was developed for a 20 in. column (Specimen No. 11).

4.4 STRAIN DISTRIBUTION DIAGRAMS

As has been pointed out in section 4.1, strain was one of the quantities directly measured. Section 3.2.2 showed how this was done by installing 1/4 in. post yield gages along the grooved bars. The resulting strain distributions along the length of the rebar gave direct insight into how much each segment of a rebar deforms. In the range below yielding of the rebar, the strains in essence give a picture of the stress distribution as well.

4.4.1 Monotonic Loading

4.4.1.1 Pull-Only Specimens

Strain distributions in the working stress range, at ± 10 ksi and ± 24 ksi, is shown in Fig. 4.16(a). Note that even at working load level, about 15 inches of the 25 in. anchorage, or 60 percent of the embedded length was strained. A significant residual strain was also observed at this level of loading. Approximately 10 in. of the rebar remained in tension with a maximum residual strain of about 80 micro in./in. This clearly indicated that, at working load level, some cracking and inelastic deformation has already occurred in the concrete immediately surrounding the rebar. However, subsequent application of two more cycles of the same peak force amplitude did not produce a noticeable change in the strain distribution, i.e., a stable response was achieved.

Strain distribution, for loads ranging from zero to initiation of rebar yielding, is shown in Fig. 4.16(b). It should be noted that in this range the length of stress varied according to the magnitude of applied load. At 20 ksi, about 14 in. responded to the applied load; at 40 ksi, the length increased to 18 in.; and at yielding, the disturbed length was 22 in. There was no increase in the transferring length from LP 6E to 6F since the applied load was virtually unchanged.

The abnormal strain reading of the second gage location from pulled-end at yielding is worth some attention (see Fig. 4.16(b)). As has been pointed out in Sec. 4.2.1, the splitting tension cracks already form (at ± 40 ksi) long before the bar begins to yield. No bond resistance is offered in the first 3 in. inside from the pulled face and therefore a yield slippage plane could develop at any section along this length.

In this test it turned out that the second gage was located on a slippage plane and resulted in a sudden jump in the strain reading, while the other two gage locations remained on the verge of slipping. Thus the second gage attained a strain-hardening reading prior to the other locations reaching the same strain level (see Fig. 4.16(c), LP 6G to 6I).

Strain distribution beyond yielding of the rebar is shown in Fig. 4.16(c). The length of the rebar being strained beyond the yielding strain propagated further inside the specimen as the applied load increased. At LP 6I, where the strain at the exposed end reached strain hardening level, the length was about 3 in.; at 6L, with 15000 micro in./in of exterior strain, the length was 5 in.; meanwhile the remainder of the rebar was in the elastic range. A similar pattern of strain distribution was observed for more advanced loading stages, Figs. 4.16(d) to 4.16(f), i.e., the length strained beyond yield was continuously increasing and thereby diminishing the part of the rebar that remained elastic.

The strain distribution at maximum pull-through stress and subsequent unloading is shown in Fig. 4.16(g). Except for LP 8Q which was LP at pull-through, the rest of the strain distributions were at declining load levels. Therefore, strain distribution at LP 8Q became the envelope curve of all measured strain distributions.

One of the major factors influencing the bond deterioration mechanism is the reduction in contact area between the concrete lug and surrounding concrete. This reduction tended to create a higher bearing pressure at the contact point which was a favorable condition for crack initiation. The mechanism of reduction in bearing area is

illustrated in Fig. 4.17. Initially (Fig. 4.17(a)), the steel lug is fully in contact with surrounding concrete. The bearing area is initially approximated by the formula

$$A_b = \pi D_{AVG} h \tag{4.1}$$

where D_{AVG} is the average of the outer and inner diameters of the deformed bar and h is the height of the lugs. As the bar is strained in tension, the diameter of the rebar reduces and thereby decreases the height of the lug in contact with concrete. The new effective bearing area is

$$A_{b_E} = \pi D_{AVG} h_E \tag{4.2}$$

where h_E denotes the new contact height; D_{AVG} was assumed unchanged. The reduction in contact area is shown in Fig. 4.18. (This diagram was based on knowledge of the strain distribution along the rebar and on the assumption that the Poisson ratio of the steel was 0.3 for the elastic range and 0.5 for strains beyond yield.) Within the elastic range of the rebar (prior to LP 6L in Fig. 4.18), the shrinkage in area was insignificant. The reduction became significant for the post-elastic range (LP 6L to 8Q).

4.4.1.2 Push-Pull Specimens

For $\pm$ 10 ksi and $\pm$ 24 ksi, working stress level, the strain distributions show consistant patterns and tend to stabilize at peak load under repeating cycles (compare Figs. 4.19(a) and (b) and Figs. 4.19(c) and (d)). However, alternating loading and unloading produced some

residual strain of order 100 micro in./in. (LP 1B and LP 3E). The presence of residual strain indicates that some damage has already occurred in the boundary layer*, as confirmed by the hysteretic loops in Fig. 4.11(a).

Strain distributions for loading from zero to yielding strain are shown in Fig. 4.19(e). The similarity between this case of push-pull loading and the case of pull-only (Fig. 4.16(b)) can be observed in the region near pulled ends; the breakaway of the unconfined concrete cone left the bar uniformly strained along its first 3 in. The approximate location of the separation is indicated by the difference in strain readings between the second and third gage locations at yielding stress level. The region near the pushed end, on the other hand, showed no major loss in bond resistance even at yielding load level, as is evident from the steep strain gradient.

As the applied load increased, the strain at the pulled end and the length of the bar strained beyond the yielding strain also increased as shown in Fig. 4.19(f). The pushed end, however, showed much less action in gaining larger strain readings. Only two gages lying close to the exposed surface showed some increase in strain readings. At LP 9Z, Fig. 4.19(g), the maximum pull-through strength of the block was reached. From then on, strain reading diminished as a result of decreasing applied load. The effective anchorage length at the failure stage is estimated at about 13 in., with about 10 in. at the pulling end and 3 in. at the pushed end strained above yielding level.

Increase and decrease in bearing area due to a contracting and expanding bar diameter is shown in Fig. 4.20. As can be seen, the change in bearing area was insignificant prior to LP 7, in elastic range

*As defined in Ref. [13].

and began to be important in the post-yield range. Note that the reduction in bearing area occurs over considerably more length than does the expansion, as is obvious from strain distribution curves previously presented.

The significant results of strain distribution for the other specimens are listed in Table 4.3. Note that only Specimen No. 7 pulled through prior to reaching yielding capacity of the rebar.

4.4.2 Cyclic Push-Pull Specimens

The response of strain distribution under $\pm$ 10 ksi and working load level was exactly the same as described in section 4.4.1.2. In this section the strain distribution at higher load level is presented.

A typical strain distribution at $\pm$ 40 ksi level, one step beyond working load, is shown in Fig. 4.21(a) and 4.21(b). The following points may be observed.

(1) At this load level, no change in the strain distribution pattern occurs under two additional cycles.

(2) At this level, bond damage has already occurred in the first few inches from the column faces during the portion of each pulling cycle. At the pushed end, bond resistance remains intact. This can be explained by the development of diagonal cracks around the rebar during pulling sequences shown in Fig. 4.21(b.1). Upon pushing the bar, it would move freely until the lugs wedged into the concrete. It requires a stress level higher than 40 ksi to produce a significant bearing failure during pushing cycles.

At the 55 ksi level, the strain distribution pattern looks similar to that at $\pm$ 40 ksi except for an increasing amount of bond

damage and resultant redistribution of strains occuring at the two subsequent repeating cycles (see LP 10D and 11D in Fig. 4.21(d) and LP 9D in Fig. 4.21(c)).

The strain distribution at first yield is shown in Fig. 4.21(e). Note that the yielding first occurs at the compression end, and at LP 12F. Subsequently the bar was loaded in the opposite direction, inducing yield in both ends, LP 12N. Once yielding began, the strain distribution diagram no longer lent itself to easily interpreting the underlying physical action. This was due mainly to the complex relation of f_s-ε_s for steel under cyclic loading. For instance, the reason the strain reading at the faces of the columns gave a high value at pushing cycle and low for pulling cycle in comparison with strain readings of the adjacent inner gages was residual strains. Unloading from yielding in compression at north face, LP 12L, the residual strain of -500 micro in./in. remained at the north face. As the specimen was loaded to LP 12N, the residual strain substracted from the additional tensile strain, resulting in lower strain readings at the column face. Stress distribution diagrams presented below in section 4.5.1.2 would be easier to interpret than the strain results.

The regions extending about 4 inches in from each column face were strained beyond elastic range (see Fig. 4.21(f) and 4.21(g)). As a result, the strain distributions adopted a peculiar shape. The remaining portion of the rebar, inside the confined core, remained elastic and therefore the strain distribution was easily interpreted according to either the tensile or compression stresses induced. Pull-through

strength of the rebar was reached at LP 19E in Fig. 4.21(h). After LP 19E the peak strain continued to diminish (LP 19K and LP 20E). Unlike monotonic loading presented in previous cases where pulled-through strengths were well beyond the inelastic range of the rebar, in the cyclic tests the bars pulled through prior to or just slightly above yielding stress, and therefore the necking and expansion of the bar diameter had a minor effect.

The listing of strain at the verge of pull-through for the other specimens tested is given in Table 4.3(b). Note that since Specimen No. 4 and No. 8 pulled through prior to yield of the rebar, a relatively low strain resulted.

4.5 STRESS DISTRIBUTION DIAGRAMS

As has been pointed out previously, the only raw data obtained directly from the experiments are the strain readings, displacements and forces. However, this directly obtained data does not always give a good picture of the physical action occurring in the rebar, especially for monotonic loading beyond the yield range and cyclic loading histories. A better illustration in these instances is found in distributions of stress along the embedded length, which shows stress attenuation in the rebar and, further, the bond-stress distribution, which gives the rate of force being transferred into the surrounding concrete. Stress distribution diagrams are to be presented in this section while the bond stress distribution diagrams are delayed until the next section.

As pointed out in Section 4.1, in order to make a conversion from a strain to a stress, a rather accurate mathematical model of f_s-ε_s

of the steel is needed. For monotonic loading, the f_s-ε_s relation possesses one to one correspondence and does not require a past history of strain to determine the corresponding stress. For post-yield cyclic loading, f_s-ε_s no longer maintains a one to one function and the past history of strains is needed. The mathematical model for f_s-ε_s adopted for carrying out strain to stress conversion is described in detail in Appendix B.

4.5 1 Monotonic Loading

4.5.1.1 Pull-Only Specimens

The stress distribution diagrams corresponding to the strain distribution diagrams of Section 4.4.1.1 are shown in Fig. 4.22. For the pre-yielding range of the rebar, (Fig. 4.22(a) and part of Fig. 4.22(b)), the stress distribution diagrams have the same shape as the strain distribution diagrams.

At yielding, the stress distribution diagrams start to look different from the strain distribution diagrams (LP 6E and 6F in Fig. 4.22(b) and 4.16(b)). As noted in Fig. 4.16(b) at LP 6E and 6F, the strain of the second gage from the pulled end shows a sharp rise in strain compared with the strains of adjacent gages. For these same LP's the stress distribution diagram (Fig. 4.22(b)) shows that yielding of the rebar extended over a segment of 2 to 3 in., as was pointed out in Section 4.4.1.1

As applied load increased, the stresses in the rebar near the pulled end of the bar increased, and the length of the bar that yielded (distinctly shown by small flat portions in the curve) also increased (see Fig. 4.22(c)). For instance, at 6G in Fig. 4.22(c), the yielding

zone extended about 2.5 in. inside the block , at LP 6K the yielding zone moved in about 4 in. Note also that the effective length in resisting the 40 ksi tension stress was about 19 in. and increased to the full width of the block after reaching yielding strength of the rebar.

It is particularly interesting to compare Fig. 4.16(g) and Fig. 4.22(g), where the rebar is on the verge of pulling through. While the strain distribution diagram gives no clue of the reduction in stress, an explicit picture of the effects of unloading in the rebar is clearly noted in the stress distribution diagram.

4.5.1.2 Push-Pull Specimens

The stress distribution diagrams corresponding to the previously described strain distribution diagrams are shown in Figs. 4.23(a) to 4.23(h). As with the pull-only case, for $\pm$ 10 ksi and working stress level, the stress distribution diagrams and the strain distribution diagrams are the same (see Figs. 4.23(a) to 4.23(d)). The similarity of the two diagrams breaks down when the bar is loaded to or above yielding stress (see LP 7K and 7L in Fig. 4.19(e) and 4.23(e)).

A distinctive characteristic in the stress distribution of the push-pull case for post-yield range is the marked difference in the distribution of stress under tension as compared to that under compression. The tension zone was distinguished by a gradual attenuation of stress. On the other hand, the stress was decreased within a much shorter length in the compression region, signifying more effectiveness in bond transfer. The better performance in pushed end region can be explained by the following facts:

(1) Because of flexural bending, the concrete in this region is in compression. The compressive stresses further increase the normal pressure on the bar, thereby increasing the frictional resistance and delaying initiation of diagonal crack.

(2) As pointed out in Section 4.4.1.2 and illustrated in Fig. 4.20, the bar under a compressive state of stress would increase in diameter, resulting in a larger bearing area and increasing the normal pressure acting on the rebar. Note that excessive expansion in the bar diameter could bring about ill effects, i.e., splitting cracks due to large hoop stresses. A study of the crack patterns formed in the test specimens showed some evidence of this type of cracking (see Fig. 4.6(c)). The cracking seemed to exert insignificant influence in reducing the bond transfer effectiveness as shown by the steep slope of the stress distribution near the pushed end.

Stress distributions for unloading and under decaying load are shown in Fig. 4.23(g). These curves, unlike the strain distribution curves, show clearly the reduction in stress as a result of a decrease in magnitude of applied load.

4.5.2 Cyclic Push-Pull Specimens

The stress distribution diagrams corresponding to the previously presented strain distribution diagrams are shown in Figs. 4.24 (a) to 4.24(h). Again in the pre-yielding range the stress distribution and strain distribution curves were both almost straight lines along the length of the bar (see Figs. 4.24(a) to 4.24(d)).

Figures 4.24(e) to 4.24(g) show the stress distribution at or beyond yielding. Note the gradual attenuation in stress along the region

affected by pulling stresses and a rapid decrease along the pushing region. This also conforms to what has been observed under monotonic loading. Stress distribution on the verge of the bar's pulling through is shown in Fig. 4.24(h). LP 19E and 19K were loading points of maximum stress and, therefore, as indicated by LP 20E and subsequent loading points, a smaller applied load at the exposed end was required for successive cycles.

4.6 BOND STRESS DISTRIBUTION DIAGRAMS

Once the stress distribution diagram is obtained, one further step is required to get the bond stress distribution. Mathematically, bond stress, u, is defined as

$$u = \frac{A_s \, \Delta f_s}{\Sigma_o \, \Delta x} \tag{4.1}$$

where Δf_s is the change in stress over a small distance Δx, and A_s and Σo are the measured cross-sectional area and effective perimeter of the rebar section, respectively (actual values for these terms are given in Table 3.1). It should be emphasized that the measured area and effective circumference were used for both grooved and ungrooved bars rather than nominal values. The effective perimeters were defined according to the sketch in Fig. 4.25, i.e., the longitudinal ribs were excluded for the ungrooved bar while the groove width was excluded in the case of a grooved bar.

The bond stress distribution diagrams give an indication of the physical interaction between the deformed bar and the surrounding concrete. Information is given by these diagrams on the rate of force transfer from the rebar to the surrounding concrete. In this respect the region where the bond has deteriorated can be clearly identified.

A few precautions must be taken in studying the bond distribution data:

(1) According to Eq. 4.1, computation of bond stress involves a mathematical operation equivalent to differentation. Therefore the accuracy of the computed bond stress depends upon the accuracy of the computed bar stress, f_s, from which it is derived. A moderate discrepancy in the proposed f_s-ε_s model can result in grossly unacceptable error in the computed bond stress.

(2) Since the bond resistance relies mainly on the mechanical wedging action between the steel lugs and the concrete, concentrations of bond stress occur in the concrete immediately surrounding the lugs. The recorded strains, which permit the determination of the bond stresses, might reflect these stress concentrations if a gage is close to a lug.

To overcome (1), attempts were made to come up with the most accurate f_s-ε_s model without excessive computational effort in the data reduction. The problem created by (2) is dealt with by interpreting the bond stress as an average value between gage locations and not as the local bond stress at a point.

4.6.1 Monotonic Loading

4.6.1.1 Pull Only Specimen

A series of bond distribution diagrams corresponding to the strain distribution and stress distribution diagrams given in Figs. 4.16(a) to 4.16(g) and Figs. 4.22(a) to 4.22(g) are shown in Figs. 4.26(a) to 4.26(g). As indicated previously in Section 4.4.1.2 for the strain distribution, the stress distributions at $\pm$ 10 ksi and working stress level (Figs. 4.26(a)) show about 16 in. of the rebar involved in resisting

the pulling load. The rest of the embedment length remained undisturbed. A peak local bond stress of about 1 ksi occurred near the exposed end. There was no noticeable redistribution of bond stress in this loading range, indicating no significant degradation in bond.

The bond distribution for loading up to yield strength is shown in Fig. 4.26(b). Fig. 4.26(b1) is a partial redrawing of the more complete Fig. 4.26(b) that emphasizes the redistribution as the load increases. At LP 6D, there was decreased resistance in the first 3 in. of embedment, and the peak bond resistance of 1.8 ksi occurred about 4 in. inside the block. A new pattern of distribution was developed at LP 6E where bond resistance was absent along the first 2.5 in. due to the breaking away of the concrete cone; the location of the maximum bond stress moved inside to about 3.25 in. from the original position of the block face.

The post yield distribution of bond is shown in Figs. 4.26(c) to 4.26(g). A gradual shifting in bond resistance from the pulling end toward the free end was the characteristic behavior in this range. A peak resistance of 2 ksi was developed within the block. At the pulling-through stage, LP 8Q in Fig. 4.26(g), the first 10 in. of embedment suffered severe loss of bond. Nevertheless, a peak bond stress of 3 ksi was developed at the free end. A summary of redistribution of bond for this loading condition of pull only is shown in Fig. 4.26(h).

4.6.1.2 Push-Pull Specimens

A series of bond distribution diagrams corresponding to the strain distribution and stress distribution diagrams given in Fig. 4.19

and Fig. 4.23 are shown in Fig. 4.27. At $\pm$ 10 ksi stress level (see Figs. 4.27(a) and 4.27(b)), the bond resistance was concentrated in the first few inches of embedment at the exposed end with peak amplitude of 0.5 ksi. At working load level (f_s = 24 ksi), Figs. 4.27(c) and 4.27(d), through LP 7B of Fig. 4.27(e), the peak bond stress increased to 1.0 ksi near the pulling end and about 2.0 for pushing. Except for regions near the end, the bond stress is surprisingly uniform in distribution. Unlike the pull-only case where, at working level, only part of the rebar length was involved in actively resisting the pulling force, in push-pull loading the whole length participated in resisting the forces applied at both ends of the bar.

The bond stress distribution ranging from zero up to the first yield is shown in Fig. 4.27(e). The bond stress at the pushing end was extremely high, from 4-6 ksi; therefore a shorter development length was required to transfer the pushing force applied to the bar. On the other hand, the bond stress was more evenly distributed in the region near the pulled end. The redistribution phenomena due to damage of the bond was confined to the first 3 in. from the pulled end.

For advanced stages of loading, a progressive bond failure occurred in the region near the pulled end, resulting in a redistribution of resistance as clearly shown in Figs. 4.27(f) to 4.27(h). The jagged appearance of the bond distribution curve for LP 7M to LP 9G characterizes the successive nature of bond failure, i.e., as the concrete around the first few lugs fails, the resistance has to rely on the wedging of concrete and steel lugs further inside the block to maintain equilibrium.

The bond stress distribution for decreasing load is shown in Fig. 4.27(h). As expected, the bond stresses diminish in accordance with the reduced applied load.

After studying the bond distributions and rebar stress distributions as well as the crack development on the tested specimens, the general characteristics of bond behavior within the column block can be deduced. Under the general case of push-pull loading, the block embedment length can be classified into three distinct regions according to the predominant bond behavior: unconfined, confined and push end regions. The unconfined region is located mostly outside the reinforcing cage and is influenced by the contraction of bar diameter. The failure mode in this region is identified by a breaking away of the concrete cone. Measuring the depth of the fracture cone after the specimen's rebar has completely pulled through indicates that the depth of cone and its radius at the column face can be approximated by assuming a 45-degree angle from the embedded bar to the close of transversed reinforcement as shown in Fig. 4.28. Heavy column reinforcement with transverse steel is characteristic of the confined region. Column longitudinal and transverse reinforcement arrests the propagation of cracks and limits the crack size. As a result the maximum bond stress it can sustain is higher than that of the unconfined region. The results obtained showed that average maximum bond capacity for the confined region was about 2.0 ksi while about 1.2 ksi was reached in the unconfined region.

The pushed-end region experiences an increase in bar diameter due to the rebar compressive stress. The increase in bar diameter increases the lug to concrete bearing area and radial normal pressure (not including

the additional pressure derived from the flexural bending induced into the block) and thereby increases the bond strength due to wedging action as well as that due to adhesive (chemical) bonding at the steel-concrete interface. Therefore the highest bond strength is achieved in this region. The average compressive bond strength derived from the experiments was about 6 ksi.

Table 4.4(a) summarizes the important characteristics of bond stress distribution for all test specimens. Except for the pushed-end region, the maximum bond stresses at different regions showed slight variation.

4.6.2 Cyclic Push-Pull Specimens

A series of bond stress distribution diagrams corresponding to the strain distribution and stress distribution diagrams given in Figs. 4.21 and Figs. 4.24 is shown in Figs. 4.29. For $\pm$ 40 ksi loading level, the bond stress was evenly distributed except for the regions near the loaded ends, as shown in Figures 4.29(a) and 4.29(b). No modification of distribution curves occurred at successive peaks of the repeating cycles, LP 7D, 8D and 7K, 8K. A similar pattern of distribution curves resulted for $\pm$ 55 ksi loading cycle, as shown in Figs. 4.29(c) and 4.29(d). As expected, the bond stress for peak loading at $\pm$ 55 ksi was higher than for $\pm$ 40 ksi. For instance, the maximum average bond stress in the confined region at $\pm$ 40 ksi was 1.2 ksi while the value at $\pm$ 55 ksi was about 1.6 to 1.7 ksi. It should also be noted that the average bond stress in the confined region (which covered the majority of column width) was almost proportional to the magnitude of applied load: zero bound

stress at zero applied load, 1.3 ksi at 40 ksi, and 1.65 ksi at 55 ksi (see LP 9A, 9C and 9D of Fig. 4.29(c)). This was due to the almost uniform distribution of bond at these load levels.

The bond stress distribution diagrams between yielding and pull-through of the rebar are shown in Figs. 4.29(e) to 4.29(h). Again, the curves are similar to those at $\pm$ 40 ksi and $\pm$ 55 ksi levels. As will be shown later, this similarity allows the use of the same mathematical rule to predict the build-up of bond stress in the confined region throughout the loading history.

A summary of the maximum bond stresses developed in all test specimens is listed in Table 4.4(b). Note that the maximum bond stress value shows little variation with varying column widths and bar sizes.

4.7 LOCAL DISPLACEMENT DISTRIBUTION DIAGRAMS

The distribution curves referred to so far do not explicitly describe the movement of the bar relative to the concrete; the local displacement distribution diagrams are designed to fill this gap. Local displacement is defined as the relative movement of the bar section with respect to a rigid concrete core or, equivalently, the center of the column. Adoption of this definition was necessary due to a lack of information regarding the deformation of concrete (which in turn depends upon cracking and strain distribution within the concrete) necessary to compute a local slip, which is the actual relative displacement between steel-concrete at their interface.

Referring to Fig. 4.30, the local displacement at section X, δ_x, is computed as follows:

$$\delta_{x1} = \delta_1 - \int_o^x \varepsilon_s(\xi)d\xi \tag{4.3}$$

$$\delta_{x2} = \int_o^{L-X} \varepsilon_s(\eta)d\eta + \delta_2 \tag{4.4}$$

$$\delta_x = \frac{\delta_{x1} + \delta_{x2}}{2} \tag{4.5}$$

where δ_1 and δ_2 are the displacements at the exposed ends, as shown in Fig. 4.30(a), $\varepsilon_s(\xi)$ is the measured strain distribution along the bar as shown in Fig. 4.30(b), and $\eta = L-\xi$. The displacement δ_{x1} satisfies displacement compatibility at one end while δ_{x2} satisfies compatibility at the opposite end; an average value, δ_x, was adopted as the displacement at the desired section, X.

4.7.1 Monotonic Loading

4.7.1.1 Pull-Only Specimen

The local displacement distribution diagrams corresponding to the strain distributions previously given are shown in Figs. 4.31(a) to 4.31(g). For $\pm$ 10 ksi working load cycles, the disturbed length of the rebar was within 16 in. of the pulled face. This agrees with what had been observed in the other diagrams. A substantial increase in local displacement was observed when the bar began to yield, LP 6D to LP 6E in Fig. 4.31(b). At yield, the length of bar showing movement extended to 18 in. within the column block.

The local displacement diagrams for post-yielding of the specimen to pull-through are shown in Figs. 4.31(c) to 4.31(g). Note that prior to pull-through the only portion of rebar that moves is near the pulled

end where the rebar is strained into the inelastic range. Also, the free end showed no significant displacement until LP 70 where the bar was at the verge of pull-through.

4.7.1.2 Monotonic Push and Pull

The local displacement diagrams for $\pm$ 10 ksi and working stress level are shown in Fig. 4.32. Unlike the behavior for pulling on one end only, where the whole bar did not start moving until a very advanced stage of loading, the push-pull loading case showed the entire bar moved even at working load cycles (see Figs. 4.32(a) to Figs. 4.32(d)). This is additional evidence in support of the phenomenon observed in the corresponding bond-distribution diagram of Figs. 4.27(a) to 4.27(d) where the bond stress had developed everywhere along the bar. Permanent displacement upon return to zero load also appeared (see LP 4F and 7 in Figs. 4.32(c) and 4.32(d)), indicating damage had already occurred in the surrounding concrete boundary layer.

The local displacement diagrams at yield and post-yield range are shown in Figs. 4.32(e) to 4.32(h). As anticipated, a larger displacement occurred as applied load increased. For example, at yield there was no point in the rebar that moved less than .01 in., as shown in Fig. 4.32(e), while at 80 ksi, the minimum local displacement was double that at yield (LP 7K) as shown in Figs. 4.32(e) and 4.32(f)).

Although the magnitude of applied load at the rebar protruding ends was equal, the displacement in the region near the pulled end was far in excess of that within the pushed end region. This is because a larger length of rebar is strained past yielding at the pull end than

at the push end (see the corresponding strain distribution diagram in Figs. 4.19(f) to 4.19(h)). The pull-through of the rebar was initiated at LP 9Z in Fig. 4.19(g). After the failure stage, the entire bar displaced almost as a rigid body, as reflected by the local displacement curves of LP 9Z, 10 0 and 10 Y as a series of parallel lines (Fig. 4.32(g)).

4.7.2 Cyclic Push-Pull Specimens

The local displacement diagrams for cyclic loading are illustrated in Fig. 4.33. These diagrams correspond to the strain, stress and bond stress distribution diagrams previously presented in Fig. 4.21. The first two local displacement diagrams, Fig. 4.33(a) and 4.33(b), are for $\pm$ 40 ksi level. Note that at zero load, LP 6, the whole bar has already displaced from its original undisturbed position as a result of subjecting the bar to $\pm$ 10 ksi and working stress cycles prior to the $\pm$ 40 ksi cycles. At the $\pm$ 40 ksi peaks, the minimum local displacement at any point in the rebar already well exceeded $\pm$ .005 in.

There was little difference in the shape of the local displacement diagrams corresponding to $\pm$ 40 ksi and + 55 ksi stress levels, as shown in Figs. 4.33(c) and 4.33(d). The only difference was that the values of these displacements were larger for the $\pm$ 55 ksi cycles. The local displacements at the peak stress, LP 9D, 9K, 11D and 11K, exceeded 0.007 in.

Local displacement diagrams for first-yielding and post-yielding cycles are shown in Figs. 4.33(e) to 4.33(h). Unlike monotonic loading, where the local displacements near the pulled end were considerably larger than those of the pushed end, cyclic loading produced almost equal displacements at opposing ends. An explanation for this difference

is given in the strain distribution diagrams in Figs. 4.21(e) to 4.21(h): there was a much more extensive straining of the bar well beyond yielding near the pulled end than near the pushed end in the monotonic loading case, and the lengths of yielding near the ends were almost the same for cyclic loading. The maximum strength of the block was reached between the load points LP 19E and LP 20E (see Figs. 4.33(h)). Although LP 19E and 20E showed equal local displacement at the pulled end, the local displacement inside the block for LP 20E was considerably larger than for LP 19E.

4.8 SUMMARY

Because of the lengthy presentation of the experimental results, a brief summary of the significant results are necessary to put them in perspective.

For monotonic loading, cone formations appeared at the pulled end as early as the 40 ksi level, while no such cracks appeared at the pushed end (for push-pull specimen) or free end (for pull-only specimens) surfaces. Cone formations occurred on both of the exposed ends of cyclic loading specimens at a stress level of about 40 to 55 ksi.

Three different concrete regions, classified according to different bond behavior, can be identified, i.e., unconfined region (lying mostly in the column cover near the pull end), confined region (inside the reinforcing cage) and pushed-end region (near the pushed end). The ultimate bond strengths were found to be about 1.0, 2.1 and 4.0 ksi for unconfined, confined and pushed-end regions, respectively. High values of bond strength at the pushed ends give an indication of the good bond of a bar embedded in confined concrete under compressive loading. For

ABSTRACT

Under reversing lateral loads, such as occur during a major earthquake, cracks can form at column faces of continuous beams framing into joints of moment-resisting frames. Reinforcement may be strained well into the inelastic range and cracks will tend to remain open. During cyclic loading, continuous longitudinal beam bars can be simultaneously pushed and pulled from opposite sides of a column, creating a severe demand on anchorage.

The performance of anchorage under conditions similar to those described above was tested experimentally. Seventeen specimens of single bars embedded in well-confined column stubs were tested under push-pull or only pull loadings. Monotonic as well as cyclic loadings were prescribed. Bar sizes #6, #8, and #10 were tested. The tendency of bond to degrade under cyclic loading was observed. Results obtained from these tests provide essential data from which a mathematical model for predicting the bond behavior that leads to the pull out or push in of a rebar is formulated.

Finite element techniques are employed to predict the cracking behavior of the surrounding concrete since this behavior could not be deduced from the experimental data. The superior performance of a bar subjected to a push load is noted. The discrepancy between the predicted and experimental results is evaluated, and the limitations of the material models used in the present analysis are described.

A model for the hysteretic behavior of a bond element when subjected to generalized loading histories is established from the experimental results. The reliability of the model for monotonic and full reversal loading histories is encouraging.

monotonic loading, degradation in bond starts to be significant after the rebar reaches yielding. A reduction in bar diameter and, hence, bearing area plays a major role in monotonic bond deterioration.

For cyclic loading, deterioration in stiffness appeared as early as working load range. Slippage over the entire bar was recorded at relatively low stresses, in the range between 24 and 40 ksi. An increase in loading intensity and number of repeating cycles led to a decrease in strength and increase in pinching of the force-deformation loops. The fractured-away cones formed at both ends of the specimens at about 40 ksi, causing a considerable reduction in the effective anchored length, leaving confined cores to resist the applied force. For the loading history used in these experiments, the ultimate bond strength in unconfined and confined regions was found to be about .8 and 1.6 ksi, respectively.

The experimental results indicate clearly that the bar embedded in a column does pull out. Table 4.5 gives an example of an approximate value of fixed-end rotation at yield for 20 in. effective beam depth (d-d'). Note that for monotonic loading the contribution from pull-out ranges from .001 to .0026 rad., or 20 to 60 percent of .005 story index commonly used; furthermore, in cyclic loading the contributions are greater, ranging from .0022 to .0034 which is 25 to 70 percent of the drift index. The substantial amount of fixed-end rotation from pull-out clearly indicates a need to reexamine the assumption that beam-column joints of moment resisting R/C frames are rigid.

5. EVALUATION OF TEST RESULTS

5.1 GENERAL

In Chapter 4 the general results and the behavior of the bond test specimens have been presented and described in detail. No attempt has been made either to evaluate the bond performance under the influence of different parameters or to give a full explanation for the differences in response. In this chapter, an attempt is made to evaluate bond behavior under the influences of:

(1) pull-only and push-pull loading conditions,

(2) loading histories, restricted to the case of monotonic and full or semi-full reversal loading,

(3) different bar size, and

(4) grooved and ungrooved bars.

5.2 PULL ONLY AND PUSH-PULL LOADINGS

As pointed out in Chapter 1, beam bars passing through an interior column joint can be subjected, under extreme loading conditions, to two general types of loading: pull-only and pull and simultaneous push with equal magnitude in force. These two loading conditions estimate upper and lower bounds on the performance of an anchored bar in an interior beam column connection.

It should be noted at this point that no test results for cyclic bond tests involving pull loads only have been presented here. The presentation on pull-only loading is restricted to a monotonic load history.

The most important characteristics for comparison between the pull-only and pull-push loading condition is the total stress-displacement at pulled end curve, f_{s1}-δ_1, as presented in Fig. 5.1. A comparison of the initial stiffness, pull-out at maximum strength, maximum strength and energy absorption capacity, as indicated by the f_{s1}-δ_1 curves follows.

(1) Initial stiffness.--There is virtually no effect of the pushing force C, on the initial stiffness of the f_{s1}-δ_1 curve for the push-pull loading prior to yielding. To explain this, and the ensuing similarity of the two types of loading in the early stages, the internal responses are studied at loading point A (60 ksi) where the two curves almost coincide, and at loading point B (85 ksi) where the two curves start to deviate.

At point A, the similarity of the bond stress, strain distribution for the pull-only and push-pull case within 15 in. from the pulled end, Fig. 5.2(a) and 5.2(b), supports the coincidence of the two f_{s1}-δ_1 curves; the local displacement diagrams for the push-pull case, however, show a slightly consistently higher value (Fig. 5.2(c)). The larger local displacement developed inside the block of the push-pull loading indicates that more damage is introduced in the surrounding concrete of the push-pull case than to that of the pull-only. Although its effect is not apparent at this stage (60 ksi), the deformation at maximum strength of the push-pull case is considerably reduced in comparison with that of pull-only. A similarity of the distribution curves within the stated 15 in. limit remained valid at point B, as shown in Figs. 5.3(a), 5.3(b) and 5.3(c). This means that up to the stress level at B, 85 ksi,

the interference from the pushing end upon the region in tension was minimal; the forces applied to the bar at the push end were transferred by the internal bond resistance within a relatively short embedment length near pushed end. This study tends to suggest that for the 25 in. column block, about 83 percent of development length required by ACI Code [23] (embedded length for grade 60, #8 bar is about 30 in.), the responses at the pull end and push end are independent up to yielding.

(2) Strength and Ductility.--Apparently from a strength point of view, the application of a pushing load in addition to a pulling load did not have a significant effect. The maximum strengths of the pull-only and push-pull specimens at failure due to pull through were 102 and 95 ksi, respectively. Meanwhile, the pull-out ductility or deformation capacity prior to failure was greatly influenced by the addition of a pushing force. As shown in Fig. 5.1, the pull-out at maximum strength was almost twice that of the push-pull case.

One of the reasons that push-pull loading cannot sustain as large a deformation as pull-only loading may be due to the presence of higher bond stress in the push-pull boundary layer concrete (see Fig. 5.4(a). Higher local bond stresses would cause more damage in the layer. This was also confirmed by the local displacement data, Fig. 5.3(c), pointed out earlier, and Fig. 5.4(b), where a significant displacement of the whole bar for push-pull loading was observed while the free (unloaded) end of pull-only remained practically stationary.

(3) Energy Absorption Capacity.--For the pull-only specimen, the absorbed energy is represented by the area under the f_{s1}-δ_1 curve only, whereas for push-pull loading, the absorbed energy is the sum of

the areas under both the f_{s1}-δ_1 and the f_{s2}-δ_2 curves. Examining the curve in Fig. 5.1 shows that there is not much difference in the energy absorption capacity at the pull end of the two cases up to about 0.45 in. displacement. At 1 in. displacement, the absorbed energy of the push-pull case of the pull end is about 72 percent of the pull-only (pull-only absorbed 64.5 k-in. at 1 in. displacement). However, in terms of total absorbed energy, the two cases show a slight difference, even at 1 in. displacement, since the contribution of energy absorbed at push end of the push-pull case compensates for the discrepancy (see f_{s2}-δ_2 in Fig. 4.10).

5.3 EFFECT OF CYCLIC LOADING

The effect of cyclic loading on bond behavior is best demonstrated by a comparison with monotonic loading, as is done in Figures 5.5(a) to 5.5(e). The following presentation includes the effects of cyclic loading on different bar sizes (#6, #8, and #10) and varying column widths (from 15 in. to 25 in.). The study indicated that:

(1) Cyclic load causes stiffness degradation characterized by pinched hysteresis loops, as early as in the working load range. The larger the amplitude and the greater the number of cycles of reversal loading, the more the degradation in stiffness resulted.

(2) Gradual incremental cyclic loading causes a decrease in the maximum pull-through capacity (see Table 5.1). The maximum strength of cyclic loading ranged from 71 to 91 percent of the monotonic strength.

(3) The deformability at maximum strength (ductility) was considerably reduced by severe reversal loading. As can be seen in

Table 5.1, no cases were observed where monotonically loaded specimens would pull through at displacement less than that of cyclic loading.

To identify the cause of the discrepancy between the two types of loadings, the typical bond stress and displacement variation at different locations along the bar are compared at stress levels prior to yielding, at yielding level and at pull-through. For the pre-yielding and yielding range, it is clearly indicated that local displacement along the bar in cyclic loading was consistently larger than the local displacement under monotonic loading (Fig. 5.7); however, there is no significant difference in bond stress distribution at the pull-through stress level (Fig. 5.6). Larger local movement in cyclic loading implies more damage being introduced into the surrounding concrete. The smaller pull-through strength of cyclic loading in comparison with monotonic is reflected in Fig. 5.8(a) where the maximum bond stress along the rebar was reached. Excepting the region near pulled end, the cyclic bond stress capacity for the rest of the bar was considerably less.

The smaller deformability under cyclic loading at maximum pull through load is again shown in Fig. 5.8(b). Further, the local displacements that the rebar in contact with concrete experiences prior to the drop in resistance when subjected to cyclic loading is considerably lower than for monotonic loading.

5.4 EFFECT OF BAR SIZE

The experimental results include the use of different bar sizes: #6, #8 and #10. Note that the dimensions of the lugs (their heights and spacings) of the bar are not proportional to the bar diameter (see

Table 5.2). For instance, the proportion of the bar dimensions of the #6 bar with respect to the #8 bar can vary from 0.58 for lug spacing to 0.75 for bar diameter. Since the bar geometry is not in proportion, the law of similitude cannot be directly applied in obtaining a result from one bar to another. The comparisons here are limited to the case of monotonically-increasing loading. This eliminates the effect of loading sequences which, for the cyclic tests, were slightly different.

As a general observation from these experiments, the smaller the bar size, the higher the average bond strength that could be developed--an observation that agrees with previous research such as that in Reference 6. Figures 5.9(a), 5.9(b) and 5.10 show this general trend, i.e., the bond strength of the #8 bar is about 87 percent of the #6 bar and the bond strength of the #10 bar is about 85 percent of the #8 bar. Further examination of the bond stress distribution of the #8 and #10 bars at pull through confirm the above observation (see Fig. 5.10).

The smaller bar diameters tend to show a higher stiffness during early stages of loading, i.e., for a given bond stress, the larger the bar size the greater the end displacements. This type of response is further explained by studying the distribution curves at the bond stress 1.81 ksi (at point A in Fig. 5.9(b)). As expected, since the average bond stress is equal, the bond stress curve showed a similar distribution, Fig. 5.11(a). A difference appears in the local displacement diagram where the result of the #10 bar shows a consistently higher value throughout the bar length (see Fig. 5.11(b)).

5.5 EFFECT OF GROOVES

As indicated in Chapter 3, in order to install strain gages to measure the strain distribution, the rebars had to be grooved. By doing so, the effective perimeter and the area of the bar are reduced. Such a reduction might significantly distort the bond performance of the grooved bar from that of the ungrooved bar. Thus, it is essential to be able to relate the behavior of the two, since in actual construction the ungrooved bars are used.

In order to evaluate the effect of grooves on the rebar, a realistic perimeter, Σ_o, reflecting the bond mechanism must be used in the computation of bond stress (as defined in Eq. 4.3). In the deformed bar the stress transfer between the steel and concrete takes place through two major mechanisms: the bearing mechanism (crushing of concrete at the lug toes) and the direct shear-off mechanism as shown in Fig. 5.12(a) and 5.12(b), respectively.

For the bearing failure mode, the bearing area of a lug plays the major role in the bond mechanism. The effective perimeter, Σ_o, in this case corresponds to the total perimeter less the width of the longitudinal rib for the ungrooved bar (see Fig. 5.12(a)) and less the widths of the grooves for the grooved section. Table 5.3(a) gives the effect of grooves on the bearing area. Note that variable $\frac{A_s}{\Sigma_o}$ is the major variable for evaluating the influence of grooves (see Eq. 4.3). For #8 and #10 bars the grooves lead to a distortion of under 10 percent, while 11 percent distortion results for the #6 grooved bar.

For direct shear failure, the effective perimeter, Σ_o, of the grooved and ungrooved section is practically the same as shown in

Fig. 5.12(b). This is because the shear off will take place along the outermost limit of the bar. The indication of the distortion introduced by the grooves for the shearing mechanism is the difference in cross-sectional area A_s. Table 5.3(b) lists the distortion for the different bar sizes. Since the groove sizes are all the same, the #10 bar section has the least distorted section (.959 of the ungrooved section), while the #6 bar gives the most distorted section (.847 of the ungrooved section).

This study indicates that there could be a variation of 0.847 to 1.11 between the bond stress of the grooved and ungrooved bar. The experimental results of the bond stress-displacement curves for the ungrooved and grooved sections somewhat confirms the above study (see Figs. 5.13 to 5.15). The bond stress is based on the bearing effective perimeter for the ungrooved and the grooved widths for the grooved section). The correlation for #6 is fair at the earlier part of the response and is better for the advanced stage of loading (see Fig. 5.13). A reasonably good agreement through the whole range of loading is observed for the #8 and #10 bars (see Fig. 5.14 and 5.15).

6. ANALYTICAL STUDY OF BOND BEHAVIOR

6.1 GENERAL

As pointed out by Bresler and Bertero [13], the bond behavior along anchored bars is directly affected by the development of internal cracking in the concrete boundary layer around the rebar. This behavior within the concrete boundary layers, however, does not lend itself to experimental observation. Major technical difficulties arise in attempting to measure this behavior without, at the same time, altering that behavior. Therefore, a nonlinear analytical simulation of this behavior was initiated; the existing experimental data obtained thus far provides an opportunity to assess the accuracy of prediction of the computer simulation scheme that was devised.

A nonlinear finite element analysis program, NONPLAX [26], which can take into account the effect of concrete cracking, was used in the present study. Sophisticated as the program was, it lacked certain features necessary for this study. First of all, the program could handle only monotonically increasing loads. Secondly, the main embedded steel had to remain in the elastic range. Because of these limitations, the program was applied only to monotonic push-pull and monotonic pull-only loading, Specimen No. 13 and Specimen No. 3, respectively. The significance of the results are discussed and suggestions for further research are given.

6.2 FINITE ELEMENT MODEL OF BOND SPECIMEN

To study the behavior of bond as displayed in the experiments, the axisymmetric model shown in Fig. 6.1 was adopted. The model consisted

of a #8 bar embedded in a concrete cylinder 25 in. long. The radius of the cylinder was 6.5 in. (13D) with its boundary restrained from displacements. It was believed that with a cylinder of this size the boundary support condition would not significantly affect results obtained for local stress in the steel-concrete interface layers where internal cracking was expected to originate. The external forces could be exerted as a pulling force on one protruding end of the rebar or as a pulling force on one end and a simultaneous pushing on the other to simulate the pull-only or pull-push loading as prescribed in the experiments.

6.3 FINITE ELEMENT MESH AND MATHEMATICAL FORMULATION

The finite element mesh of the deformed #8 bar and the surrounding concrete are shown in Fig. 6.2. The finite element used to represent the steel bar and concrete prism was the 4-node linear strain axisymmetric quadrilateral, (see Fig. 6.3). This element can also be collapsed into a triangular element by specifying two nodes at the same location. It should be noted that the exact shape of the steel lugs could not be simulated with this mesh because the embedded length of the rebar was too large in comparison to the lug size. Otherwise, a great number of elements must be included to describe the geometry of the specimen realistically, making computational costs prohibitive. In the average sense, the finite element meshes adopted retained all the significant bond behavior and yet required a moderate computation effort. The compatibility in the nodal displacement of the rebar-concrete layer common nodes closely simulated the wedging action of the steel lug on the surrounding concrete.

For the 4-node linear-strain axisymmetric isoparametric quadrilateral element (Fig. 6.3), the relationship between the displacement field inside the element (u_r, u_z) and the displacement at nodes (u_{ri}, u_{zi}) is given by:

$$u_r = \sum_{i=1}^{4} h_i \, u_{ri} \tag{6.1}$$

$$u_z = \sum_{i=1}^{4} h_i \, u_{zi} \tag{6.2}$$

where the displacement interpolation functions, h_i, are:

$$h_1 = \frac{1}{4} (1-s) (1-t)$$

$$h_2 = \frac{1}{4} (1+s) (1-t)$$

$$h_3 = \frac{1}{4} (1+s) (1+t)$$

$$h_4 = \frac{1}{4} (1-s) (1+t)$$

where s and t are local element coordinates. In mapping the local coordinates to r-z structural coordinates, identical interpolation functions are used:

$$r = \sum_{i=1}^{4} h_i \, r_i \tag{6.3}$$

$$z = \sum_{i=1}^{4} h_i \, z_i \tag{6.4}$$

In the axisymmetric problem, the shear strains, $\gamma_{r\theta}$ and $\gamma_{z\theta}$, are zero, using symmetry. The relationship between the non-zero strains and the displacement is:

$$\underline{\varepsilon} = \begin{Bmatrix} \varepsilon_{zz} \\ \varepsilon_{rr} \\ \varepsilon_{\theta\theta} \\ \gamma_{rz} \end{Bmatrix} = \begin{Bmatrix} u_{z,z}^{*} \\ u_{r,r} \\ u_r/r \\ u_r/z + u_{z,r} \end{Bmatrix} \tag{6.5}$$

Now substitute Eq. 6.1 into Eq. 6.5 to obtain the strain and nodal displacement relationships:

$$\underline{\varepsilon} = \underline{H}(s,t)\underline{u} = \begin{bmatrix} \underline{H},z & \underline{0} \\ \underline{0} & \underline{H},r \\ \underline{0} & \underline{H}/r \\ \underline{H},r & \underline{H},z \end{bmatrix} \begin{Bmatrix} u_z \\ u_r \end{Bmatrix}$$

where u_z and u_r are nodal displacement vectors, and

$$\underline{H} = [h_1 \quad h_2 \quad h_3 \quad h_4]$$

$$\underline{H},z = [h_{1,z} \; h_{2,z} \; h_{3,z} \; h_{4,z}]$$

$$\underline{h},r = [h_{1,r} \; h_{2,r} \; h_{3,r} \; h_{4,r}]$$

The internal stresses, σ_{rr}, σ_{zz}, $\sigma_{\theta\theta}$, and σ_{rz} (Fig. 6.3), are computed by multiplying the strain vector, $\underline{\varepsilon}$ (Eq. (6.6)), by the appropriate material property matrices specified in Sect. 6.4.

6.4 MATERIAL MODEL FOR CONCRETE

The basic assumptions for the concrete material behavior are listed below (see Section 6.11):

(1) Under uniaxial stress, concrete is assumed to be elasto-perfectly plastic in compression where the elastic limit is defined by f_c', and to fail in compression when reaching a specified crushing

---

*$u_{z,z} = \dfrac{\partial u_z}{\partial z}$

strain.* Cracking (tensile failure) is assumed to occur as the principal tensile stress reaches a specified tensile strength* and the internal element force in the cracked direction is redistributed to the remainder of the structure.

(2) Under a triaxial stress, cracking is allowed to occur at the principal stress directions in the r-z plane and in the hoop direction (Fig. 6.3). Thus,

Elastic, uncracked concrete element:

$$\begin{bmatrix} \sigma_{rr} \\ \sigma_{zz} \\ \sigma_{\theta\theta} \\ \sigma_{rz} \end{bmatrix} = \frac{E_c}{(1+\nu)(1-2\nu)} \begin{bmatrix} 1-\nu & \nu & \nu & 0 \\ & 1-\nu & \nu & 0 \\ & & \nu & 0 \\ \text{sym} & & & \frac{1-2\nu}{2} \end{bmatrix} \begin{bmatrix} \varepsilon_{rr} \\ \varepsilon_{zz} \\ \varepsilon_{\theta\theta} \\ \varepsilon_{rz} \end{bmatrix} \tag{6.7}$$

Concrete element cracked perpendicular to principal stress direction 1 in the r-z plane:

$$\begin{bmatrix} \sigma_1 \\ \sigma_2 \\ \sigma_3 \\ \sigma_{12} \end{bmatrix} = \frac{E_c}{1-\nu^2} \begin{bmatrix} 0 & 0 & 0 & 0 \\ & 1 & 0 & 0 \\ & & 1 & 0 \\ \text{sym} & & & \frac{G^*(1-\nu^2)}{E_c} \end{bmatrix} \begin{bmatrix} \varepsilon_1 \\ \varepsilon_2 \\ \varepsilon_3 \\ \gamma_{12} \end{bmatrix} \tag{6.8}$$

where G^* is the shear modulus of the cracked element = 0.0;

Concrete element cracked perpendicular to principal stress direction 2 in the r-z plane:

$$\begin{bmatrix} \sigma_1 \\ \sigma_2 \\ \sigma_3 \\ \sigma_{12} \end{bmatrix} = \frac{E_c}{1-\nu^2} \begin{bmatrix} 1 & 0 & 0 & 0 \\ & 0 & 0 & 0 \\ & & 1 & 0 \\ \text{sym} & & & \frac{G^*(1-\nu^2)}{E_c} \end{bmatrix} \begin{bmatrix} \varepsilon_1 \\ \varepsilon_2 \\ \varepsilon_3 \\ \gamma_{12} \end{bmatrix} \tag{6.9}$$

*For the specified values used in the analysis, see Section 6.6.

Concrete cracked in the hoop direction:

$$\begin{Bmatrix} \sigma_{rr} \\ \sigma_{zz} \\ \sigma_{\theta\theta} \\ \sigma_{rz} \end{Bmatrix} = \frac{E_c}{1-\nu^2} \begin{bmatrix} 1 & \nu & 0 & 0 \\ & 1 & 0 & 0 \\ & & 0 & 0 \\ & & & G \end{bmatrix} \begin{Bmatrix} \varepsilon_{rr} \\ \varepsilon_{zz} \\ \varepsilon_{\theta\theta} \\ \gamma_{rz} \end{Bmatrix} \tag{6.10}$$

6.5 MATERIAL MODEL FOR REINFORCING BAR

The bar was modeled by plane stress elements. A linear-elastic stress-strain relationship (Eq. (6.7)) was used. The steel was assumed to remain in the elastic range throughout the loading applications.

6.6 MATERIAL PROPERTIES OF CONCRETE AND REBAR USED IN THE ANALYSIS

The material properties used in the analysis work were typical of those of the bond tests. The modulus of rupture of concrete (490 psi) was used for determining the cracking strength of concrete elements. The other mechanical characteristics of the concrete were its crushing strength of 4500 psi, crushing strain of .0025, elastic stiffness of 3,380,000 psi and Poisson's ratio of 0.15. The mechanical properties of elastic steel were the Young's modulus of 29 x 10^3 ksi and a Poisson ratio of 0.30.

6.7 NONLINEAR ANALYSIS SCHEME

The standard step-by-step nonlinear analysis solution procedure was employed. For each loading increment, Newton-Raphson iterations were carried out using a force convergence criteria. The structural stiffness was reformed at each iteration for speeding up convergence.

6.8 ANALYTICAL RESULTS

The basic results in bond behavior, paralleling those obtained in the experiments, are presented. In addition, the behavior of the surrounding layer of concrete which was unobtainable from the tests is given. The results of two cases are presented: monotonic push-pull and monotonic pull-only.

6.8.1 Monotonic Push-Pull Specimen

The load deformation diagram, f_{s1}-δ_1, at the pull end is shown in Fig. 6.4. Because cracking developed in the concrete, a nonlinear response curve resulted.

Sequence of internal cracking as predicted by the analytical work is shown in Fig. 6.5. Listing of stresses, f_{s1}-f_{s2}, at cracks is also given in the figure. Note that from zero to 60 ksi level all the cracking is diagonally inclined. No splitting tension cracks formed. This deviation from the probable real behavior presented in section 4.2 may be due to the size of finite element meshes used; they may be too coarse to detect the splitting cracks which are likely to concentrate only at the pulled surfaces. The first crack formed near the pulled end at the stress of 5 ksi. The second, third and fourth cracks are also formed near the pulled end at 11.8, 23, and 24.5 ksi, respectively. Note that 24.5 ksi (about working range) cracking already covers half of the embedment length. Cracks near the push end did not form until 25 ksi and required the stress of 35 ksi to form another crack (see crack no. (6) in Fig. 6.5). The late formation of the crack near the push end indicates the better performance of this region. The cone formation at the pull end can be quantitatively identified by the continuation of cracking of (7) to (1) at 37 ksi.

Fig. 6.6 shows the stress distribution in concrete. As expected, along most of the embedment length the concrete was under compressive stress, while a tension stress existed for only a small length near the pull end. It should be noted that a compressive state of stress in the region near the pull end was also possible. This occurred primarily due to tensile cracking of the concrete that allowed the concrete elements to arrange themselves to transfer load through compression strut action. Even at 55 ksi the maximum compressive stress in concrete along the rebar is less than 2.4 ksi which is about half of the concrete compressive strength; therefore no crushing in concrete is developed.

Stress distribution along the rebar is shown in Fig. 6.7. The corresponding strain distribution diagram is identical to the stress diagram, except that the vertical stress scale is proportionally reduced by a factor of $1/E_s$. As expected, the result indicates high local rebar stress concentrations near the loaded ends of the cylinder. Transfer of force from rebar to immediately adjacent concrete through bonding action is shown in Fig. 6.8. Again most of the force transfer occurs around the applied loaded end and gradually lessens toward the middle of the block. A dropping in the bond stress at about 1 in. from the pulled end (at stress 39 ksi, see Fig. 6.8) was due to cracking, while no reduction occurred at the pushed end due to the formation of cracks.

6.8.2 Monotonic Pull Only Specimen

Results similar to the set given above for push-pull loading were obtained. For pull-only loading, only a few selected results are presented, i.e., cracking sequences in Fig. 6.9, rebar stress distribution in Fig. 6.10, and bond stress distributions in Fig. 6.11.

6.9 COMPARISON BETWEEN EXPERIMENTAL AND ANALYTICAL RESULTS

Although cracking in the concrete was included in formulating the mathematical model for concrete, the analytical results show a stiffer response than that obtained experimentally. This is clearly indicated in Fig. 6.12(a) for push-pull loading, and Fig. 6.12(b) for pull-only. The underlying cause of a stiffer response is primarily due to the concrete model used. It produces a higher element stiffness. This can be seen from the compared stress-strain diagrams shown in Fig. 6.13 where the analytical results give a more rapid rate of attenuation than the tests.

In spite of a stiffer concrete element, the general trend of bond distribution could be fairly well predicted (see Fig. 6.14). Moderate discrepancy occurs at the region close to the pushed end.

6.10 SUMMARY OF ANALYTICAL STUDY

The analytical results clearly indicate that cracking in the concrete surrounding the bar can initiate at stress levels in the steel as low as 5 ksi, about one-fifth of working stress. Diagonal cracking can occur at regions close to both the pulled and pushed ends, although a much higher force is required to produce a first crack near the push end. The concrete cracking model is capable of reproducing the loss of bond due to cracking rather well; therefore a reasonably accurate picture of concrete strain distribution close to the rebar, unobtainable from the experiment, could be obtained from this analytical study. The present method of handling cracking in concrete must be considerably modified if it will be used for predicting cyclic loading. The main limitation lies in the lack of a crack width history which is required

to prescribe the opening and closing states of the cracks under cyclic-reversal loading of the model.

6.11 RECOMMENDATIONS FOR FURTHER ANALYTICAL STUDY

(1) To obtain more significant results, the NONPLAX program must be modified to incorporate the yielding of the rebar. This is essential because the major degradation in bond occurs at and after the yielding.

(2) Obviously, from this study, a better correlation between experimental and analytical results can be obtained by prescribing a softer material around the rebar such as the approach employed by Bresler and Bertero (Ref. 13). Softer mechanical properties should be established.

7. FORMULATION OF BOND MODEL AND ITS APPLICATION

7.1 GENERAL

As pointed out in the introduction of Chapter 1 and in the results from the bond tests reported in Chapter 4, the fixed-end rotation of an interior joint caused by the slippages of the main beam bars can be an important source of stiffness degradation in the lateral load-deformation relationship of moment-resisting frame. This fixed-end rotation must be included in an analysis of building response; otherwise, a gross error in predictions will result.

The fixed-end rotation caused by the pull-out and push-in of a bar at an interior beam column joint has been described in detail in Chapter 1 (see Fig. 1.4). In short, the fixed-end rotations are defined as

$$\theta_{FE} = \frac{|\delta_1| + |\delta_2|}{(d-d')} \tag{7.1}$$

where δ_1 and δ_2 are the pulled out and pushed in displacements at the column faces measured with respect to column axis, and d-d' is approximately the distance from the top to the bottom reinforcement. Equation 7.1 clearly suggests that the first step toward calculation of the rotation is to obtain δ_1 and δ_2 from a bar embedded in a well confined block as shown in Fig. 7.1. In this chapter, an attempt is made to mathematically formulate bond elements and to devise an analytical procedure to calculate the embedded bar load-displacement relations at the exposed ends. The analytical method is useful in predicting the load-deformation relation of a bar embedded in a column block.

7.2 REVIEW OF MATHEMATICAL MODELING OF BOND

The problem of predicting the amount of pull-out and push-in of an embedded bar has received considerable attention by researchers such as Morita and Kaku [19], Houde [11], and Hassan and Hawkins [22].

Houde [11], based on his experimental results, proposed a local bond-slip relation for monotonic loading. His analytical finite element layout is shown in Fig. 7.2 where the 4 node-quadrilateral elements for the steel and the surrounding concrete are connected by one degree of freedom bond link elements. Considering the large number of degrees of freedom in this type of idealization, the cost of computation can be prohibitively high. Therefore, the analytical work using this approach has been limited to the monotonic working load range, where initiation of cracking in concrete controls the behavior.

An approach similar to Houde was taken by Morita [19]. In Morita's approach, the interaction between the steel and concrete and deformation of the surrounding concrete are lumped together, resulting in a one-dimensional element. A uniaxial truss element is employed for steel. The idealization of the bar embedded in concrete block is shown in Fig. 7.3. The reliability of the proposed model was tested against experimental results of Bresler and Bertero [13]. The model is able to handle a generalized loading history.

Hassan and Hawkins [22] took a rather different approach to the problem. Instead of modeling the pull-out specimen by an assemblage of steel, concrete and bond elements as employed by the previous investigators, the bond stress distributions along the bar were assumed. The concrete along the bar was subdivided into three regions: elastic uncracked, cracked and extensively cracked regions. A bond stress

distribution taking into consideration the number of cycles as well as displacement ductilities associated with each region was assigned. A cyclic f_s-ε_s relation was also incorporated in the analysis. The validity of this approach was tested against experimental results.

7.3 IDEALIZATION OF BOND MODEL

The actual behavior of a bar embedded in a concrete block can be idealized as a round bar surrounded by an axisymmetric soft concrete layer as shown in Fig. 7.4. The deformation of concrete is assumed to occur in the soft layer only; the rest of the concrete block remains in an undeformed configuration. The layer is composed of many small elements strung together along the rebar. Each element has a thickness of t and a longitudinal length of ℓ_e (see Fig. 7.4(a)). Upon application of load at bar ends, the soft layer elements are stressed and deformed as shown in Fig. 7.4(b). Note that each element of the soft layer is acted on by the shearing stress τ resulting in the shearing deformation γ. The behavior of the shear element, therefore, is described by the τ-γ relation. This relation will be established on the basis of the obtained experimental data.

7.4 EXPERIMENTAL τ-γ CURVES

The τ-γ curves for the idealized shear elements located along the embedded bar can be determined from the experiments conducted as follows:

(1) A shear stress, τ_x, acting on the shear elements at distance x from the exposed face [Fig. 7.5] is computed by

$$\tau_x = \frac{\Delta f_s \, A_s}{\Sigma_o \, \ell_e} \tag{7.2}$$

where Δf_s is the difference in the rebar stresses at the two faces of the element; A_s and Σ_o are the area and perimeter of the bar section; and ℓ_e is the length of the shear element. Δf_s is readily calculated from the stress distribution diagram (see section 4.4).

(2) A corresponding shear deformation, γ_x, (as shown in Fig. 7.4(b)), can be related to local displacement, δ_x, by

$$\gamma_x = \frac{\delta_x}{t} \tag{7.3}$$

where t is the layer thickness. δ_x is defined in section 4.6 as the local displacement of the bar.

As has been pointed out in Chapter 4, three types of bond mechanisms can be identified for push-pull loading of an embedded bar: unconfined, confined and pushed end region. Consequently, there are also three types of τ-γ curves associated with these three different regions. The average τ-γ curves for these regions are illustrated in Fig. 7.6 for monotonic loading and Fig. 7.7 for cyclic loading.

7.5 THEORY OF BOND RESISTANCE MECHANISM

The purpose of developing a theory for bond mechanism is two fold:

(1) To understand the basic mechanism of bond resistance so that steps can be taken to improve the performance of an anchored bar by appropriate detailing.

(2) To form a rational basis for developing hysteretic rules for the bond behavior under generalized loading. This allows the systematic development of an analytical method for predicting pull-out and push-in of a bar.

Prior to presenting the mechanism of bond, a brief review of past developments in the theory is given. For the type of reinforcement used in the present tests on deformed bars, bond is mainly due to the bearing of bar lugs on concrete and the strength of concrete between lugs. Some of the bond resistance comes from friction and from the chemical adhesion between the concrete and bar surface [6]. However, it has been demonstrated experimentally by Goto [10] that even a few repeating cycles at low stress level are adequate to destroy the chemical bond.

The variables that have been found to affect bond effectiveness are local stress level, history of loading, lug geometry (height, spacing, thickness and inclination of deformations), size of bar, confinement (offered either by concrete cover or by main and secondary reinforcement), properties of the concrete surrounding the bar (i.e., tensile and compressive concrete strengths), type of aggregate (normal weight or lightweight) and external forces such as axial loads, interaction between bond and diagonal tension and dowel action. Among these parameters, the effect of loading history has received the most attention in the present study. The general conclusions on the effect of cyclic loading, as reported in Chapter 5, can be summarized as follows:

(1) Bond deterioration is sensitive to the previous loading history. The greater the magnitude of the previous peak stress, the greater the disruption of the local bond and the less effective the bond at lower stress levels [13, 17 and 22].

(2) A limited number of repeated loading and unloading cycles in tension, below the proportional limit of the steel, does not induce appreciable bond deterioration. However, once the steel has undergone several complete stress reversals from tension to compression, bond deterioration can be readily observed [13,17].

A theoretical explanation of the bond deterioration mechanism under repeating tension loading and unloading has been proposed by Bresler and Bertero [13] as a failure in the concrete boundary layer adjacent to the steel-concrete interface. This failure occurs when the stress reaches a critical value and local fracture and inelastic deformation take place. Damage to the concrete boundary layer from previous loading tends to accumulate and is irreversible. The actual physical bond failure mechanism has been identified by Goto [10]. Ma [9], based on the experimental results of Morita, has proposed a bond deterioration mechanism for cyclic-reversal loading.

The theories developed so far are strictly applicable to unconfined concrete. To extend these theories to apply to a rebar embedded in a typical well-confined beam-column joint requires some modification which will be presented below.

For convenience in presentation, the bond mechanism associated with unconfined, confined and pushed-end regions as shown in Fig. 4.28 will be separately described.

7.5.1 Bond Deterioration Mechanism Under Monotonic Loading

7.5.1.1 Unconfined Region

The deterioration of bond in an unconfined region has been described by Goto [10] and Ma [9] as inclined cracks initiating at relatively low stress at the point of contact between steel lug and concrete as shown in Fig. 7.8(a). With a sufficiently large amplitude of loading, the crack emerges at the exposed face of the column. Once this occurs, a cone-like piece of concrete comes loose from the rest of the concrete-block, and this will cause a sudden drop in bond resistance, as shown in Fig. 7.8(b). The hysteretic loop of this region is characterized by low bond strength and low ductility as reflected by an apparently brittle mode of failure.

7.5.1.2 Confined Region

A behavior similar to that occurring in the unconfined region repeats itself in the confined region at the early stages of loading, i.e., initiation of inclined cracks, as shown in Fig. 7.9(a). For further increases in applied load, instead of prolonging the crack lengths and enlarging the crack widths, the lengths and widths of cracks are arrested by the restraint offered by the presence of the transverse steel. A large imposed displacement will cause a progressive crushing at the points of contact and inelastic deformation in the cracked concrete which now transfer the wedging force by "strut" action (see Fig. 7.9(b)). Furthermore, the crushing of the concrete before the lugs leads to a reduction in the shear resisting area of concrete between lugs. Finally, with continuously diminishing shear area, the stress build up is so high that the concrete is sheared off. Note that the primary sources

of degradation of stiffness in this region derive from a combination of bearing failure, inelastic deformations of the concrete "strut" and reducing in the effective shearing area of the concrete. This results in a ductile response, as characterized by a gradually decaying curve after the maximum bond strength is reached. Its superior performance over the unconfined region, where diagonal cracking controls the behavior, is apparent in Fig. 7.6.

7.5.1.3 Pushed End Region

Unlike behavior within the unconfined and confined regions where the inclined cracks are generally formed at relatively low stress levels, the pushed-end region requires a higher load for crack initiation (see Section 6.8.1). Immediately after the cracks form, the crack length and size are limited because the applied pushing force induces compressive stresses that restrain further crack propagation. The displacement of the bar lugs induces crushing, inelastic deformation of compressed concrete and reduction in shearing area (see Fig. 7.10), without the extensive cracking that occurs in the confined region. Nevertheless, the pushed end region poses a distinct advantage over the unconfined and confined regions surrounding an end of a pulled bar, i.e., the expansion of the bar diameter that leads to an increase in bearing area between steel lug and concrete as well as an increase in the radial pressure induced by pushing the end of the bar. This pressure considerably increases the resistance against shear failure along the shear failure plane. Because of the benefits of the bar expansion in the pushed-end region, its load-deformation curve is very much superior to that of the other regions.

7.5.2 Bond Deterioration Mechanism Under Cyclic Loading

7.5.2.1 Unconfined Region

For the first half of the loading cycle A-B-C (see Fig. 7.11(a)), the response is exactly the same as described in section 7.5.1.1: the wedging of steel lugs against the inclined concrete cracks causes the wedge to rotate, producing a high radial pressure at the lug toe. Because the crack is irrecoverable, the radial pressure will not vanish, even after complete unloading (from C to D in Fig. 7.11(a)). At this stage there is a gap, Δ_{AD}, existing between the lug and surrounding concrete. A frictional resistance develops that hinders the rebar in moving from D to E. By applying a force large enough to overcome the frictional resistance, the gap, Δ_{AD}, can be closed. At G, the other face of the steel lug starts to contact with the concrete (see Fig. 7.11(b)). Due to the concrete blocking any further advancement of the bar lug, a sharp rise in stiffness of the hysteretic curve GH occurs. At H, new diagonal cracks start to form almost perpendicular to the old cracks, which at this stage are not yet fully closed. As loading proceeds to point I, the stiffness of the curve continuously degrades as a result of an extension of the new cracks and closing of the old, as shown in Fig. 7.11(c). With an adequately large imposed displacement, the path of the old and new cracks may join. Response under further loading is controlled by crushing at points of contact as well as inelastic deformation of the broken concrete. The wedging of the lug on the broken concrete recreates a locking effect similar to what was described earlier in this section.

A permanent deformation is created upon complete unloading from point I to point J (see Fig. 7.11(d)). This produces a gap, Δ_{DJ}, between

the lug and the concrete. The bond mechanism of reloading along path J-K-L is similar to the loading D-E-F-G described earlier (see Fig. 7.11(e)). At point L the lug starts to contact the loose pieces of concrete. This leads to gaining stiffness, LM in Fig. 7.11(f). Through path LM the lugs begin to push the broken pieces of concrete forward, thereby opening up the cracks previously closed and closing the cracks previously opened (see Fig. 7.11(e)). The stiffness over path LM is relatively low in comparison to the previous stiffness over path AB, where the surrounding concrete was in a crack-free state, and less than the stiffness over path GH, where cracks formed only to one side of the lugs. At M, the broken piece is moved forward far enough to close the crack completely and ensure full contact. Along path MN, the wedging action of the lugs causes a build up of bearing stress and compressive stress in the broken concrete pieces. With sufficiently large imposed force or displacement, the inclined crack will propagate to the exposed face of the column in the form of a cone. Once the cone fractures away from the main body of the block, the bond resistance offered by the first lug vanishes.

7.5.2.2 Confined Region

The bond mechanism in the confined region differs from that of the unconfined region as follows:

(1) The heavy transverse reinforcement will inhibit propagation and widening of cracks. Therefore the merging of the diagonal cracks which tend to occur in an unconfined region is delayed or may not even take place.

(2) The successive crushing (bearing failure) and inelastic deformation in the compressed concrete are the primary causes of degradation in stiffness, eventually causing failure by shearing off the concrete between the lugs.

A few significant stages in the evaluation of the bond mechanism for the confined region are given in Fig. 7.12.

7.5.2.3 Pushed End Region

For a gradual and incremental series of load reversals, there is virtually no distinction between the unconfined and pushed-end regions (see Figs. 7.7(a) and (c)). The tension portion of the cycle that each end undergoes controls the behavior. The difference in the two regions becomes clear only under monotonic loading where a significant expansion of bar diameter occurred in the pushed-end region.

7.6 IDEALIZED HYSTERETIC RULES OF τ-γ FOR GENERALIZED LOADING

As pointed out in section 7.5, there are many parameters that control the bond behavior. The parameters investigated experimentally were confinement, loading history and bar sizes. Other parameters are held fixed, i.e., 4000 - 5000 psi stone aggregate concrete, spiral lug deformation pattern with surface geometry shown in Fig. 2.7, and no axial load applied to the column blocks. Therefore τ-γ relationships to be formulated bear the same limitations.

The development of the bond model involves the following steps:

(1) Idealization of monotonic skeleton curves.

(2) Construction of monotonic skeleton curves for push-pull loading conditions.

(3) Reduction of skeleton curve due to repeating load.

(4) Formulation of hysteretic rules for generalized cyclic loading.

7.6.1 Idealized Monotonic Skeleton Curve

A four stage piece-wise linear approximation of the experimental τ-γ curves is used (see Fig. 7.13). The idealized curves are identified by stage 1, stage 2, stage 3 and stage 4 as shown in Fig. 7.14. Each stage reflects a distinctive behavior in bond:

-- Stage 1 represents adhesive bond and absence of diagonal cracks and is characterized by the highest stiffness.

-- Stage 2 represents the initiation of diagonal cracks and some crushing of concrete at the steel lug, leading to a less stiff curve in comparison with stage 1.

-- Stage 3 signifies the beginning of failure in the surrounding concrete. An increase in shear deformation results in a reduction of shear resistance.

-- Stage 4 represents the exhaustion of the shear resistance offered by wedging between the steel lug and a broken piece of concrete. The small remaining resistance is from friction.

The construction of this four-stage curve is established by assigning the coordinates of the controlling points A, B, and C (see Fig. 7.15). A listing of the coordinates of the controlling points for different regions and bar sizes obtained after an extensive review of the experimental τ-γ curves is given in Table 7.1. A general formulation based on curve fitting of the tabulated values is shown in Table 7.2.

7.6.2 Monotonic Skeleton Curve for Push-Pull Loading

After obtaining the monotonic skeleton curves for the unconfined, confined and pushed end regions in Fig. 7.14, a complete monotonic

skeleton curve can be constructed for the push-pull loading condition. Observe that there are two possibilities for monotonic loading at each region, i.e., pull all the way or push all the way. The monotonic skeleton of this two-way generalized loading is shown in Fig. 7.15. For instance, in the unconfined region, the τ-γ curve is composed of an unconfined curve for pulling as described in the first quadrant of τ-γ curve and a push-end curve for pushing as described in the third quadrant of τ-γ curve. It should be noted that the stages -1, -2, -3 and -4 are used to identify the skeleton curves in the third quadrant.

7.6.3 Modification of Skeleton Curve Due to Cyclic Loading

As shown in Chapter 5, upon application of repeating loads with sufficient intensity, the cumulative and irreversible damage induced in the concrete boundary layer is considerably more severe than is the case with monotonic loading. The greater the magnitude of the previous peak stress and the higher the number of cycles, the greater the softening of the layer and the less the effectiveness of the bond resistance. Typical reductions from monotonic skeleton curve due to cyclic load at an unconfined region are shown in Fig. 7.16.

According to Fig. 7.16, one approach toward incorporating both the monotonic and cyclic loading sequences in a generalized curve is to formulate a rule as a function of loading history to describe the reduction of the monotonic skeleton curve used to obtain the cyclic envelope curve. For the idealized piece-wise linear curve used in the approximation of the experimental curve, this can be done by assigning appropriate values for τ and γ to the controlling points of the curves (points A, B, C, A', B' and C').

A few assumptions are needed for constructing the reduced curves:

(1) Initial loading, back and forth, within the limit of stage 1 produces no effect on the skeleton modification. This is the same as assuming no significant damage is introduced into the boundary layer within this stage. Reductions start to be effective when unloading occurs beyond stage 1 (Fig. 7.17(a)).

(2) Reduction in the skeleton curve will occur when unloading proceeds beyond point E (see Fig. 7.17(b)). Unloading and reloading along path XE results in no modification. This conforms to what has been observed during experiments [19] (see Fig. 7.18), i.e., no appreciable difference in reduction in strength occurs between monotonic and half-cycle loading.

(3) Reduction in skeleton curves is assumed to be a function of cumulative shear deformations having magnitudes larger than those of the previous loading cycles (see Fig. 7.19). For instance, the shear deformations that will be included in the expression for reducing the skeleton curve for the next loading cycle are γ_1 and γ_1' in Fig. 7.19(a) and $(\gamma_1 + \gamma_2)$, $(\gamma_1' + \gamma_2')$ in Fig. 7.19(b).

In order to describe how the reduction algorithm works, a τ-γ curve for reversal loading is taken as an example. A series of figures are used for the illustrations.

Prior to the description of the example, a clear definition of the monotonic skeleton curve is necessary. The four stage piece-wise linear approximation is shown in Fig. 7.20. The points A, B, C, A', B' and C' are the controlling points, whose coordinates are τ_a, γ_a for

point A, and τ_b, γ_b for point B, τ_c, γ_c for point C, $\tau_{a'}$, $\gamma_{a'}$ for point A', $\tau_{b'}$, $\gamma_{b'}$ for point B' and $\tau_{c'}$, $\gamma_{c'}$ for point C', respectively.

Consider that the OP_1E_1 loading sequence is imposed on the τ-γ curve (see Fig. 7.21(a)). Physically, this corresponds to moving the bar at rest to a new position. Positive displacements are shown in the first and fourth quadrants of the τ-γ curve (Fig. 7.21(a)). Movement of the bar in the opposite direction is shown in the third quadrant. Unloading from point P_1 gives rise to the reduction from the skeleton OABC and OA'B'C' to OAB_1C_1 and $OA_1'B_1'C_1'$ respectively. The shifting from OABC to the new skeleton OAB_1C_1 is accomplished by reducing the τ at B by $\Delta\tau_{b1}$ and τ and γ at C by $\Delta\tau_{c1}$ and $\Delta\gamma_{c1}$. The reductions can be formulated mathematically as

$$\Delta\tau_{b_1} = \tau_b \, \alpha_{\tau b} \, \frac{(\gamma_1/\gamma_b)}{P_b} \, \xi_{\tau b} \tag{7.4}$$

$$\Delta\tau_{c_1} = \tau_c \, \alpha_{\tau c} \, \frac{(\gamma_1/\gamma_c)}{P_c} \, \xi_{\tau c} \tag{7.5}$$

$$\Delta\gamma_{c_1} = \gamma_c \, \alpha_{\gamma c} \, \frac{(\gamma_1/\gamma_c)}{P_c} \, \xi_{\gamma c} \tag{7.6}$$

where τ_b, γ_b, τ_c and γ_c are the coordinates of points B and C of the monotonic skeleton curve as shown in Fig. 7.20; $\alpha_{\tau b}$, $\alpha_{\tau c}$ and $\alpha_{\gamma c}$ are the proportionality factors that take into account the contribution of loading history to the curve reduction; $\xi_{\tau b}$, $\xi_{\tau c}$ and $\xi_{\gamma c}$ are the weight factors controlling the rate of reduction; P_b, P_c and P_c', which are defined later, are the constants designed to facilitate the evaluation of

the proportionality factors from the experimental results and the quantities (γ_1/γ_b) and (γ_1/γ_c) are the accumulated dimensionless shear deformations which comprise the past loading history. It should be pointed out that a linear relation between the skeleton reduction and the past history is assumed. This assumption is appropriate for the present since a lack of experimental data does not justify a more complicated relation.

The reduction for the skeleton OA'B'C' can similarly be expressed as:

$$\Delta\tau_{b_1'} = \tau_{b'}\,\beta_{\tau b'}\frac{(\gamma_1/\gamma_b)}{P_b}\,\xi_{\tau b'} \tag{7.7}$$

$$\Delta\tau_{c_1'} = \tau_{c'}\,\beta_{\tau c'}\frac{(\gamma_1/\gamma_c)}{P_c}\,\xi_{\tau c'} \tag{7.8}$$

$$\Delta\gamma_{c_1'} = \gamma_{c'}\,\beta_{\gamma c'}\frac{(\gamma_1/\gamma_c)}{P_c}\,\xi_{\gamma c'} \tag{7.9}$$

where $\tau_{b'}$, $\tau_{c'}$ and $\gamma_{c'}$ are defined in Fig. 7.20; $\beta_{\tau b'}$, $\beta_{\tau c'}$ and $\beta_{\gamma c'}$ are the proportionality factors reflecting the effect of past history. The distinction between $\alpha_{\tau b}$, $\alpha_{\tau c}$ and $\alpha_{\gamma c}$ vs. $\beta_{\tau b'}$, $\beta_{\tau c'}$ and $\beta_{\gamma c'}$ are that the α's are designed for the reduction in the skeleton curve where the maximum shear and the reductions are in the same quadrant, while the β's apply to the condition where the maximum shear lies in a different quadrant from the skeleton curve to be modified (see Fig. 7.21(c)).

Further reloading and unloading as represented by path $EP_1'E'$ as shown in Fig. 7.21(b), leads to the establishment of new skeleton curves, OAB_2C_2 and $OAB_2'C_2'$, from OAB_1C_1 and $OAB_1'C_1'$ curves. The reduction

in τ and γ of point B_1, C_1, B_1' and C_1' as a result of undergoing the shear deformation γ_1' are

$$\Delta\tau_{b2} = \tau_b \, \beta_{\tau b} \frac{(\gamma_1'/\gamma_{b'})}{P_{b'}} \xi_{\tau b} \tag{7.10}$$

$$\Delta\tau_{c2} = \tau_c \, \beta_{\tau c} \frac{(\gamma_1'/\gamma_{c'})}{P_{c'}} \xi_{\tau c} \tag{7.11}$$

$$\Delta\gamma_{c2} = \gamma_c \, \beta_{\gamma c} \frac{(\gamma_1'/\gamma_{c'})}{P_{c'}} \xi_{\gamma c} \tag{7.12}$$

$$\Delta\tau_{b'2} = \tau_{B'} \, \alpha_{\tau b'} \frac{(\gamma_1'/\gamma_{b'})}{P_{b'}} \xi_{\tau b'} \tag{7.13}$$

$$\Delta\tau_{c'2} = \tau_{c'} \, \alpha_{\tau c'} \frac{(\gamma_1'/\gamma_{c'})}{P_{c'}} \xi_{\tau c'} \tag{7.14}$$

$$\Delta\gamma_{c'2} = \gamma_{c'} \, \alpha_{\gamma c'} \frac{(\gamma_1'/\gamma_{c'})}{P_{c'}} \xi_{\gamma c'} \tag{7.15}$$

Note that, because the definition of α's and β's have to do with the position of maximum shear, γ_1', with respect to the skeleton curve, the reductions $\Delta\tau_{b2}$, $\Delta\tau_{c2}$, and $\Delta\gamma_{c2}$ involve β's while $\Delta\tau_{b'2}$, $\Delta\tau_{c'2}$ and $\Delta\gamma_{c'2}$ are related to α's.

The expressions for further reduction in the skeleton curve from OAB_2C_2 and $OAB_2'C_2'$ to OAB_3C_3 and $OA'B_3'C_3'$ as a result of loading $E_1'P_2E_2$ are given in Fig. 7.21(c).

This example can be easily extended to the more generalized cases like the cyclic loading shown in Fig. 7.22. The total reduction in τ of point B due to the repeating loading is

$$\Delta\tau_b = \Delta\tau_{b1} + \Delta\tau_{b2} + \Delta\tau_{b3} + \ldots + \Delta\tau_{bn}$$

$$= \tau_b \left[\alpha_{\tau b} \frac{(\gamma_1 + \gamma_2 + \gamma_3 + \ldots + \gamma_n)/\gamma_b}{P_b} + \right.$$

$$\left. + \beta_{\tau b} \frac{(\gamma_1' + \gamma_2' + \ldots + \gamma_n')/\gamma_{b'}}{P_{b'}} \right] \xi_{\tau b} \qquad (7.16)$$

Similarly, for points C, B' and C', the reductions are

$$\Delta\tau_c = \tau_c \left[\alpha_{\tau c} \frac{(\gamma_1 + \gamma_2 + \ldots + \gamma_n)/\gamma_b}{P_c} + \beta_{\tau c} \frac{(\gamma_1' + \gamma_2' + \ldots + \gamma_n')/\gamma_{b'}}{P_c'}\right] \xi_{\tau c} \qquad (7.17)$$

$$\Delta\gamma_c = \gamma_c \left[\alpha_{\gamma c} \frac{(\gamma_1 + \gamma_2 + \ldots + \gamma_n)/\gamma_c}{P_c} + \beta_{\gamma c} \frac{(\gamma_1' + \gamma_2' + \ldots + \gamma_n')/\gamma_{c'}}{P_c'}\right] \xi_{\gamma c} \qquad (7.18)$$

$$\Delta\tau_{b'} = \tau_{b'} \left[\beta_{\tau b'} \frac{(\gamma_1 + \gamma_2 + \ldots \gamma_n)/\gamma_b}{P_b} + \alpha_{\tau b'} \frac{(\gamma_1' + \gamma_2' + \ldots + \gamma_n')/\gamma_{b'}}{P_b'}\right] \xi_{\tau b'} \qquad (7.19)$$

$$\Delta\tau_{c'} = \tau_{c'} \left[\beta_{\tau c} \frac{(\gamma_1 + \gamma_2 + \ldots + \gamma_n)/\gamma_c}{P_c} + \alpha_{\tau c'} \frac{(\gamma_1' + \gamma_2' + \ldots + \gamma_n')/\gamma_{c'}}{P_c'}\right] \xi_{\tau c'} \qquad (7.20)$$

$$\Delta\gamma_{c'} = \gamma_{c'} \left[\beta_{\gamma c'} \frac{(\gamma_1 + \gamma_2 + \ldots + \gamma_n)/\gamma_c}{P_c} + \alpha_{\gamma c'} \frac{(\gamma_1' + \gamma_2' + \ldots + \gamma_n')/\gamma_{c'}}{P_c'}\right] \xi_{\gamma c'} \qquad (7.21)$$

According to the experimental data obtained for cyclic reversal loading and from the equations above, it is suggested that the definition of the constants should be in the form

$$P_b = (\gamma_1 + \gamma_2 + \ldots + \gamma_b)/\gamma_b \qquad (7.22)$$

as the summing up of the shear deformation until the deformation of the last included loop just exceeds γ_b. As shown in Fig. 7.23, γ_b is the summation of γ_1 to γ_6. The definition of the other P's are similarly defined as

$$P_b' = (\gamma_1' + \gamma_2' + \ldots + \gamma_b')/\gamma_b', \tag{7.23}$$

$$P_c = (\gamma_1 + \gamma_2 + \ldots + \gamma_c)/\gamma_c \tag{7.24}$$

$$P_c' = (\gamma_1' + \gamma_2' + \ldots + \gamma_c')/\gamma_c', \tag{7.25}$$

where γ_1, γ_2,..., γ_c and γ_1', γ_2',..., γ_c' are shown in Fig. 7.23. The constants of P_b, P_b', P_c and P_c' for different bar sizes and different regions as evaluated from the experiment results are listed in Table 7.3. The adoption of such a definition of the P's lends itself readily to determining the values of the other parameters to fit the experimental results. Selecting values of $\alpha_{\tau b}$, $\alpha_{\tau c}$, $\alpha_{\gamma c}$, $\alpha_{\tau c}$, and $\alpha_{\gamma c}$, of 0.7 and $\beta_{\tau b}$, $\beta_{\tau c}$, $\beta_{\gamma c}$, $\beta_{\tau c}$, and $\beta_{\gamma c}$, of 0.3 produced an idealized τ-γ curve that closely matched the experimental curves $\xi_{\tau b}$, $\xi_{\tau b}$,, $\xi_{\tau c}$, $\xi_{\tau c}$,, $\xi_{\gamma c}$ and $\xi_{\gamma c}$, for different bar sizes and regions (listed in Table 7.3).

7.6.4 Hysteretic Rules for Generalized Loading

In this section, except for the formulation of how the monotonic skeleton curve can be constructed, the rules for plotting the τ-γ curve are presented. The presentation of the rules are best illustrated by a series of figures covering all the possible stages of loading, unloading and reloading history. Whenever possible, the relationship of the rules to the bond deterioration mechanism will also be described.

Unloading from stages 2, 3, 4 in the first quadrant of the monotonic curve, or -2, -3 and -4 in the third quadrant, will result in permanent set, i.e., a permanent relative slippage of the bars (see Fig. 7.24(a)). The unloading stiffness is assigned to be equal to k_1, which is the smaller slope value of either curve 0A or 0'A of the monotonic skeleton curves as described in section 7.6.2. The limit of unloading from the above stages is set by point E and E' whose coordinates are defined by

$$\tau_e = \tau_c' \tag{7.26}$$

$$\tau_{e'} = \tau_c \tag{7.27}$$

$$\gamma_e = \gamma_1 - (\tau_1 - \tau_e)/k_1 \tag{7.28}$$

$$\gamma_e' = \gamma_1' - (\tau_1' - \tau_e)/k_1 \tag{7.29}$$

where τ_c and τ_c' are the shear stress set by the skeleton curve in stage 4 and -4; and τ_1, γ_1, τ_1' and γ_1' are the coordinates of points on the skeleton curve where unloading takes place (see Fig. 7.24(a)).

Displacing beyond γ_e or γ_e' will follow the friction path, EF and E'F' as shown in Figs. 7.24(b) and 7.24(c). If in Fig. 7.24(b) further deformation takes place until γ is less than γ_f where

$$\tau_f = \tau_c' \tag{7.30}$$

$$\gamma_f = \tau_c'/k_1' \tag{7.31}$$

k_1' is the stiffness of curve OA'; a new modified skeleton $OA'B_1'$ will be followed. Path OA' will be taken only when the deformation enters the third quadrant for the first time; otherwise a path described in Figs. 7.24(d) and (e) will be taken.

A similar rule is set for the releasing of deformation occurring in the other direction of deformation, as shown in Fig. 7.24(c). In this case, point F' is defined by

$$\tau_f' = \tau_c \tag{7.32}$$

$$\gamma_{f'} = \tau_c/k_1 \tag{7.33}$$

where k_1 is the stiffness of curve OA or OA', whichever is smaller.

It should be noted that the rules described above are derived from the bond mechanism in Figs. 7.11(b) and 7.11(c). A bond hysteretic curve corresponding to a B_1 full or semi-full load reversal is illustrated in Fig. 7.24(d). The loading sequence is O-A-B-P-E-F-A'-B_1'-P'-E-L-D. As soon as deformation from point P proceeds beyond point E, new controlling points P_1, D and L are established. Point P_1, defined by τ_{p1} and γ_{p1}, is generated from the intersection between unloading curve PE and reduced skeleton curve B_1C, if unloading occurs from stage 3, and AB_1 if from stage 2. Point D and L are related to point P_1 by

$$\tau_d = \tau_{p1}\ \beta_1 \tag{7.34}$$

$$\gamma_d = \gamma_{p1} - (1-\beta_1)\tau_{p1}/k_1 \tag{7.35}$$

$$\tau_{\ell} = \tau_c \tag{7.36}$$

$$\gamma_{\ell} = \gamma_a + [\gamma_d - \gamma_a - (\tau_d - \tau_c)/k_1]\alpha_1 \tag{7.37}$$

where τ_c, τ_d and τ_{ℓ} are the shearing stress of point C, D and L, respectively; γ_a, γ_c, γ_d and γ_{ℓ} are the shear deformation of the points A, C, D and L; and β_1 and α_1 are the parameters designed to determine what the stiffness of the ascending LD curve will be as shown in Fig. 7.24(d). The larger the β_1 and the smaller the α_1, the steeper the curve. Note that, if $\beta_1 = 1.0$, point P_1 and P coincide, and if $\alpha_1 = 1$ yields $\gamma_L = \gamma_d - (\tau_d - \tau_c)/k_1$ (from Eq. 7.25), i.e., point L is in the unloading branch PE. From reviewing the experimental results obtained, it is indicated that α_1 equal to .4 and β_1 equal to .9 gives a reasonable agreement with the test data.

The same pattern is applied for unloading from point P' in the other direction of loading, i.e., new controlling points P_1', D' and L' are created (see Fig. 7.24(e)). The bond mechanism associated with the rules in Figs. 7.24(d) and (e) has been described in Section 7.5.

Thus far some of the general rules for cyclic-repeating loading have been presented. Samples of the effect of full- and semi-full reversal loading histories on hysteretic rules for bond are illustrated. The next presentation will concentrate on repeating half-cycle loading. Rules applied for one direction of loading as depicted in the first quadrant of the τ-γ curve will be used to describe the entire curve since, by virtue of symmetry, a similar rule for first quadrant can be used for the third quadrant (loaded in the opposite direction) with minor

modifications. A series of figures will be used to demonstrate the rules.

The rules for repeating half cycle history O-A-B-P-E-U-V-L-D-R and O-A-B-P-E-U-V-D-R are illustrated in Fig. 7.24(f) and 7.24(g). Unloading from point P, the control points D, L and LL are established. The coordinates of point D and L are given in Eqs. (7.22) to (7.25), respectively. Point LL is defined by

$$\tau_{\ell\ell} = \tau'_c \tag{7.38}$$

and

$$\gamma_{\ell\ell} = \gamma_\ell - (\tau_c - \tau'_c)/k_1 \tag{7.39}$$

where τ_c and τ'_c are the shear stresses of point C and C', respectively. Note that as the reloading is made, starting from point U whose coordinate is defined by τ_u and γ_u, the stiff slope (k_1) of path UV is taken first. Point V is defined by

$$\tau_v = \tau_c \tag{7.40}$$

$$\gamma_v = \gamma_u + (\tau_c - \tau'_c)/k_1 \tag{7.41}$$

At V there are two possible paths to be taken. If $\gamma_u < \gamma_{\ell\ell}$, then the VL path, which is characterized by flat slope, is taken. However, if $\gamma_u \geq \gamma_{\ell\ell}$, then it is necessary to consider the stiff path VD (see Fig. 7.24(g)) whose stiffness is

$$k_{vd} = (\tau_d - \tau_v)/(\gamma_d - \gamma_v) \tag{7.42}$$

where τ_d and γ_d are defined in Eqs. (7.34) and (7.35).

The bond mechanism associated with the establishment of the rules for either the VL or VD path is dependent on how far the retraction of the lugs is made before reloading takes place. If sufficient retraction is made, a small gap between the steel lug and disrupted concrete (as denoted by $\Delta_{u\ell}$ in Fig. 7.24(f_1) and 7.24(g_1)) is created. Therefore, to move the bar forward, the force required to overcome the friction resistance is needed (see Fig. 7.24(f_1)). On the other hand, if the retraction is not far enough, the lugs and the surrounding concrete remain in contact (see Fig. 7.24(g_1)). Therefore, the forward motion is met by a stiff resistance.

The rule for unloading from a point of the τ-γ curve is always characterized by the steep descending slope of k_1. Figures 7.24(h) and (i) shows another example of reloading and unloading (path O-A-B-P-E-U-L-M-N) where unloading path MN takes place before the reloading path LM meets the skeleton curve B_1C_1.

Figure 7.24(j) shows the loadings, unloadings and reloadings within two friction paths, V-L and U-LL. The friction paths occur only within the region damaged by path O-A-B-P. Note that the unloading and reloading paths connected between the path VL and U-LL are characterized by stiff slope k_1. Zero stiffness results if loading and reloading occur within the friction paths.

Another possibility of loading and reloading that may occur is as shown in Fig. 7.24(k). In this figure, the loading and unloading along the path O-A-B-P-E-U-V-L-M takes place before unloading and reloading along the MNST path. Note that point M already is in ascending path LD prior to unloading. Slope of stiffness k_1 is assigned to path MN and ST, while zero stiffness is given to path NS. The rationality behind

such a rule can be similarly deduced without further explanation from previous descriptions of the bond mechanism as shown in Figs. 7.24(f1) and 7.24(g1).

The hysteretic rule for unloading and reloading after the bar is pulled and pushed until its bond capacity is almost exhausted is shown in Fig. 7.24(ℓ). The path O-A-B-C-P is imposed prior to the unloading. Note that point P, where unloading takes place, is already in stage 4 of the idealized skeleton curve. Unloading and reloading after passing through stage 4 are governed by two friction paths, QR and ST, as shown in the figure. Slope k_1 is assigned to connect between the QR and ST paths. The bond mechanism behind the establishment of the above rules is rather obvious, i.e., the steel lug has moved far enough to either knock off the entire piece of the cracking concrete as might occur in the unconfined region or completely shear off the damaging concrete filled in between the lugs as may occur in the confined and pushing end regions (see Figs. 7.24(ℓ_1) and ℓ_2). Subsequently, the bar can move freely once the force applied is high enough to overcome the frictional resistance.

The rules for repeating half-cycle loading is shown in Fig. 7.24(m). The same path for unloading and reloading of stiffness k_1 is assigned. As pointed out in section 7.6.4, there is no reduction in skeleton curve for this type of loading sequence.

It is believed that the above presentation includes all the possible basic stages of loading and unloading. Any complex loading history can be broken down into a combination of the above loading and unloading stages.

7.7 APPLICATION OF BOND DETERIORATION MODEL

7.7.1 Idealization of Physical Behavior

As pointed out at the beginning of this chapter, the major objective of this analytical work is to attempt to predict the force-displacement relationship of a rebar embedded in a concrete block. Physically the problem is visualized as a rebar surrounded by a soft layer (Fig. 7.4 and 7.25). Two types of elements are needed for modeling the physical behavior of a bar embedded in a concrete block. The behavior of the soft layer is represented by a string of shear elements which typically have a dimension of length L_e and thickness t (see Fig. 7.25). An average shear stress and shear deformation at the center of the element are used to represent the overall behavior of the shear element. Adopting the average shear and deformation, the degree of freedom of each element is reduced to one; mathematically the element is equivalent to a spring, as shown in Fig. 7.26. The other essential component to simulate the physical problem is the reinforcing bar element. The reinforcing bar in this case is subjected to axial load only and therefore it can be idealized as a one dimension truss element, with two degrees of freedom as shown in Fig. 7.25.

The material properties of steel needed for the uni-axial truss element are given in the stress-strain relation, f_s-ε_s. The mathematical model of f_s-ε_s for monotonic as well as cyclic loading used in constructing the steel elements is given in Appendix B. Proper assemblage of the two elements to simulate a reinforcing bar embedded in a concrete block results in an idealized mathematical layout shown in Fig. 7.26, i.e., a one degree of freedom spring element directly connected to a two degrees of freedom steel element.

To convert the τ-γ relation of the shear elements to the force-local displacement curve, R-δ, of the spring elements, the following relations are established

$$R = \tau \Sigma_o L_e \tag{7.43}$$

$$\delta = \gamma t \tag{7.44}$$

where Σ_o is the effective circumference of rebar, L_e is the length of soft layer element, and t is the thickness of the soft layer.

7.7.2 Subroutines for Steel and Bond Deterioration Elements

With the availability of ANSR-I, a general finite element program for nonlinear analysis [27], it is relatively easy to incorporate the steel element and bond element into the program. The steel element and bond element are arbitrarily referred to as elements no. 6 and no. 10, respectively, by the ANSR-I base program. The input instructions and the Fortran listings of the steel element and the bond element are given in Appendix C and D, respectively.

Basically, the element subroutines consist of several routines. INEL, STIF, RESP and REST. The INEL routine accepts input data for all elements and initializes all the variables used. The function of the STIF routine is to compute a change in element stiffness and to transfer the change to the base program for subsequent assemblage into the structural stiffness matrix. The task of the RESP routine is to perform the following functions: compute the element deformations and actions; determine the change in state, if any; compute equivalent nodal loads in equilibrium with the current state of stress; accumulate envelope values of element

deformations and actions; update the element information and print the stress and strain results. The REST routines provide a mathematical formulation of hysteretic rules for either steel or bond elements.

Various types of solution schemes can be selected from the package program. These include step-by-step procedures (without iteration), Newton-Raphson iteration, constant stiffness iteration with stiffness reformulation every step, constant stiffness iteration using initial stiffness throughout, and mixed iteration procedure in which Newton-Raphson iterations are followed by constant stiffness iterations. Choice of a particular scheme depends mainly on the characteristics of nonlinearity introduced into the problem. For the material nonlinearity as introduced in the bond and steel elements, it was found that the Newton-Raphson iteration scheme probably was the most effective. Therefore, this scheme was exclusively used for the analytical prediction.

7.7.3 Prescription of Loading History for the Analytical Model

In most of the bond experiments, the bar was subjected to simultaneous pull and push forces, of equal intensity, at the protruding ends. The same loading history had to be prescribed in the analytical work. The displacement-controlled loading history is selected for the analytical model to prevent the occurrence of solution instability at the pull-through stage. Since the analytical and experimental responses are matched according to the end displacements, the indication of how good the agreement is between the two can be judged by the discrepancy in the end resulting forces (or stresses).

7.8 ASSESSMENT OF ANALYTICAL PREDICTION

7.8.1 Comparison with Experimental Results

Several computer runs were carried out to investigate the reliability of the proposed bond model. These runs can be classified as follows:

(1) Monotonic loading

a) pull on one end, #8 bar 25 in. column

b) pull and push simultaneously for

#6 bar, 15 in. column

#8 bar, 25 in. column

#10 bar, 25 in. column

(2) Cyclic loading

b) push and pull simultaneously on

#8 bar, 15 in. column

#8 bar, 25 in. column

#10 bar, 25 in. column

An example of the information needed for carrying out an analytical prediction of #8 bar, 25 in. column, push-pull loading is shown in Fig. 7.27. The soft layer is divided longitudinally into shear elements. Three types of elements are identified with different regions in the concrete block (unconfined, confined and pushed end regions). Knowing the length and thickness (t = 3.5 in.) of the soft layer element and the perimeter of the steel bar (Σ_o = 2.5 in.), an equivalent spring is derived (see Fig. 7.27(b)). The mechanical properties of the soft layer element (τ-γ curves) and their corresponding spring element (R-δ curves) are given in Fig. 7.27(c).

Comparison between the analytical and experimental results is shown in Figs. 7.28 and 7.29. For monotonic loading, the agreement is quite good, although in most of the cases the analytical results give a slightly higher stress (not more than 10 percent higher). A fair agreement is obtained for cyclic load. The cyclic predictions can reproduce nearly every aspect of significant response as recorded from the tests, i.e., stiffness degradation (pinching effect) upon approaching zero stress, degradation in strength for the repeating loops of the same displacements, and yielding of the rebar.

7.8.2 Computation Cost

Due to the highly nonlinear material properties of bond and steel elements, the computational procedure had to resort to a step-by-step load incremental approach. The step size was specified as large as possible to reduce computation cost while achieving a reasonable convergence of solution. Experience with the runs showed that even with the large step size, many steps were necessary to capture all the essential parts of the responses. Table 7.4 lists the computational costs for the runs. Note that even with few degrees of freedom, the calculation cost for cyclic loading can be very high.

Experience with several runs points out the limitation of employing more elaborate and more realistic idealization for analysis. As indicated at the beginning of Sec. 7.8, the simplified hysteretic model used had combined the concrete and steel-concrete interaction responses. Such a model, although very useful in obtaining the displacement of the rebar at the ends with respect to a

fixed axis, could not give information regarding cracking behavior of the surrounding concrete. To obtain concrete cracking response, the concrete may have to be divided into an element mesh, as shown in Fig. 7.2. The concrete elements next to the rebar would be connected to the rebar by bond-link elements whose hysteretic rules are similar to what has been discussed. Many more degrees of freedoms would be necessary with this approach and, as a result, the computational effort would be excessive. Therefore, the level of hysteretic model proposed is the only way to obtain an estimation of load displacement at a reasonable cost at present.

7.9 REMARKS AND RECOMMENDATIONS FOR FURTHER STUDY

Although the results obtained from the analytical work look very promising, it should be recognized that the model is still in a development stage and requires more test runs. The bond hysteretic model and f_s-ε_s of steel were developed for generalized loading, but the analytical works conducted so far were restricted to cases of monotonic and full or semi-full reversal loading histories, as were the actual tests. How reliable the predictions of other types of loading histories, such as repeating half cycle loading or one large excursion (shock load) followed by a series of small excursions, remains to be seen.

The size of the column in the analysis was 25 in. It will be interesting to see how good an agreement can be achieved between the prediction and the experimental results for different widths of column. It would be of help for earthquake resistance design if this developing model could be used to reliably predict, within acceptable accuracy, the minimum

anchorage length required for a rebar to be able to develop yield strength or strain-hardening strength, or even fracture of the rebar before pull-through occurs.

To be able to predict f_{s1}-δ_1 and f_{s2}-δ_2 with precision is only a first step. Attention should be placed on extending the procedure for obtaining the moment fixed-end-rotation which is essential for predicting the response of a structure. The analytical reproduction of the moment-fixed-end rotation relation will provide an important tool for pinpointing the significance of the other parameters important in actual beam-column joints. For instance, the extent of possible anchorage of the main bars in concrete before slippage, or the significance of the beam-column interface shear which introduces the dowel action on the beam main rebar, can be investigated.

The parameters α, β, α_1 and β_1 assigned in the generalized bond model were held constant. More tests are needed to identify how they are effected by different loading histories.

Lastly, the bond hysteretic rule was developed for a fixed rebar surface geometry, 4000 - 5000 psi concrete and no axial load applied to the column; extension of this model to other rebar surfaces, different concrete strength range, or even different aggregate (light-weight) requires further experimental and analytical investigation.

8. CONCLUSIONS AND SUGGESTIONS FOR FUTURE RESEARCH

8.1 CONCLUSIONS FROM EXPERIMENTAL STUDIES

Due to the large number of parameters involved, a comprehensive study of the deterioration in bond under generalized loading usually requires a wide-range investigation. However, a significant understanding of the behavior may be obtained from a relatively small investigation, if it is performed through well-coordinated experimental and analytical effort. It is with this belief that the present investigation was carried out. From the results obtained in this investigation, the following main observations are drawn.

8.1.1 Performance of Testing Facility and Instrumentation

In general, the performance of the testing facility was good. Tracing the prescribed load or displacement histories by continuous monitoring of the force deformation on XY recorders proved effective. MTS controllers used for automatically controlling the pull and push hydraulic rams performed adequately throughout the series of tests. The large amount of instrumentation (mostly electronic transducers) provided valuable data for obtaining overall response of the embedded bars, as well as for studying in detail their deformation and bond resistance mechanisms. Data from the continuously recorded hysteretic force-deformation diagrams provided excellent information on the overall behavior since the history of stiffness degradation and strength degradation was easily deduced from such data. The measurement of the strain along the embedded rebar by post-yield gages, specially installed, was reliable.

8.1.2 Performance of Bars Embedded in the Column Block

Some of the most important observations on the performance of the test bars in elastic and inelastic ranges are listed below.

(1) Stiffness Degradation.--The observed stiffness degradation occurring in the response of an embedded bar was very sensitive to the loading history. Significant degradation in stiffness readily occurred at stress level in the steel as low as $\pm$ 24 ksi (working load range). The response was stable for subsequent repeating cycles at this level. At stress levels exceeding working stress, the initial stiffness and energy dissipation per cycle was observed to degrade continuously in subsequent reversals. Stiffness degradation also occurred due to repeated applications of loading reversals at cycles of constant large displacement.

(2) Mechanism of Failure.--Although all the specimens were failed in a pull-through mode (bond failure), it is essential to distinguish the bond of unconfined concrete in the column cover from that in the confined core which was heavily reinforced and to further distinguish the region near the pushed end. The bond strengths of these regions were considerably different. The confined bond strength was about twice the unconfined strength, while the pushed-end bond strength could be two to three times that of the confined region. The development length for pushed end to resist an applied load is much smaller in comparison to those of the unconfined and confined regions.

8.1.3 Application for Seismic Design

(1) The assumption that beam-column joints of moment-resisting R/C frames are rigid needs to be reexamined. The main reinforcing

bars of the beams do pull out. At yielding stress of the beam bar, it can amount to 20 to 70 percent of the allowable drift (see Table 4.5), thereby causing beams to experience fixed-end rotation. The consequences of this behavior on the overall structural response must be examined.

(2) Under severe cyclic loading, due to the formation of cracks on both sides of a column, the continuous beam reinforcement can be subjected simultaneously to tensile and compressive forces and therefore may pull through the column, causing a large decrease in joint stiffness. This effect may contribute to a loss of the overall stability of a frame. In seismic resistant design, it is not sufficient to develop the calculated moment capacity of members; the deformations at which such moments can be attained must be known.

(3) Presently the ACI [4] and UCB [24] codes have no provision for computing the development length of main rebars passing through an R/C interior connection, since it is assumed that ample anchorage length is provided on the opposite framing beam. However, this is not true for severe cyclic loading where the concrete in this beam can also be damaged. Recognition of the formations of cracks at the column surface, which leads to cyclic push-pull loading of the main beam bars, should be made, and some modifications of the present code specifications are necessary.

8.2 CONCLUSIONS FROM ANALYTICAL STUDIES

Analytical studies were carried out to formulate a reliable mathematical model for predicting hysteretic behavior of a bar embedded in a well-confined column. Studies were also made on the behavior of an embedded bar and its surrounding concrete. From these studies, the

following observations can be made.

(1) The mathematical model developed for the bond element offers a reasonably good prediction of the hysteretic force-deformation of push-pull experiments with moderate effort of computation. The bond element proved to be effective for both the monotonic and cyclic loading histories. The computer-oriented approach for formulating the hysteresis rules for the bond element can be used for any type of loading history.

(2) Applying an existing non-linear finite-element method to the study of the mechanical behavior of the concrete boundary layer around a reinforcing bar subjected to monotonically-increasing tension contributed to an understanding of the bond behavior along anchored main bars. The results indicated that increasing stress transfer from steel to concrete will cause propagation of internal cracking in the concrete boundary layer. Also, the formation of a 'cone' in the unconfined regions could be approximately identified. This cracking could initiate in the concrete at very low stress level (about 5 ksi). The analysis shows that internal concrete cracking reduces the stiffness of the concrete boundary layer, and thus the axial stiffness of the embedded bar. The analysis results tended to yield a stiffer response than that of the actual case, and an investigation should be taken to find an equivalent softer material to improve the prediction of the response.

8.3 RECOMMENDATIONS FOR FUTURE RESEARCH

While the experimental and analytical studies reported herein have clarified some aspects of the bond behavior of confined and unconfined regions subjected to monotonic and cyclic loading, some

areas have not yet been fully explored and should be the subject of future research.

(1) Further experiments to supply results for developing a generalized bond model are needed. Such work must include a broad range of bar sizes and types of bar deformation (lugs), and use of specimens with more than one bar (interaction effect) and with different amounts of confinement.

(2) The implication of the effect of fixed end rotation on the behavior of an R/C structural system should be studied analytically.

(3) Additional research effort should be devoted to developing a concrete cracking model under cyclic loading. The model must be able to keep track of crack widths so that opening and closing of cracks can be simulated. Such a model is necessary to gain a better insight of the bond deterioration mechanism in a beam column joint.

(4) The reduction in anchorage performance due to disruption of bond as a consequence of the shear that develops in the bar due to dowel action at the interface cracks should be considered.

(5) Finally, a comparison of the results obtained herein with other bond research should be made so that a more precise identification of the effect of each parameter can be achieved.

REFERENCES

1. ACI Committee 352, "Recommendations for Design of Beam-Column Joints in Monolithic Reinforced Concrete Structures," ACI Journal Proceedings V. 73, No. 7, July 1976, pp. 375-393.

2. V. V. Bertero and E. P. Popov, "Seismic Behavior of Ductile Moment-Resisting Reinforced Concrete Frames," Reinforced Concrete Structures in Seismic Zones, Publication SP-53, ACI, 1977.

3. S. Viwathanatepa, E. P. Popov and V. V. Bertero, "The Behavior of Original and Epoxy Repaired Interior R/C Beam Column Connections," in preparation.

4. ACI Committee 318, "Building Code Requirements for Reinforced Concrete, (ACI 318-77)," ACI, 1977.

5. ATC Publication ATC 3-06, "Tentative Provisions for the Development of Seismic Regulations for Buildings," National Bureau of Standards, June 1978.

6. ACI Committee 408, "Bond Stress--The State of the Art," ACI Journal, Vol. 63, No. 11, November 1966.

7. T. Takeda, M. A. Sozen, and N. N. Nielsen, "Reinforced Concrete Response to Simulated Earthquakes," Journal of the Structural Division, ASCE, Vol. 96, No. ST 12, December 1970, pp. 2557-2573.

8. M. A. Ismail, and J. O. Jirsa, "Behavior of Anchored Bars under Low Cyclic Overloads Producing Inelastic Strains," Journal of the American Concrete Institute, Vol. 69, No. 7, July 1972, pp. 433-438.

9. S-Y. Ma, V. V. Bertero, and E. P. Popov, "Experimental and Analytical Studies on the Hysteretic Behavior of Reinforced Concrete Rectangular and T-Beams," Report No. EERC 76-2, Earthquake Engineering Research.

10. Y. Goto, "Cracks Formed in Concrete Around Deformed Tension Bars," ACI Journal, Vol. 68, No. 4, April 1971, pp. 244-251.

11. J. Houde, "Study of Force-Displacement Relationships for the Finite Element Analysis of Reinforced Concrete," Structural Concrete Series No. 73-2, Department of Civil Engineering and Applied Mechanics, McGill University, Dec. 1973.

12. A. H. Nilson, "Internal Measurement of Bond Slip," ACI Journal, Vol. 69, No. 7, July 1972, pp. 439-441.

13. B. Bresler and V. Bertero, "Behavior of Reinforced Concrete Under Repeated Load," J. of the Structural Division, ASCE, Vol. 94, No. ST6, June 1968, pp. 1567-1590.

14. S. Zagajeski, "Deterioration of Bond in Reinforced Concrete Beams Due to Cyclic Load Reversals," Graduate Student Report, Structural Engineering and Structural Mechanics, University of California, Berkeley, Winter 1974.

15. C. O. Orangun, J. O. Jirsa, and J. E. Breen, "A Re-evaluation of Test Data on Development Length and Splices," ACI Journal, Vol. 74, No. 3, March 1977, pp. 114-122.

16. L. A. Lutz, "Information of the Bond of Deformed Bars from Special Pull-Out Tests," ACI Journal, Vol. 68, No. 11, November 1970, pp. 885-887.

17. J. Minor, and J. O. Jirsa, "Behavior of Bent Bar Anchorages," ACI Journal, Vol. 72, No. 4, April 1975, pp. 141-149.

18. J. L. G. Marques, and J. O. Jirsa, "A Study of Hooked Bar Anchorages in Beam-Column Joints," ACI Journal, Vol. 72, No. 5, pp. 198-209.

19. S. Morita, and T. Kaku, "Local Bond Stress-Slip Relationship and Repeated Loading," IABSE Symposium, Resistance and Ultimate Deformability of Structures Acted on by Well Defined Repeated Loads, Lisboa, 1973, pp. 221-227.

20. S. Morita, and T. Kaku, "Splitting Bond Failures of Large Deformed Reinforcing Bars," Preprint, ACI 1977 Annual Convention, San Diego, California, March 1977.

21. R. H. Brown, and J. O. Jirsa, "Reinforced Concrete Beams Under Load Reversals," ACI Journal, Vol. 68, No. 3, May 1971, pp. 380-390.

22. Hassan, F. M. and Hawkins, N. M., "Effects of Post-Yield Loading Reversals on Bond Between Reinforcing Bars and Concrete," Report SM73-2, Dept. of Civil Engineering, University of Washington, Seattle, Washington, March 1973.

23. "Building Code Requirements for Reinforced Concrete," ACI Standard 318-71, Detroit, Michigan.

24. Uniform Building Code, International Conference of Building Officials, Pasadena, 1974 edition.

25. J. L. Cobb, Jr., "The Influence of Shock Loading and Axial Compression Upon Bond Deterioration Under Cyclic Loading," M. Eng. Thesis, Dept. of C. E., University of California, Berkeley, June 1977.

26. D. Liu, "Nonlinear Analysis of Axisymmetric Reinforced Concrete Structures," Graduate Student Report No. 559, Division of Structural Engineering and Structural Mechanics, Department of Civil Engineering, University of California, Berkeley, California, Fall 1972.

27. D. P. Mondkar and G. H. Powell, "ANSR-I, General Purpose Program for Analysis of Nonlinear Structural Response," Report No. EERC 75-37, Earthquake Engineering Research Center, University of California, Berkeley, December 1975.

28. D. Watstein, and B. Bresler, "Bond and Cracking in Reinforced Concrete," Chapter 4, Reinforced Concrete Engineering, John Wiley International, 1974.

29. "Building Code Requirements for Reinforced Concrete," ACI Standard 318-63, Detroit, Michigan.

TABLE 2.1 MECHANICAL PROPERTIES OF CONCRETE

Specimen No.	ϵ_c' (in./in.)	f_c' (psi)	E_c (ksi)	f_r (psi)	f_{sp} (psi)
2	.00265	4,910	3,158	520	449
3	.0026	4,720	3,265	585	509
4	.00258	3,890	3,047	540	377
5	.00285	4,130	3,098	536	513
6	.00285	4,790	3,251	600	467
7	.00265	4,680	3,453	608	504
8	.00265	4,640	3,455	571	499
9	.0025	4,700	3,583	580	490
10	.0028	4,410	3,177	572	454
11	.00255	4,230	3,313	504	478
12	.0025	4,470	3,495	501	392
13	.0026	4,700	3,524	541	419
14	.00275	4,740	3,558	548	510
15	.0022	3,900	3,113	508	498
16	.0022	4,270	3,490	450	416
17	.0026	4,290	3,326	534	496
18	.0025	4,320	3,443	590	479
Avg.	.002601	4,471	3,319.5	584.4	470
Standard Deviation	.00018	300	177	16	43

Notes: f_c' denotes maximum concrete strength in compression

ϵ_c' is the strain at f_c'

E_c is the secant tangent modulus at the early part of f_c-ϵ_c curve.

f_r is the tensile strength of concrete, obtained from the flexural test of a prism. It is usually referred to as modulus of rupture.

f_{sp} is the tensile strength of concrete obtained from split tension.

TABLE 3.1

AREA AND CIRCUMFERENCE OF GROOVED AND UNGROOVED SECTIONS

Bar Size	Ungrooved Section* Nominal		Ungrooved Section Measured		Grooved Section Measured	
	Area ($in.^2$)	Circum. (in.)	Area + ($in.^2$)	Effective Circum. (in.) Δ	Area + ($in.^2$)	Effective Circum. (in.) Δ
# 6	.442	2.36	.438	2.13	.371	1.62
# 8	.785	3.14	.774	2.94	.700	2.50
#10	1.227	3.93	1.223	3.98	1.173	3.49

* The norminal area and circumference of an ungrooved section are computed according to $\frac{\pi D^2}{4}$ and πD, respectively.

\+ The areas are obtained from calculation and measurement. Pieces of rebars, 10 in. in length, are carefully weighed. Knowing the specific gravity of the steel and weight of rebar, an average volume of the steel can be computed. The measured area is obtained from dividing the volume by 10 in. length.

Δ A rebar was cut and trimmed to obtain a smooth section surface. Carbon dye then smeared over the surface. Subsequently, the section was duplicated on a piece of white paper where its circumference can be traced and measured. Note that the effective circumference for grooved and ungrooved are defined according to the figures below, i.e., deducting the groove widths from the total circumference for a grooved section and the longitudinal ribs for an ungrooved section.

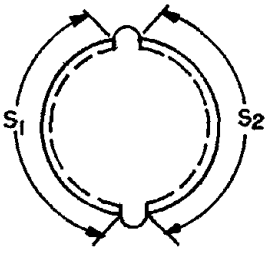

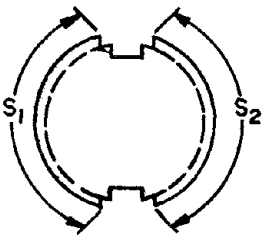

The effective circumference is $s_1 + s_2$

TABLE 3.2

TEST SPECIMENS

Specimen No.	Bar Size	Block Width (in.)	+ Sections of Bars	Δ Loading History
2	# 6	15	G	M
3	# 8	25	G	M
4	# 6	15	G	C
5	# 6	15	U	M
6	# 6	15	U	C
7	# 8	15	G	M
8	# 8	15	G	C
9	# 8	15	U	C
10	# 6	20	G	M
11	# 6	20	G	C
12	# 6	20	U	C
13	# 8	25	G	M
14	# 8	25	G	C
15	# 8	25	U	C
16	#10	25	G	M
17	#10	25	G	C
18	#10	25	U	C

Note: Except Specimen No. 3, which was subjected to pull only, the rest were under pull and push with pull equal to push.

\+ G = Grooved

U = Ungrooved

Δ M = Monotonic

C = Cyclic

TABLE 4.1

IMPORTANT STAGES OF CRACK DEVELOPMENT
(PUSH-PULL TESTS)

(a) Monotonic Loading

Specimen No.	First Appearance of			Average Radius of Cone (in.)	Depth of Cone (in.)
	Split Tension Crack (ksi)	Longitudinal Crack (ksi)	Cone Formation (ksi)		
2	49	46	46	4.0	3.0
3	50	52	48	3.8	3.5
5	48	51	45	3.6	3.0
7	40	40	48	5.0	3.3
10	45	45	54	3.5	3.2
13	40	40	56	5.0	3.4
16	36	45	54	5.0	3.2

(b) Cyclic Loading

Specimen No.	First Appearance of			Average Radius of Cone (in.)	Depth of Cone (in.)
	Split Tension Crack (ksi)	Longitudinal Crack (ksi)	Cone Formation (ksi)		
4	51	50	48	4.0	3.0
6	53	55	50	3.6	2.8
8	42	43	43	3.4	3.2
9	40	40	40	3.0	3.5
11	55	55	50	4.3	2.9
12	55	55	48	4.0	2.7
14	40	40	47	4.0	3.2
15	40	40	46	4.0	3.3
17	40	40	48	4.0	3.2
18	40	40	46	4.0	3.4

TABLE 4.2 STRESSES AND END DISPLACEMENTS

(a) Monotonic Loading*

Specimen No.	Bar Size	Block Width (in.)	Maximum Stress (ksi)	Average Bond Stress (ksi)	Displacement at Maximum Stress	
					Pulling End (in.)	Pushing End (in.)
2	# 6	15	77	2.42	.104	-.037
3	# 8	25	102	1.14	.98	-.065
5	# 6	15	80	2.19	.123	-.052
7	# 8	15	56	2.09	.06	-.048
10	# 6	20	89	2.10	.35	-.035
13	# 8	25	95	2.13	.45	-.096
16	#10	25	87	2.34	.169	-.060

*Except for specimen no. 3 which is subjected to pull on one end only, the rest are under pull and push with pull equal to push.

(b) Cyclic Loading

For pull equal to push.

Specimen No.	Bar Size	Block Width (in.)	Max. Stress (ksi)	Average Bond Stress (ksi)	End Displacement at Max. Stress (in.)	
					δ_1	δ_2
4	# 6	15	55	1.73	.067	-.065
6	# 6	15	64	1.6	.048	-.041
8	# 8	15	51	1.52	.039	-.034
9	# 8	15	50	1.67	.040	-.031
11	# 6	20	67	1.58	.062	-.027
12	#16	20	72	1.35	.054	-.025
14	# 8	25	72	1.283	.060	-.030
15	# 8	25	74	1.49	.071	-.032
17	#10	25	68	1.62	.052	-.033
18	#10	25	66	1.86	.054	-.038

TABLE 4.3: STRAIN AT PULLED THROUGH STAGE

(a) Monotonic Loading

Specimen No.	Bar Size	Block Width (in.)	Strain in Micro In./In.	
			Pull End	Push End
2	# 6	15	24,000	-12,000
3$^{\Delta}$	# 8	25	61,000	0
7*	# 8	15	1,860	-1,800
10	# 6	20	51,000	-20,000
13	# 8	25	42,000	-21,000
16	#10	25	24,000	-8,000

* Pull-through at a stress smaller than the yielding stress of rebar.

Δ Subjected to pulled on one end only.

(b) Cyclic Loading

Specimen No.	Bar Size	Block Width (in.)	Strain in Micro In.In.	
			Pull End	Push End
4*	# 6	15	1,900	-1,850
8**	# 8	15	1,800	-1,500
11	# 6	20	10,000	-3, -3,000
14	# 8	25	11,000	-7,500
17	#10	25	9,000	-6,000

*Pull-through strength is 55 ksi less than yield strength of rebar.

**Pull-through strength is 50 ksi.

TABLE 4.4

ESTIMATED MAXIMUM BOND STRESSES IN DIFFERENT REGIONS

(a) Monotonic Loading

Specimen No.	Block Width (in.)	Maximum Bond Stress (ksi)		
		Unconfined Region	Confined Region	Pushed End Region
2	15	1.05	2.3	5.3
3*	25	1.1	2.2	
7	15	1.02	1.9	2.8
10	20	0.95	2.2	4.8
13	25	1.2	2.3	7.0
16	25	0.9	2.3	6.3

* Subjected to pull on one end only. There is no push end region in this test.

(b) Cyclic Loading

Specimen No.	Block Width (in.)	Maximum Bond Stress (ksi)		
		* Unconfined Region	* Confined Region	* Pushed End Region
4	15	0.9	1.9	4.3
8	15	0.7	1.7	4.5
11	20	0.9	2.0	4.9
14	25	0.9	1.9	7.0
17	25	0.8	1.9	4.8

* Note: The unconfined, confined and pushed end regions are defined according to the figure shown.

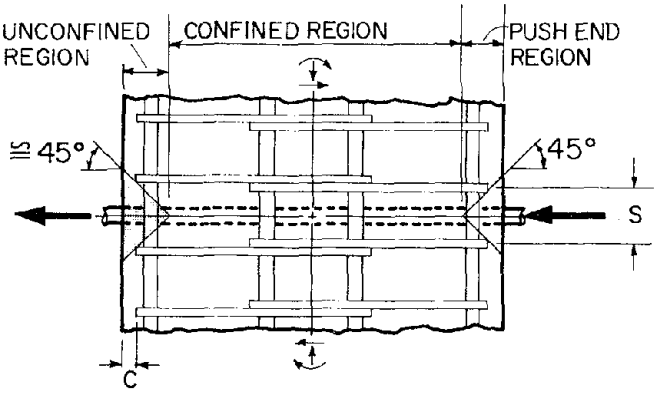

Where s is the space between transverse or longitudinal reinforcement, whichever is narrower, and c is the cover thickness of column.

TABLE 4.5: APPROXIMATED FIXED END ROTATION AT YIELD

(a) Monotonic Loading

Specimen No.	Bar Size	Block Width (in.)	Fixed End Rotation at Yield (rad.)
2	# 6	15	.0018
2	# 8	25	.0010
10	# 6	20	.0014
13	# 8	25	.00135
16	#10	25	.0026

(b) Cyclic Loading

Specimen No.	Bar Size	Block Width (in.)	Fixed End Rotation at Yield (rad.)
11	# 6	20	.0028
12*	# 6	20	.0030
14	# 8	25	.0022
15*	# 8	25	.0026
17	#10	25	.0030
18*	#10	25	.0034

*Ungrooved Bar

Note: An effective depth (d-d') of 20 in. is assumed in the estimation of the fixed end rotation.

TABLE 5.1: COMPARISON OF CYCLIC AND MONOTONIC LOADING

Bar Size	Block Size (in.)	Strength Ratio Cyclic over Monotonic	Max. Strength (ksi)		δ_1 at Max. Strength (in.)		δ_2 at Max. Strength (in.)	
			Mono	Cyclic	Mono	Cyclic	Mono	Cyclic
# 6	15	.71	77	55	.104	.067	-.037	-.065
# 6	20	.75	89	67	.35	.062	-.035	-.027
# 8	15	.91	56	51	.06	.039	-.035	-.034
# 8	25	.76	95	72	.45	.06	-.096	-.030
#10	25	.78	87	68	.169	.052	-.060	-.033

TABLE 5.2: PROPORTION OF DEFORMED BAR DIMENSION (#8 BAR AS BASIS)

Bar Size	Proportion of		
	Bar Diameter	Lug Height	Lug Spacing
# 6	.75	.58	.75
#10	1.27	1.08	1.23

TABLE 5.3(a): EFFECT OF GROOVES ON BEARING FAILURE MODE

Bar Size	(A_s/Σ_o)		Ratio of Grooved to Ungrooved Bearing Area
	Ungrooved Bar	Grooved Bar	
# 6	.206	.229	1.11
# 8	.263	.280	1.07
#10	.307	.336	1.09

*A_s and Σ_o is the measured area and the perimeter of a bar.

TABLE 5.3(b): EFFECT OF GROOVES ON DIRECT SHEAR FAILURE MODE

Bar Size	$A_s(in.^2)$		Ratio of Grooved to Ungrooved Shear Surface
	Ungrooved Bar	Grooved Bar	
# 6	.438	.371	.847
# 8	.774	.700	.904
#10	1.223	1.173	.959

TABLE 7.1 MONOTONIC SKELETON CURVE FOR DIFFERENT BAR DIAMETERS

(a) #6 BAR

Regions	τ_A	γ_A	τ_B	γ_B	τ_C	γ_C
Unconfined	.4	.00069	1.1	.0083	0.	.011
Confined	.5	.00069	1.9	.0084	.05	.0772
Pushed End	.5	.00069	3.2	.0110	.1	.083

(b) #8 BAR

Regions	τ_A	γ_A	τ_B	γ_B	τ_C	γ_C
Unconfined	.4	.00071	1.3	.00714	0.	.012
Confined	.5	.00071	2.1	.0086	.05	.0857
Pushed End	.5	.00071	3.07	.0086	.10	.10

(c) #10 BAR

Regions	τ_A	γ_A	τ_B	γ_B	τ_C	γ_C
Unconfined	.4	.00071	1.3	.0101	0.	.012
Confined	.5	.00074	2.6	.0104	.05	.0889
Pushed End	.5	.00074	4.3	.01511	.10	.1289

Note: τ in ksi unit

γ in Rad.

TABLE 7.2 EXPRESSIONS OF τ-γ RELATION FOR MONOTONIC SKELETON CURVES

(a) UNCONFINED REGION

$$\tau_A = .4$$
$$\gamma_A = .00008D^2 - .00006D + .00069$$
$$\tau_B = -1.6D^2 + 3.6D - .7$$
$$\gamma_B = .033D^2 - .0623D + .0365$$
$$\tau_C = 0.$$
$$\gamma_C = -.008D^2 + .018D + .002$$

(b) CONFINED REGION

$$\tau_A = .5$$
$$\gamma_A = .00008D^2 - .00006D + .00069$$
$$\tau_B = 2.4D^2 - 3.4D + 3.1$$
$$\gamma_B = .0128D^2 - .0216D + .0174$$
$$\tau_C = .05$$
$$\gamma_C = -.0424D^2 + .1082D + .0199$$

(c) PUSHED END REGION

$$\tau_A = .5$$
$$\gamma_A = .00008D^2 - .00006D + .00069$$
$$\tau_B = 10.88D^2 - 19.56D + 11.75$$
$$\gamma_B = .0713D^2 - .1343D + .0717$$
$$\tau_C = .10$$
$$\gamma_C = .0952D^2 - .0986D + .0104$$

TABLE 7.3: CYCLIC PARAMETERS

(a) #8 BAR

Regions	P_b	$P_{b'}$	P_c	$P_{c'}$	$\xi_{\tau b}$	$\xi_{\tau c}$	$\xi_{\gamma c}$	$\xi_{\tau b'}$	$\xi_{\tau c'}$	$\xi_{\gamma c'}$
Unconfined	9.47	3.53	7.10	2.38	.20	.6	0	.64	.6	.543
Confined	6.63	6.63	3.05	3.05	.43	.50	.333	.43	.5	.333
Pushed End	9.47	3.53	2.38	7.10	.64	.6	.543	.20	.64	.543

(b) #10 BAR

Regions	P_b	$P_{b'}$	P_c	$P_{c'}$	$\xi_{\tau b}$	$\xi_{\tau c}$	$\xi_{\gamma c}$	$\xi_{\tau b'}$	$\xi_{\tau c'}$	$\xi_{\gamma c'}$
Unconfined	9.47	3.53	7.4	3.25	.20	.6	0	.32	.40	.56
Confined	6.63	6.63	3.56	3.56	.40	.40	.333	.40	.40	.333
Pushed End	3.53	9.47	3.25	7.4	.32	.40	.40	.20	.6	.0

Table 7.4 COMPUTATION COSTS IN ANALYTICAL PREDICTIONS

Type of Loading History	No. of Bond Elements	No. of Steel Elements	No. of Steps	* Time (sec.)	** Cost ($)
MONO-Sp.3	12	11	35	97.5	D $18
MONO-SP.10	11	9	48	65.0	D $12
MONO-SP.13	11	9	52	75.8	D $13
MONO-SP.16	11	9	80	86.7	D $15
CYC-SP.8	8	6	253	23.8	D $43
CYC-SP.14	8	6	635	65.0	I $60
CYC-SP.17	8	6	601	54.1	D $99

* Estimated effective time, including printing costs.

** The estimated cost of a run was charged according to CDC 6400 computer Table. D and I denote the priority of the job run.

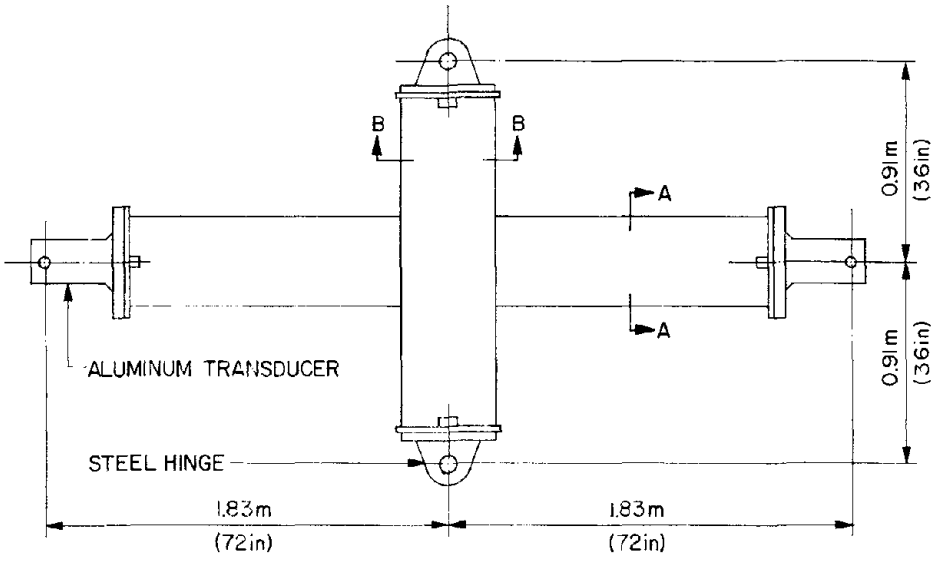

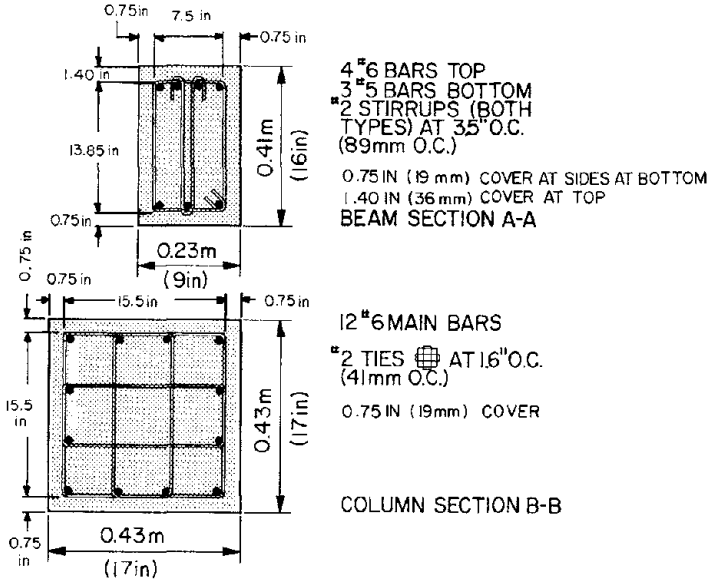

Fig. 1.1 Beam-Column Specimen

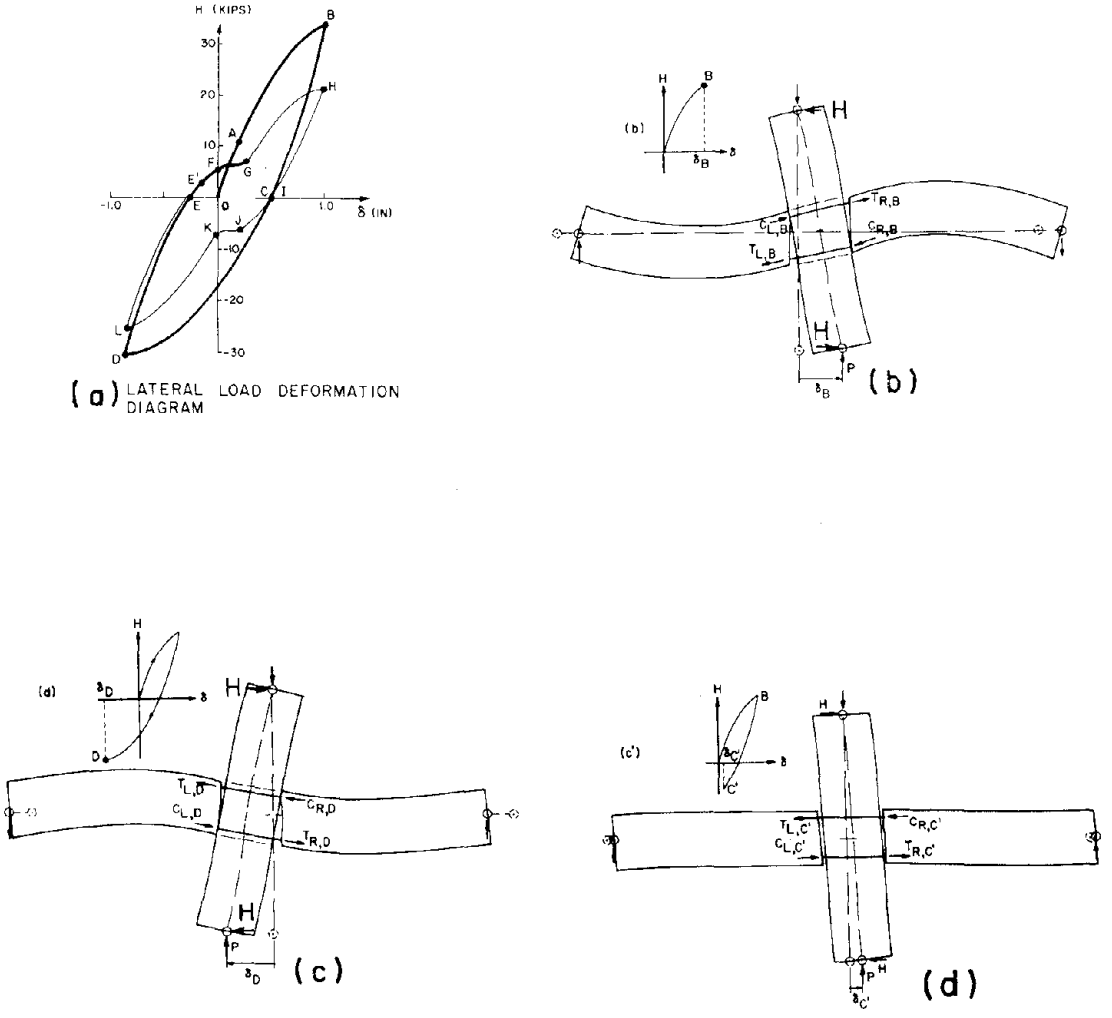

Fig. 1.2 Mechanism of Stiffness Degradation

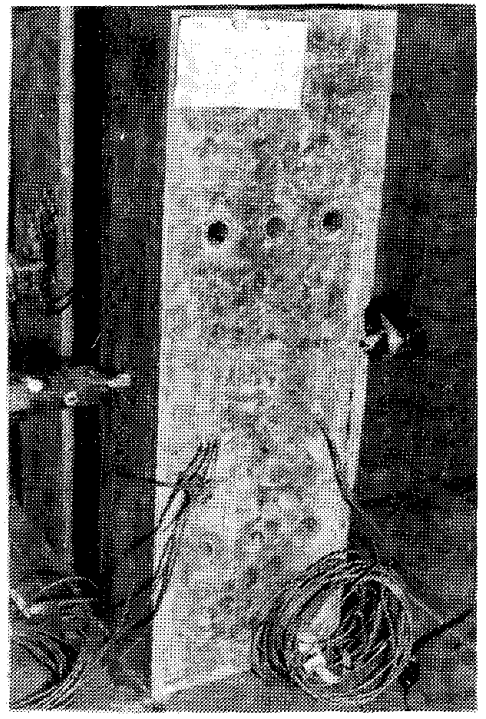

Fig. 1.3 Photograph of a Specimen After Test

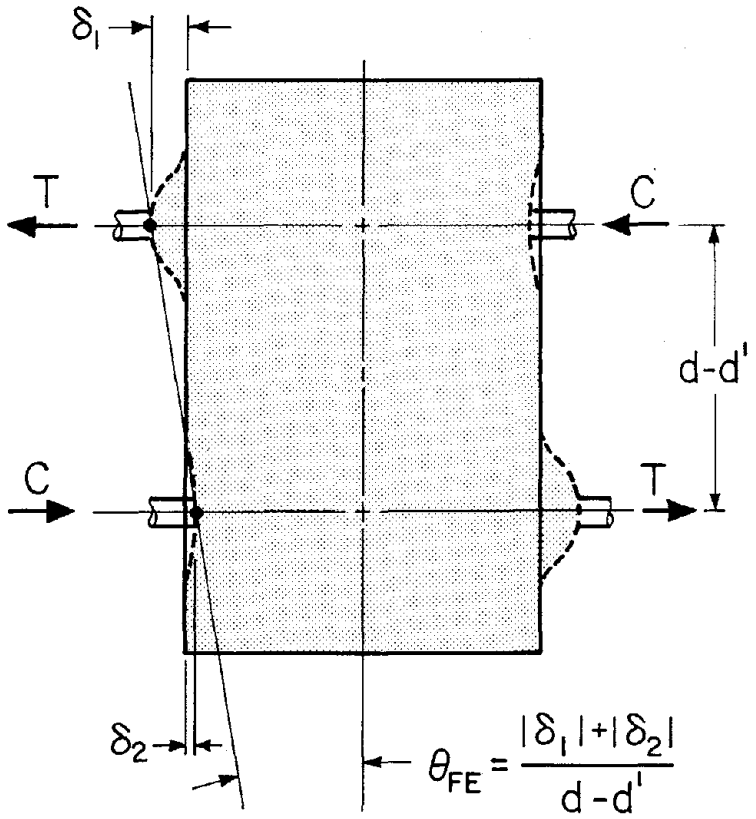

Fig. 1.4 Fixed-End Rotations at Interior Column

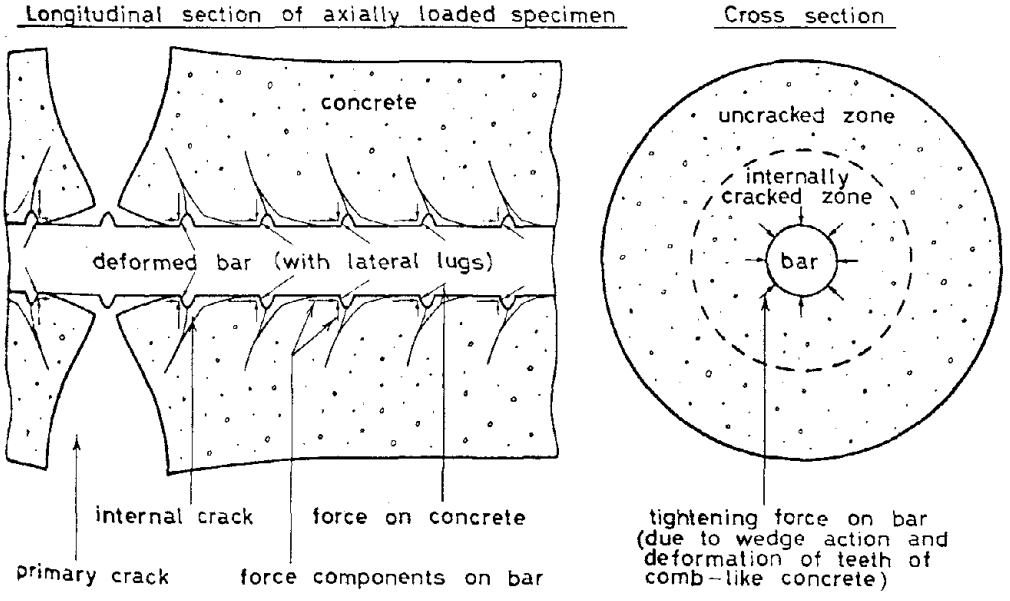

Fig. 1.5 Deformation of Concrete Around Reinforcing Bars [10]

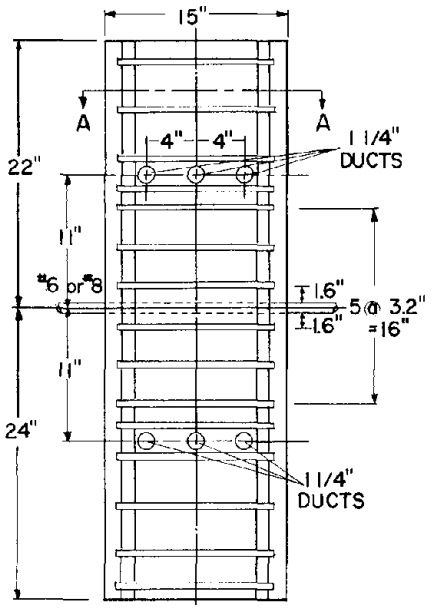

(a) ELEVATION

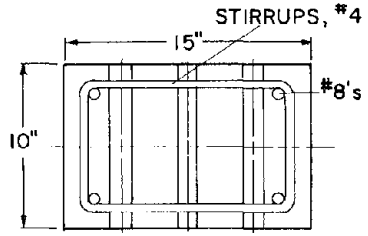

(b) SECTION A-A

Fig. 2.1 Reinforcing Cage for 15 in. Specimen

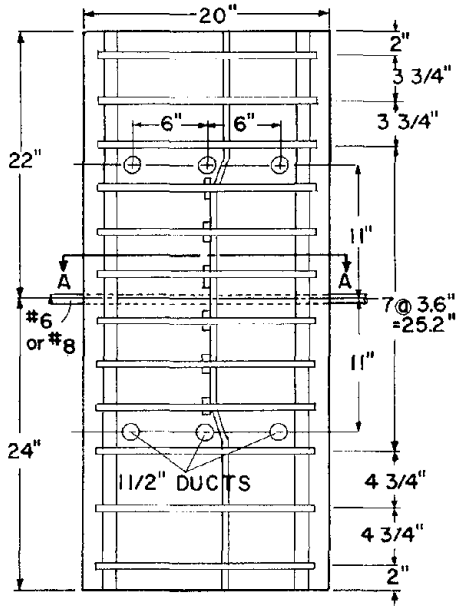

(a) ELEVATION

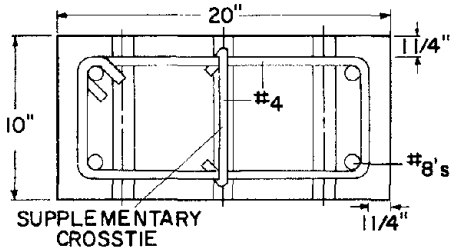

(b) SECTION A-A

Fig. 2.2 Reinforcing Cage for 20 in. Specimen

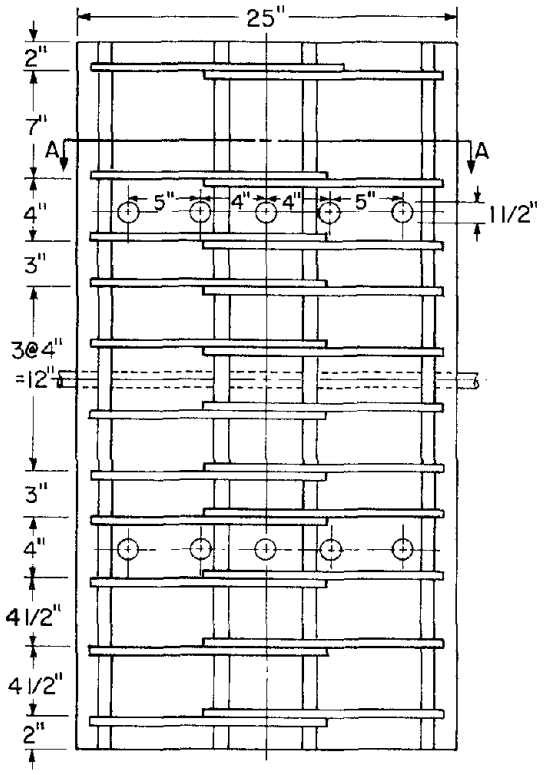

(a) ELEVATION

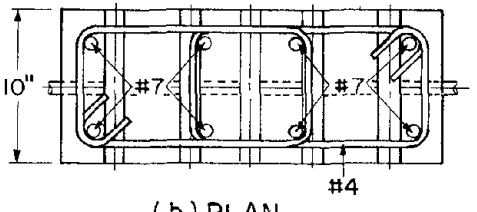

(b) PLAN

Fig. 2.3 Reinforcing Cage for 25 in. Specimen

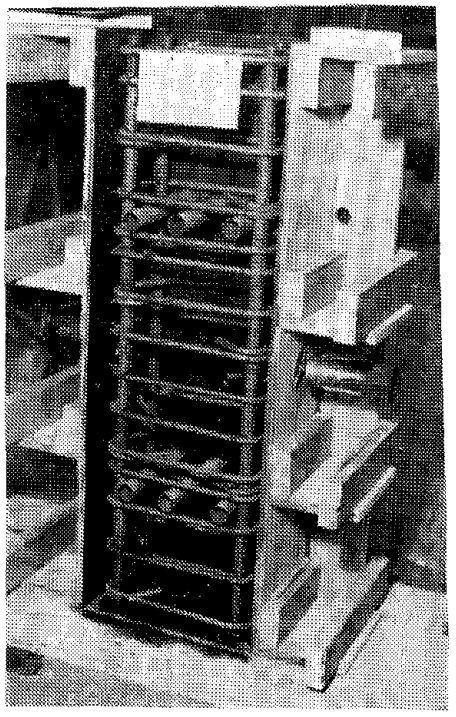

(a) 15 in. Column

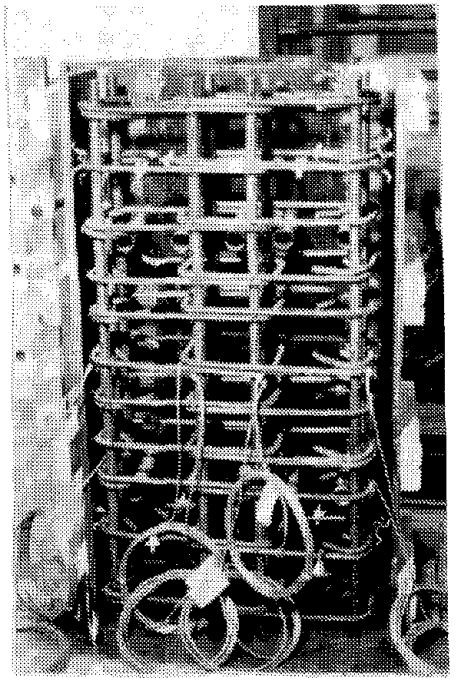

(b) 25 in. Column

Fig. 2.4 Reinforcing Cages

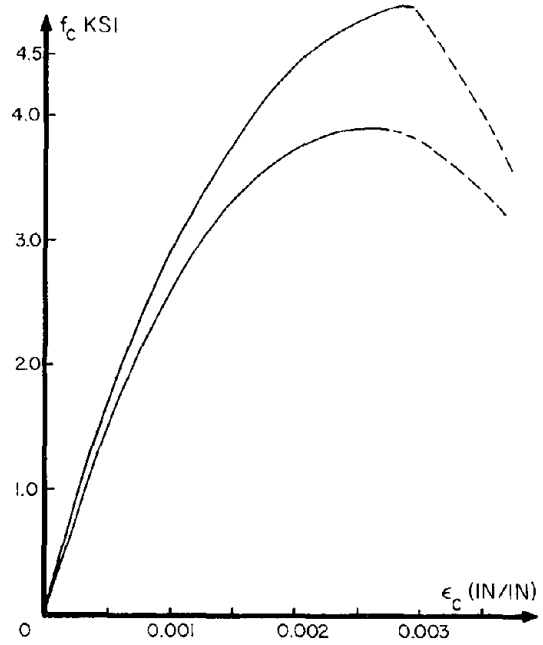

Fig. 2.5 Upper and Lower Bound of Concrete Stress-Strain Curve

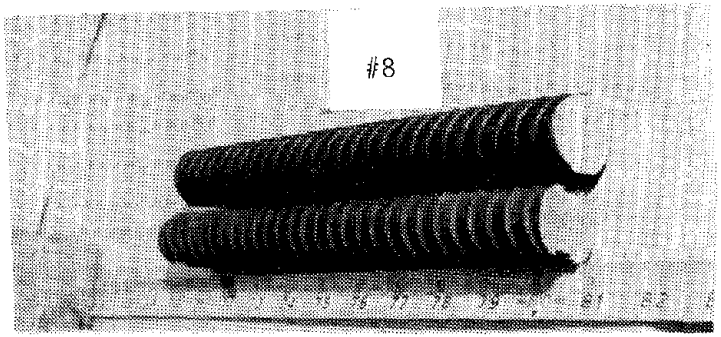

Fig. 2.6 Typical Deformed Pattern of Embedded Reinforcing Bar

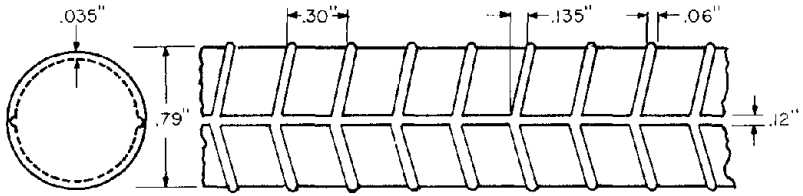

(a) #6

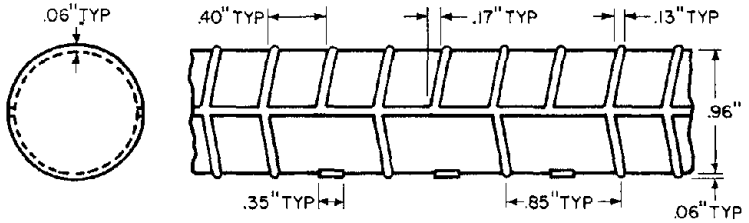

(b) #8

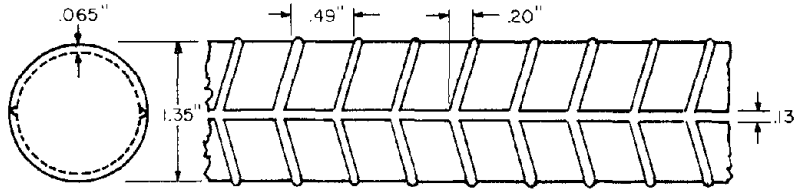

(c) #10

Fig. 2.7 Geometry of Ungrooved Bars

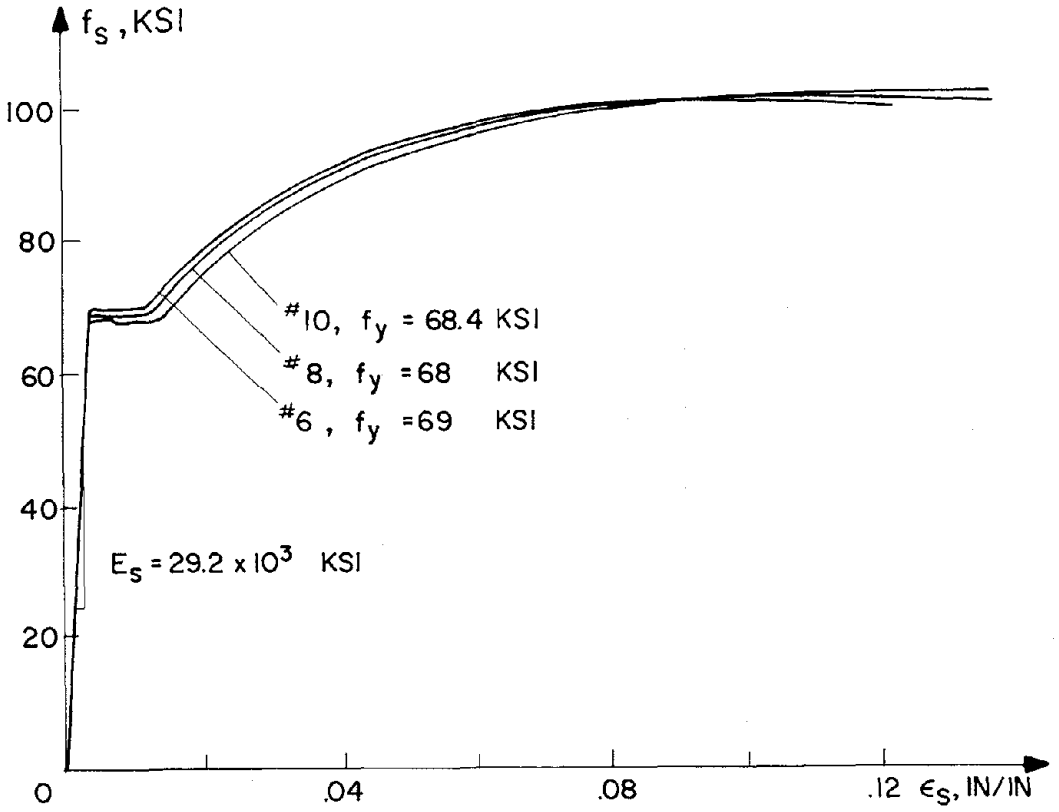

Fig. 2.8 $f_s - \varepsilon_s$ Diagram of Embedded Bars

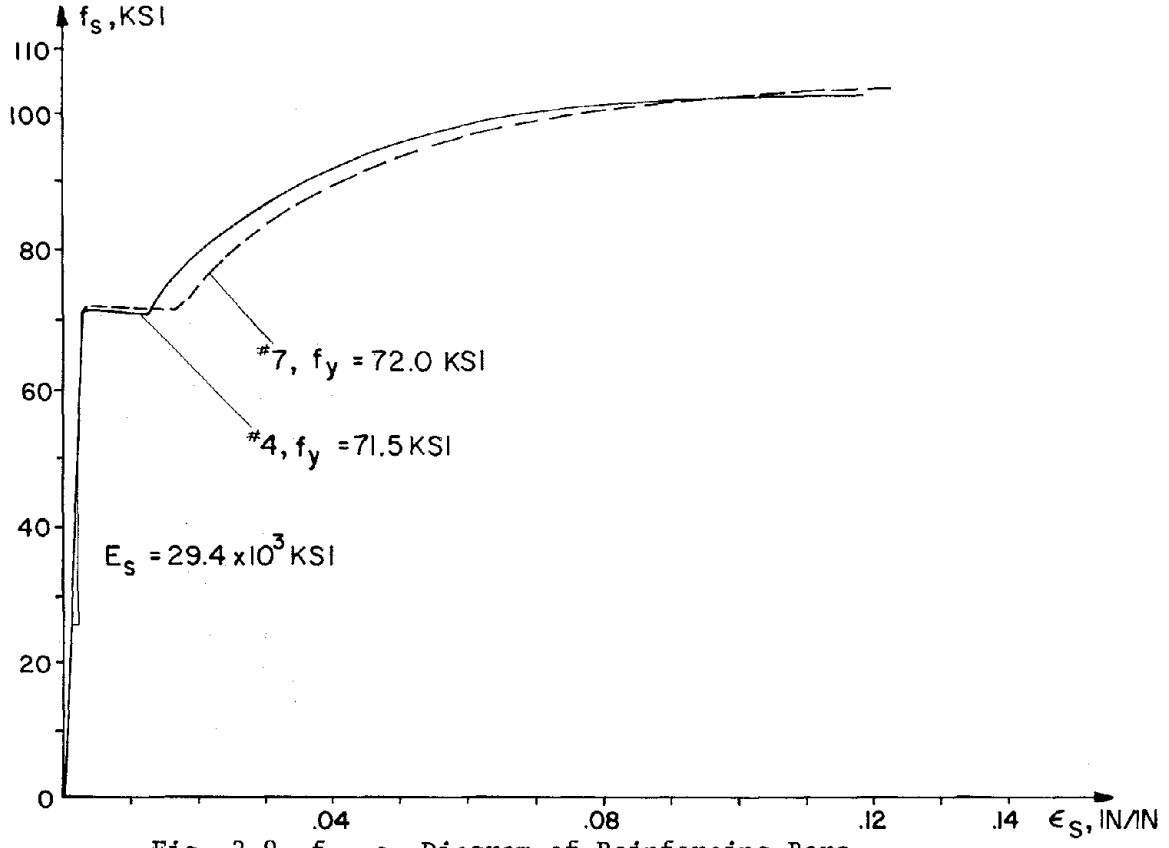

Fig. 2.9 $f_s - \varepsilon_s$ Diagram of Reinforcing Bars

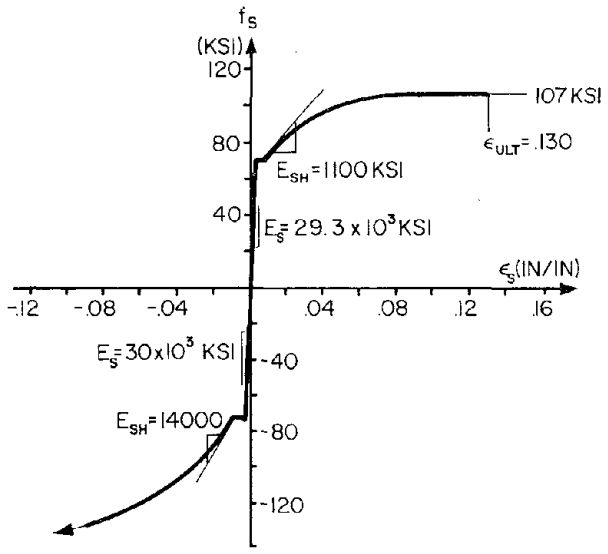

Fig. 2.10 Typical $f_s - \varepsilon_s$ Curve of Reinforcing Bar Under Monotonic Tension and Compression

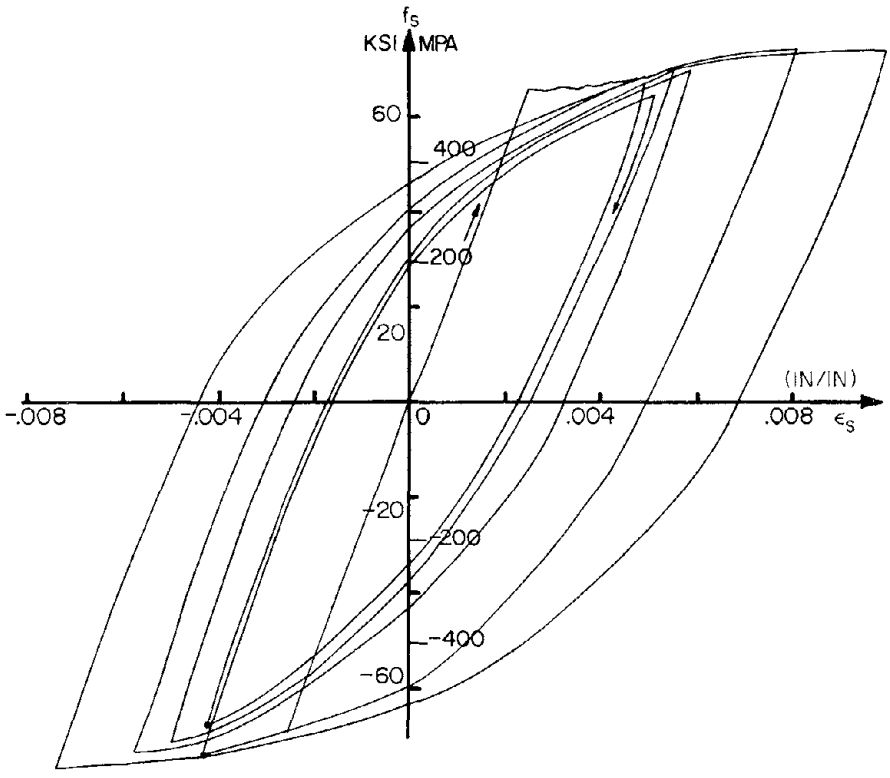

Fig. 2.11 Typical $f_s - \varepsilon_s$ Curve of Reinforcing Bar Under Cyclic Loading

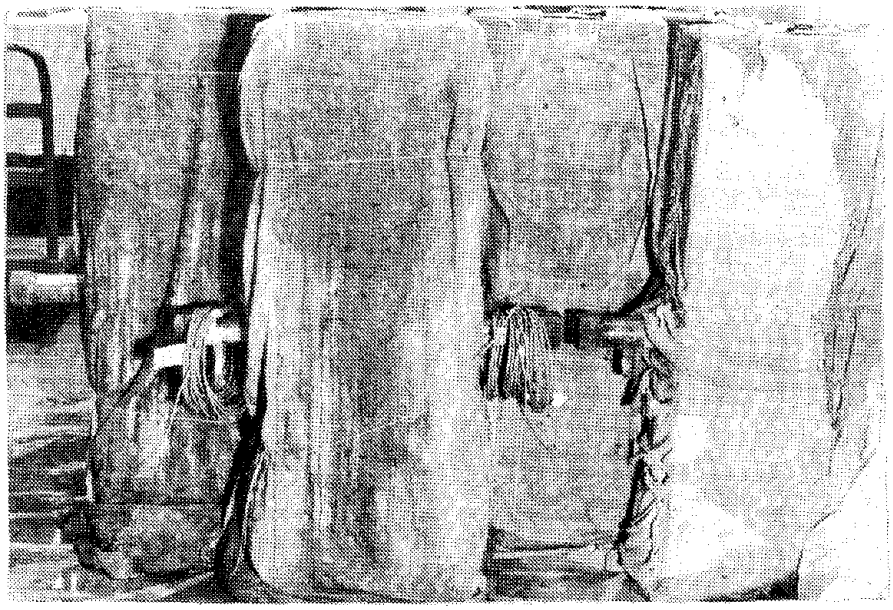

Fig. 2.12 Specimens Curing

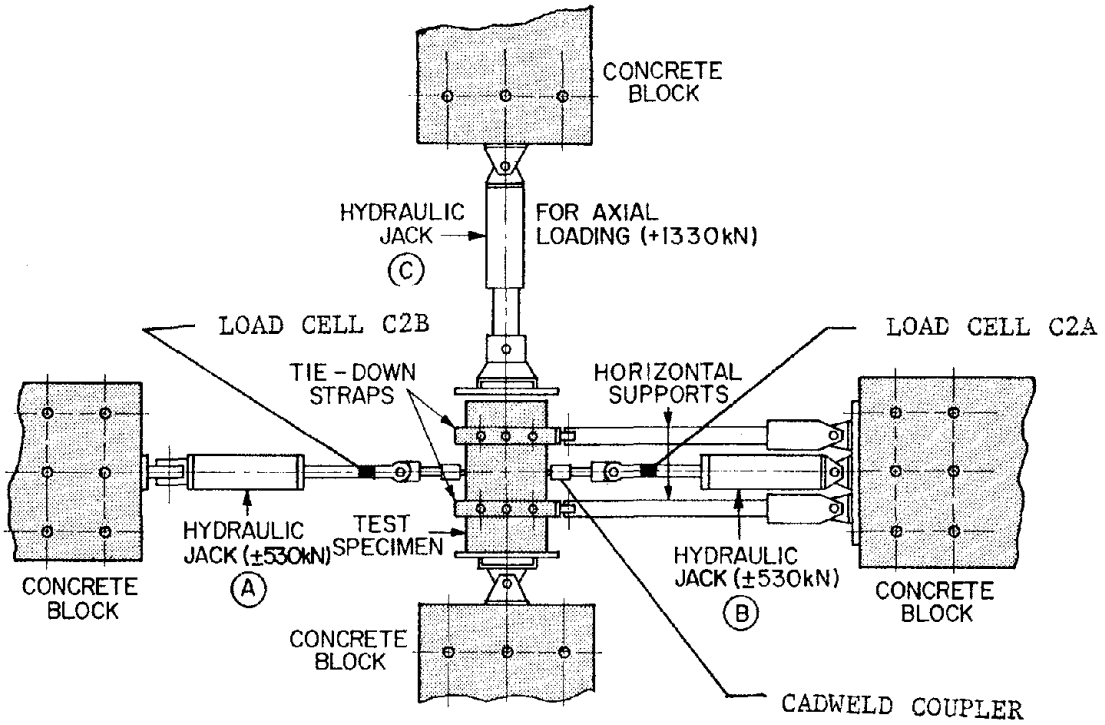

(a) Schematic Diagram of Test Set-Up

Fig. 3.1 Test Facility

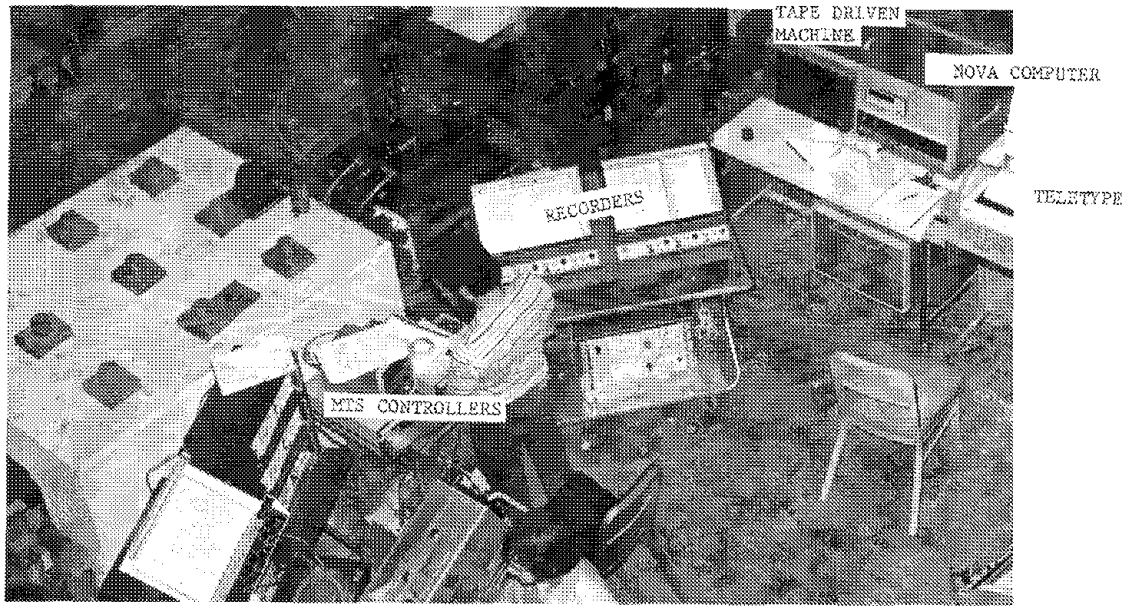

(b) Test Set-Up and Data Acquisition System

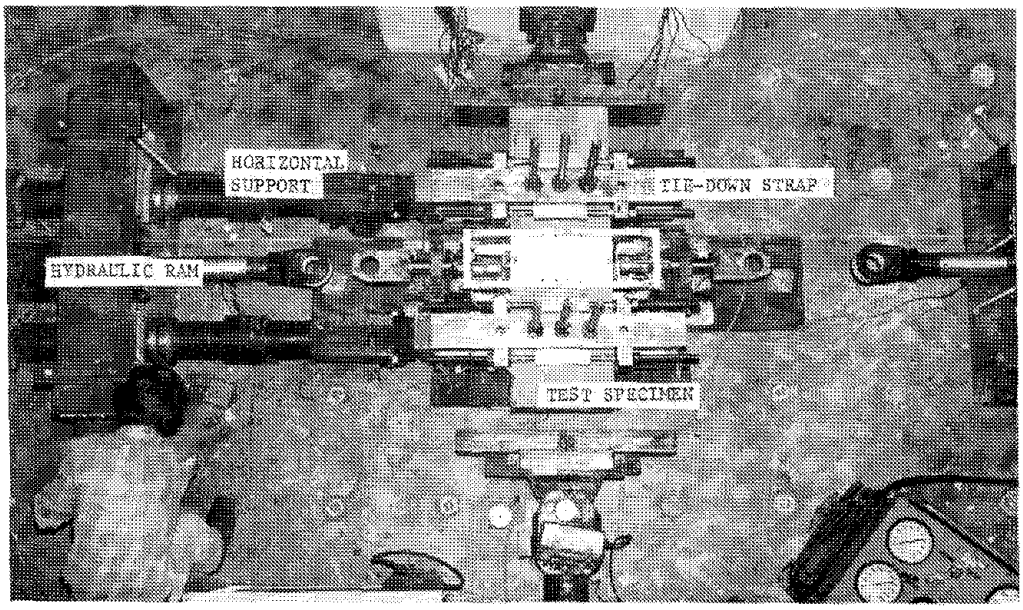

(c) Specimen in Testing Bed

Fig. 3.1 Test Facility

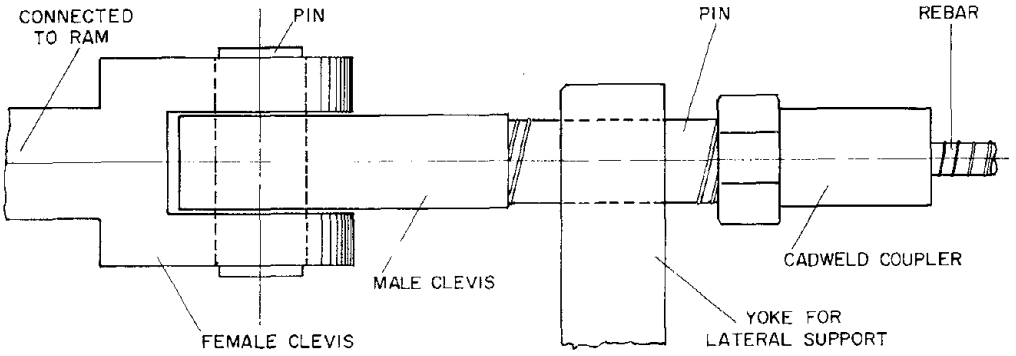

Fig. 3.2 Transmission of Force to Rebar

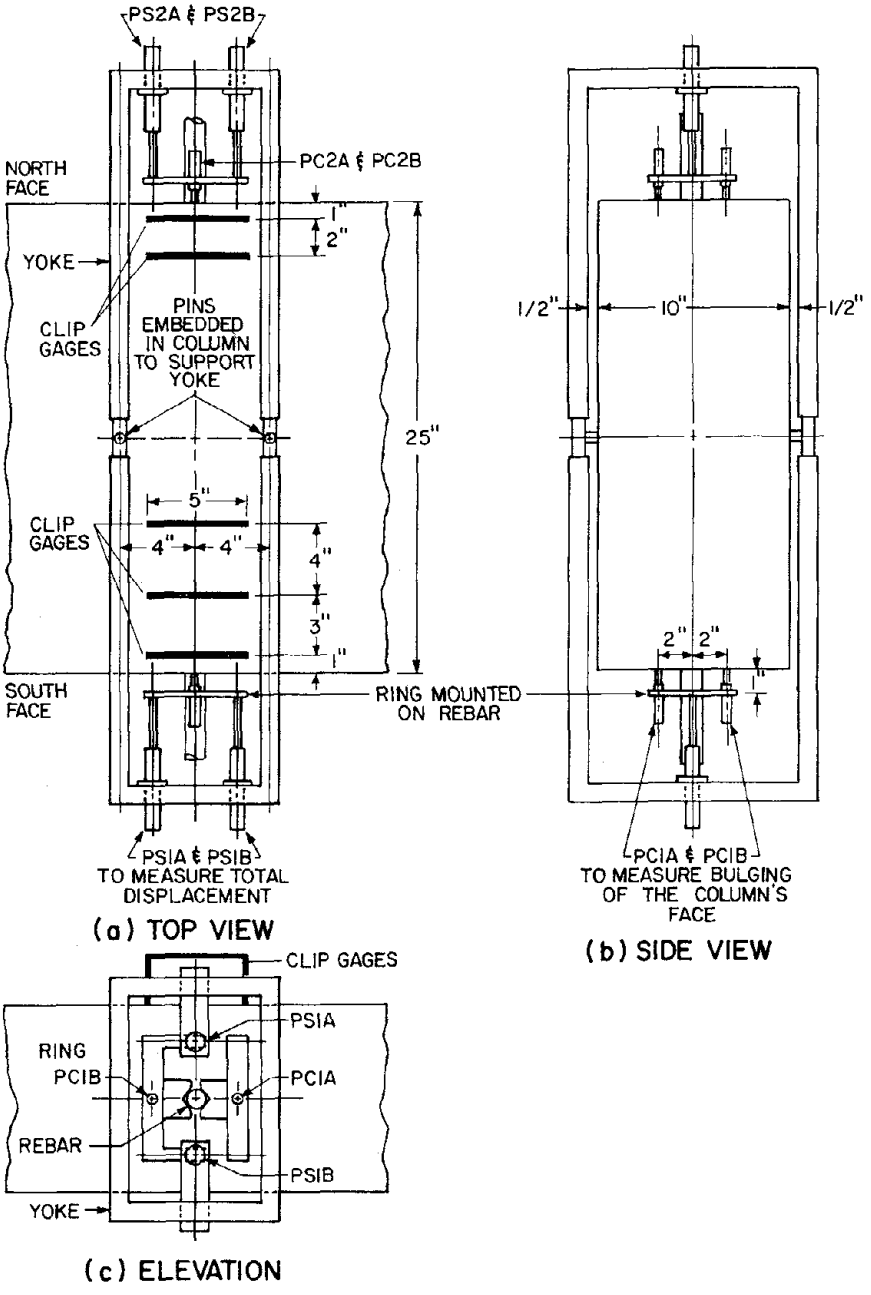

Fig. 3.3 External Instrumentation

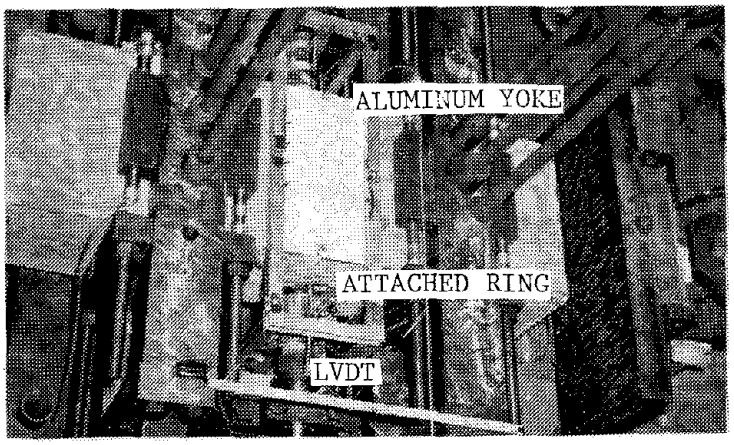

Fig. 3.4 Close-Up of External Instrumentation

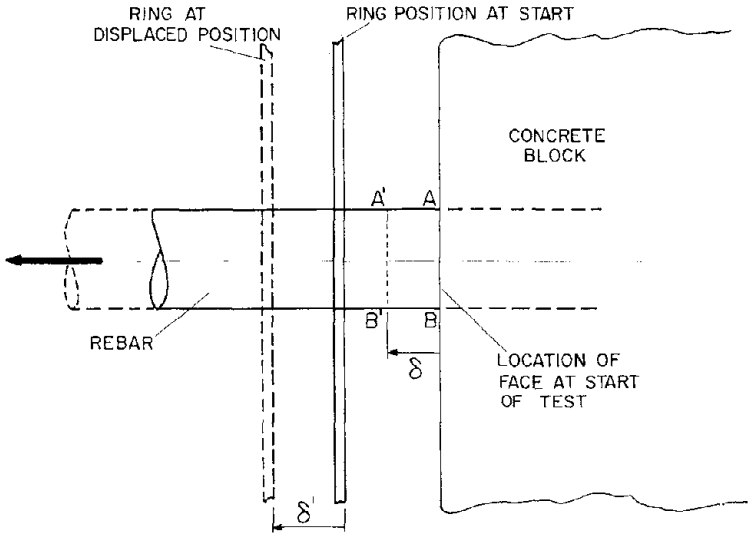

Fig. 3.5 Definition of δ and δ'

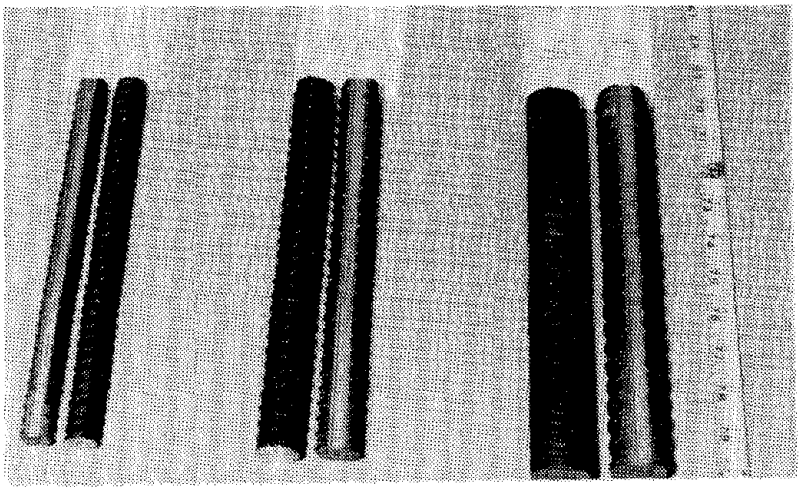

Fig. 3.6 Grooved and Ungrooved Bars

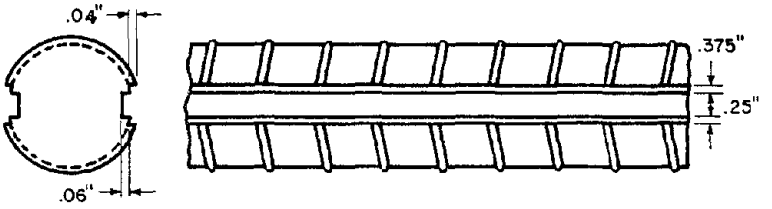

(a) #6 Bar

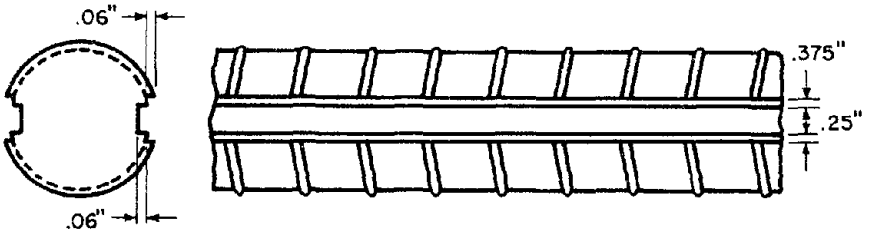

(b) #8 Bar

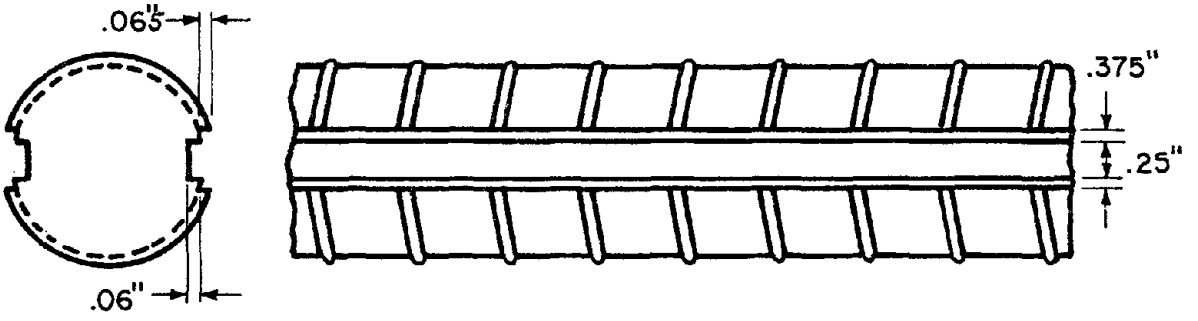

(c) #10 Bar

Fig. 3.7 Geometry of Grooved Bars

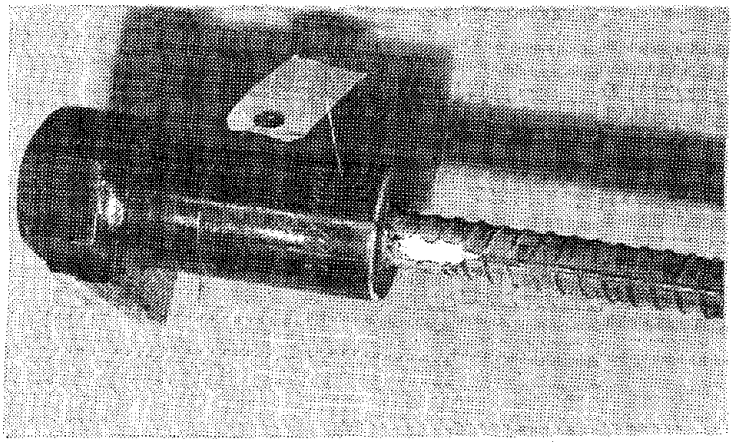

Fig. 3.8 Cadweld Coupler at End of Bar

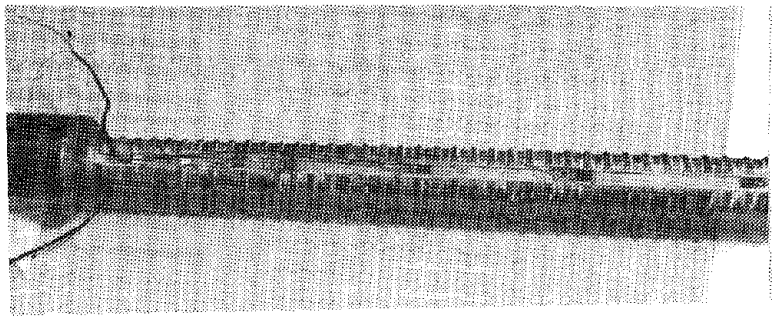

Fig. 3.9 Installed Strain Gages in Groove

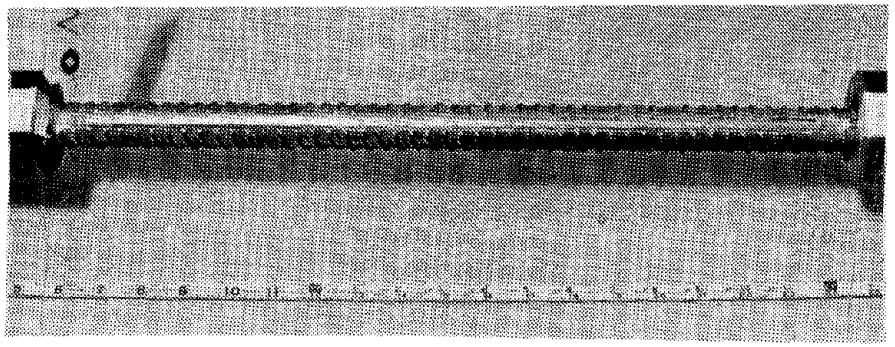

Fig. 3.10 Bar with Complete Strain Gage Instrumentation Installation

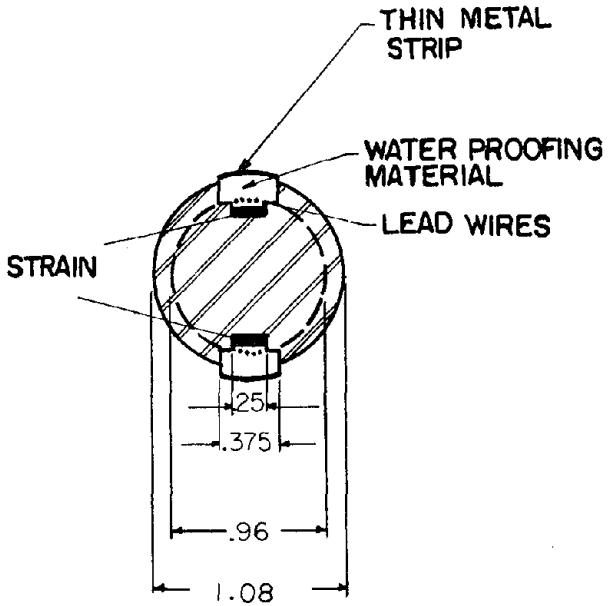

Fig. 3.11 Typical Section of Instrumented Grooved Bar

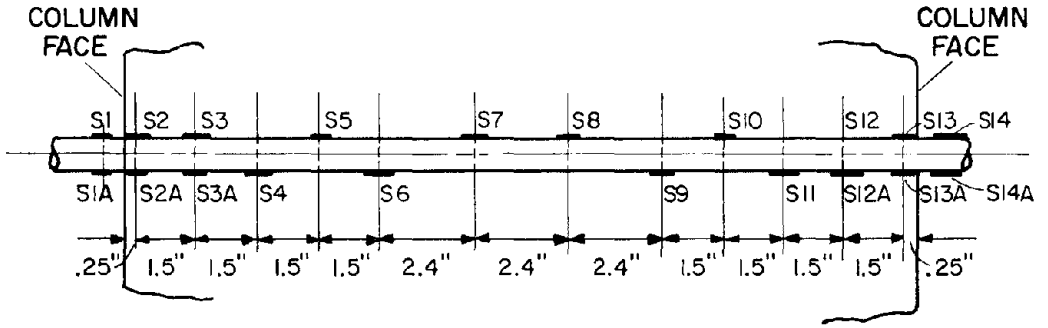

Fig. 3.12 Typical Layout of Strain Gages Along Grooved Bar

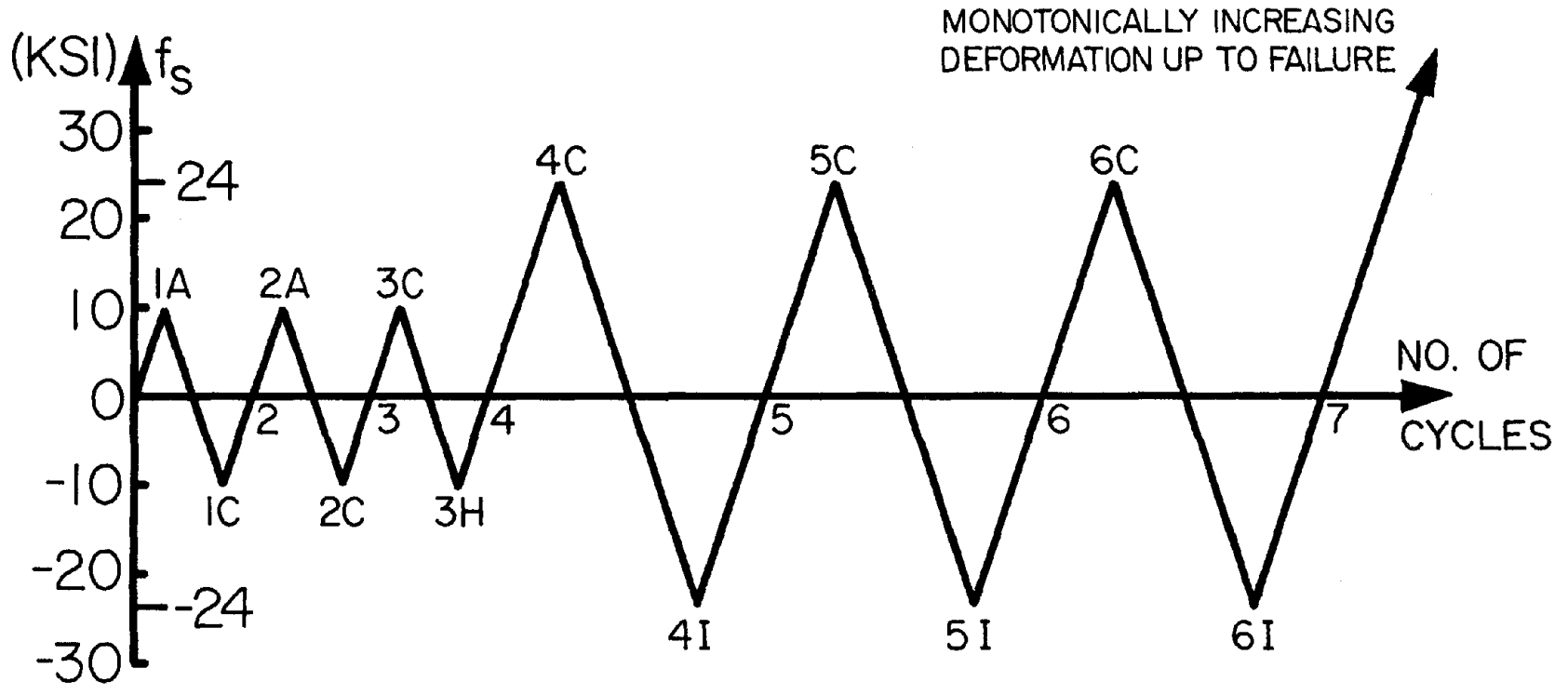

Fig. 3.13 Typical Monotonic Loading History

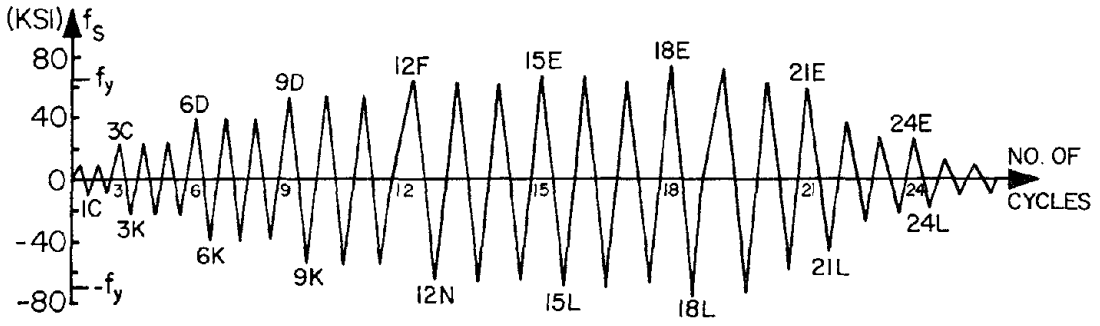

(a) Force or Stress History

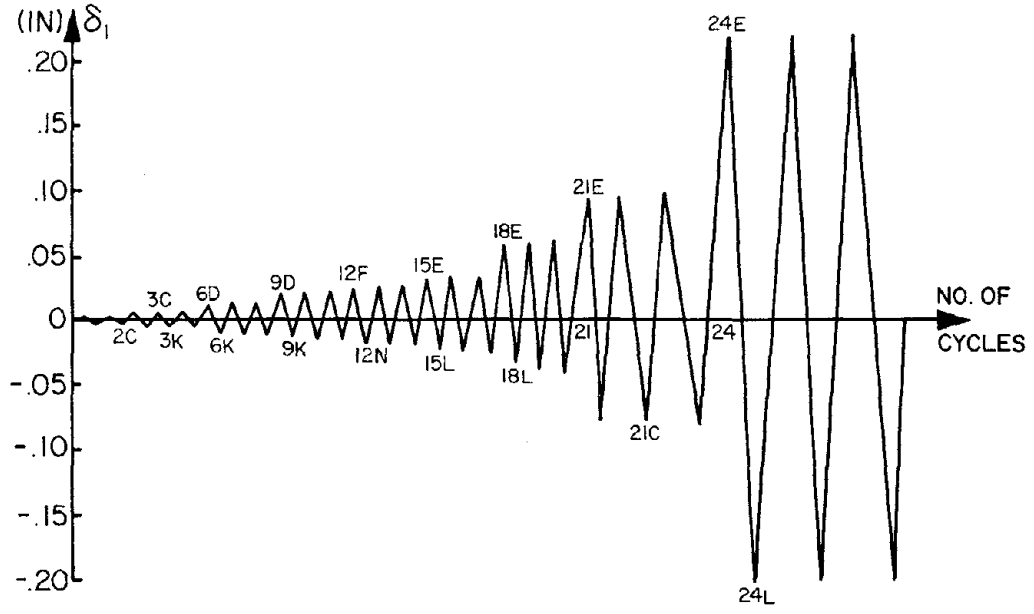

(b) Displacement History

Fig. 3.14 Typical Cyclic Loading History

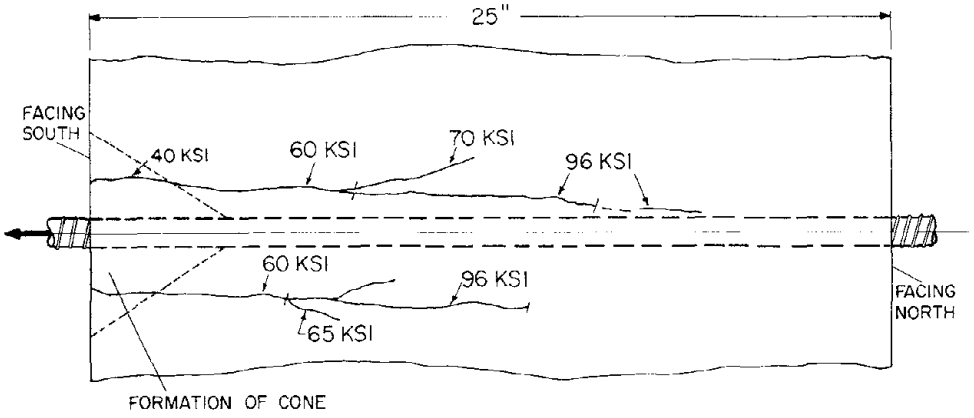

(a) Top Face of the Column Block

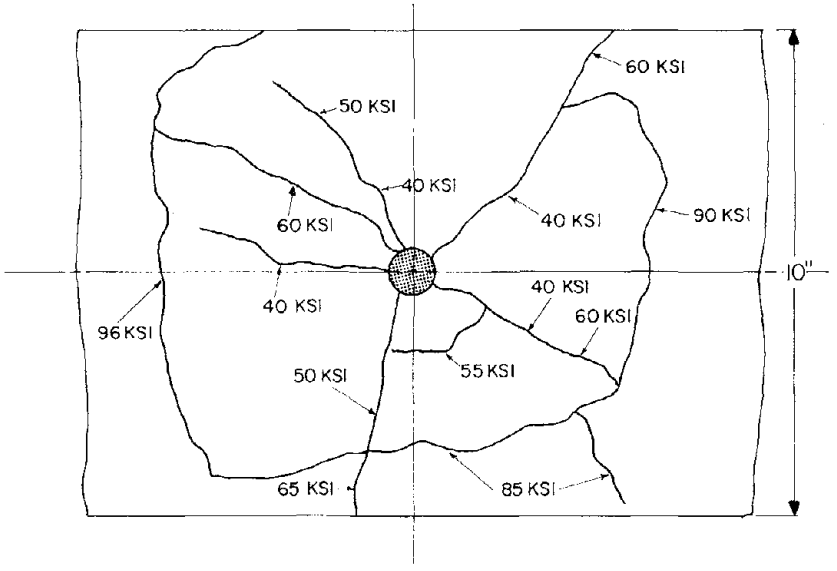

(b) At Pull Face

Fig. 4.1 Crack Pattern (Pull Only)

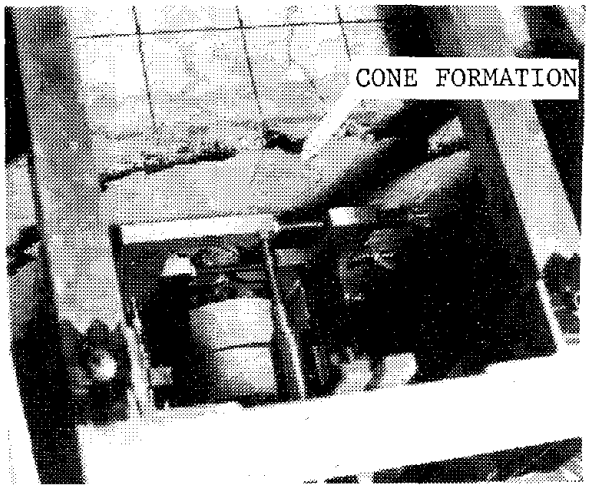

Fig. 4.2 Cone Formation at Pull End

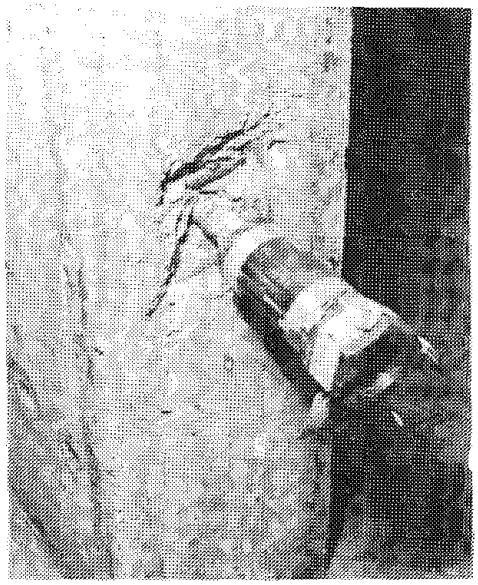

Fig. 4.3 Seat of Cone Formation

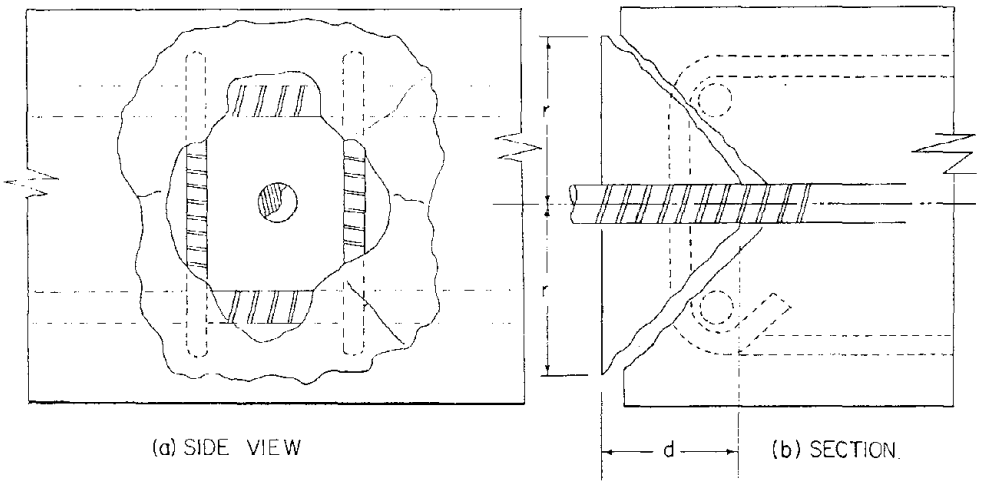

Fig. 4.4 Geometry of Cone

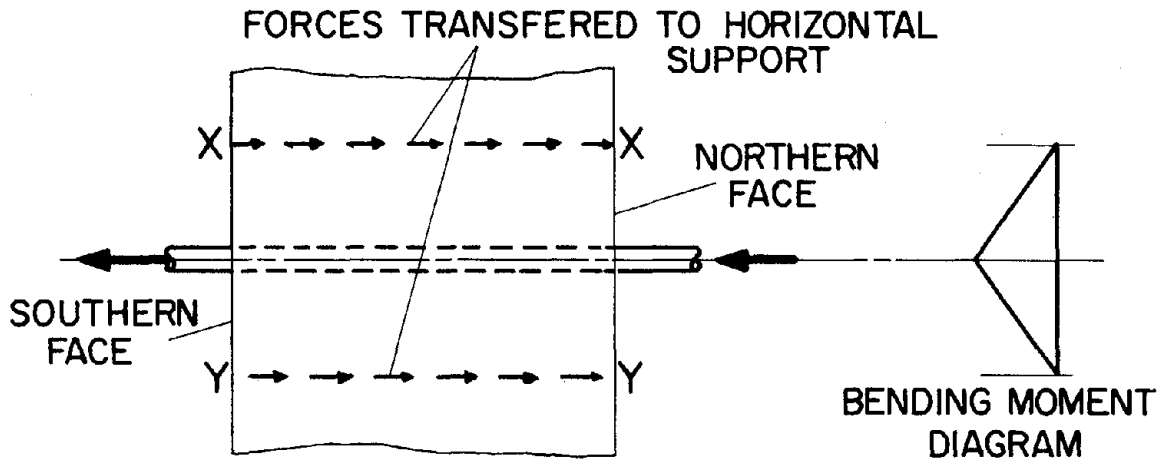

Fig. 4.5 Free Body Diagram of Concrete Block

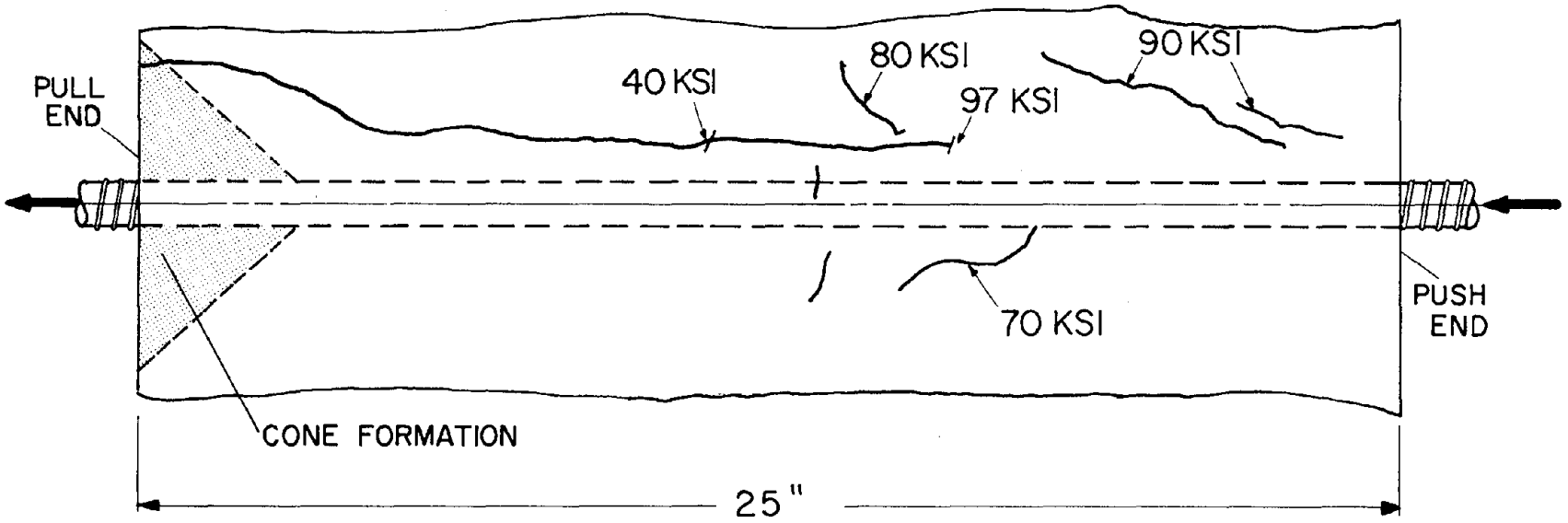

Fig. 4.6 Typical Crack Pattern of Monotonic Pull-Push Specimen, (a) At Top Face

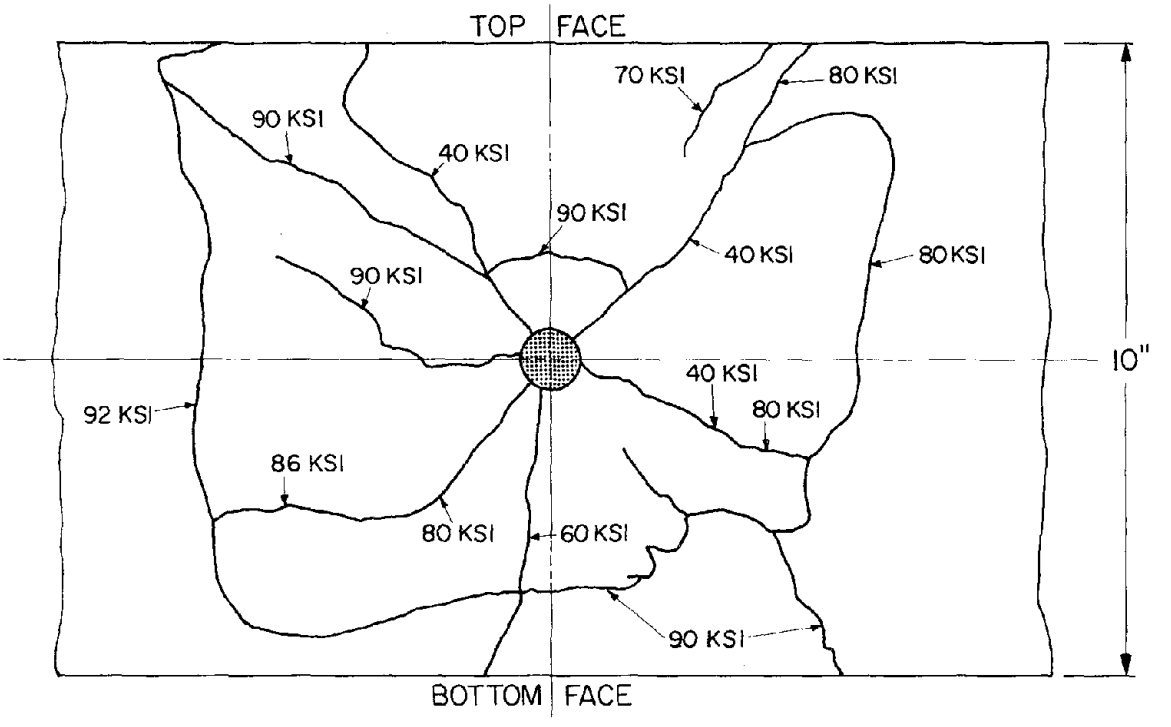

(b) At Pull End Face

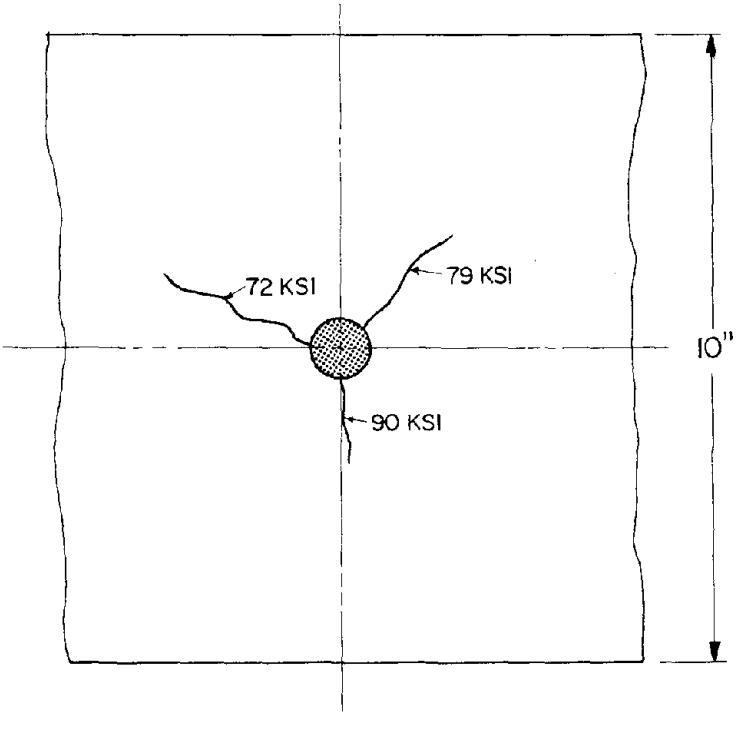

(c) At Pushed End Face

Fig. 4.6 Typical Crack Pattern of Monotonic Push-Pull Specimen

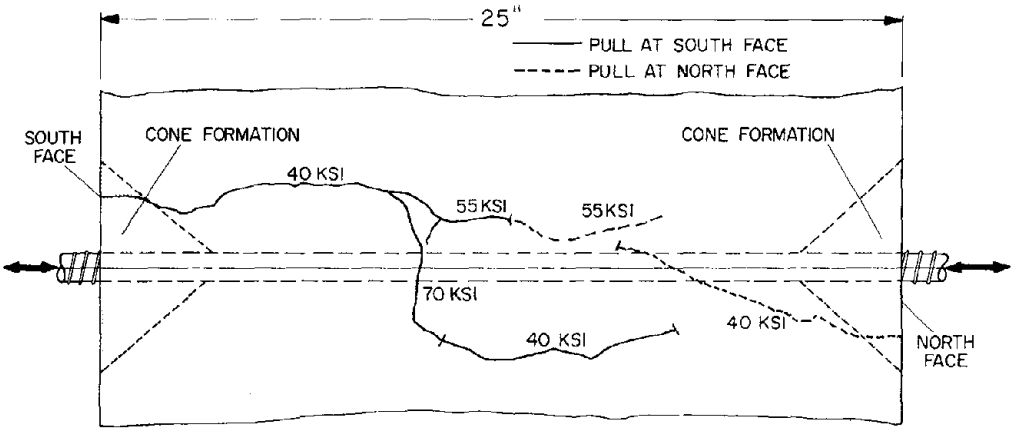

(a) At Top Face

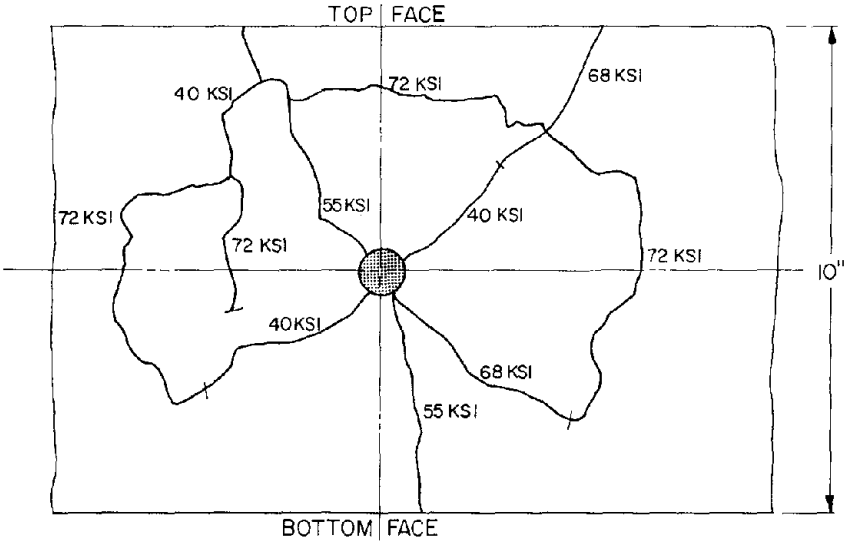

(b) At South Face

Fig. 4.7 Typical Crack Pattern Under Bond Reversal

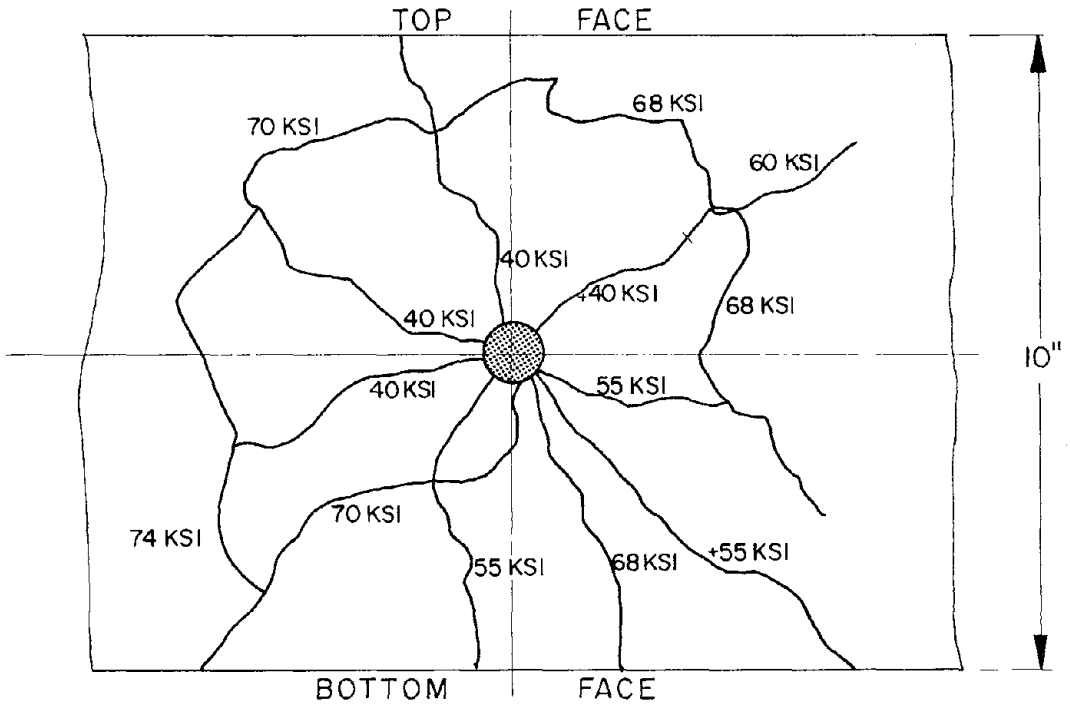

(c) At North Face

Fig. 4.7 Typical Crack Pattern Under Bond Reversal

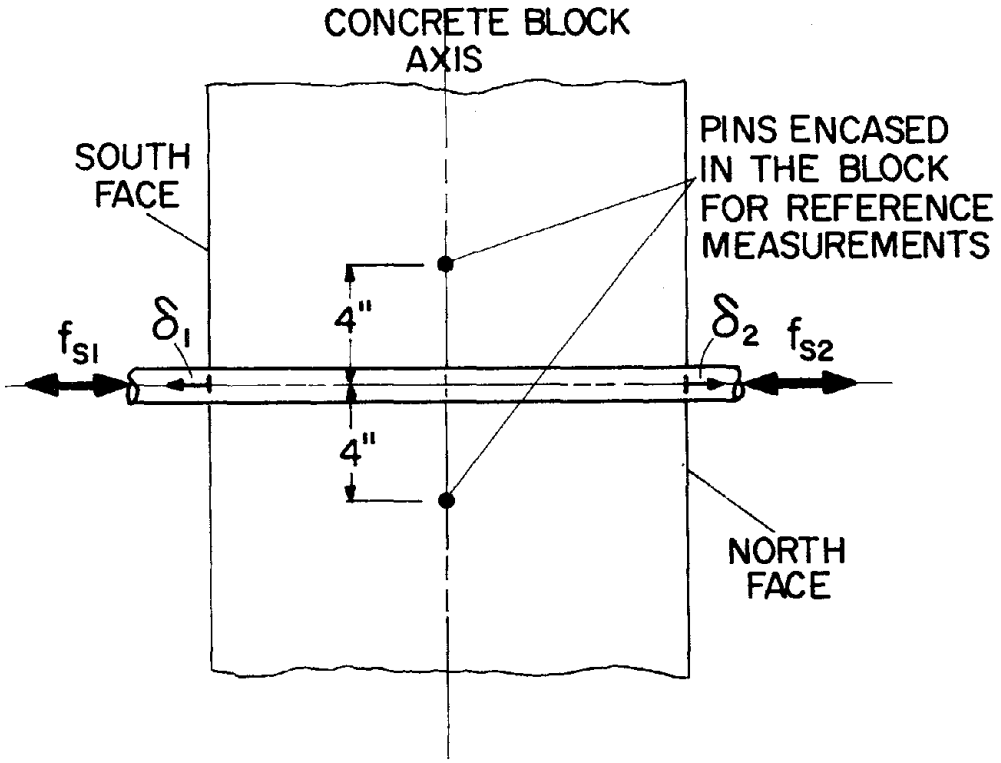

Fig. 4.8 Definitions of External Forces and Displacement

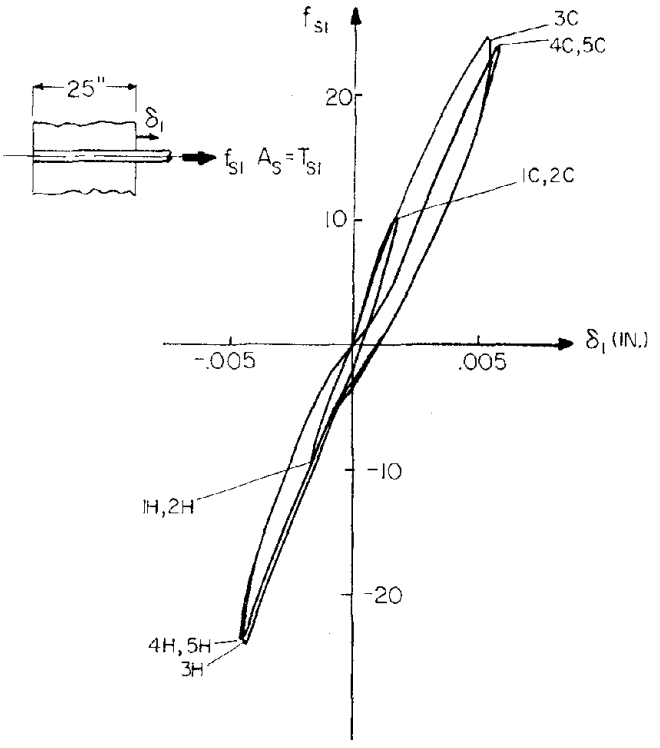

(a) Working Load Range

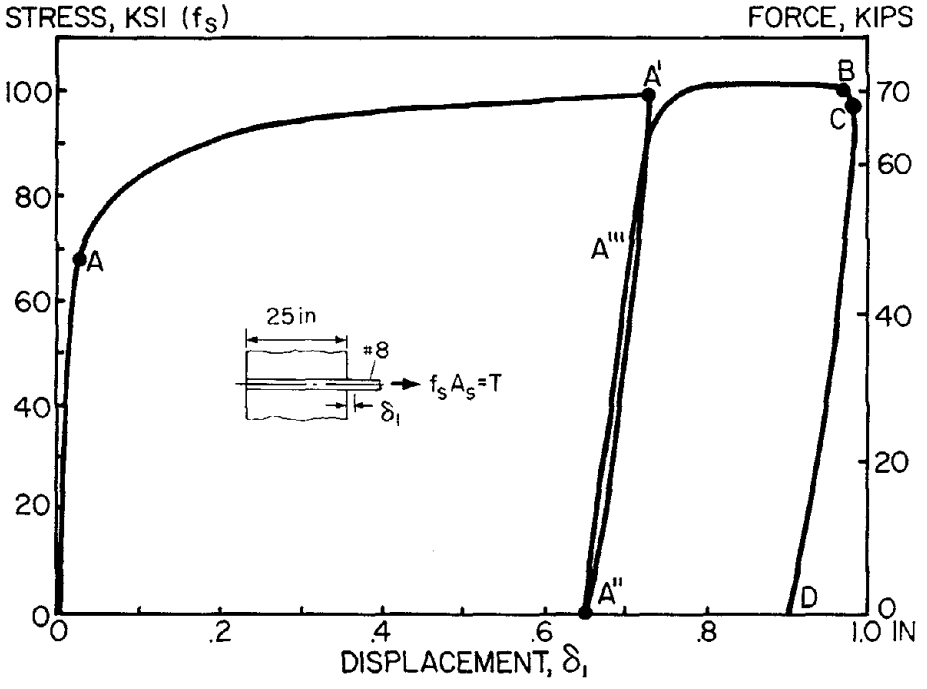

(b) Monotonic Loading

Fig. 4.9 $f_{s1} - \delta_1$ Diagram (Pull Only)

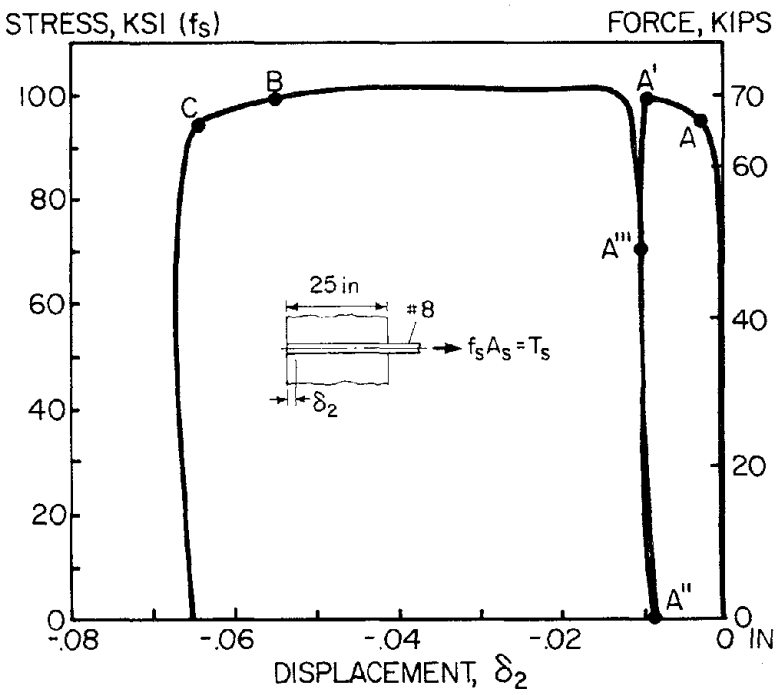

Fig. 4.10 $f_{s1} - \delta_2$ Diagram (Pull Only)

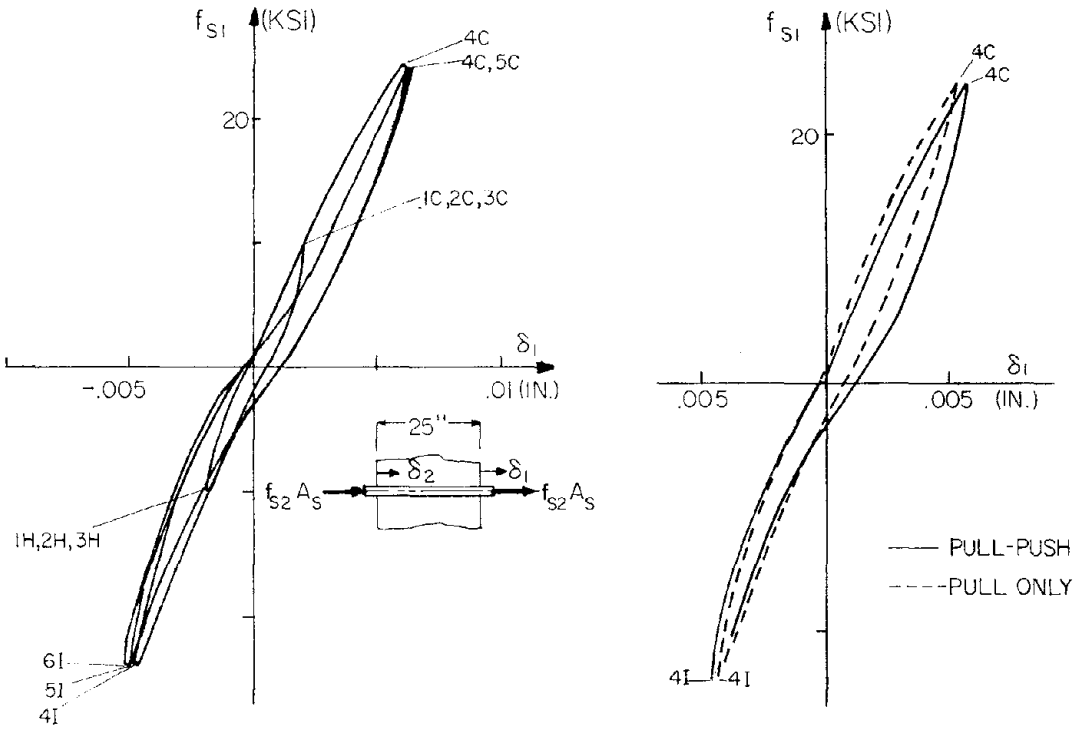

(a) Working Load Range

(b) Pull Only vs. Push-Pull Loading

Fig. 4.11 Typical Stress Displacement Diagram of Push-Pull Test

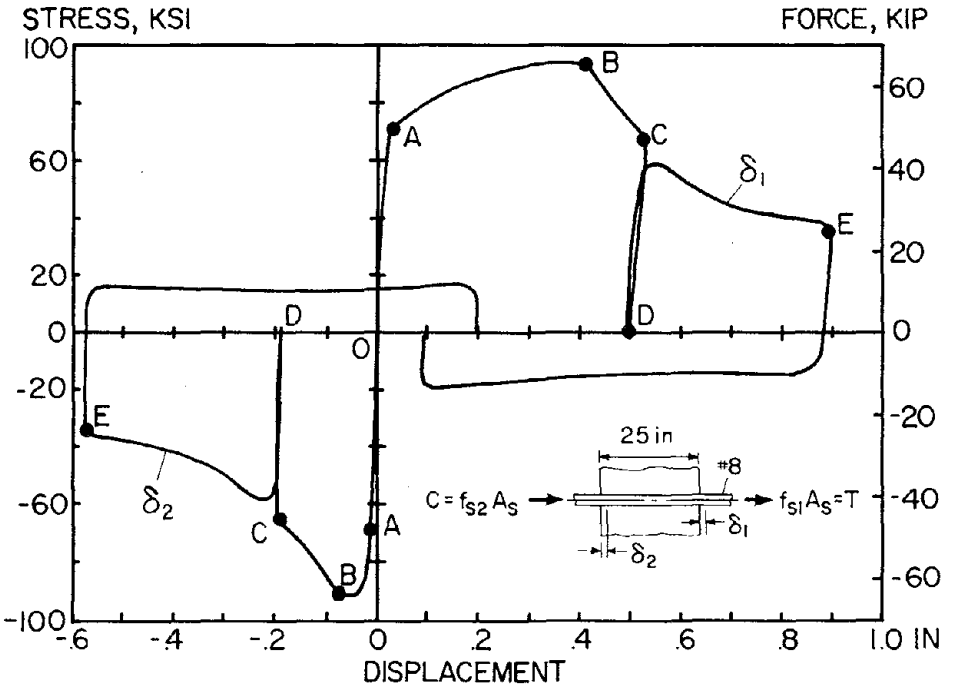

(c) Monotonic Loading

Fig. 4.11 Typical Stress Displacement Diagram of Push-Pull Test

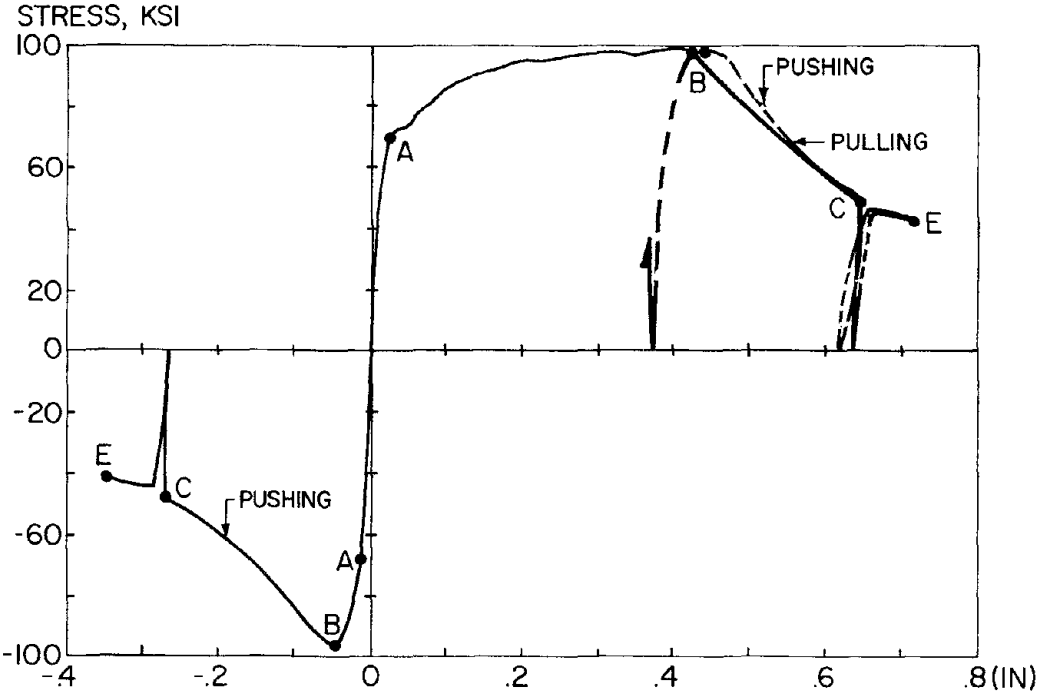

Fig. 4.12 Verification of Pull-Through

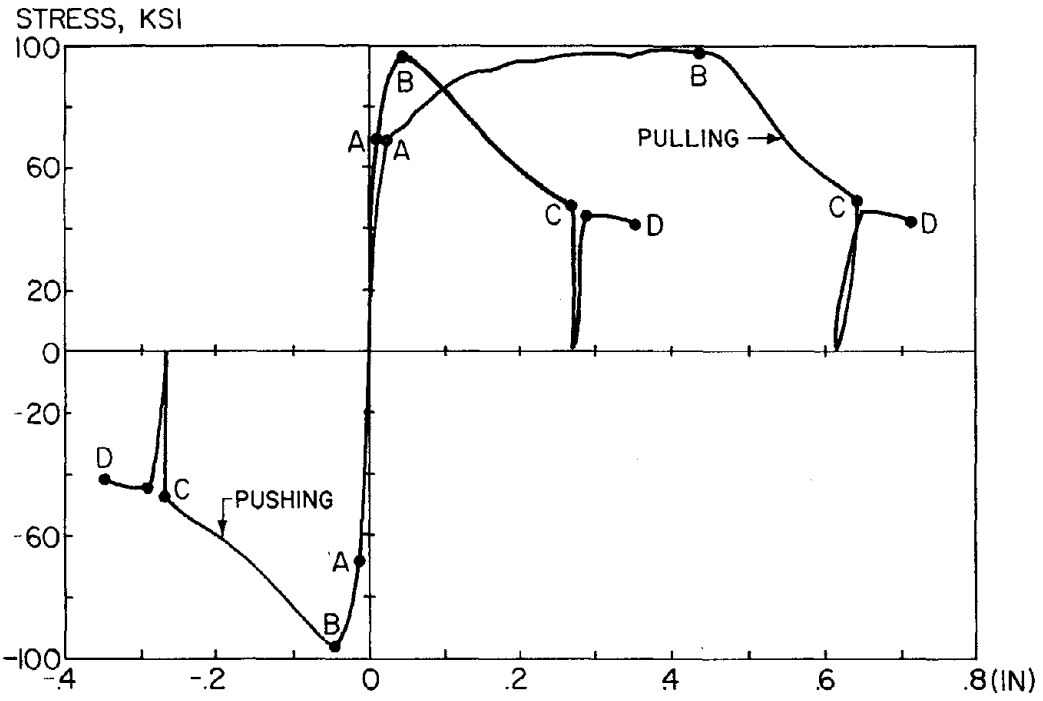

Fig. 4.13 Pull End vs. Push End Response

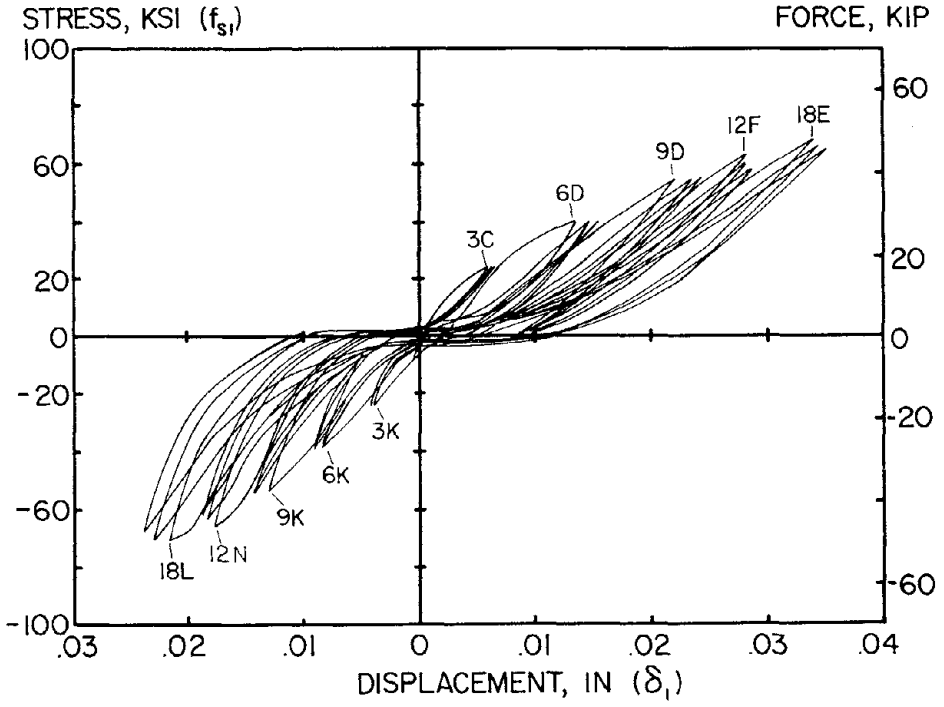

(a) Up to Initiation of Yielding

Fig. 4.14 $f_{s1} - \delta_1$ Diagram (Cyclic Loading)

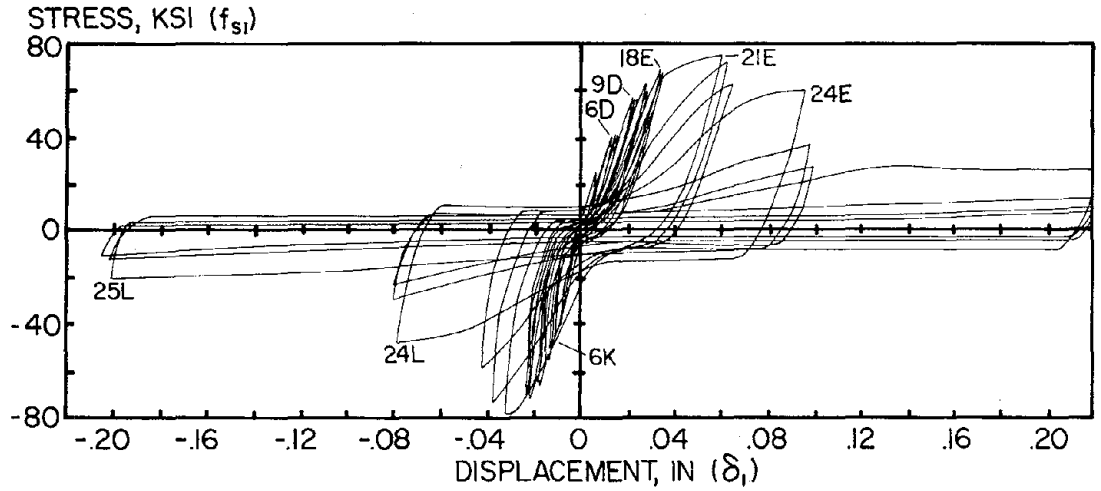

(b) Whole Range

Fig. 4.14 $f_{s1} - \delta_1$ Diagram (Cyclic Loading)

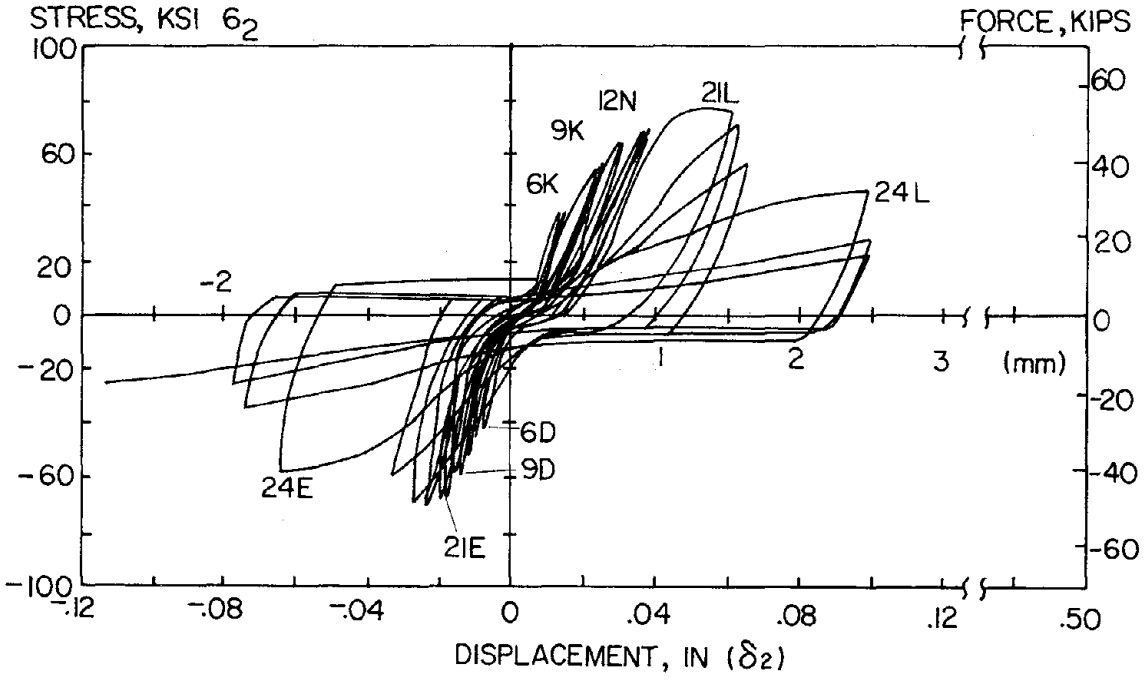

Fig. 4.15 $f_{s2} - \delta_2$ Diagram (Cyclic Loading)

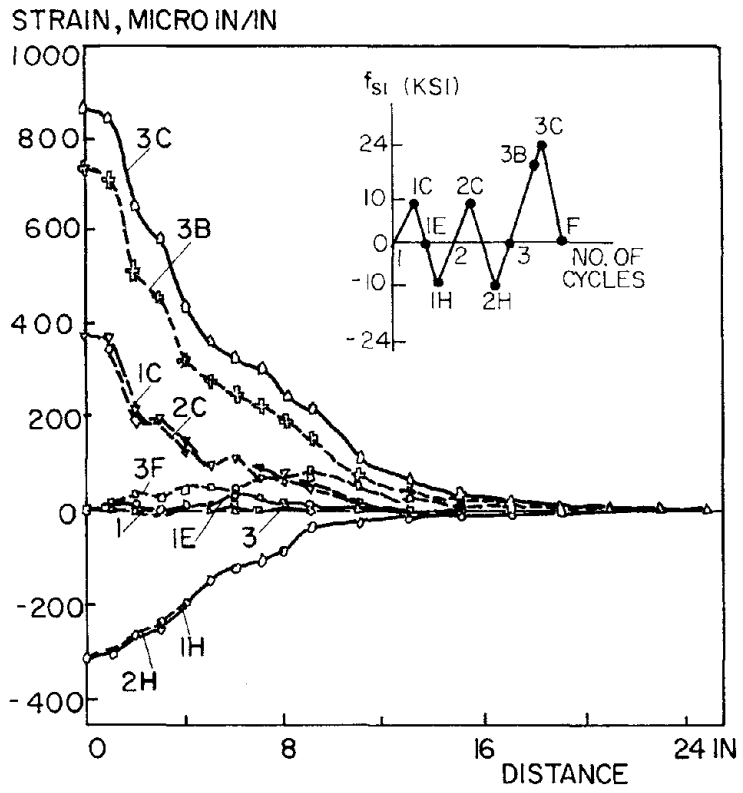

(a) Working Load Range

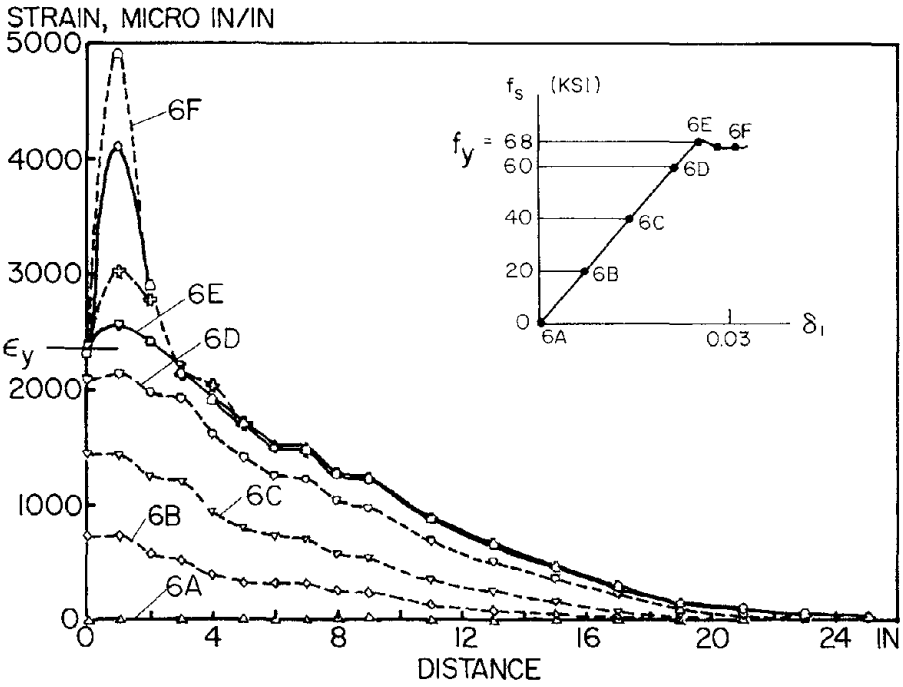

(b) Load Up to Yield

Fig. 4.16 Strain Distribution Diagrams (Pull Only)

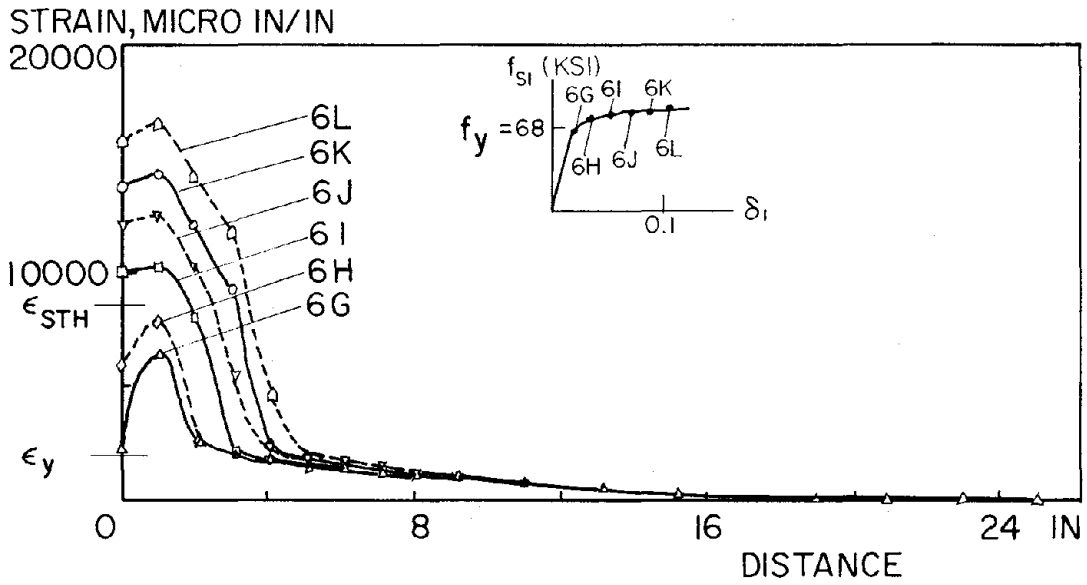

(c) First Post-Yield Range

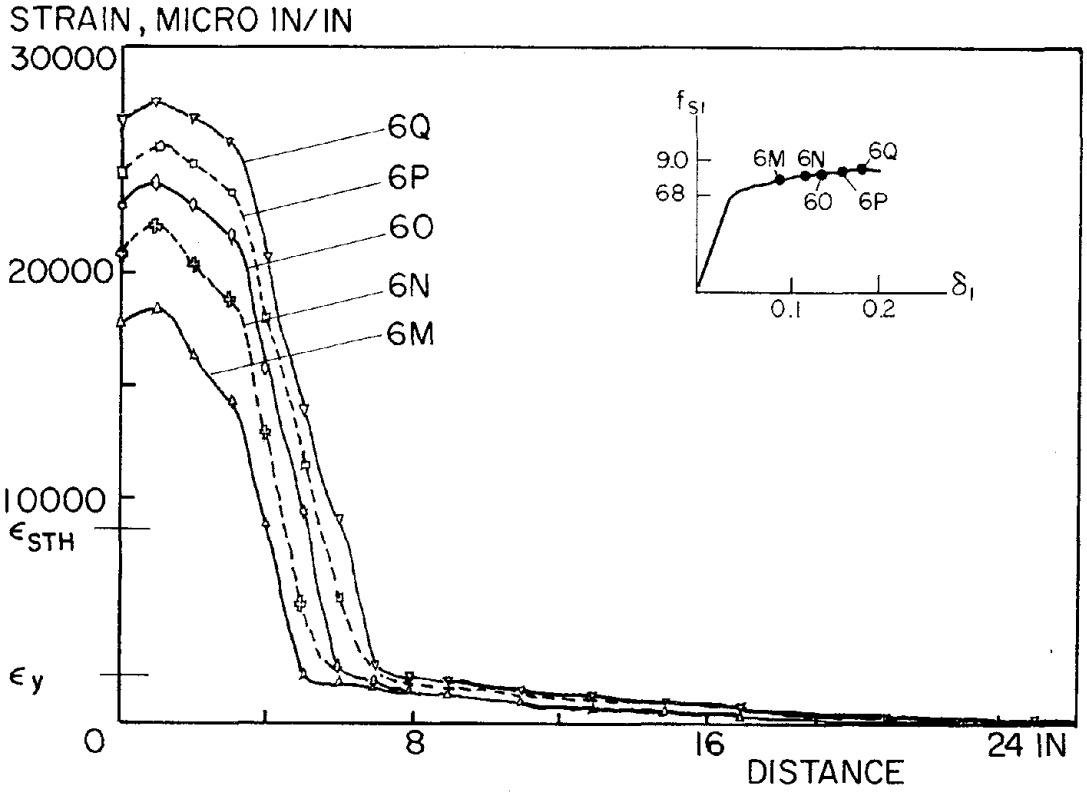

(d) Second Post-Yield Range

Fig. 4.16 Strain Distribution Diagrams (Pull Only)

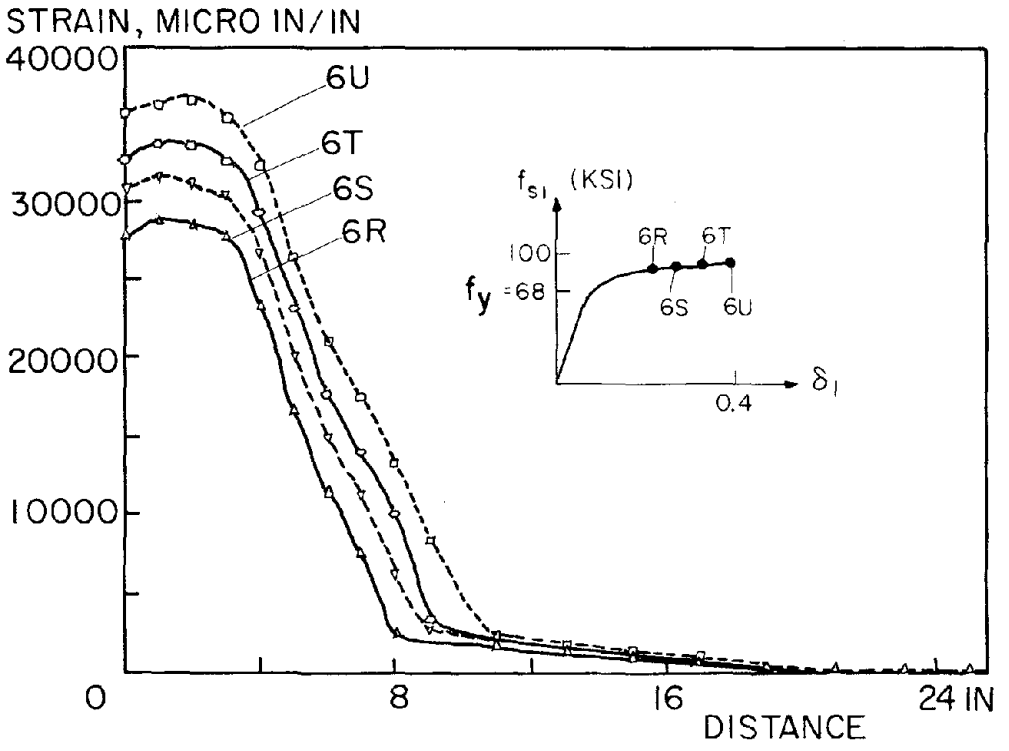

(e) Third Post-Yield Range

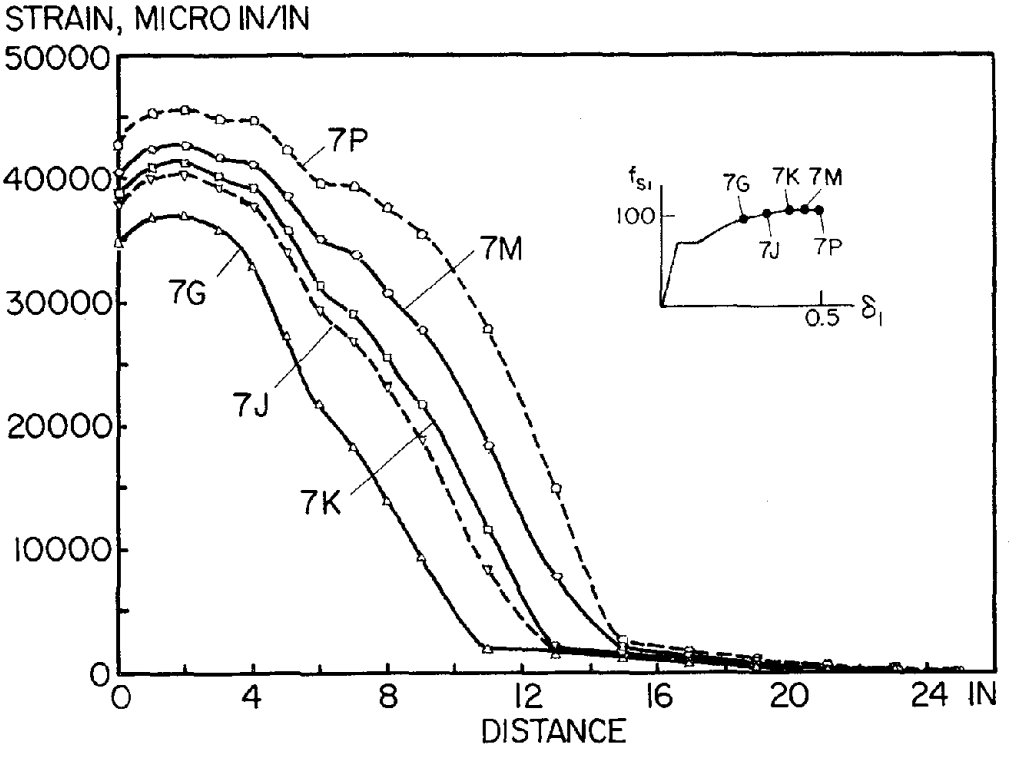

(f) Fourth Post-Yield Range

Fig. 4.16 Strain Distribution Diagrams (Pull Only)

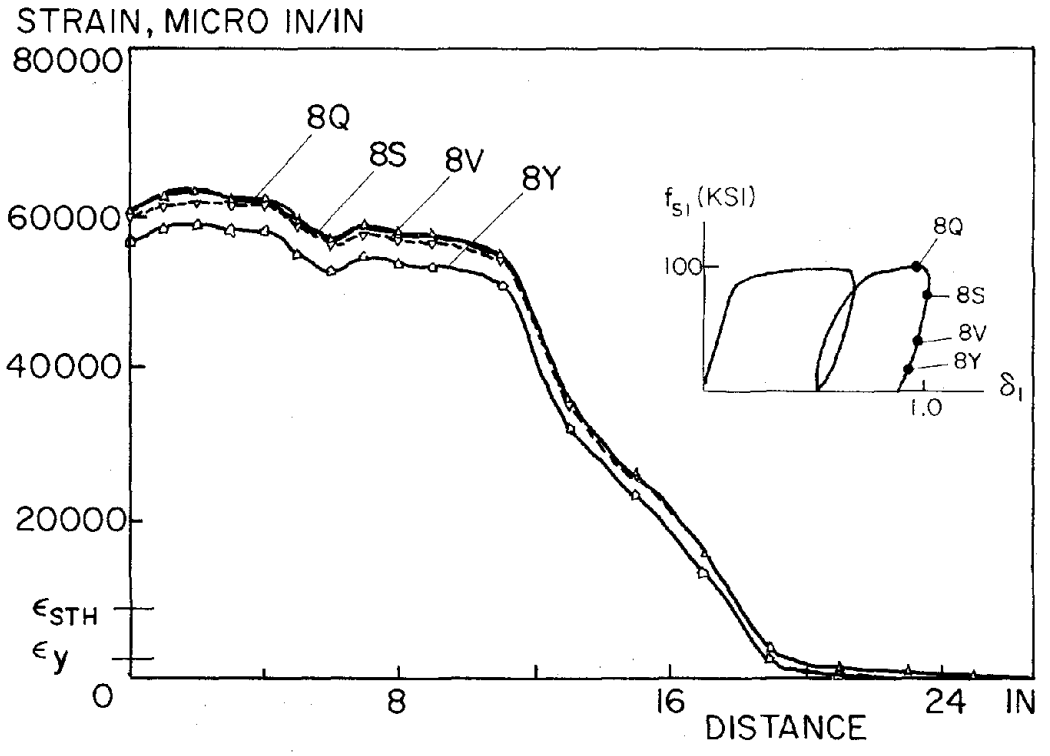

(g) Pull-Through Stage

Fig. 4.16 Strain Distribution Diagrams (Pull Only)

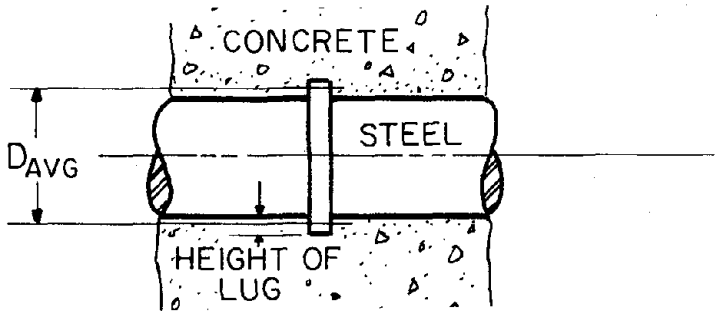

(a) No Reduction in Diameter

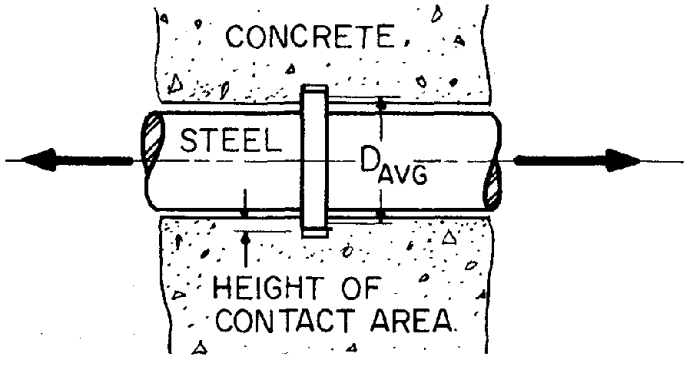

(b) Necking in Bar Diameter

Fig. 4.17 Reduction in Contact Area

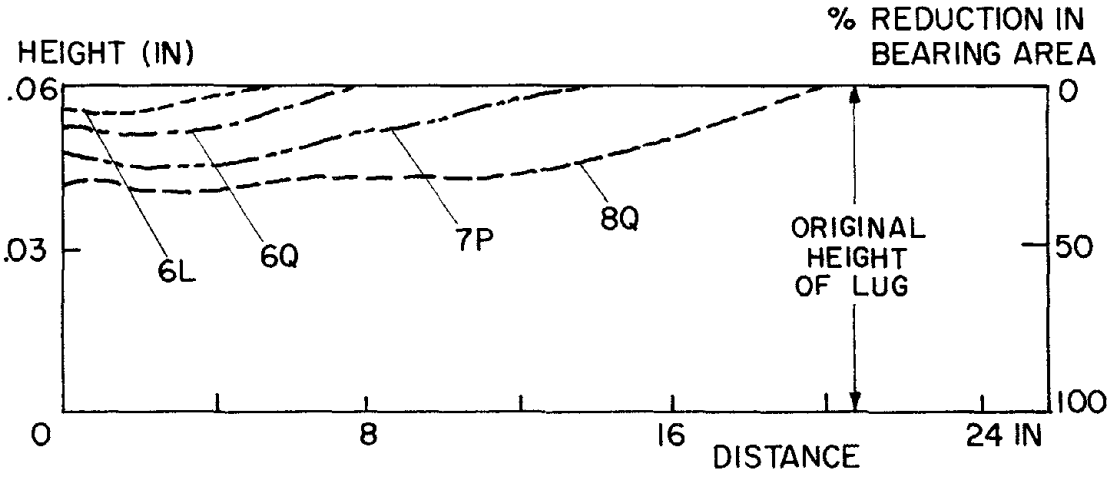

Fig. 4.18 Reduction in Bearing Area Along Rebar

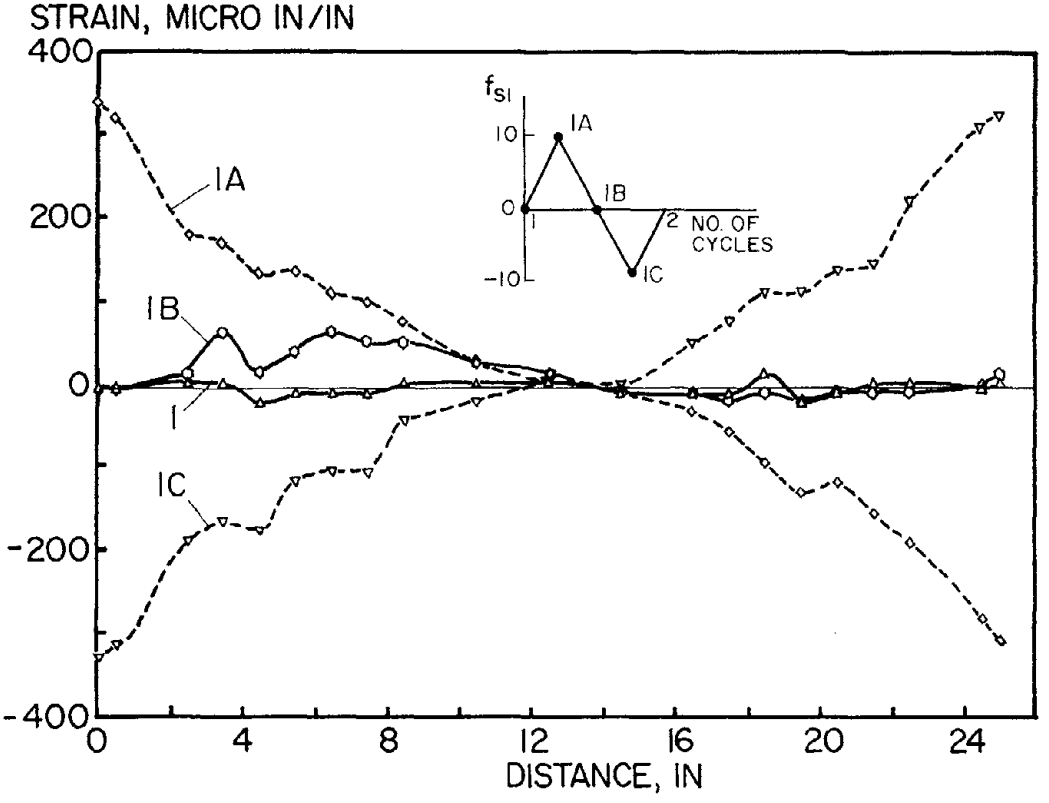

(a) 10 ksi Level (First Cycle)

Fig. 4.19 Strain Distribution Diagram (Monotonic Push-Pull)

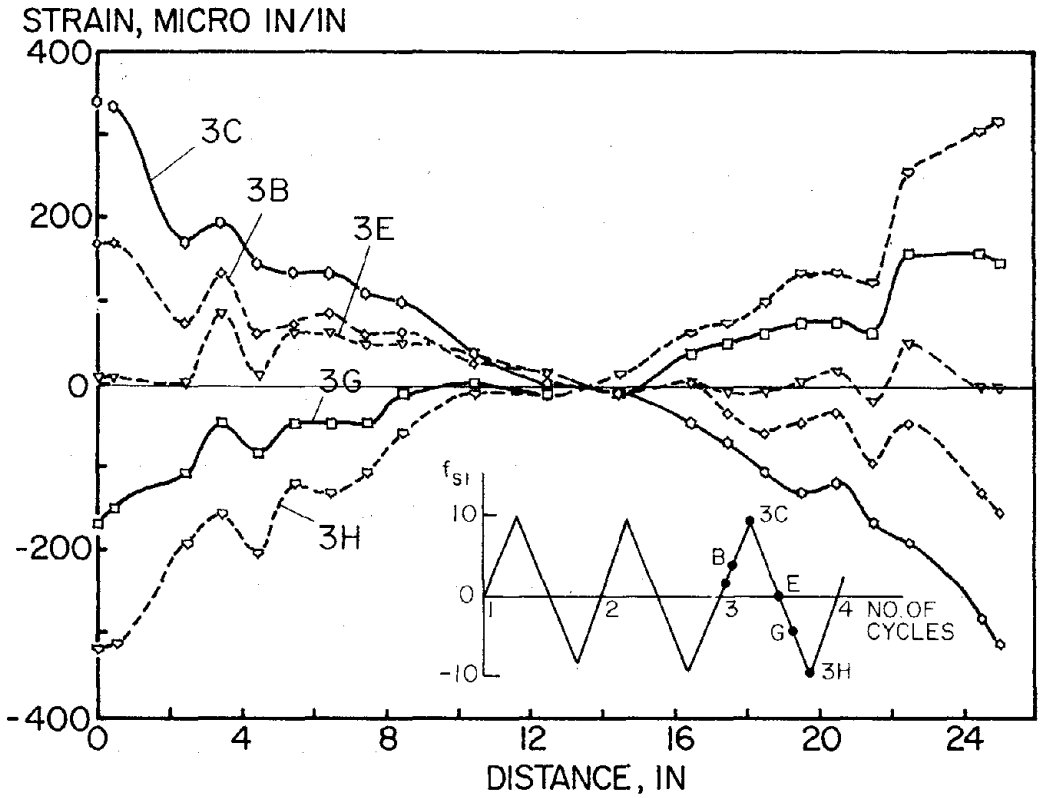

(b) 10 ksi Level (Repeating Cycle)

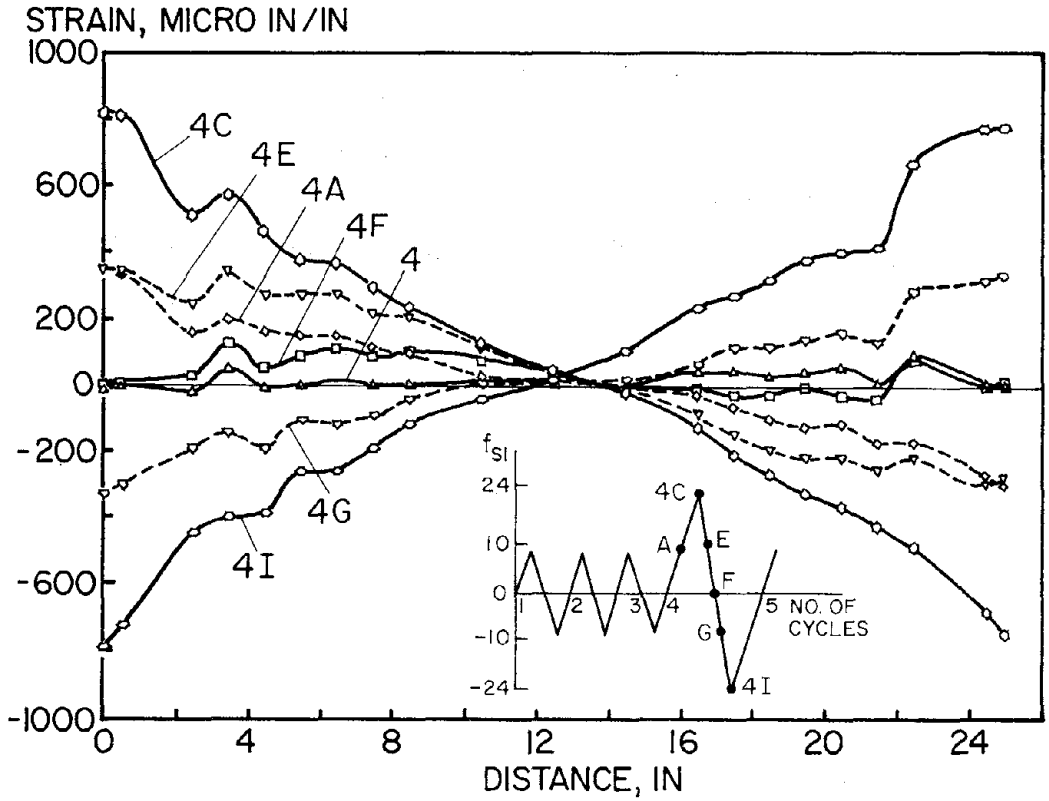

(c) Working Load Level (First Cycle)

Fig. 4.19 Strain Distribution Diagram (Monotonic Push-Pull)

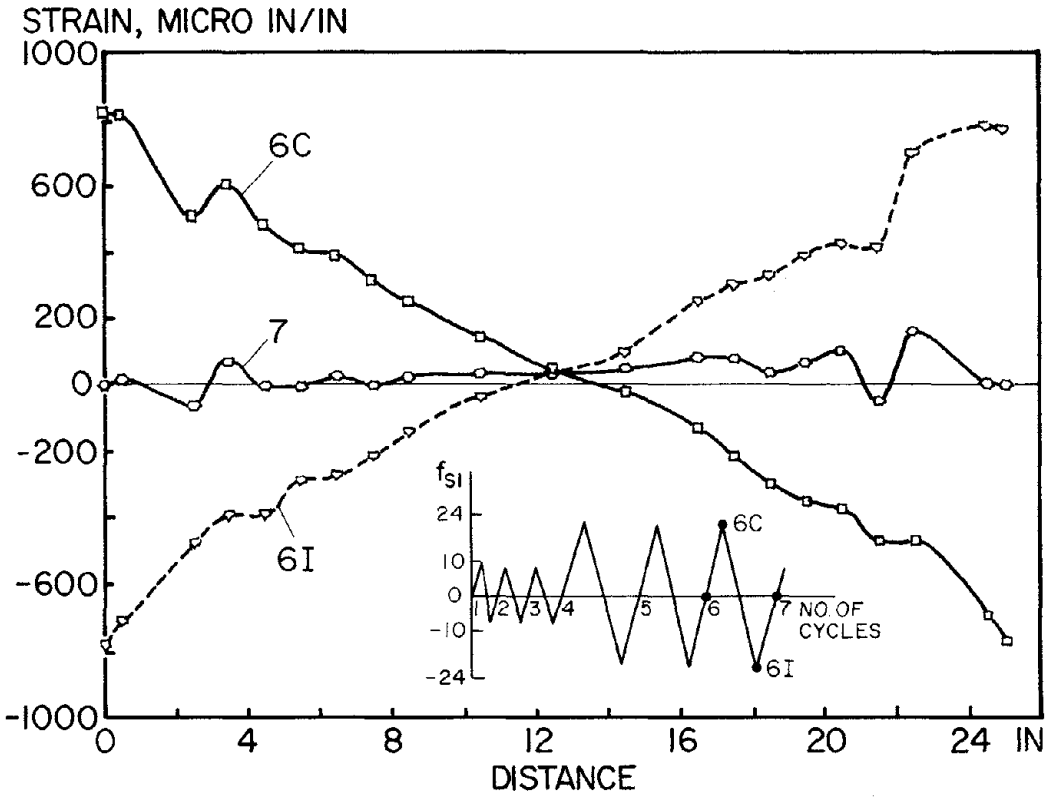

(d) Working Load Level (Repeating Cycle)

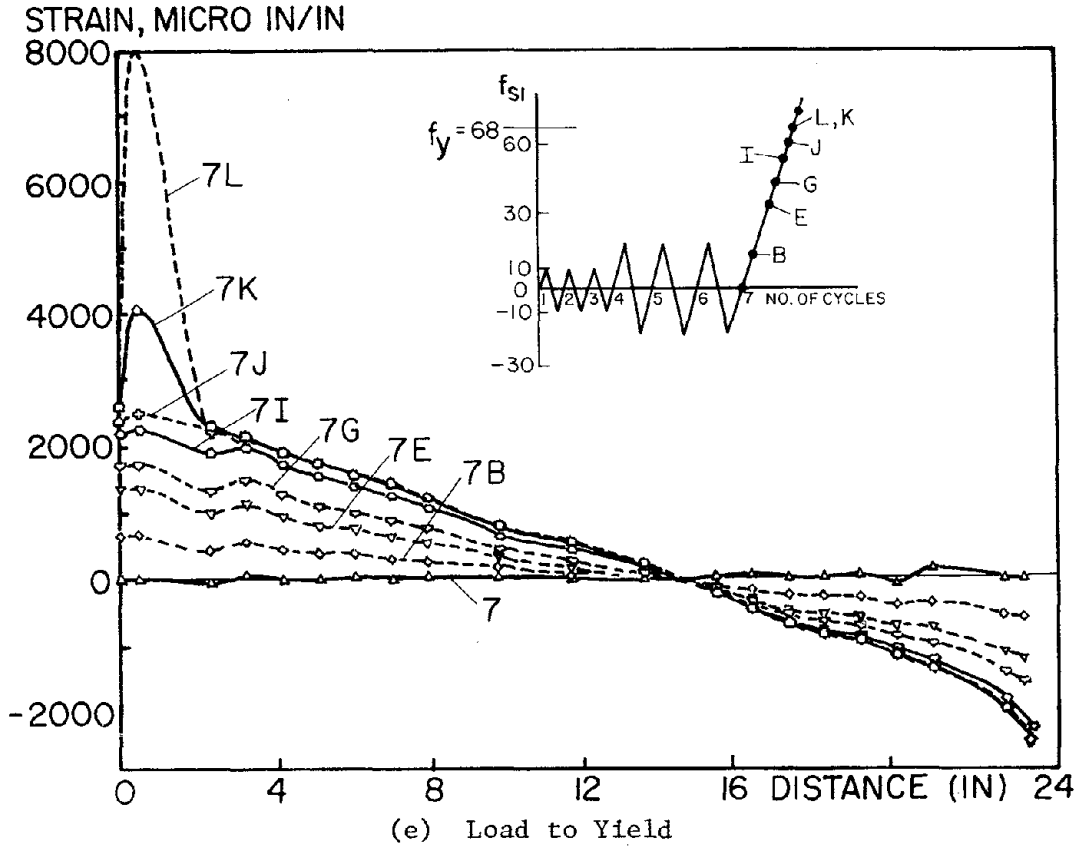

(e) Load to Yield

Fig. 4.19 Strain Distribution Diagram (Monotonic Push-Pull)

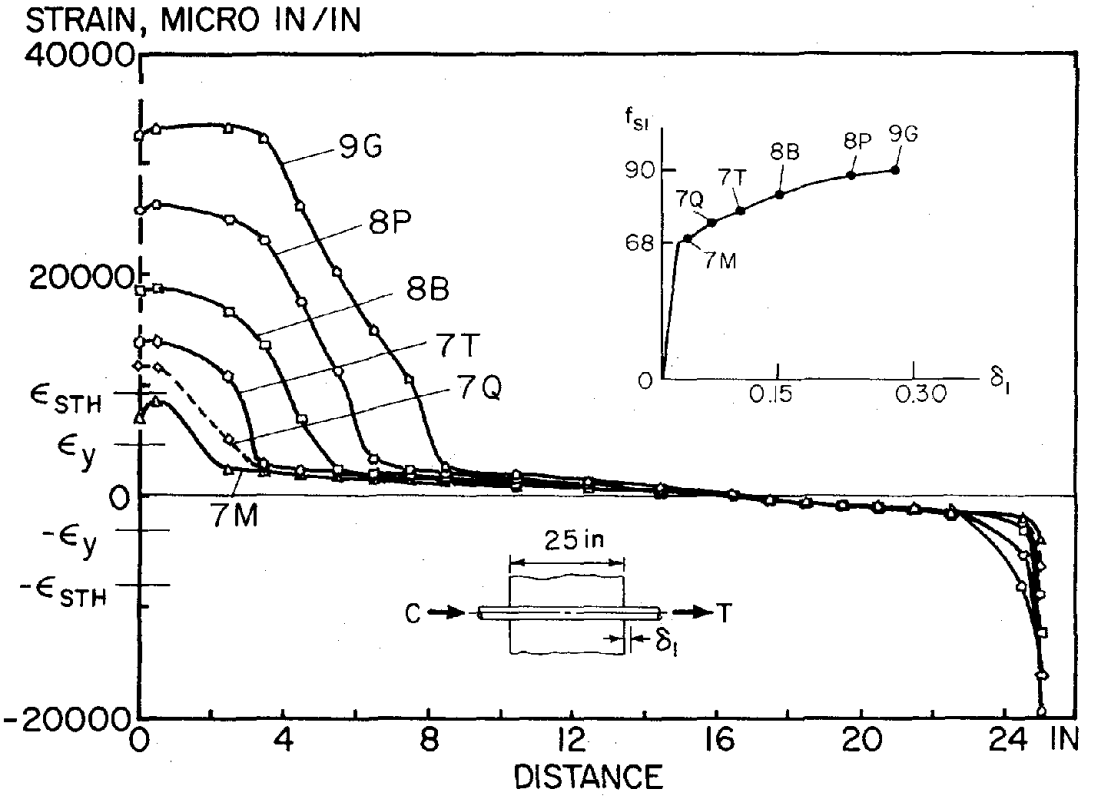

(f) Post-Yield Range

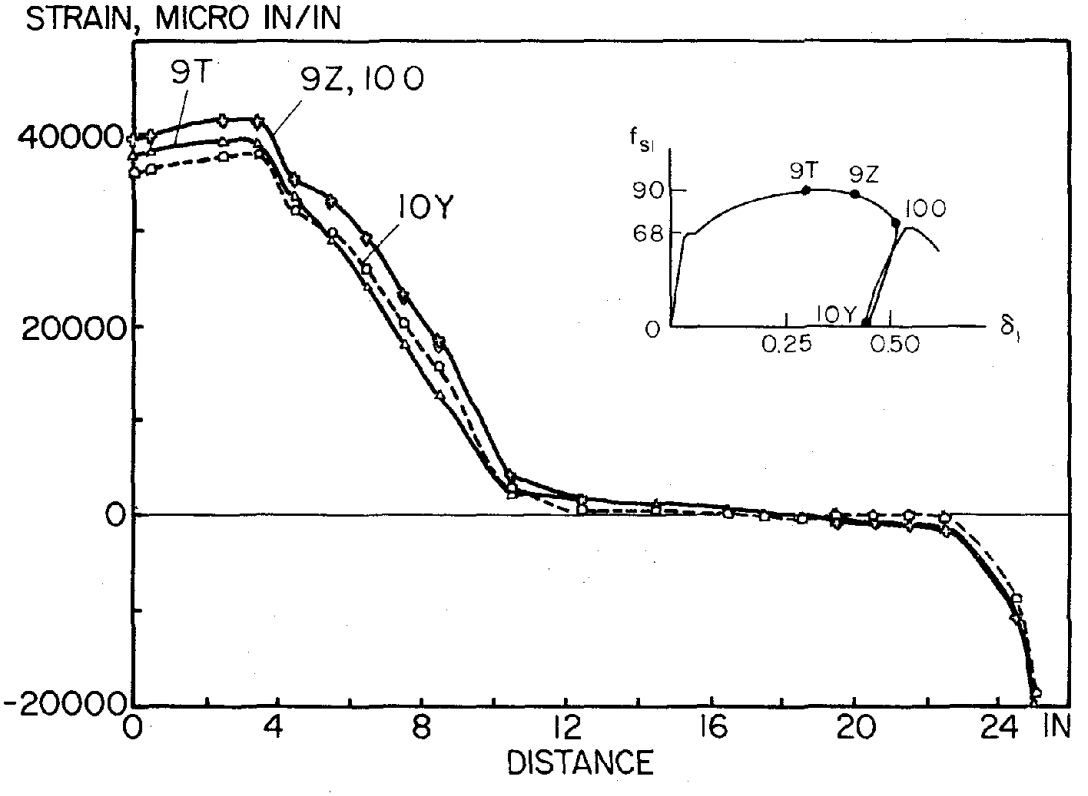

(g) Pull-Through Stage

Fig. 4.19 Strain Distribution Diagram (Monotonic Push-Pull)

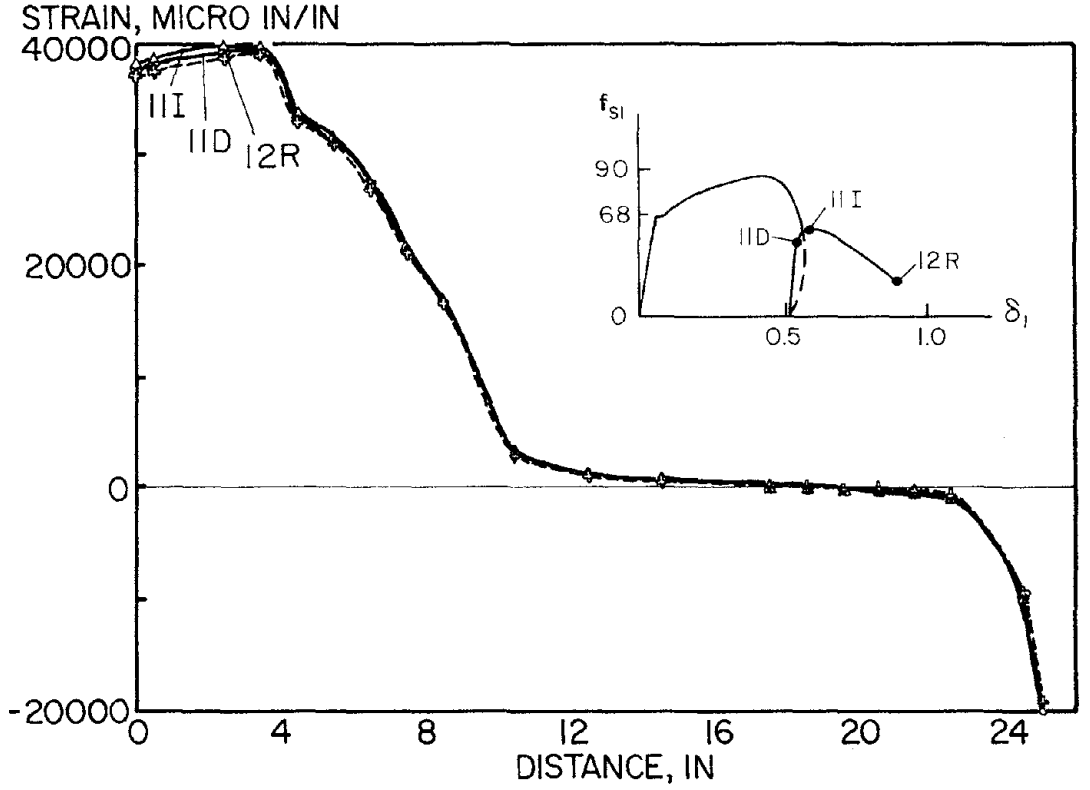

(h) Post Pull-Through Range

Fig. 4.19 Strain Distribution Diagram (Monotonic Push-Pull)

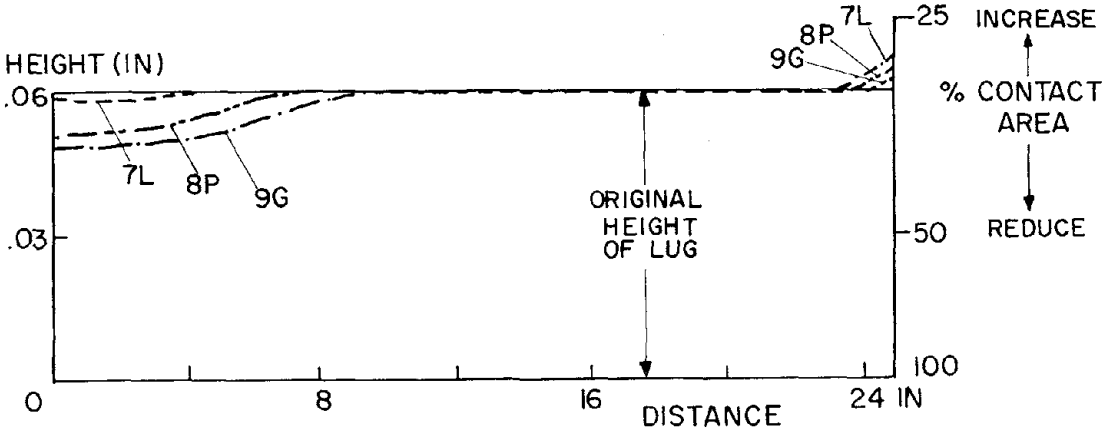

Fig. 4.20 Variation of Contact Area Along Rebar

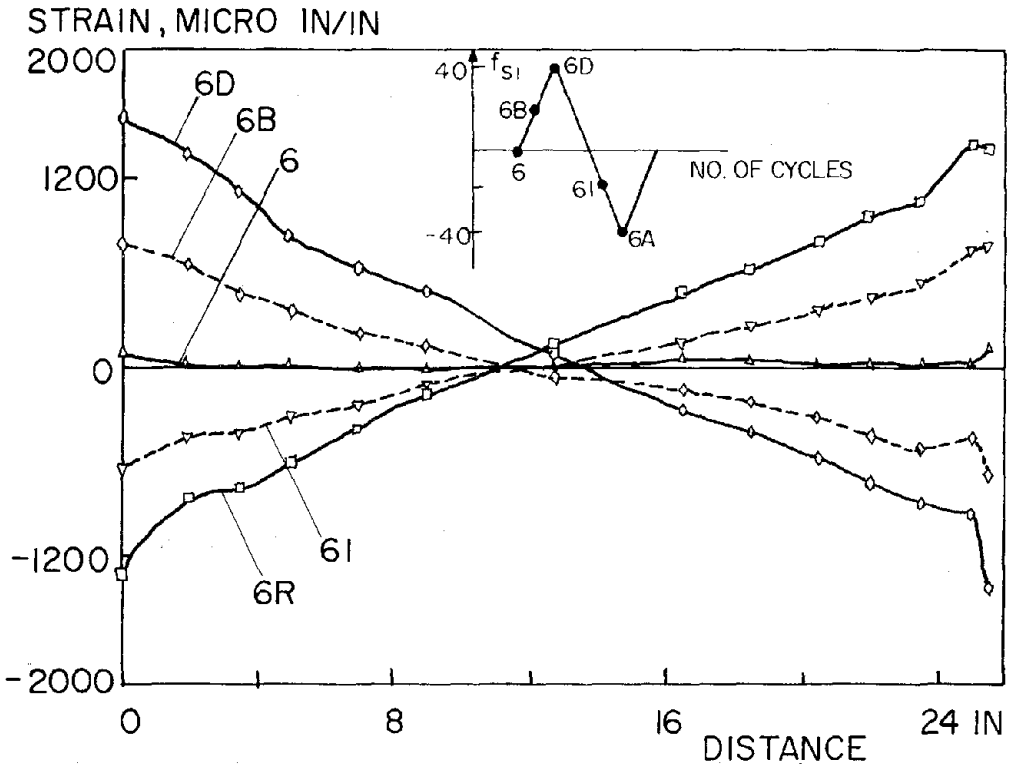

(a) ± 40 ksi Level (First Cycle)

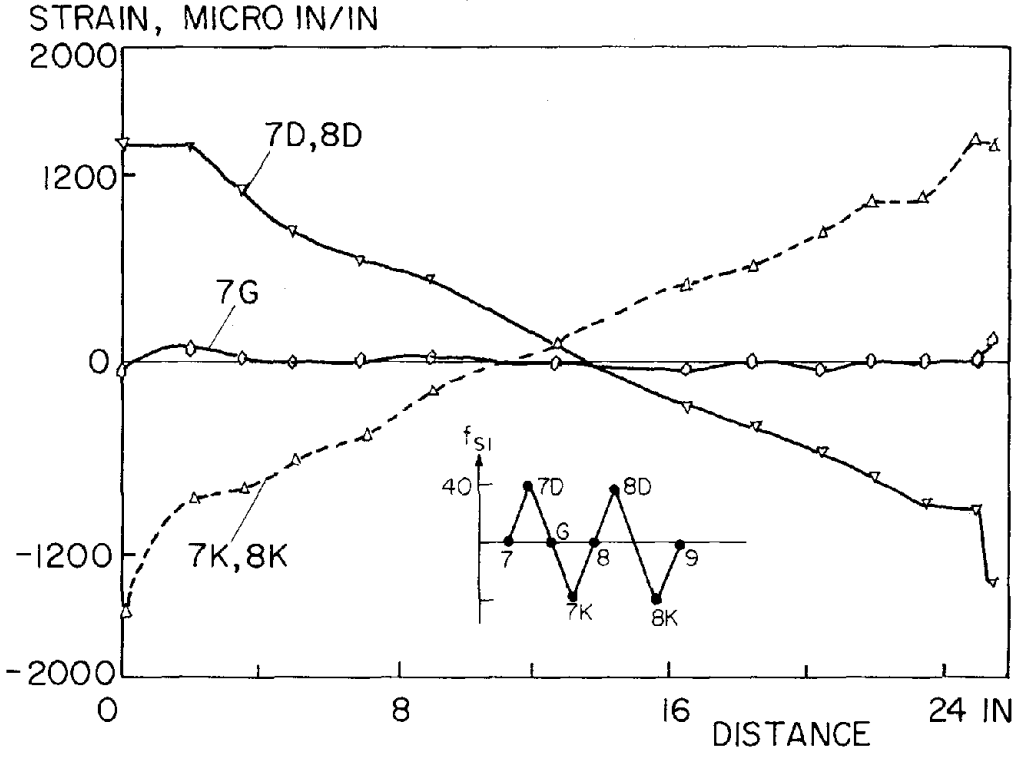

(b) ± 40 ksi Level (Repeating Cycle)

Fig. 4.21 Typical Strain Distribution Diagrams (Cyclic Loading)

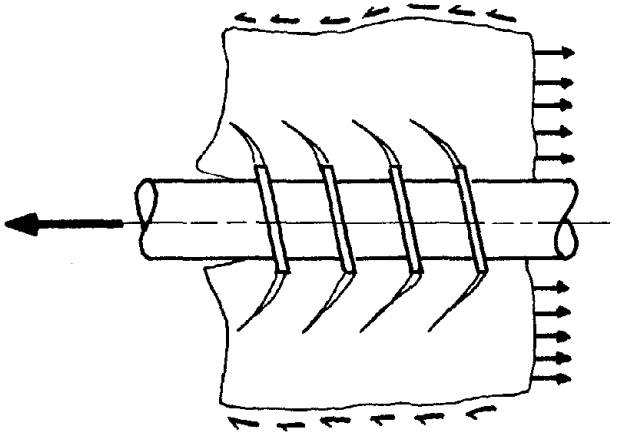

(b.1.1) Crack Developed at Pulling Cycle

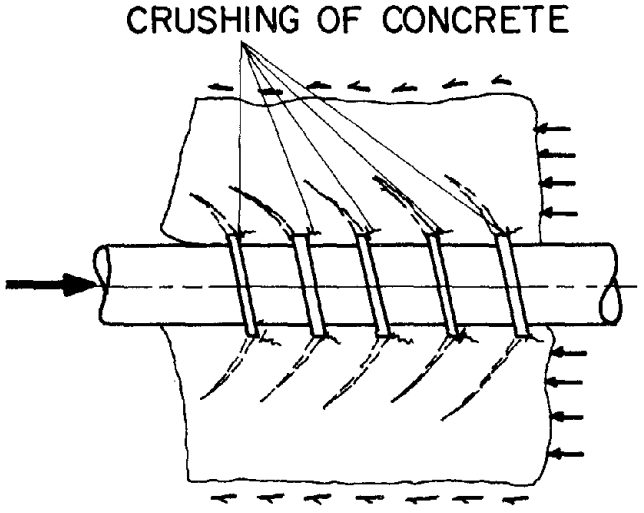

(b.1.2) Lugs in Contact with Uncracked Concrete at Pushing Cycle

(b.1) Postulation of Cracking and Crushing of Surrounding Concrete

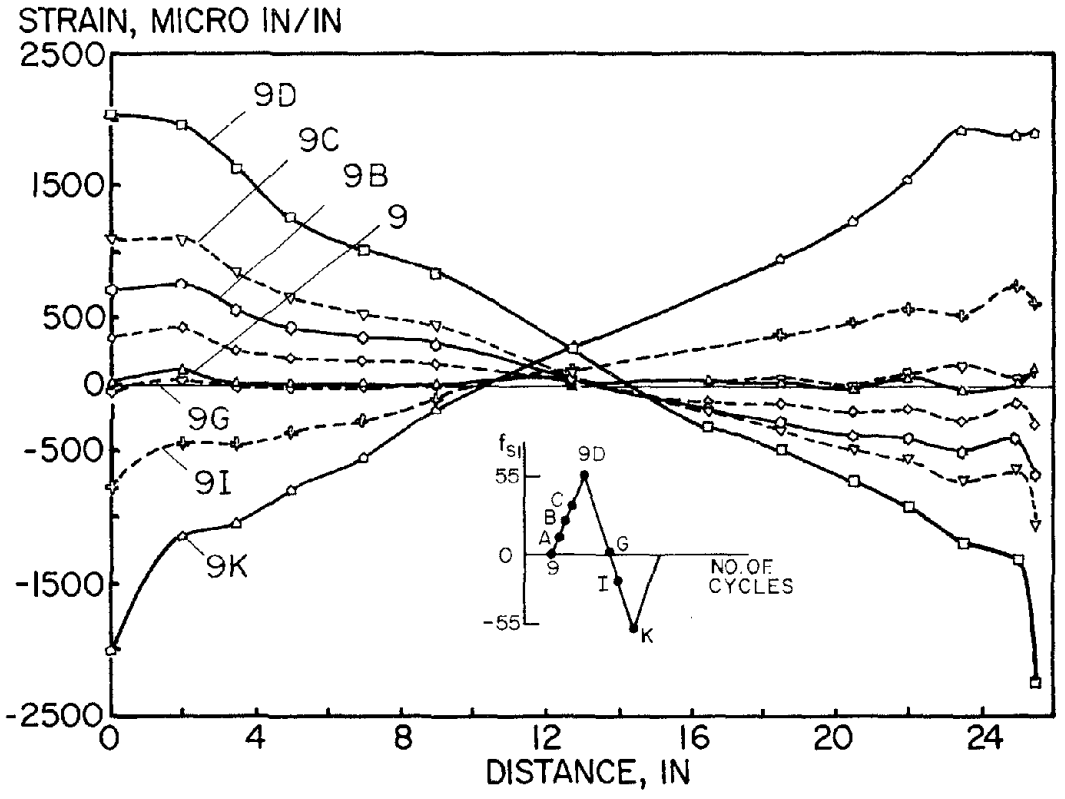

(c) ± 55 ksi Level (First Cycle)

Fig. 4.21 Typical Strain Distribution Diagrams (Cyclic Loading)

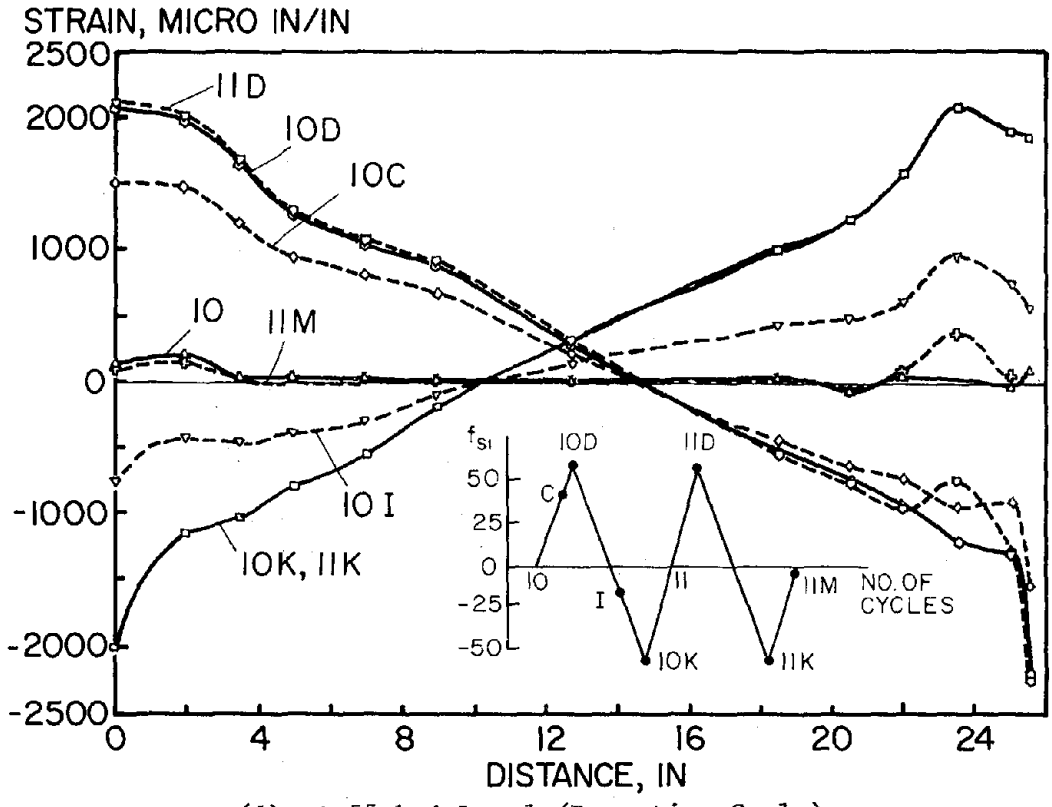

(d) ± 55 ksi Level (Repeating Cycle)

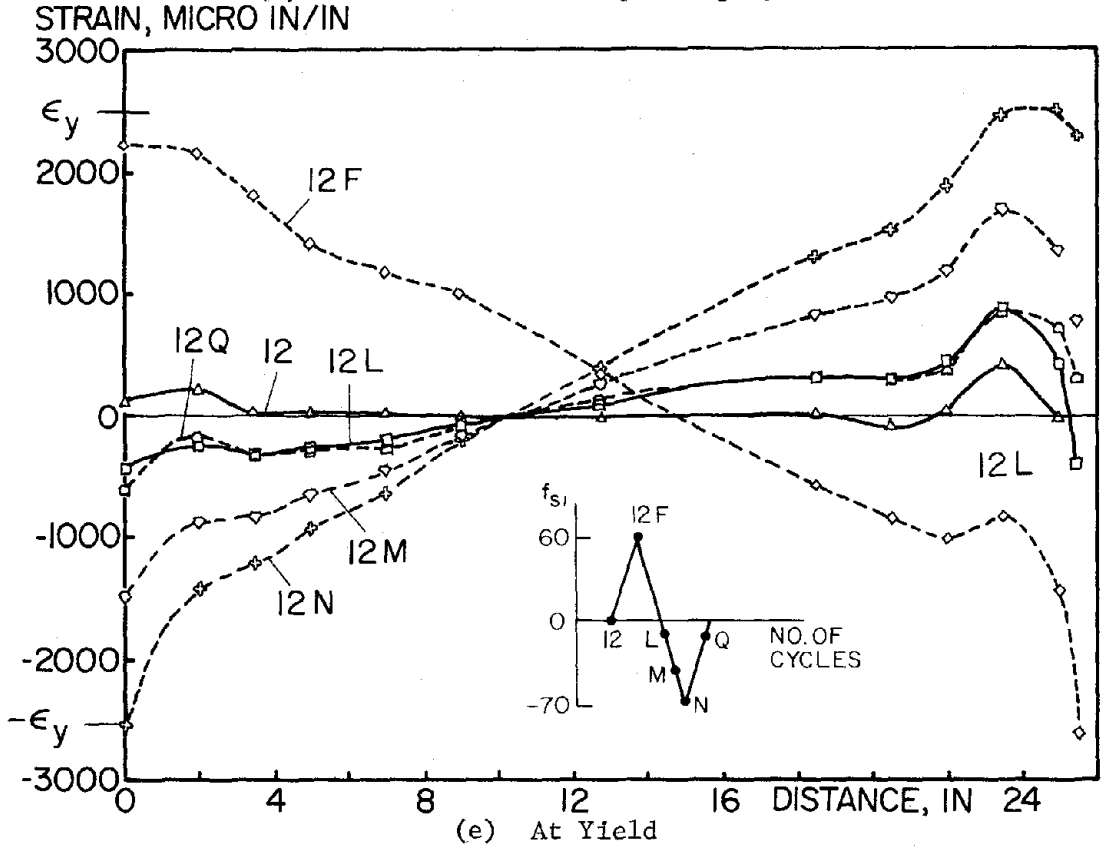

(e) At Yield

Fig. 4.21 Typical Strain Distribution Diagrams (Cyclic Loading)

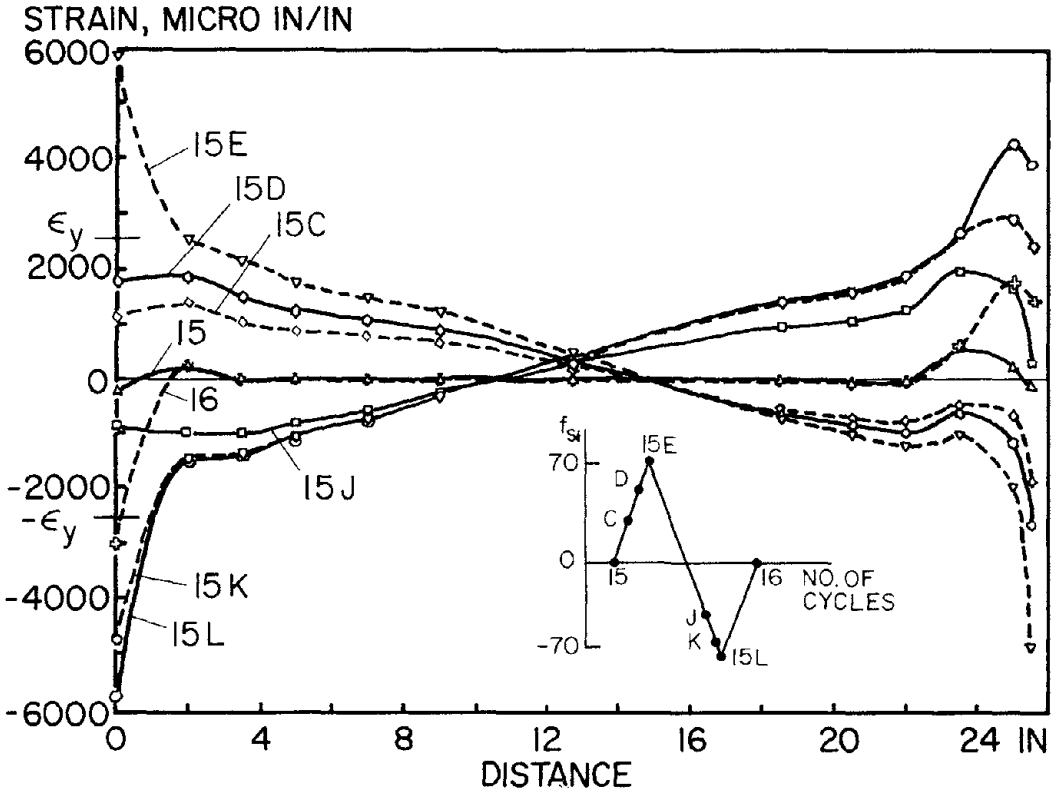

(f) First Post-Yield Range

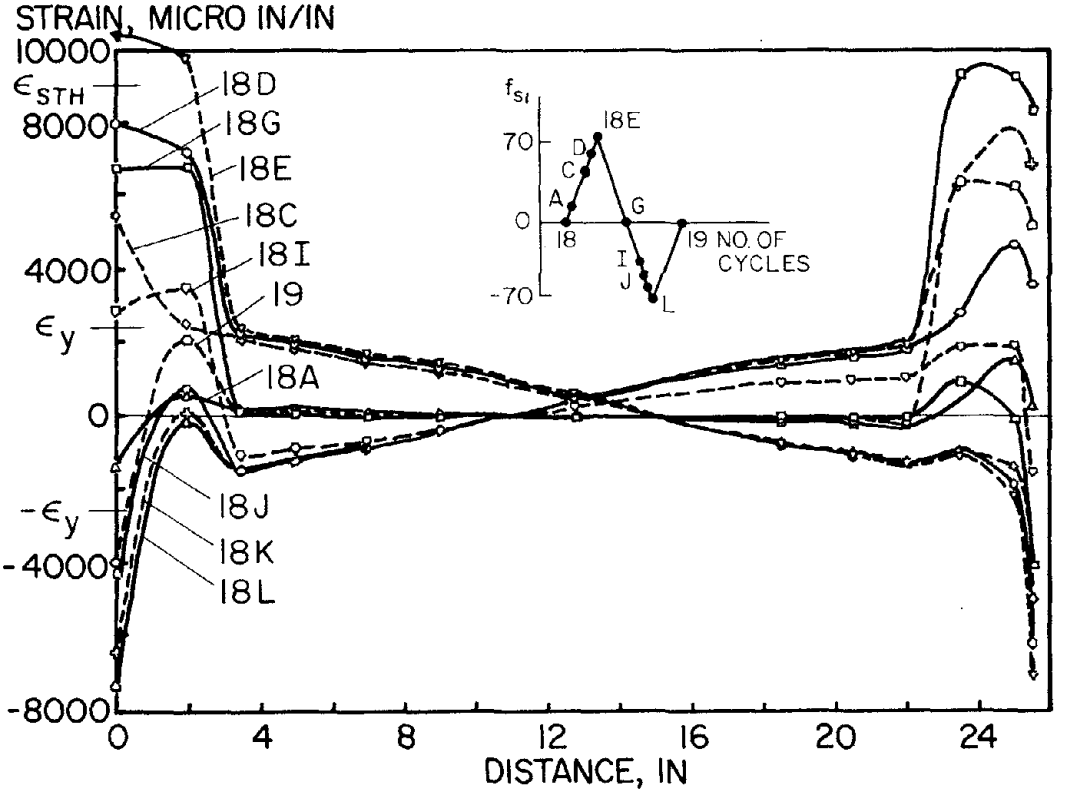

(g) Second Post-Yield Range

Fig. 4.21 Typical Strain Distribution Diagrams (Cyclic Loading)

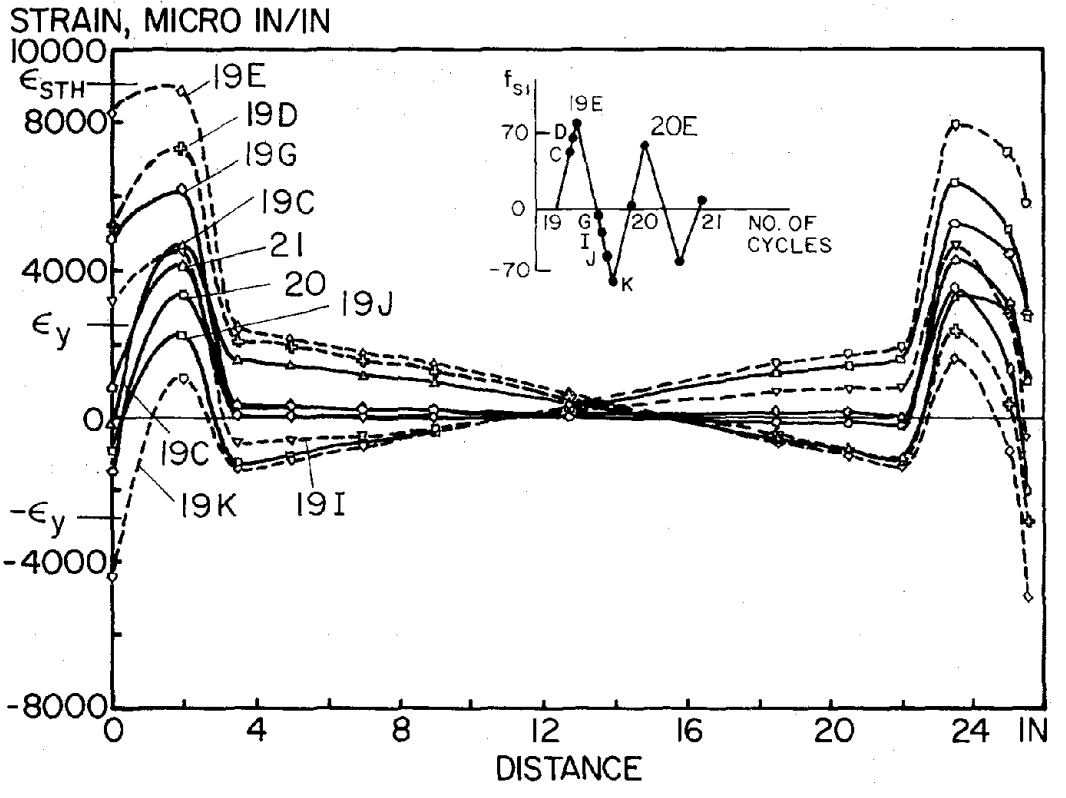

(h) Pull-Through Stage

Fig. 4.21 Typical Strain Distribution Diagrams (Cyclic Loading)

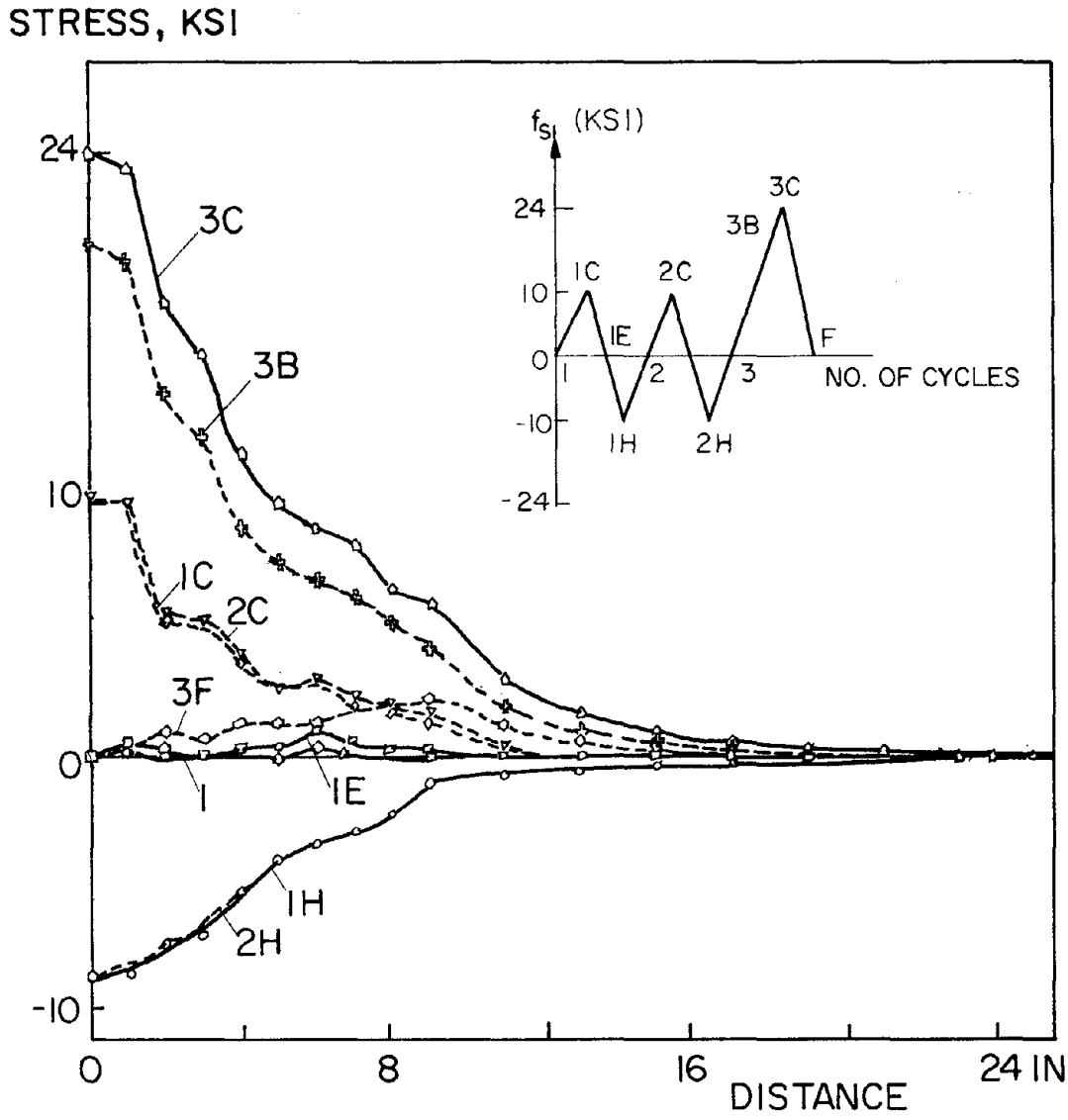

(a) Working Load Range

Fig. 4.22 Stress Distribution Diagrams (Monotonic Pull Only)

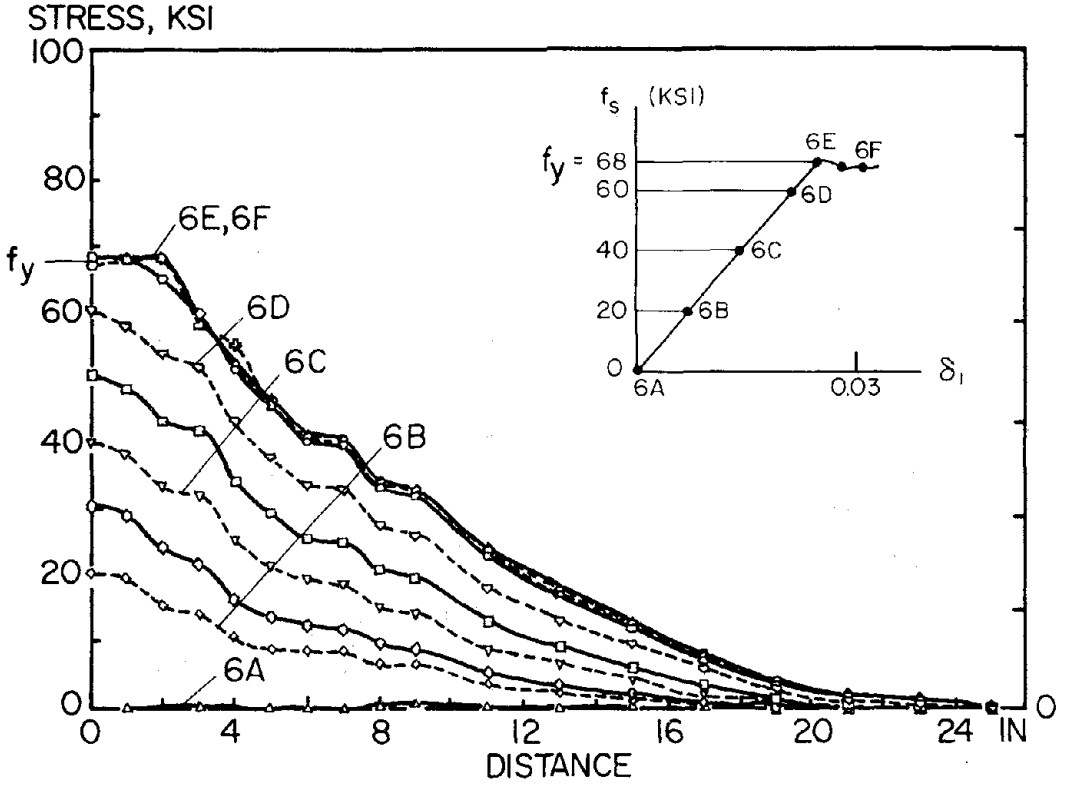

(b) Loaded Up to Yield

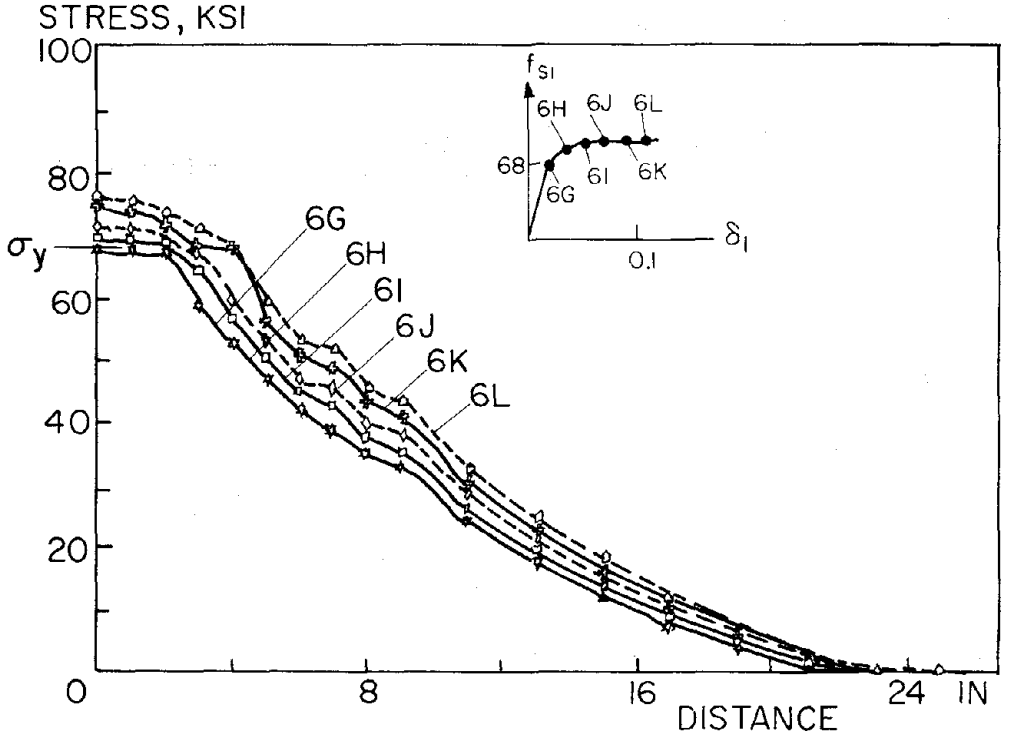

(c) First Post-Yield Range

Fig. 4.22 Stress Distribution Diagrams (Monotonic Pull Only)

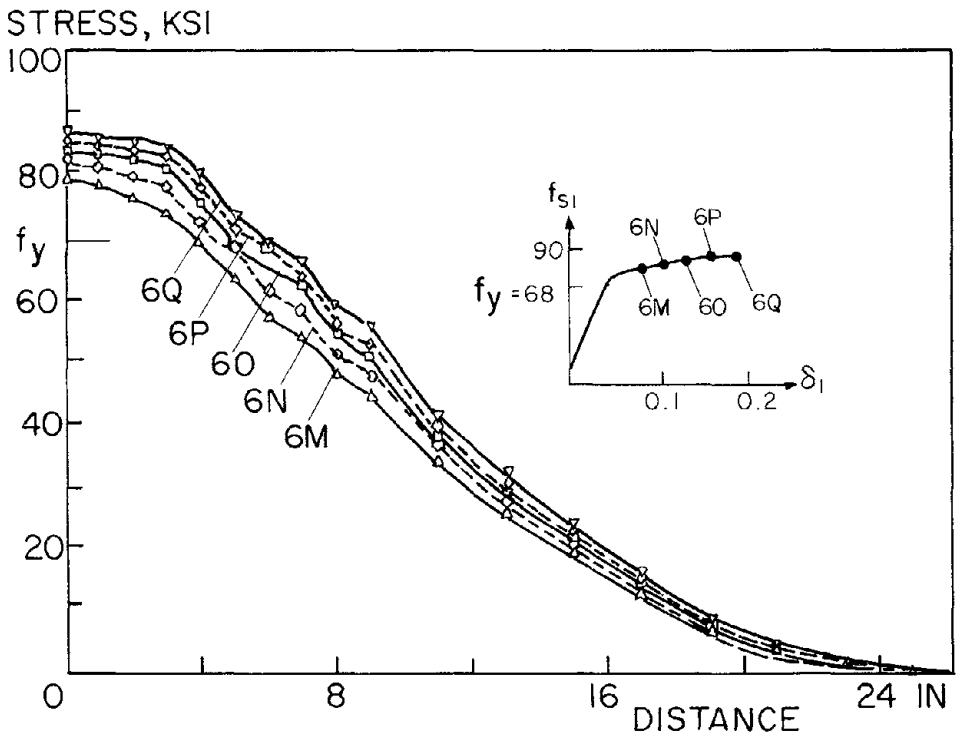

(d) Second Post-Yield Range

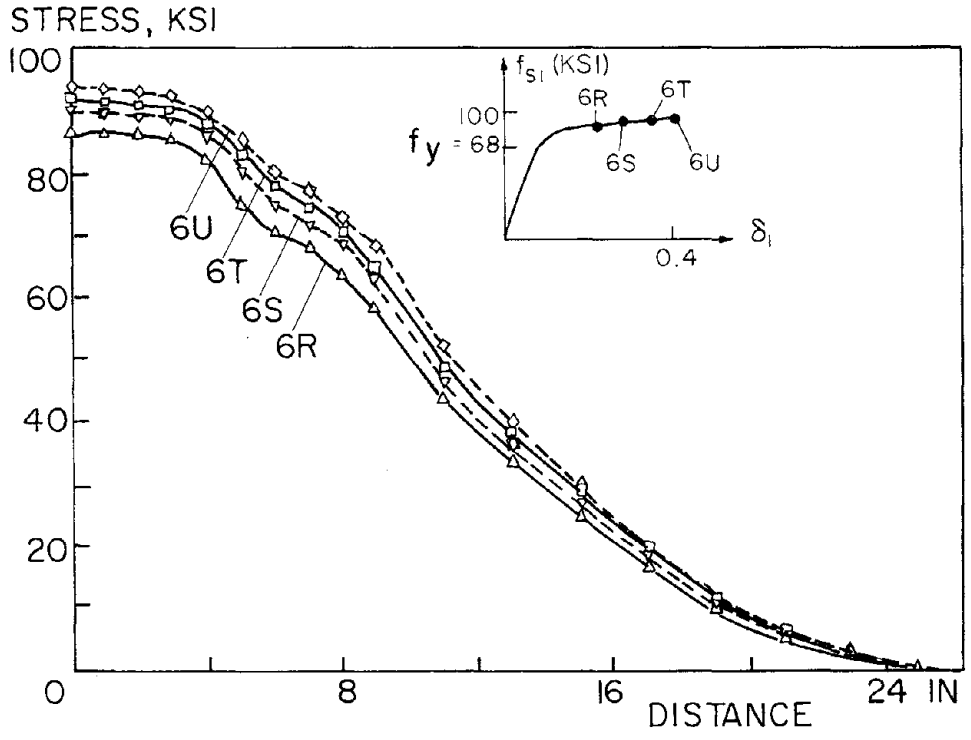

(e) Third Post-Yield Range

Fig. 4.22 Stress Distribution Diagrams (Monotonic Pull Only)

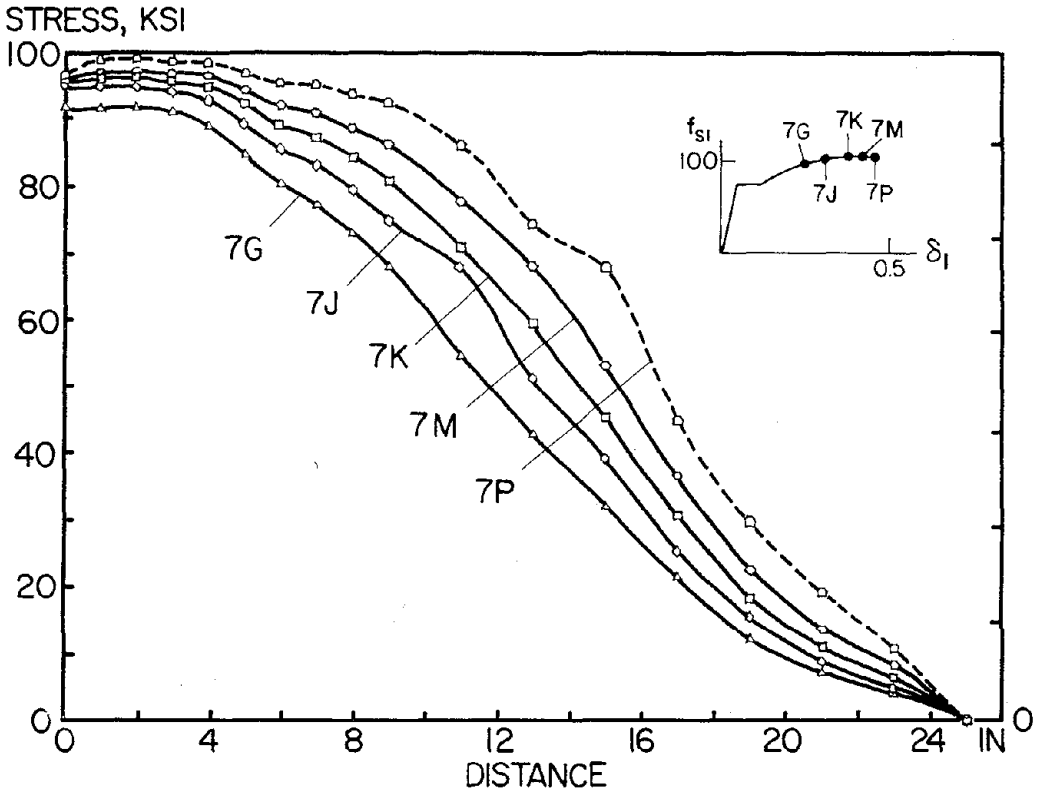

(f) Fourth Post-Yield Range

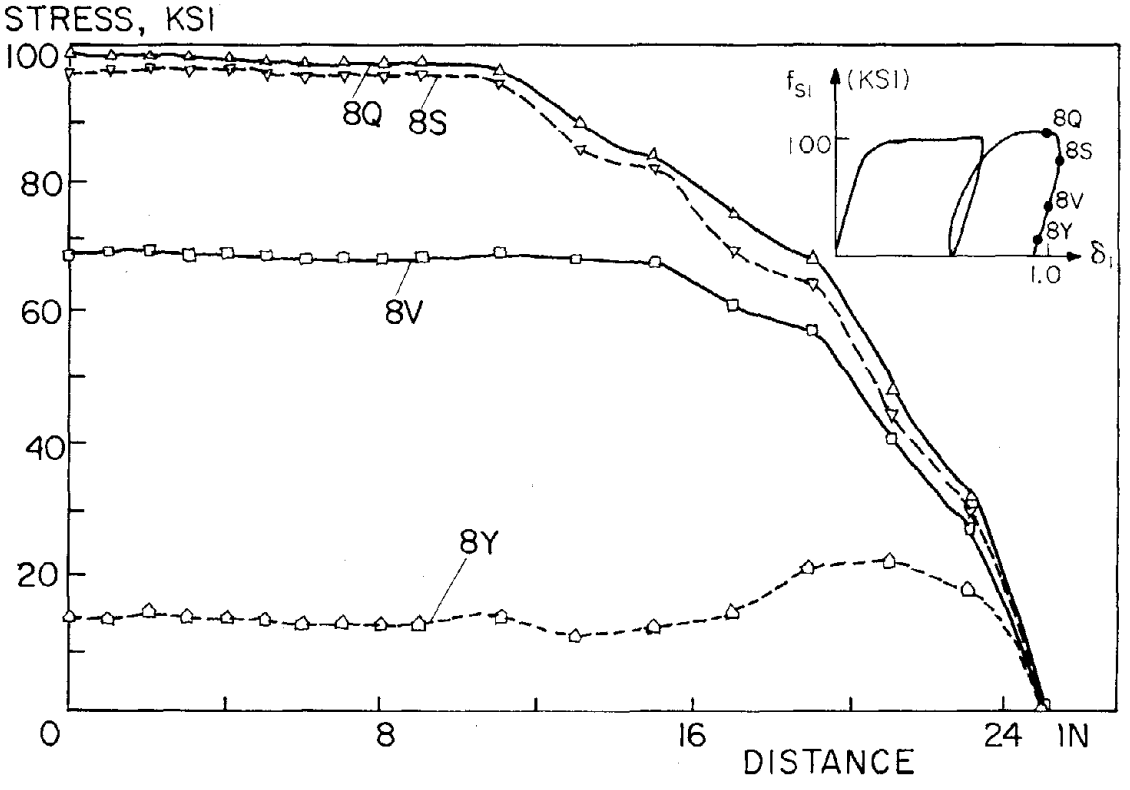

(g) Pull-Through Level

Fig. 4.22 Stress Distribution Diagrams (Monotonic Pull Only)

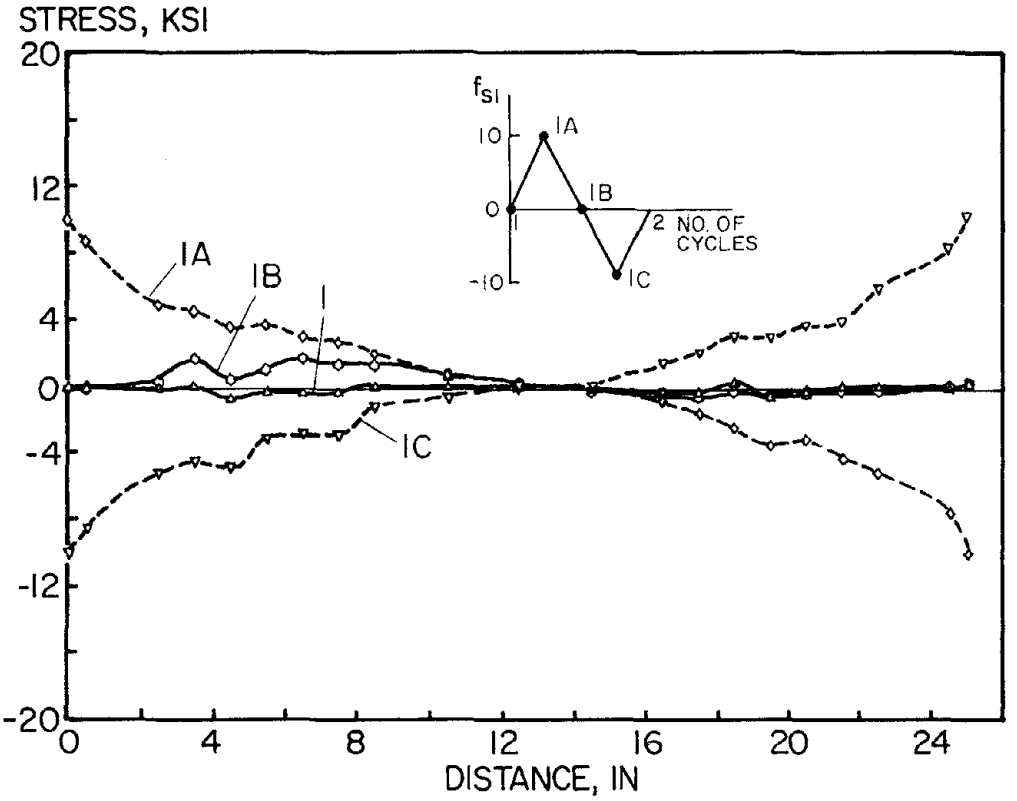

(a) 10 ksi Level (First Cycle)

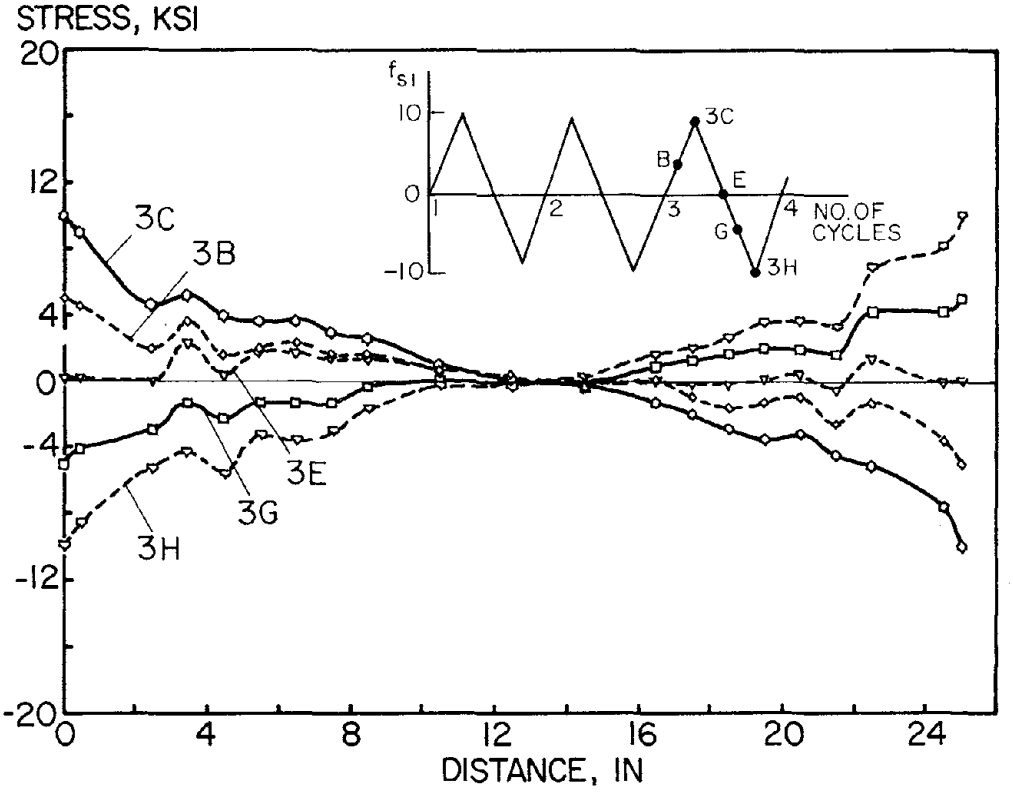

(b) 10 ksi Level (Repeating Cycle)

Fig. 4.23 Stress Distribution Diagrams (Monotonic Push-Pull)

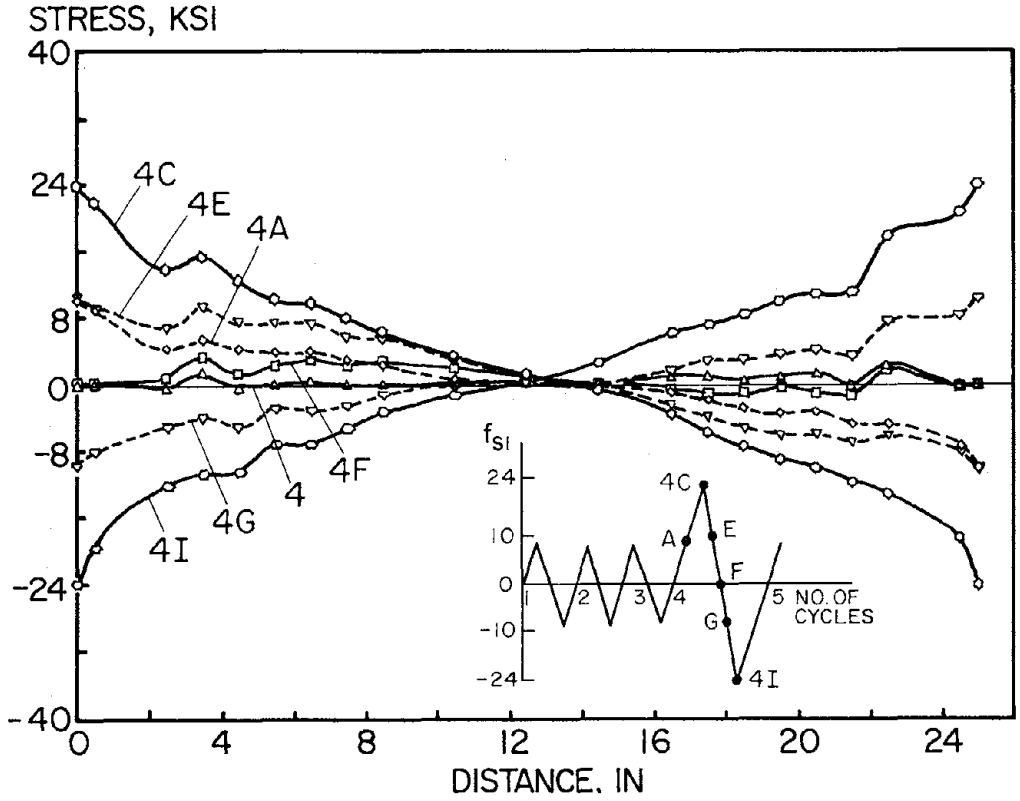

(c) Working Load Cycle (First Cycle)

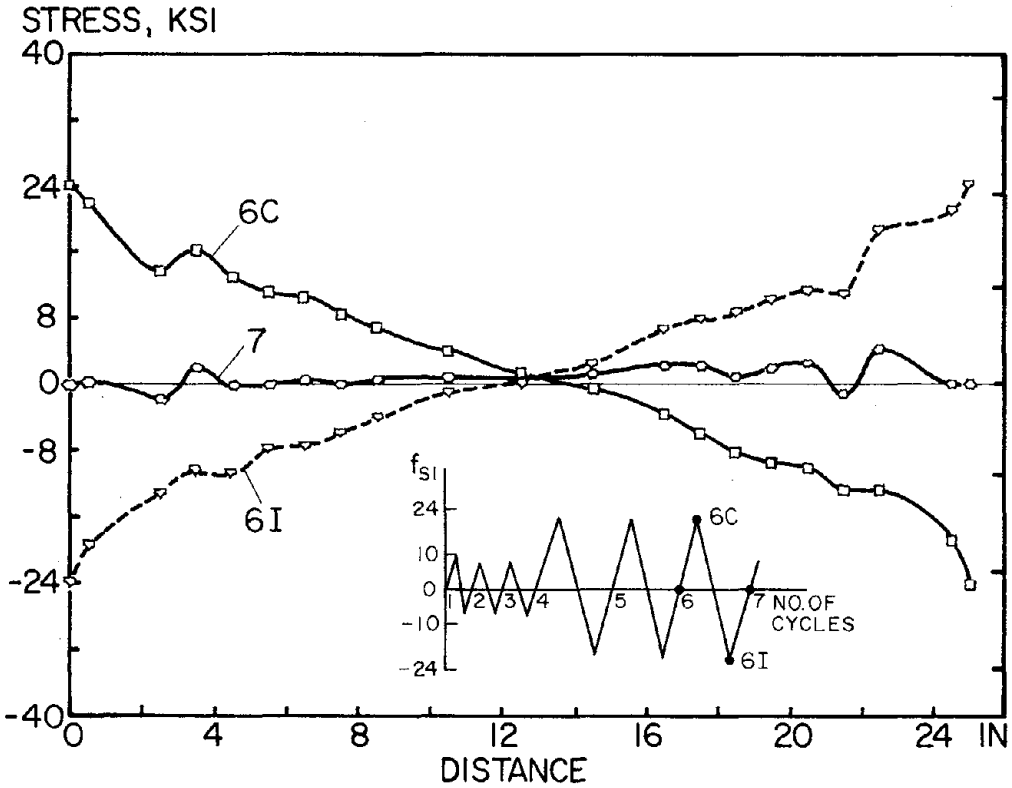

(d) Working Load Cycle (Repeating Cycle)

Fig. 4.23 Stress Distribution Diagrams (Monotonic Push-Pull)

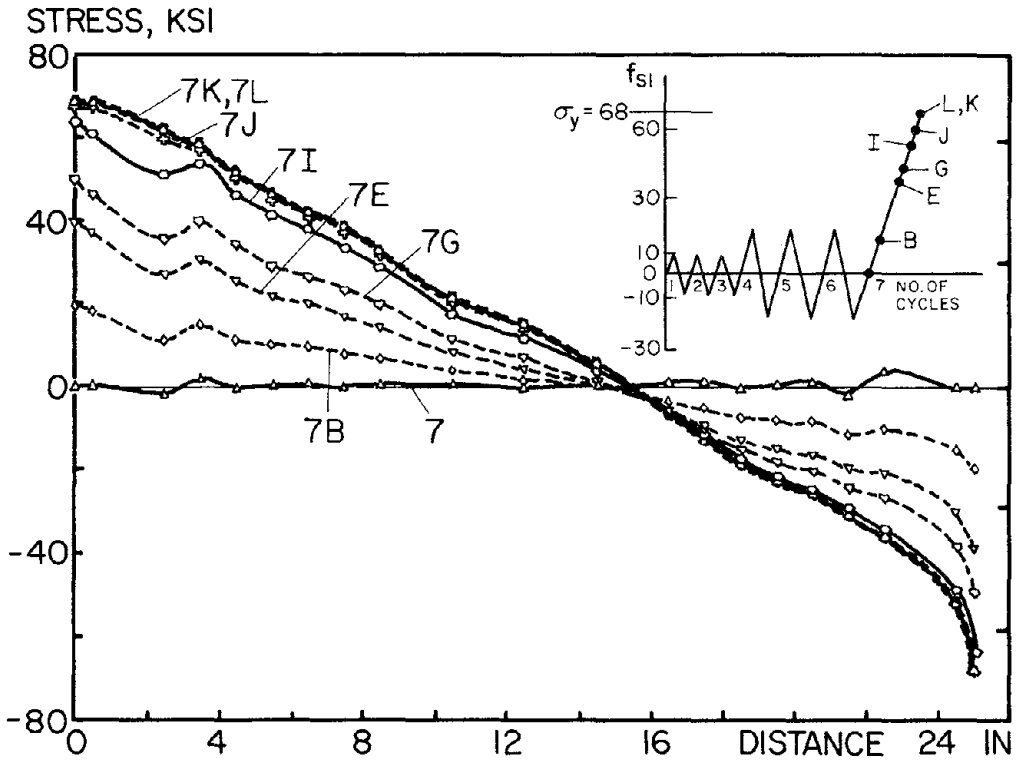

(e) Load to First Yield

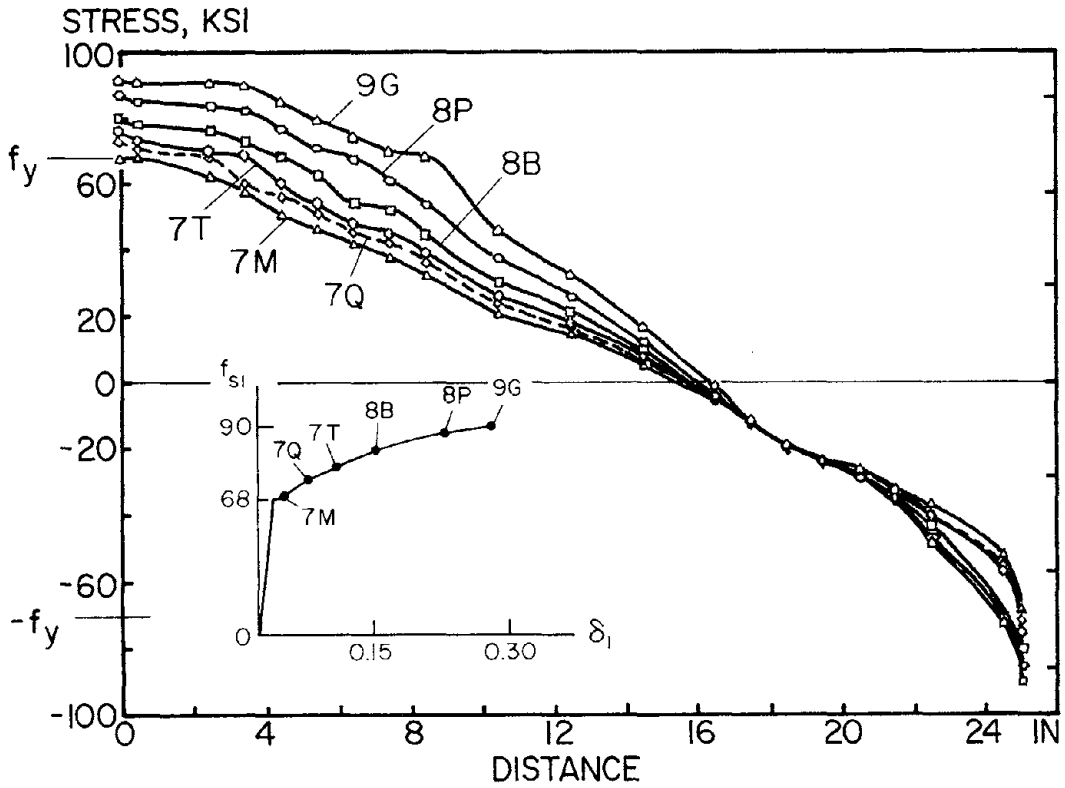

(f) Post-Yield Range

Fig. 4.23 Stress Distribution Diagrams (Monotonic Push-Pull)

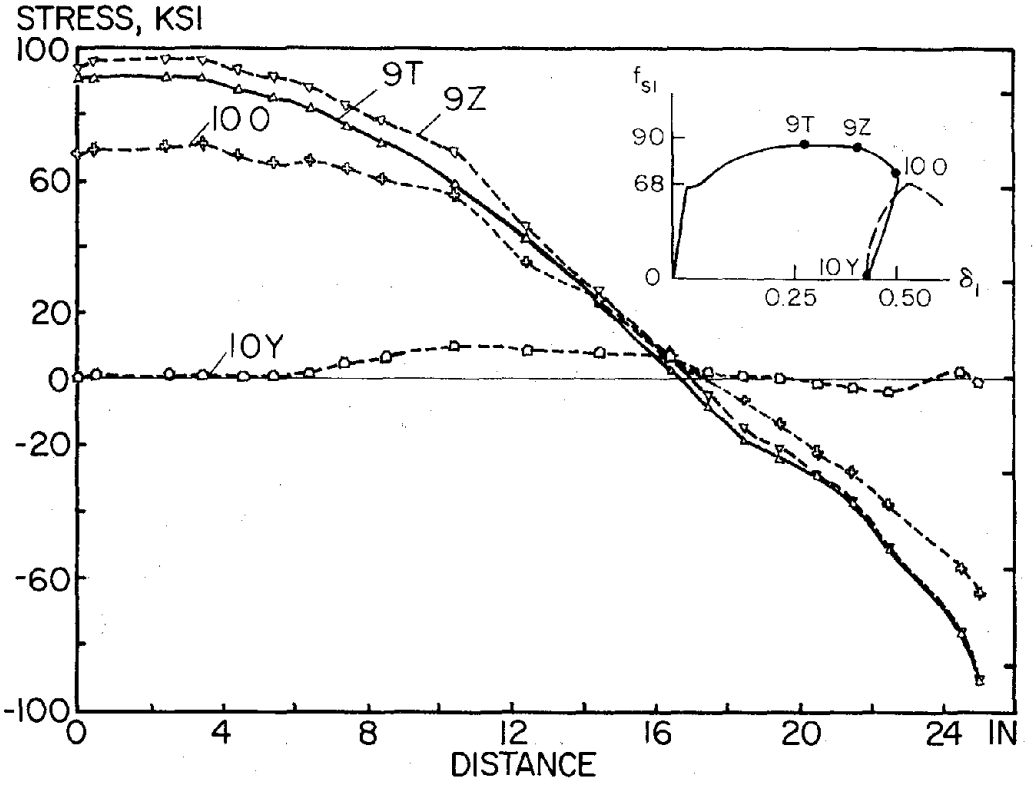

(g) Pull-Through Stage

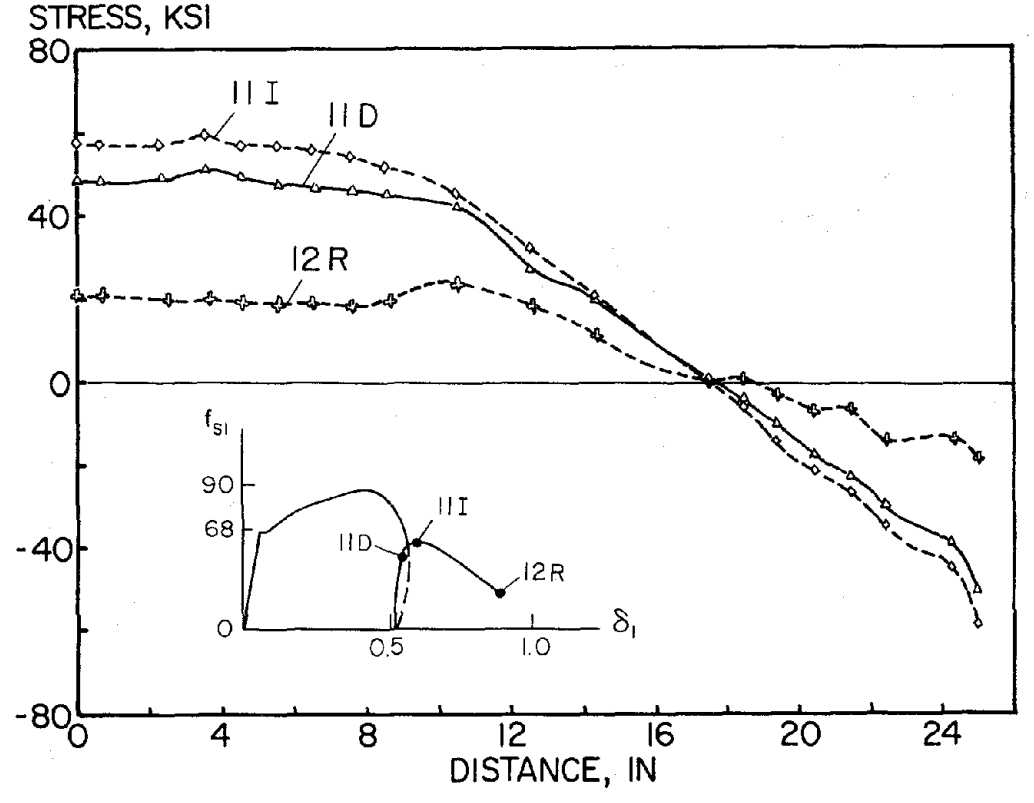

(h) Post-Pull-Through Stage

Fig. 4.23 Stress Distribution Diagrams (Monotonic Push-Pull)

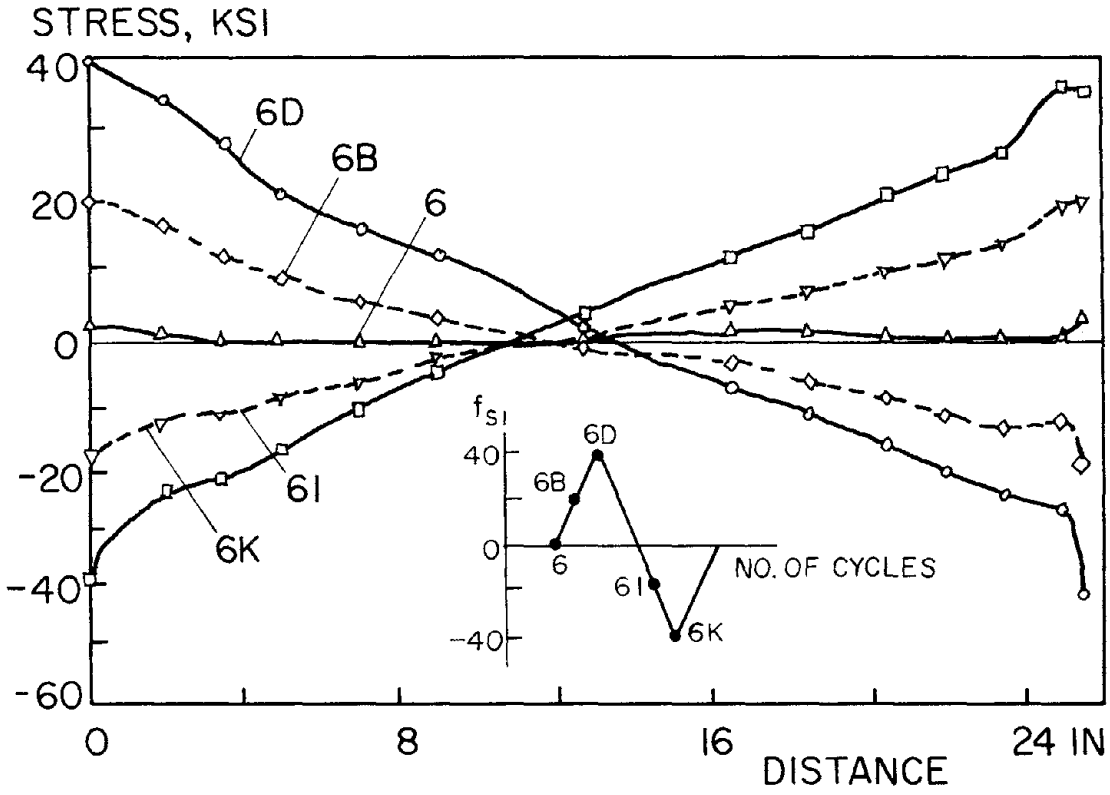

(a) 40 ksi Level (First Cycle)

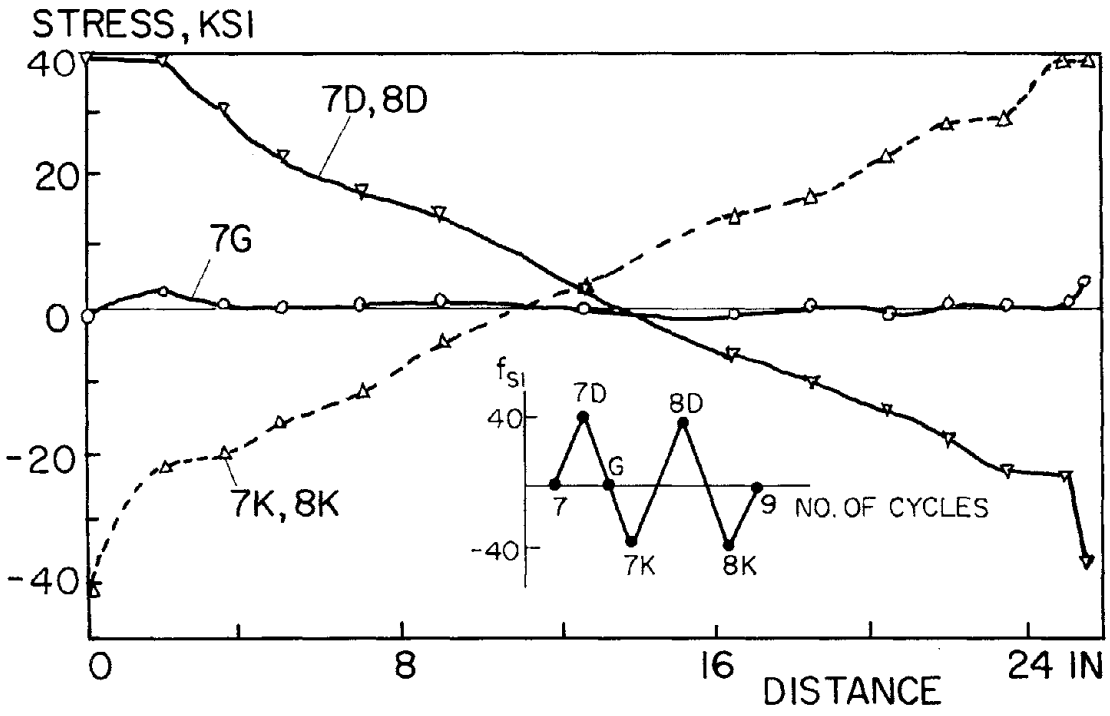

(b) 40 ksi Level (Repeating Cycle)

Fig. 4.24 Stress Distribution Diagrams (Cyclic Loading)

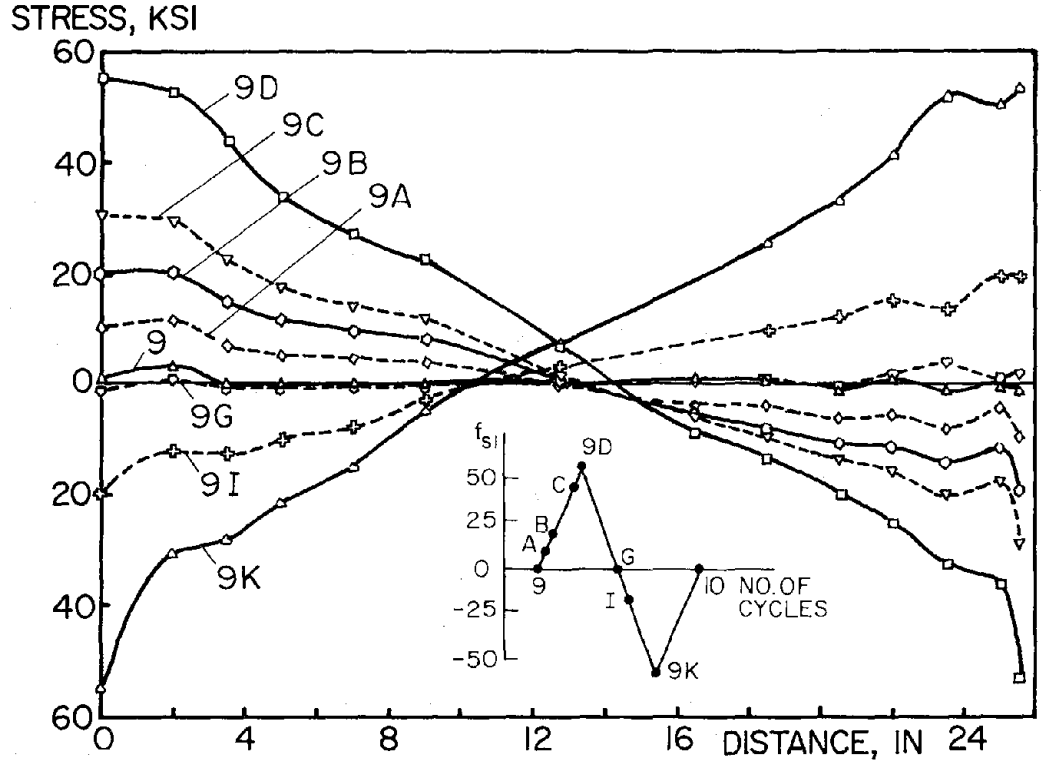

(c) 55 ksi Level (First Cycle)

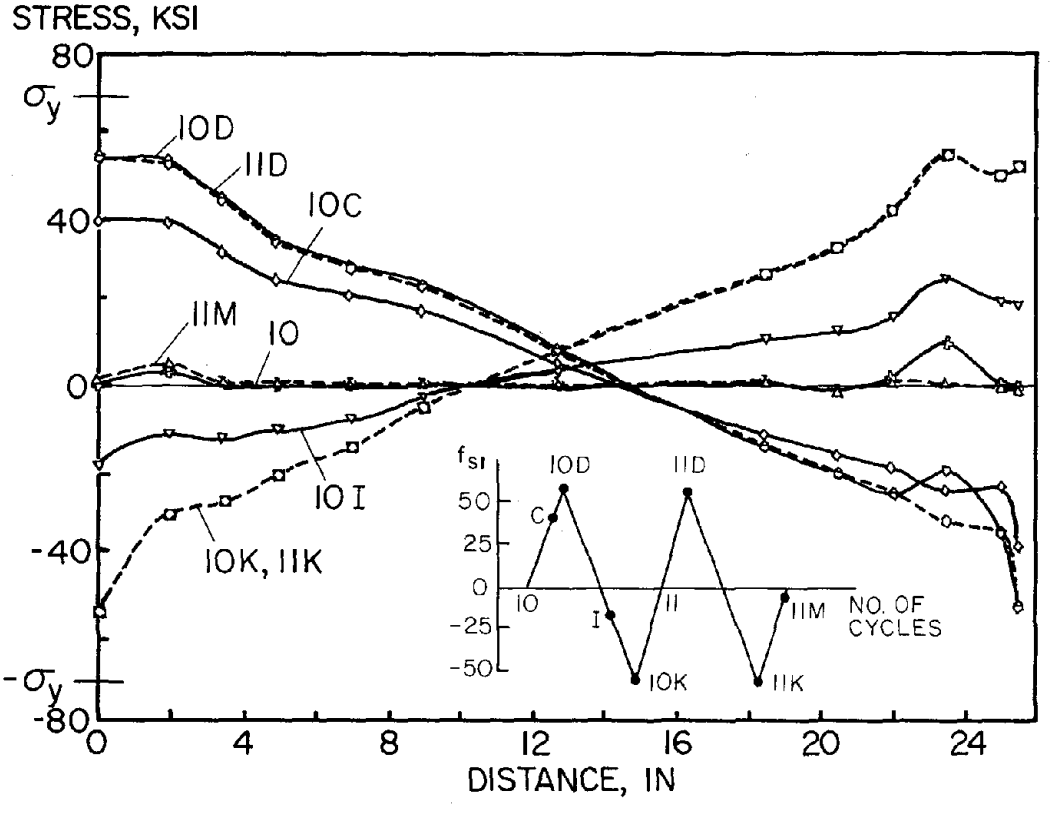

(d) 55 ksi Level (Repeating Cycle)

Fig. 4.24 Stress Distribution Diagrams (Cyclic Loading)

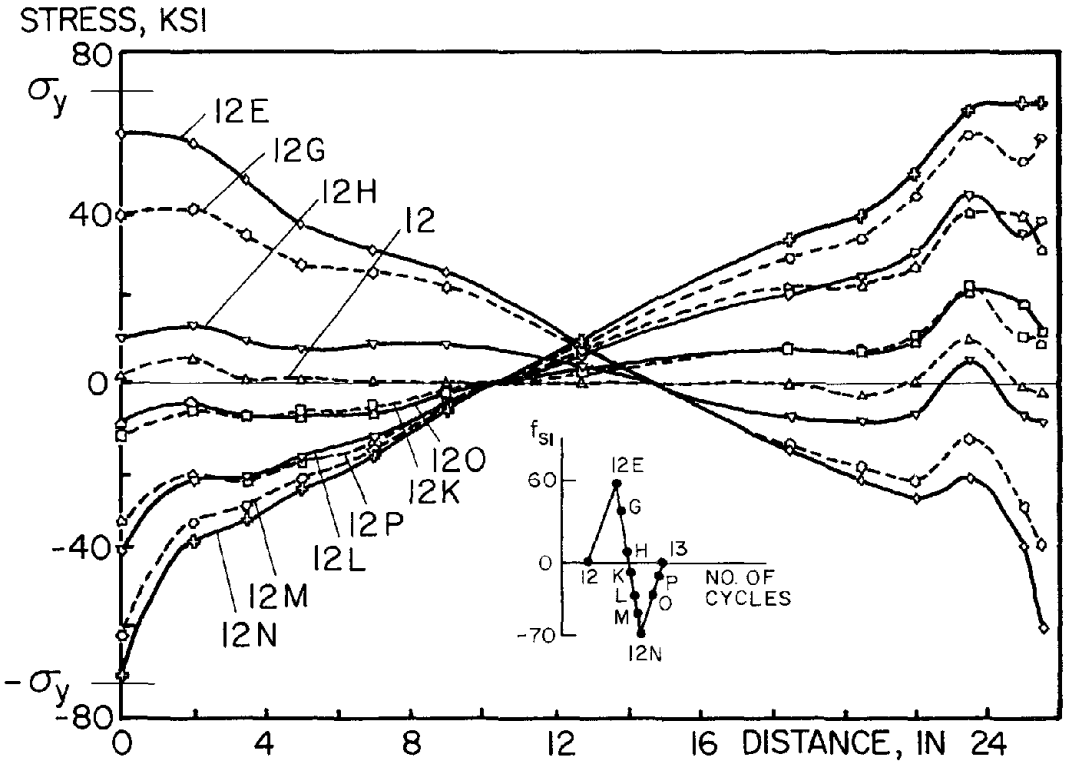

(e) Up to Yield

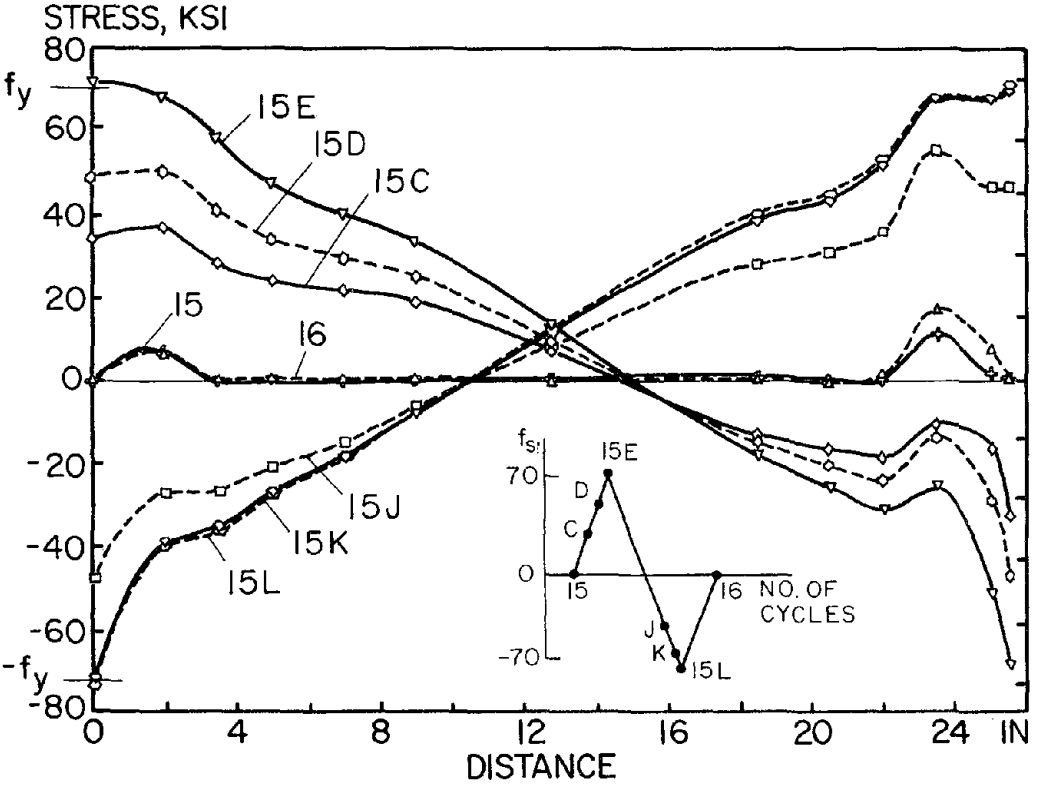

(f) First Post-Yield Range

Fig. 4.24 Stress Distribution Diagrams (Cyclic Loading)

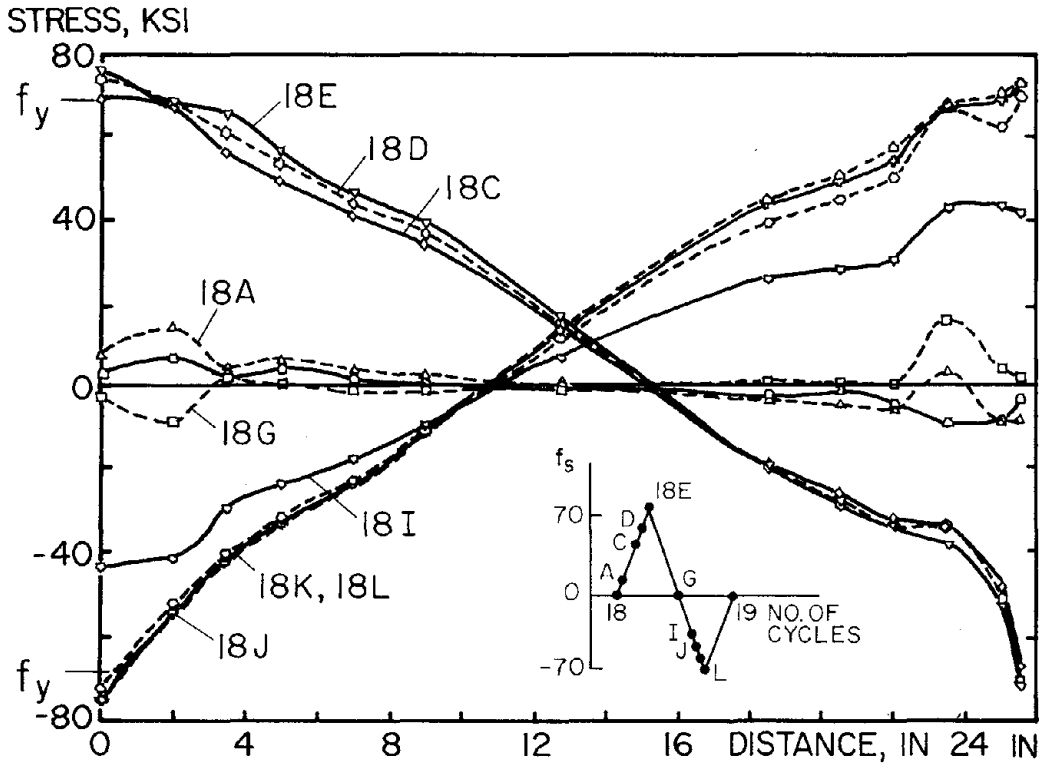

(g) Second Post-Yield Range

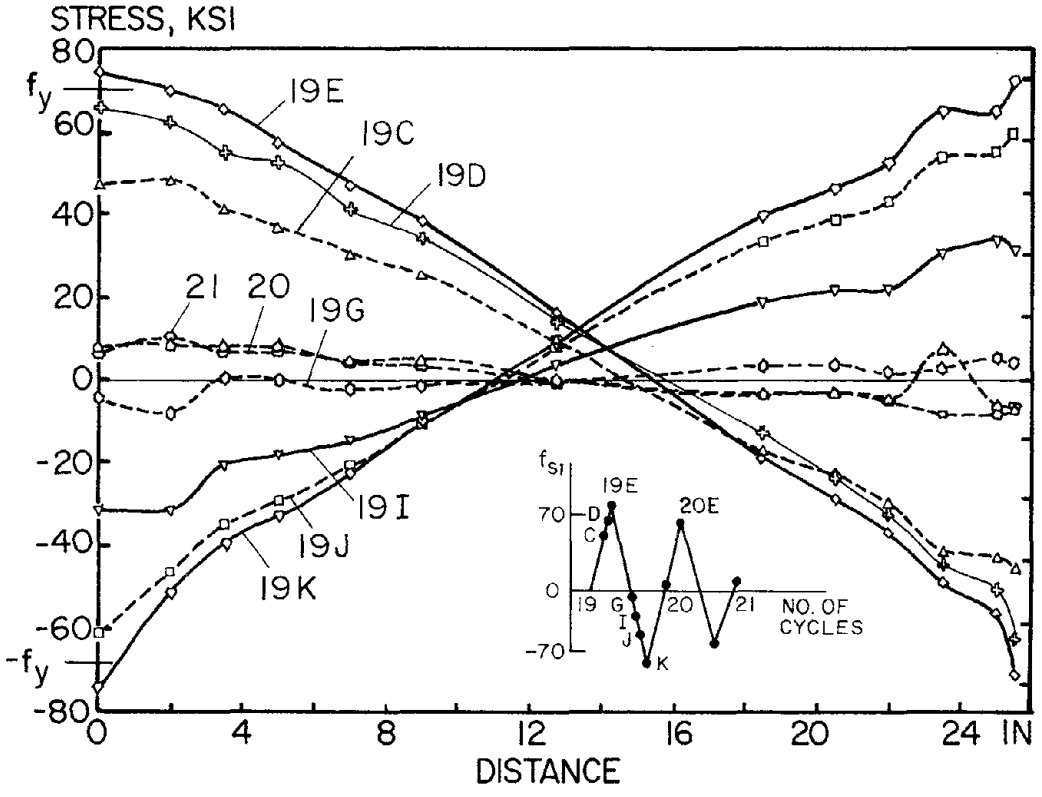

(h) Pull-Through Range

Fig. 4.24 Stress Distribution Diagrams (Cyclic Loading)

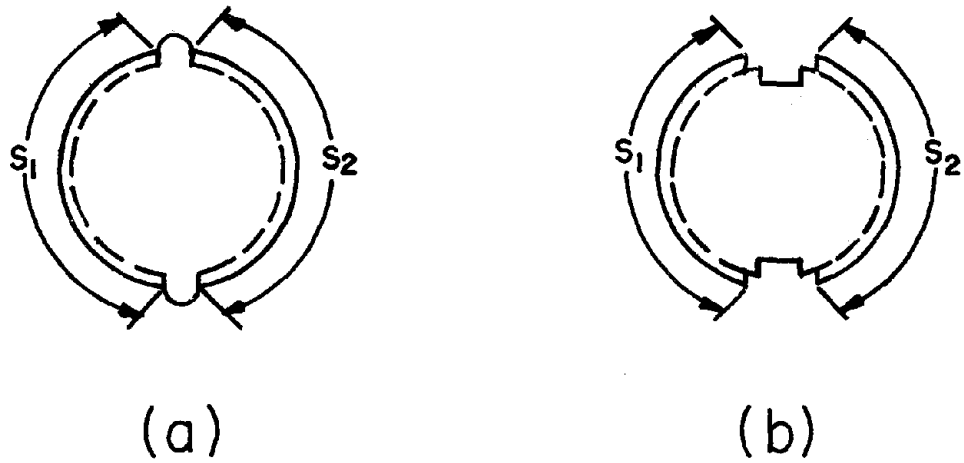

Fig. 4.25 Effective Circumference

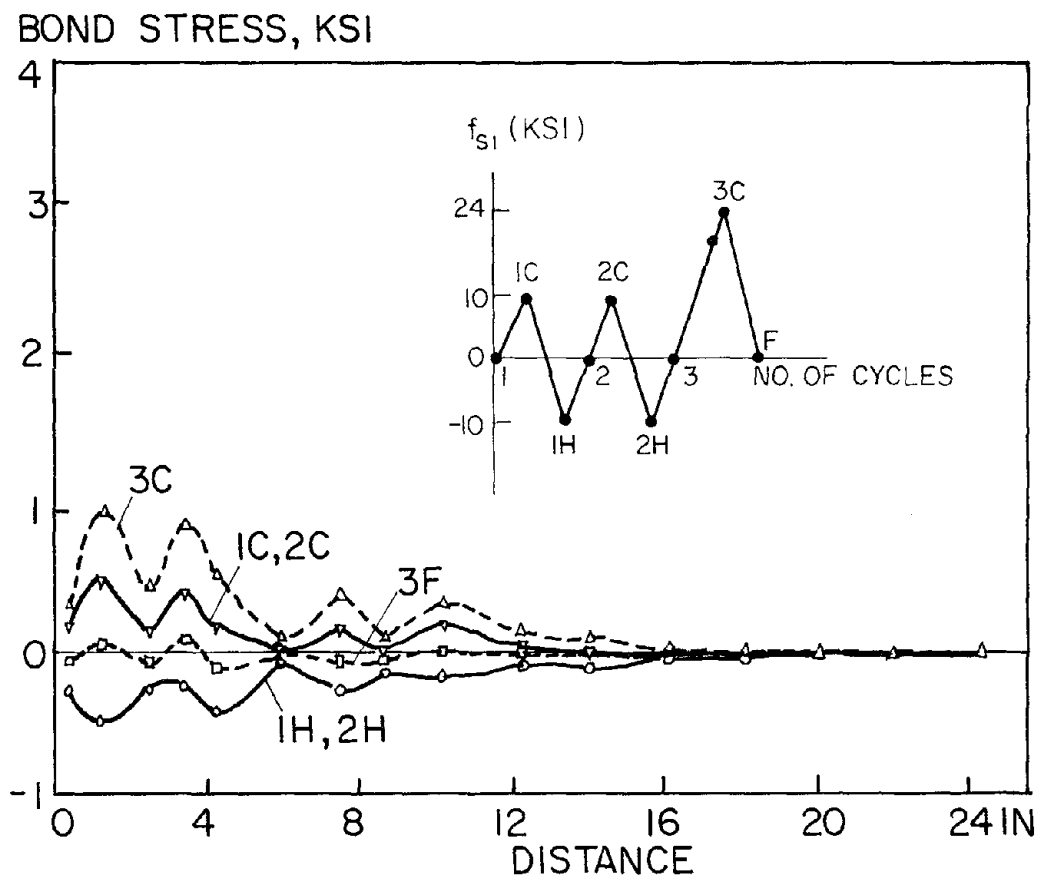

(a) Working Load Range

Fig. 4.26 Bond Stress Distribution Diagrams (Pull Only)

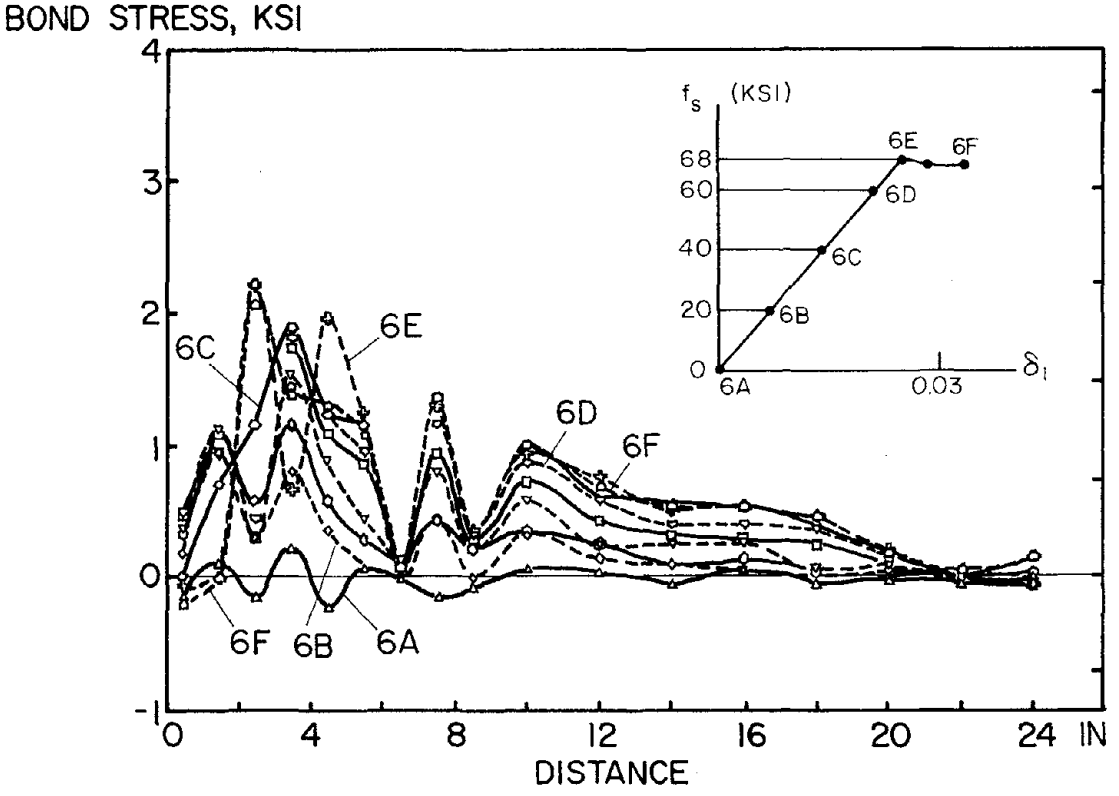

(b) Up to Yield

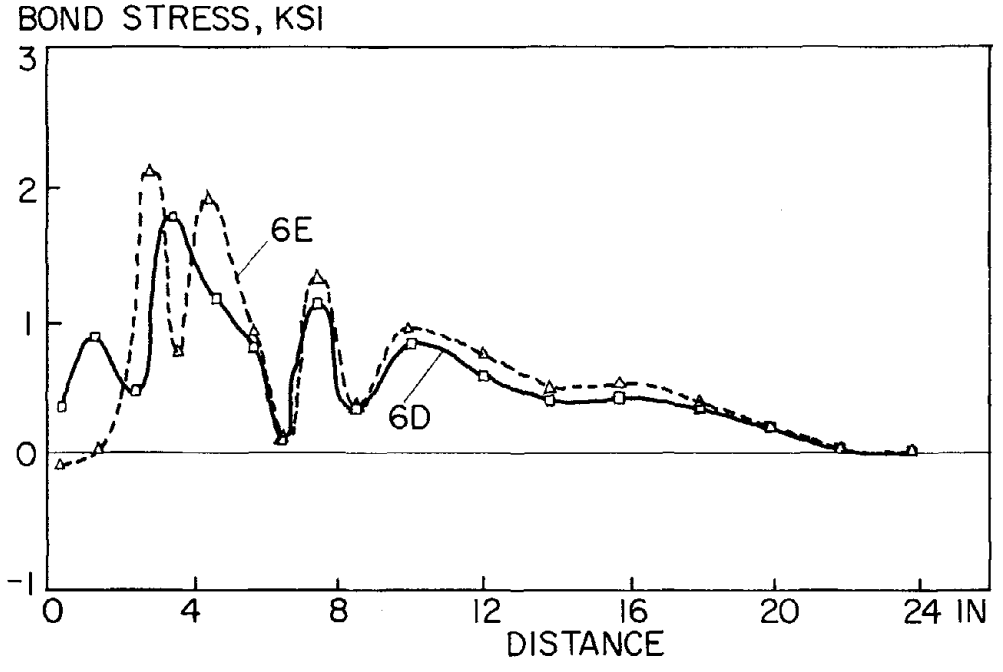

(b.1) LP 6D and 6E Isolated from (b)

Fig. 4.26 Bond Stress Distribution Diagrams (Pull Only)

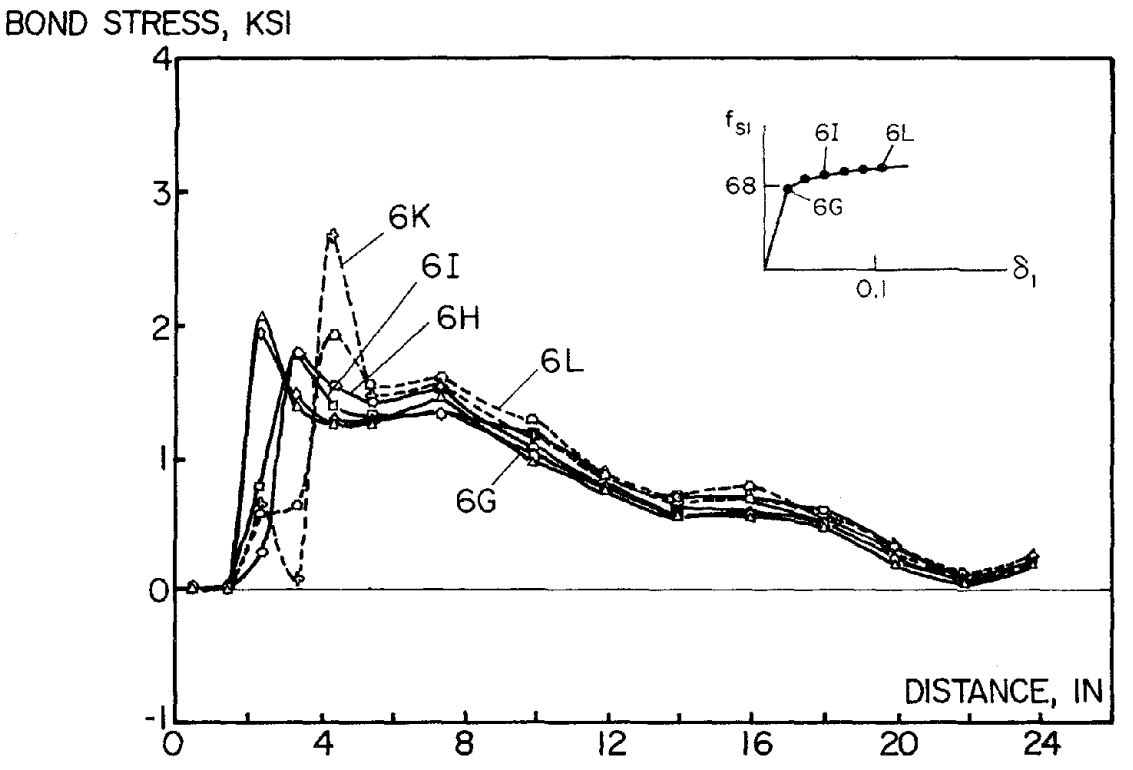

(c) First Post-Yield Range

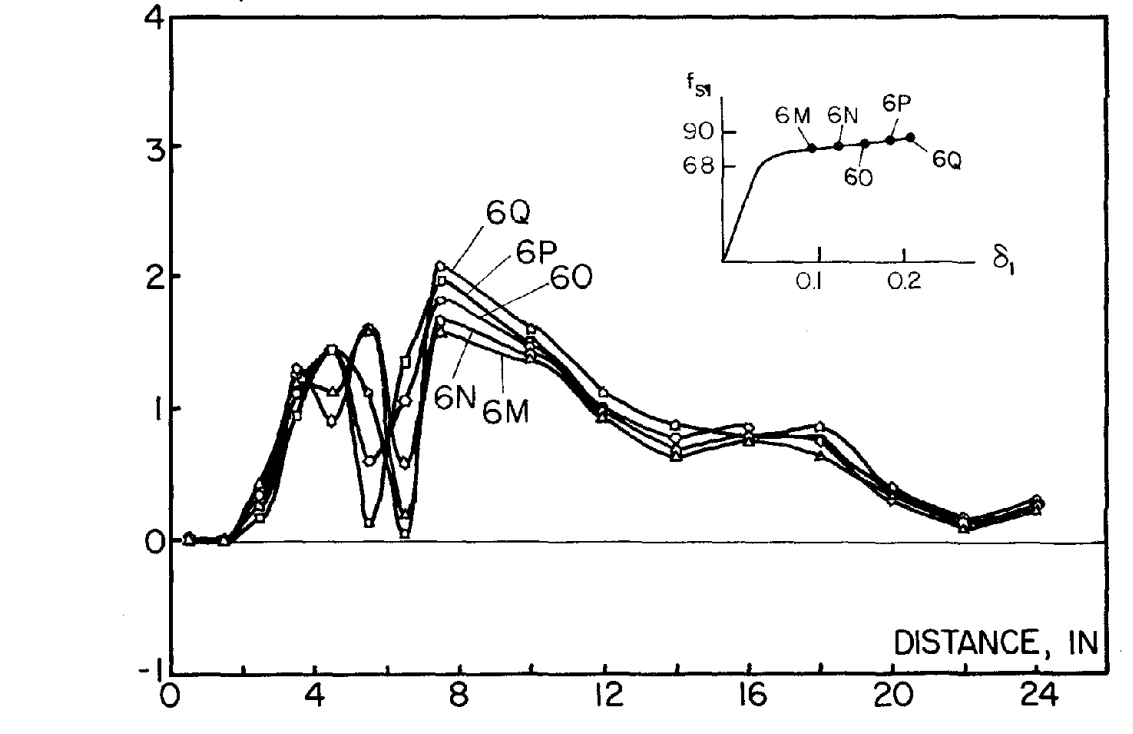

(d) Second Post-Yield Range

Fig. 4.26 Bond Stress Distribution Diagrams (Pull Only)

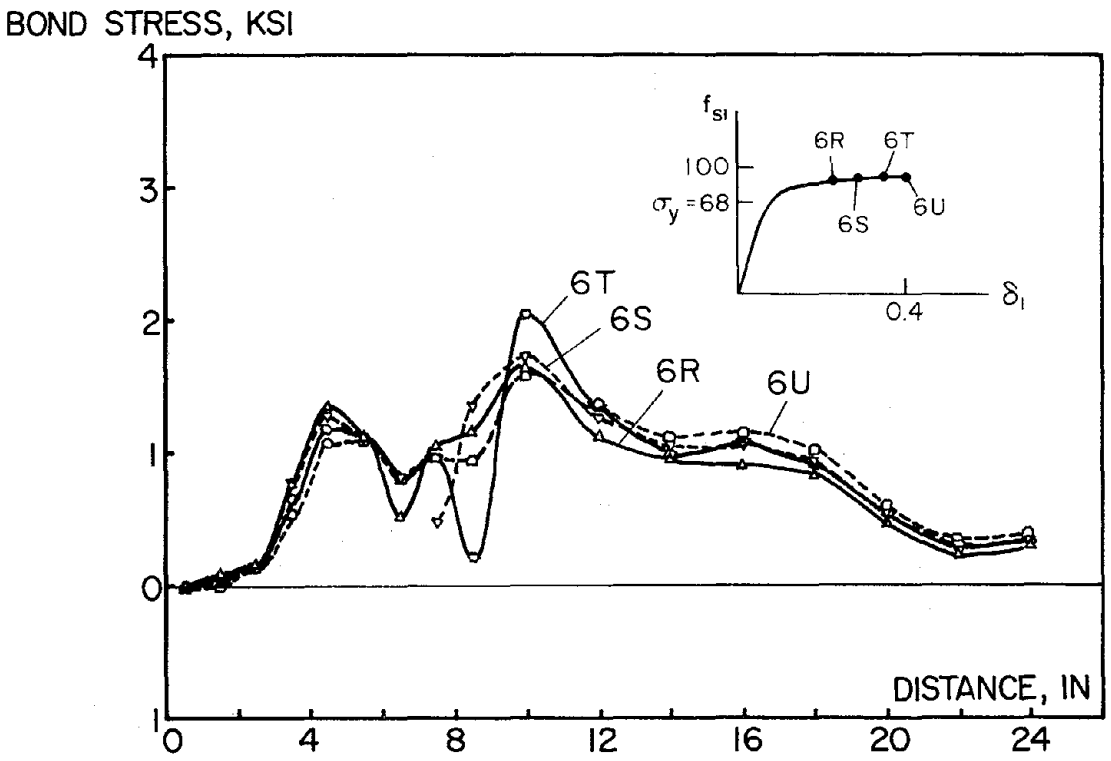

(e) Third Post-Yield Range

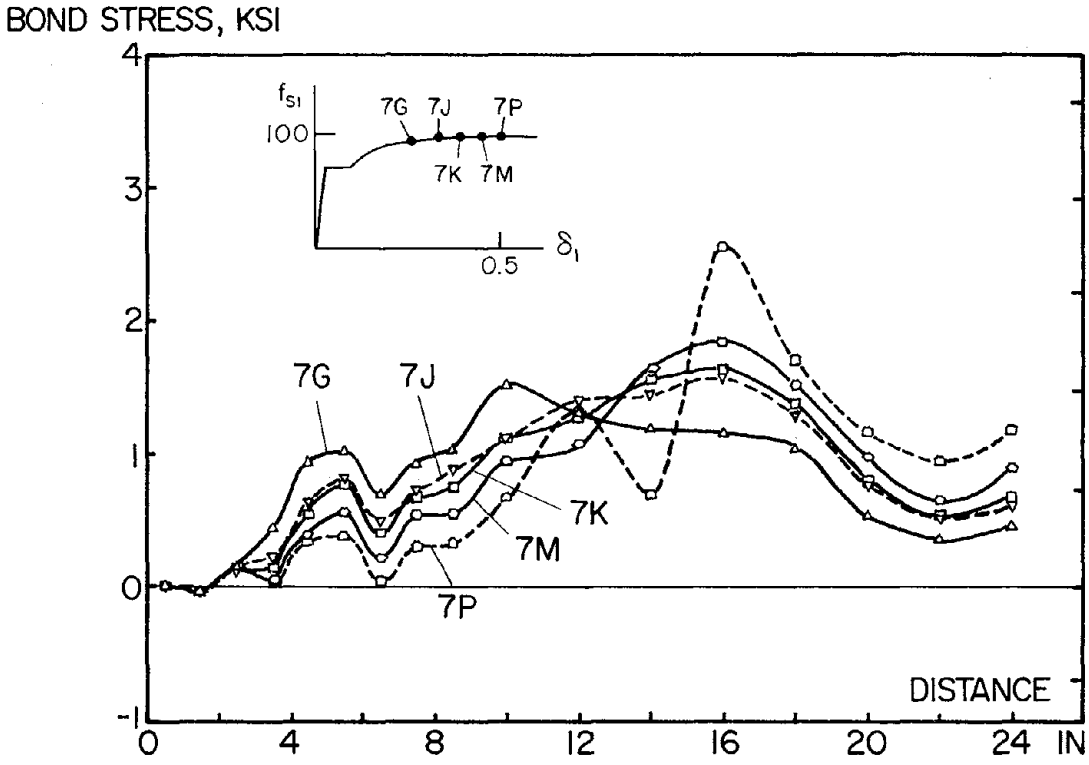

(f) Fourth Post-Yield Range

Fig. 4.26 Bond Stress Distribution Diagrams (Pull Only)

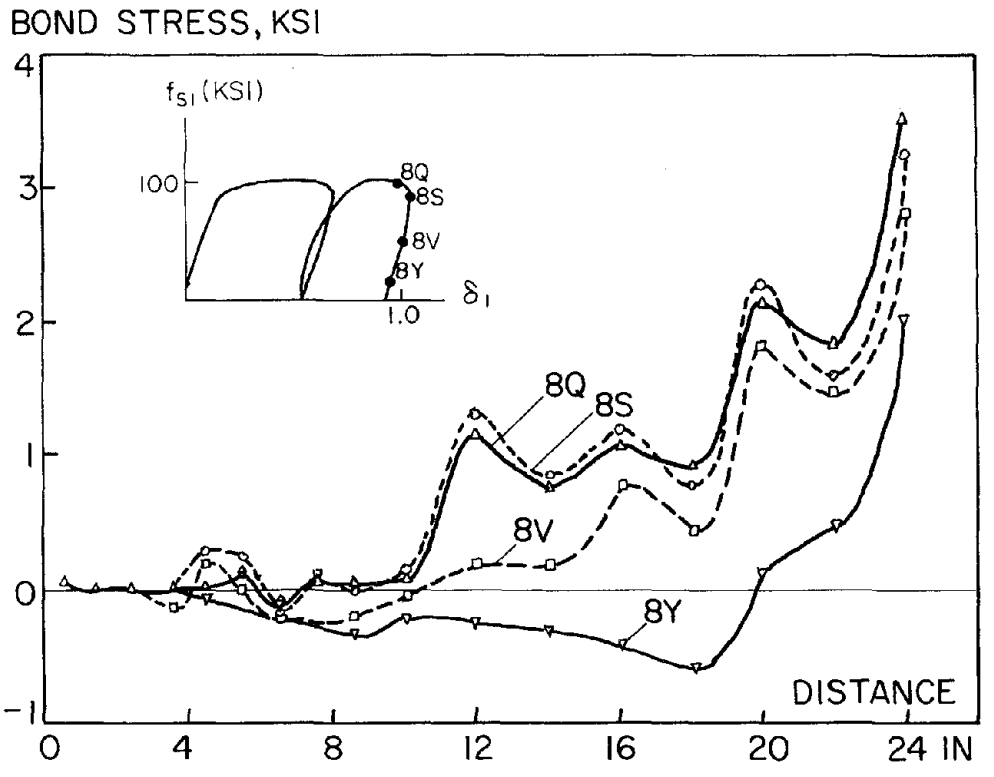

(g) Pull-Through Stage

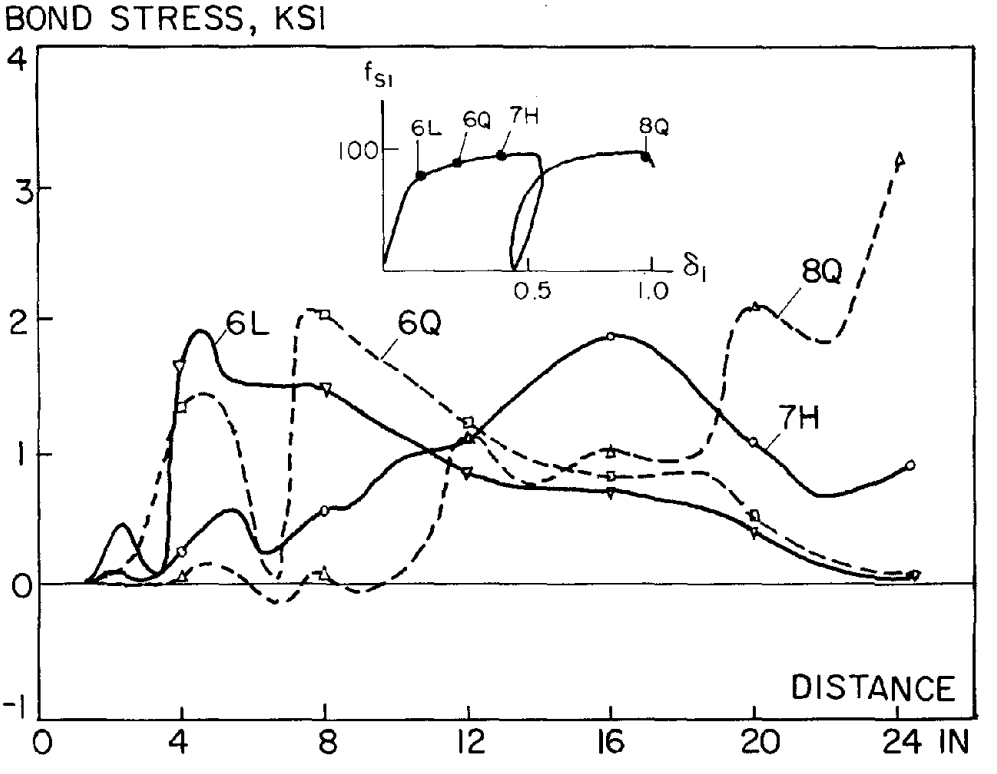

(h) Summary of Bond Stress Distribution in Post-Yield Range

Fig. 4.26 Bond Stress Distribution Diagrams (Pull Only)

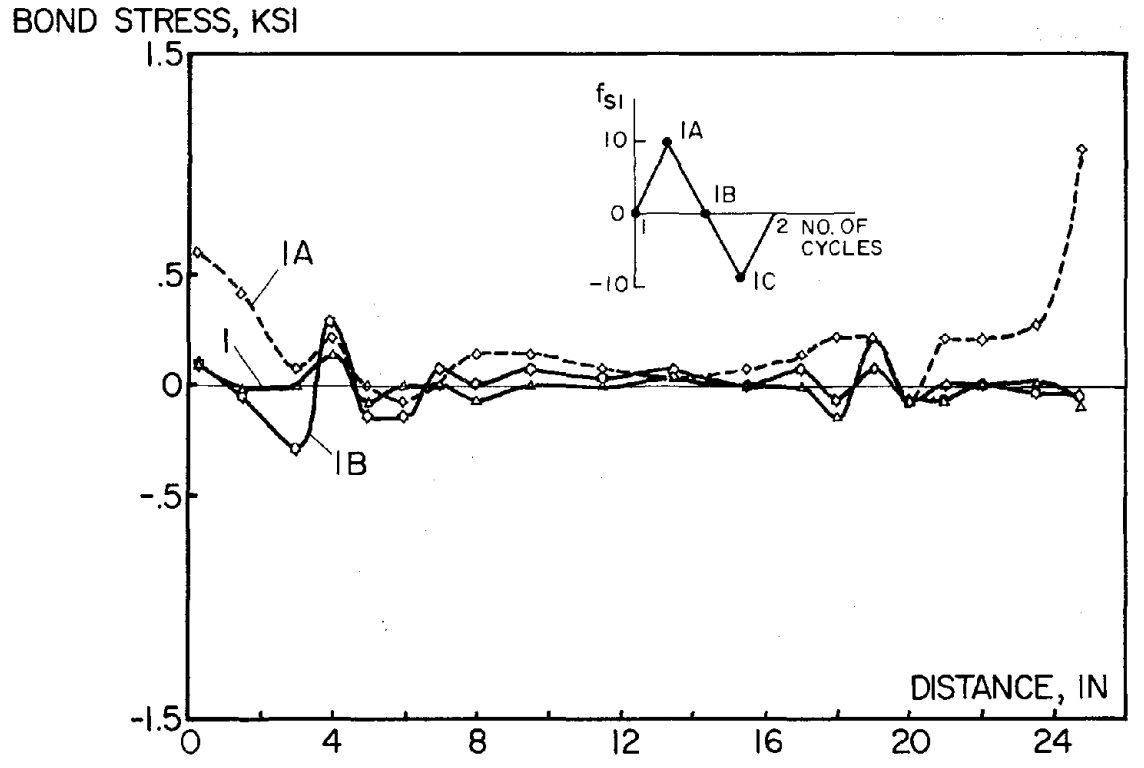

(a) 10 ksi Level (First Cycle)

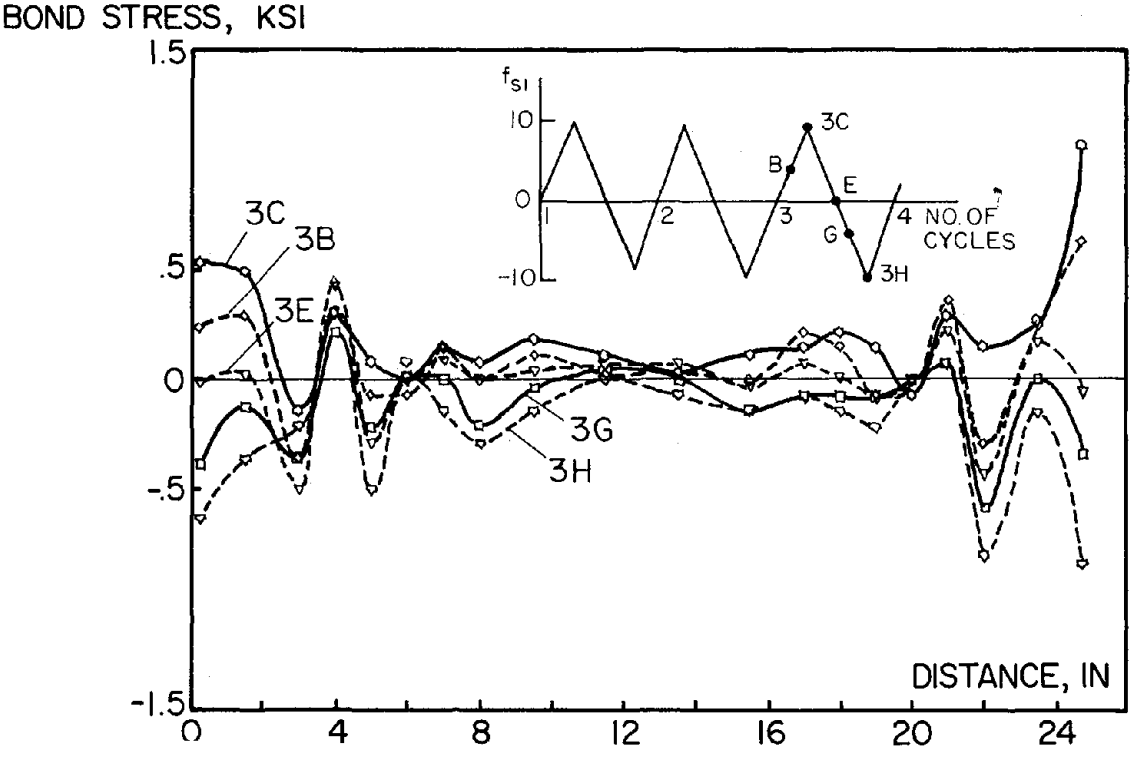

(b) 10 ksi Level (Repeating Cycle)

Fig. 4.27 Bond Stress Distribution Diagrams (Push-Pull)

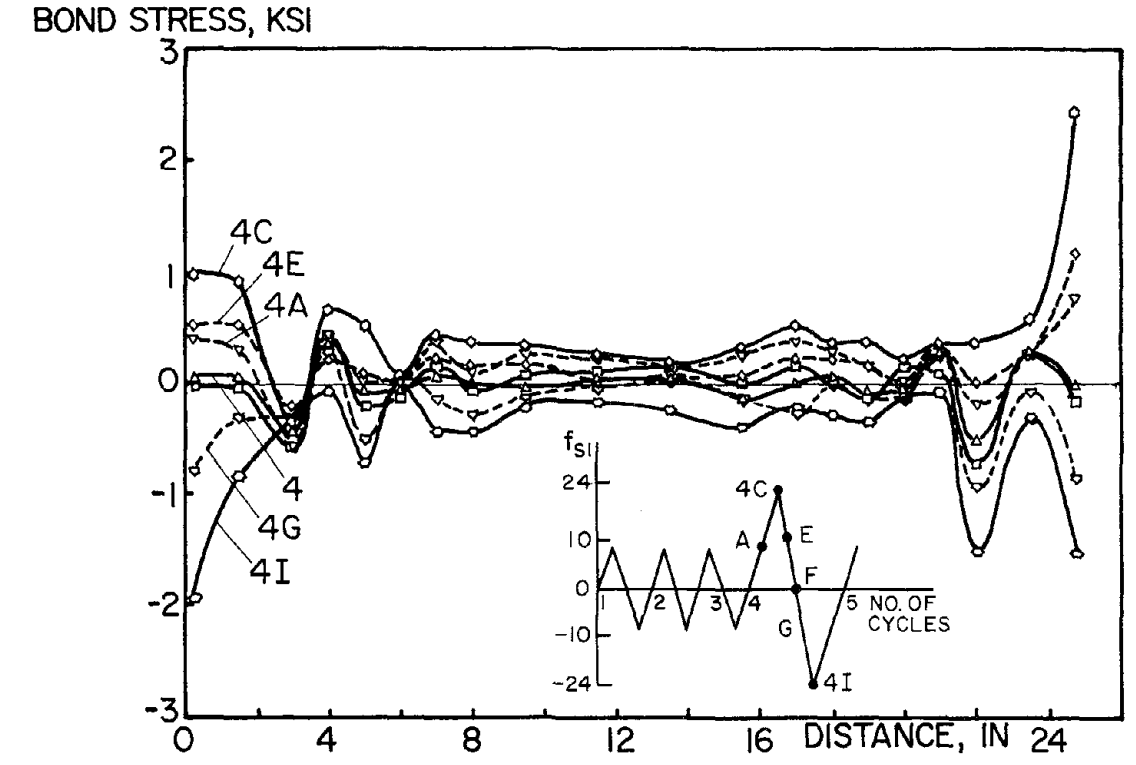

(c) Working Load Range (First Cycle)

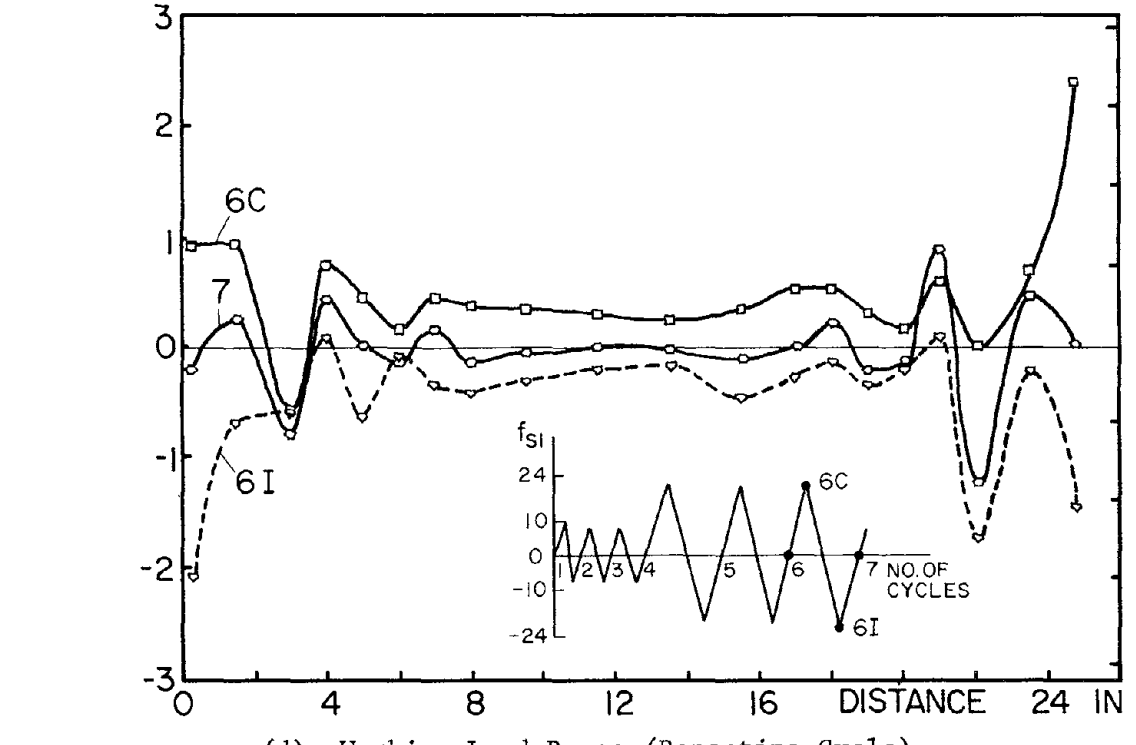

(d) Working Load Range (Repeating Cycle)

Fig. 4.27 Bond Stress Distribution Diagrams (Push-Pull)

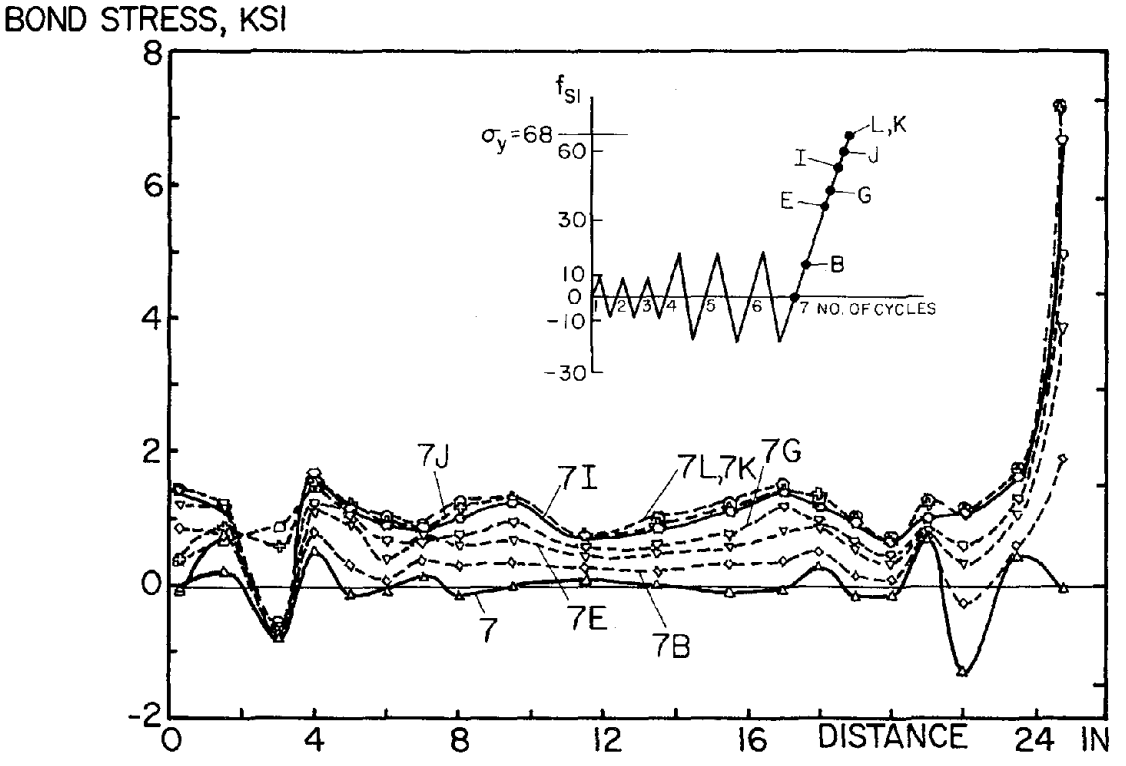

(e) Load Up to Yield

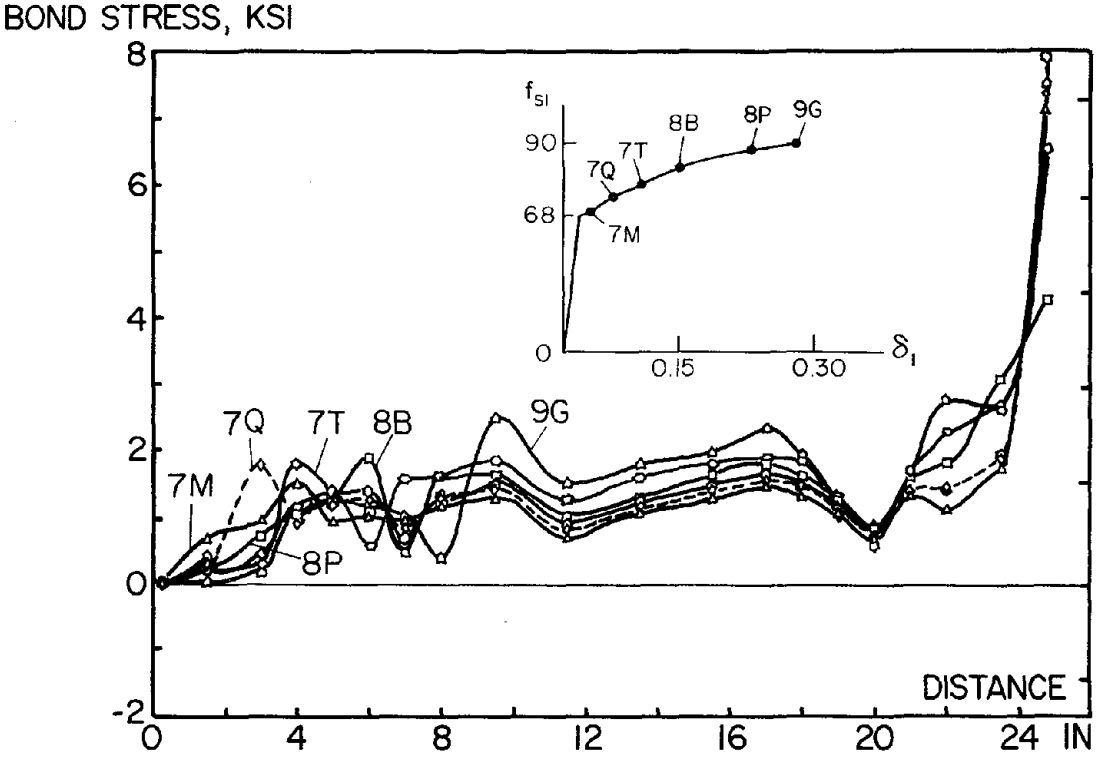

(f) Post Yield Range

Fig. 4.27 Bond Stress Distribution Diagrams (Push-Pull)

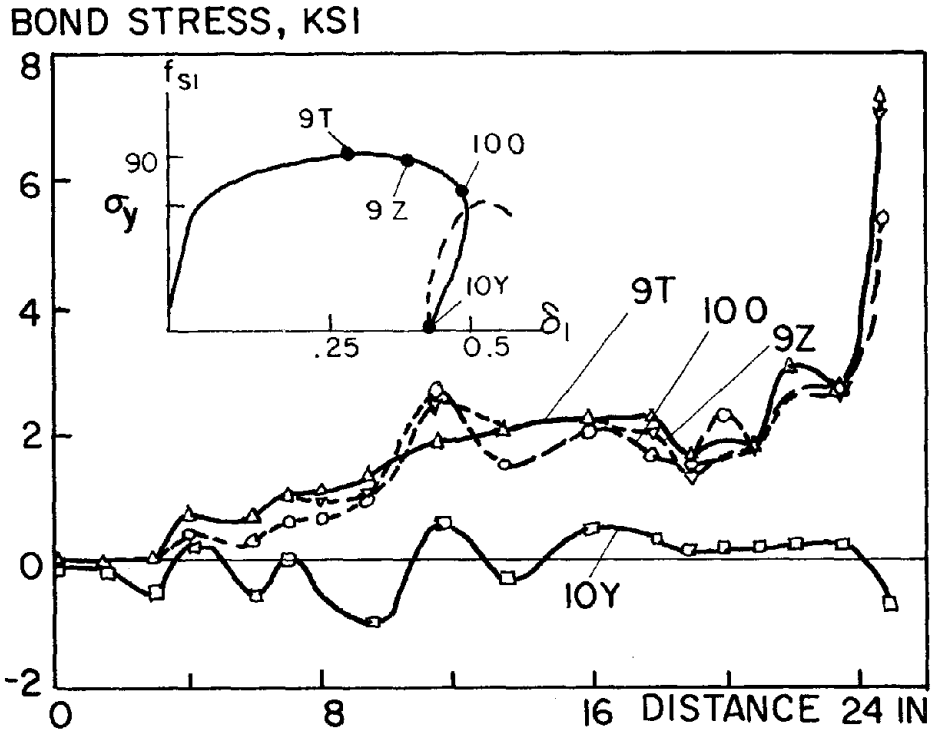

(g) Pull-Through Stage

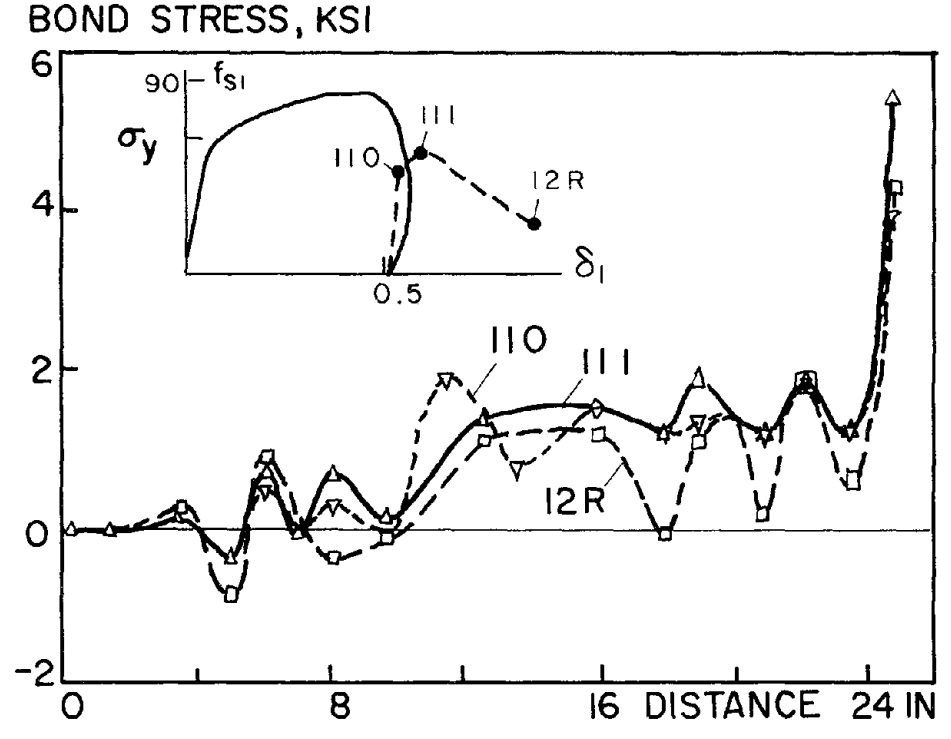

(h) Post-Pull-Through Range

Fig. 4.27 Bond Stress Distribution Diagrams (Push-Pull)

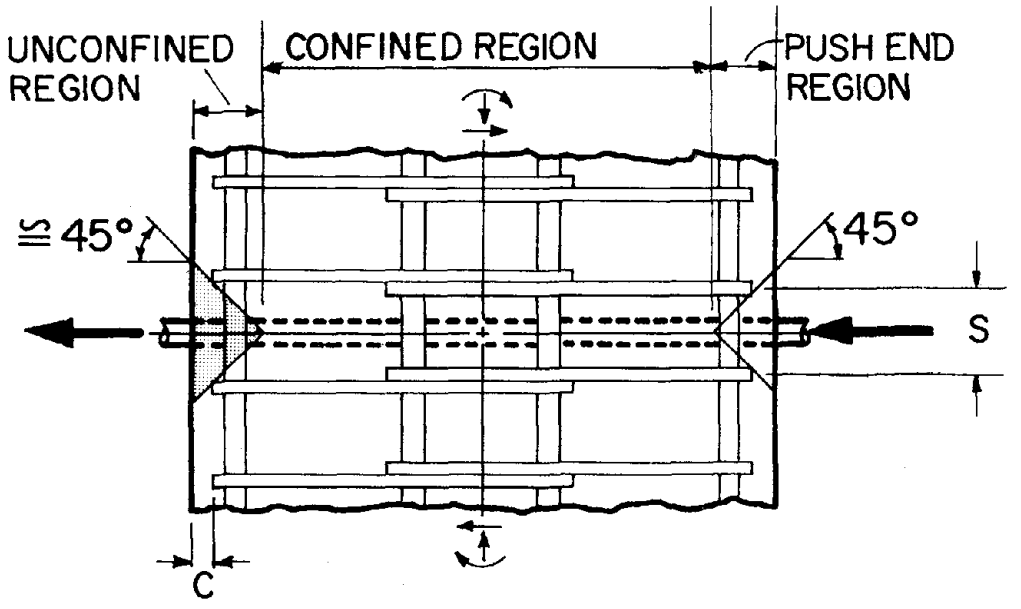

Fig. 4.28 Regions in Concrete Block

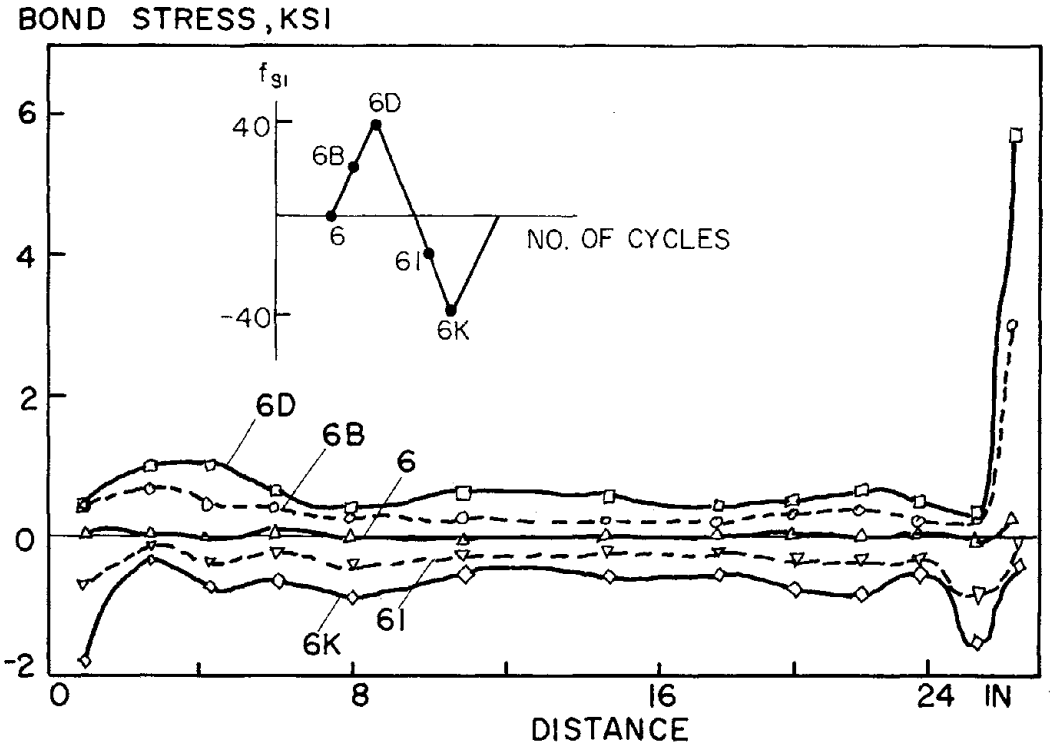

(a) 40 ksi Level (First Cycle)

Fig. 4.29 Bond Stress Distribution Diagrams (Push-Pull)

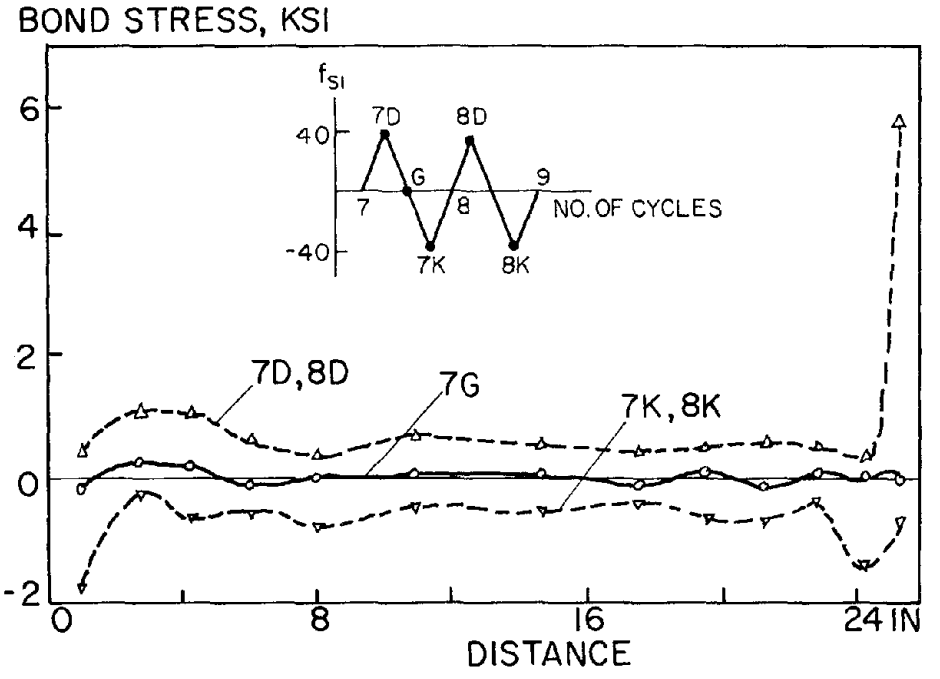

(b) 40 ksi Level (Repeating Cycle)

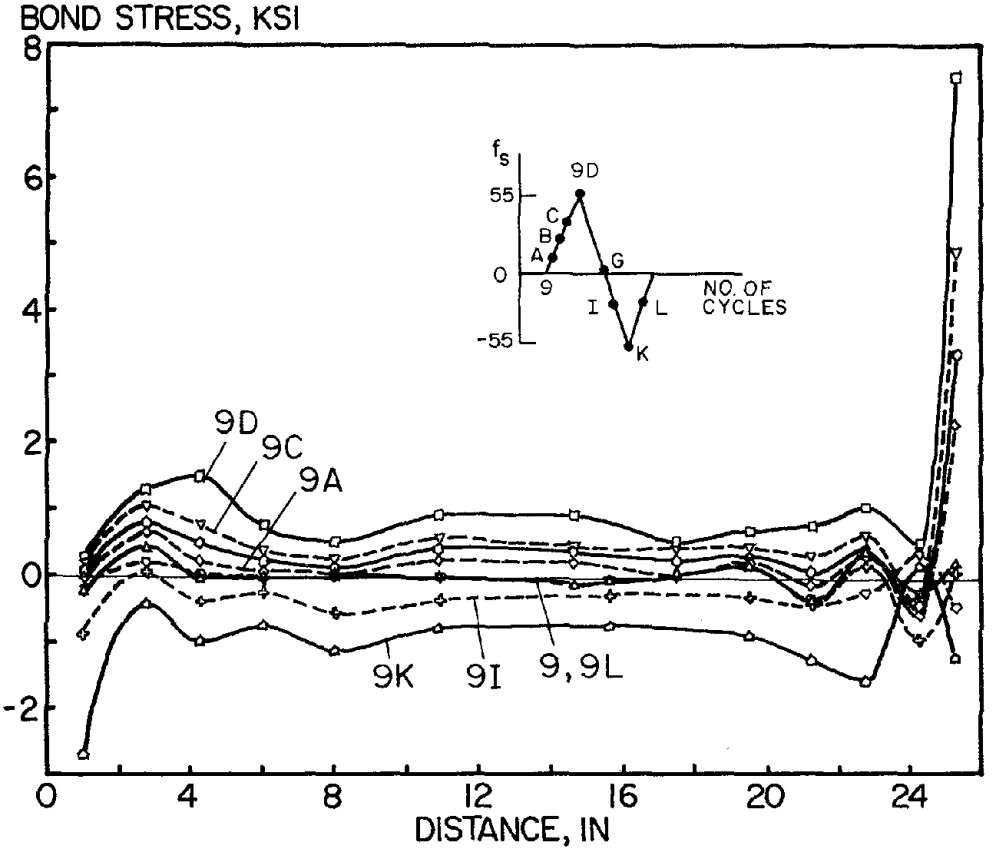

(c) 55 ksi Level (First Cycle)

Fig. 4.29 Bond Stress Distribution Diagrams (Push-Pull)

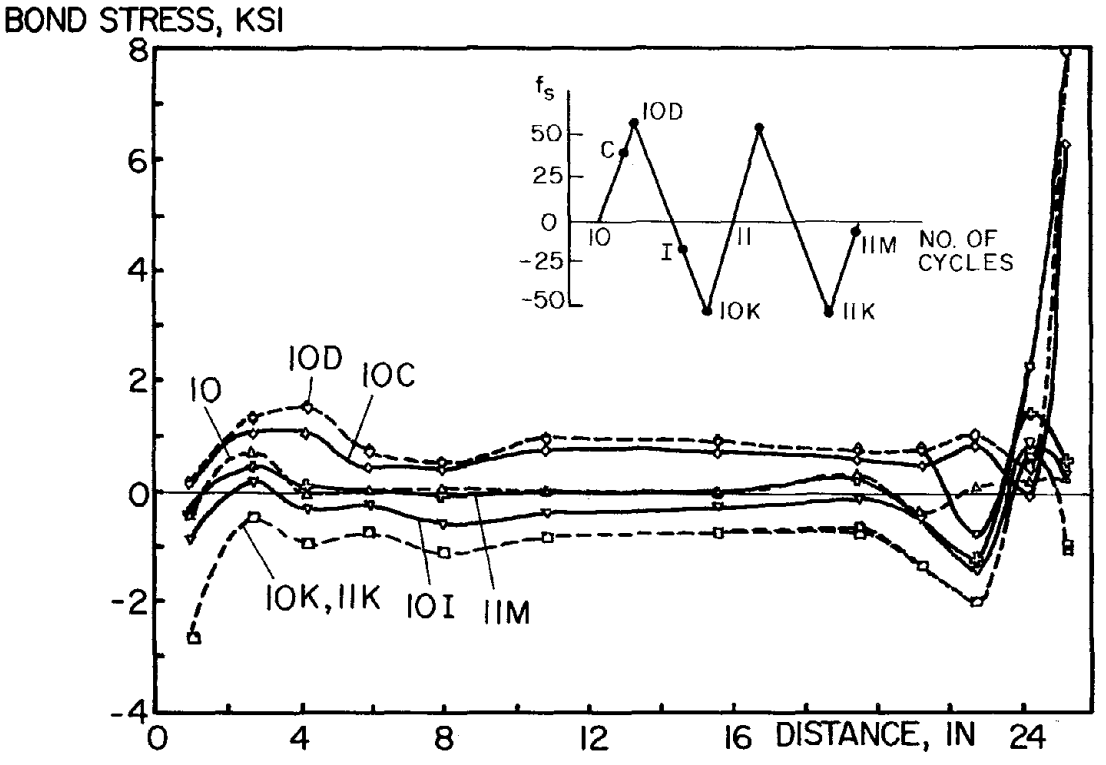

(d) 55 ksi Level (Repeating Cycle)

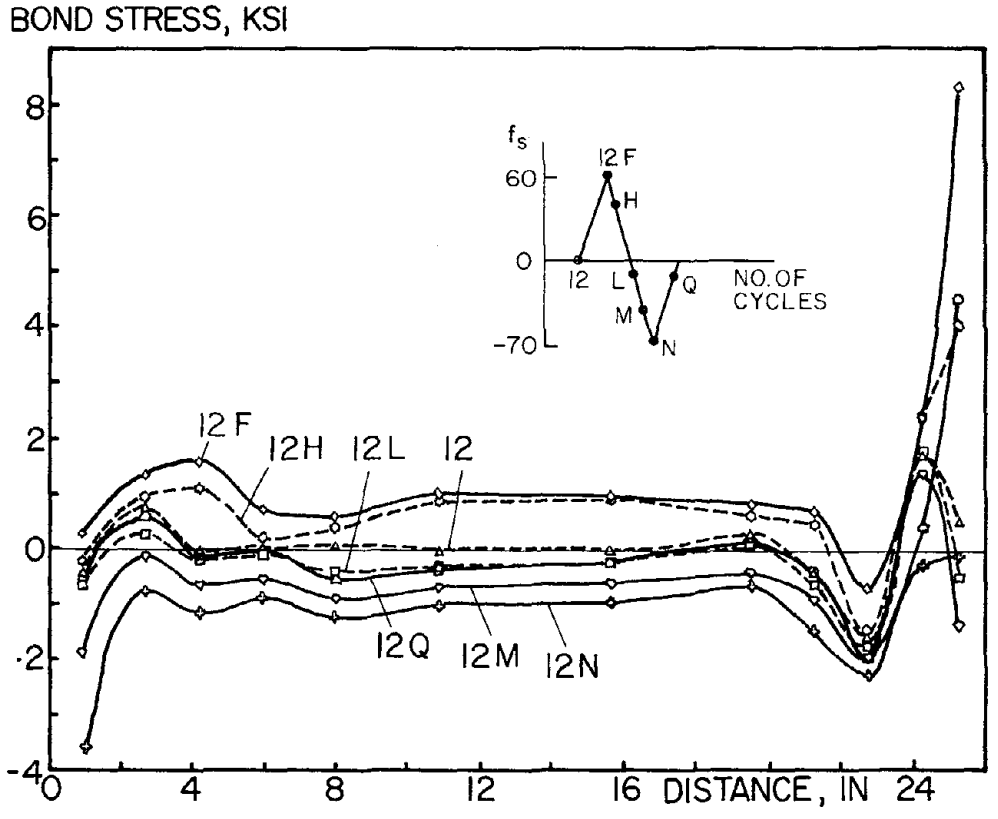

(e) Up to Yield

Fig. 4.29 Bond Stress Distribution Diagrams (Push-Pull)

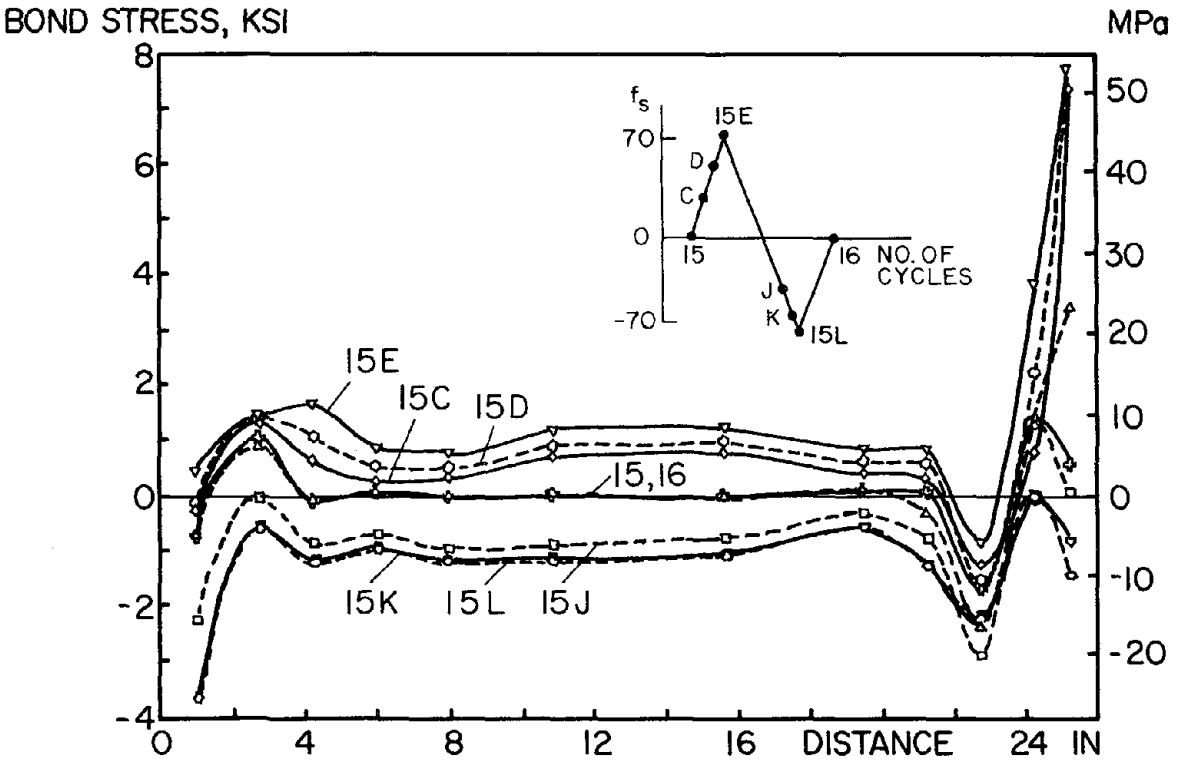

(f) First Post-Yield Range

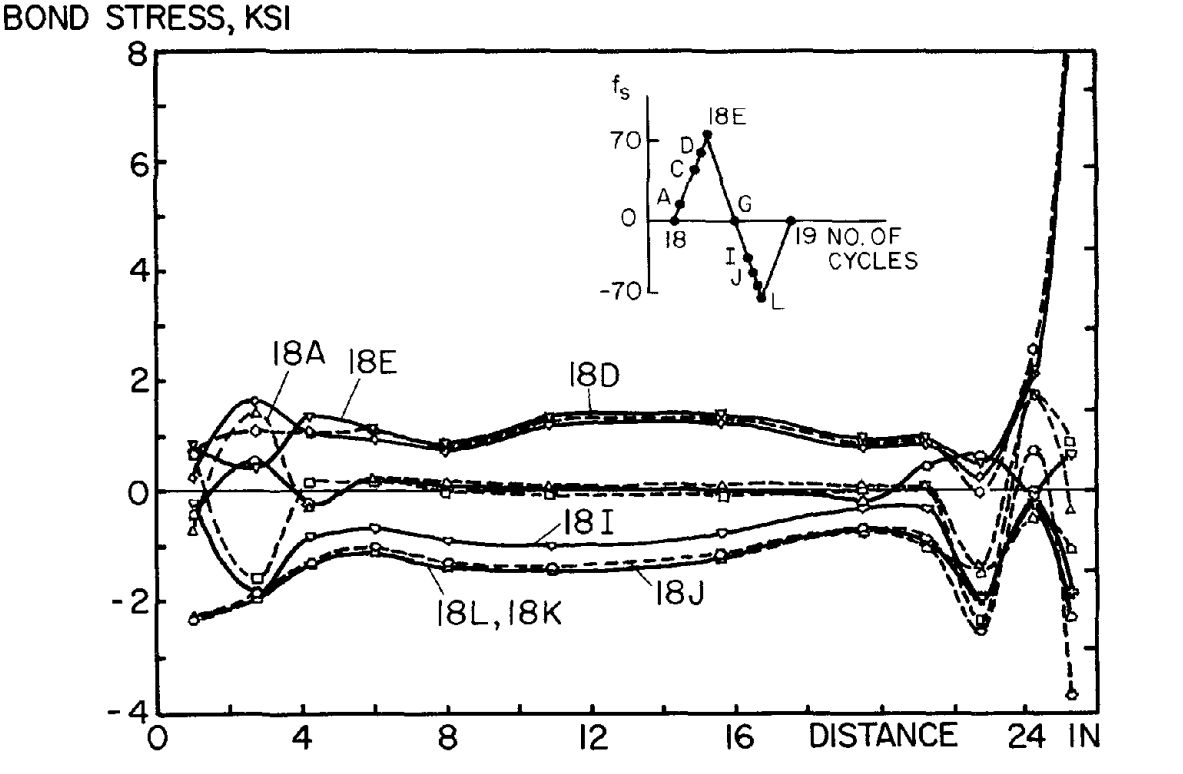

(g) Second Post-Yield Range

Fig. 4.29 Bond Stress Distribution Diagrams (Push-Pull)

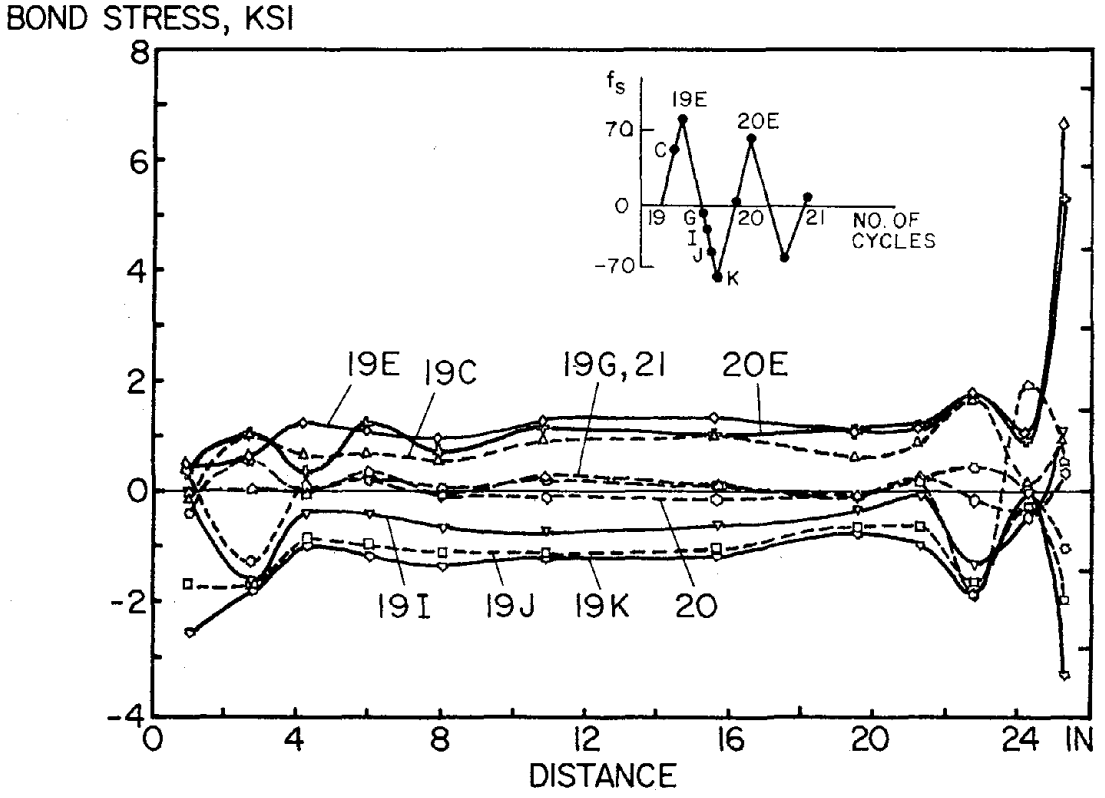

(h) Pull-Through Range

Fig. 4.29 Bond Stress Distribution Diagrams (Push-Pull)

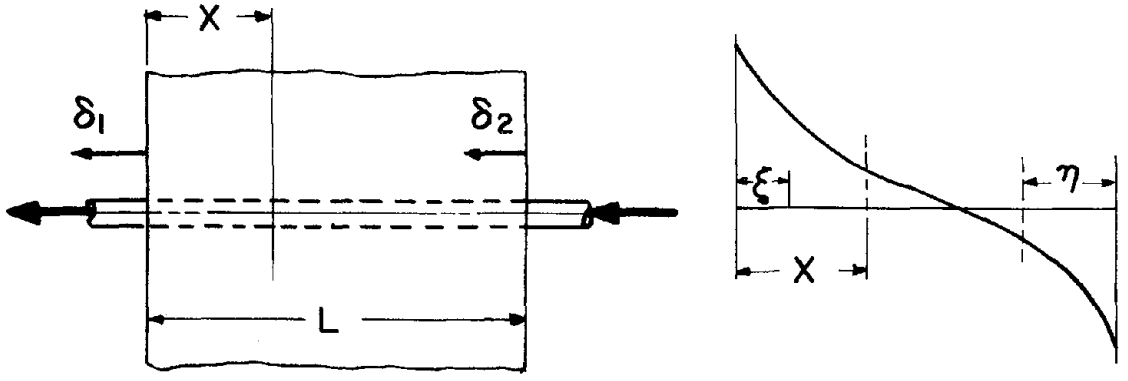

(a) Displacement at Exposed Ends

(b) Strain Distribution, $\varepsilon_s(\xi)$

Fig. 4.30 Data for Calculation of Local Displacement

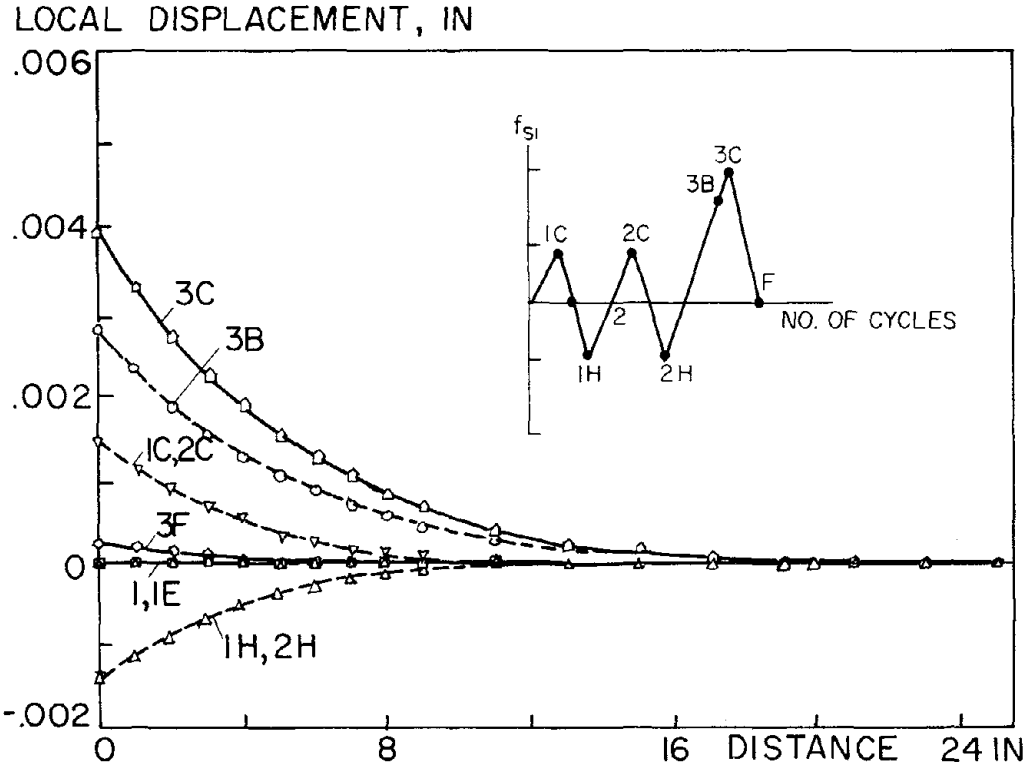

(a) Working Load Range

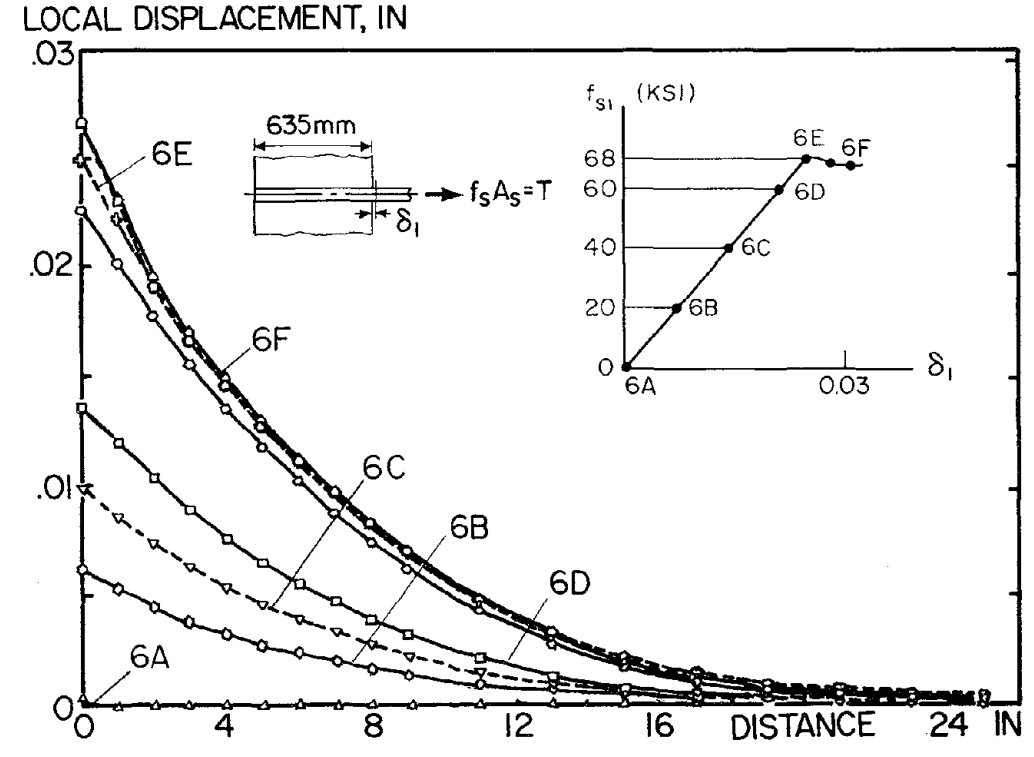

(b) Load Up to Yield

Fig. 4.31 Local Displacement Distribution Diagrams (Pull Only)

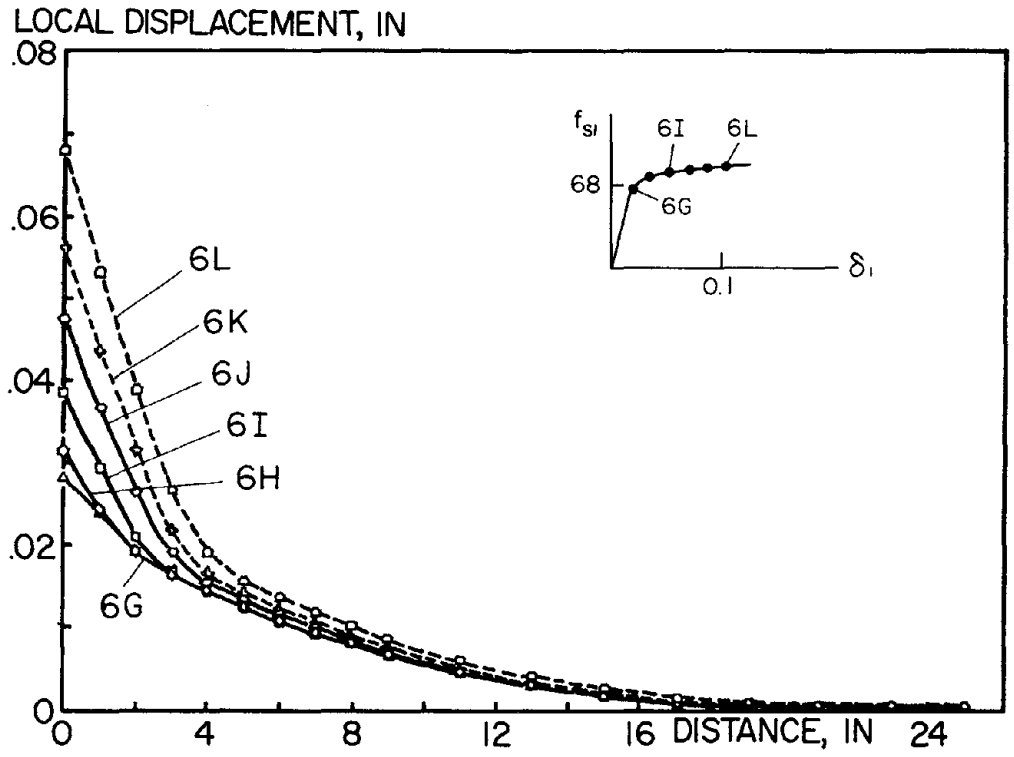

(c) First Post-Yield Range

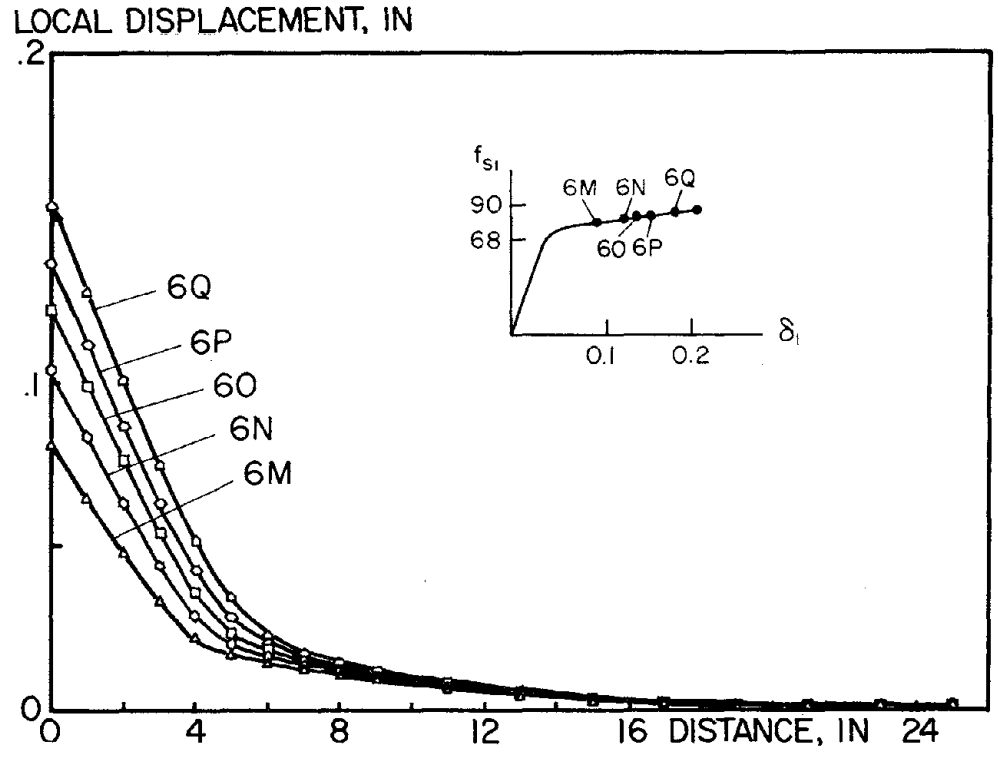

(d) Second Post-Yield Range

Fig. 4.31 Local Displacement Distribution Diagrams (Pull Only)

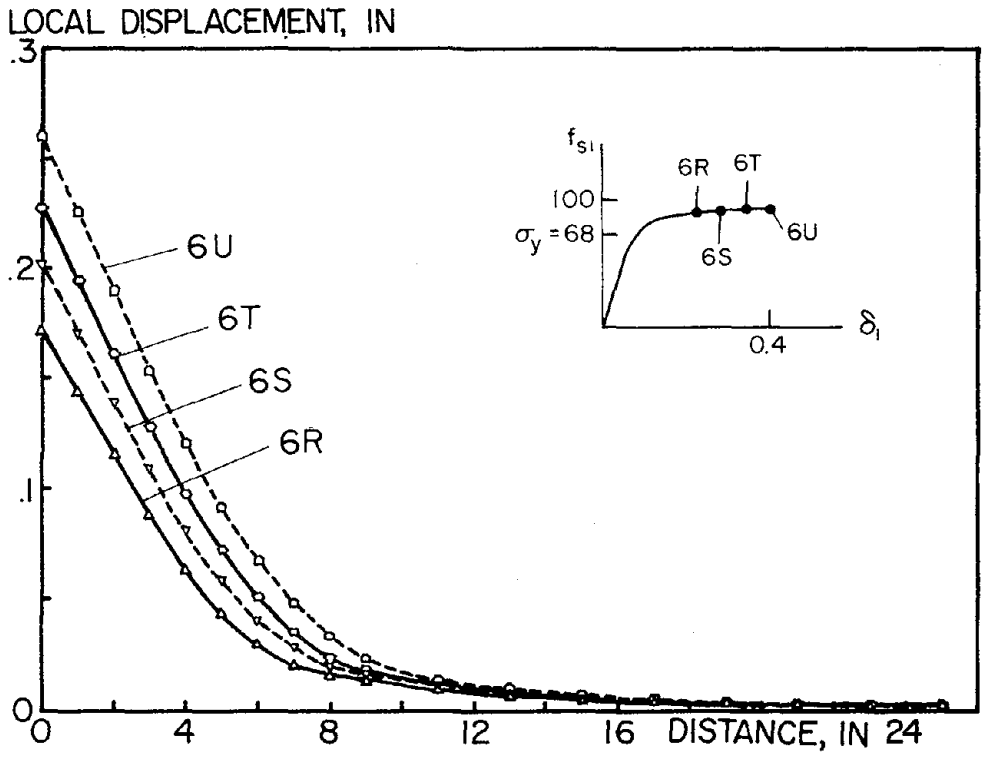

(e) Third Post-Yield Range

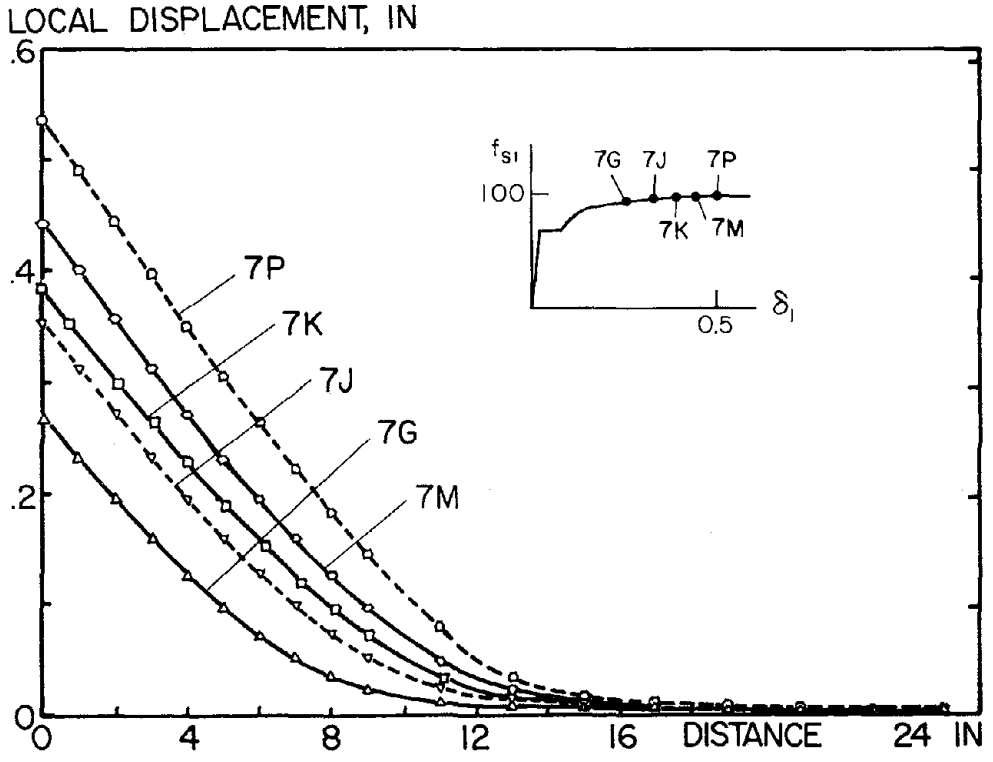

(f) Fourth Post-Yield Range

Fig. 4.31 Local Displacement Distribution Diagrams (Pull Only)

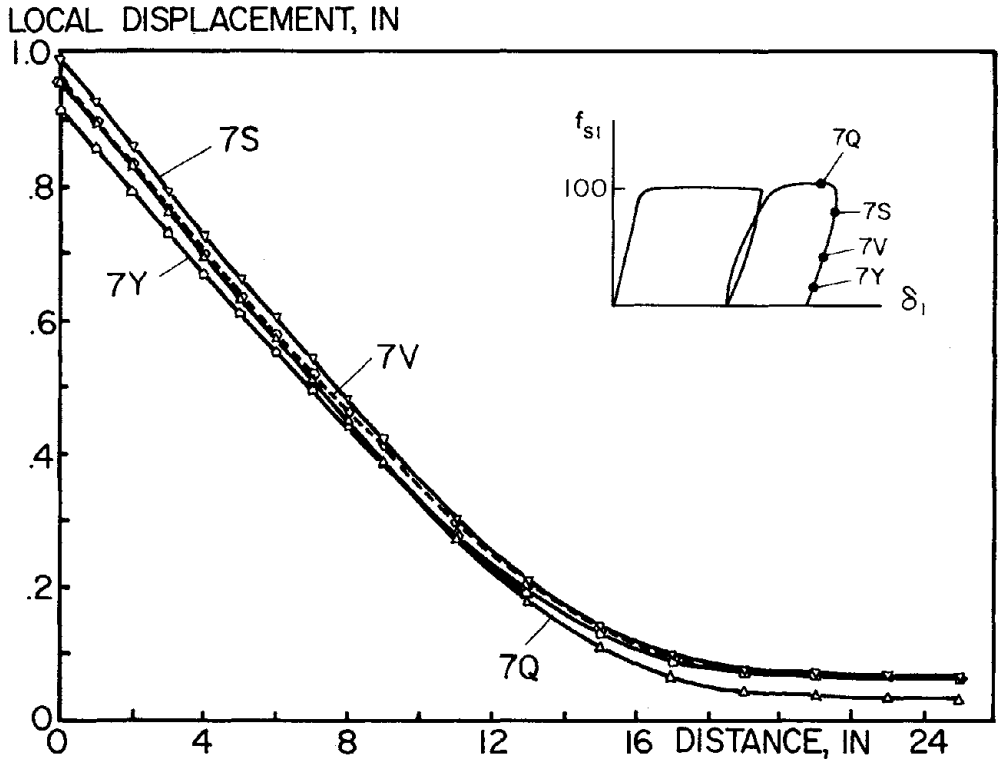

(g) Pull-Through Range

Fig. 4.31 Local Displacement Distribution Diagrams (Pull Only)

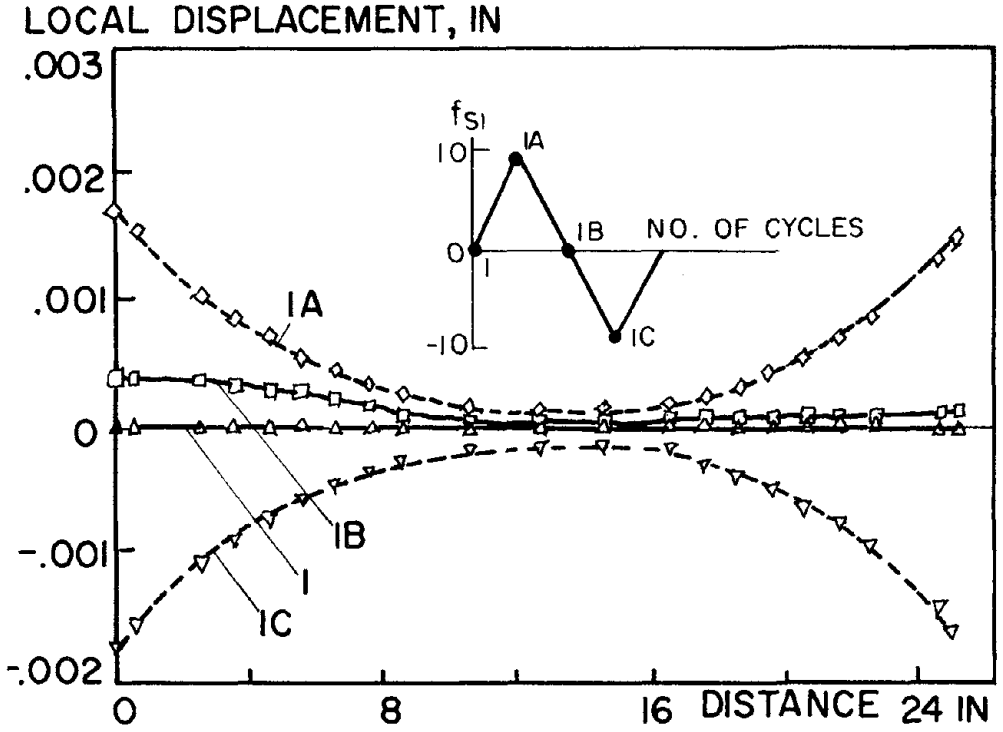

(a) 10 ksi Level (First Cycle)

Fig. 4.32 Local Displacement Distribution Diagrams (Push-Pull)

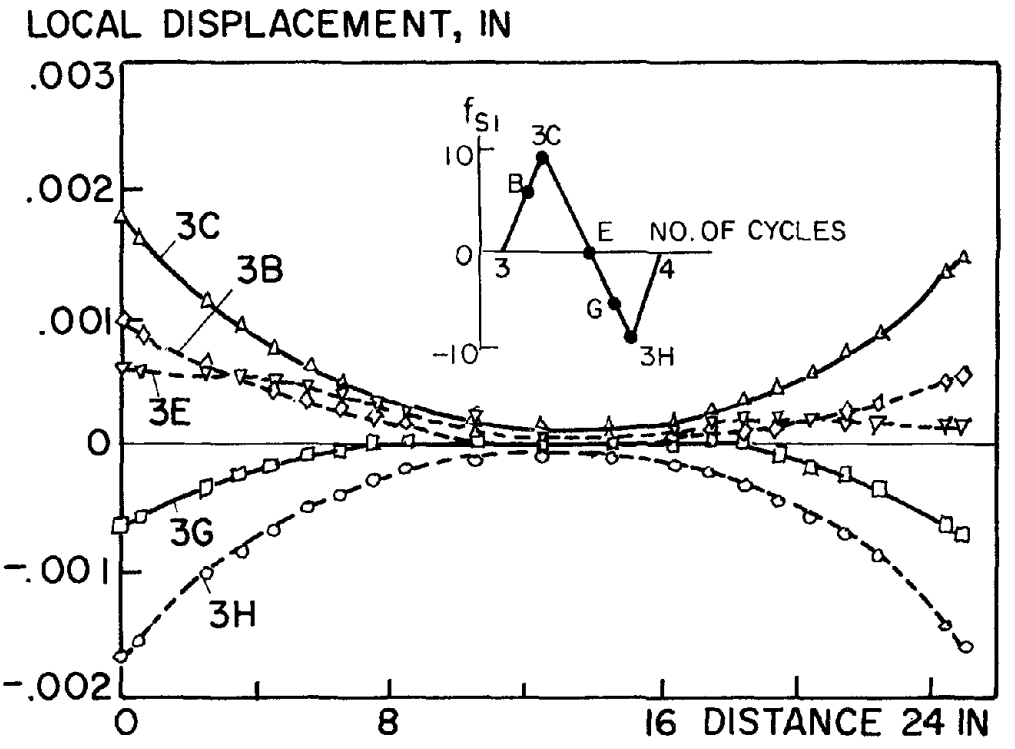

(b) 10 ksi Level (Repeating Cycle)

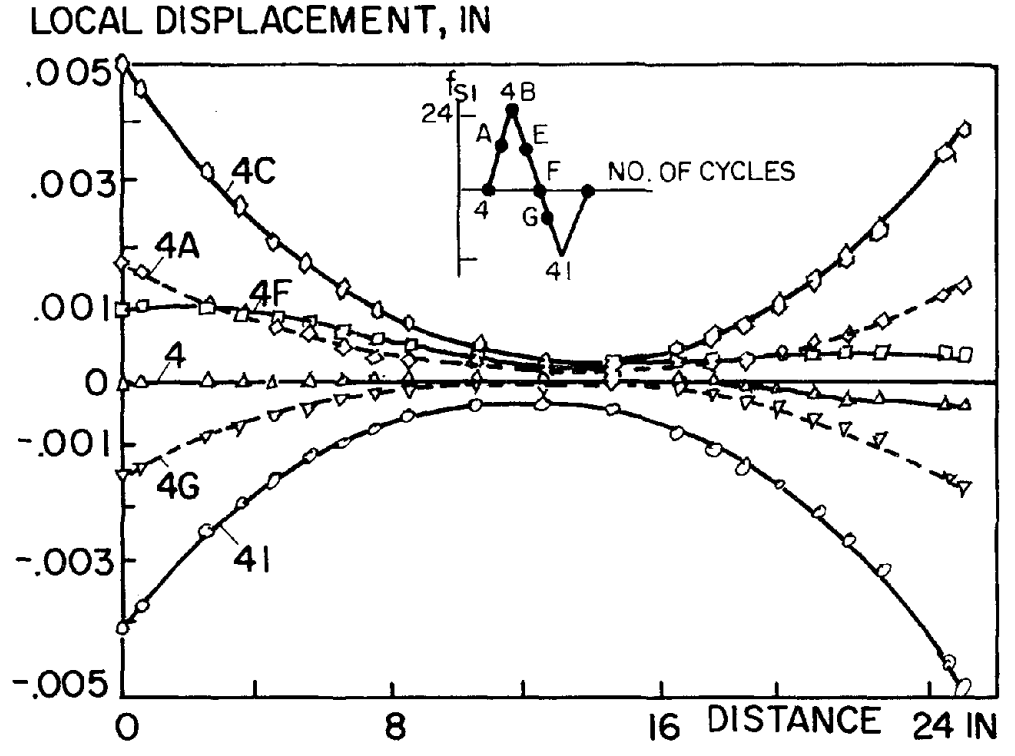

(c) Working Load Cycle (First Cycle)

Fig. 4.32 Local Displacement Distribution Diagrams (Push-Pull)

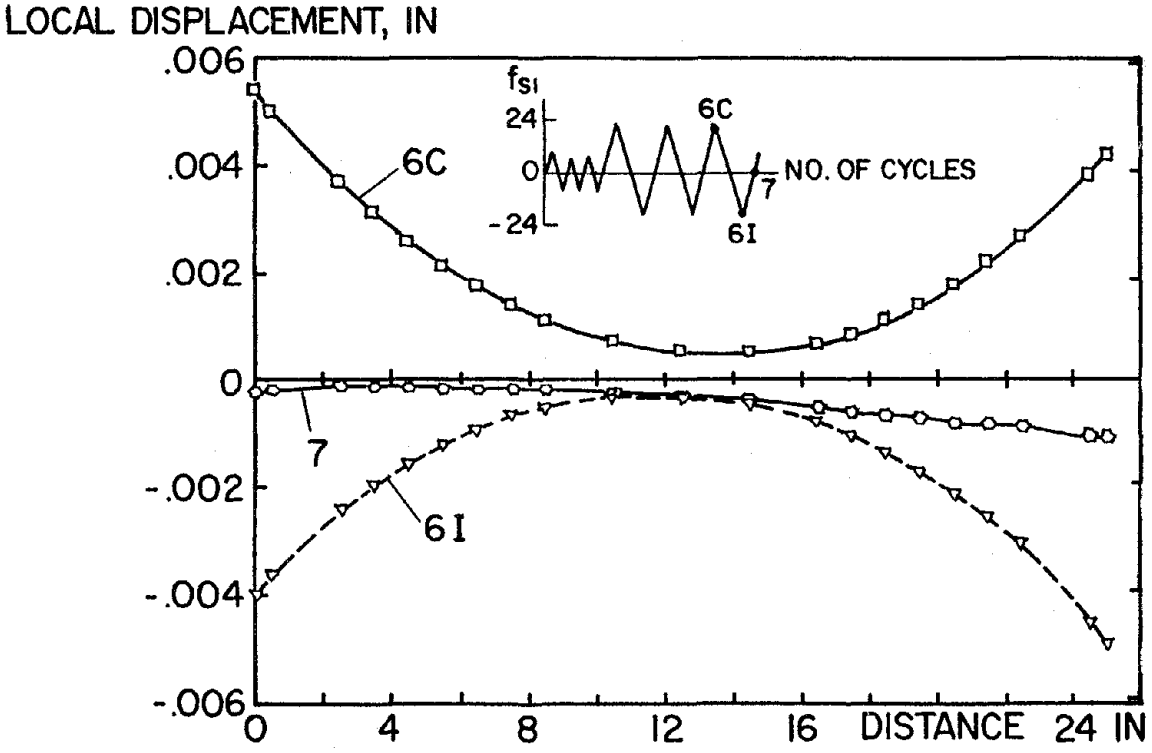

(d) Working Load Cycle (Repeating Cycle)

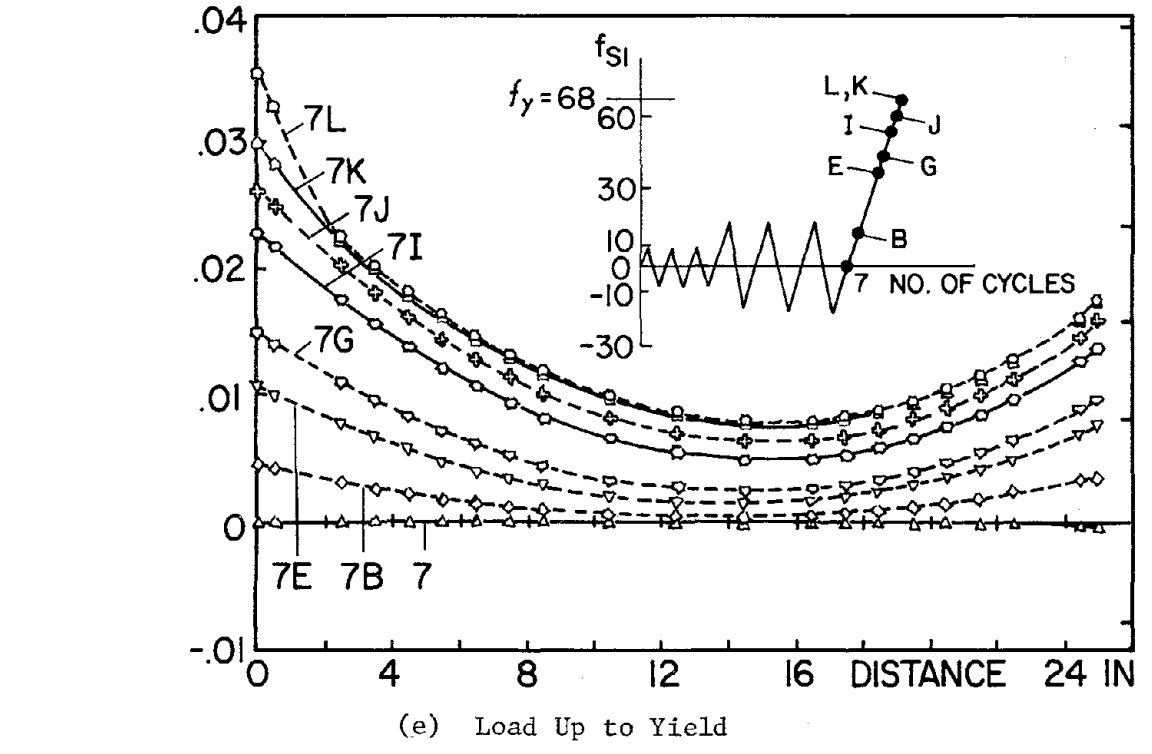

(e) Load Up to Yield

Fig. 4.32 Local Displacement Distribution Diagrams (Push-Pull)

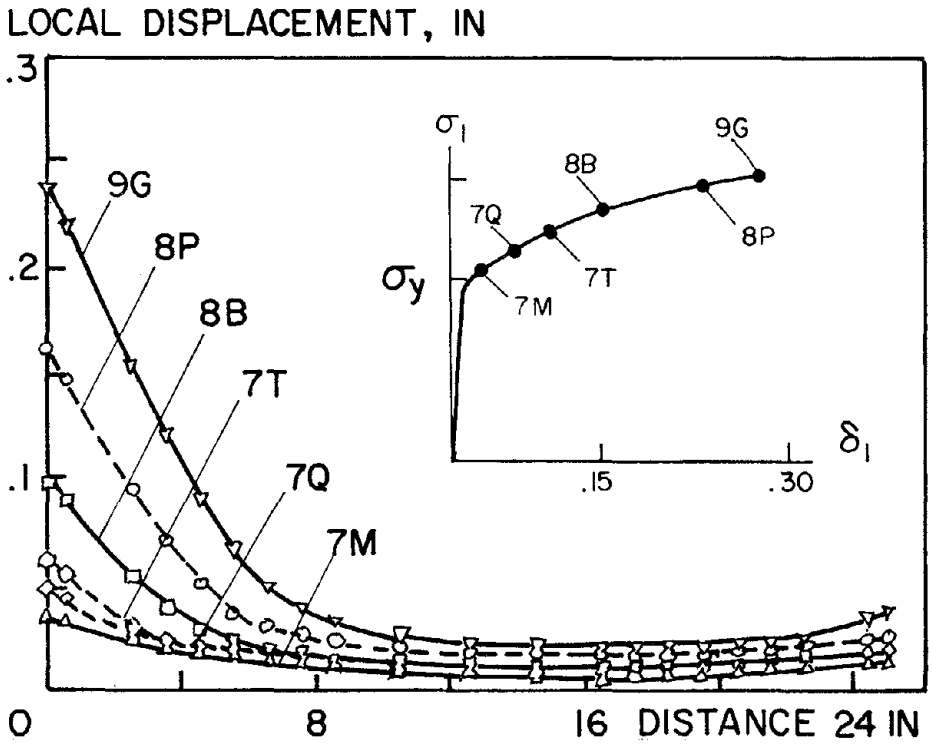

(f) Post-Yield Range

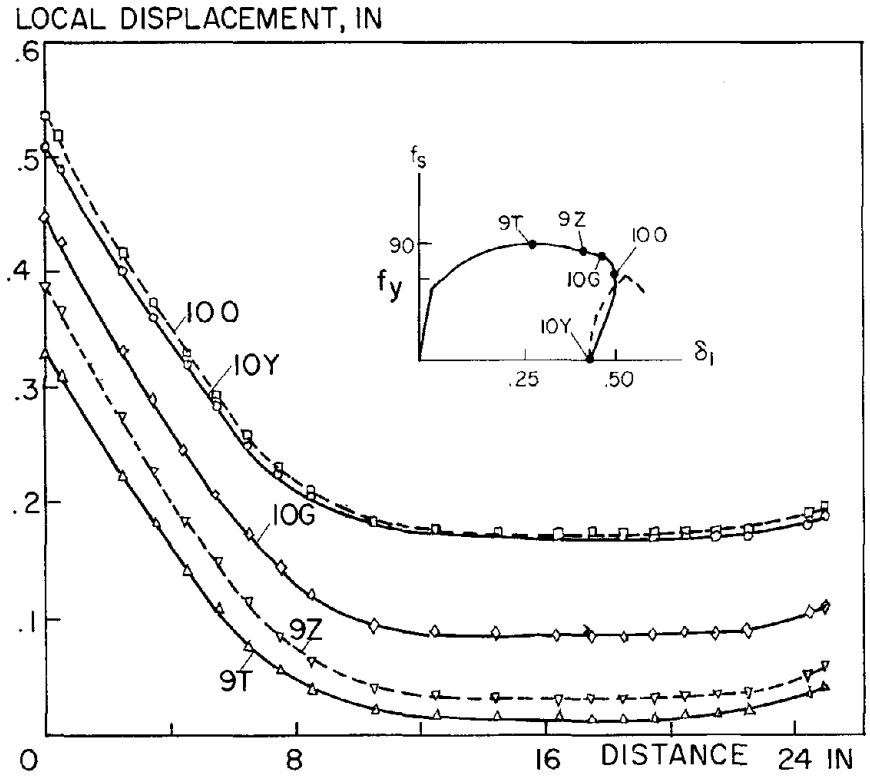

(g) Pull-Through Stage

Fig. 4.32 Local Displacement Distribution Diagrams (Push-Pull)

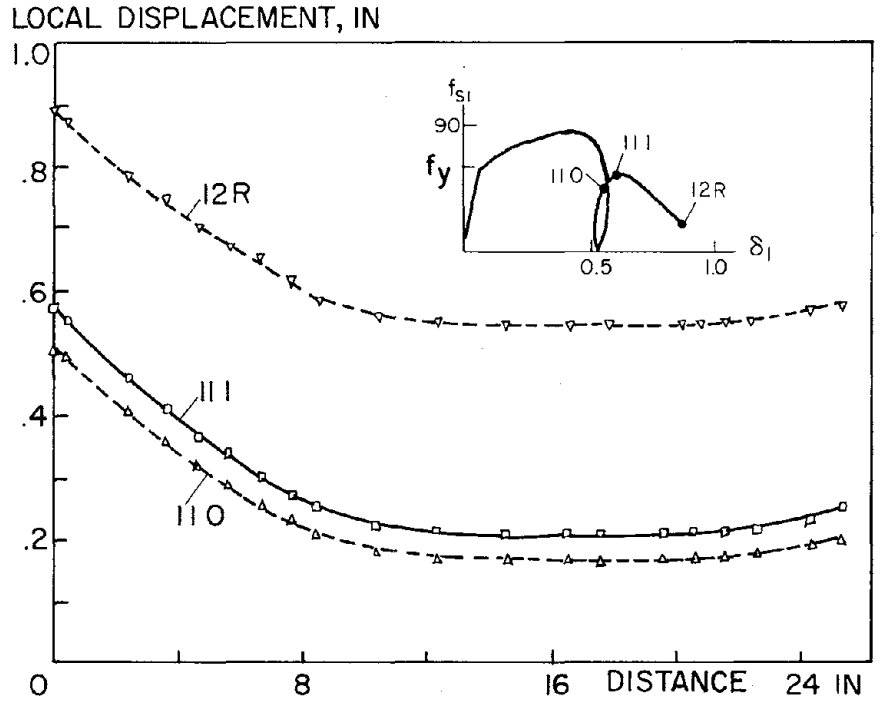

(h) Post-Pull-Through Range

Fig. 4.32 Local Displacement Distribution Diagrams (Push-Pull)

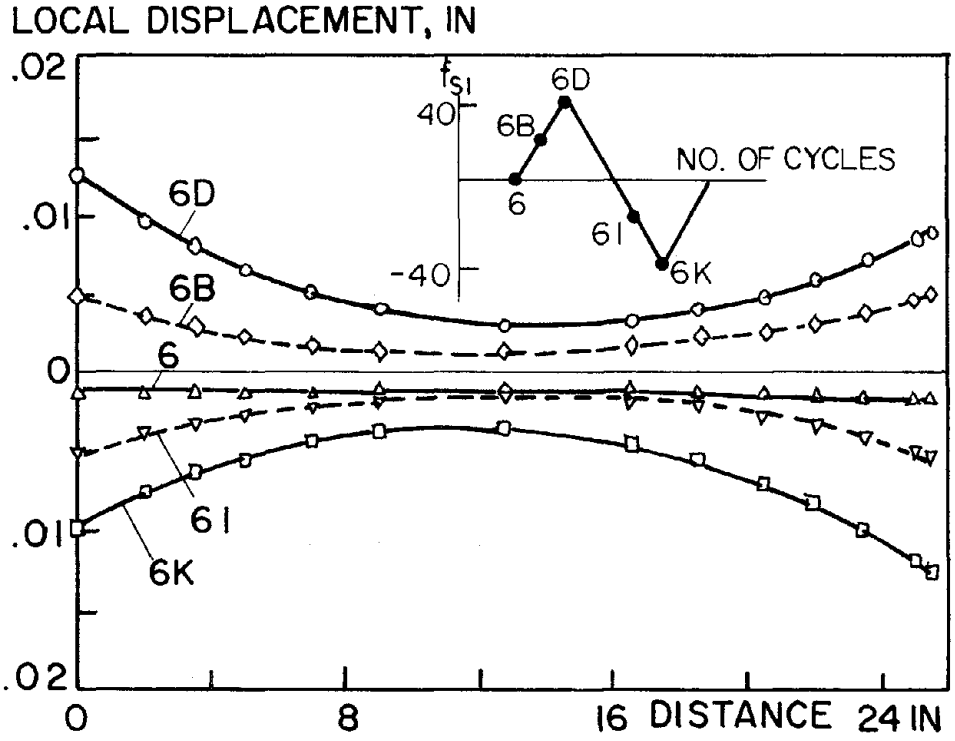

(a) 40 ksi Level (First Cycle)

Fig. 4.33 Local Displacement Distribution Diagrams (Cyclic Push-Pull Loading)

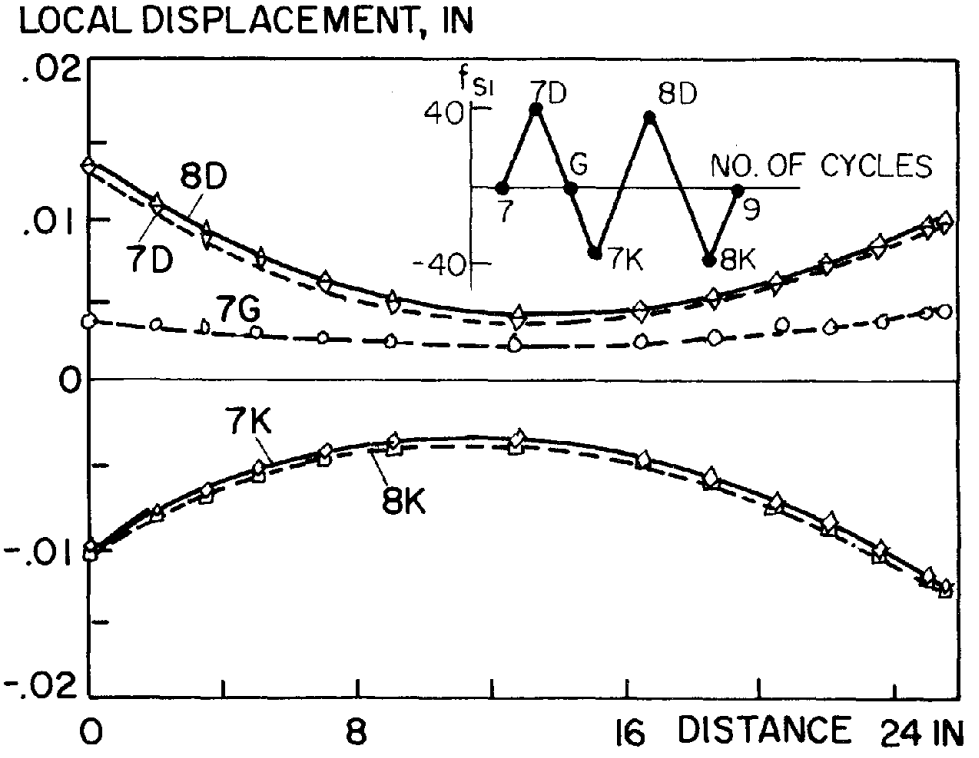

(b) 40 ksi Level (Repeating Cycle)

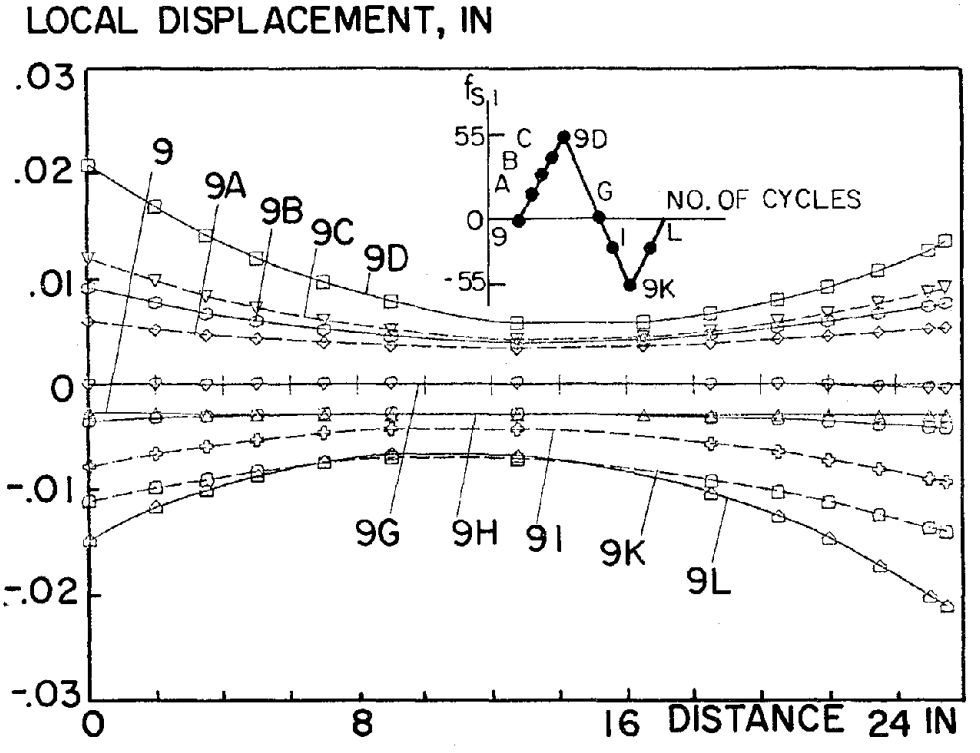

(c) 55 ksi Level (First Cycle)

Fig. 4.33 Local Displacement Distribution Diagrams (Cyclic Push-Pull Loading)

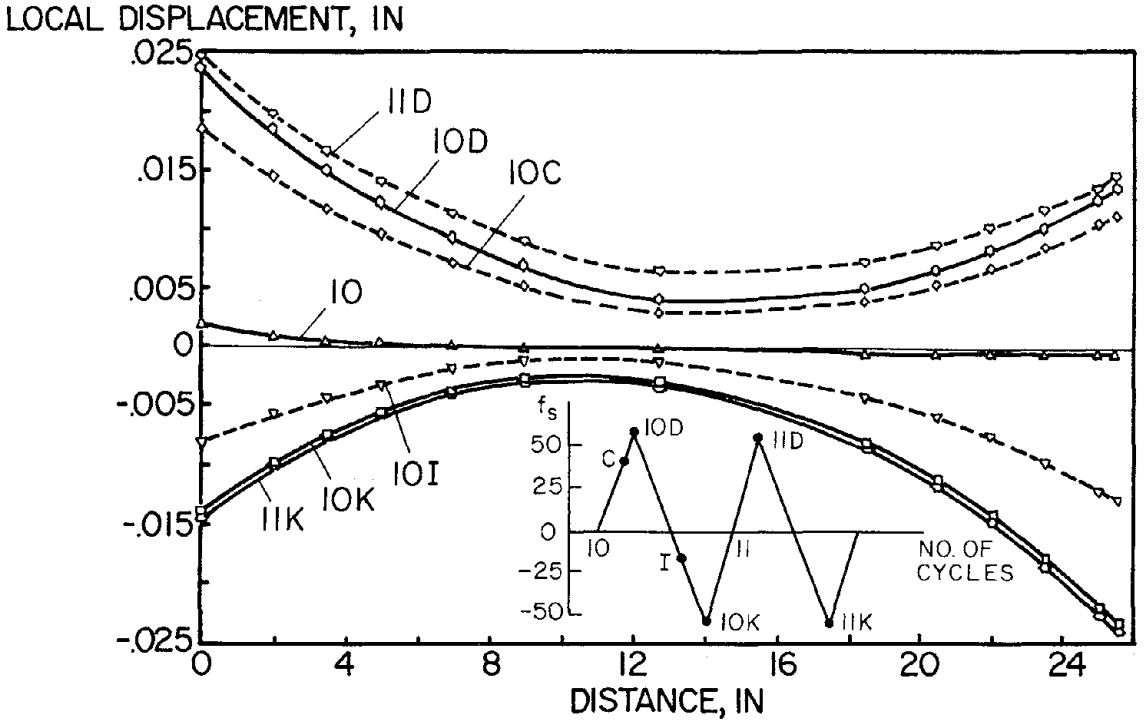

(d) 55 ksi Level (Repeating Cycle)

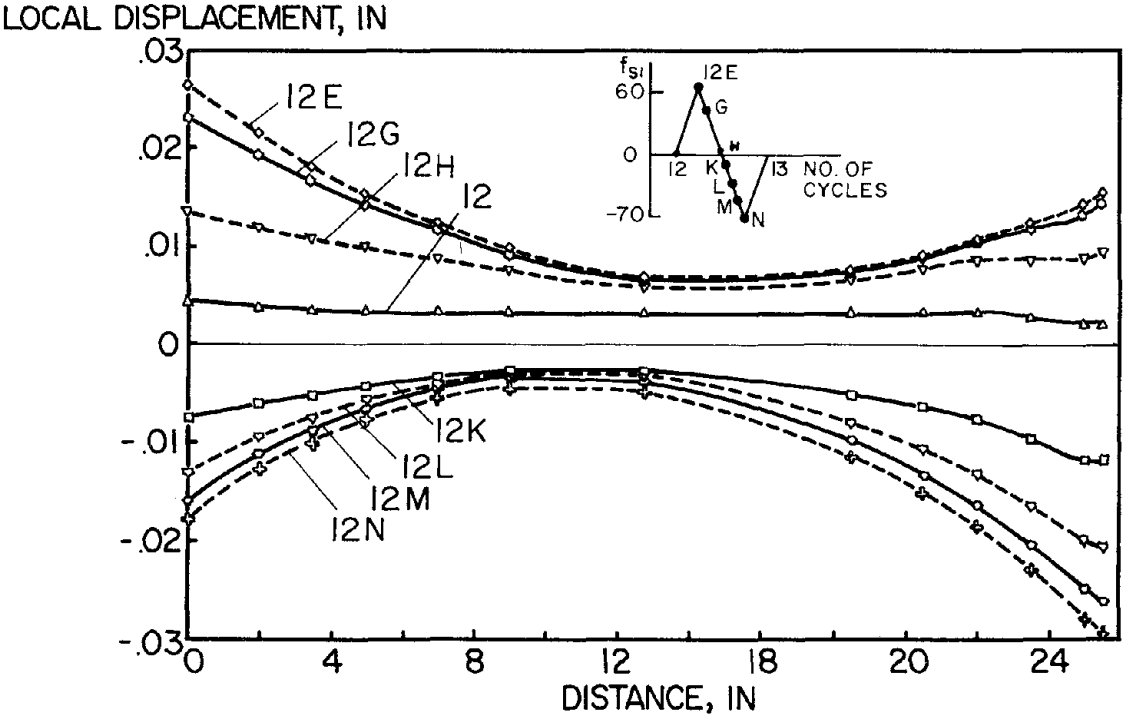

(e) Up to Yield

Fig. 4.33 Local Displacement Distribution Diagrams (Cyclic Push-Pull Loading)

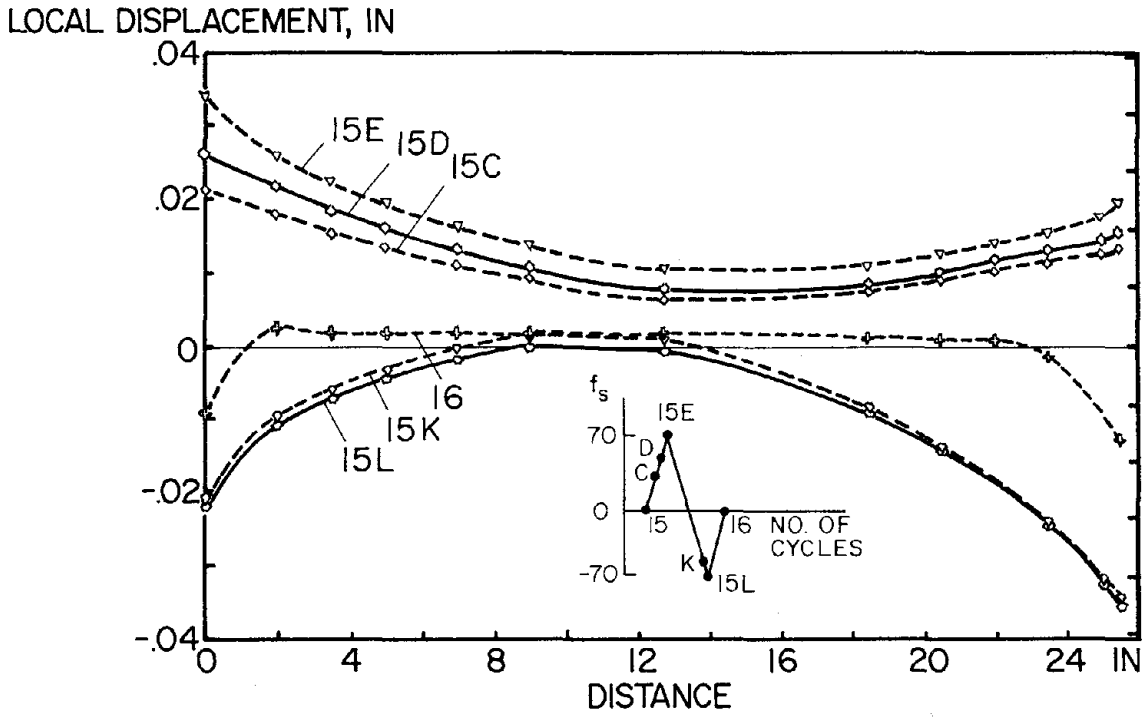

(f) First Post-Yield Range

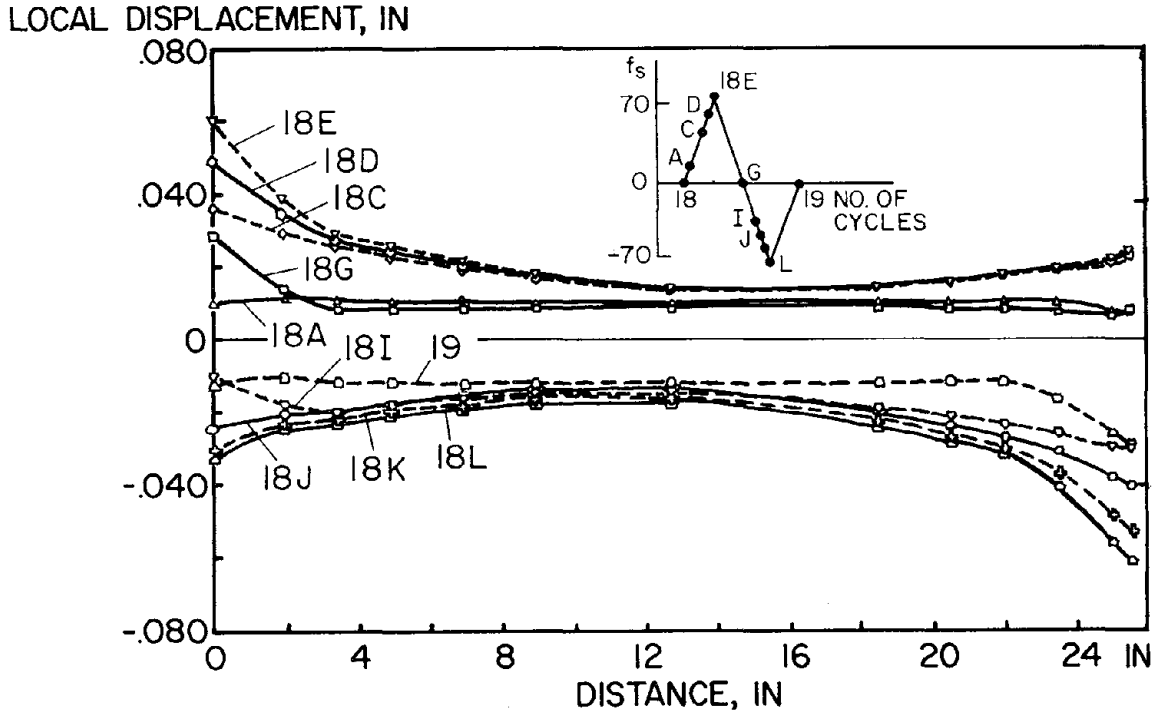

(g) Second Post-Yield Range

Fig. 4.33 Local Displacement Distribution Diagrams (Cyclic Push-Pull Loading)

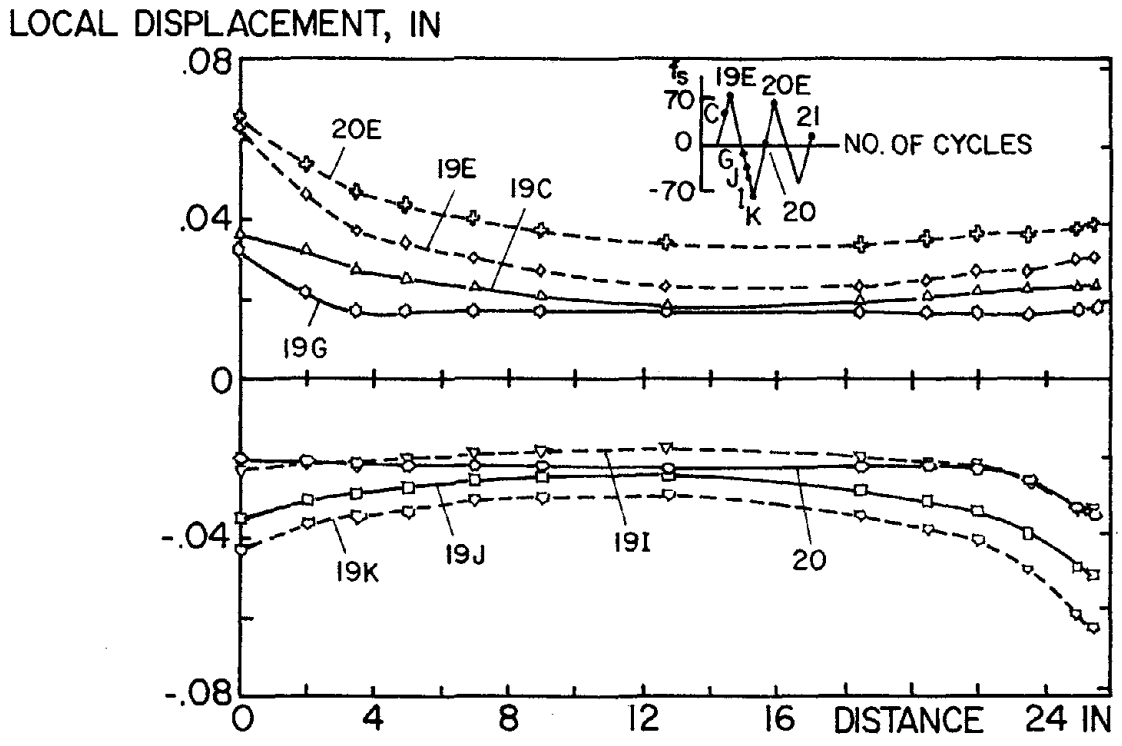

(h) Pull-Through Range

Fig. 4.33 Local Displacement Distribution Diagrams (Cyclic Push-Pull Loading)

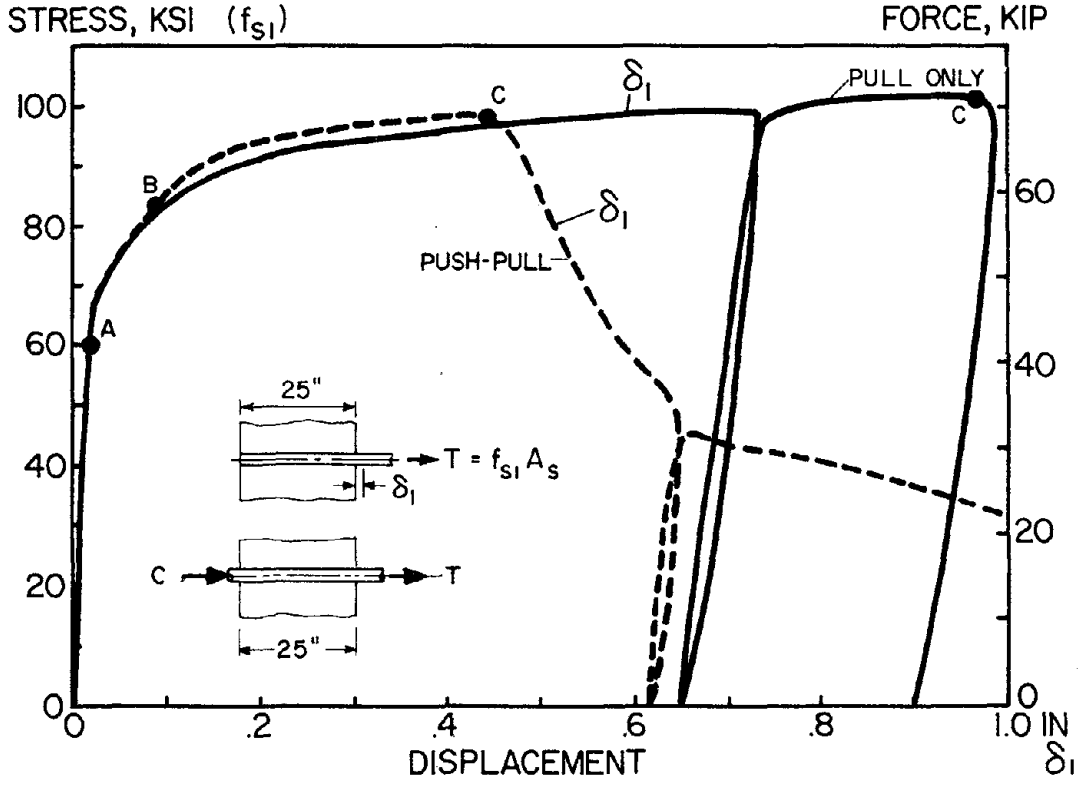

Fig. 5.1 $f_{sl} - \delta_l$ Curve for Pull Only vs. Curve for Push-Pull

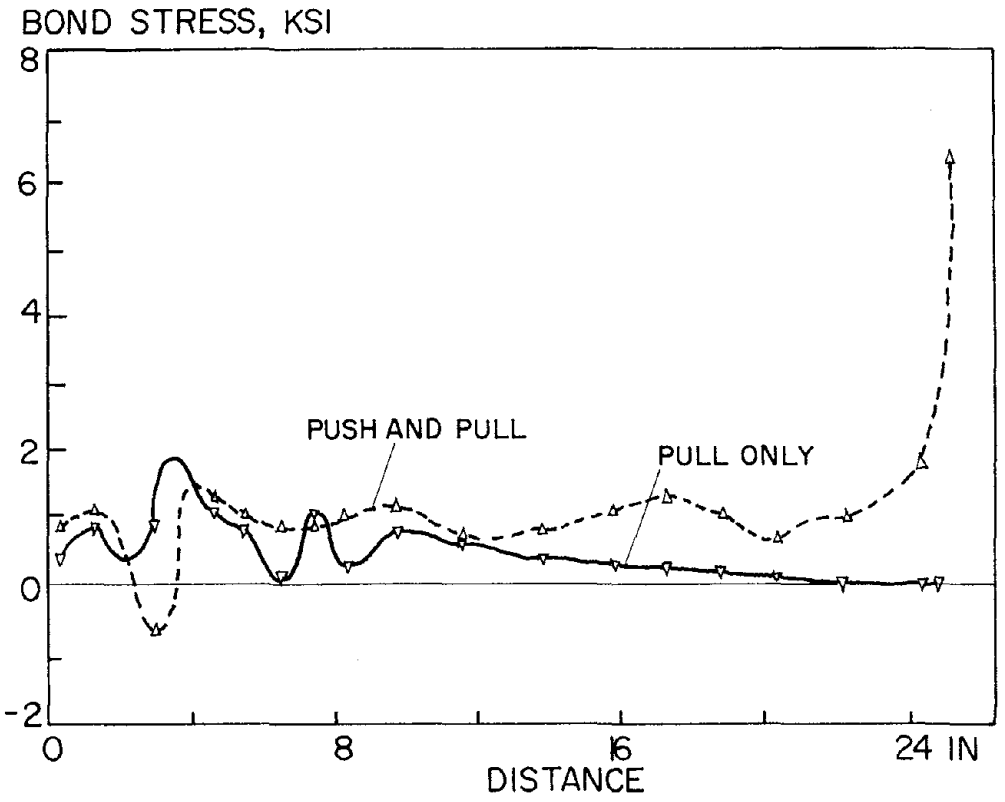

(a) Bond Stress Distribution at 60 ksi

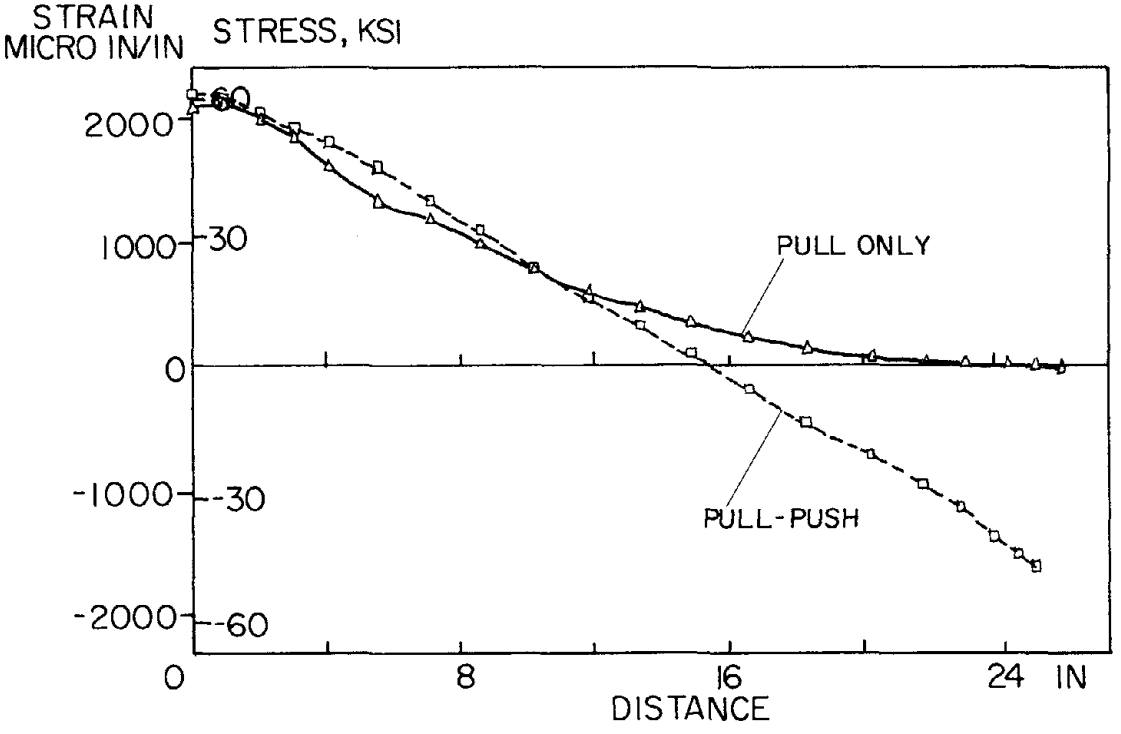

(b) Strain Distribution at 60 ksi

Fig. 5.2 Distribution Diagrams for Pull Only vs. Push-Pull

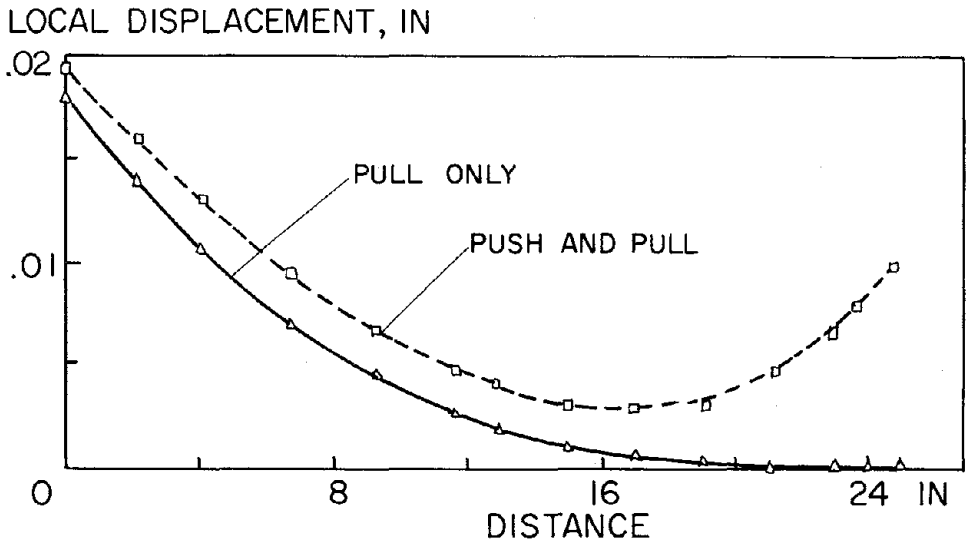

(c) Local Displacement Distribution at 60 ksi

Fig. 5.2 Distribution Diagrams for Pull Only vs. Push-Pull

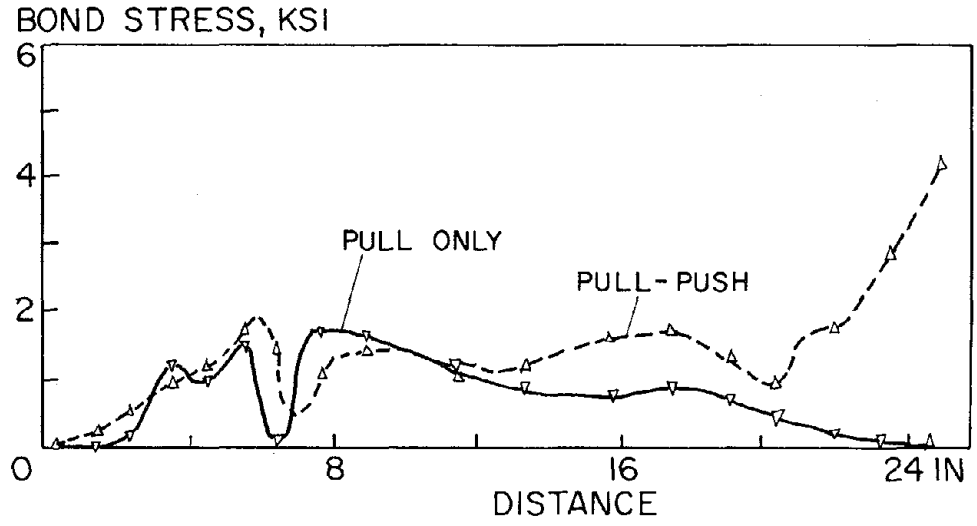

(a) Bond Stress Distribution

Fig. 5.3 Distribution Diagrams for Pull Only vs. Push-Pull at 85 ksi

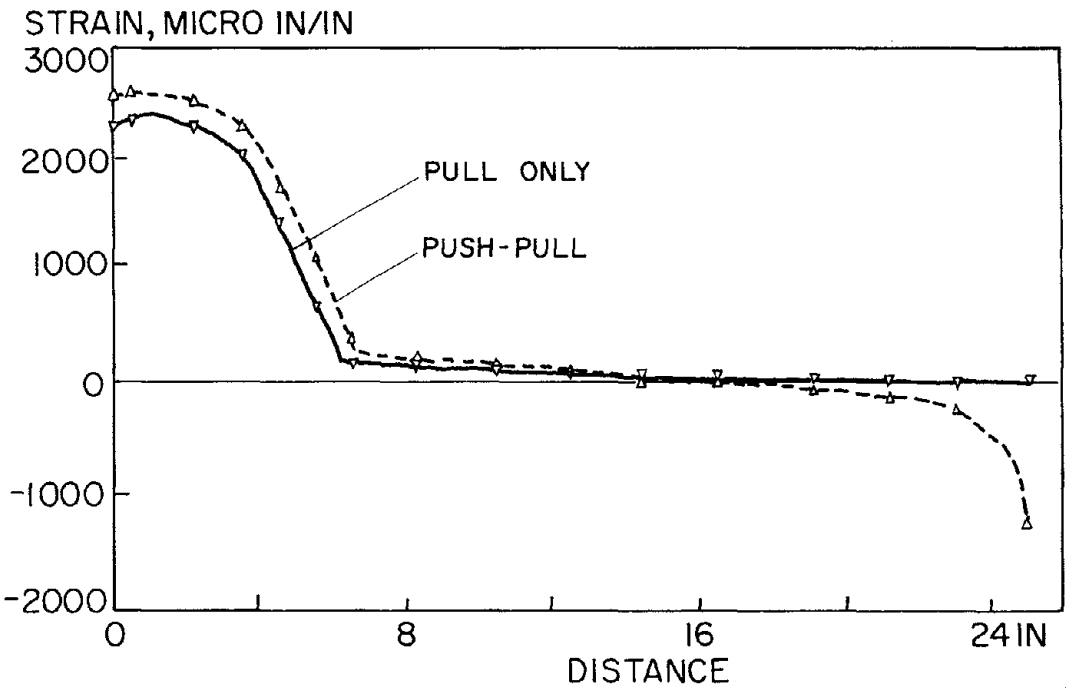

(b) Strain Distribution

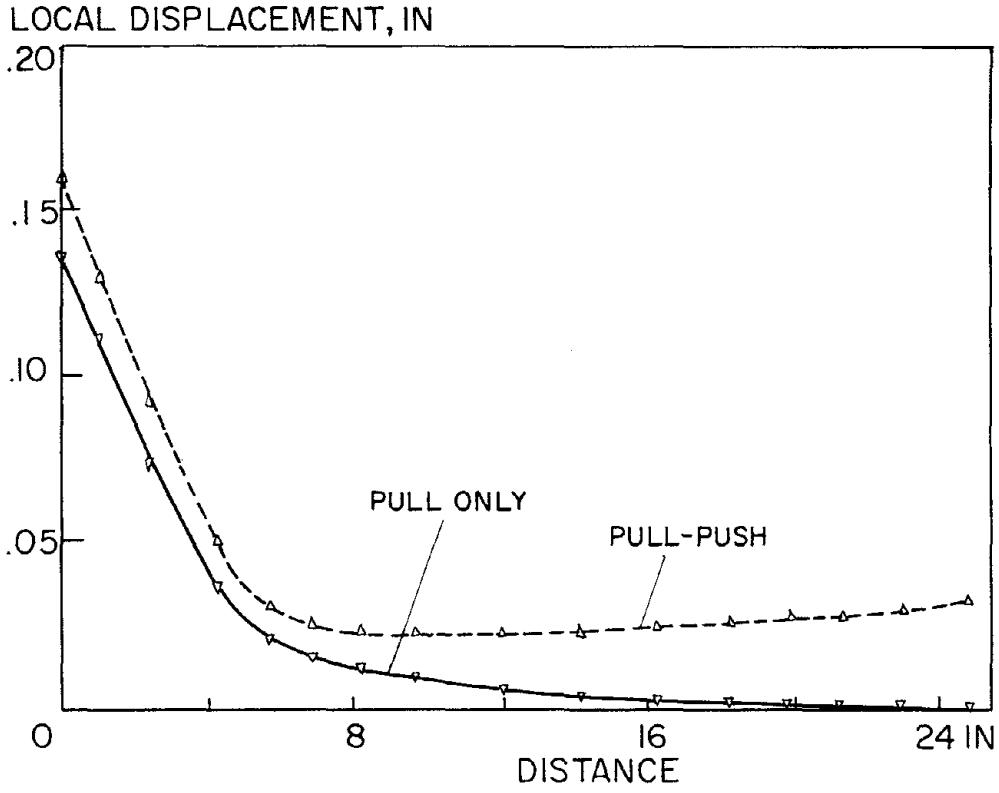

(c) Local Displacement Distribution

Fig. 5.3 Distribution Diagrams for Pull Only vs. Push-Pull at 85 ksi

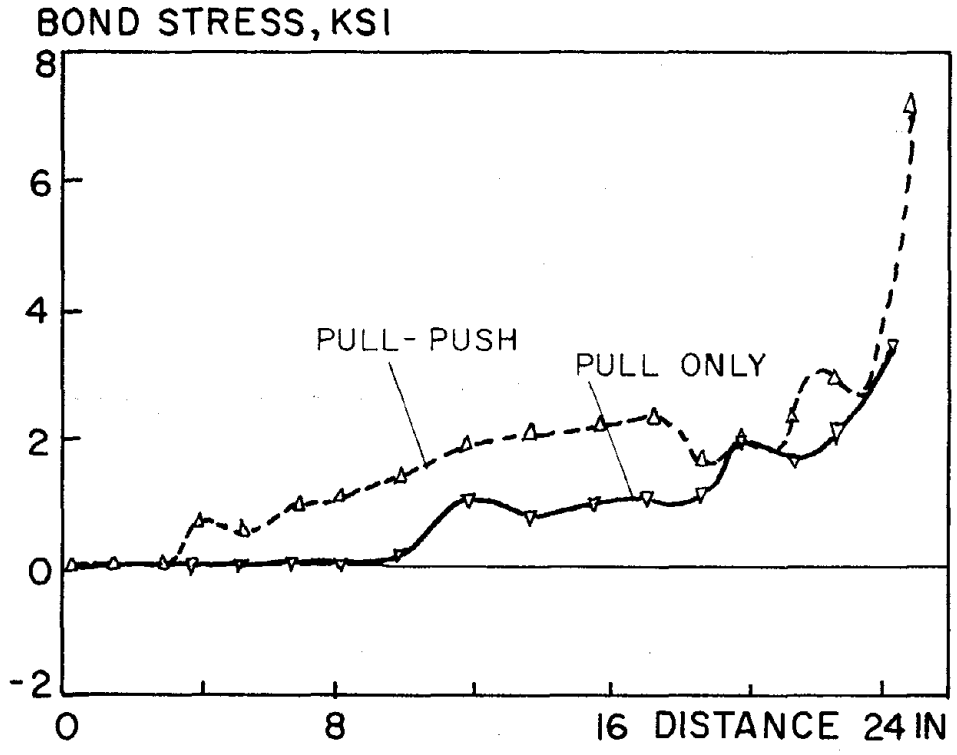

(a) Bond Stress Distribution

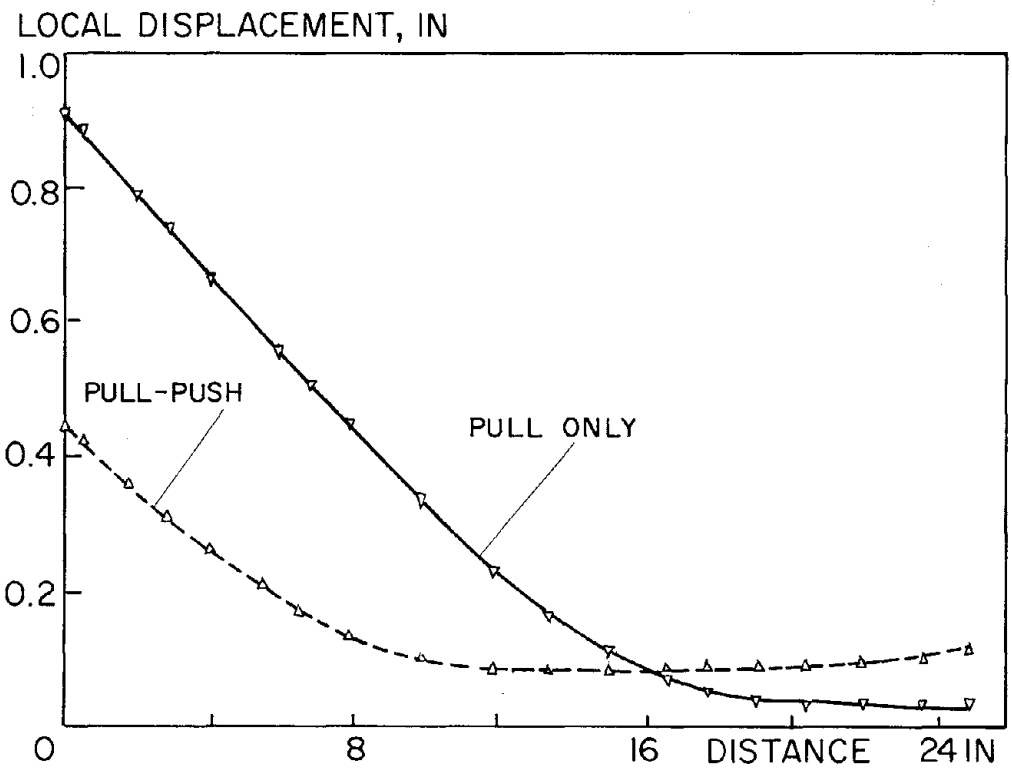

(b) Local Displacement Distribution at Verge of Pull-Through

Fig. 5.4 Distribution Diagrams for Pull Only vs. Push-Pull (At Verge of Pull-Through)

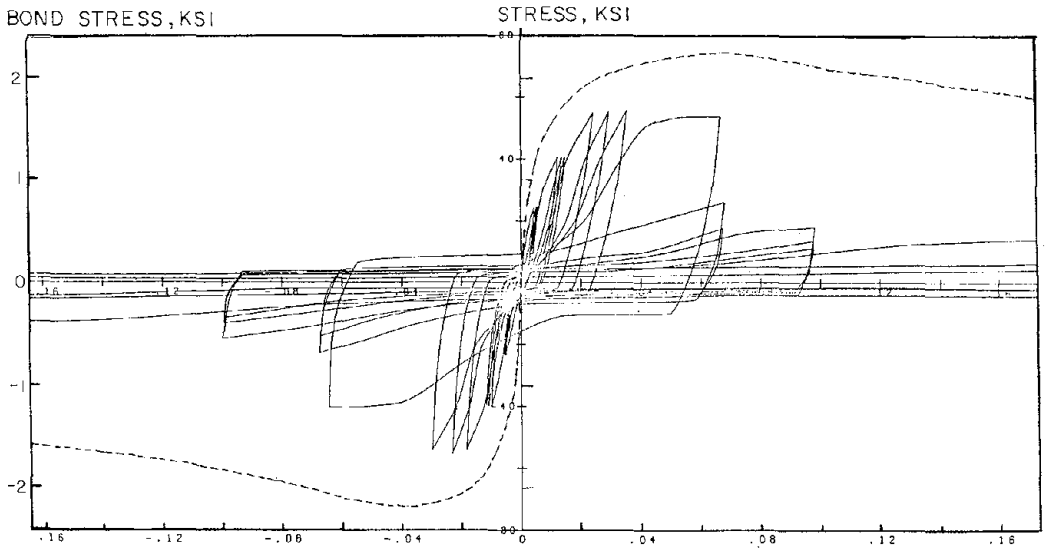

(a) #6 Bar in 15 in. Block

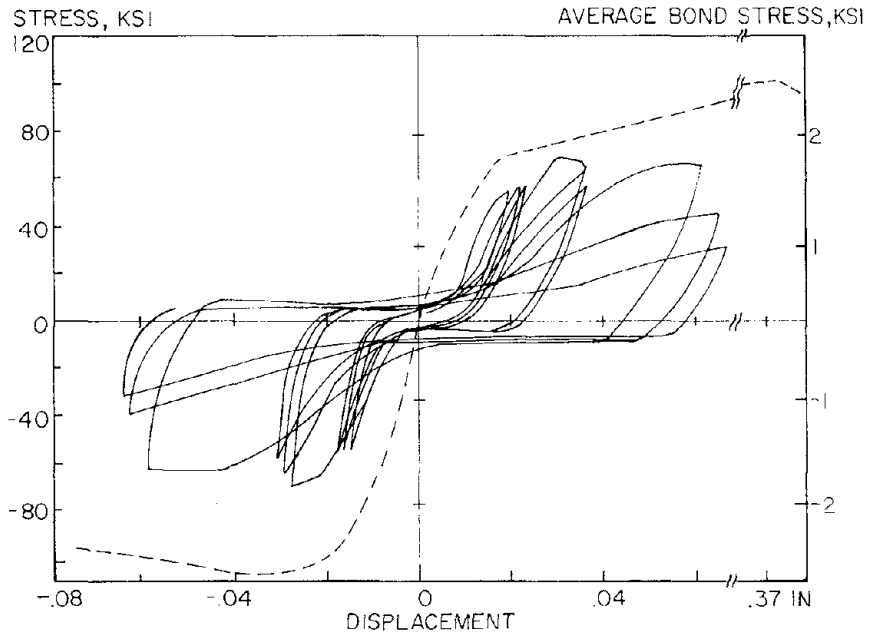

(b) #6 Bar in 20 in. Block

Fig. 5.5 Comparison of Monotonic vs. Cyclic Loading Response

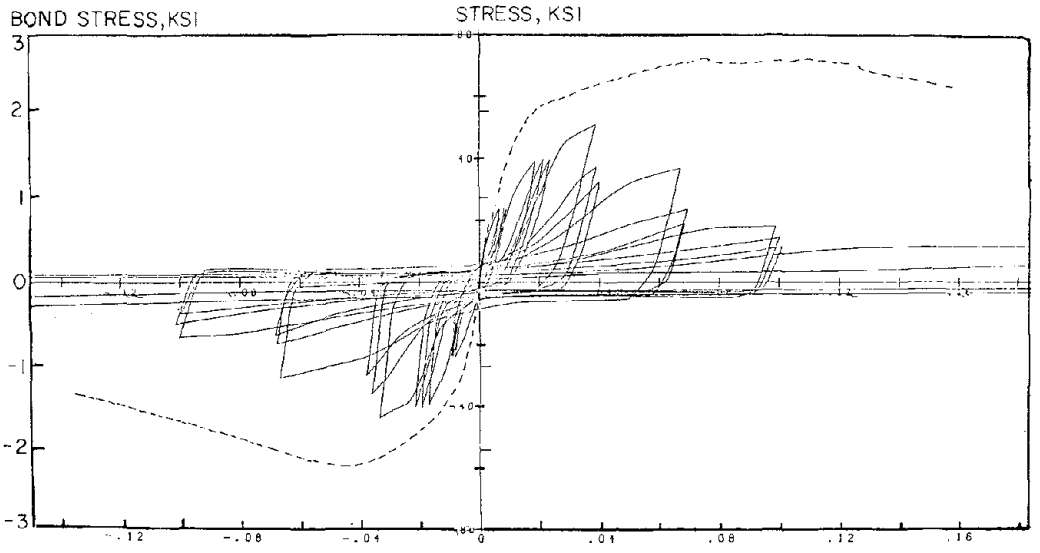

(c) #8 Bar in 15 in. Block

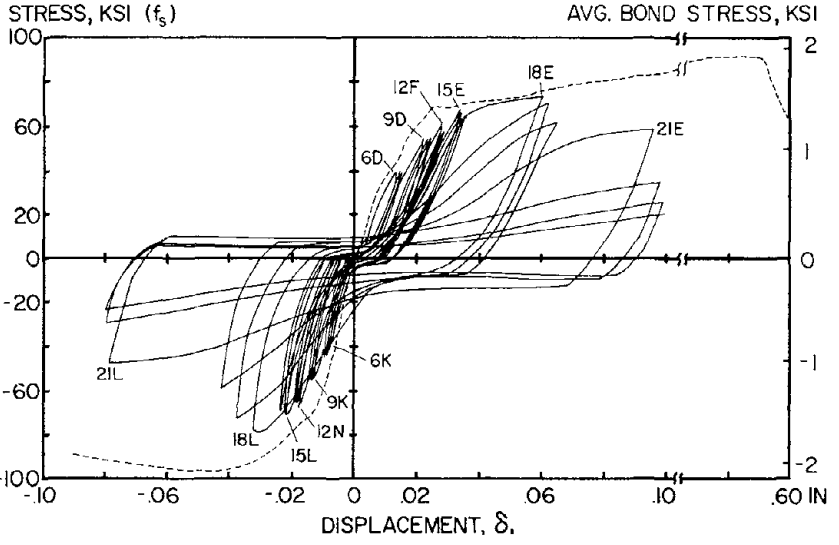

(d) #8 Bar in 25 in. Block

Fig. 5.5 Comparison of Monotonic vs. Cyclic Loading Response

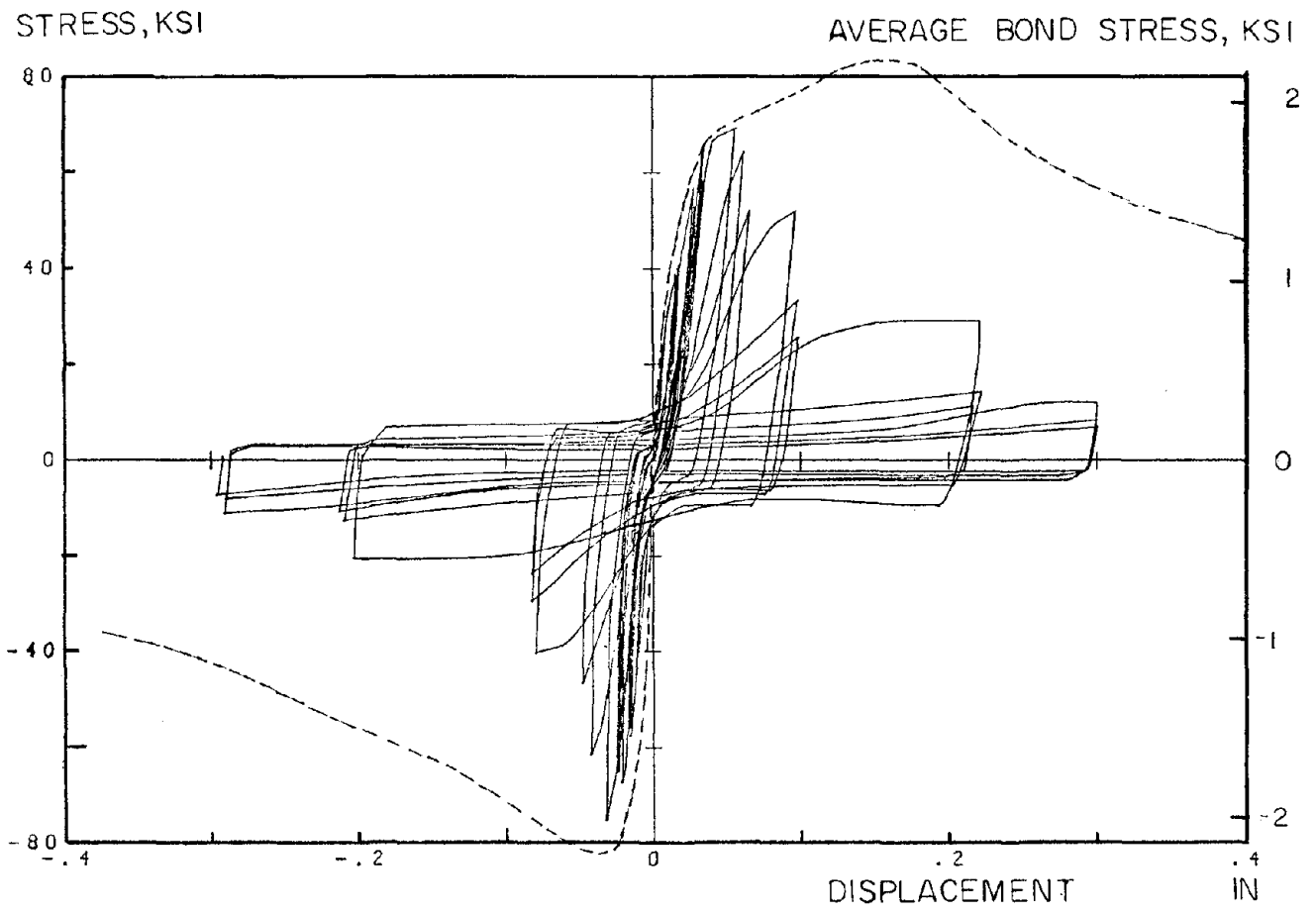

(e) #10 Bar in 25 in. Block

Fig. 5.5 Comparison of Monotonic vs. Cyclic Loading Response

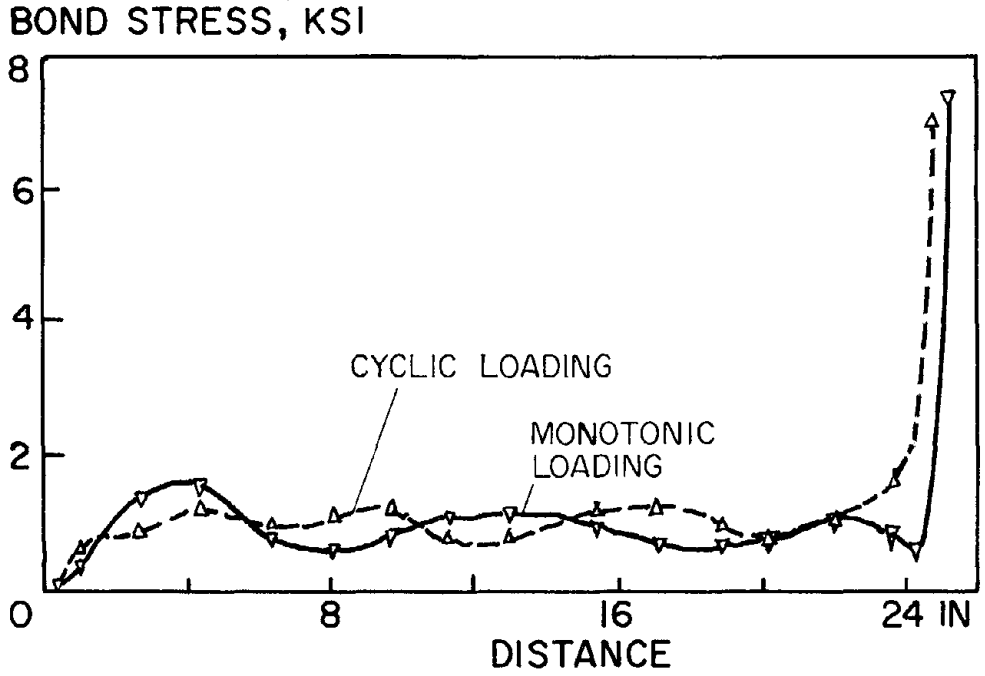

(a) Bond Stress Distribution

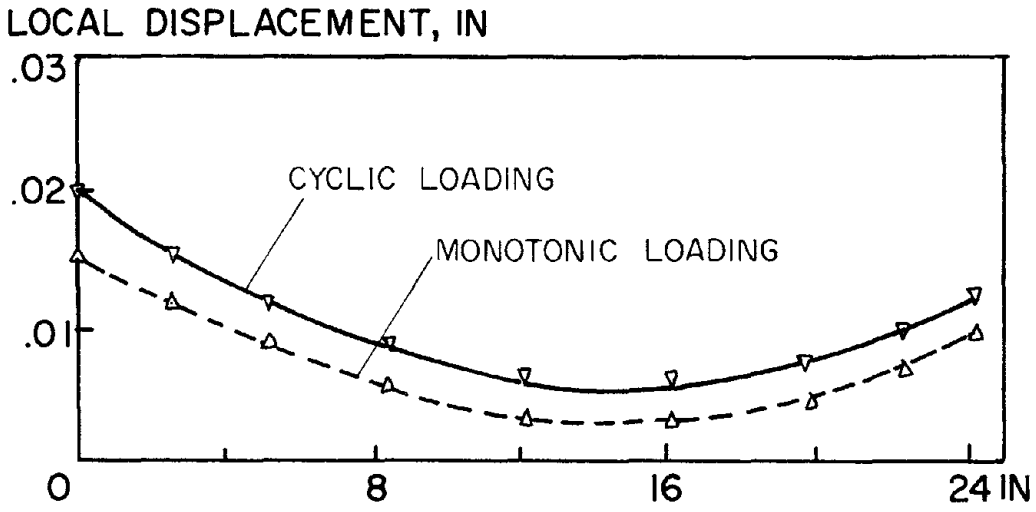

(b) Local Displacement Distribution

Fig. 5.6 Distribution Diagrams of Cyclic vs. Monotonic Loading (at 55 ksi)

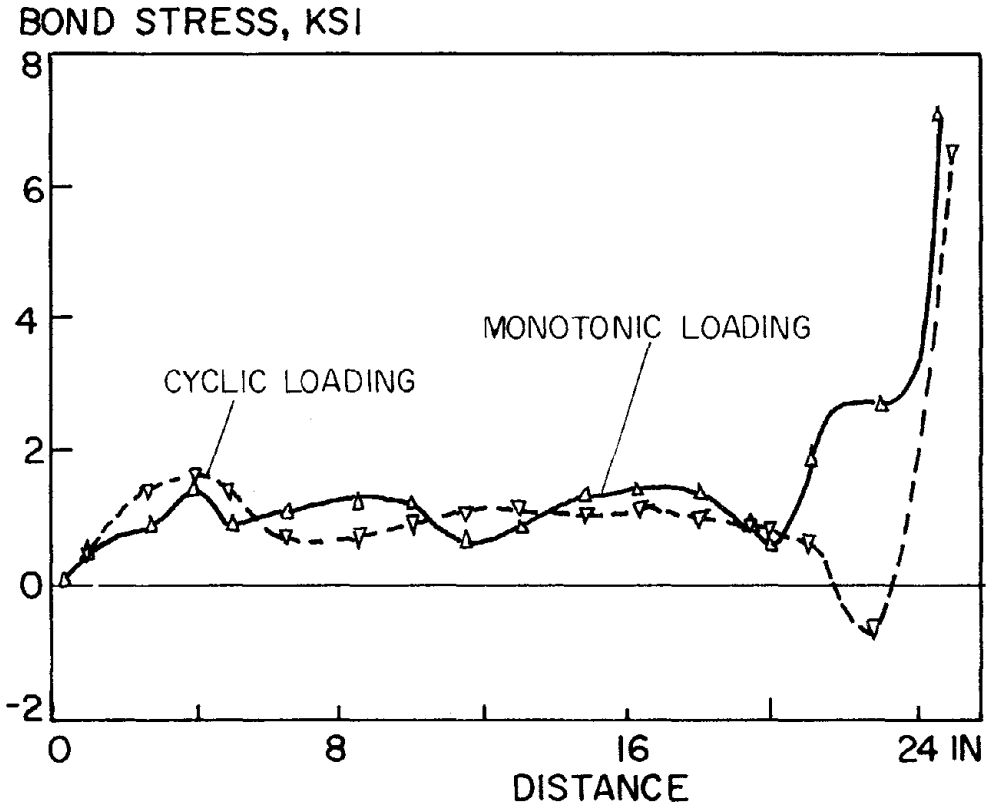

(a) Bond Stress Distribution (#8 Bar)

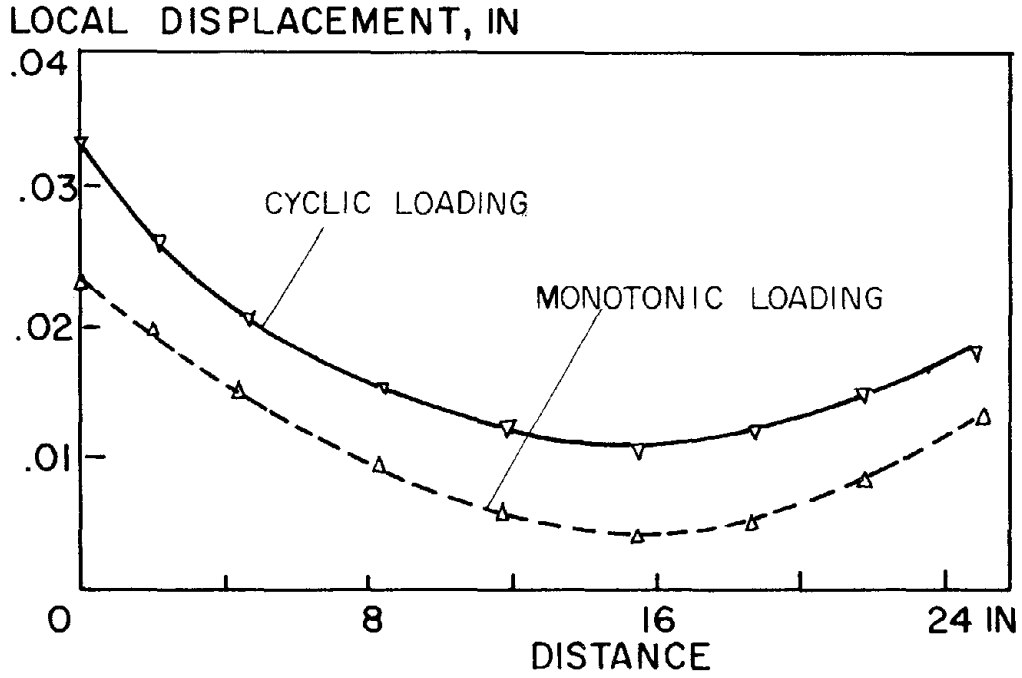

(b) Local Displacement Distribution (#8 Bar)

Fig. 5.7 Distribution Diagrams of Cyclic vs. Monotonic Loading (At Yield)

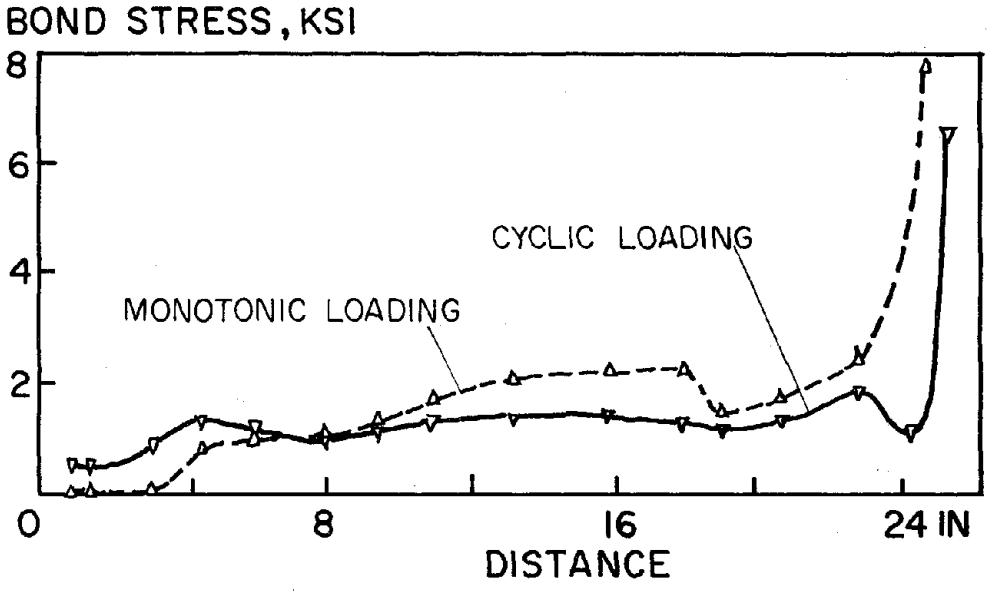

(a) Bond Stress Distribution (#8 Bar)

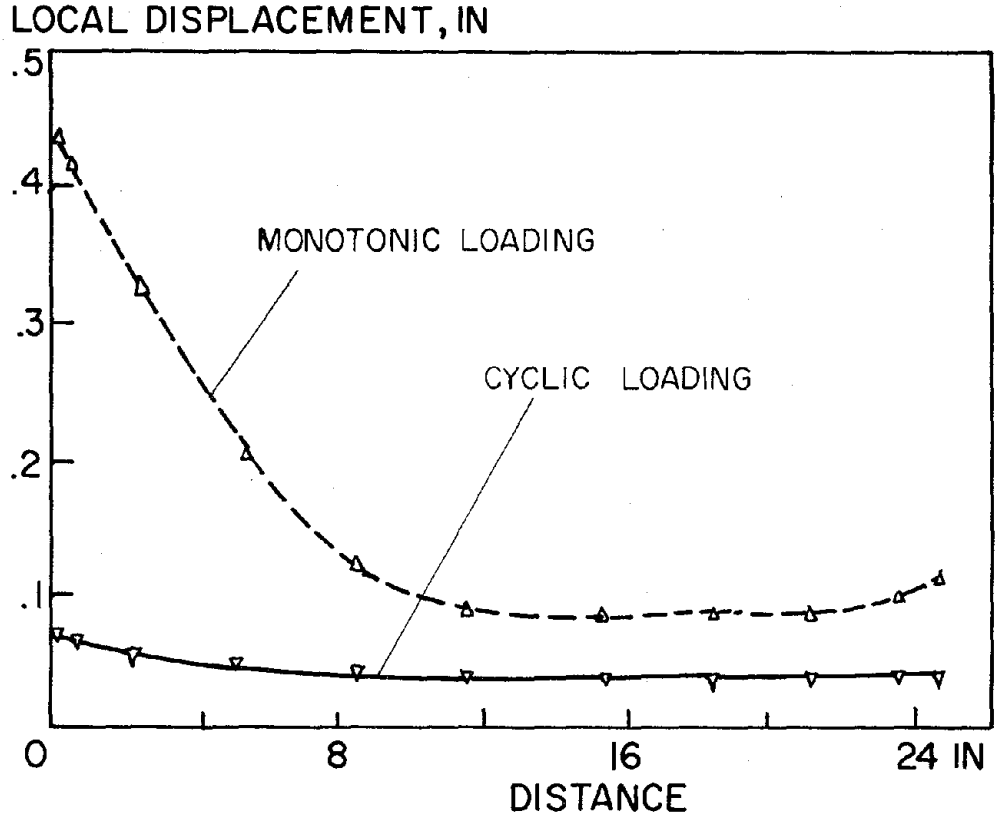

(b) Local Displacement Distribution (#8 Bar)

Fig. 5.8 Distribution Diagrams, Bond Stresses, and Local Displacements of Cyclic vs. Monotonic Loading (At Pull-Through)

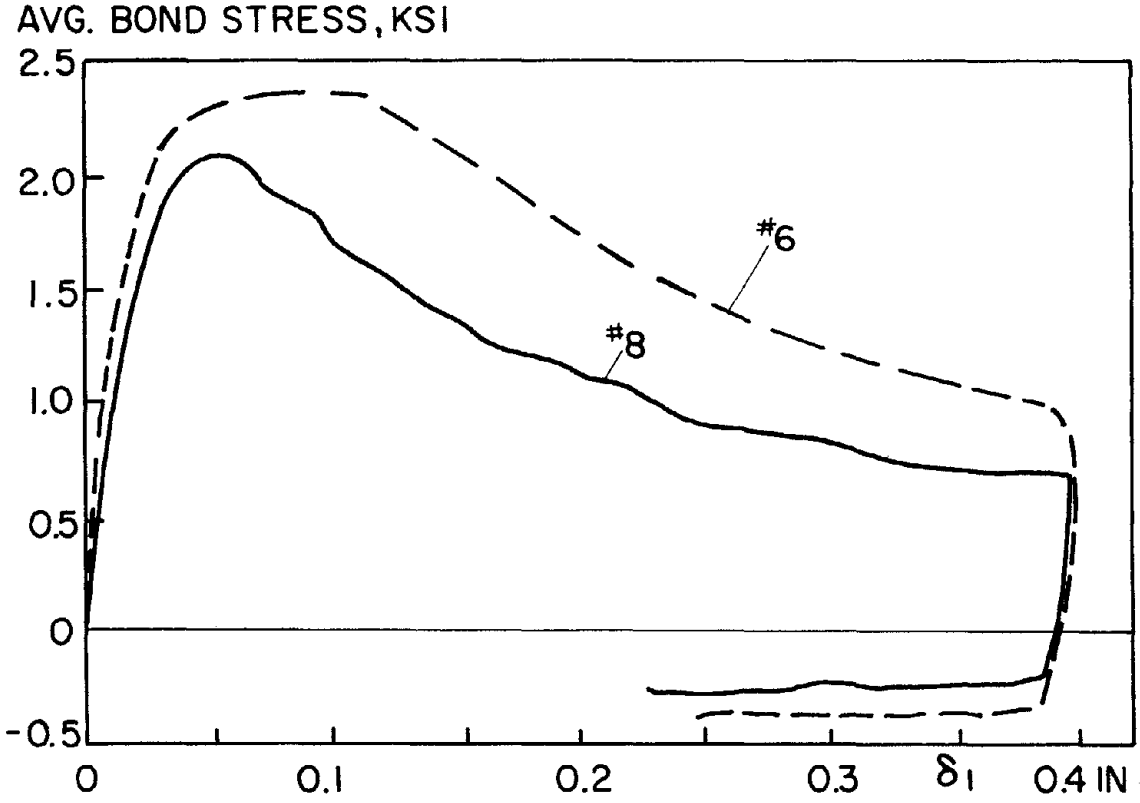

(a) #6 vs. #8

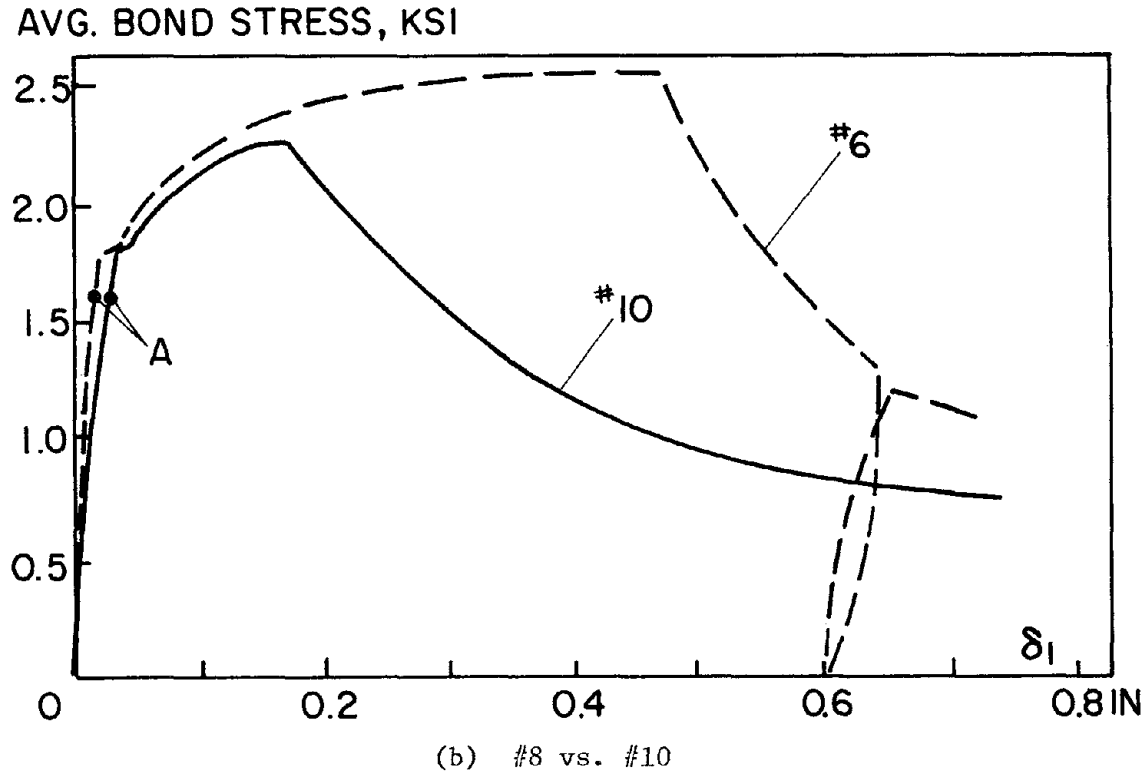

(b) #8 vs. #10

Fig. 5.9 Bond Stress Displacement Diagrams for Different Bar Sizes

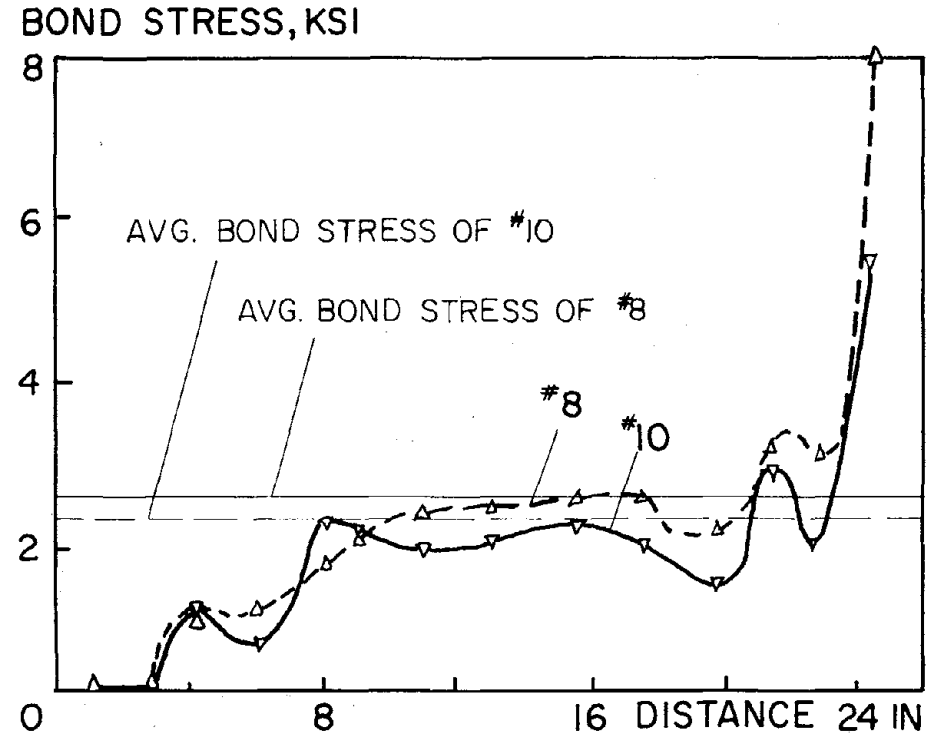

Fig. 5.10 Bond Stress Distribution at Verge of Pull-Through

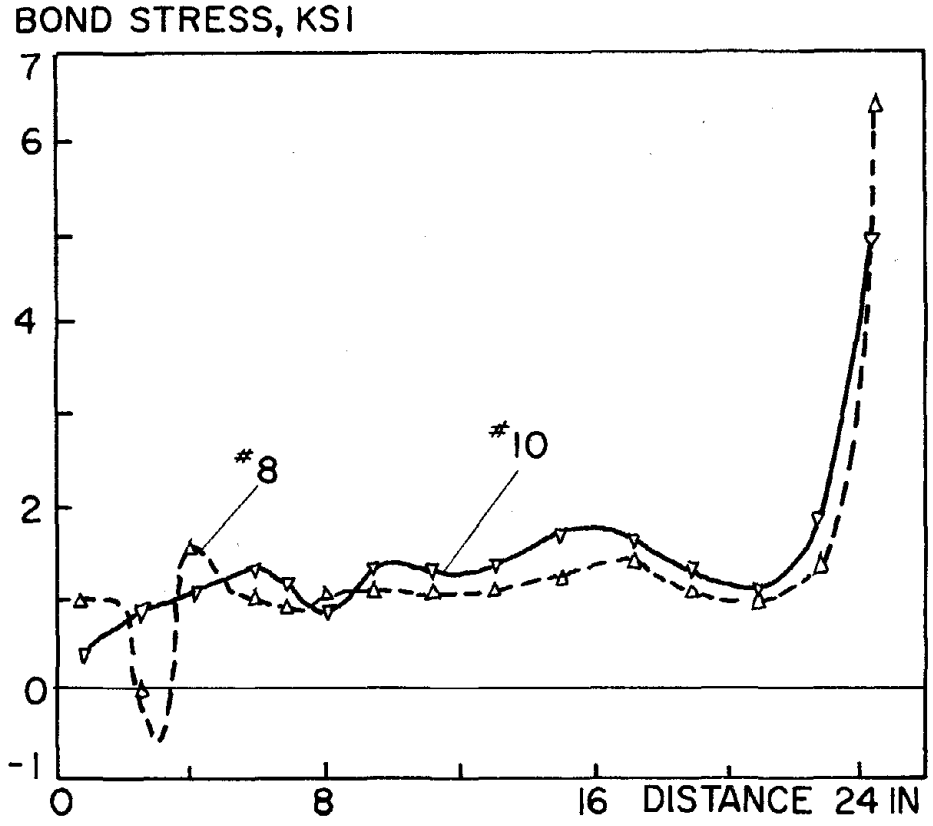

(a) Bond Stress Distribution

Fig. 5.11 Distribution Diagrams of #8 vs. #10 Bar (At Point A)

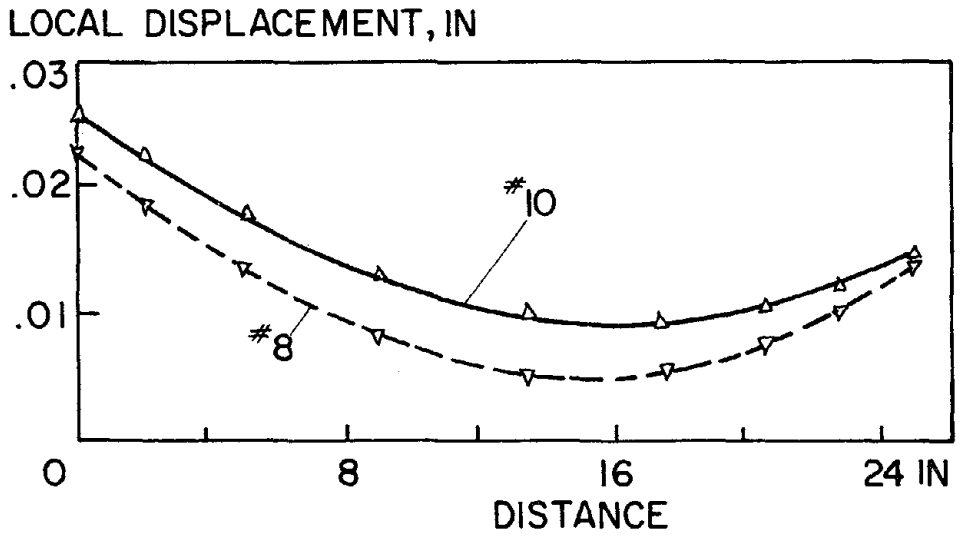

(b) Local Displacement Distribution

Fig. 5.11 Distribution Diagrams of #8 vs. #10 Bar (At Point A)

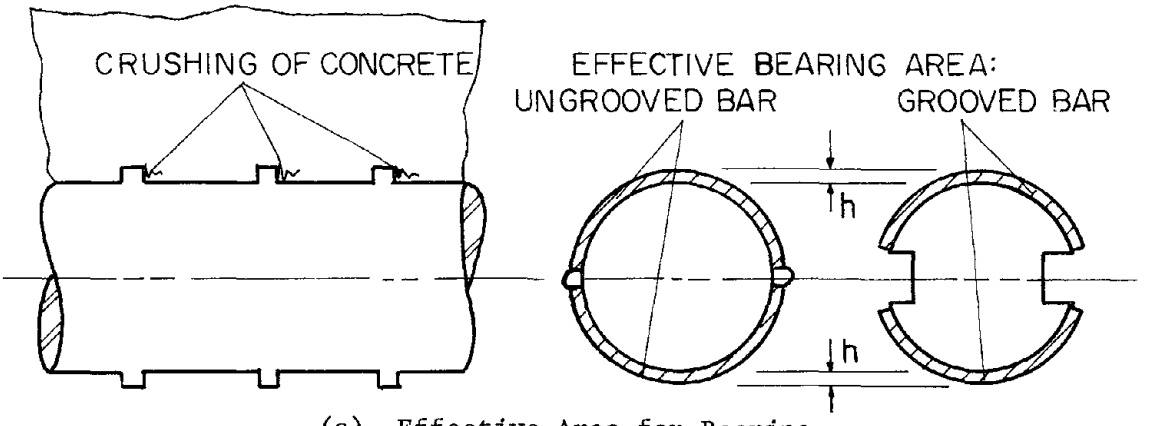

(a) Effective Area for Bearing

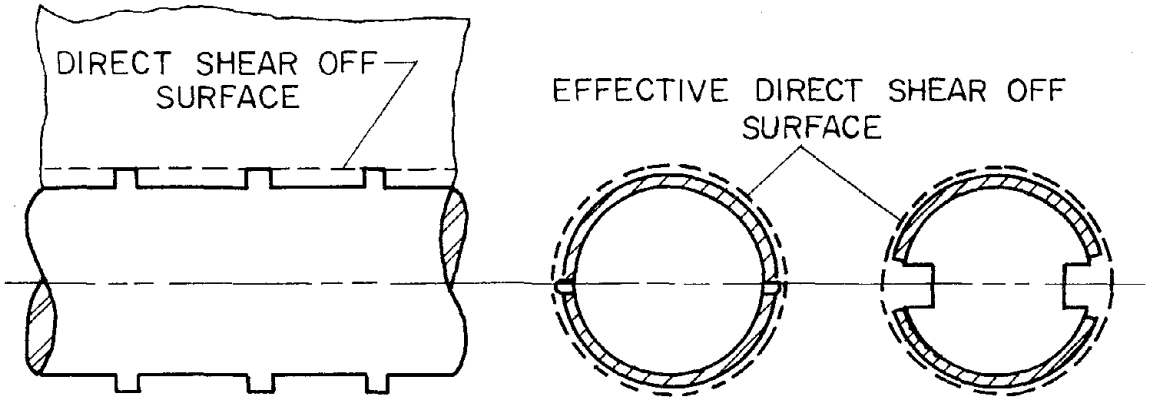

(b) Effective Surface for Direct Shear Off

Fig. 5.12 Effective Area for Various Bond Mechanisms

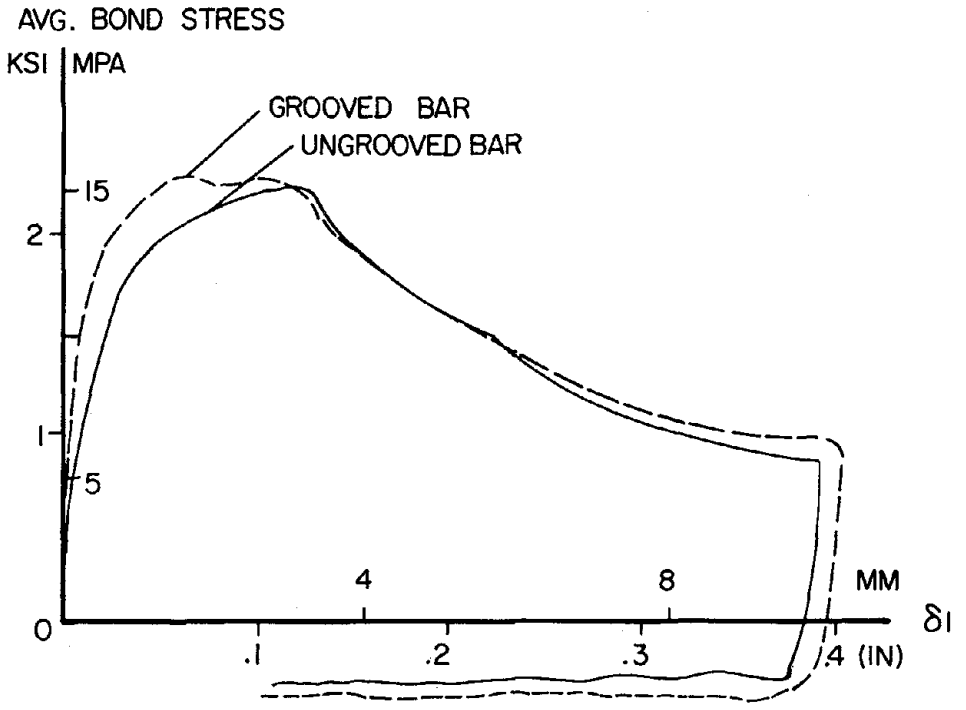

Fig. 5.13 Response of #6 Grooved Bar vs. Ungrooved

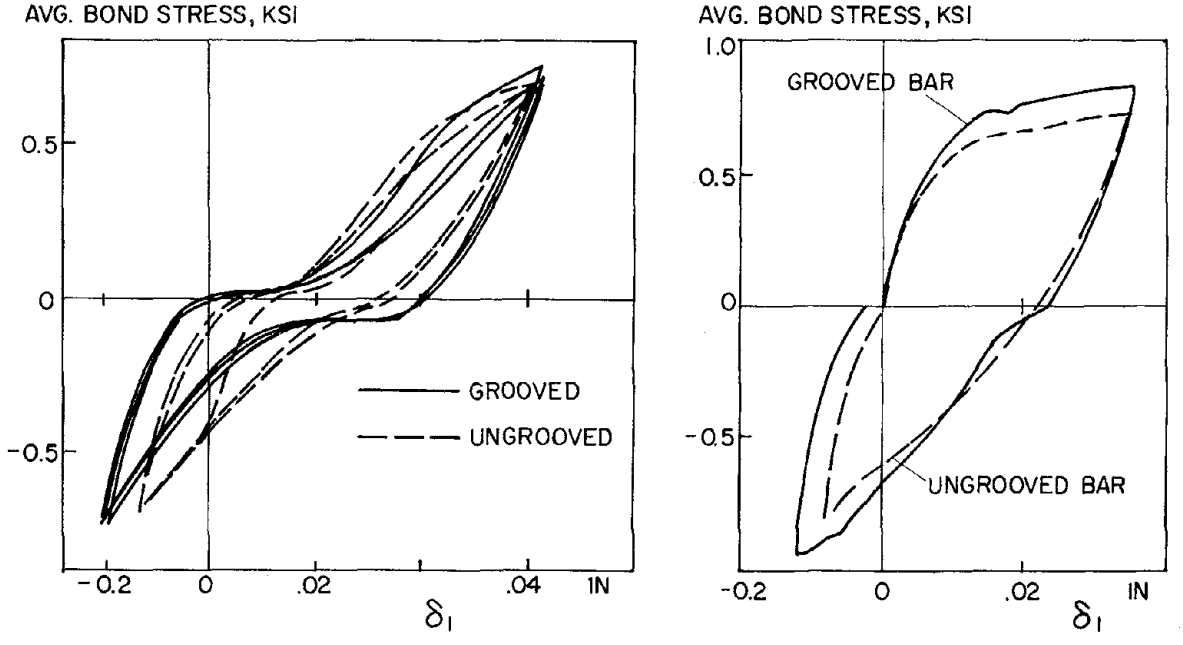

(a) Cycle at .07 in. [Ref. 25]

(b) Shook Load [Ref. 25]

Fig. 5.14 Response of #8 Grooved Bar vs. Ungrooved

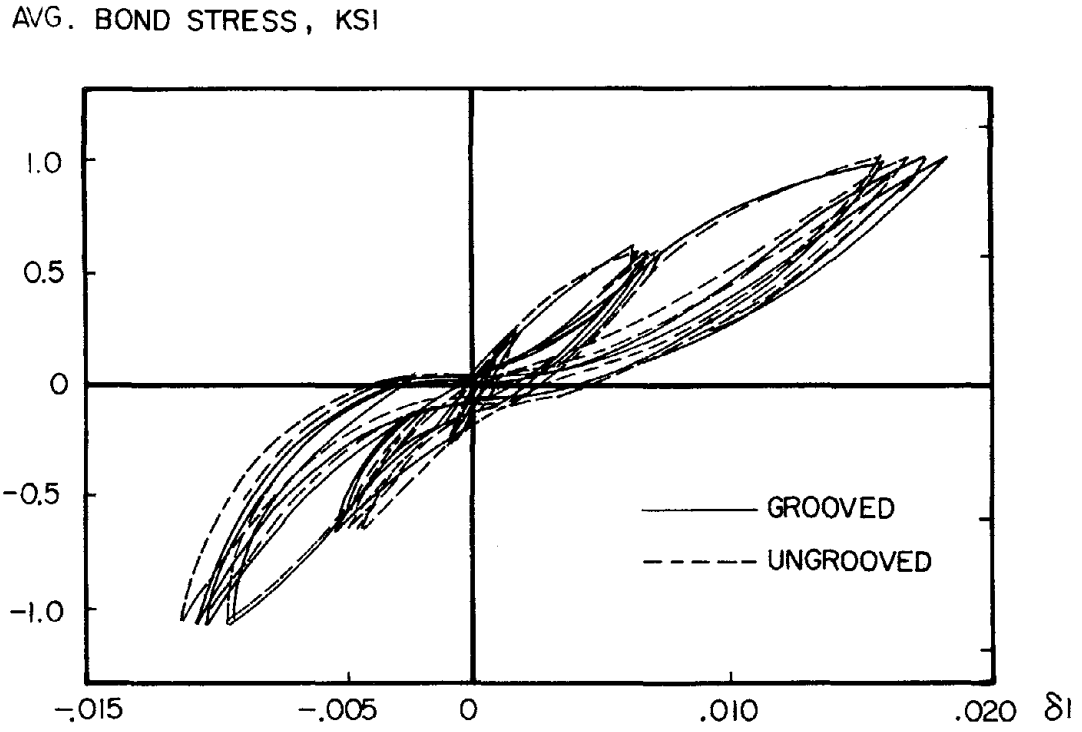

(a) Cycles Before Yielding

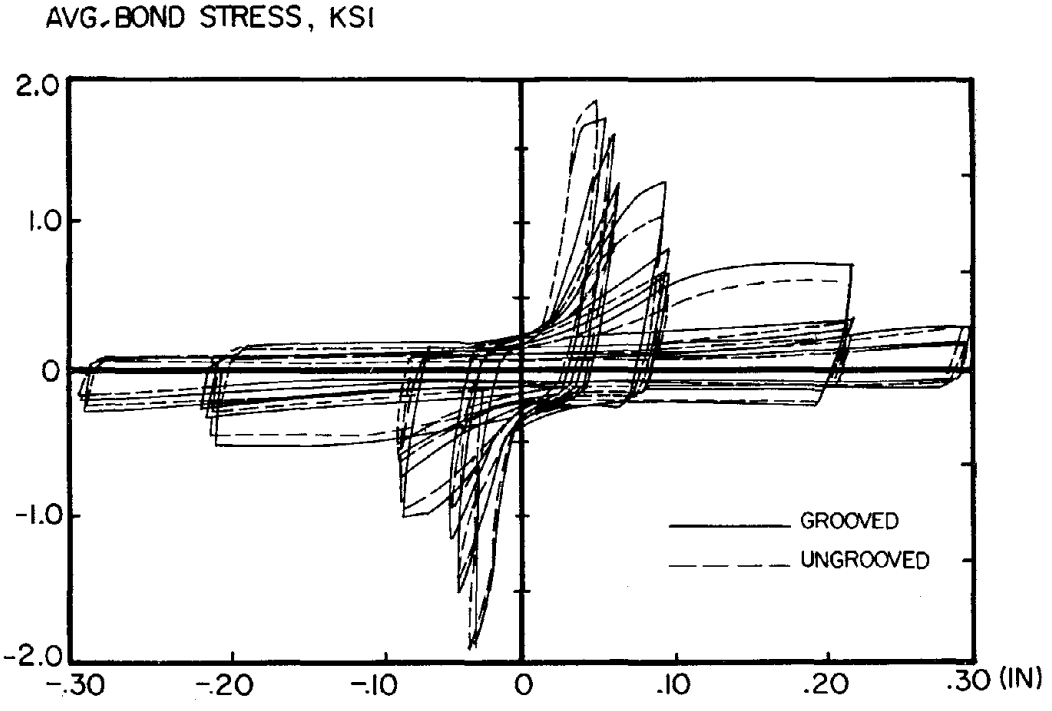

(b) Cycles After Yielding

Fig. 5.15 Response of #10 Grooved Bar vs. Ungrooved

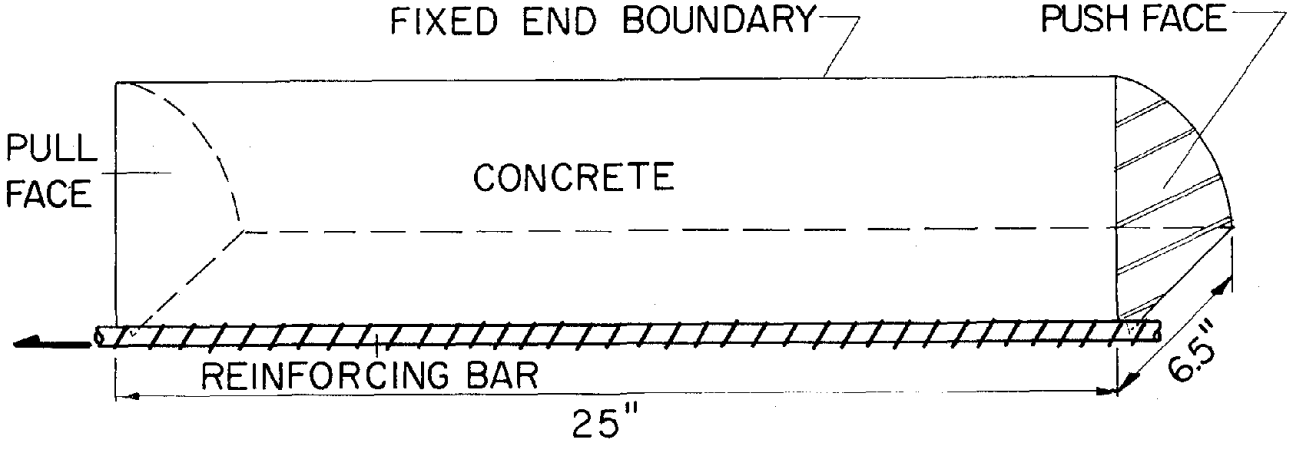

Fig. 6.1 Axisymmetric Model of Analysis

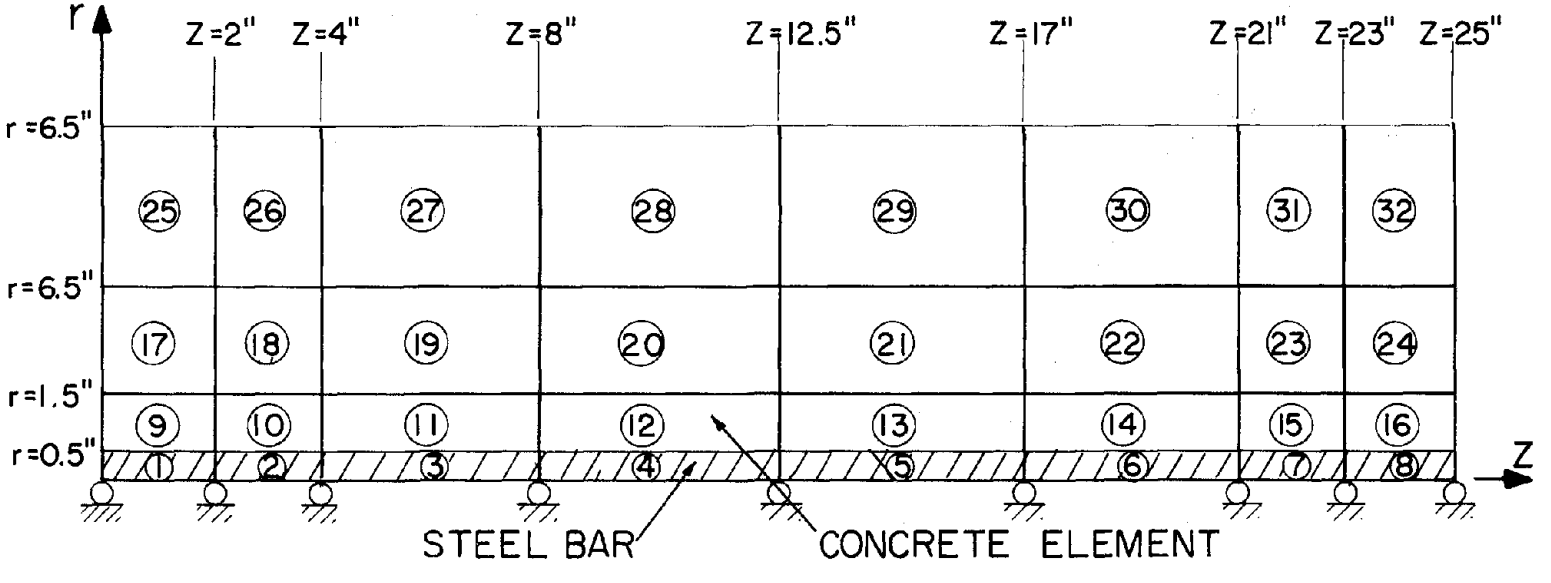

Fig. 6.2 Finite Element Mesh for Analytical Model

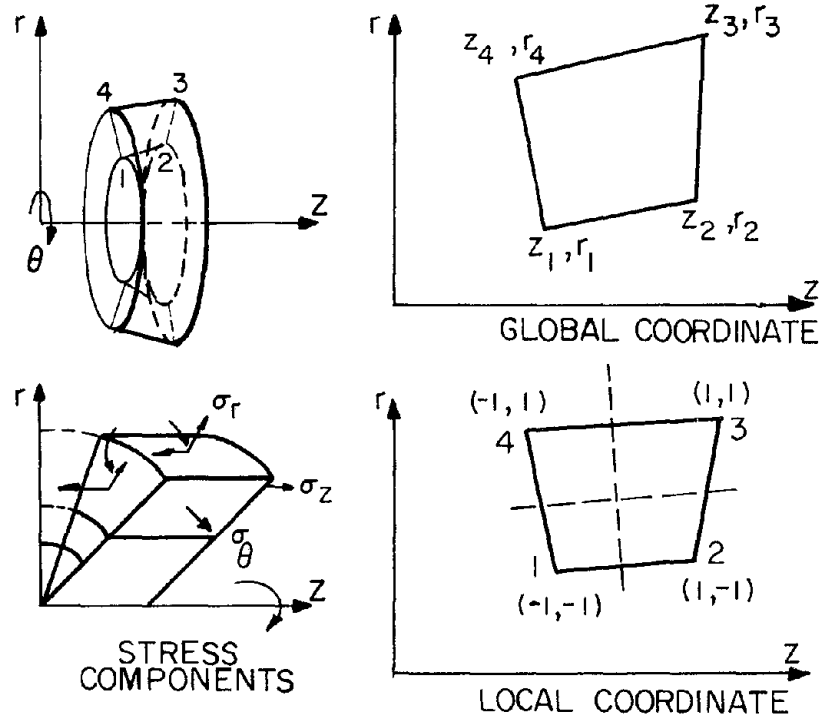

Fig. 6.3 Quadrilateral Axisymmetric Element

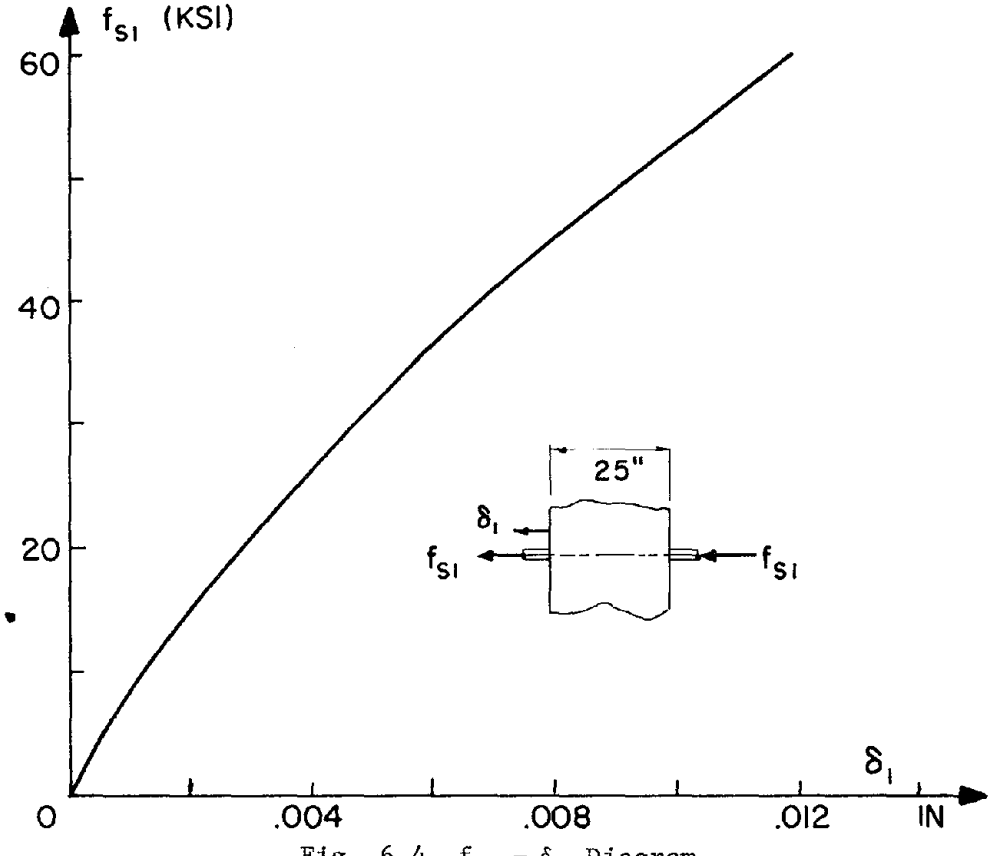

Fig. 6.4 $f_{s1} - \delta_1$ Diagram

Crack Seq. No.	Stress at Crack ($f_{s1} = f_{s2}$) (KSI)	Type of Cracks
1	5.0	Diagonal
2	11.8	"
3	23.0	"
4	24.5	"
5	25.0	"
6	35.0	"
7	37.0	"
8	39.0	"

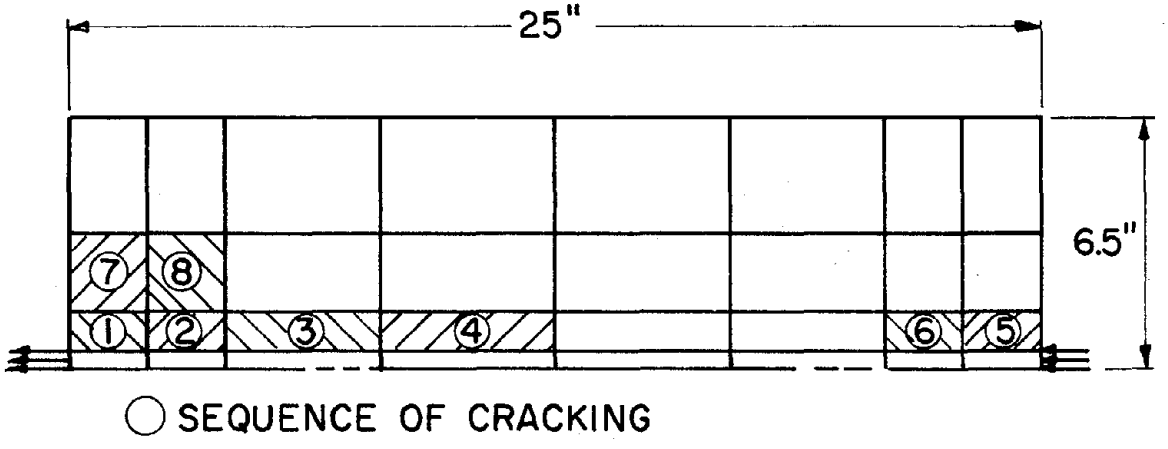

Fig. 6.5 Crack Sequence and Load for Push-Pull

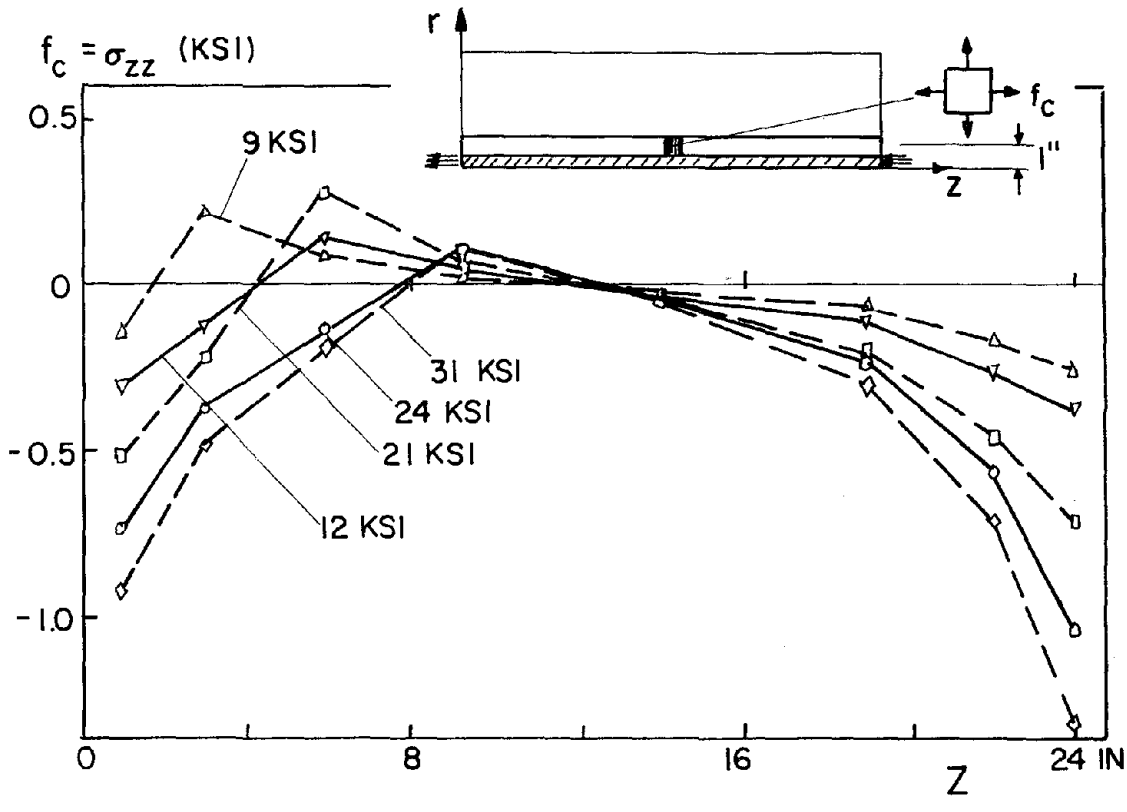

(a) From 0 to 31 ksi Stress

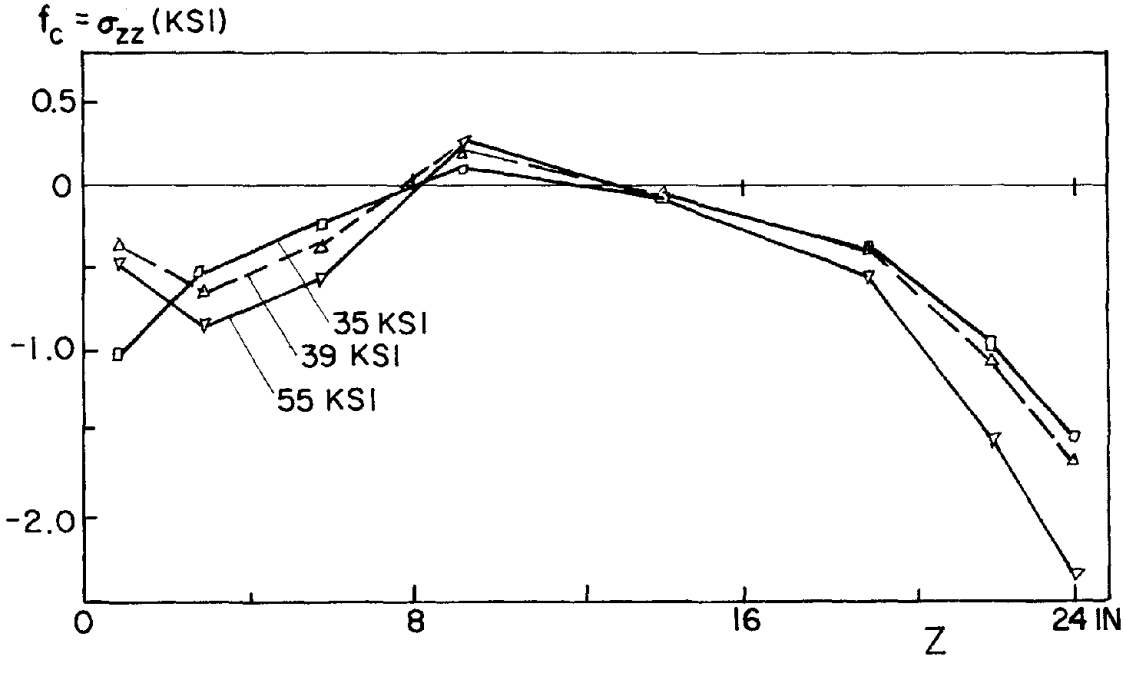

(b) From 35 to 55 ksi Stress

Fig. 6.6 Stress Distribution in Concrete (1 inch from center)

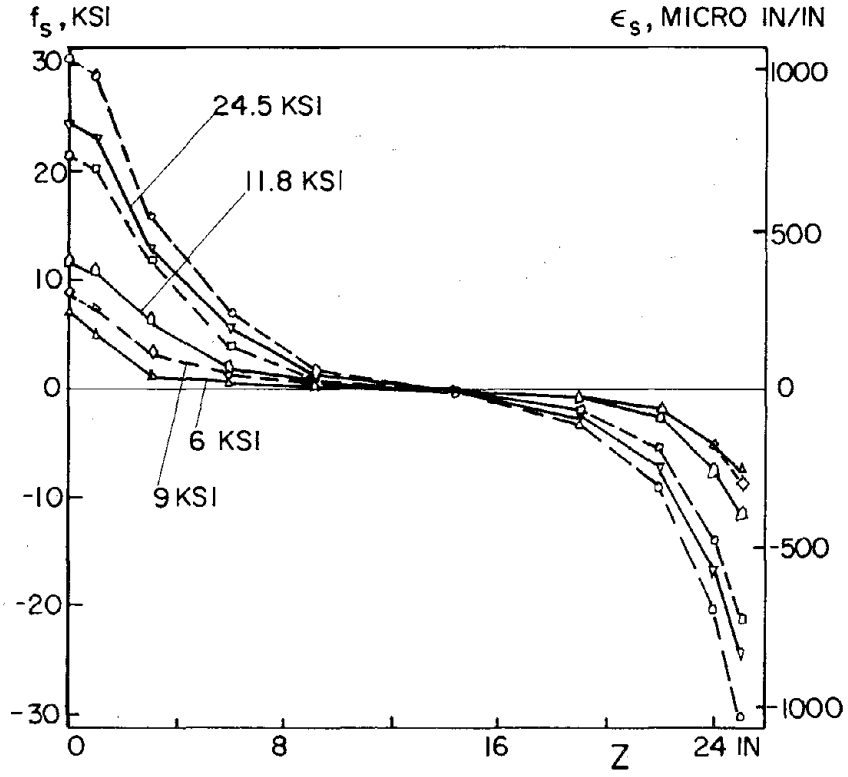

(a) From 0 to 30 ksi Stress

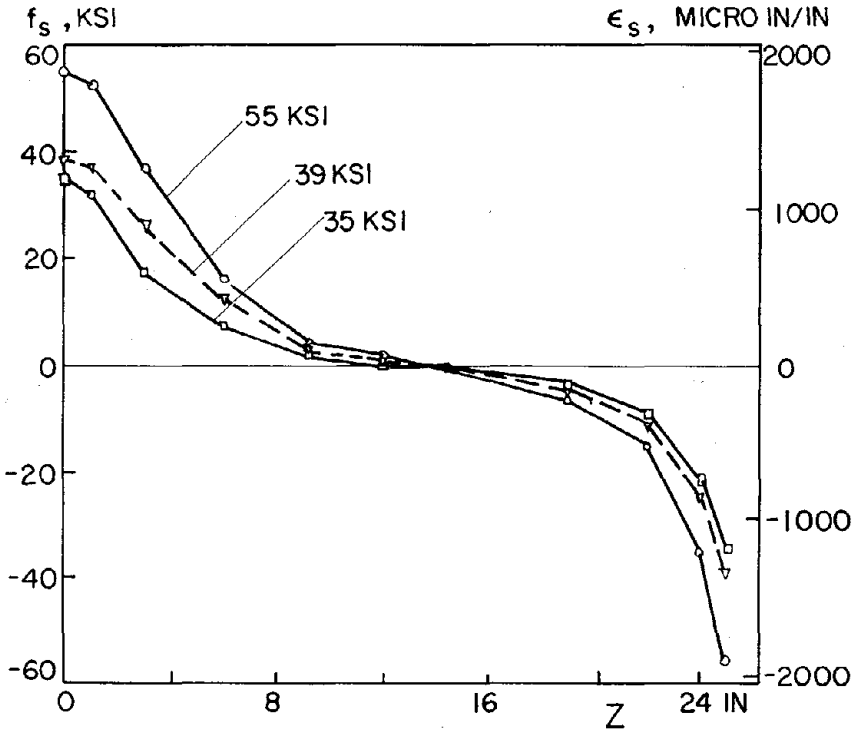

(b) From 35 to 55 ksi Stress

Fig. 6.7 Stress, Strain Distribution Diagram in Rebar (Push-Pull)

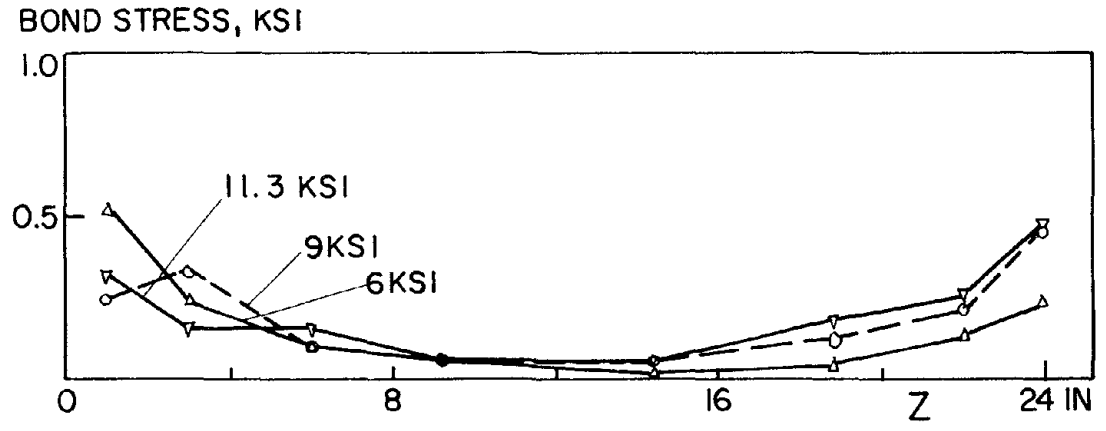

(a) From 0 to 11.8 ksi

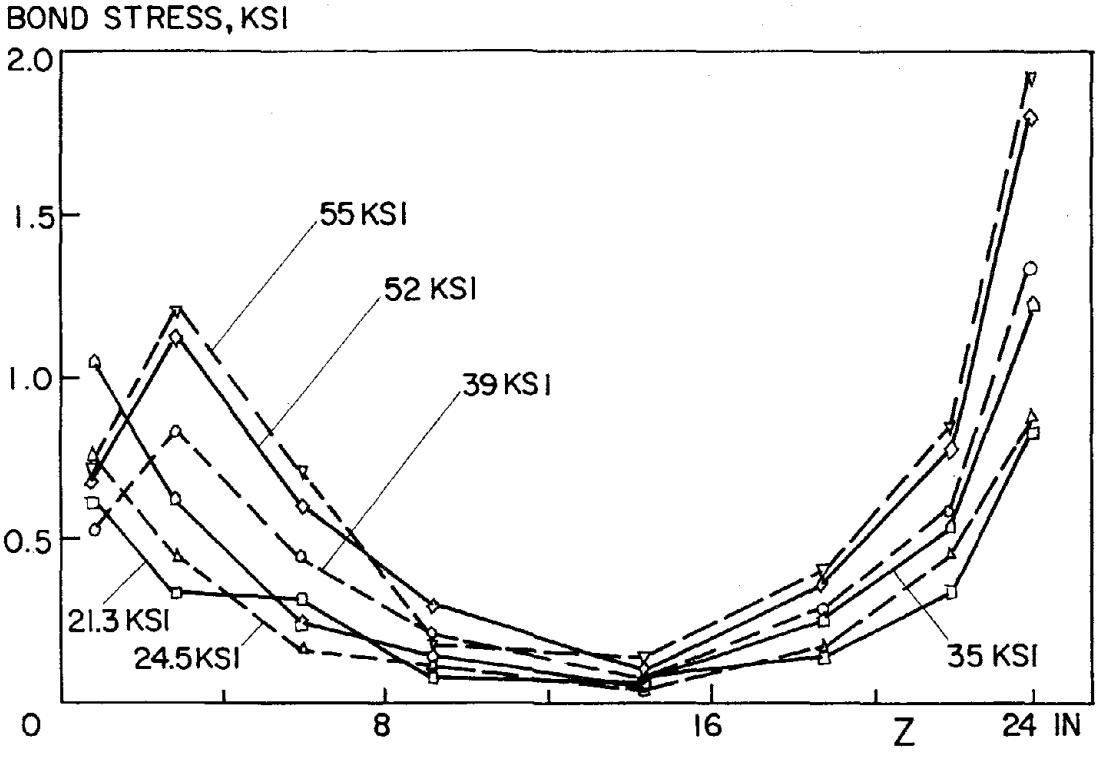

(b) From 21 to 55 ksi

Fig. 6.8 Bond Stress Distribution for Push-Pull Loading

Crack Seq. No.	Stress at Crack (KSI)
1	8
2	12
3	26
4	38
5	40
6	57

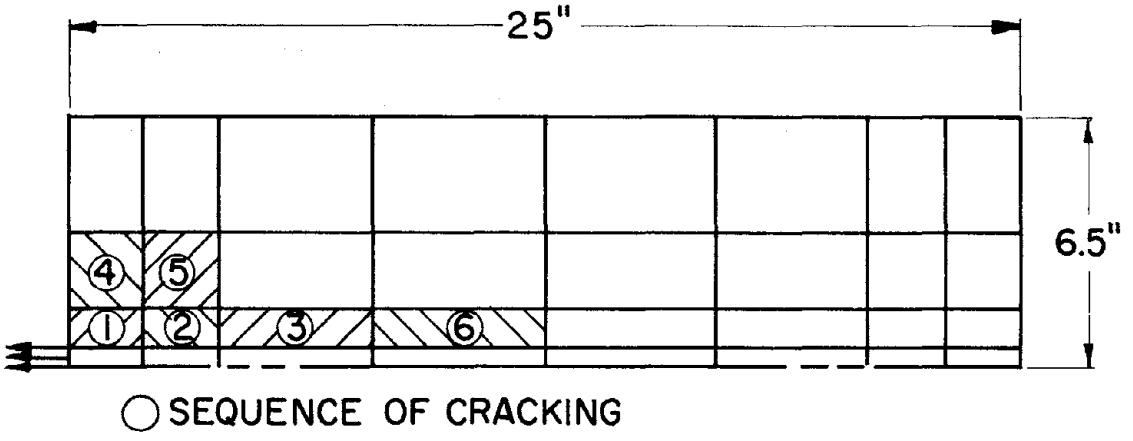

Fig. 6.9 Crack Sequence and Load for Pull Only

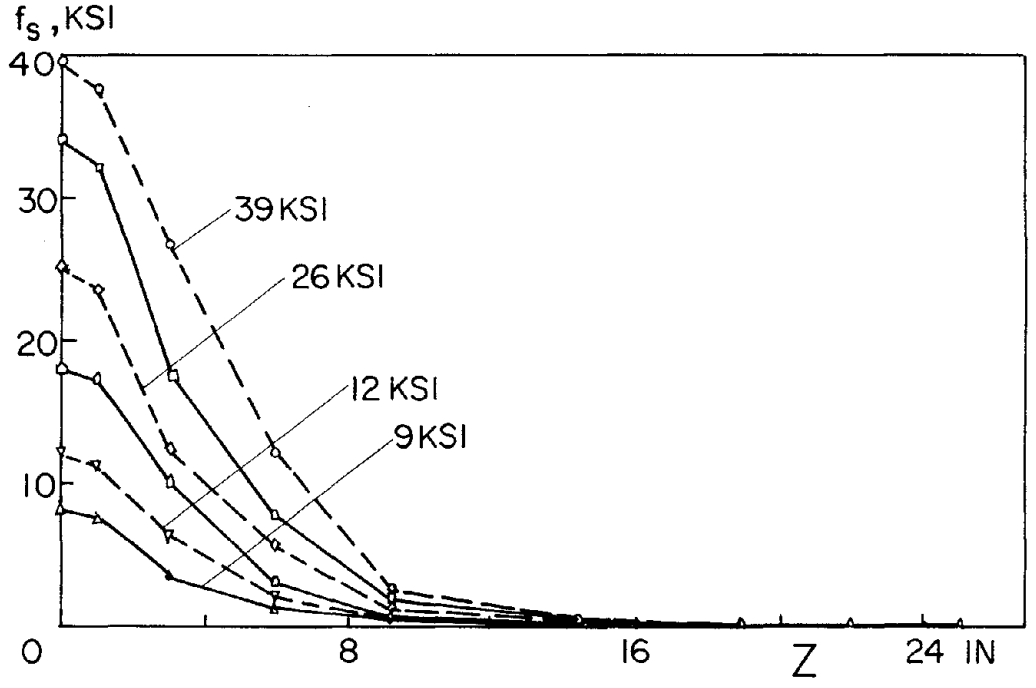

(a) From 0 to 40 ksi

Fig. 6.10 Stress Distribution Diagram (Pull Only)

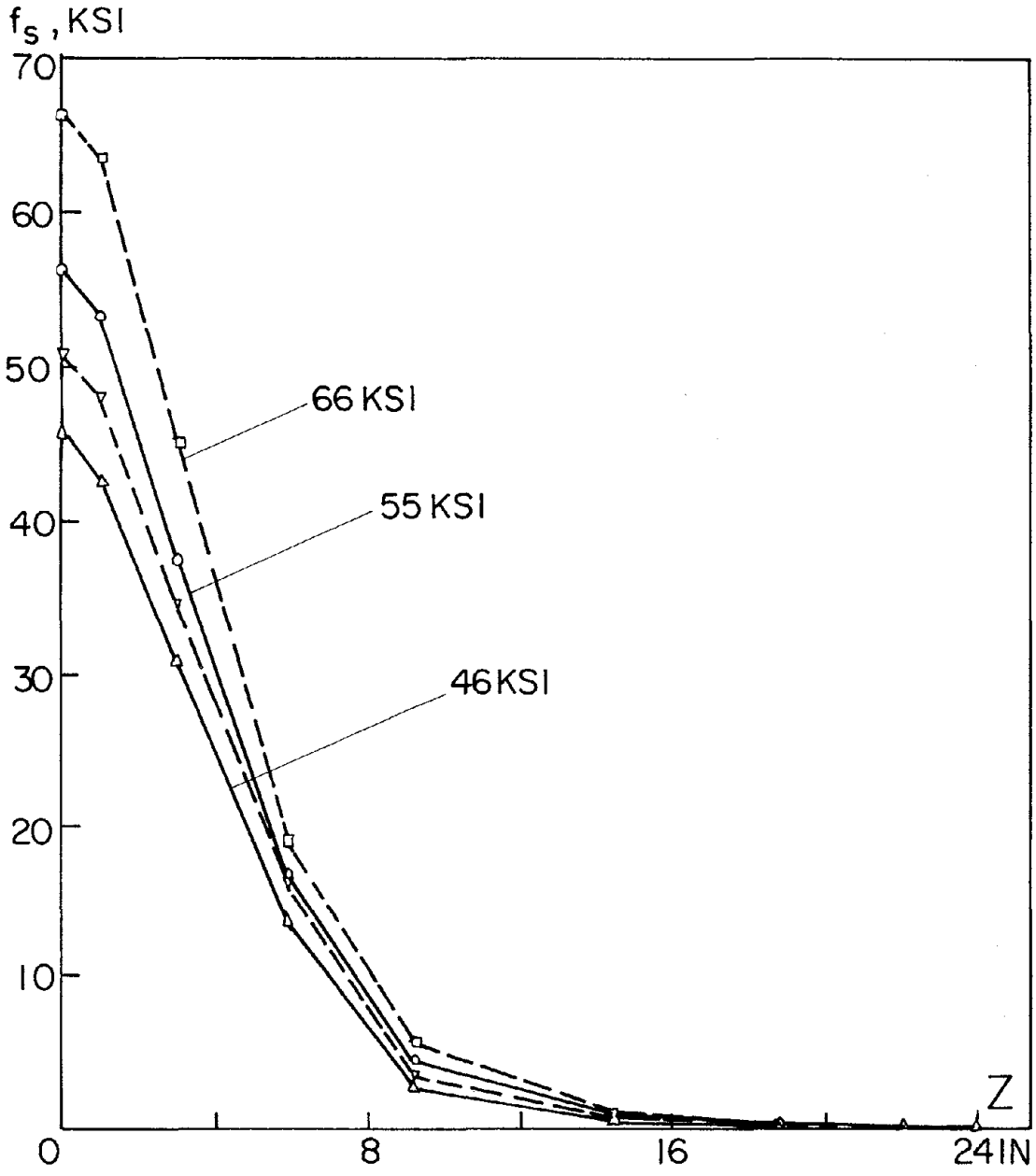

(b) From 45 to 65 ksi

Fig. 6.10 Stress Distribution Diagram (Pull Only)

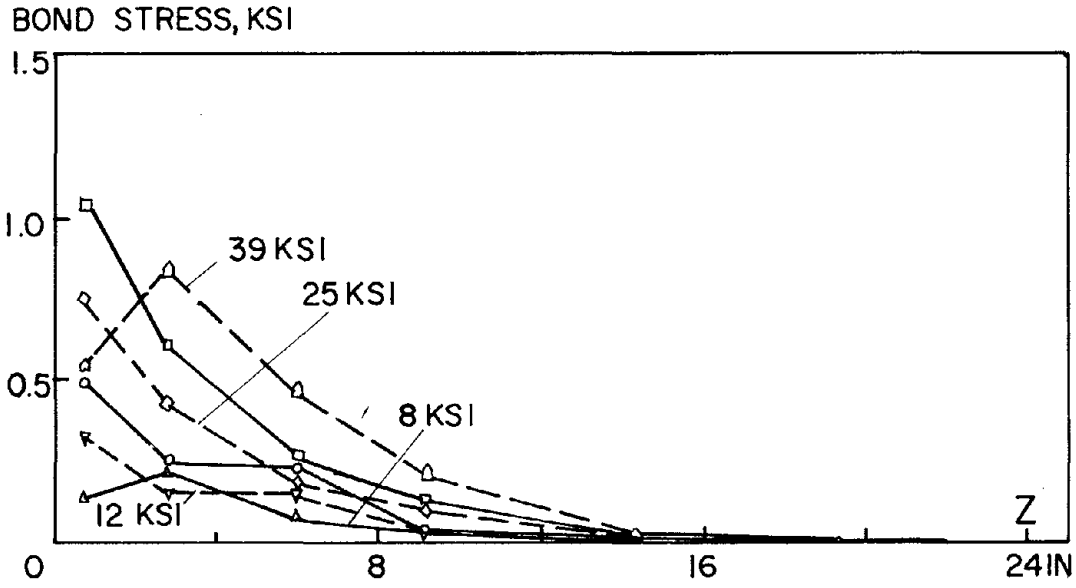

(a) From 0 to 40 ksi

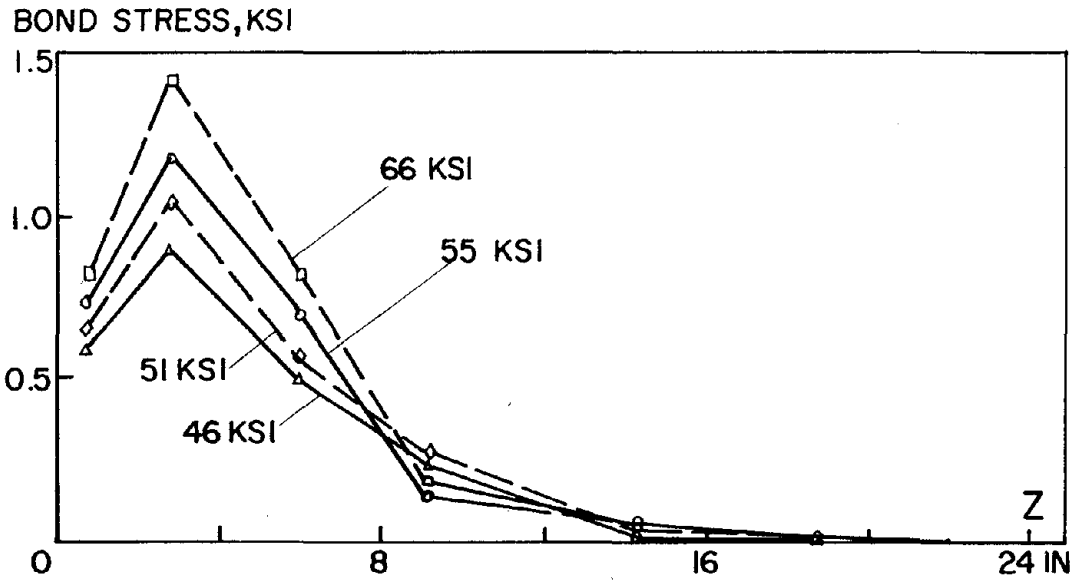

(b) From 45 to 65 ksi

Fig. 6.11 Bond Stress Distribution (Pull Only)

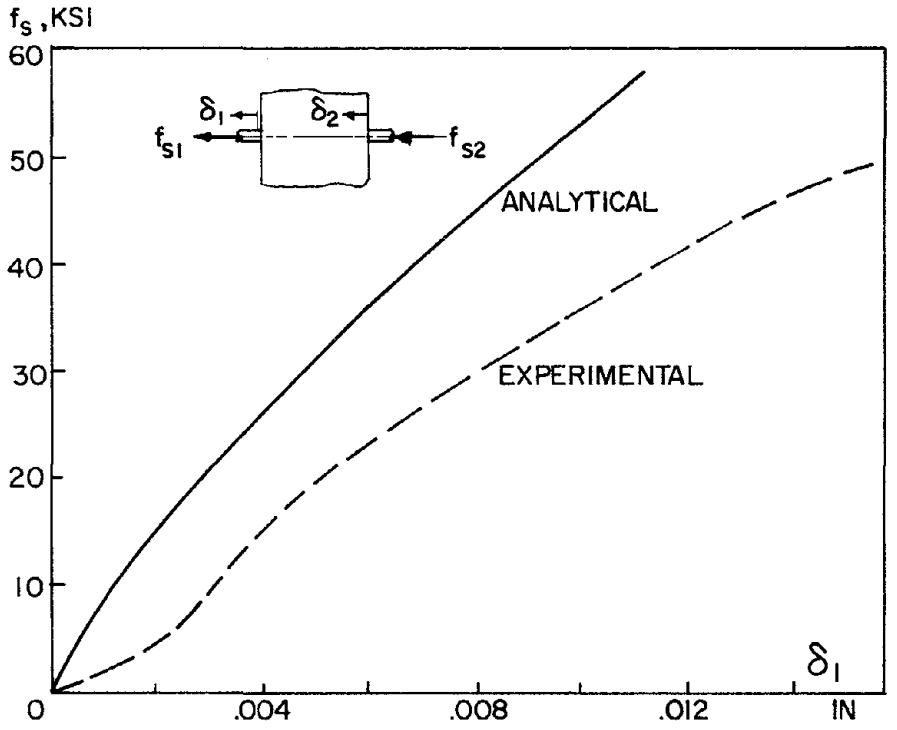

(a) Pull-Push

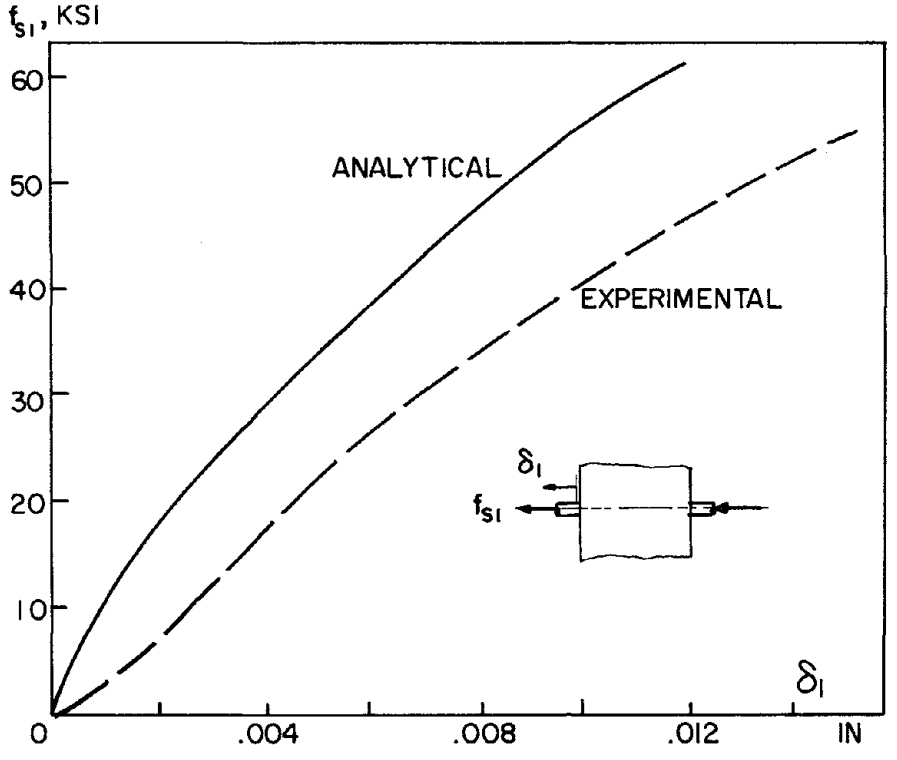

(b) Pull Only

Fig. 6.12 Analytical vs. Experimental Results of $f_{s1} - \delta_1$ Curve

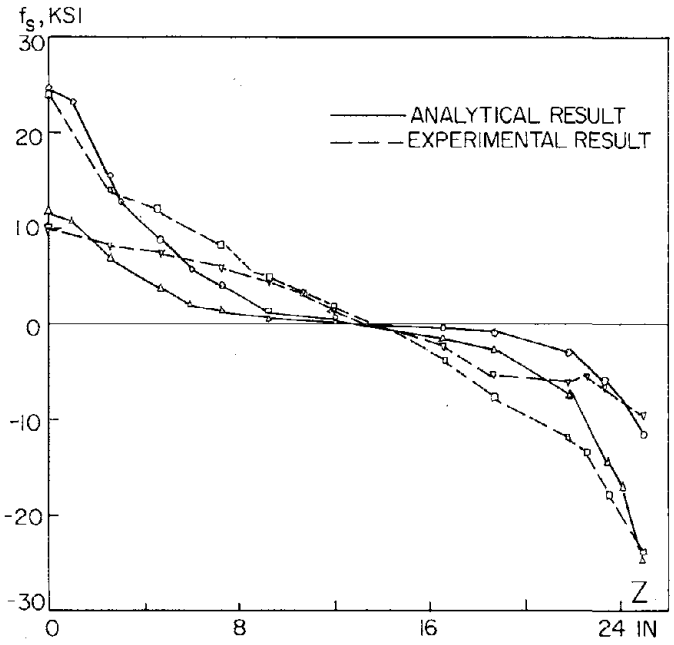

(a) At Low Stresses (Push-Pull)

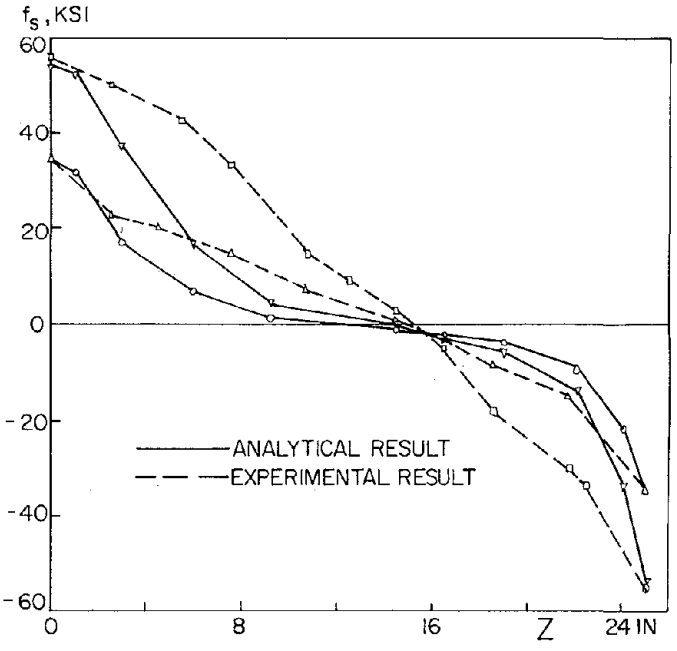

(b) At Higher Stresses (Push-Pull)

Fig. 6.13 Analytical vs. Experimental Stress Distribution Diagram

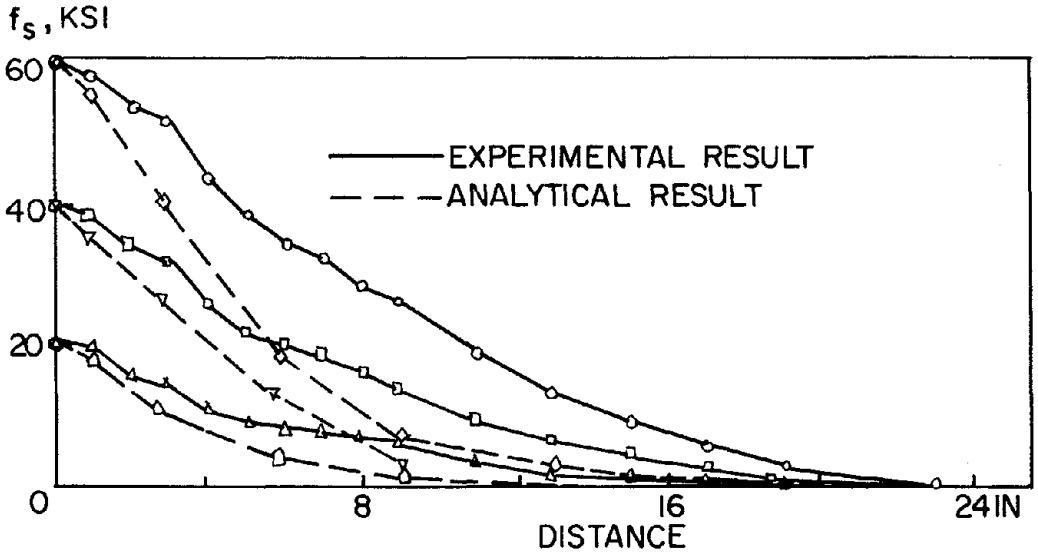

(c) Pull Only

Fig. 6.13 Analytical vs. Experimental Stress and Strain Distribution Diagram

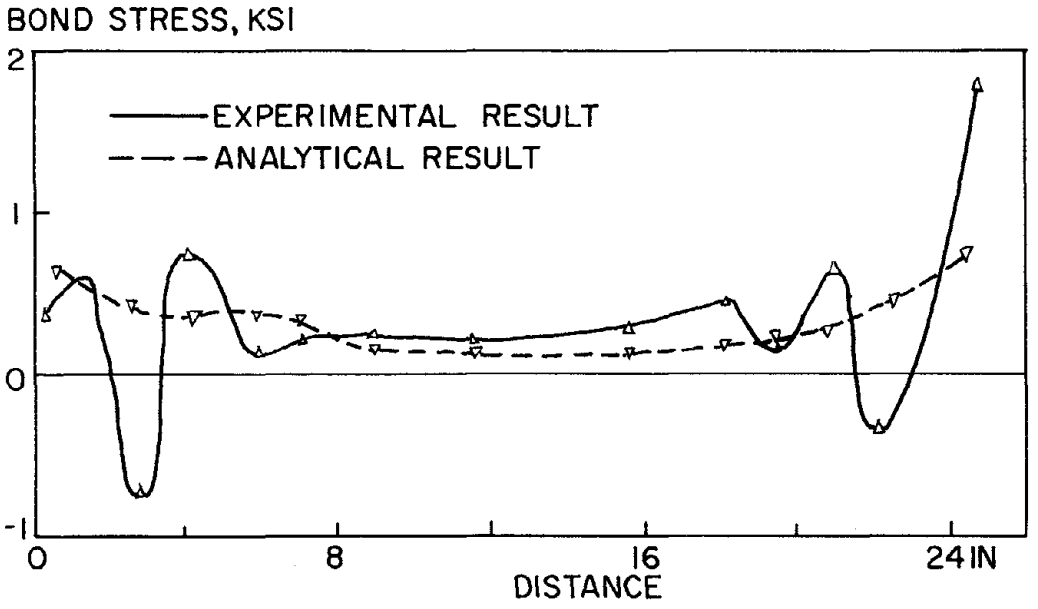

(a) At 12 ksi

Fig. 6.14 Analytical vs. Experimental Bond Stress Distribution

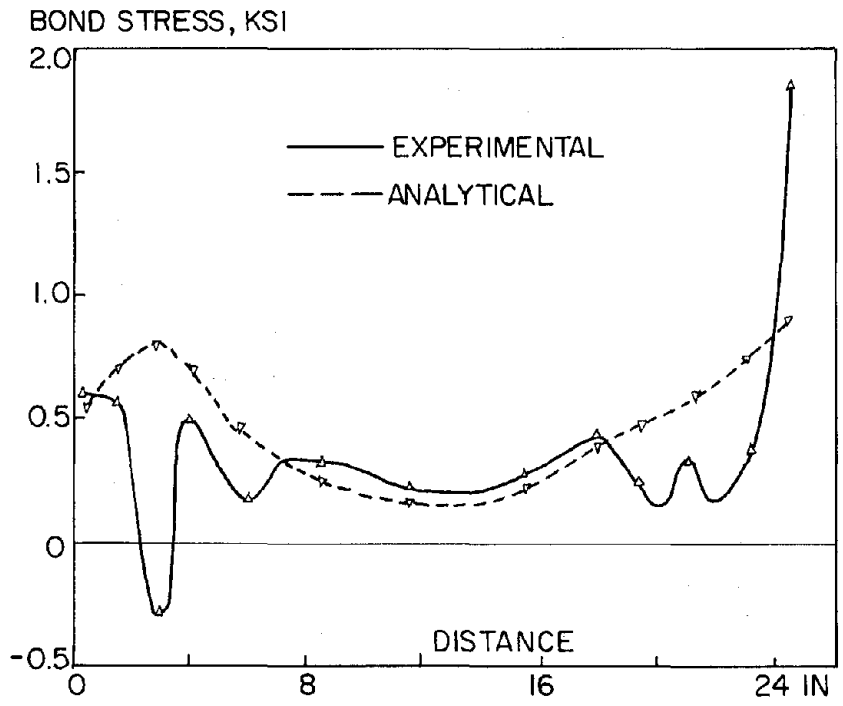

(b) At 39 ksi

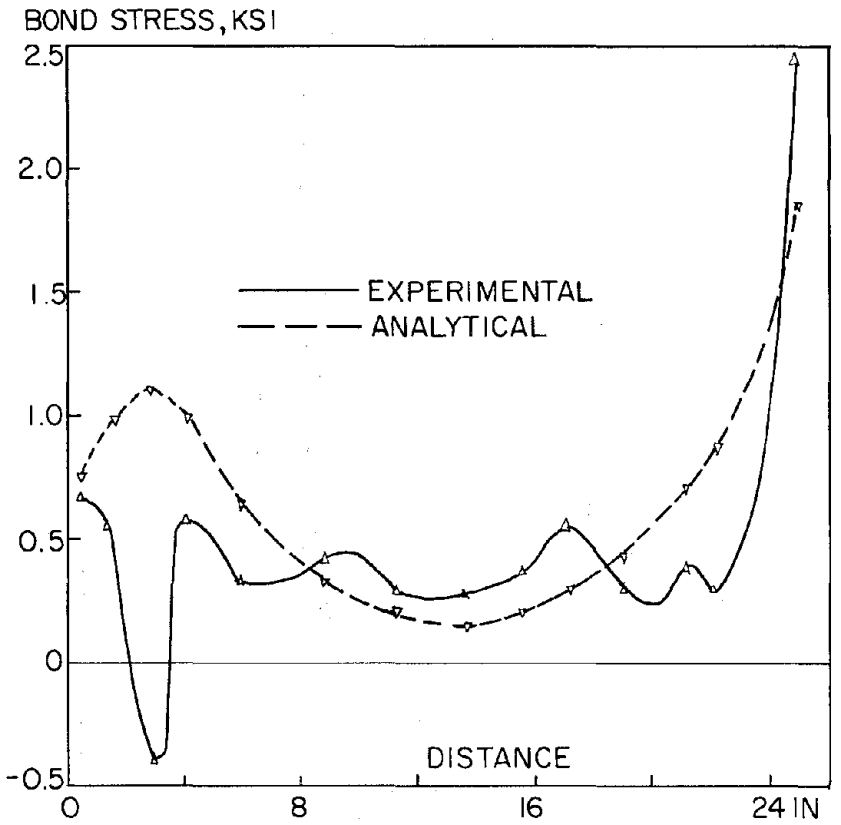

(c) At 50 ksi

Fig. 6.14 Analytical vs. Experimental Bond Stress Distribution

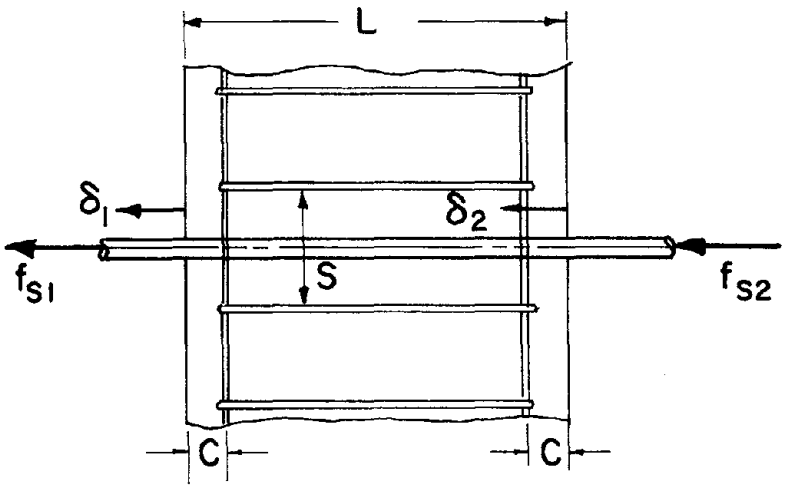

Fig. 7.1 Bar Embedded in Confined Concrete Block

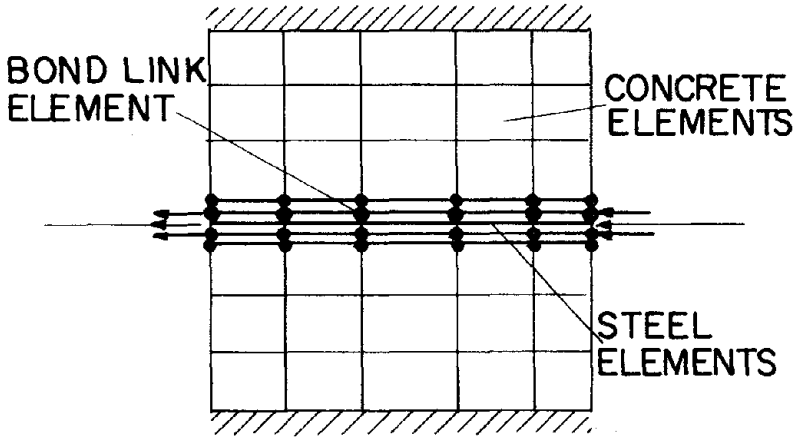

Fig. 7.2 Finite Element Mesh of Bar and Concrete Block

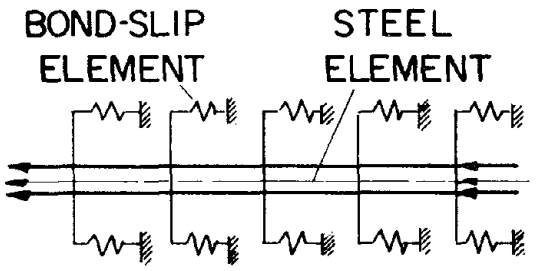

Fig. 7.3 Steel Bar and Nonlinear Spring Model

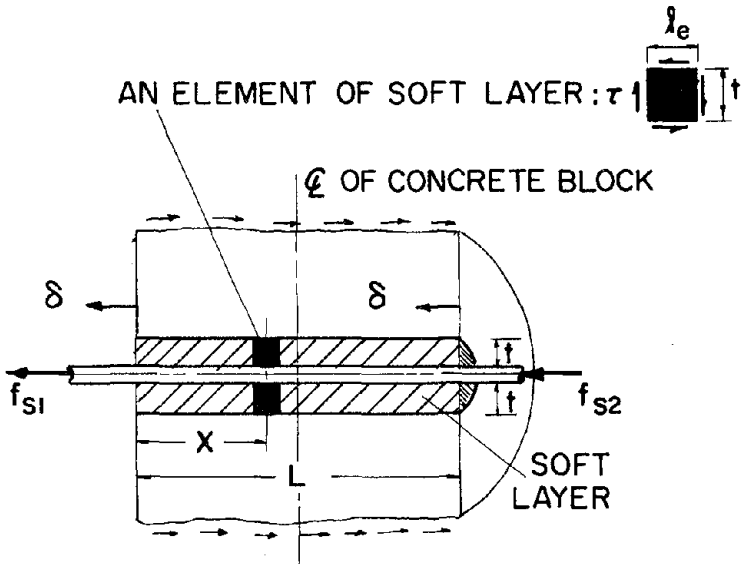

(a) Concrete Block and Soft Layer Element at Undeformed Position

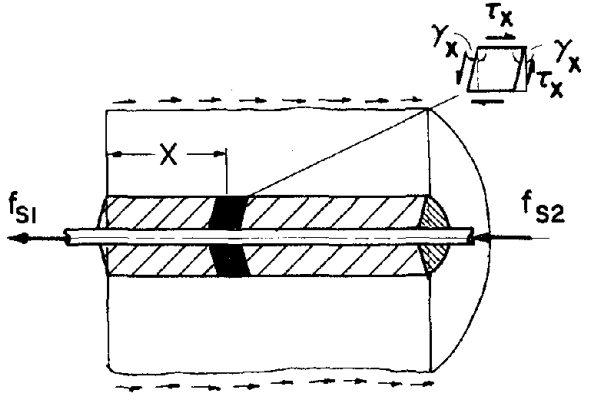

(b) Deformed Soft Layer

Fig. 7.4 Idealized Deformation of Soft Layer

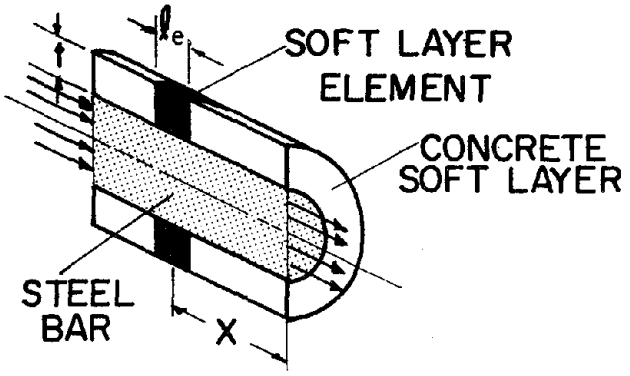

(a) Free Body Diagram of Soft Layer

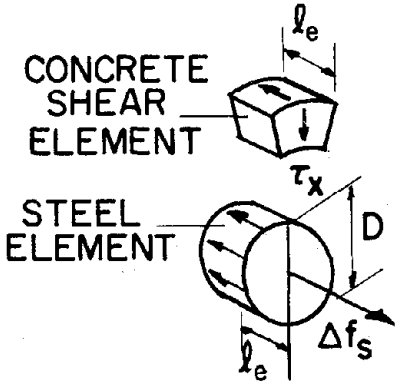

(b) Free Body Diagram of Shear Element

Fig. 7.5 Free Body of Soft Layer and Shear Element

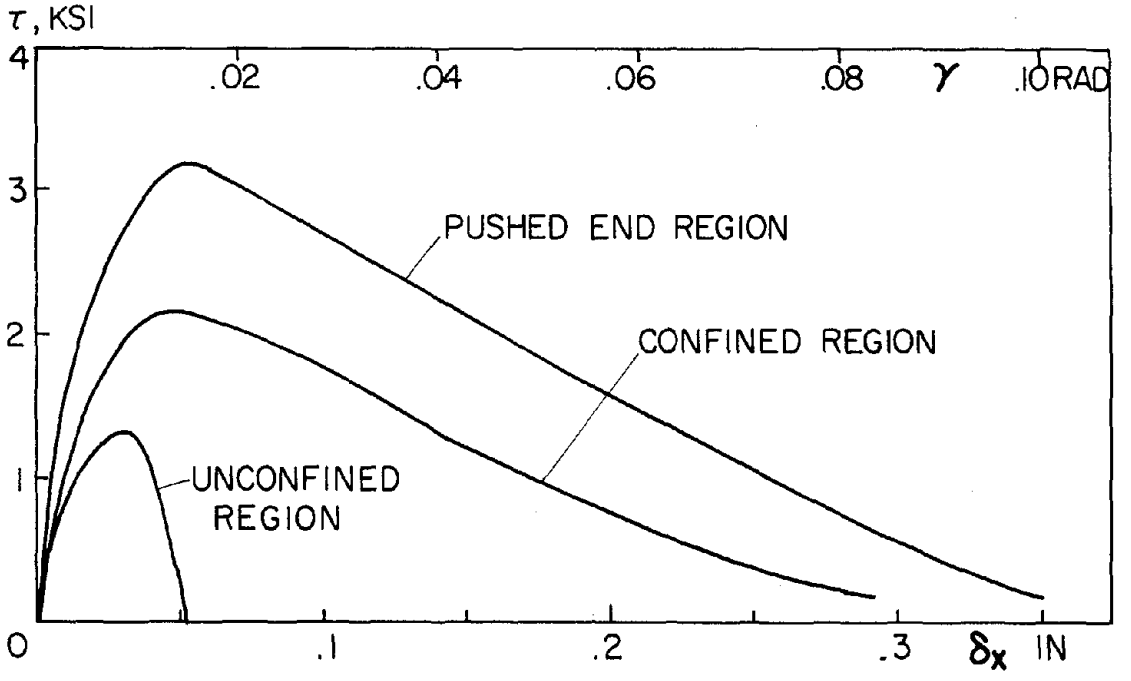

Fig. 7.6 Typical τ-γ Curves of Different Regions (Monotonic Loading)

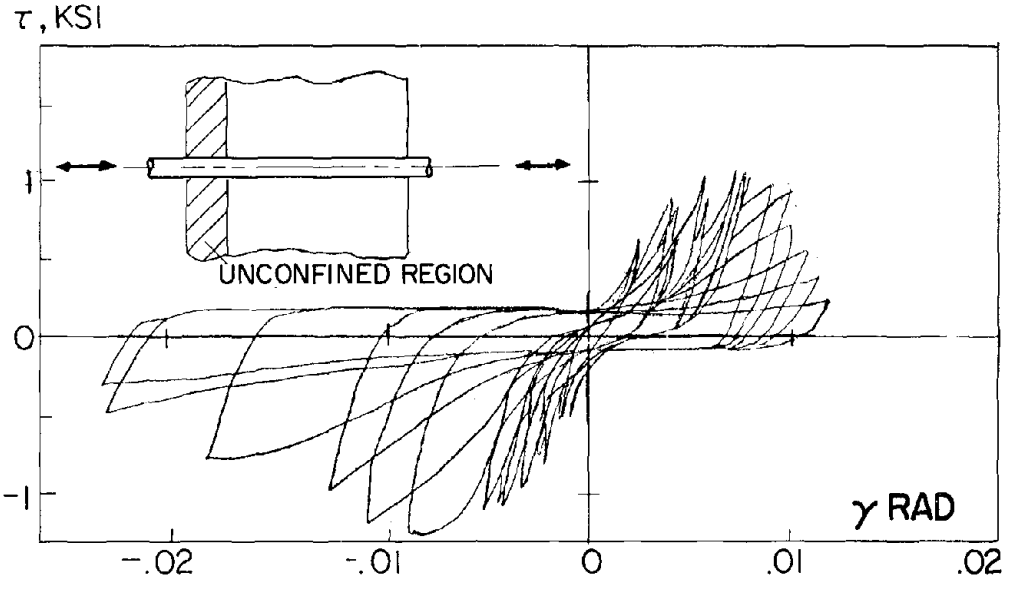

(a) Unconfined Region

Fig. 7.7 Typical τ-γ Curve of Cyclic Loading at Different Regions

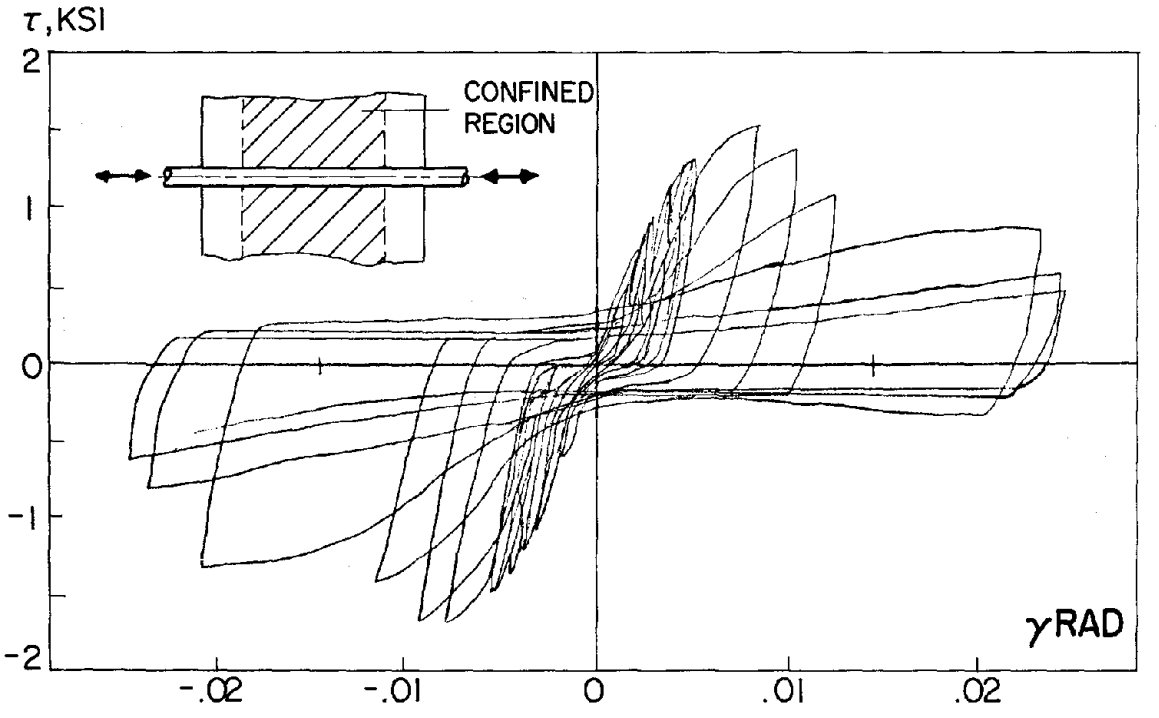

(b) Confined Region

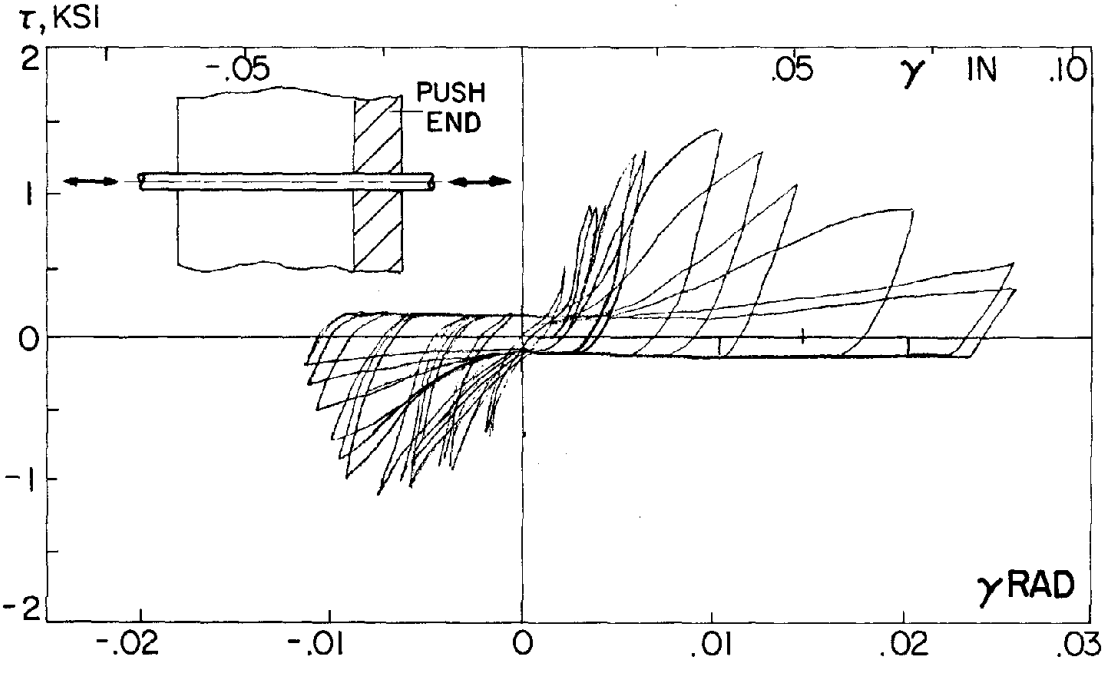

(c) Pushed End Region

Fig. 7.7 Typical τ-γ Curve of Cyclic Loading at Different Regions

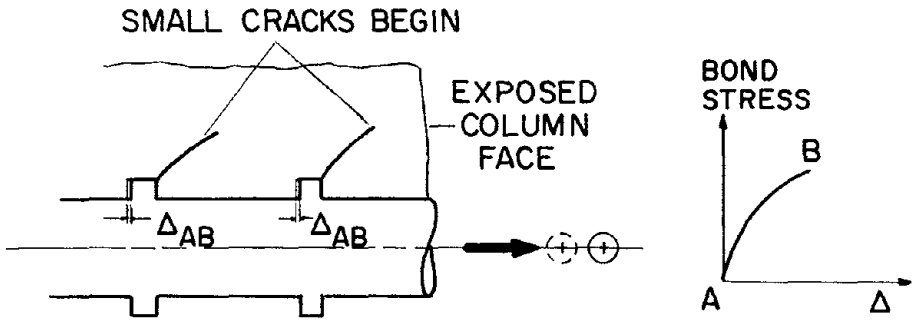

(a) Cracks Initial Stage: Load from A-B

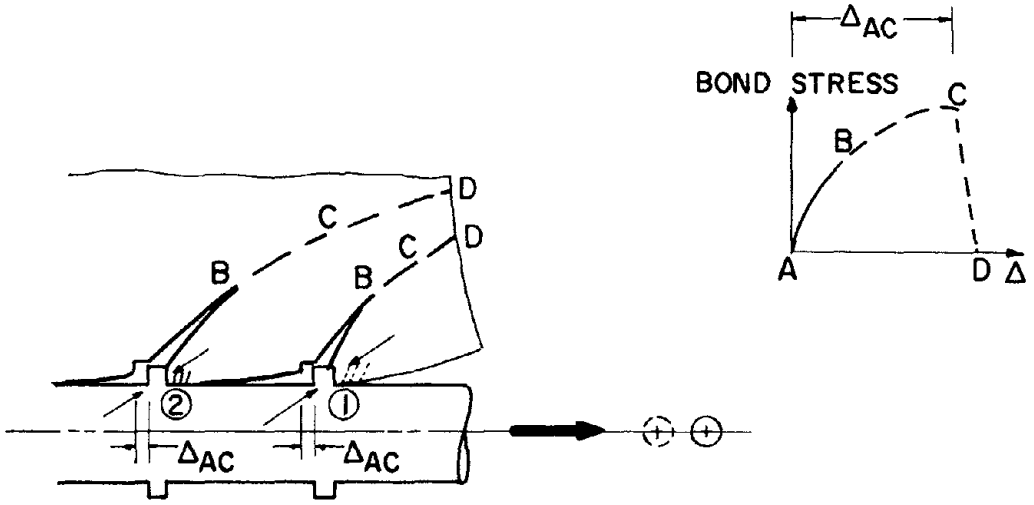

(b) Crack Propagation Stage (Loaded from A-B-C-D) and Failure Mode

Fig. 7.8 Mechanism of Bond Resistance in Unconfined Region (For Monotonic Loading)

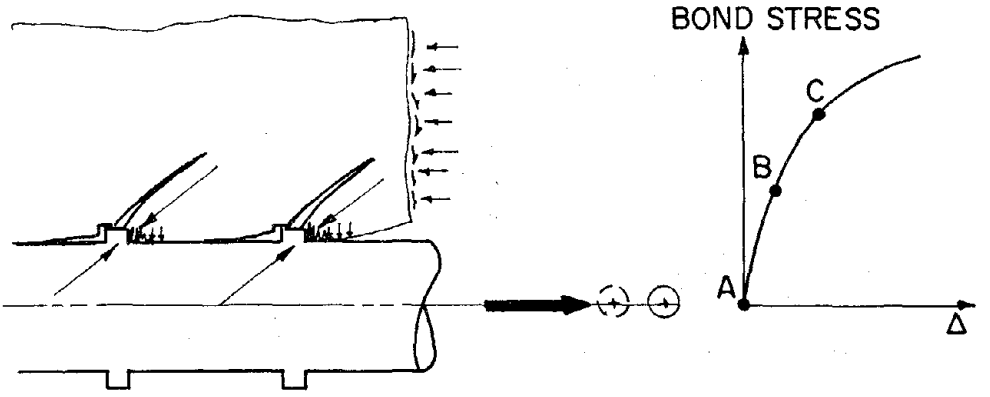

(a) Crack Initiation and Propagation Stage

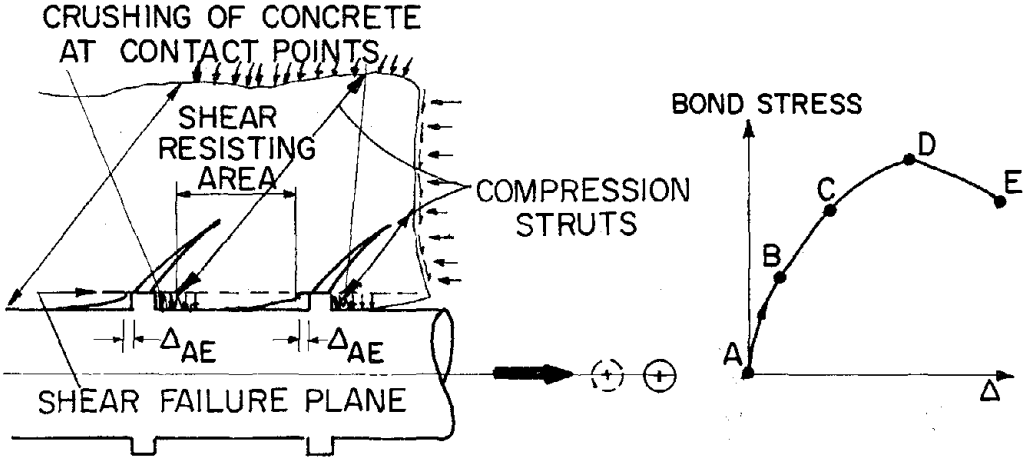

(b) Crushing, Inelastic Deformation of Compression Strut and Successive Reduction in Shear Area

Fig. 7.9 Mechanism of Bond Resistance in Confined Region (for Monotonic Loading)

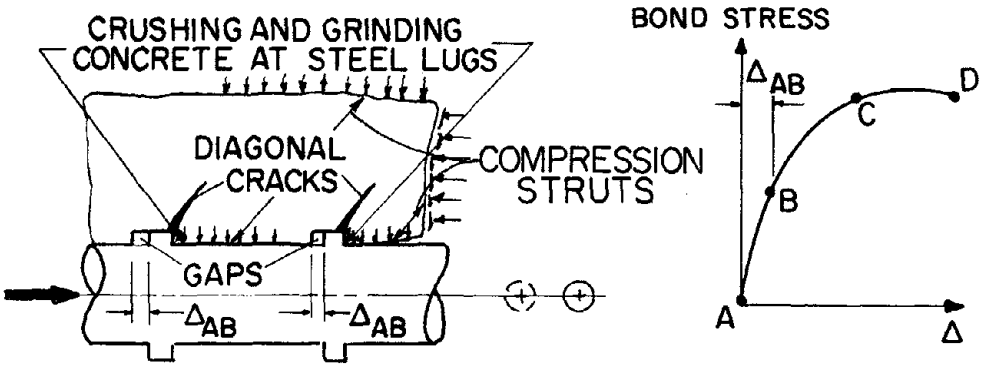

(a) Early Part of Loading: Crushing, Inelastic Deformation of Compression Strut and Increasing in Normal Pressure Around Bar

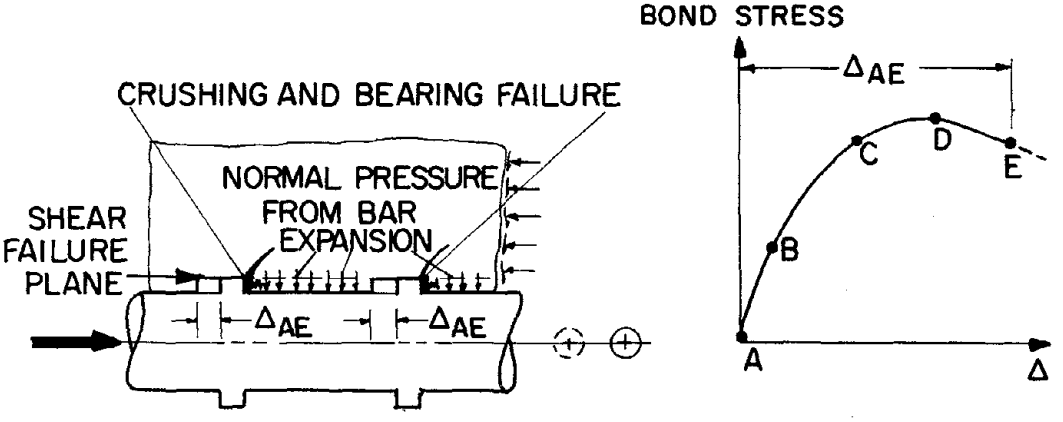

(b) Advanced Stage of Loading: Crushing, Grinding Concrete at Contact Point and Successive Reduction in Concrete Shear Area

Fig. 7.10 Mechanism of Bond Resistance in Pushed End Region (for Monotonic Loading)

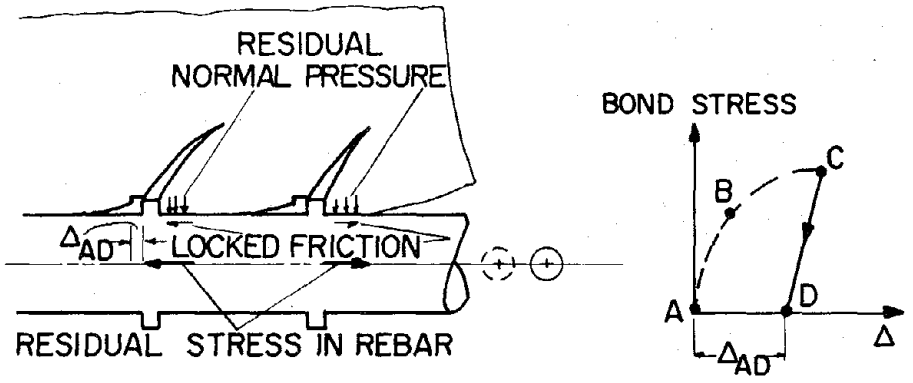

(a) Complete Unloading at D

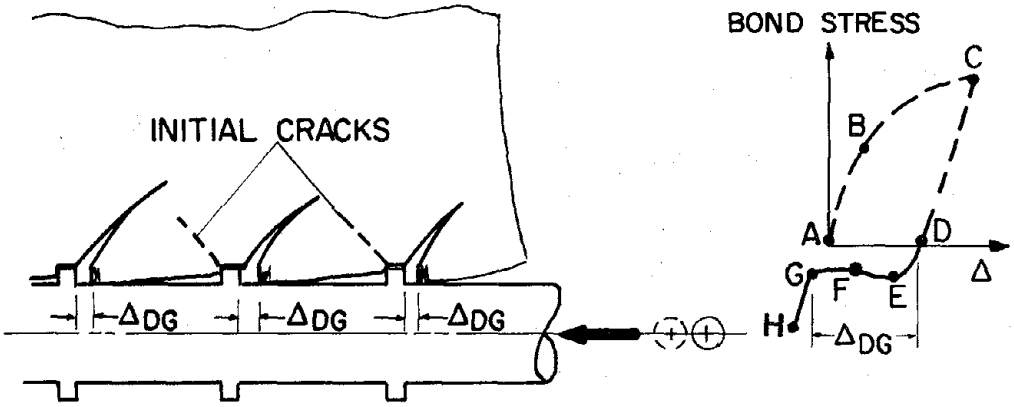

(b) Overcome Friction Resistance (Loading D-E-F-G)

Fig. 7.11 Bond Mechanism of Unconfined Region for Cyclic Loading

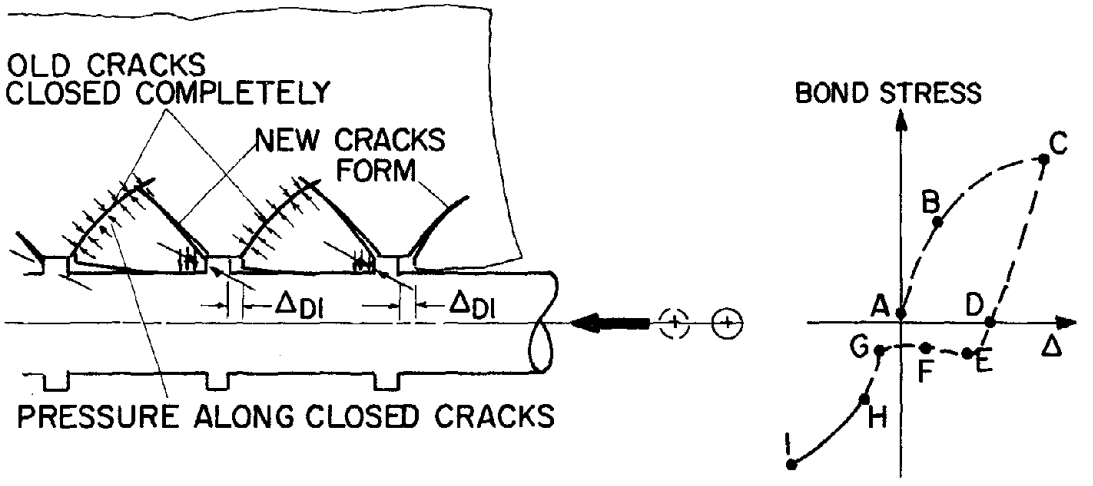

(c) Close Old Cracks and Open New Cracks

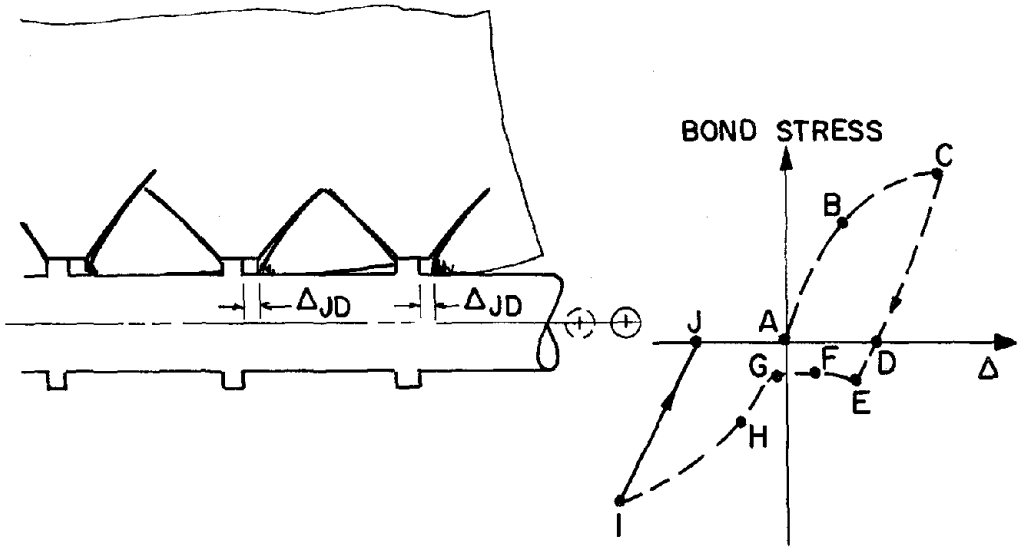

(d) Complete Unloading at J

Fig. 7.11 Bond Mechanism of Unconfined Region for Cyclic Loading

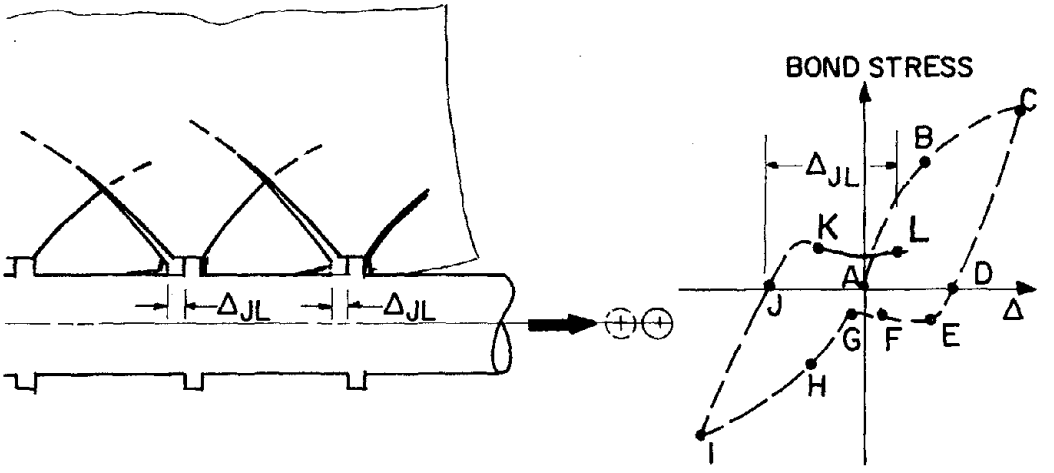

(e) Lugs in Contact with Broken Pieces of Concrete (Loading from K-L)

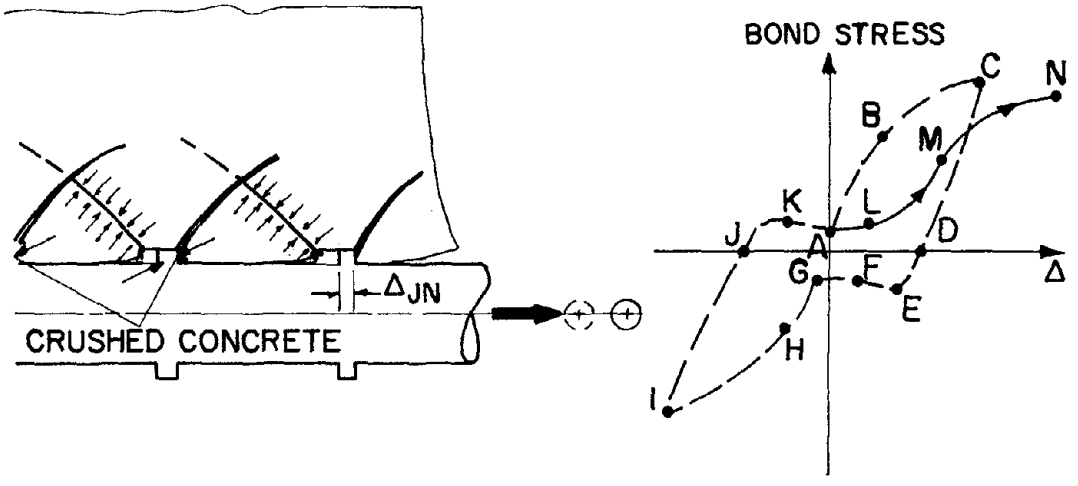

(f) Closing Cracks, Wedging Against Broken Pieces and Failure Mode (Loading from L-M-N-O)

Fig. 7.11 Bond Mechanism of Unconfined Region for Cyclic Loading

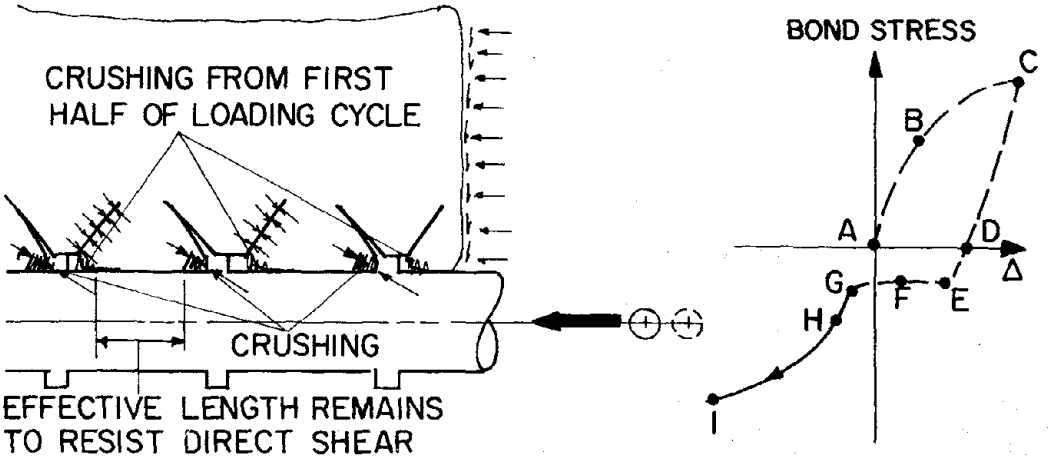

(a) Loading A-B-C, Unloading C-D and Reloading D-E-F-G-H-I

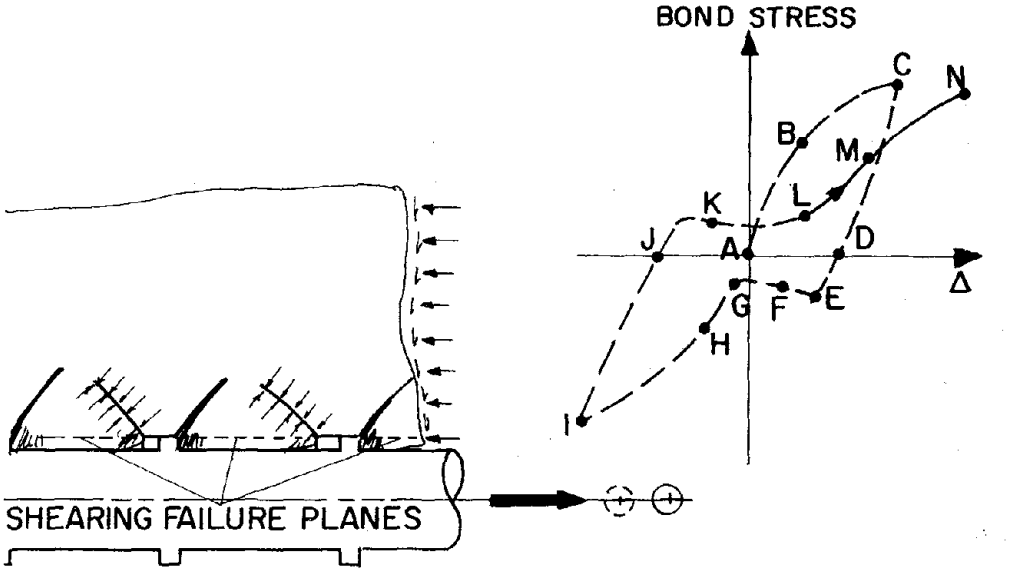

(b) Unloading I-J, Reloading J-K-L-M-N

Fig. 7.12 Bond Mechanism of Confined Region (Cyclic Loading)

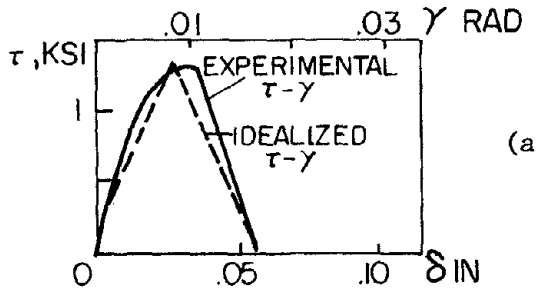

(a) Unconfined Region

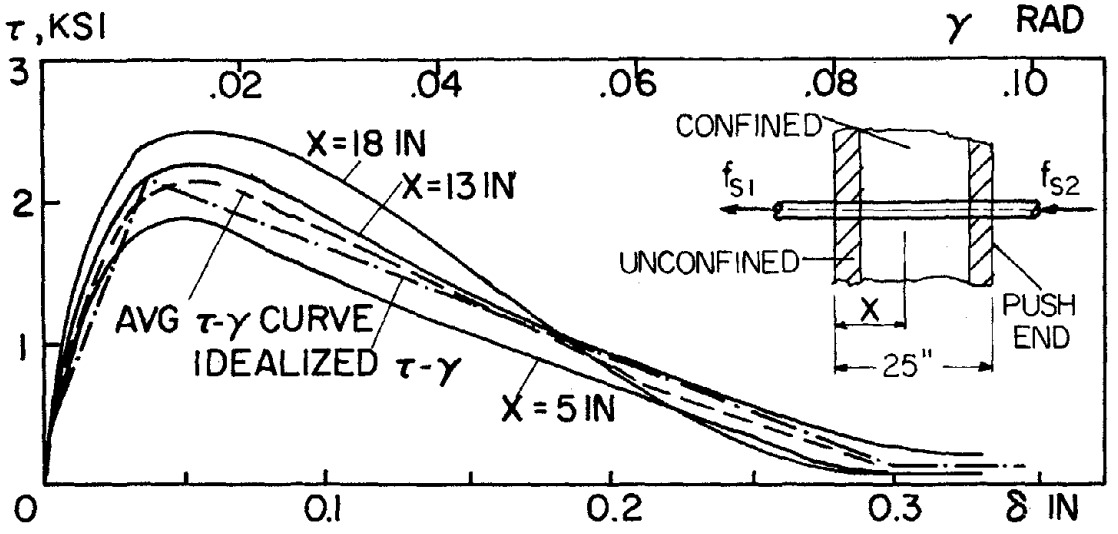

(b) Confined Region

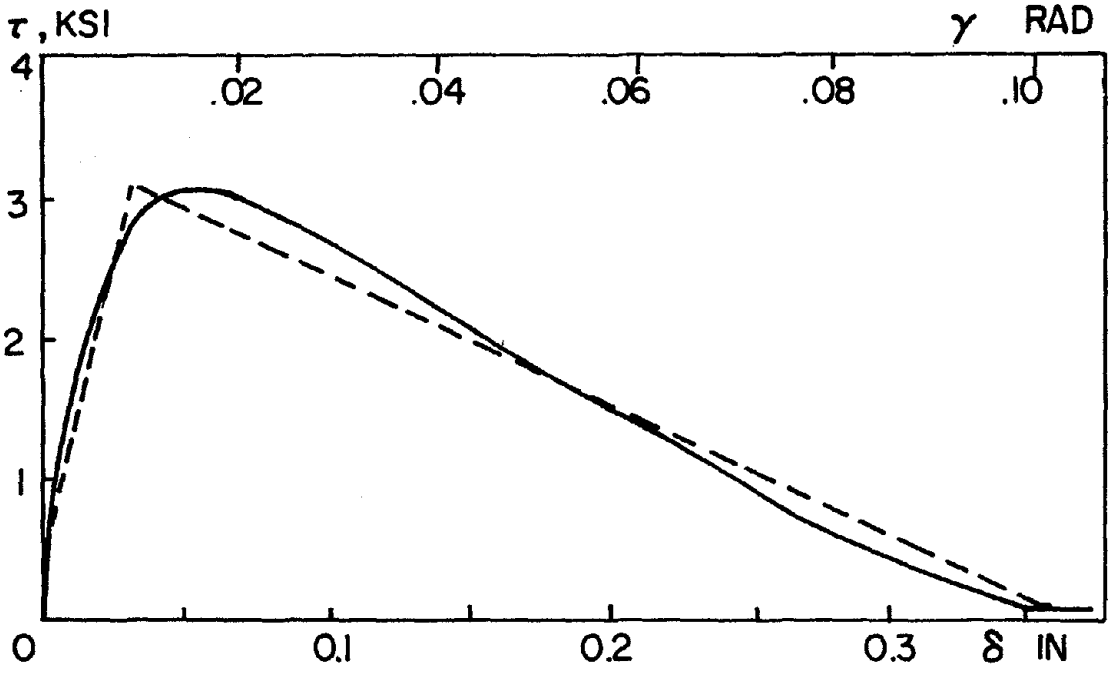

(c) Push-End Region

Fig. 7.13 Experimental and Idealized τ-γ Curve for Monotonic Loading

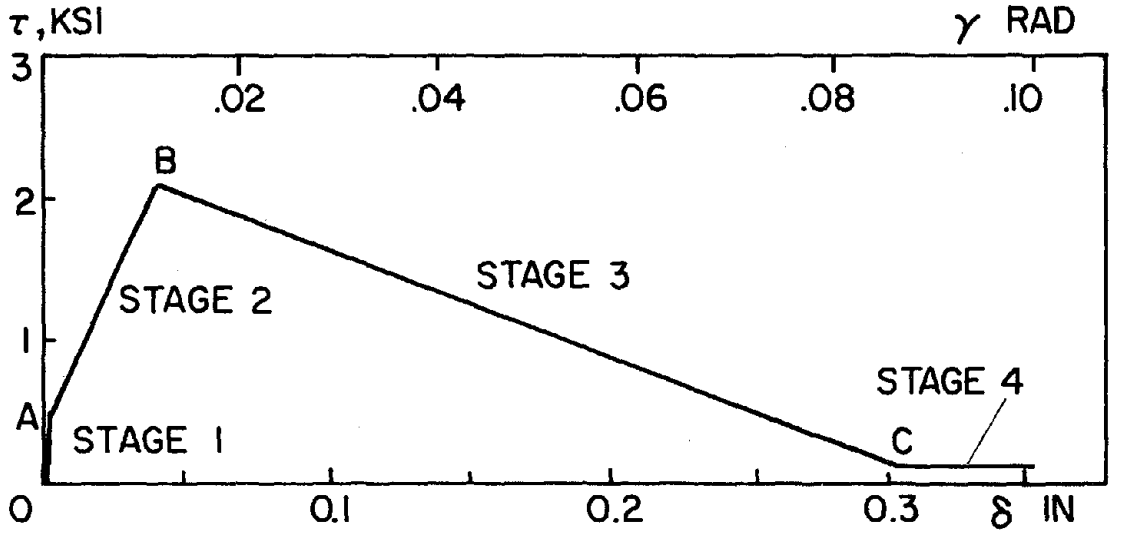

Fig. 7.14 Stages in Idealized Monotonic Skeleton Curve

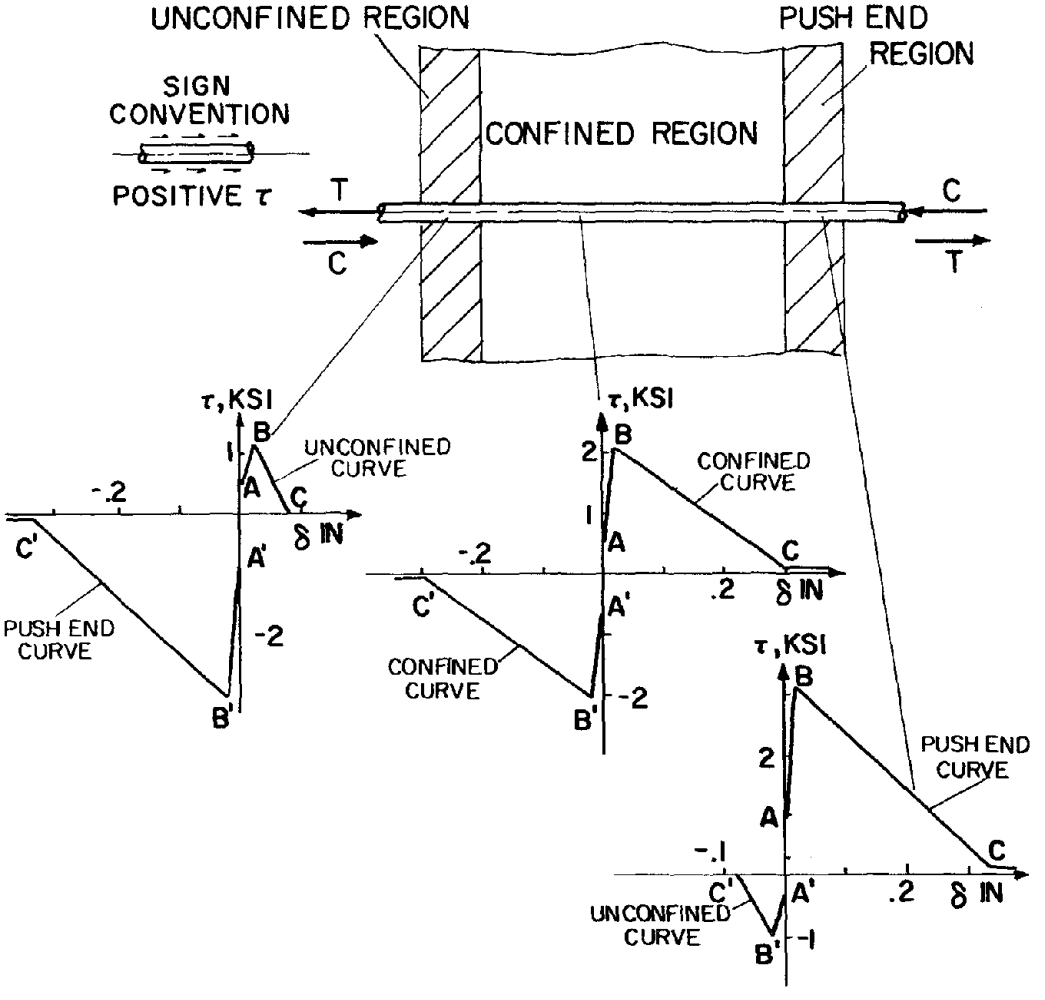

Fig. 7.15 Skeleton Curve for Push and Pull Loading

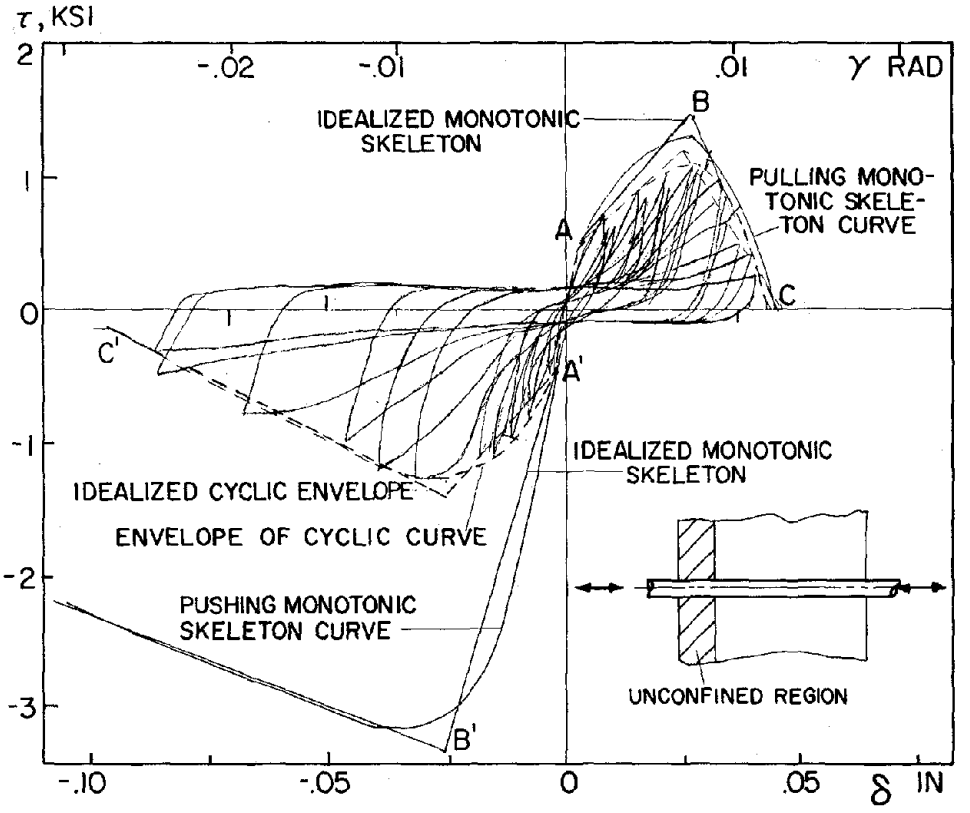

Fig. 7.16 Typical τ-γ Curve for Monotonic and Cyclic Loading (Unconfined Region)

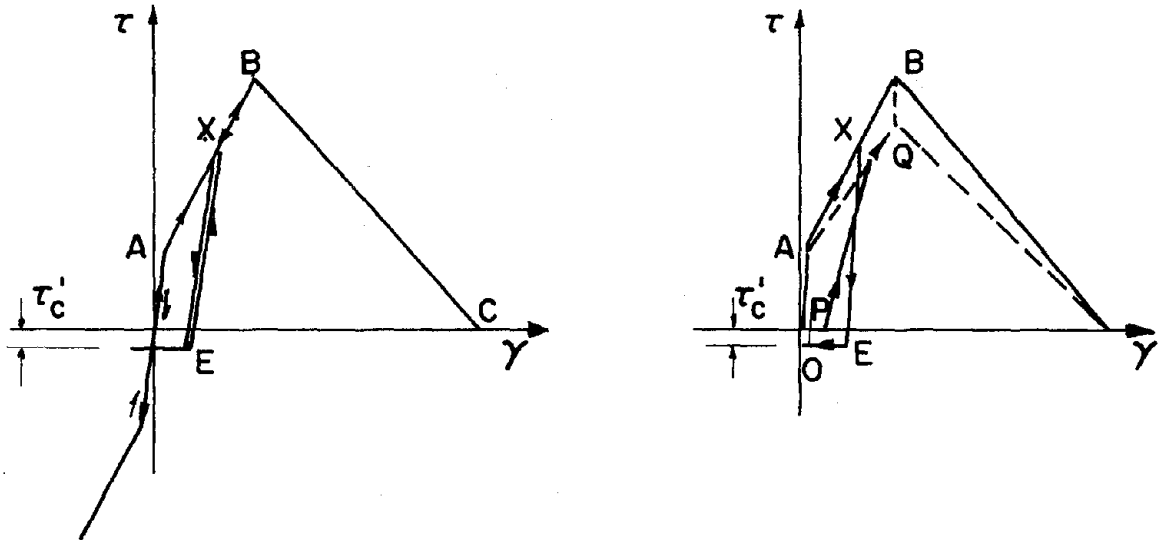

(a) No Reduction: Unloading and Reloading within XE Curve

(b) Reduction: Unloading Past Point E

Fig. 7.17 Loading History Leading to Reduction in Skeleton Curve

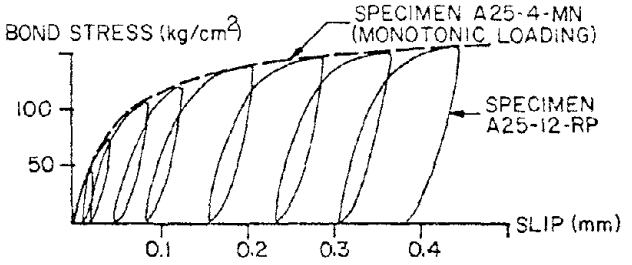

(a) Onesided Loading

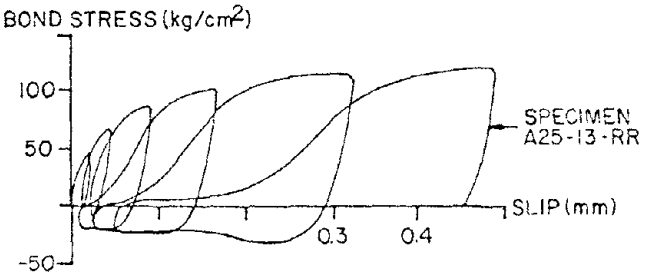

(b) Onesided Loading with Partial Reversal (Pushing)

Fig. 7.18 Experimental Results for Oneside Loading of Bond Slip Curve [Ref. 19]

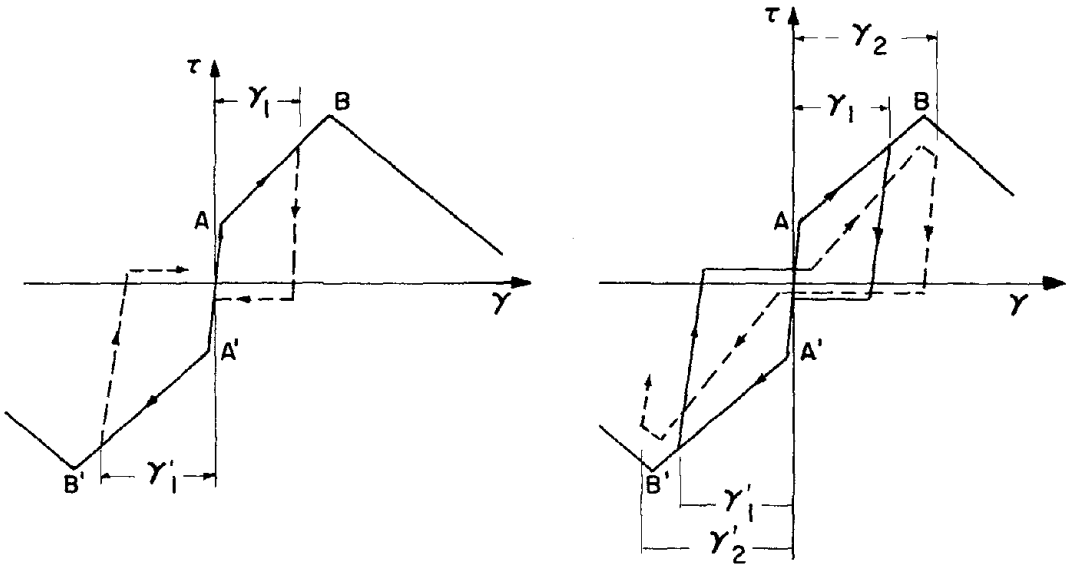

(a) γ_1 and γ_1' (b) γ_1, γ_1', γ_2 and γ_2'

Fig. 7.19 Definition of Effective Past History, γ_i and γ_i'

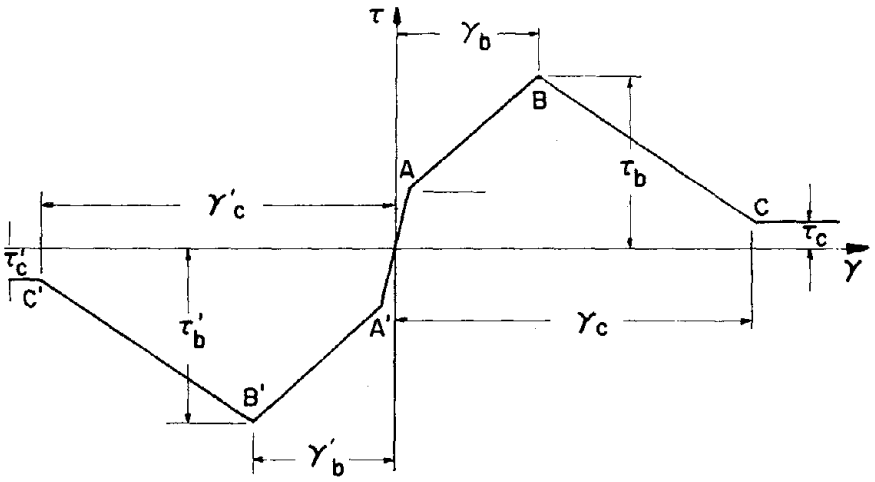

Fig. 7.20 Definition of Monotonic Skeleton Curve

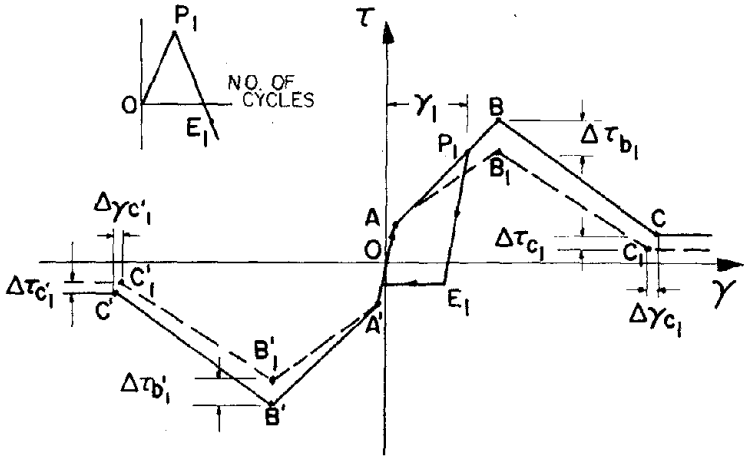

(a) Loading Sequence OP_1E_1

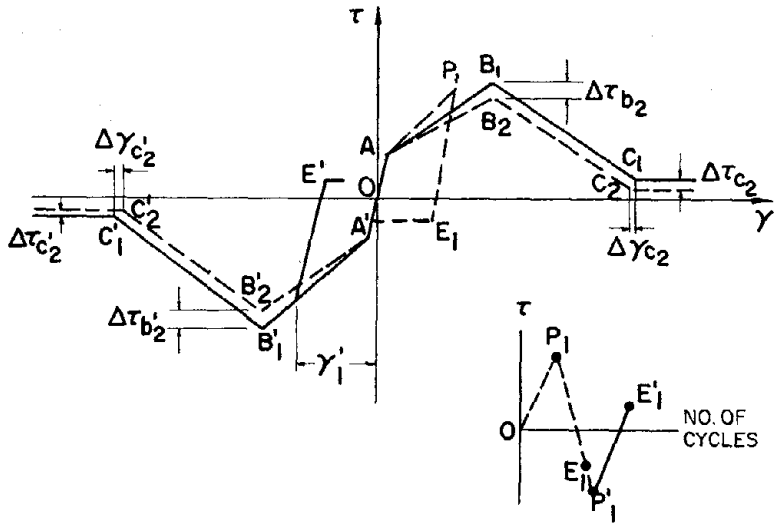

(b) Second Half of Loading Sequence $E_1P_1E'_1$

Fig. 7.21 Sample of Mathematical Formulation for Skeleton Reduction

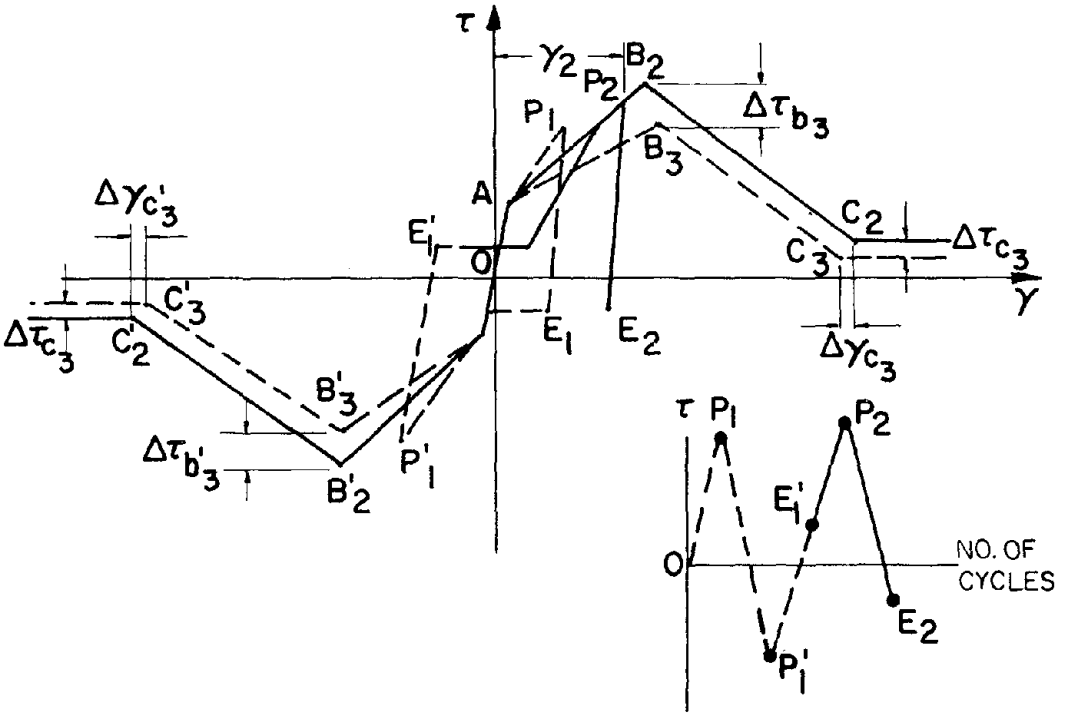

$$\Delta\gamma_{c'3} = \gamma_c \beta_{\gamma c'} \frac{(\gamma_2/\gamma_c)}{P_c} \xi_{\gamma c'} \qquad \Delta\tau_{b3} = \tau_b \alpha_{\tau b} \frac{(\gamma_2/\gamma_b)}{P_b} \xi_{\tau b}$$

$$\Delta\tau_{c'3} = \tau_{c'} \beta_{\tau c'} \frac{(\gamma_2/\gamma_c)}{P_c} \xi_{\gamma c'} \qquad \Delta\tau_{c3} = \tau_c \alpha_{\tau c} \frac{(\gamma_2/\gamma_c)}{P_c} \xi_{\tau c}$$

$$\Delta\tau_{b'3} = \tau_{b'} \beta_{\tau b} \frac{(\gamma_2/\gamma_b)}{P_b} \xi_{\tau b'} \qquad \Delta\gamma_{c3} = \gamma_c \alpha_{\gamma c} \frac{(\gamma_2/\gamma_c)}{P_c} \xi_{\gamma c}$$

(c) Third Half of Loading Sequence $E'_1 P_2 E_2$

Fig. 7.21 Sample of Mathematical Formulation for Skeleton Reduction

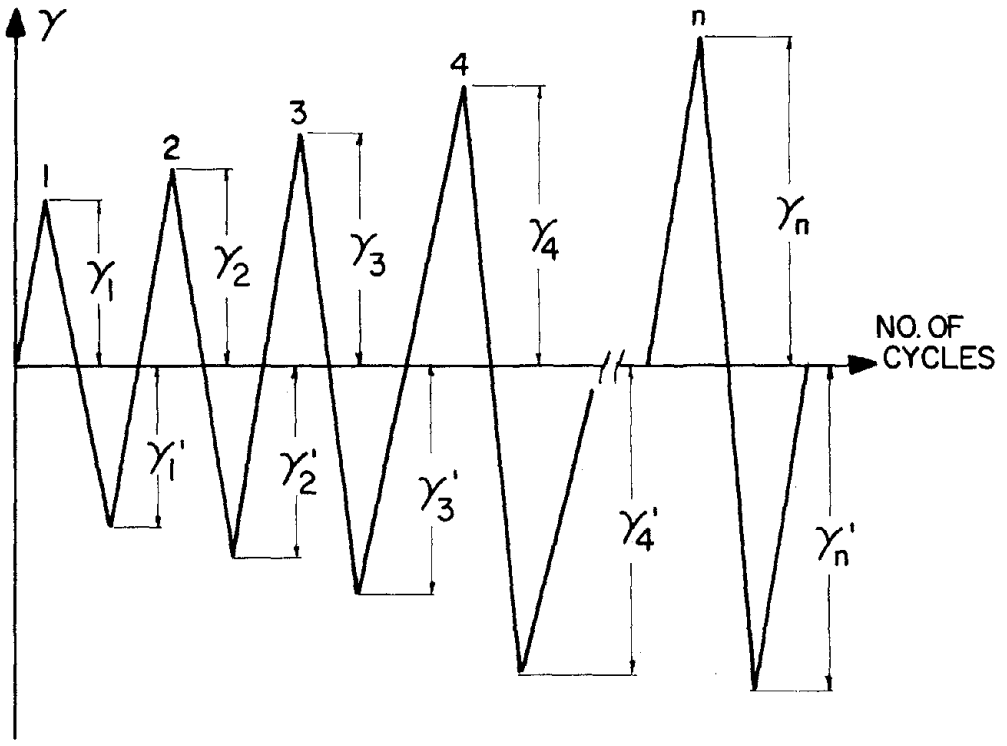

Fig. 7.22 Cyclic Loading History

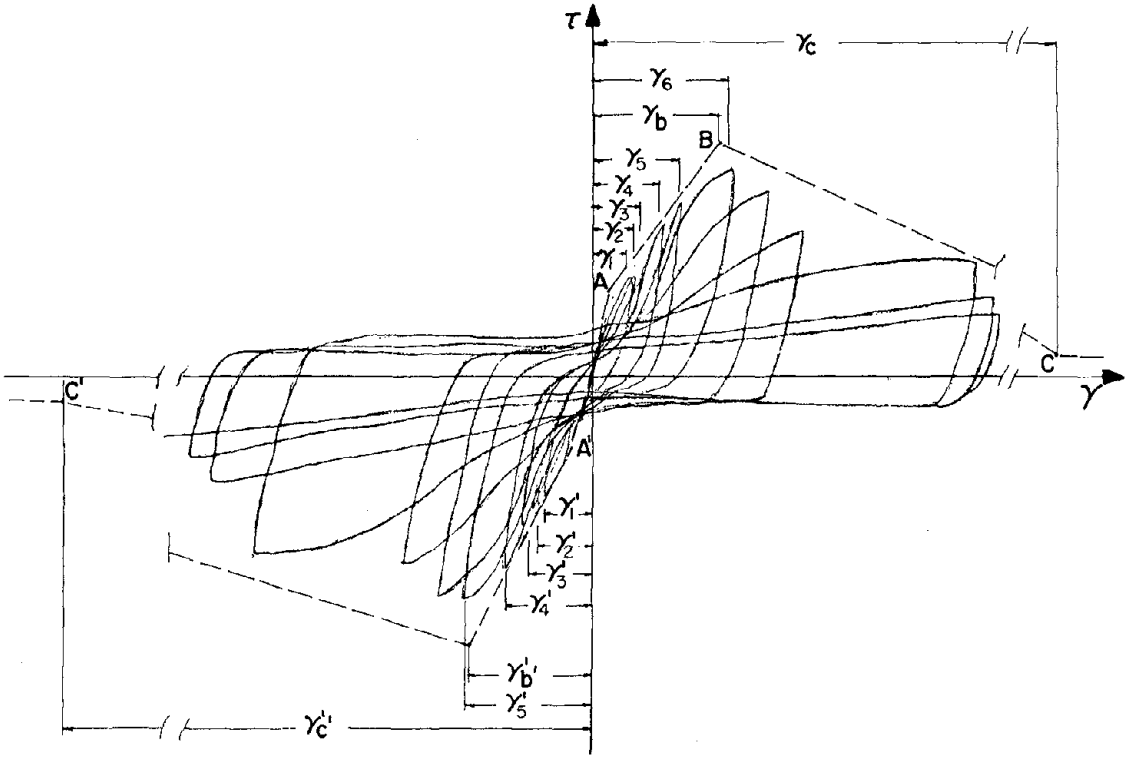

Fig. 7.23 Estimation of γ_s and γ_s' from Experimental Results

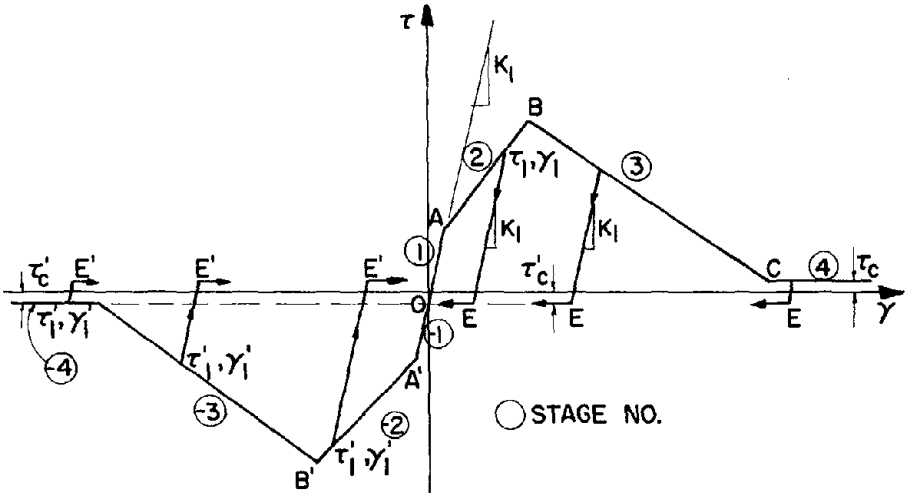

(a) Unloading from Stage 2, 3, 4, -2, -3 and -4 Produce Permanent Set

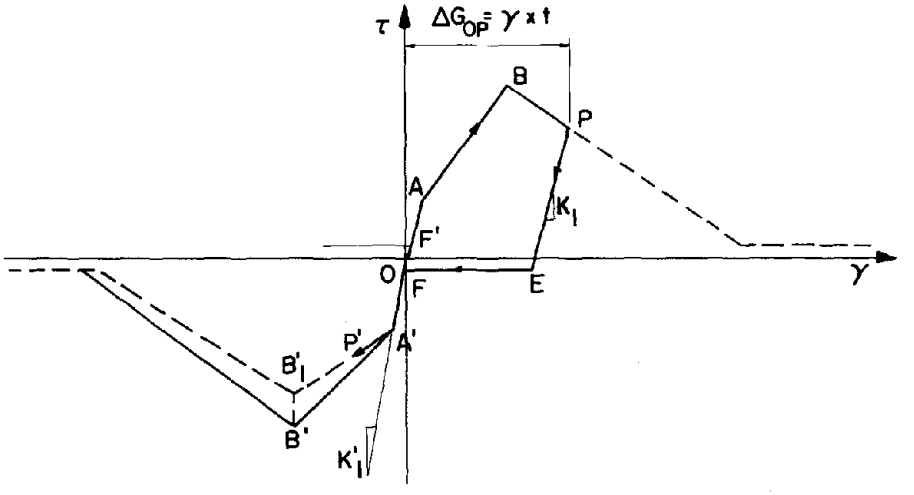

(b) Loading Sequence O-A-B-P-E-F-A'-P'
(First Time to Enter Third Quadrant)

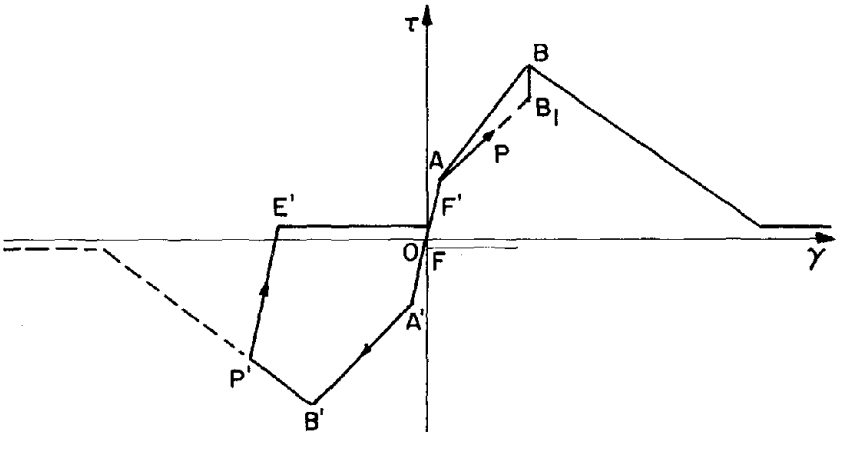

(c) Loading Sequence O-A'-B'-P'-E'-F'-A-P

Fig. 7,24 Hysteretic Rules for Bond (Cyclic Loading)

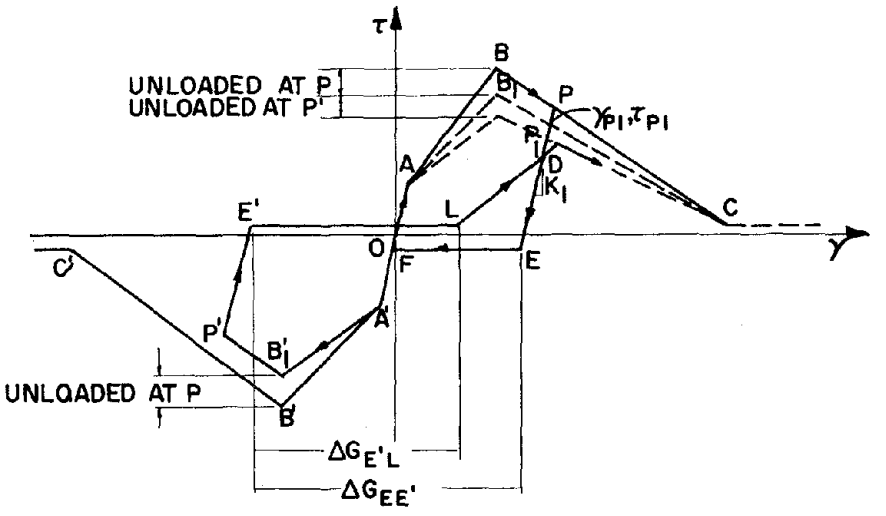

(d) Loading Reversal Sequence O-A-B-P-E-F-A'-B_1'-P'-E'-L-D
(Creation of Controlling Points P_1, D, E, P)

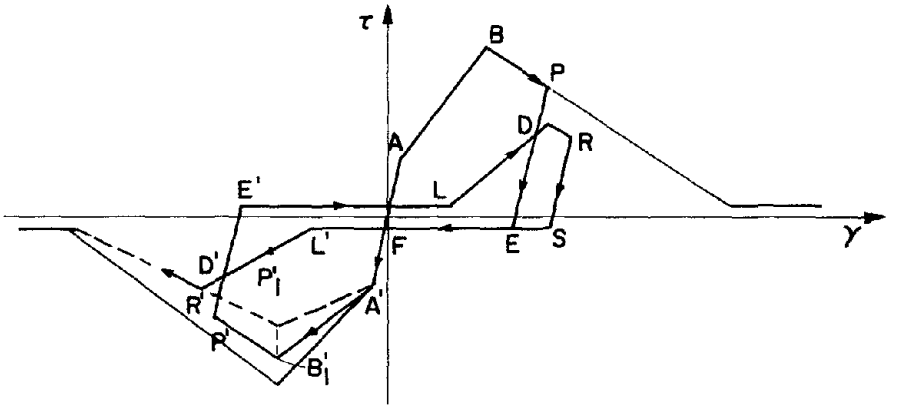

(e) Load Reversal Sequence O-A-B-P-E-F-A'-B_1'-P'-E'-L-D-R-S-L'-D'-R'
(Creation of Controlling Point P_1', D', E', P', L')

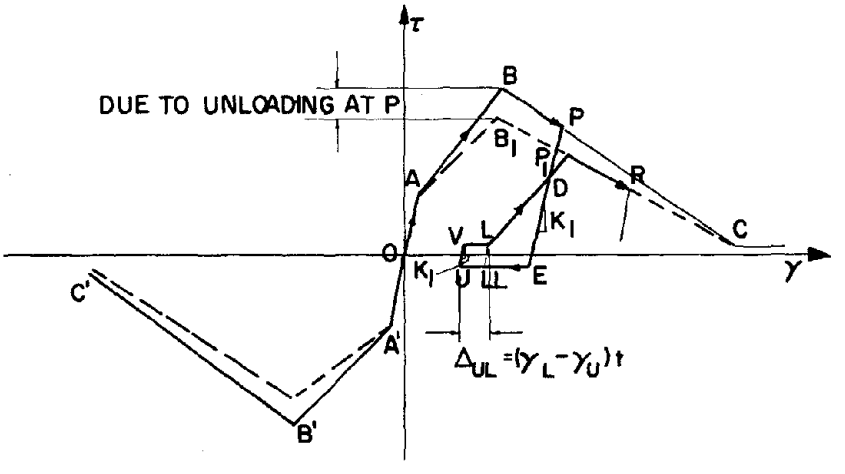

(f) Loading Path O-A-B-P-E-U-V-L-D-R ($\gamma_u \geq \gamma_{\ell\ell}$)

Fig. 7.24 Hysteretic Rules for Bond (Cyclic Loading)

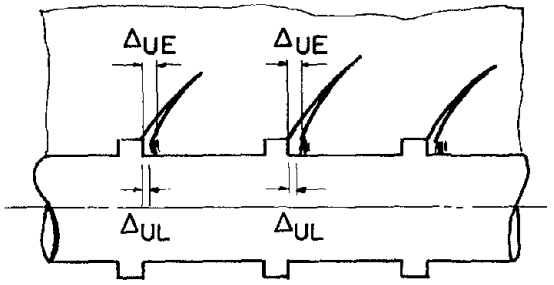

(f_1) Bar Retracted Far Enough Before Reloading

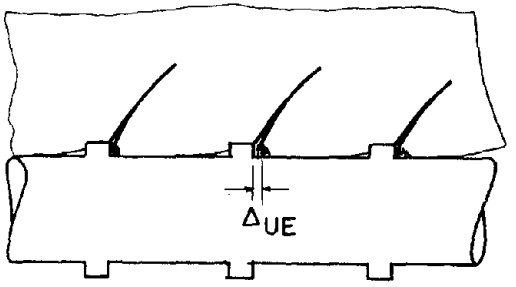

(g_1) Lug in Contact with Disrupted Concrete

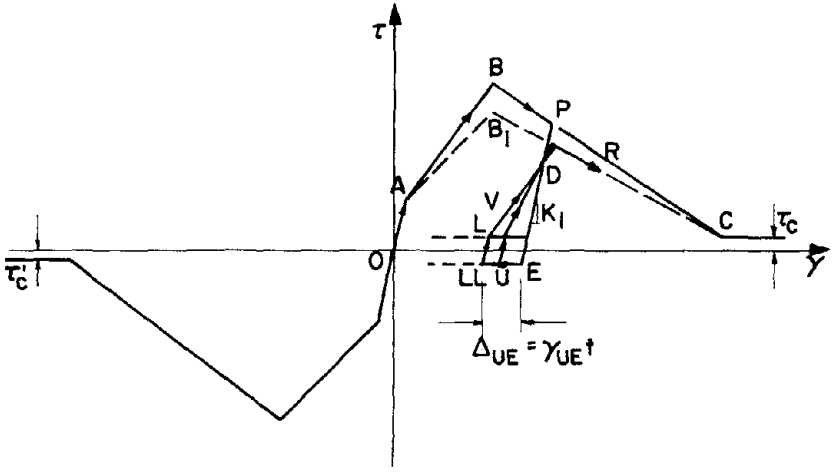

(g) Loading Path O-A-B-P-E-U-V-D-R ($\gamma_u < \gamma_{\ell\ell}$)

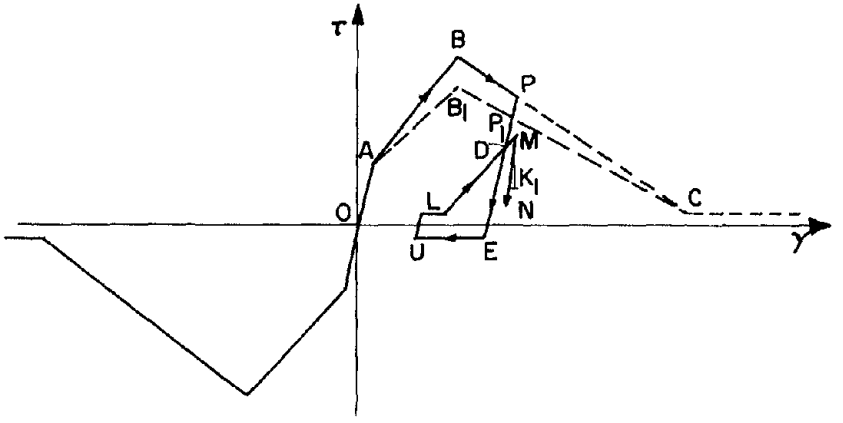

(h) Loading Path O-A-B-P-E-U-O-M-N
(Unloading from Secondary Curve $\gamma_M > \gamma_d$)

Fig. 7.24 Hysteretic Rules for Bond (Cyclic Loading)

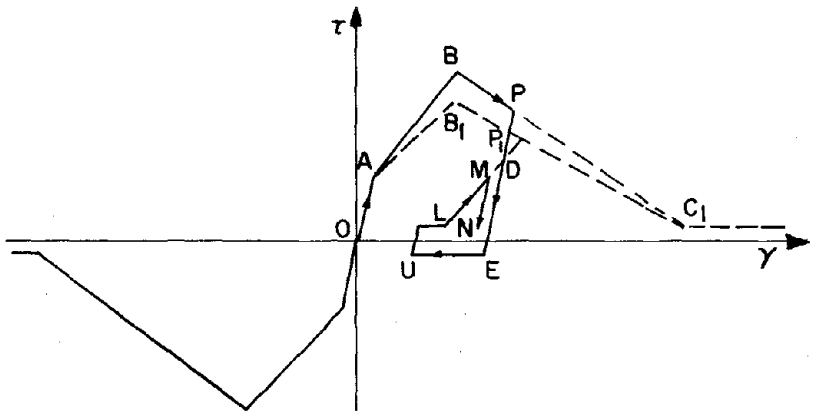

(i) Loading Path O-A-B-P-E-U-L-M-N
(Unloading from Secondary Curve $\gamma_M < \gamma_d$)

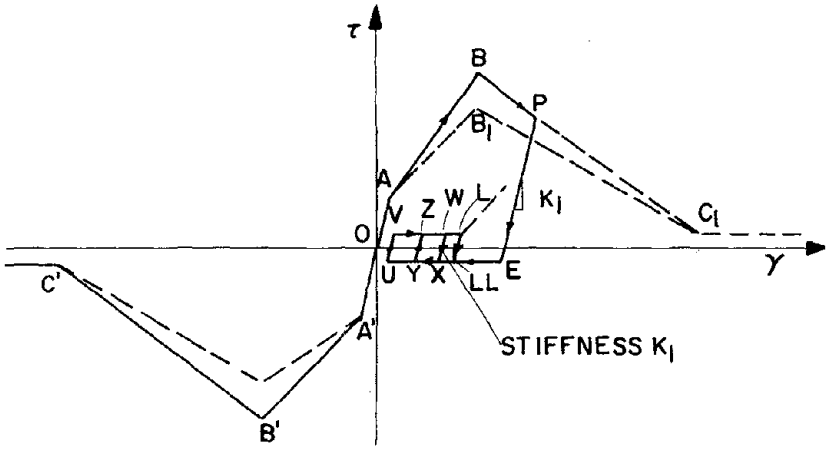

(j) Loading Path O-A-B-P-E-U-V-W-X-Y-Z
(Reload and Unload within Friction Range)

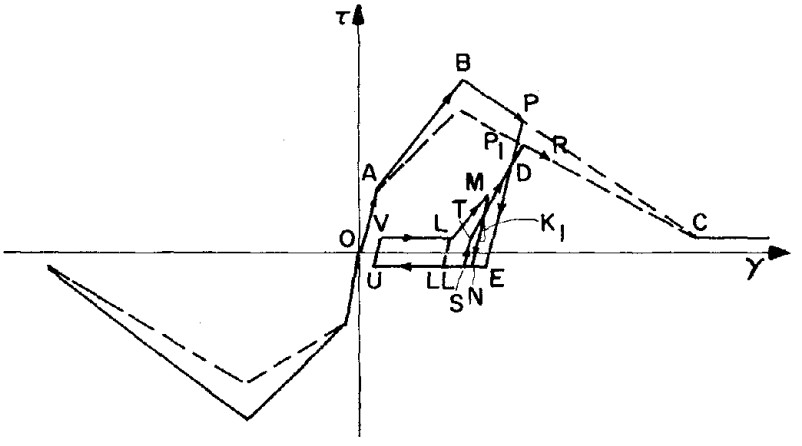

(k) Loading Path O-A-B-P-E-U-V-L-M-N-S-D-T
(L-M-N-S-T-D Loading and Unloading, $\gamma_{LL} < \gamma < \gamma_d$)

Fig. 7.24 Hysteretic Rules for Bond (Cyclic Loading)

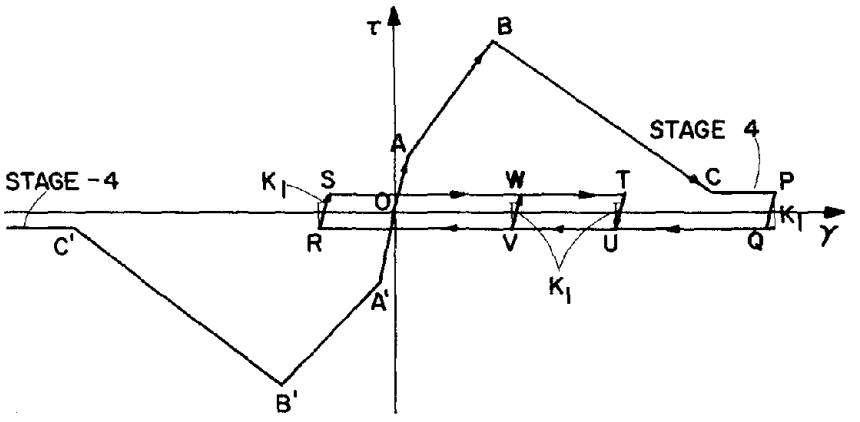

(ℓ) Loading Path O-A-B-C-P-Q-R-S-T-U-V-W
(Loading Back and Forth After Entry Stage 4 and -4)

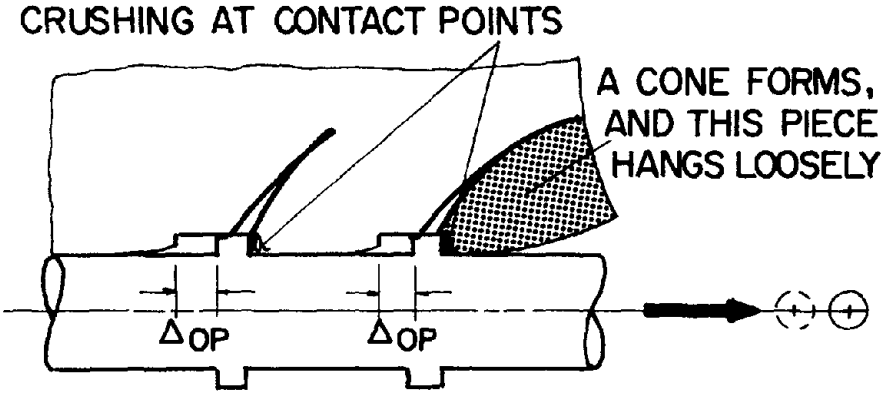

(ℓ_1) Failure Mode (Unconfined Region)

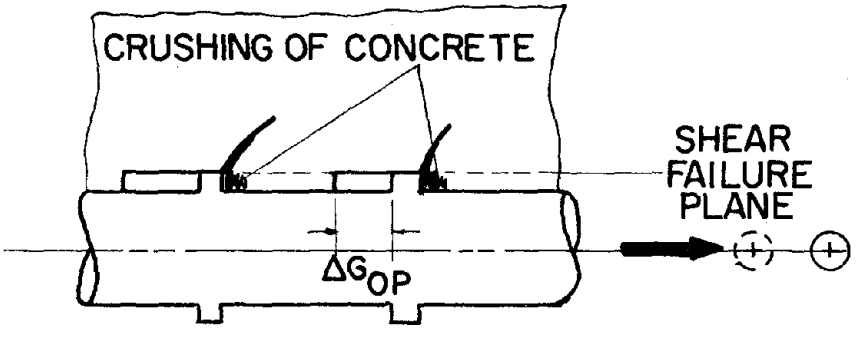

(ℓ_2) Failure Mode (Confined and Pushed End Regions)

Fig. 7.24 Hysteretic Rules for Bond (Cyclic Loading)

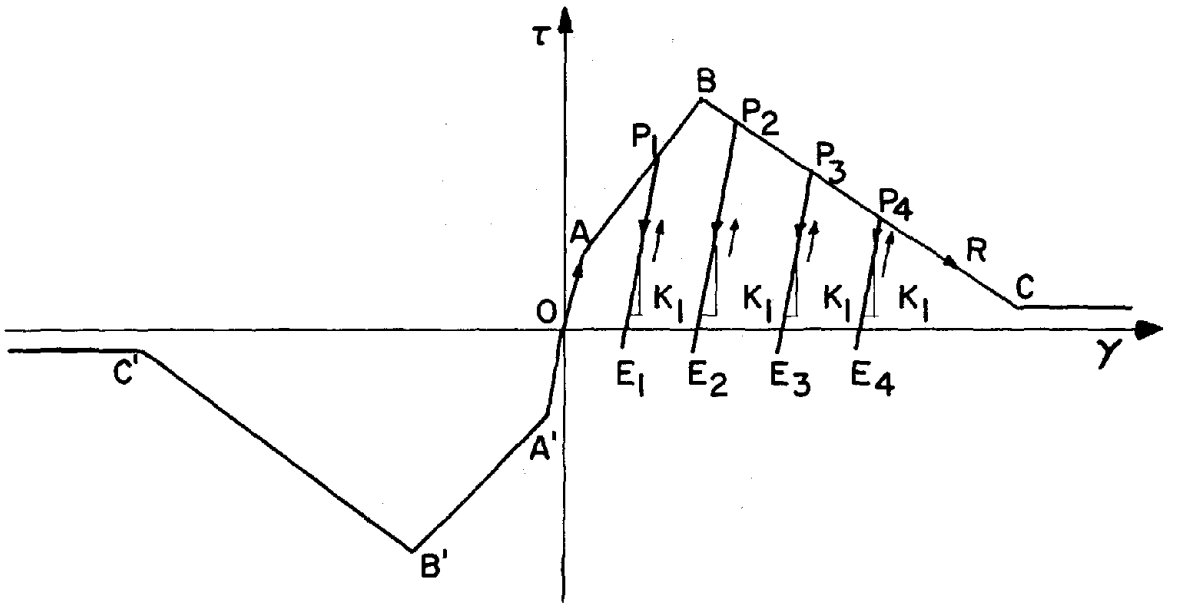

(m) Repeating One Sided Loading

Fig. 7.24 Hysteretic Rules for Bond (Cyclic Loading)

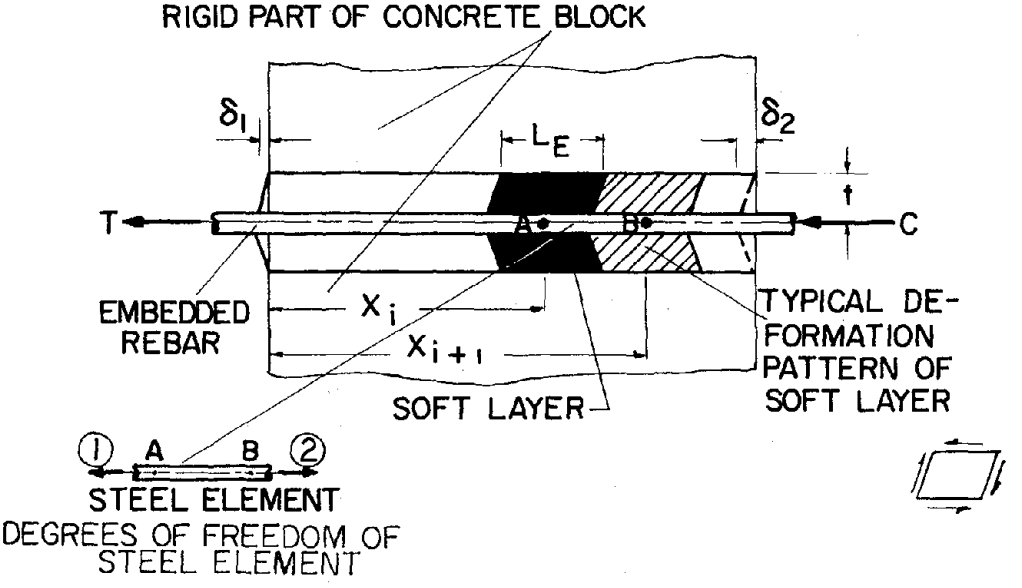

Fig. 7.25 Physical Prescription of Concrete Block

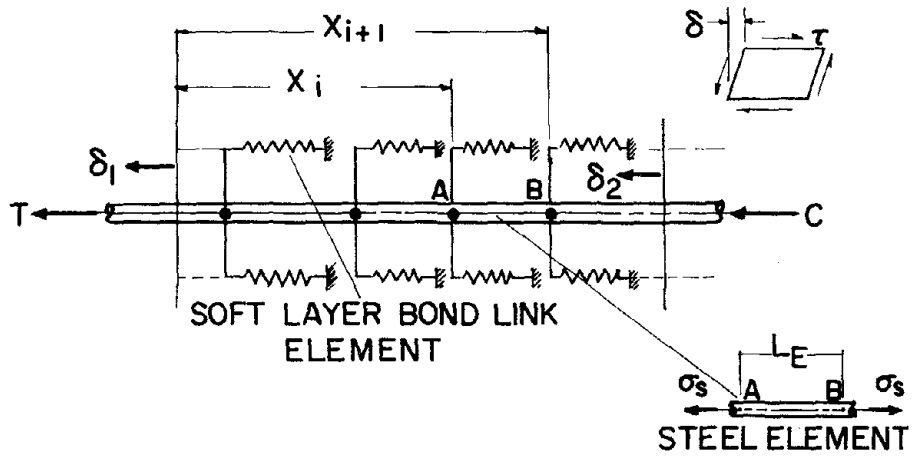

Fig. 7.26 Idealization of Concrete Block with a Bar Embedded

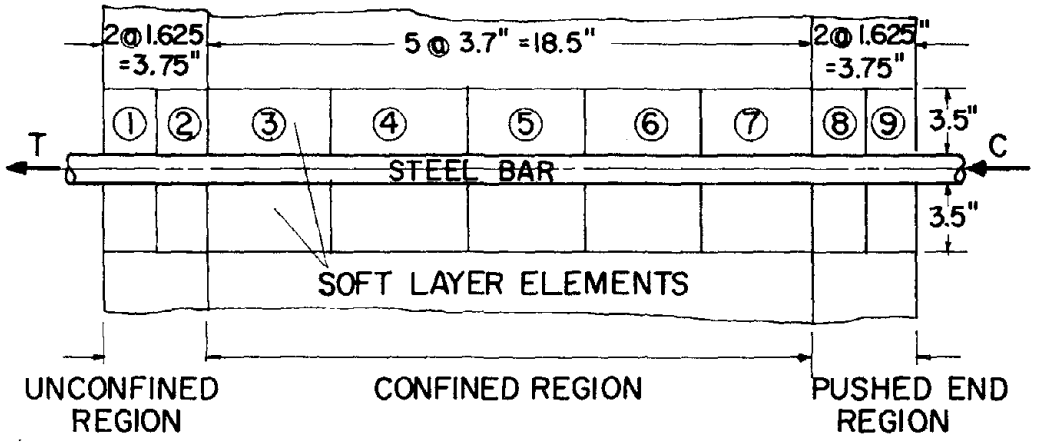

(a) Layout of Steel and Soft Layer Elements

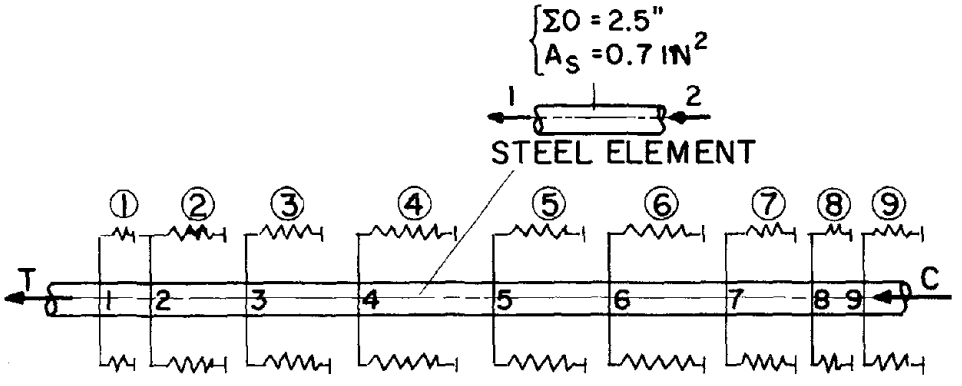

(b) Mathematical Model

Fig. 7.27 Information for Analytical Prediction of #8 Bar, Push-Pull Loading

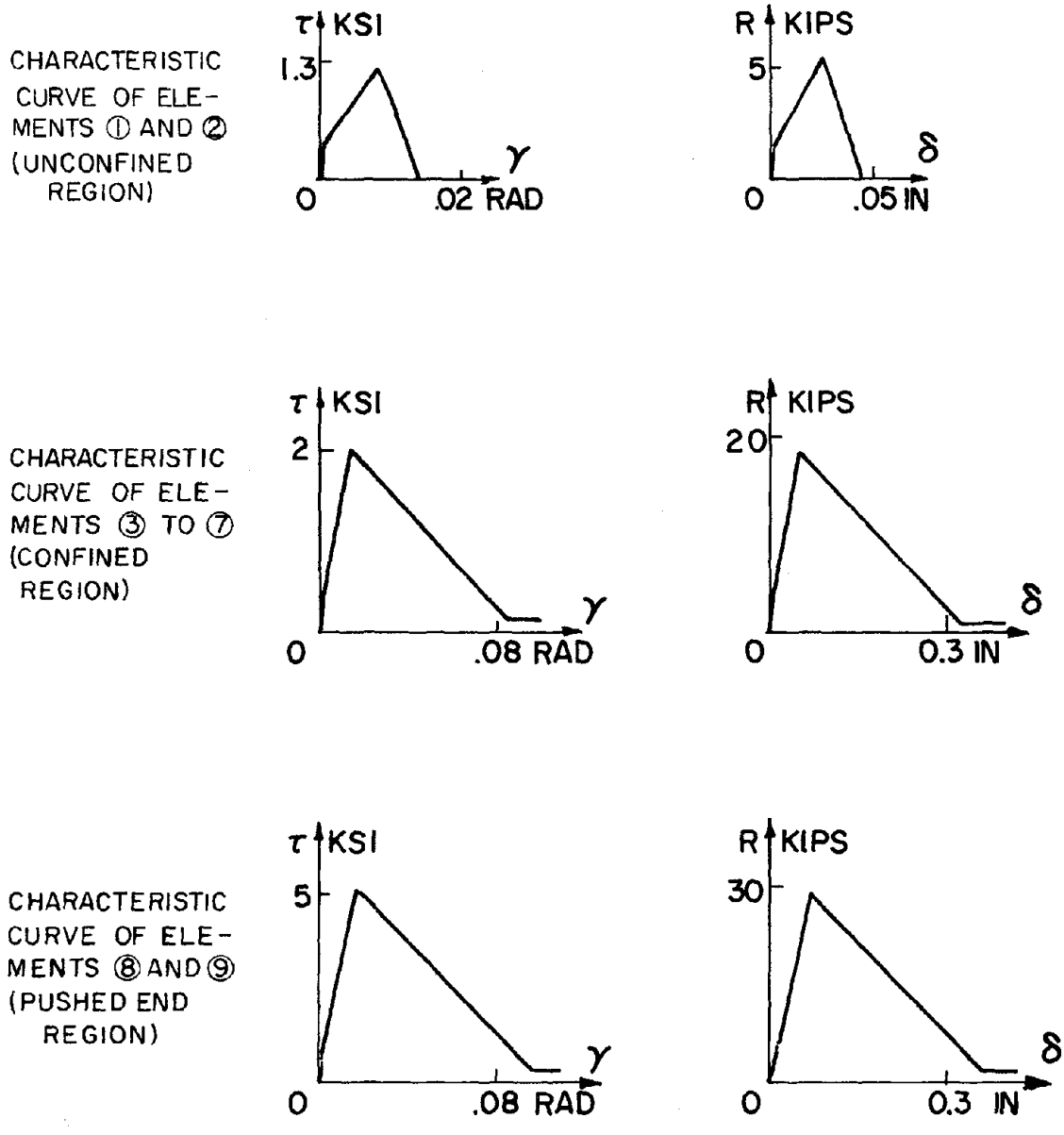

(c) Mechanical Properties of Soft Layer Elements

Fig. 7.27 Information for Analytical Prediction of #8 Bar, Push-Pull Loading

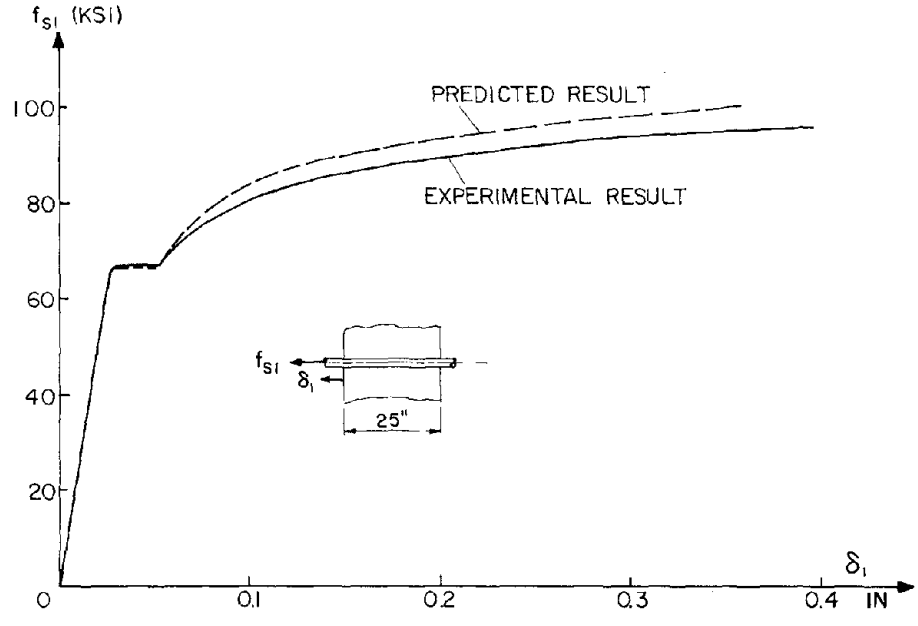

(a) #8 Pull Only, 25 in. Column (Specimen No. 7)

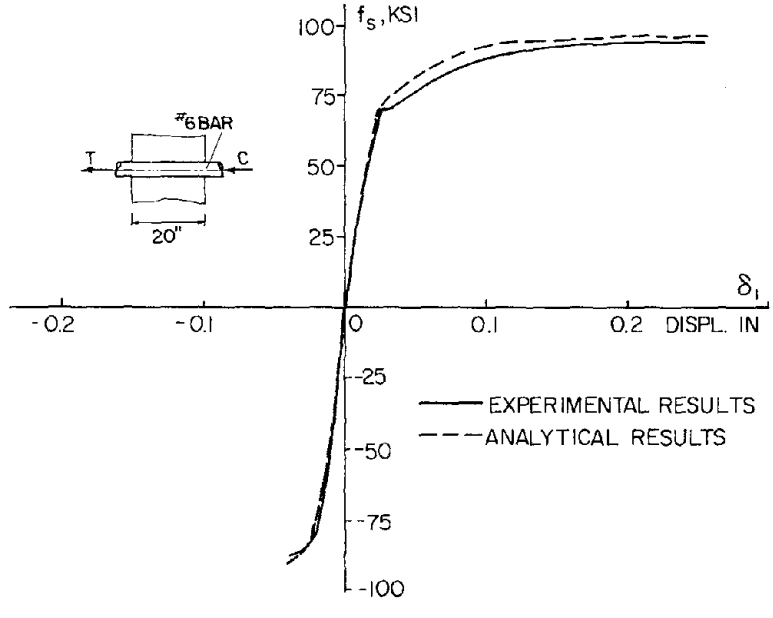

(b) #6, 20 in. Column (Specimen No. 10)

Fig. 7.28 Analytical Prediction vs. Experimental Results for Monotonic Loading

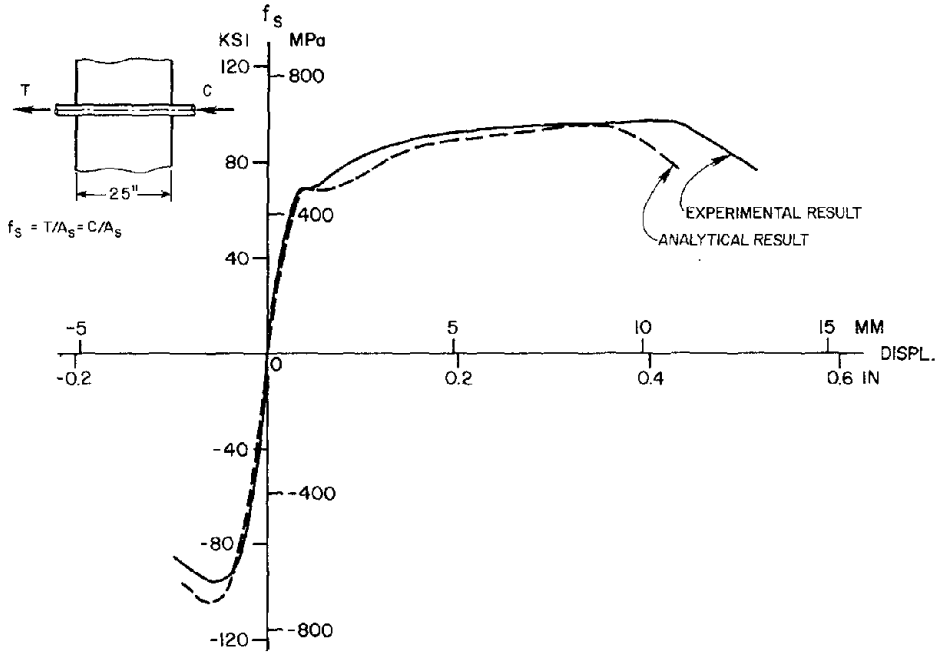

(c) #8, 25 in. Column (Specimen No. 13)

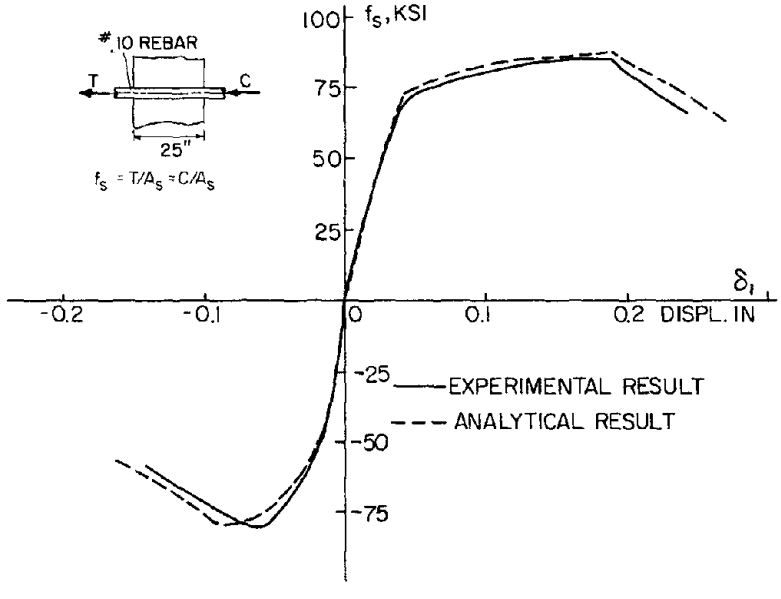

(d) #10, 25 in. Column (Specimen No. 13)

Fig. 7.28 Analytical Prediction vs. Experimental Results for Monotonic Loading

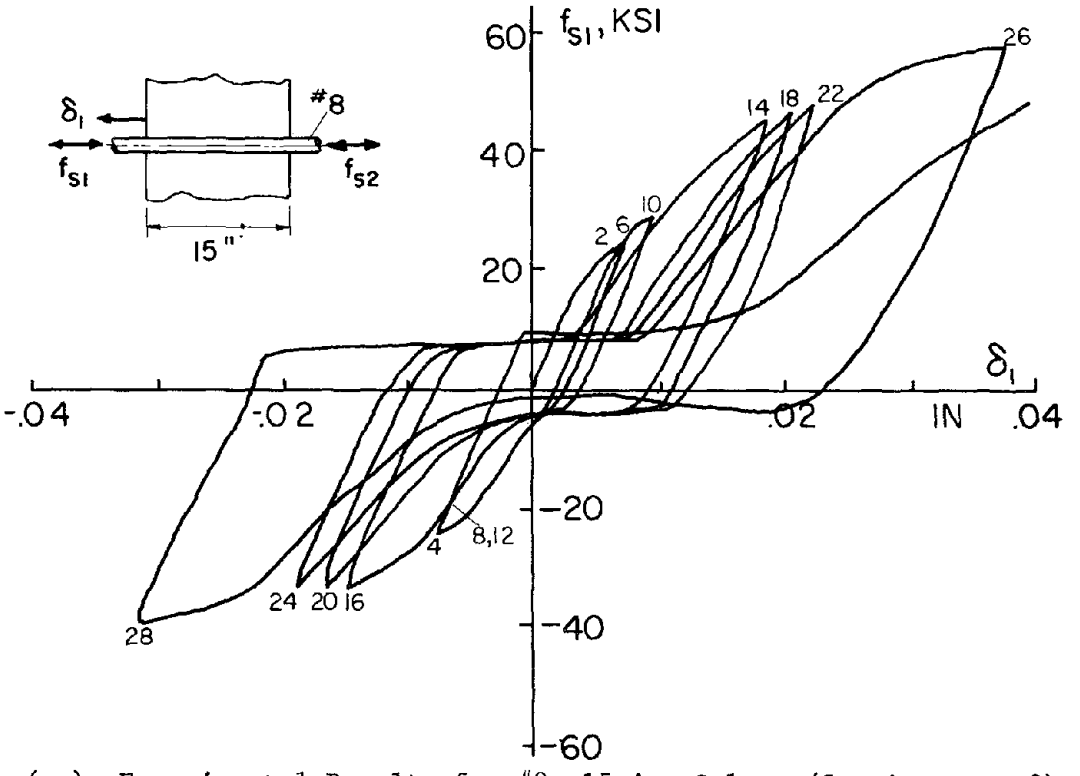

(a_1) Experimental Results for #8, 15 in. Column (Specimen No. 8)

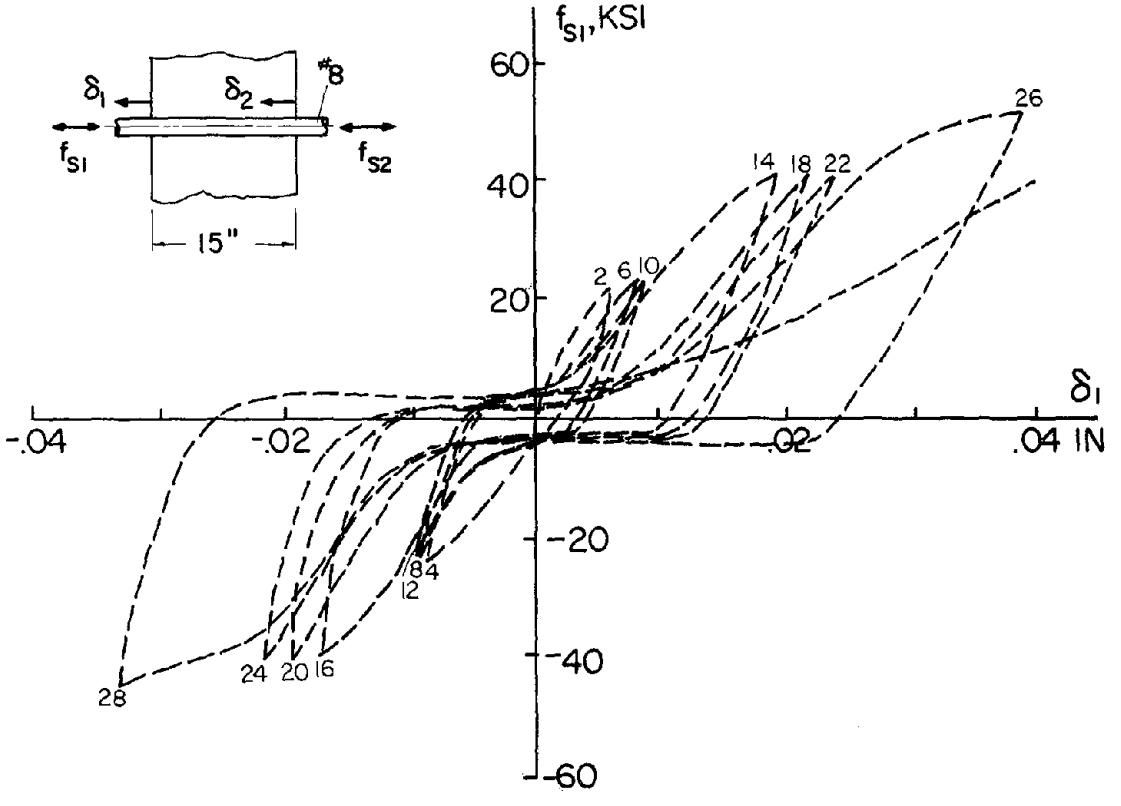

(a_2) Analytical Prediction for #8, 15 in. Column (Specimen No. 8)

Fig. 7.29 Experimental vs. Analytical Prediction for Cyclic Loading

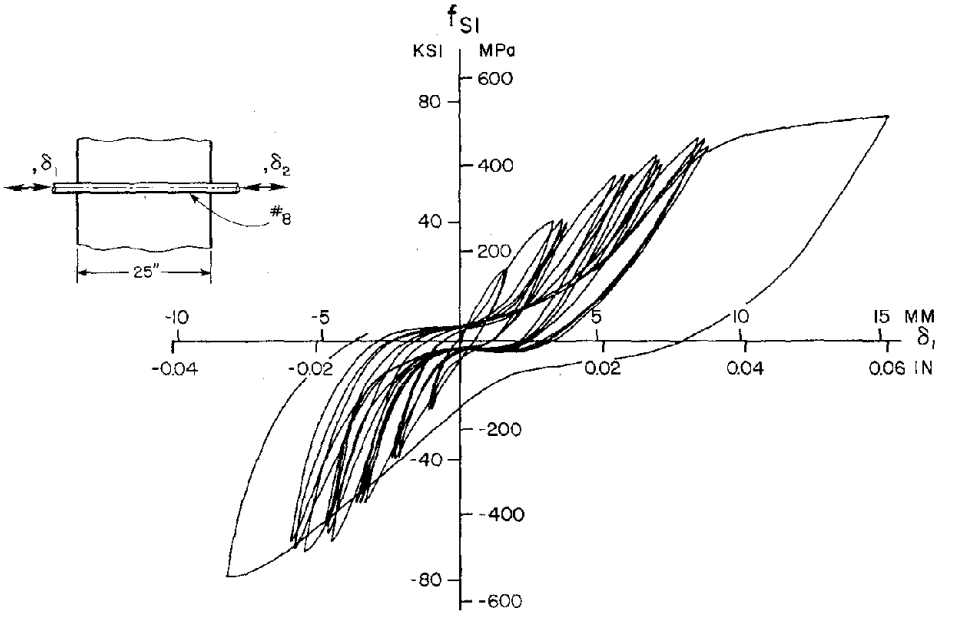

(b_1) Experimental Result for #8, 25 in. Column (Specimen No. 14)

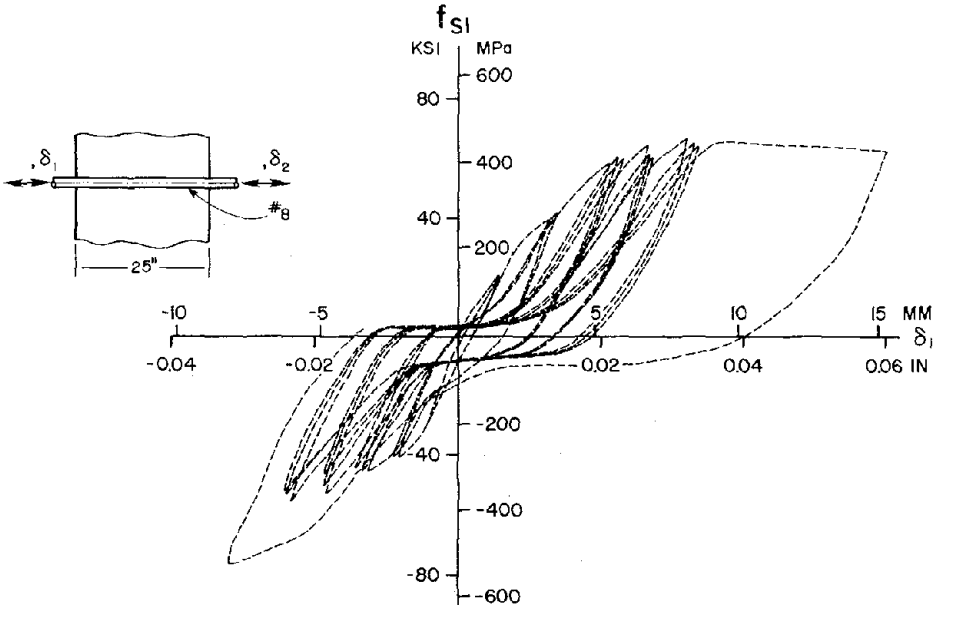

(b_2) Analytical Prediction for #8, 25 in. Column (Specimen No. 14)

Fig. 7.29 Experimental vs. Analytical Prediction for Cyclic Loading

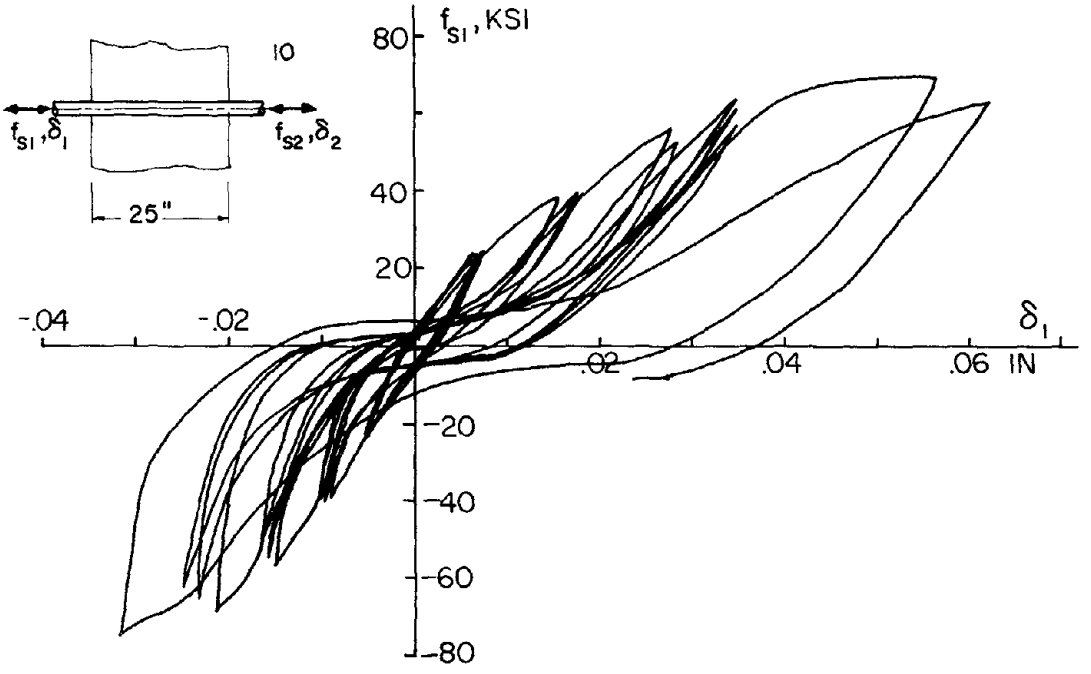

(c_1) Experimental Result for #10, 25 in. Column (Specimen No. 17)

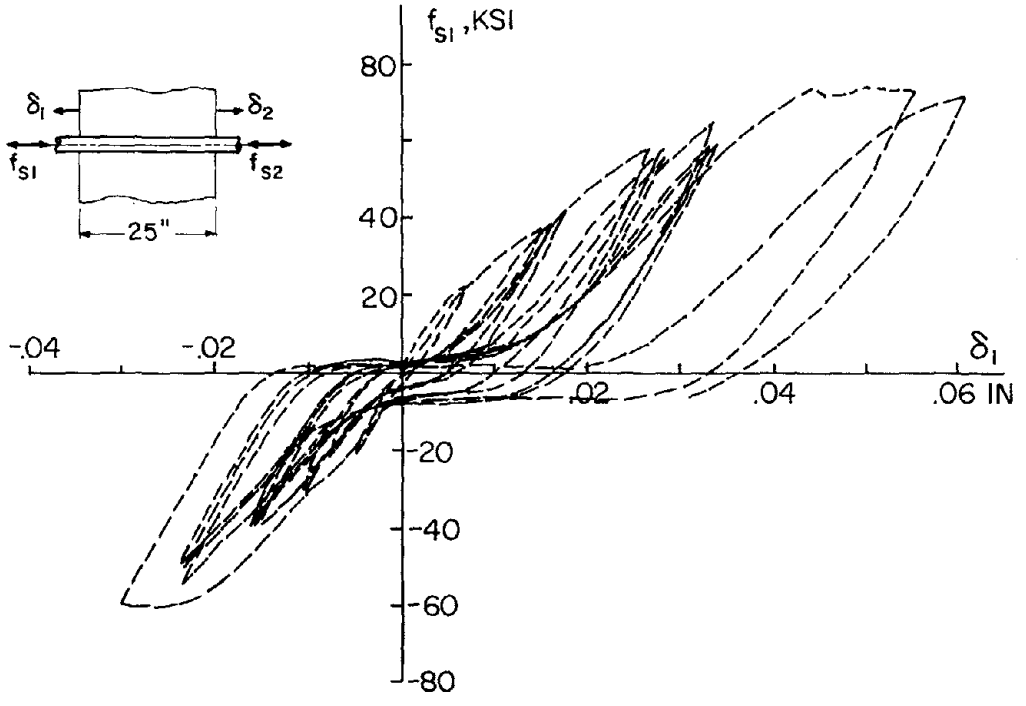

(c_2) Analytical Prediction for #10, 25 in. Column (Specimen No. 17)

Fig. 7.29 Experimental vs. Analytical Prediction for Cyclic Loading

APPENDIX A

DESIGN OF TEST SPECIMENS

A.1 GENERAL

In order to simulate the anchorage conditions in the interior beam-column connections observed in the tests [4] where practically no cracks appeared, three design criteria must be met. The column must have its concrete well confined and must be strong enough to prevent failure in shear, and must limit the size and propagation of cracks caused by flexural bending. With a sufficient amount of transverse reinforcement and column thickness, the shear mode of failure of the column can be suppressed. Acceptable limits for size and extension of flexural cracks can be controlled by providing enough longitudinal steel.

A trial and error approach was used to arrive at an acceptable column thickness. Before computation for a required transverse and longitudinal reinforcement was made, various arbitrary thicknesses were assumed for the column depths which varied from 15 in. to 31 in. After lengthy computations, it was found that the thickness of 10 in. gave a reasonable balance for the required longitudinal and transverse reinforcement.

In the following sections, a computation for the reinforcement is described in detail. This computation was made after arriving at a 10 in. thickness.

A.2 TEST SPECIMEN FOR A #6 BAR IN A 15 IN. COLUMN

A.2.1 Design for Shear

The critical loading condition to be designed for is when the embedded bar is simultaneously pulled and pushed. Calculation for the

shear reinforcement of grade 60 steel, $f_y \simeq 60$ ksi, and concrete strength f'_c of 4,000 psi, is given below. Figure A.1 shows the external forces applied to the test specimen.

The ultimate shear capacity of concrete allowed by code [23] is given by

$$v_c = 2(1 + .0005\ Nu/Ag)\ \sqrt{f'_c} \qquad (11\text{-}6)^*$$

However, v shall not exceed:

$$v_c = 3.5\ \sqrt{f'_c}\ \sqrt{1 + 0.002\ Nu/Ag} \qquad (11\text{-}7)^*$$

When N_u is assumed to be zero, Eq. (11-6) gives a conservative estimate of v_c.

$$v_c = 2\sqrt{f'_c} = 2\sqrt{4000} = 126.5 \text{ psi}$$

The ultimate shear force, V_c, can be computed as

$$V_c = v_c bd$$

where

$$b = 10 \text{ in.}, \quad d = 13.5 \text{ in.}$$

$$V_c = 126.5 \times 10 \times 13.5 = 17 \times 10^3 \text{ lb}$$

$$v_u = \frac{V_u}{bd} = \frac{26.5 \times 10^3}{10 \times 13.5} = 196 \text{ psi}$$

The maximum possible shear stress which can be developed by the shear reinforced section is:

$$8\sqrt{f'_c} + v_c = 10\sqrt{f'_c} = 632.5 > 196 \text{ psi}$$

*These equations are numbered according to ACI 1971 Code [23].

Computing the required shear reinforcement (Section 11.6.4 of ACI 1971 Code):

$$A_v = \frac{(v_u - v_c)bS}{f_y}$$

$$= \frac{(196 - 126.5)\ 10\ S}{60 \times 10^3} = 0.0125\ S$$

Using two #3 bars

$A_v = 2(0.11\ \text{in.}^2)$ (provided)

$$S = \frac{2(0.11)}{0.012} = 18\ \text{in.}$$

A.2.2 Design for Confinement

Referring to section A.6.42 of ACI 1971 Code [23] and Fig. A.2,

$$p_s = 0.45\left(\frac{A_g}{A_c} - 1\right)\frac{f'_c}{f_y} = 0.138\frac{f'_c}{f_y} > 0.12\frac{f'_c}{f_y}$$

$$p_s = \frac{0.138 \times 4}{60} = 0.0092$$

$$A_{sh} = \frac{L_h\, p_s\, S_h}{2}$$

$$= \frac{13.5 \times .0092}{2} S_h = .0622\ S_h \qquad \text{(A.6.3.2)*}$$

Maximum center-to-center spacing between hoops shall not exceed 4 in.

$A_{sh} = .0622 \times 4$ (one leg)

$= .249\ \text{in.}^2$

Using a #4 bar

$A_{sh} = 0.20\ \text{in.}^2$ (Ash provided)

$$S_h = \frac{0.20}{.0622} = 3.2\ \text{in.}$$

---

*The equation is numbered according to ACI 1971 code [23].

A #4 bar at 3.2 in. center-to-center provides a more than adequate shear reinforcement.

A.2.3 Design for Longitudinal Reinforcement

In order to confine crack propagation and limit the crack size caused by the external flexural bending moment, adequate longitudinal reinforcement must be provided. The amount of strain induced in the longitudinal bars must be well within the elastic limit and therefore the elastic theory is directly applicable for the design.

k is computed by including the contribution of the compression steel as follows.

$$k = \left[2(2n-1)p'\frac{d'}{d} + 2pn + n^2(2p' + p - \frac{p'}{n})^2\right]^{\frac{1}{2}} - n\ (2p' + p - \frac{p'}{n})$$

$$E_s = 29 \times 10^3 \text{ ksi} \quad , \quad E_c = 33w^{3/2}\sqrt{f'_c}$$

For

$$w = 150\ \frac{\text{lb}}{\text{ft}^3} \quad , \quad f'_c = 4000 \text{ psi}$$

$$E_c = 33(150)^{1.5}\sqrt{4000} = 3.83 \times 10^3 \text{ ksi}$$

$$n = \frac{29 \times 10^3}{3.83 \times 10^3} = 7.56$$

$$d = 13 \text{ in.} \quad , \quad d' = 2 \text{ in.}$$

$$p = \frac{A_s}{bd} = \frac{2 \times 0.785}{10 \times 13} = 0.012 \quad , \quad p' = p = 0.012$$

$$k = \left[2(2 \times 7.56 - 1) \times 0.012 \times \frac{2}{13} + 2 \times 0.012 \times 7.56 + (7.56)^2 (2 \times 0.012 + 0.012 - \frac{0.012}{7.56})^2\right]^{\frac{1}{2}} - 7.56(2\times0.012+0.012 - \frac{0.012}{7.56})$$

$$k = 0.289, \text{ hence } kd = 3.8 \text{ in.}$$

$$jd = (d - z) = 13 - 1.50 = 11.5$$

$$M = A_s \sigma_s jd$$

$$\sigma_s = \frac{M}{A_s(jd)} = \frac{M}{2 \times .785 \times 11.5} = 0.055\,M \qquad (A.1)$$

Note that $\varepsilon_s = f_s/E_s$ and M can be related to pulling stress f_s by

$$M = A_s f_s L \qquad (A.2)$$

(See Fig. A.1.)

σ_s and ε_s, at different levels of loading, are computed from Eq. (A.1) and listed in Table A.1.

The compression strain in concrete, ε_c, can be expressed as

$$\varepsilon_c = \frac{\varepsilon_s k}{(1-k)} \qquad (A.3)$$

If the concrete displaced is neglected

$$k = \left[2n\left(p'\frac{d'}{d} + p\right) + n^2(p' + p)^2\right]^{\frac{1}{2}} - n(p + p')$$

$$= \left[2 \times 7.56\left(\frac{0.012 \times 2}{13} + 0.012\right) + (7.56)^2(0.012 + 0.012)^2\right]^{\frac{1}{2}}$$

$$- 7.56 \times 2 \times 0.012 = 0.311$$

The distance from top fiber to the center of compression force, z, as shown in Fig. A.3, is

$$z = \frac{(d/6)k^2 + p'(2n-1)(1 - d'/kd)d'}{\frac{k}{2} + p'(2n-1)(1 - d'/kd)}$$

$$= \left(\frac{13}{6}\right)(0.289)^2 + 0.012(2 \times 7.56 - 1)\left(1 - \frac{2}{3.70}\right) \times 2$$

$$\frac{0.289}{2} + 0.012(2 \times 7.56 - 1)\left(1 - \frac{2}{3.76}\right) = 1.52 \text{ in.}$$

The values of z given by the two formulas do not differ significantly.

TABLE A.1

Level of Loading	M (k-in)	σ_s^* (ksi)	ε_s^* (in/in)	$\varepsilon_c^\dagger$ (in/in)
Working load $f_s = 24$ ksi	116.2	6.43	.0002	.00010
Yielding of rebar $f_s = 68$ ksi	329.1	18.22	.0006	.00028
Fracture of reinforcing bar $f_s = 100$ ksi	484	26.79	.00092	.00042

*σ_s and ε_s are stress and strain, respectively, in longitudinal bar

†ε_c is compressive strain of concrete at top fiber

Ultimate strength capacity of the section can be estimated by

$$M_u = bd^2 f'_c \, q(1 - 0.59q)$$

$$q = \frac{A_s}{bd}\frac{f_y}{f'_c} = \frac{0.01 \times 60}{4} = 0.180$$

$$M_u = 10 \times 13^2 \times 4 \times 0.18(1 - 0.59 \times 0.18) = 1087 \text{ k-in.} > 484 \text{ k-in.}$$

Therefore the assumption of elastic behavior of the longitudinal steel bars is justified.

A.2.4 Length of Longitudinal Bar

Adequate anchor length must be provided for the longitudinal steel to ensure that maximum steel stress, f_s, can be developed. The maximum stress in the bar is found to be 26.8 ksi. The development length, ℓ_d, needed can be computed as follows using ACI 1963 code [29].

$$u \text{ (allowable bond stress)} = 4.8\sqrt{f'_c} = 304 \text{ psi} < 500 \text{ psi}$$

$$\ell_d = \frac{A_s f_s}{(\pi d)u} = 22.1 \text{ in.}$$

The detailing of the specimen shown in Fig. 2.1 satisfied this anchoring requirement.

See Fig. 2.1 for details of specimen reinforcement.

A.3 TEST SPECIMEN FOR A #8 BAR IN A 15 IN. COLUMN

The same procedure outlined in section A.2 is employed in designing a test specimen for a #8 bar, 15 in. column as shown below. (See the forces applied to the designed specimen in Fig. A.4.)

$$v_c = 2\sqrt{f'_c} = 126.6 \text{ psi}$$

$$v_u = \frac{47.12}{10 \times 13} = 0.393 \text{ ksi}$$

$$A_v = \frac{(393 - 126.6)\,10S}{60 \times 10^3} = 0.04435 \text{ in.}^2$$

For S = 4 in., $A_v = 0.177$ in.^{2}

A.3.2 Design for Confinement

The procedure is the same as that outlined in section A.2.2, i.e., #4 bar, S_h = 3.2 in. center-to-center.

A.3.3 Design for Longitudinal Reinforcement

The following quantities are obtained:

$$k = 0.311 \quad , \quad z = 1.498 \text{ in.}, \left[\sigma_s = 0.055\, M\right]^*$$

$$\left[M = 8.635\, f_s\right]^*, \quad M_u = 1087 > 863.5 \text{ k-in.}$$

---

* Ts is in ksi, and M is in K-in.

TABLE A.2

Stage of Loading	M (k-in)	σ_s (ksi)	ε_s (in/in)	ε_c (in/in)
Working Load $f_s = 24$ ksi	207.24	11.39	.0004	.00018
Yielding of the pulling rebar $f_y = 68$ ksi	587.2	32.3	.0011	.0005
Fracture of the pulled rebar $f_s = 100$ ksi	863.5	47.5	.0016	.00074

The test specimen for the #8 bar is identical to that for the #6 bar. (See Fig. 2.1 for details of the specimen.)

A.4 TEST SPECIMEN FOR #6 BAR IN A 20 IN. COLUMN

The same procedure outlined in section A.2 is employed in designing a specimen for a #6 bar, 20 in. column. See Fig. A.5 for the external applied forces.

A.4.1 Design for Shear

$$v_c = 2\sqrt{f'_c} = 2\sqrt{4000} = 126.6 \text{ psi}$$

$$v_u = \frac{V_u}{bd} = \frac{26.5 \times 10^3}{10 \times 18} = 147.22 \text{ psi}$$

$$b = 10 \quad , \quad d = 18 \text{ in.}$$

$$A_v = \frac{(v_u - v_c)bS}{f_y} = \frac{(147.2 - 126.6)\,10\,S}{60 \times 10^3} = .00343\,S$$

For S = 4 in., $A_v = 0.0137$ in.^{2}

A.4.2 Design for Confinement

Refer to Fig. A.6 for the cross section of the 20 in. column.

$$p_s = 0.45\left(\frac{A_g}{A_c} - 1\right)\frac{f'_c}{f_y} = 0.45\left(\frac{10 \times 20}{8 \times 17.5} - 1\right)\frac{f'_c}{f_y}$$

$$= 0.193\,\frac{f'_c}{f_y} > 0.12\,\frac{f'_c}{f_y} = \frac{0.193 \times 4}{60} = 0.0129$$

$$A_{sh} = \frac{L_h p_s S_h}{2}$$

$$L_h = 8.75 \text{ in.}$$

$$A_{sh} = \frac{8.75 \times 0.0129}{2} S_h = 0.0563\, S_h$$

$$S_h = 4 \text{ in.} \quad , \quad A_{sh} = 0.23 \text{ in.}^2 \text{ (for one leg)}$$

$$A_{sh} = 0.20 \text{ in.}^2$$

$$S_h = \frac{0.20}{0.0563} = 3.6 \text{ in.}$$

If a #4 bar is used at 3.6 in. center-to-center, this provision is adequate for shear requirement.

A.4.3 Design for Longitudinal Reinforcement

$$k = \left[\, 2n\left(p'\frac{d'}{d} + p\right) + n^2\, p' \,\right]^{\frac{1}{2}} - n(p + p')$$

$$E_s = 29 \times 10^3 \quad , \quad E_c = 33w^{3/2}\sqrt{f'_c} = 3.83 \times 10^3 \text{ ksi}$$

$$n = 7.56 \quad , \quad d = 18 \text{ in.} \quad , \quad d = 2 \text{ in.}$$

$$p = \frac{2 \times .785}{10 \times 18} = .00872 \quad , \quad p' = p = .00872$$

$$k = \left[2 \times 7.56\left(.00872 \times \frac{2}{18} + .00872\right) + (7.56)^2(2 \times .00872)^2\right]^{\frac{1}{2}}$$

$$- 7.56 \times 2 \times .00872 = 0.273$$

$$kd = 4.91 \text{ in.}$$

$$z = \frac{(d/6)k^2 + p'nd'(1 - d'/kd)}{\frac{k}{2} + p'n(1 - d'/kd)}$$

$$= \frac{(\frac{18}{6})(.273)^2 + .00872 \times 7.56 \times 2(1 - \frac{2}{4.91})}{\frac{0.273}{2} + .00872 \times 7.56 \times 2(1 - \frac{2}{4.91})} = \frac{0.3018}{0.215} = 1.41 \text{ in.}$$

$$jd = 18 - 1.41 = 16.60 \text{ in.}$$

$$\sigma_s = \frac{M}{2 \times .785 \times 16.60} = 0.0384\, M$$

$$M = 0.44\, f_s \times 11 = 4.84\, f_s$$

TABLE A.3

Level of Loading	M (k-in)	σ_s (ksi)	ε_s (in/in)	ε_c (in/in)
Working load $f_s = 24$ ksi	116.2	4.46	.00015	.00006
Yielding of rebar $f_s = 68$ ksi	329.1	12.63	.00044	.00016
Fracture of pulling rebar $f_s \simeq 100$ ksi	484	18.57	.00064	.00024

The approximate yield capacity of the section is:

$$M_u = bd^2 f'_c q(1 - 0.59q)$$

$$q = \frac{A_s}{bd}\frac{f_y}{f'_c} = \frac{.00872 \times 60}{4} - 0.131$$

$$M_u = 10 \times 18^2 \times 4 \times 0.131(1 - 0.59 \times 1.31)$$

$$= 1567 \text{ k-in.} >> 484 \text{ k-in.}$$

See Fig. 2.2 for details of specimen reinforcement.

A.5 TEST SPECIMEN FOR A #8 BAR IN A 20 IN. COLUMN

A.5.1 Design for Shear

Refer to Fig. A.7 for the externally applied at yielding forces on the designed specimen.

$$v_c = 126.6 \text{ psi}$$

$$v_u = \frac{4712 \times 10^3}{10 \times 18} = 261 \text{ psi}$$

$$A_v = \frac{(261 - 127)}{60 \times 10^3} \times 10 \; S = 0.0223 \, S$$

For $S = 4$ in., $A_v = 0.0893$ in.^{2}

A.5.2 Design for Confinement

Using the same procedure employed in the design for confinement of a #6 bar in a 20 in. column yields

$$S_h = 3.6 \text{ in.} \quad , \quad \#4 \text{ rebar}$$

It is evident from a comparison of the transverse reinforcement required for shear and for confinement that the confinement requirement governs the design.

A.5.3 Design for Longitudinal Reinforcement

Refer to 20 in. column #6 bar in section A.4.3.

$$k = 0.273 \quad , \quad kd = 4.91 \text{ in.} \quad , \quad z = 1.41 \text{ in.}$$

$$\sigma_s = 0.03841 \; M \quad , \qquad M = 0.785 \times 11 \, f_s = 8.635 \, f_s$$

TABLE A.4

Level of Loading	M (k-in)	σ_s (ksi)	ε_s (in/in)	ε_c (in/in)
Working load level $f_s = 24$ ksi	207.2	7.96	.0003	.00007
Yielding of rebar $f_y = 60$ ksi	518.1	19.9	.0007	.00019
Fracture of pulling rebar $f_s = 100$ ksi	863.5	33.16	.0011	.00031

The approximate yield capacity of the section is:

$$M_u = 1567 \text{ k-in.} > 863.5 \text{ k-in.}$$

The reinforcement detailing is identical to that for the #6 bar, 20 in. column specimen shown in Fig. 2.2.

A.6 TEST SPECIMEN FOR A #8 BAR IN A 25 IN. COLUMN

Following the same procedure as presented in section A.2 yields the design requirements detailed below.

A.6.1 Design for Shear

Based on the design of the 20 in. column, the shear requirement will not govern the design of the transversed reinforcement. See Fig. A.8 for the external applied forces.

A.6.2 Design for Confinement

Refer to Fig. A.9 for the cross section of the 25 in. column.

$$p_s = 0.45\left(\frac{A_g}{A_c} - 1\right)\frac{f'_c}{f_y} = 0.45\left(\frac{10 \times 25}{23 \times 8} - 1\right)\frac{f'_c}{f_y}$$

$$= 0.1614\,\frac{f'_c}{f_y} > 0.12\,\frac{f'_c}{f_y} = \frac{0.1614 \times 4}{60} = 0.0108$$

$$A_{sh} = \frac{L_h p_s S_h}{2}$$

$$L_h = 8 \text{ in.} \quad , \quad S_h = 4 \text{ in.}$$

$$A_{sh} = \frac{8 \times 0.0108 \times 4}{2} = 0.172 \text{ in.}^2 \qquad \text{(one leg)}$$

Using a #4 bar, $A_{sh} = 0.20$ with 4 in. center-to-center.

A.6.3 Design of Longitudinal Reinforcement

Refer to Section A-A of the column illustrated in Fig. A.10.

$$\varepsilon_1 = \frac{\varepsilon_c}{kd}(kd - 2) = \varepsilon_s \frac{(kd - 2)}{(23 - kd)}$$

$$\varepsilon_2 = \frac{\varepsilon_s}{(23 - kd)}(9.5 - kd)$$

$$\varepsilon_3 = \frac{\varepsilon_s}{(23 - kd)}(15.5 - kd)$$

$$\varepsilon_c = \frac{\varepsilon_s}{(23 - kd)} kd$$

$$C = \frac{1}{2} b\, kd\, \varepsilon_c E_c = \frac{1}{2} b\, kd\, E_c \frac{\varepsilon_s kd}{(23 - kd)} = \frac{1}{2} b \frac{E_c \varepsilon_s (kd)^2}{(23 - kd)}$$

$$C'_s = 2 A_s E_s \frac{\varepsilon_s (kd - 2)}{(23 - kd)}$$

$$T_1 = A_s \varepsilon_s E_s \frac{(9.5 - kd)}{(23 - kd)}$$

$$T_2 = A_s E_s \varepsilon_s \frac{(15.5 - kd)}{(23 - kd)}$$

$$T_3 = A_s \varepsilon_s E_s$$

$$C + C'_s = T_1 + T_2 + T_3$$

$$\frac{1}{2} b E_c \frac{\varepsilon_s (kd)^2}{(23-kd)} + 2 A_s E_s \varepsilon_s \frac{(kd-2)}{(23-kd)} = A_s \varepsilon_s E_s \frac{(9.5-kd)}{(23-kd)}$$

$$+ A_s E_s \varepsilon_s \frac{(15.5-kd)}{(23-kd)} + A_s \varepsilon_s E_s$$

$$\frac{1}{2} b (kd)^2 + 2 A_s n(kd-2) = A_s n(9.5-kd) + A_s n(15.5-kd) + A_s n(23-kd)$$

$$\frac{1}{2} b(kd)^2 + A_s n[2kd - 4 - 9.5 + kd - 15.5 + kd - 23 + kd] = 0$$

$$\frac{1}{2} b(kd)^2 + A_s n[5kd - 52] = 0$$

Substitute $b = 10$, $d = 23$, $A_s = 2\frac{\pi}{4}(\frac{7}{8})^2 = 1.203$, $n = 7.56$.

$$\frac{1}{2} \times 10\, k^2 (23)^2 + 1.203 \times 7.56\, [5k \times 23 - 52] = 0$$

$$2645k^2 + 1045.6k - 472.8 = 0$$

$$k^2 + 0.395k - 0.178 = 0$$

$$k = \frac{-0.395 + \sqrt{0.395^2 + 4 \times 0.178}}{2} = \frac{-0.395 \pm 0.933}{2}$$

$$k = 0.27$$

$$kd = 6.20 \text{ in.}$$

$$M = \frac{2}{3} C\, kd + C'_s (kd-2) + T_1 (9.5-kd) + T_2 (15.5-kd) + T_3 (23-kd)$$

$$= (9.319 + 2.509 + .785 + 6.202 + 20.225) E_s \varepsilon_s$$

$$M = 35.9\ E_s \varepsilon_s = 35.9\ \sigma_s \text{ k-in.}$$

$$M = 8.64\ f_s \text{ k-in.} \quad , \quad \varepsilon_c = \frac{\varepsilon_s k}{(1-k)}$$

TABLE A.5

Level of Loading	M (k-in)	σ_s (ksi)	ε_s (in/in)	ε_c (in/in)
Working load $f_s = 24$ ksi	207.3	5.77	.0002	.00010
Yielding level $f_y = 68$ ksi	587.5	16.35	.0006	.00021
Fracture of pulling rebar $f_s = 100$ ksi	863.9	22.12	.0008	.00028

Yield capacity of the heavily reinforced section proceeds as follows:

Assume that ε_2, ε_3, $\varepsilon_s \geq \varepsilon_y$ while $\varepsilon_1 < \varepsilon_y$. From this assumption the equilibrium of the section can be expressed as (see Fig. A.11):

$$(0.85 f'_c)(0.85c)b + \frac{0.003(c-2)}{c} E_s A_s = 3A_s f_y \qquad (A.4)$$

Recognizing that b = 10 in., $A_s = 1.203$, $f_y = 60$ ksi and $E_s = 29 \times 10^3$ ksi, Eq. (A.1) can be rewritten as

$$28.9 c^2 - 111.84 c - 209.3 = 0$$

or

$$c^2 - 3.87 c - 7.243 = 0 \qquad (A.5)$$

The solution of Eq. (A.2) yields,

$$c = 5.25 \text{ in.}$$

The assumption that ε_2, ε_3, $\varepsilon_s \geq \varepsilon_y$ while $\varepsilon_1 < \varepsilon_y$ is proved to be correct when c = 5.25 in.

$$M_u = (.85 \times 4 \times .85 \times 10c)(c - \frac{a}{2}) + \frac{0.003(c-2)}{c} A_s E_s (c-2)$$

$$+ A_s f_y (9.5 - c) + A_s f_y (15.5 - c) + A_s f_y (23 - c)$$

$$= 457.95 + 210.53 + 306.8 + 739.87 + 1281.22$$

$$= 2996.4 \text{ k-in.} \quad 863.9 \text{ k-in.}$$

Therefore, there is no danger of yielding in the section.

The dimensions and reinforcement detailing of the specimen for a #8 bar, 25 in. column are given in Fig. 2.3.

A.7 TEST SPECIMEN FOR A #10 BAR IN A 25 IN. COLUMN

Following the same procedure as presented in section A.2 yields:

A.7.1 Design for Shear

Refer to Fig. A.12:

$$v_c = 2\sqrt{f'_c} = 2\sqrt{4000} = 126.5 \text{ psi}$$

$$v_u = \frac{73.8 \times 10^3}{10 \times 23} = 320.87 \text{ psi}$$

For S = 4 in. spacing, the required A_v is

$$A_v = \frac{(v_u - v_c)}{f_y} bS = \frac{(320.9 - 126.5)}{60 \times 10^3} \times 10 \times 4$$

$$= 0.1296 \text{ in.}^2 \quad \text{(two legs)}$$

A.7.2 Design for Confinement

Refer to the previous calculation in section A.6.2.

$$A_{sh} = 0.172 \text{ in.}^2 \quad \text{(one leg)}$$

For a #4 bar, $A_{sh} = 0.20$ in.^{2} at 4 in. center-to-center will be adequate.

A.7.3 Design of Longitudinal Reinforcement

Using the same calculation as presented in section A.6.3 yields

$$M = 39.04 E_s \varepsilon_s = 35.93 \sigma_s \text{ k-in.}$$

$$M = 1.23 \times 11 f_s \text{ k-in.}$$

[Where T_s, f_s are in ksi and M is in k-in.]

$$\sigma_s = \frac{1.23 \times 11}{35.93} f_s \text{ ksi} = 0.368 f_s \text{ ksi}$$

For a fracture of the rebar ($f_s = 100$ ksi), the maximum moment induced is 1353 k-in.

TABLE A.6

Level of Loading	σ_s (ksi)	ε_s (in/in)	ε_c (in/in)
Working stress $f_s = 24$ ksi	8.84	.0003	.00008
Yielding $f_s = 68$ ksi	25.04	.0009	.00023
Fracture of rebar $f_s = 100$ ksi	36.83	.0013	.00034

The yielding capacity of the test specimen section is 2996.4 k-in. (from section A.6.3), which is larger than the maximum moment of 1353 k-in. Therefore, there is no danger of yielding the longitudinal bar.

From above results, the dimensions and reinforcement detail of the test specimen shown in Fig. 2.3 are adequate.

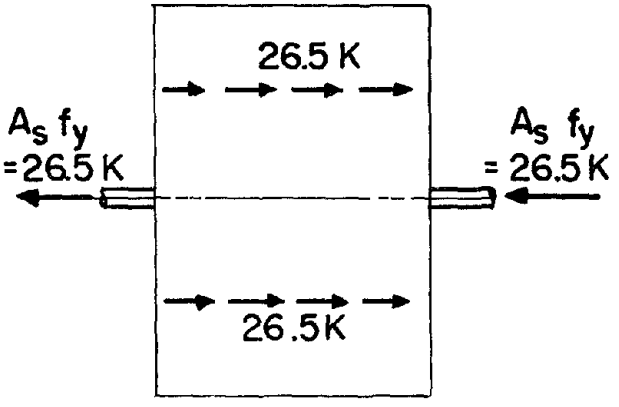

Fig. A.1 Forces in Test Specimen at Yield of #6 Bar

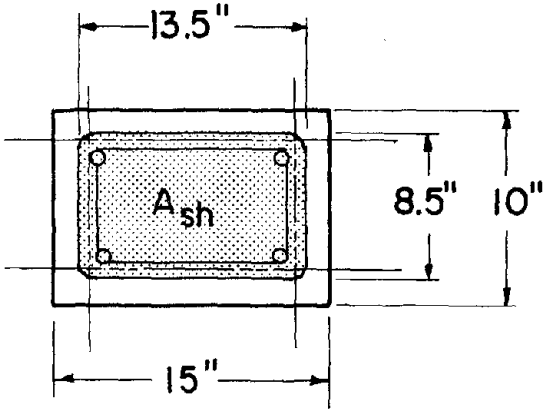

Fig. A.2 Cross Section of 15 in. Col.

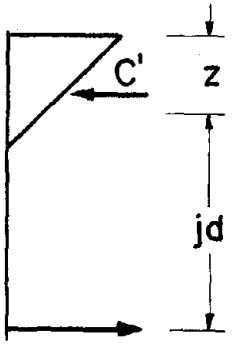

Fig. A.3 Force Diagram

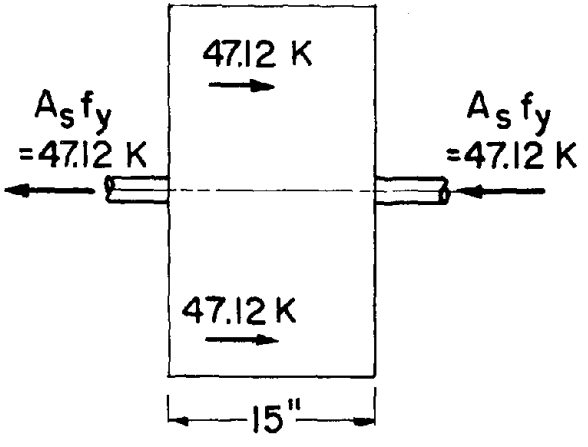

Fig. A.4 Forces in Test Specimen at Yield of #8 Bar

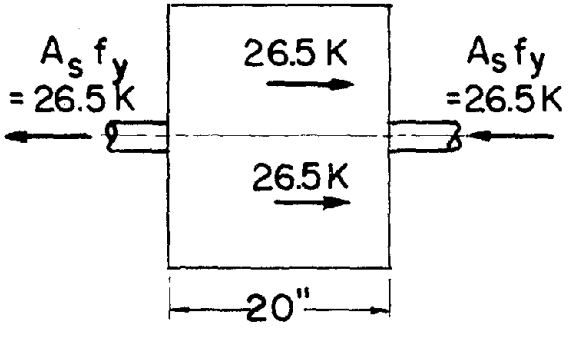

Fig. A.5 Forces in Test Specimen at Yield of #6 Bar

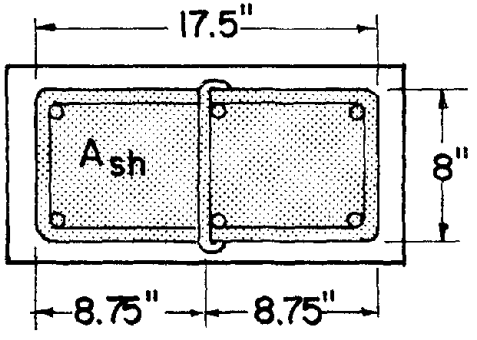

Fig. A.6 Cross Section of 20 in. Column

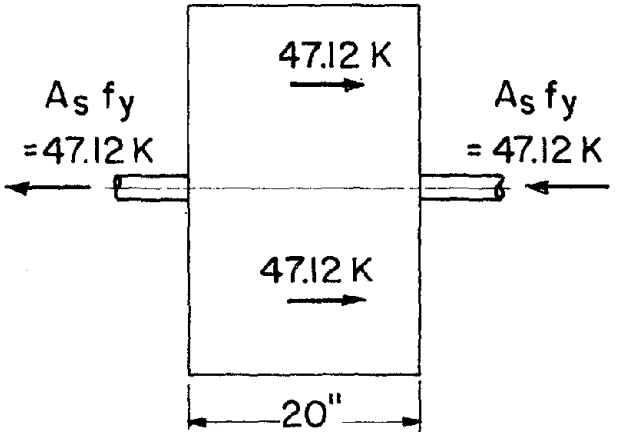

Fig. A.7 Forces in Test Specimen at Yield of #8 Bar

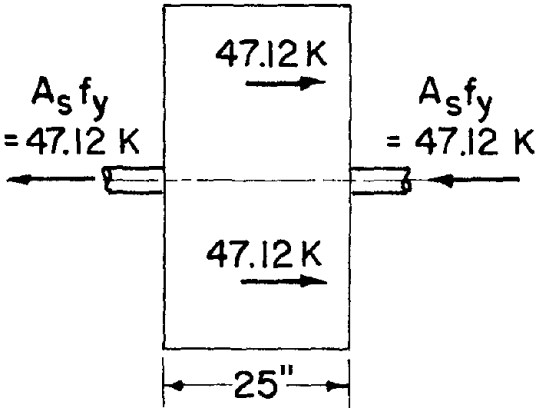

Fig. A.8 Forces in Test Specimen at Yield of #8 Bar

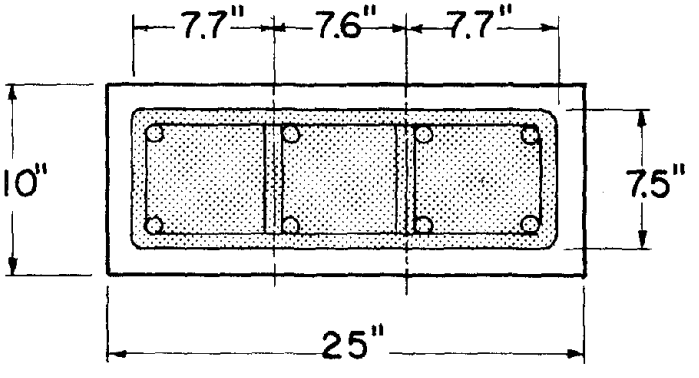

Fig. A.9 Cross Section of 25 in. Column

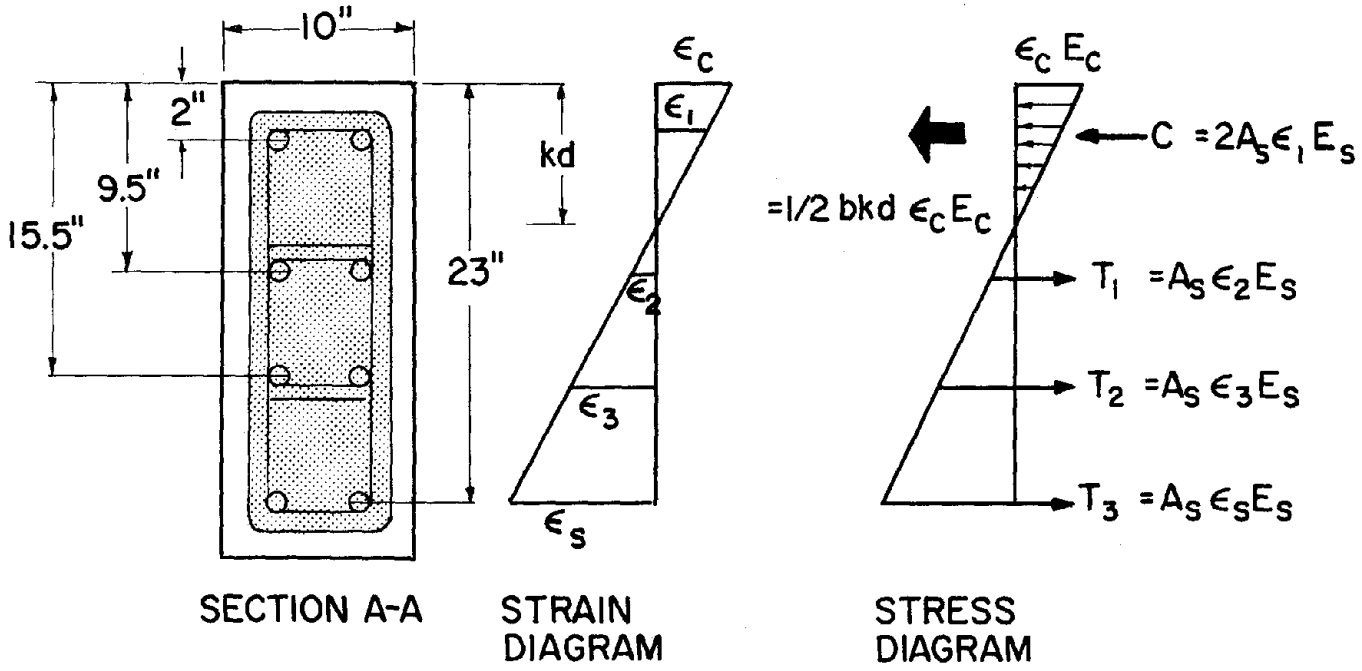

Fig. A.10 Free Body Diagram of Section A-A $\varepsilon_1 = \frac{\varepsilon_c}{kd}(kd - 2)$

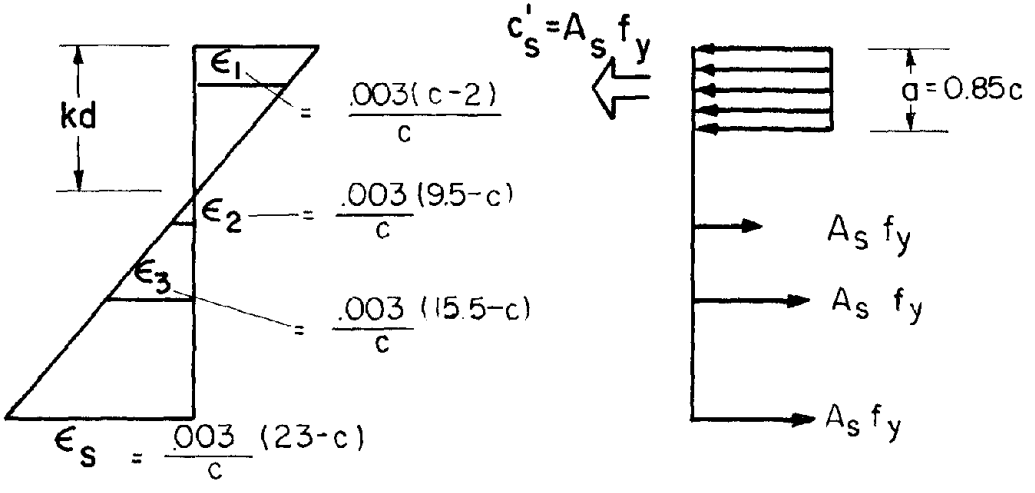

Fig. A.11 Calculation of Ultimate Moment

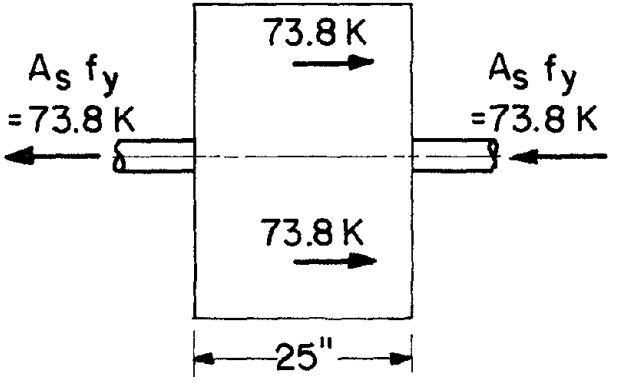

Fig. A.12 Forces in Test Specimen at Yield of #10 Bar

APPENDIX B

MATHEMATICAL MODEL OF STRESS-STRAIN RELATION OF REINFORCING STEEL

B.1 GENERAL

The purpose of developing f_s-ε_s of reinforcing steel is to meet the following needs:

(1) To determine the steel stress corresponding to the measured strain. Once the steel has yielded and strain reversal has taken place, the stress-strain relationship becomes history dependent. Since there is no direct way of measuring steel stress in the bond tests, the corresponding stress is computed from the measured strain value.

(2) To establish the hysteretic behavior of reinforcing steel for the analytical prediction of the inelastic behavior of push-pull specimens.

B.2 MATHEMATICAL MODEL FOR f_s-ε_s OF STEEL

The hysteretic f_s-ε_s of steel used herein is adopted from the one developed by Ma *et. al.* [9] with the following modifications:

(1) Monotonic skeleton curve under tension after yielding. Instead of supplying enough data points on post-yield range, curve BC of Fig. B.1--a cubic polynonial curve like the one used by Ma *et. al.* [9]--is employed with the following constraints:

At the onset of strain hardening, point B in Fig. B.1, the

$$f(\varepsilon_{sh}) = f_y$$

and

$$f'(\varepsilon_{sh}) = E_{sh} \quad *$$

---

* $f'(\varepsilon_{sh})$ denotes $df/d\varepsilon$ at $\varepsilon = \varepsilon_{sh}$

At point C

$$f(\varepsilon_{smax}) = f_{smax}$$

and

$$f'(\varepsilon_{smax}) = 0$$

where $f(\varepsilon_s)$ is the proposed cubic polynomial function, ε_{sh} is strain at onset of strain hardening, f_y is yielding stress in tension, E_{sh} is the tangent stiffness of strain hardening, and f_{smax} and ε_{smax} are the stress and strain at maximum stress. The equation for BC is given by

$$f_s = [E_{shr} - 2(f_{smax} - f_y)] \left(\frac{s}{r}\right)^3 + 3 \left[(f_{smax} - f_y) - \frac{2}{3} E_{sh}r\right] \left(\frac{s}{r}\right)^2 + E_{sh}s + f_y \qquad (B.1)$$

where $r = \varepsilon_{smax} - \varepsilon_{sh}$ and $s = \varepsilon_s - \varepsilon_{sh}$

(2) Monotonic skeleton curve under compression after yielding.

According to experimental data, the f_s-ε_s curve for axial compression in the post yield range is significantly different from that in tension. A more accurate mathematical expression is prescribed in parabolic form.

This curve satisfies the following constraint conditions;

At point B'

$$f(\varepsilon_{shc}) = f_{yc}$$

$$f'(\varepsilon_{shc}) = E_{shc}$$

At point C

$$f(\varepsilon_{maxc}) = f_{maxc}$$

where ε_{shc} and E_{shc} are the strain and tangent stiffness at strain hardening in compression, respectively; as shown in Fig. B.2 ε_{maxc} and f_{maxc} are the strain and stress at maximum compressive load from test. Further loading lead to the buckling of the test specimens.

According to the experimental data, the equation of BC is

$$f_s = [T' - E_{shc} r'] \left(\frac{s'}{r'}\right)^2 + E_{shc} s' + f_{yc} \qquad (B.2)$$

where $T = f_{maxc} - f_{yc}$, $r' = \varepsilon_{maxc} - \varepsilon_{shc}$ and $s' = \varepsilon_s - \varepsilon_{shc}$

(3) Parameters for f_s-ε_s curve under cyclic loading.

A Ramberg Osgood equation was used in modeling the cyclic f_s-ε_s relation (see [9]). Mathematically, it is

$$\bar{\varepsilon}_s = \beta(\bar{f}_s + \alpha \mid \bar{f}_s \mid^n)$$

where

$$\bar{\varepsilon}_s = \frac{\varepsilon_s}{\gamma \varepsilon_y} \quad \text{and} \quad \bar{f}_s = \frac{f_s}{\gamma f_y}$$

It was found that $\beta = 1.0$, $\alpha = .6$ and $\gamma = .9$, and $n = 8$ gave good agreement with the experimental results.

B.3 ACCURACY OF THE PROPOSED MATHEMATICAL MODEL

A comparison of analytical prediction and experimental results for #8 bar are shown in Fig. B.3 and B.4. An excellent agreement is observed for monotonic loading and reasonably good agreement for cyclic loading.

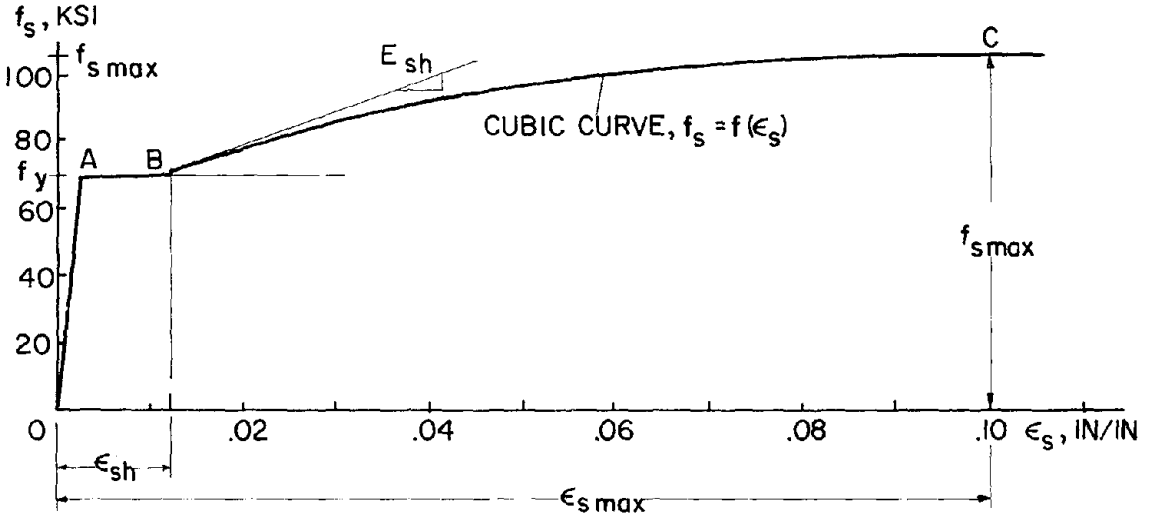

Fig. B.1 Idealized $f_s - \varepsilon_s$ Relation for Monotonic Tension

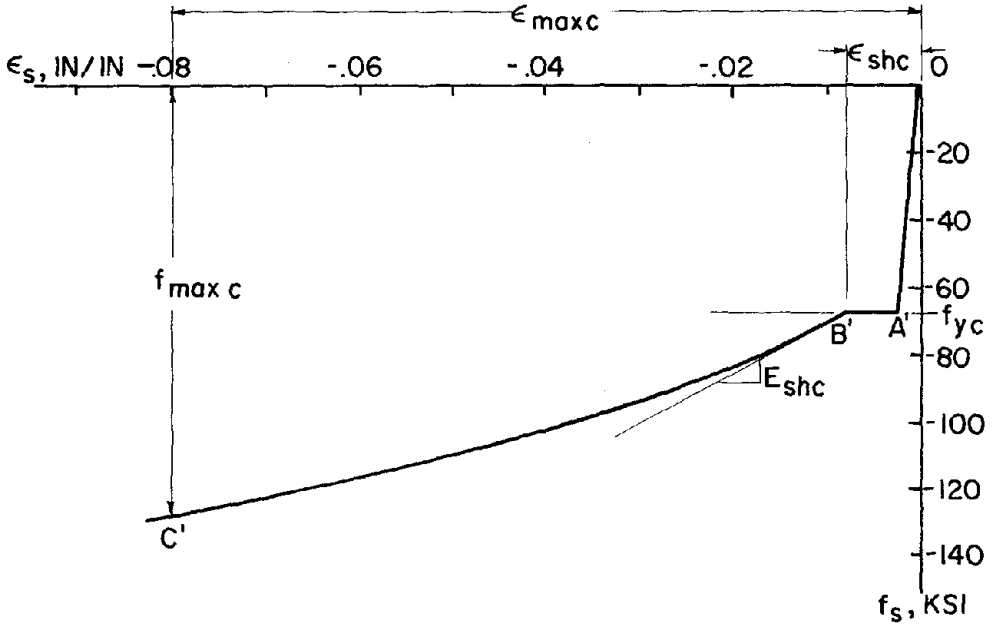

Fig. B.2 Idealized $f_s - \varepsilon_s$ Relation for Monotonic Compression

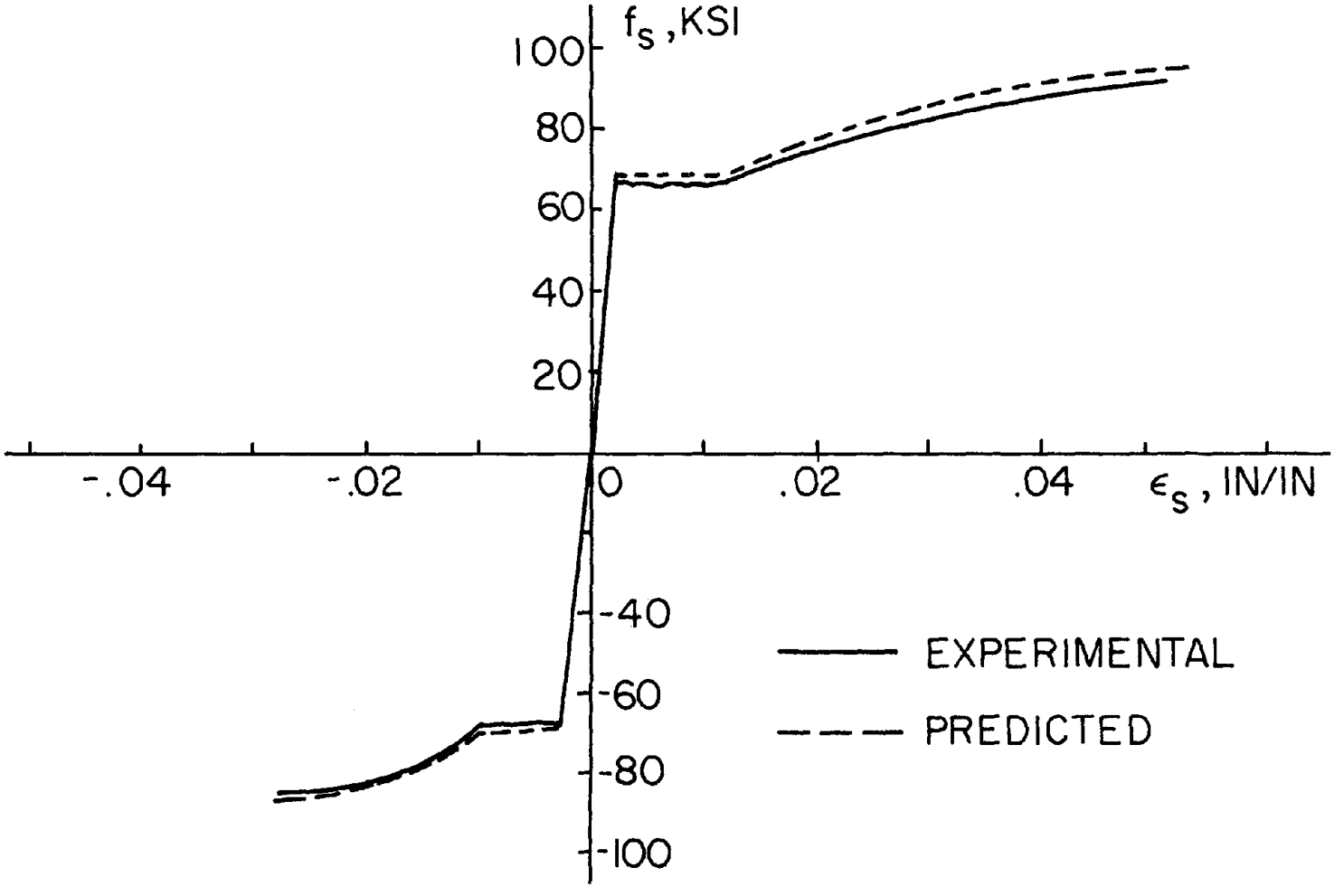

Fig. B.3 $f_s - \varepsilon_s$ Curves (Experimental vs. Predicted Result)

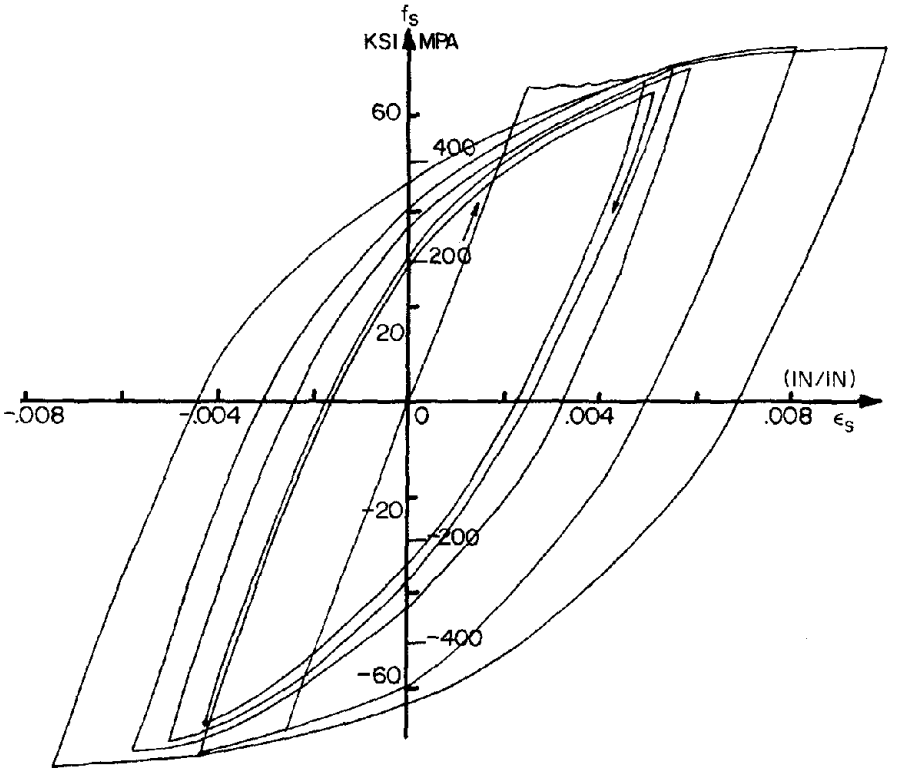

(a) Experimental Result

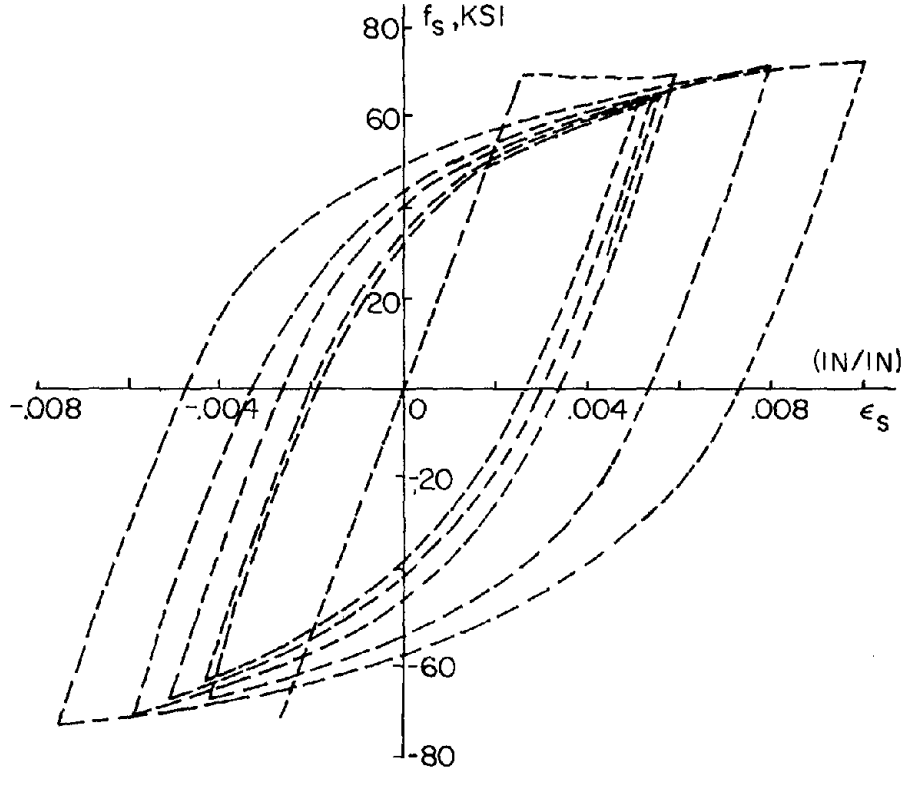

(b) Analytical Result

Fig. B.4 $f_s - \epsilon_s$ Curve of Reinforcing Bar Under Cyclic Loading

APPENDIX C

INPUT INSTRUCTION AND COMPUTER PROGRAM LISTING OF STEEL ELEMENT

APPENDIX D

INPUT INSTRUCTION AND COMPUTER PROGRAM LISTING OF BOND ELEMENT

APPENDIX E

DATA REDUCTION PROGRAMS

The reader is referred to the doctoral dissertation of S. Viwathanatepa on which this report is based for Appendices C, D, and E, which contain detailed information on the above topics. These have been omitted from the present volume due to limitations on length.

EARTHQUAKE ENGINEERING RESEARCH CENTER REPORTS

NOTE: Numbers in parenthesis are Accession Numbers assigned by the National Technical Information Service; these are followed by a price code. Copies of the reports may be ordered from the National Technical Information Service, 5285 Port Royal Road, Springfield, Virginia, 22161. Accession Numbers should be quoted on orders for reports (PB --- ---) and remittance must accompany each order. Reports without this information were not available at time of printing. Upon request, EERC will mail inquirers this information when it becomes available.

EERC 67-1 "Feasibility Study Large-Scale Earthquake Simulator Facility," by J. Penzien, J.G. Bouwkamp, R.W. Clough and D. Rea - 1967 (PB 187 905)A07

EERC 68-1 Unassigned

EERC 68-2 "Inelastic Behavior of Beam-to-Column Subassemblages Under Repeated Loading," by V.V. Bertero - 1968 (PB 184 888)A05

EERC 68-3 "A Graphical Method for Solving the Wave Reflection-Refraction Problem," by H.D. McNiven and Y. Mengi - 1968 (PB 187 943)A03

EERC 68-4 "Dynamic Properties of McKinley School Buildings," by D. Rea, J.G. Bouwkamp and R.W. Clough - 1968 (PB 187 902)A07

EERC 68-5 "Characteristics of Rock Motions During Earthquakes," by H.B. Seed, I.M. Idriss and F.W. Kiefer - 1968 (PB 188 338)A03

EERC 69-1 "Earthquake Engineering Research at Berkeley," - 1969 (PB 187 906)A11

EERC 69-2 "Nonlinear Seismic Response of Earth Structures," by M. Dibaj and J. Penzien - 1969 (PB 187 904)A08

EERC 69-3 "Probabilistic Study of the Behavior of Structures During Earthquakes," by R. Ruiz and J. Penzien - 1969 (PB 187 886)A06

EERC 69-4 "Numerical Solution of Boundary Value Problems in Structural Mechanics by Reduction to an Initial Value Formulation," by N. Distefano and J. Schujman - 1969 (PB 187 942)A02

EERC 69-5 "Dynamic Programming and the Solution of the Biharmonic Equation," by N. Distefano - 1969 (PB 187 941)A03

EERC 69-6 "Stochastic Analysis of Offshore Tower Structures," by A.K. Malhotra and J. Penzien - 1969 (PB 187 903)A09

EERC 69-7 "Rock Motion Accelerograms for High Magnitude Earthquakes," by H.B. Seed and I.M. Idriss - 1969 (PB 187 940)A02

EERC 69-8 "Structural Dynamics Testing Facilities at the University of California, Berkeley," by R.M. Stephen, J.G. Bouwkamp, R.W. Clough and J. Penzien - 1969 (PB 189 111)A04

EERC 69-9 "Seismic Response of Soil Deposits Underlain by Sloping Rock Boundaries," by H. Dezfulian and H.B. Seed 1969 (PB 189 114)A03

EERC 69-10 "Dynamic Stress Analysis of Axisymmetric Structures Under Arbitrary Loading," by S. Ghosh and E.L. Wilson 1969 (PB 189 026)A10

EERC 69-11 "Seismic Behavior of Multistory Frames Designed by Different Philosophies," by J.C. Anderson and V. V. Bertero - 1969 (PB 190 662)A10

EERC 69-12 "Stiffness Degradation of Reinforcing Concrete Members Subjected to Cyclic Flexural Moments," by V.V. Bertero, B. Bresler and H. Ming Liao - 1969 (PB 202 942)A07

EERC 69-13 "Response of Non-Uniform Soil Deposits to Travelling Seismic Waves," by H. Dezfulian and H.B. Seed - 1969 (PB 191 023)A03

EERC 69-14 "Damping Capacity of a Model Steel Structure," by D. Rea, R.W. Clough and J.G. Bouwkamp - 1969 (PB 190 663)A06

EERC 69-15 "Influence of Local Soil Conditions on Building Damage Potential during Earthquakes," by H.B. Seed and I.M. Idriss - 1969 (PB 191 036)A03

EERC 69-16 "The Behavior of Sands Under Seismic Loading Conditions," by M.L. Silver and H.B. Seed - 1969 (AD 714 982)A07

EERC 70-1 "Earthquake Response of Gravity Dams," by A.K. Chopra - 1970 (AD 709 640)A03

EERC 70-2 "Relationships between Soil Conditions and Building Damage in the Caracas Earthquake of July 29, 1967," by H.B. Seed, I.M. Idriss and H. Dezfulian - 1970 (PB 195 762)A05

EERC 70-3 "Cyclic Loading of Full Size Steel Connections," by E.P. Popov and R.M. Stephen - 1970 (PB 213 545)A04

EERC 70-4 "Seismic Analysis of the Charaima Building, Caraballeda, Venezuela," by Subcommittee of the SEAONC Research Committee: V.V. Bertero, P.F. Fratessa, S.A. Mahin, J.H. Sexton, A.C. Scordelis, E.L. Wilson, L.A. Wyllie, H.B. Seed and J. Penzien, Chairman - 1970 (PB 201 455)A06

EERC 70-5 "A Computer Program for Earthquake Analysis of Dams," by A.K. Chopra and P. Chakrabarti - 1970 (AD 723 994)A05

EERC 70-6 "The Propagation of Love Waves Across Non-Horizontally Layered Structures," by J. Lysmer and L.A. Drake 1970 (PB 197 896)A03

EERC 70-7 "Influence of Base Rock Characteristics on Ground Response," by J. Lysmer, H.B. Seed and P.B. Schnabel 1970 (PB 197 897)A03

EERC 70-8 "Applicability of Laboratory Test Procedures for Measuring Soil Liquefaction Characteristics under Cyclic Loading," by H.B. Seed and W.H. Peacock - 1970 (PB 198 016)A03

EERC 70-9 "A Simplified Procedure for Evaluating Soil Liquefaction Potential," by H.B. Seed and I.M. Idriss - 1970 (PB 198 009)A03

EERC 70-10 "Soil Moduli and Damping Factors for Dynamic Response Analysis," by H.B. Seed and I.M. Idriss - 1970 (PB 197 869)A03

EERC 71-1 "Koyna Earthquake of December 11, 1967 and the Performance of Koyna Dam," by A.K. Chopra and P. Chakrabarti 1971 (AD 731 496)A06

EERC 71-2 "Preliminary In-Situ Measurements of Anelastic Absorption in Soils Using a Prototype Earthquake Simulator," by R.D. Borcherdt and P.W. Rodgers - 1971 (PB 201 454)A03

EERC 71-3 "Static and Dynamic Analysis of Inelastic Frame Structures," by F.L. Porter and G.H. Powell - 1971 (PB 210 135)A06

EERC 71-4 "Research Needs in Limit Design of Reinforced Concrete Structures," by V.V. Bertero - 1971 (PB 202 943)A04

EERC 71-5 "Dynamic Behavior of a High-Rise Diagonally Braced Steel Building," by D. Rea, A.A. Shah and J.G. Bouwkamp 1971 (PB 203 584)A06

EERC 71-6 "Dynamic Stress Analysis of Porous Elastic Solids Saturated with Compressible Fluids," by J. Ghaboussi and E. L. Wilson - 1971 (PB 211 396)A06

EERC 71-7 "Inelastic Behavior of Steel Beam-to-Column Subassemblages," by H. Krawinkler, V.V. Bertero and E.P. Popov 1971 (PB 211 335)A14

EERC 71-8 "Modification of Seismograph Records for Effects of Local Soil Conditions," by P. Schnabel, H.B. Seed and J. Lysmer - 1971 (PB 214 450)A03

EERC 72-1 "Static and Earthquake Analysis of Three Dimensional Frame and Shear Wall Buildings," by E.L. Wilson and H.H. Dovey - 1972 (PB 212 904)A05

EERC 72-2 "Accelerations in Rock for Earthquakes in the Western United States," by P.B. Schnabel and H.B. Seed - 1972 (PB 213 100)A03

EERC 72-3 "Elastic-Plastic Earthquake Response of Soil-Building Systems," by T. Minami - 1972 (PB 214 868)A08

EERC 72-4 "Stochastic Inelastic Response of Offshore Towers to Strong Motion Earthquakes," by M.K. Kaul - 1972 (PB 215 713)A05

EERC 72-5 "Cyclic Behavior of Three Reinforced Concrete Flexural Members with High Shear," by E.P. Popov, V.V. Bertero and H. Krawinkler - 1972 (PB 214 555)A05

EERC 72-6 "Earthquake Response of Gravity Dams Including Reservoir Interaction Effects," by P. Chakrabarti and A.K. Chopra - 1972 (AD 762 330)A08

EERC 72-7 "Dynamic Properties of Pine Flat Dam," by D. Rea, C.Y. Liaw and A.K. Chopra - 1972 (AD 763 928)A05

EERC 72-8 "Three Dimensional Analysis of Building Systems," by E.L. Wilson and H.H. Dovey - 1972 (PB 222 438)A06

EERC 72-9 "Rate of Loading Effects on Uncracked and Repaired Reinforced Concrete Members," by S. Mahin, V.V. Bertero, D. Rea and M. Atalay - 1972 (PB 224 520)A08

EERC 72-10 "Computer Program for Static and Dynamic Analysis of Linear Structural Systems," by E.L. Wilson, K.-J. Bathe, J.E. Peterson and H.H.Dovey - 1972 (PB 220 437)A04

EERC 72-11 "Literature Survey - Seismic Effects on Highway Bridges," by T. Iwasaki, J. Penzien and R.W. Clough - 1972 (PB 215 613)A19

EERC 72-12 "SHAKE-A Computer Program for Earthquake Response Analysis of Horizontally Layered Sites," by P.B. Schnabel and J. Lysmer - 1972 (PB 220 207)A06

EERC 73-1 "Optimal Seismic Design of Multistory Frames," by V.V. Bertero and H. Kamil - 1973

EERC 73-2 "Analysis of the Slides in the San Fernando Dams During the Earthquake of February 9, 1971," by H.B. Seed, K.L. Lee, I.M. Idriss and F. Makdisi - 1973 (PB 223 402)A14

EERC 73-3 "Computer Aided Ultimate Load Design of Unbraced Multistory Steel Frames," by M.B. El-Hafez and G.H. Powell 1973 (PB 248 315)A09

EERC 73-4 "Experimental Investigation into the Seismic Behavior of Critical Regions of Reinforced Concrete Components as Influenced by Moment and Shear," by M. Celebi and J. Penzien - 1973 (PB 215 884)A09

EERC 73-5 "Hysteretic Behavior of Epoxy-Repaired Reinforced Concrete Beams," by M. Celebi and J. Penzien - 1973 (PB 239 568)A03

EERC 73-6 "General Purpose Computer Program for Inelastic Dynamic Response of Plane Structures," by A. Kanaan and G.H. Powell - 1973 (PB 221 260)A08

EERC 73-7 "A Computer Program for Earthquake Analysis of Gravity Dams Including Reservoir Interaction," by P. Chakrabarti and A.K. Chopra - 1973 (AD 766 271)A04

EERC 73-8 "Behavior of Reinforced Concrete Deep Beam-Column Subassemblages Under Cyclic Loads," by O. Küstü and J.G. Bouwkamp - 1973 (PB 246 117)A12

EERC 73-9 "Earthquake Analysis of Structure-Foundation Systems," by A.K. Vaish and A.K. Chopra - 1973 (AD 766 272)A07

EERC 73-10 "Deconvolution of Seismic Response for Linear Systems," by R.B. Reimer - 1973 (PB 227 179)A08

EERC 73-11 "SAP IV: A Structural Analysis Program for Static and Dynamic Response of Linear Systems," by K.-J. Bathe, E.L. Wilson and F.E. Peterson - 1973 (PB 221 967)A09

EERC 73-12 "Analytical Investigations of the Seismic Response of Long, Multiple Span Highway Bridges," by W.S. Tseng and J. Penzien - 1973 (PB 227 816)A10

EERC 73-13 "Earthquake Analysis of Multi-Story Buildings Including Foundation Interaction," by A.K. Chopra and J.A. Gutierrez - 1973 (PB 222 970)A03

EERC 73-14 "ADAP: A Computer Program for Static and Dynamic Analysis of Arch Dams," by R.W. Clough, J.M. Raphael and S. Mojtahedi - 1973 (PB 223 763)A09

EERC 73-15 "Cyclic Plastic Analysis of Structural Steel Joints," by R.B. Pinkney and R.W. Clough - 1973 (PB 226 843)A08

EERC 73-16 "QUAD-4: A Computer Program for Evaluating the Seismic Response of Soil Structures by Variable Damping Finite Element Procedures," by I.M. Idriss, J. Lysmer, R. Hwang and H.B. Seed - 1973 (PB 229 424)A05

EERC 73-17 "Dynamic Behavior of a Multi-Story Pyramid Shaped Building," by R.M. Stephen, J.P. Hollings and J.G. Bouwkamp - 1973 (PB 240 718)A06

EERC 73-18 "Effect of Different Types of Reinforcing on Seismic Behavior of Short Concrete Columns," by V.V. Bertero, J. Hollings, O. Küstü, R.M. Stephen and J.G. Bouwkamp - 1973

EERC 73-19 "Olive View Medical Center Materials Studies, Phase I," by B. Bresler and V.V. Bertero - 1973 (PB 235 986)A06

EERC 73-20 "Linear and Nonlinear Seismic Analysis Computer Programs for Long Multiple-Span Highway Bridges," by W.S. Tseng and J. Penzien - 1973

EERC 73-21 "Constitutive Models for Cyclic Plastic Deformation of Engineering Materials," by J.M. Kelly and P.P. Gillis 1973 (PB 226 024)A03

EERC 73-22 "DRAIN - 2D User's Guide," by G.H. Powell - 1973 (PB 227 016)A05

EERC 73-23 "Earthquake Engineering at Berkeley - 1973," (PB 226 033)A11

EERC 73-24 Unassigned

EERC 73-25 "Earthquake Response of Axisymmetric Tower Structures Surrounded by Water," by C.Y. Liaw and A.K. Chopra 1973 (AD 773 052)A09

EERC 73-26 "Investigation of the Failures of the Olive View Stairtowers During the San Fernando Earthquake and Their Implications on Seismic Design," by V.V. Bertero and R.G. Collins - 1973 (PB 235 106)A13

EERC 73-27 "Further Studies on Seismic Behavior of Steel Beam-Column Subassemblages," by V.V. Bertero, H. Krawinkler and E.P. Popov - 1973 (PB 234 172)A06

EERC 74-1 "Seismic Risk Analysis," by C.S. Oliveira - 1974 (PB 235 920)A06

EERC 74-2 "Settlement and Liquefaction of Sands Under Multi-Directional Shaking," by R. Pyke, C.K. Chan and H.B. Seed 1974

EERC 74-3 "Optimum Design of Earthquake Resistant Shear Buildings," by D. Ray, K.S. Pister and A.K. Chopra - 1974 (PB 231 172)A06

EERC 74-4 "LUSH - A Computer Program for Complex Response Analysis of Soil-Structure Systems," by J. Lysmer, T. Udaka, H.B. Seed and R. Hwang - 1974 (PB 236 796)A05

EERC 74-5 "Sensitivity Analysis for Hysteretic Dynamic Systems: Applications to Earthquake Engineering," by D. Ray 1974 (PB 233 213)A06

EERC 74-6 "Soil Structure Interaction Analyses for Evaluating Seismic Response," by H.B. Seed, J. Lysmer and R. Hwang 1974 (PB 236 519)A04

EERC 74-7 Unassigned

EERC 74-8 "Shaking Table Tests of a Steel Frame - A Progress Report," by R.W. Clough and D. Tang - 1974 (PB 240 869)A03

EERC 74-9 "Hysteretic Behavior of Reinforced Concrete Flexural Members with Special Web Reinforcement," by V.V. Bertero, E.P. Popov and T.Y. Wang - 1974 (PB 236 797)A07

EERC 74-10 "Applications of Reliability-Based, Global Cost Optimization to Design of Earthquake Resistant Structures," by E. Vitiello and K.S. Pister - 1974 (PB 237 231)A06

EERC 74-11 "Liquefaction of Gravelly Soils Under Cyclic Loading Conditions," by R.T. Wong, H.B. Seed and C.K. Chan 1974 (PB 242 042)A03

EERC 74-12 "Site-Dependent Spectra for Earthquake-Resistant Design," by H.B. Seed, C. Ugas and J. Lysmer - 1974 (PB 240 953)A03

EERC 74-13 "Earthquake Simulator Study of a Reinforced Concrete Frame," by P. Hidalgo and R.W. Clough - 1974 (PB 241 944)A13

EERC 74-14 "Nonlinear Earthquake Response of Concrete Gravity Dams," by N. Pal - 1974 (AD/A 006 583)A06

EERC 74-15 "Modeling and Identification in Nonlinear Structural Dynamics - I. One Degree of Freedom Models," by N. Distefano and A. Rath - 1974 (PB 241 548)A06

EERC 75-1 "Determination of Seismic Design Criteria for the Dumbarton Bridge Replacement Structure, Vol. I: Description, Theory and Analytical Modeling of Bridge and Parameters," by F. Baron and S.-H. Pang - 1975 (PB 259 407)A15

EERC 75-2 "Determination of Seismic Design Criteria for the Dumbarton Bridge Replacement Structure, Vol. II: Numerical Studies and Establishment of Seismic Design Criteria," by F. Baron and S.-H. Pang - 1975 (PB 259 408)A11 (For set of EERC 75-1 and 75-2 (PB 259 406))

EERC 75-3 "Seismic Risk Analysis for a Site and a Metropolitan Area," by C.S. Oliveira - 1975 (PB 248 134)A09

EERC 75-4 "Analytical Investigations of Seismic Response of Short, Single or Multiple-Span Highway Bridges," by M.-C. Chen and J. Penzien - 1975 (PB 241 454)A09

EERC 75-5 "An Evaluation of Some Methods for Predicting Seismic Behavior of Reinforced Concrete Buildings," by S.A. Mahin and V.V. Bertero - 1975 (PB 246 306)A16

EERC 75-6 "Earthquake Simulator Study of a Steel Frame Structure, Vol. I: Experimental Results," by R.W. Clough and D.T. Tang - 1975 (PB 243 981)A13

EERC 75-7 "Dynamic Properties of San Bernardino Intake Tower," by D. Rea, C.-Y. Liaw and A.K. Chopra - 1975 (AD/A008 406) A05

EERC 75-8 "Seismic Studies of the Articulation for the Dumbarton Bridge Replacement Structure, Vol. I: Description, Theory and Analytical Modeling of Bridge Components," by F. Baron and R.E. Hamati - 1975 (PB 251 539)A07

EERC 75-9 "Seismic Studies of the Articulation for the Dumbarton Bridge Replacement Structure, Vol. 2: Numerical Studies of Steel and Concrete Girder Alternates," by F. Baron and R.E. Hamati - 1975 (PB 251 540)A10

EERC 75-10 "Static and Dynamic Analysis of Nonlinear Structures," by D.P. Mondkar and G.H. Powell - 1975 (PB 242 434)A08

EERC 75-11 "Hysteretic Behavior of Steel Columns," by E.P. Popov, V.V. Bertero and S. Chandramouli - 1975 (PB 252 365)A11

EERC 75-12 "Earthquake Engineering Research Center Library Printed Catalog," - 1975 (PB 243 711)A26

EERC 75-13 "Three Dimensional Analysis of Building Systems (Extended Version)," by E.L. Wilson, J.P. Hollings and H.H. Dovey - 1975 (PB 243 989)A07

EERC 75-14 "Determination of Soil Liquefaction Characteristics by Large-Scale Laboratory Tests," by P. De Alba, C.K. Chan and H.B. Seed - 1975 (NUREG 0027)A08

EERC 75-15 "A Literature Survey - Compressive, Tensile, Bond and Shear Strength of Masonry," by R.L. Mayes and R.W. Clough - 1975 (PB 246 292)A10

EERC 75-16 "Hysteretic Behavior of Ductile Moment Resisting Reinforced Concrete Frame Components," by V.V. Bertero and E.P. Popov - 1975 (PB 246 388)A05

EERC 75-17 "Relationships Between Maximum Acceleration, Maximum Velocity, Distance from Source, Local Site Conditions for Moderately Strong Earthquakes," by H.B. Seed, R. Murarka, J. Lysmer and I.M. Idriss - 1975 (PB 248 172)A03

EERC 75-18 "The Effects of Method of Sample Preparation on the Cyclic Stress-Strain Behavior of Sands," by J. Mulilis, C.K. Chan and H.B. Seed - 1975 (Summarized in EERC 75-28)

EERC 75-19 "The Seismic Behavior of Critical Regions of Reinforced Concrete Components as Influenced by Moment, Shear and Axial Force," by M.B. Atalay and J. Penzien - 1975 (PB 258 842)A11

EERC 75-20 "Dynamic Properties of an Eleven Story Masonry Building," by R.M. Stephen, J.P. Hollings, J.G. Bouwkamp and D. Jurukovski - 1975 (PB 246 945)A04

EERC 75-21 "State-of-the-Art in Seismic Strength of Masonry - An Evaluation and Review," by R.L. Mayes and R.W. Clough 1975 (PB 249 040)A07

EERC 75-22 "Frequency Dependent Stiffness Matrices for Viscoelastic Half-Plane Foundations," by A.K. Chopra, P. Chakrabarti and G. Dasgupta - 1975 (PB 248 121)A07

EERC 75-23 "Hysteretic Behavior of Reinforced Concrete Framed Walls," by T.Y. Wong, V.V. Bertero and E.P. Popov - 1975

EERC 75-24 "Testing Facility for Subassemblages of Frame-Wall Structural Systems," by V.V. Bertero, E.P. Popov and T. Endo - 1975

EERC 75-25 "Influence of Seismic History on the Liquefaction Characteristics of Sands," by H.B. Seed, K. Mori and C.K. Chan - 1975 (Summarized in EERC 75-28)

EERC 75-26 "The Generation and Dissipation of Pore Water Pressures during Soil Liquefaction," by H.B. Seed, P.P. Martin and J. Lysmer - 1975 (PB 252 648)A03

EERC 75-27 "Identification of Research Needs for Improving Aseismic Design of Building Structures," by V.V. Bertero 1975 (PB 248 136)A05

EERC 75-28 "Evaluation of Soil Liquefaction Potential during Earthquakes," by H.B. Seed, I. Arango and C.K. Chan - 1975 (NUREG 0026)A13

EERC 75-29 "Representation of Irregular Stress Time Histories by Equivalent Uniform Stress Series in Liquefaction Analyses," by H.B. Seed, I.M. Idriss, F. Makdisi and N. Banerjee - 1975 (PB 252 635)A03

EERC 75-30 "FLUSH - A Computer Program for Approximate 3-D Analysis of Soil-Structure Interaction Problems," by J. Lysmer, T. Udaka, C.-F. Tsai and H.B. Seed - 1975 (PB 259 332)A07

EERC 75-31 "ALUSH - A Computer Program for Seismic Response Analysis of Axisymmetric Soil-Structure Systems," by E. Berger, J. Lysmer and H.B. Seed - 1975

EERC 75-32 "TRIP and TRAVEL - Computer Programs for Soil-Structure Interaction Analysis with Horizontally Travelling Waves," by T. Udaka, J. Lysmer and H.B. Seed - 1975

EERC 75-33 "Predicting the Performance of Structures in Regions of High Seismicity," by J. Penzien - 1975 (PB 248 130)A03

EERC 75-34 "Efficient Finite Element Analysis of Seismic Structure - Soil - Direction," by J. Lysmer, H.B. Seed, T. Udaka, R.N. Hwang and C.-F. Tsai - 1975 (PB 253 570)A03

EERC 75-35 "The Dynamic Behavior of a First Story Girder of a Three-Story Steel Frame Subjected to Earthquake Loading," by R.W. Clough and L.-Y. Li - 1975 (PB 248 841)A05

EERC 75-36 "Earthquake Simulator Study of a Steel Frame Structure, Volume II - Analytical Results," by D.T. Tang - 1975 (PB 252 926)A10

EERC 75-37 "ANSR-I General Purpose Computer Program for Analysis of Non-Linear Structural Response," by D.P. Mondkar and G.H. Powell - 1975 (PB 252 386)A08

EERC 75-38 "Nonlinear Response Spectra for Probabilistic Seismic Design and Damage Assessment of Reinforced Concrete Structures," by M. Murakami and J. Penzien - 1975 (PB 259 530)A05

EERC 75-39 "Study of a Method of Feasible Directions for Optimal Elastic Design of Frame Structures Subjected to Earthquake Loading," by N.D. Walker and K.S. Pister - 1975 (PB 257 781)A06

EERC 75-40 "An Alternative Representation of the Elastic-Viscoelastic Analogy," by G. Dasgupta and J.L. Sackman - 1975 (PB 252 173)A03

EERC 75-41 "Effect of Multi-Directional Shaking on Liquefaction of Sands," by H.B. Seed, R. Pyke and G.R. Martin - 1975 (PB 258 781)A03

EERC 76-1 "Strength and Ductility Evaluation of Existing Low-Rise Reinforced Concrete Buildings - Screening Method," by T. Okada and B. Bresler - 1976 (PB 257 906)A11

EERC 76-2 "Experimental and Analytical Studies on the Hysteretic Behavior of Reinforced Concrete Rectangular and T-Beams," by S.-Y.M. Ma, E.P. Popov and V.V. Bertero - 1976 (PB 260 843)A12

EERC 76-3 "Dynamic Behavior of a Multistory Triangular-Shaped Building," by J. Petrovski, R.M. Stephen, E. Gartenbaum and J.G. Bouwkamp - 1976 (PB 273 279)A07

EERC 76-4 "Earthquake Induced Deformations of Earth Dams," by N. Serff, H.B. Seed, F.I. Makdisi & C.-Y. Chang - 1976 (PB 292 065)A08

EERC 76-5 "Analysis and Design of Tube-Type Tall Building Structures," by H. de Clercq and G.H. Powell - 1976 (PB 252 220) A10

EERC 76-6 "Time and Frequency Domain Analysis of Three-Dimensional Ground Motions, San Fernando Earthquake," by T. Kubo and J. Penzien (PB 260 556)A11

EERC 76-7 "Expected Performance of Uniform Building Code Design Masonry Structures," by R.L. Mayes, Y. Omote, S.W. Chen and R.W. Clough - 1976 (PB 270 098)A05

EERC 76-8 "Cyclic Shear Tests of Masonry Piers, Volume 1 - Test Results," by R.L. Mayes, Y. Omote, R.W. Clough - 1976 (PB 264 424)A06

EERC 76-9 "A Substructure Method for Earthquake Analysis of Structure - Soil Interaction," by J.A. Gutierrez and A.K. Chopra - 1976 (PB 257 783)A08

EERC 76-10 "Stabilization of Potentially Liquefiable Sand Deposits using Gravel Drain Systems," by H.B. Seed and J.R. Booker - 1976 (PB 258 820)A04

EERC 76-11 "Influence of Design and Analysis Assumptions on Computed Inelastic Response of Moderately Tall Frames," by G.H. Powell and D.G. Row - 1976 (PB 271 409)A06

EERC 76-12 "Sensitivity Analysis for Hysteretic Dynamic Systems: Theory and Applications," by D. Ray, K.S. Pister and E. Polak - 1976 (PB 262 859)A04

EERC 76-13 "Coupled Lateral Torsional Response of Buildings to Ground Shaking," by C.L. Kan and A.K. Chopra - 1976 (PB 257 907)A09

EERC 76-14 "Seismic Analyses of the Banco de America," by V.V. Bertero, S.A. Mahin and J.A. Hollings - 1976

EERC 76-15 "Reinforced Concrete Frame 2: Seismic Testing and Analytical Correlation," by R.W. Clough and J. Gidwani - 1976 (PB 261 323)A08

EERC 76-16 "Cyclic Shear Tests of Masonry Piers, Volume 2 - Analysis of Test Results," by R.L. Mayes, Y. Omote and R.W. Clough - 1976

EERC 76-17 "Structural Steel Bracing Systems: Behavior Under Cyclic Loading," by E.P. Popov, K. Takanashi and C.W. Roeder - 1976 (PB 260 715)A05

EERC 76-18 "Experimental Model Studies on Seismic Response of High Curved Overcrossings," by D. Williams and W.G. Godden - 1976 (PB 269 548)A08

EERC 76-19 "Effects of Non-Uniform Seismic Disturbances on the Dumbarton Bridge Replacement Structure," by F. Baron and R.E. Hamati - 1976 (PB 282 981)A16

EERC 76-20 "Investigation of the Inelastic Characteristics of a Single Story Steel Structure Using System Identification and Shaking Table Experiments," by V.C. Matzen and H.D. McNiven - 1976 (PB 258 453)A07

EERC 76-21 "Capacity of Columns with Splice Imperfections," by E.P. Popov, R.M. Stephen and R. Philbrick - 1976 (PB 260 378)A04

EERC 76-22 "Response of the Olive View Hospital Main Building during the San Fernando Earthquake," by S. A. Mahin, V.V. Bertero, A.K. Chopra and R. Collins - 1976 (PB 271 425)A14

EERC 76-23 "A Study on the Major Factors Influencing the Strength of Masonry Prisms," by N.M. Mostaghel, R.L. Mayes, R. W. Clough and S.W. Chen - 1976 (Not published)

EERC 76-24 "GADFLEA - A Computer Program for the Analysis of Pore Pressure Generation and Dissipation during Cyclic or Earthquake Loading," by J.R. Booker, M.S. Rahman and H.B. Seed - 1976 (PB 263 947)A04

EERC 76-25 "Seismic Safety Evaluation of a R/C School Building," by B. Bresler and J. Axley - 1976

EERC 76-26 "Correlative Investigations on Theoretical and Experimental Dynamic Behavior of a Model Bridge Structure," by K. Kawashima and J. Penzien - 1976 (PB 263 388)A11

EERC 76-27 "Earthquake Response of Coupled Shear Wall Buildings," by T. Srichatrapimuk - 1976 (PB 265 157)A07

EERC 76-28 "Tensile Capacity of Partial Penetration Welds," by E.P. Popov and R.M. Stephen - 1976 (PB 262 899)A03

EERC 76-29 "Analysis and Design of Numerical Integration Methods in Structural Dynamics," by H.M. Hilber - 1976 (PB 264 410)A06

EERC 76-30 "Contribution of a Floor System to the Dynamic Characteristics of Reinforced Concrete Buildings," by L.E. Malik and V.V. Bertero - 1976 (PB 272 247)A13

EERC 76-31 "The Effects of Seismic Disturbances on the Golden Gate Bridge," by F. Baron, M. Arikan and R.E. Hamati - 1976 (PB 272 279)A09

EERC 76-32 "Infilled Frames in Earthquake Resistant Construction," by R.E. Klingner and V.V. Bertero - 1976 (PB 265 892)A13

UCB/EERC-77/01 "PLUSH - A Computer Program for Probabilistic Finite Element Analysis of Seismic Soil-Structure Interaction," by M.P. Romo Organista, J. Lysmer and H.B. Seed - 1977

UCB/EERC-77/02 "Soil-Structure Interaction Effects at the Humboldt Bay Power Plant in the Ferndale Earthquake of June 7, 1975," by J.E. Valera, H.B. Seed, C.F. Tsai and J. Lysmer - 1977 (PB 265 795)A04

UCB/EERC-77/03 "Influence of Sample Disturbance on Sand Response to Cyclic Loading," by K. Mori, H.B. Seed and C.K. Chan - 1977 (PB 267 352)A04

UCB/EERC-77/04 "Seismological Studies of Strong Motion Records," by J. Shoja-Taheri - 1977 (PB 269 655)A10

UCB/EERC-77/05 "Testing Facility for Coupled-Shear Walls," by L. Li-Hyung, V.V. Bertero and E.P. Popov - 1977

UCB/EERC-77/06 "Developing Methodologies for Evaluating the Earthquake Safety of Existing Buildings," by No. 1 - B. Bresler; No. 2 - B. Bresler, T. Okada and D. Zisling; No. 3 - T. Okada and B. Bresler; No. 4 - V.V. Bertero and B. Bresler - 1977 (PB 267 354)A08

UCB/EERC-77/07 "A Literature Survey - Transverse Strength of Masonry Walls," by Y. Omote, R.L. Mayes, S.W. Chen and R.W. Clough - 1977 (PB 277 933)A07

UCB/EERC-77/08 "DRAIN-TABS: A Computer Program for Inelastic Earthquake Response of Three Dimensional Buildings," by R. Guendelman-Israel and G.H. Powell - 1977 (PB 270 693)A07

UCB/EERC-77/09 "SUBWALL: A Special Purpose Finite Element Computer Program for Practical Elastic Analysis and Design of Structural Walls with Substructure Option," by D.Q. Le, H. Peterson and E.P. Popov - 1977 (PB 270 567)A05

UCB/EERC-77/10 "Experimental Evaluation of Seismic Design Methods for Broad Cylindrical Tanks," by D.P. Clough (PB 272 280)A13

UCB/EERC-77/11 "Earthquake Engineering Research at Berkeley - 1976," - 1977 (PB 273 507)A09

UCB/EERC-77/12 "Automated Design of Earthquake Resistant Multistory Steel Building Frames," by N.D. Walker, Jr. - 1977 (PB 276 526)A09

UCB/EERC-77/13 "Concrete Confined by Rectangular Hoops Subjected to Axial Loads," by J. Vallenas, V.V. Bertero and E.P. Popov - 1977 (PB 275 165)A06

UCB/EERC-77/14 "Seismic Strain Induced in the Ground During Earthquakes," by Y. Sugimura - 1977 (PB 284 201)A04

UCB/EERC-77/15 "Bond Deterioration under Generalized Loading," by V.V. Bertero, E.P. Popov and S. Viwathanatepa - 1977

UCB/EERC-77/16 "Computer Aided Optimum Design of Ductile Reinforced Concrete Moment Resisting Frames," by S.W. Zagajeski and V.V. Bertero - 1977 (PB 280 137)A07

UCB/EERC-77/17 "Earthquake Simulation Testing of a Stepping Frame with Energy-Absorbing Devices," by J.M. Kelly and D.F. Tsztoo - 1977 (PB 273 506)A04

UCB/EERC-77/18 "Inelastic Behavior of Eccentrically Braced Steel Frames under Cyclic Loadings," by C.W. Roeder and E.P. Popov - 1977 (PB 275 526)A15

UCB/EERC-77/19 "A Simplified Procedure for Estimating Earthquake-Induced Deformations in Dams and Embankments," by F.I. Makdisi and H.B. Seed - 1977 (PB 276 820)A04

UCB/EERC-77/20 "The Performance of Earth Dams during Earthquakes," by H.B. Seed, F.I. Makdisi and P. de Alba - 1977 (PB 276 821)A04

UCB/EERC-77/21 "Dynamic Plastic Analysis Using Stress Resultant Finite Element Formulation," by P. Lukkunapvasit and J.M. Kelly - 1977 (PB 275 453)A04

UCB/EERC-77/22 "Preliminary Experimental Study of Seismic Uplift of a Steel Frame," by R.W. Clough and A.A. Huckelbridge 1977 (PB 278 769)A08

UCB/EERC-77/23 "Earthquake Simulator Tests of a Nine-Story Steel Frame with Columns Allowed to Uplift," by A.A. Huckelbridge - 1977 (PB 277 944)A09

UCB/EERC-77/24 "Nonlinear Soil-Structure Interaction of Skew Highway Bridges," by M.-C. Chen and J. Penzien - 1977 (PB 276 176)A07

UCB/EERC-77/25 "Seismic Analysis of an Offshore Structure Supported on Pile Foundations," by D.D.-N. Liou and J. Penzien 1977 (PB 283 180)A06

UCB/EERC-77/26 "Dynamic Stiffness Matrices for Homogeneous Viscoelastic Half-Planes," by G. Dasgupta and A.K. Chopra - 1977 (PB 279 654)A06

UCB/EERC-77/27 "A Practical Soft Story Earthquake Isolation System," by J.M. Kelly, J.M. Eidinger and C.J. Derham - 1977 (PB 276 814)A07

UCB/EERC-77/28 "Seismic Safety of Existing Buildings and Incentives for Hazard Mitigation in San Francisco: An Exploratory Study," by A.J. Meltsner - 1977 (PB 281 970)A05

UCB/EERC-77/29 "Dynamic Analysis of Electrohydraulic Shaking Tables," by D. Rea, S. Abedi-Hayati and Y. Takahashi 1977 (PB 282 569)A04

UCB/EERC-77/30 "An Approach for Improving Seismic - Resistant Behavior of Reinforced Concrete Interior Joints," by B. Galunic, V.V. Bertero and E.P. Popov - 1977 (PB 290 870)A06

UCB/EERC-78/01 "The Development of Energy-Absorbing Devices for Aseismic Base Isolation Systems," by J.M. Kelly and D.F. Tsztoo - 1978 (PB 284 978)A04

UCB/EERC-78/02 "Effect of Tensile Prestrain on the Cyclic Response of Structural Steel Connections, by J.G. Bouwkamp and A. Mukhopadhyay - 1978

UCB/EERC-78/03 "Experimental Results of an Earthquake Isolation System using Natural Rubber Bearings," by J.M. Eidinger and J.M. Kelly - 1978 (PB 281 686)A04

UCB/EERC-78/04 "Seismic Behavior of Tall Liquid Storage Tanks," by A. Niwa - 1978 (PB 284 017)A14

UCB/EERC-78/05 "Hysteretic Behavior of Reinforced Concrete Columns Subjected to High Axial and Cyclic Shear Forces," by S.W. Zagajeski, V.V. Bertero and J.G. Bouwkamp - 1978 (PB 283 858)A13

UCB/EERC-78/06 "Inelastic Beam-Column Elements for the ANSR-I Program," by A. Riahi, D.G. Row and G.H. Powell - 1978

UCB/EERC-78/07 "Studies of Structural Response to Earthquake Ground Motion," by O.A. Lopez and A.K. Chopra - 1978 (PB 282 790)A05

UCB/EERC-78/08 "A Laboratory Study of the Fluid-Structure Interaction of Submerged Tanks and Caissons in Earthquakes," by R.C. Byrd - 1978 (PB 284 957)A08

UCB/EERC-78/09 "Model for Evaluating Damageability of Structures," by I. Sakamoto and B. Bresler - 1978

UCB/EERC-78/10 "Seismic Performance of Nonstructural and Secondary Structural Elements," by I. Sakamoto - 1978

UCB/EERC-78/11 "Mathematical Modelling of Hysteresis Loops for Reinforced Concrete Columns," by S. Nakata, T. Sproul and J. Penzien - 1978

UCB/EERC-78/12 "Damageability in Existing Buildings," by T. Blejwas and B. Bresler - 1978

UCB/EERC-78/13 "Dynamic Behavior of a Pedestal Base Multistory Building," by R.M. Stephen, E.L. Wilson, J.G. Bouwkamp and M. Button - 1978 (PB 286 650)A08

UCB/EERC-78/14 "Seismic Response of Bridges - Case Studies," by R.A. Imbsen, V. Nutt and J. Penzien - 1978 (PB 286 503)A10

UCB/EERC-78/15 "A Substructure Technique for Nonlinear Static and Dynamic Analysis," by D.G. Row and G.H. Powell - 1978 (PB 288 077)A10

UCB/EERC-78/16 "Seismic Risk Studies for San Francisco and for the Greater San Francisco Bay Area," by C.S. Oliveira - 1978

UCB/EERC-78/17 "Strength of Timber Roof Connections Subjected to Cyclic Loads," by P. Gülkan, R.L. Mayes and R.W. Clough - 1978

UCB/EERC-78/18 "Response of K-Braced Steel Frame Models to Lateral Loads," by J.G. Bouwkamp, R.M. Stephen and E.P. Popov - 1978

UCB/EERC-78/19 "Rational Design Methods for Light Equipment in Structures Subjected to Ground Motion," by J.L. Sackman and J.M. Kelly - 1978 (PB 292 357)A04

UCB/EERC-78/20 "Testing of a Wind Restraint for Aseismic Base Isolation," by J.M. Kelly and D.E. Chitty - 1978 (PB 292 833)A03

UCB/EERC-78/21 "APOLLO - A Computer Program for the Analysis of Pore Pressure Generation and Dissipation in Horizontal Sand Layers During Cyclic or Earthquake Loading," by P.P. Martin and H.B. Seed - 1978 (PB 292 835)A04

UCB/EERC-78/22 "Optimal Design of an Earthquake Isolation System," by M.A. Bhatti, K.S. Pister and E. Polak - 1978 (PB 294 735)A06

UCB/EERC-78/23 "MASH - A Computer Program for the Non-Linear Analysis of Vertically Propagating Shear Waves in Horizontally Layered Deposits," by P.P. Martin and H.B. Seed - 1978 (PB 293 101)A05

UCB/EERC-78/24 "Investigation of the Elastic Characteristics of a Three Story Steel Frame Using System Identification," by I. Kaya and H.D. McNiven - 1978

UCB/EERC-78/25 "Investigation of the Nonlinear Characteristics of a Three-Story Steel Frame Using System Identification," by I. Kaya and H.D. McNiven - 1978

UCB/EERC-78/26 "Studies of Strong Ground Motion in Taiwan," by Y.M. Hsiung, B.A. Bolt and J. Penzien - 1978

UCB/EERC-78/27 "Cyclic Loading Tests of Masonry Single Piers: Volume 1 - Height to Width Ratio of 2," by P.A. Hidalgo, R.L. Mayes, H.D. McNiven and R.W. Clough - 1978

UCB/EERC-78/28 "Cyclic Loading Tests of Masonry Single Piers: Volume 2 - Height to Width Ratio of 1," by S.-W.J. Chen, P.A. Hidalgo, R.L. Mayes, R.W. Clough and H.D. McNiven - 1978

UCB/EERC-78/29 "Analytical Procedures in Soil Dynamics," by J. Lysmer - 1978

UCB/EERC-79/01 "Hysteretic Behavior of Lightweight Reinforced Concrete Beam-Column Subassemblages," by B. Forzani, E.P. Popov, and V.V. Bertero - 1979

UCB/EERC-79/02 "The Development of a Mathematical Model to Predict the Flexural Response of Reinforced Concrete Beams to Cyclic Loads, Using System Identification," by J.F. Stanton and H.D. McNiven - 1979

UCB/EERC-79/03 "Linear and Nonlinear Earthquake Response of Simple Torsionally Coupled Systems," by C.L. Kan and A.K. Chopra - 1979

UCB/EERC-79/04 "A Mathematical Model of Masonry for Predicting Its Linear Seismic Response Characteristics," by Y. Mengi and H.D. McNiven - 1979

UCB/EERC-79/05 "Mechanical Behavior of Lightweight Concrete Confined by Different Types of Lateral Reinforcement," by M.A. Manrique, V.V. Bertero and E.P. Popov - 1979

UCB/EERC-79/06 "Static Tilt Tests of a Tall Cylindrical Liquid Storage Tank," by R.W. Clough and A. Niwa - 1979

UCB/EERC-79/07 "The Design of Steel Energy Absorbing Restrainers and Their Incorporation Into Nuclear Power Plants for Enhanced Safety: Volume 1 - Summary Report," by P.N. Spencer, V.F. Zackay, and E.R. Parker - 1979

UCB/EERC-79/08 "The Design of Steel Energy Absorbing Restrainers and Their Incorporation Into Nuclear Power Plants for Enhanced Safety: Volume 2 - The Development of Analyses for Reactor System Piping," "Simple Systems" by M.C. Lee, J. Penzien, A.K. Chopra, and K. Suzuki "Complex Systems" by G.H. Powell, E.L. Wilson,R.W. Clough and D.G. Row - 1979

UCB/EERC-79/09 "The Design of Steel Energy Absorbing Restrainers and Their Incorporation Into Nuclear Power Plants for Enhanced Safety: Volume 3 - Evaluation of Commerical Steels," by W.S. Owen, R.M.N. Pelloux, R.O. Ritchie, M. Faral, T. Ohhashi, J. Toplosky, S.J. Hartman, V.F. Zackay, and E.R. Parker - 1979

UCB/EERC-79/10 "The Design of Steel Energy Absorbing Restrainers and Their Incorporation Into Nuclear Power Plants for Enhanced Safety: Volume 4 - A Review of Energy-Absorbing Devices," by J.M. Kelly and M.S. Skinner - 1979

UCB/EERC-79/11 "Conservatism In Summation Rules for Closely Spaced Modes," by J.M. Kelly and J.L. Sackman - 1979

UCB/EERC-79/12 "Cyclic Loading Tests of Masonry Single Piers Volume 3 - Height to Width Ratio of 0.5," by P.A. Hidalgo, R.L. Mayes, H.D. McNiven and R.W. Clough - 1979

UCB/EERC-79/13 "Cyclic Behavior of Dense Coarse-Grained Materials in Relation to the Seismic Stability of Dams," by N.G. Banerjee, H.B. Seed and C.K. Chan - 1979

UCB/EERC-79/14 "Seismic Behavior of Reinforced Concrete Interior Beam-Column Subassemblages," by S. Viwathanatepa, E.P. Popov and V.V. Bertero - 1979

UCB/EERC-79/15 "Optimal Design of Localized Nonlinear Systems with Dual Performance Criteria Under Earthquake Excitations," by M.A. Bhatti - 1979

UCB/EERC-79/16 "OPTDYN - A General Purpose Optimization Program for Problems with or without Dynamic Constraints," by M.A. Bhatti, E. Polak and K.S. Pister - 1979

UCB/EERC-79/17 "ANSR-II, Analysis of Nonlinear Structural Response, Users Manual," by D.P. Mondkar and G.H. Powell - 1979

UCB/EERC-79/18 "Soil Structure Interaction in Different Seismic Environments," A. Gomez-Masso, J. Lysmer, J.-C. Chen and H.B. Seed - 1979

UCB/EERC-79/19 "ARMA Models for Earthquake Ground Motions," by M.K. Chang, J.W. Kwiatkowski, R.F. Nau, R.M. Oliver and K.S. Pister - 1979

UCB/EERC-79/20 "Hysteretic Behavior of Reinforced Concrete Structural Walls," by J.M. Vallenas, V.V. Bertero and E.P. Popov - 1979

UCB/EERC-79/21 "Studies on High-Frequency Vibrations of Buildings I: The Column Effects," by J. Lubliner - 1979

UCB/EERC-79/22 "Effects of Generalized Loadings on Bond Reinforcing Bars Embedded in Confined Concrete Blocks," by S. Viwathanatepa, E.P. Popov and V.V. Bertero - 1979